Exploiting the Potential of Carbon Nanotubes and Fullerenes Through Their Interaction with Specially Designed π-Conjugated Iptycenes

by

Serxho Selmani

A thesis

presented to the University of Waterloo

in fulfillment of the

thesis requirement for the degree of

Doctor of Philosophy

In

Chemistry

Waterloo, Ontario, Canada, 2020

Examining Committee Membership

The following served on the Examining Committee for this thesis. The decision of the Examining Committee is by majority vote.

External Examiner: Dr. Alexander Adronov

Supervisor: Dr. Derek Schipper

Internal Member: Dr. Shirley Tang

Internal Member: Dr. Adrian Schwan

Internal-External Member: Dr. Michael Pope

Author’s Declaration

I hereby declare that I am the sole author of this thesis. This is a true copy of the thesis, including any required final revisions, as accepted by my examiners.

I understand that this thesis may be made electronically available to the public.

Abstract

Electronics have become integrated into every aspect of modern life, from work to leisure we rely on electronics for key tasks in our daily routine. Recent research efforts have seen a push towards flexible electronic devices, creating a plethora of new potential applications. Carbon nanomaterials have emerged as excellent candidates for implementation into flexible electronic devices from transistors to solar cells, but despite their high potential, their commercial relevance has been hampered by several key challenges that have yet been unresolved. Here, I exhibit that through the merging of techniques from organic chemistry and nanoscience, I have been able to overcome several of the practical challenges facing both carbon nanotubes and fullerenes. This has been accomplished through the interaction of these carbon nanomaterials with shape complementary iptycene molecules. The concave shape of iptycenes allows them to interact very strongly with the convex carbon nanotubes and fullerenes. This has led us to develop a new technique for the simultaneous alignment and sorting of carbon nanotubes based on diameter and length, as well as the large-scale purification of fullerenes via flash chromatography. Furthermore, in the search for new iptycene derivatives, a new ligand for the formation of metal-organic frameworks has been discovered and studied.

Acknowledgements

The path to this degree has been filled with difficult challenges, self-doubt, and dead ends, but also moments of incredible self-fulfillment, and I would have never been able to accomplish what I have without the support of all the people in my life.

First and foremost, I would like to thank Vanessa Bellemore for always being there for me, for listening to me, helping me, and making me feel like I could do anything. Your love has continuously given me the strength that I need to continue to push myself to accomplish everything that I am capable of. If it weren't for you, I don't know how I would have handled all the hard nights of failed experiments, the nights when I felt like the world was collapsing on me. You have been the light of my life and you bring me everlasting joy. I'm proud to call you my fiancée, and I cannot wait to call you my wife. Thank you for everything that you do for me.

Next, I would like to thank Domenika and Marash Selmani, my wonderful parents. You have both given up so much for me, you have sacrificed your way of life to give me all of the opportunities that I have been presented. You have raised me to be a hard worker, and you have taught me to never give up. You have made me the man I am today, and I cannot thank you enough for everything you have done.

Dr. Derek Schipper, you have been a great supervisor to me throughout the course of my degree. You took me on as a bright-eyed, young scientist and have help form me into a well-seasoned, if a bit cynical, researcher. You have placed a lot of faith in me,

have taught me more than I thought I would have ever learned, and you have been a good friend to boot. Thank you for all of your hard work and time that you put into me.

I've met so many incredible people during my time at the University of Waterloo, and I have had the pleasure of working with a truly unforgettable cast of students in the Schipper group. Geoff Sinclair, thank you for being such a great friend to me throughout this crazy journey, your rants, ideas, jokes, shopping obsession, board game craze, magician phase, fermentation phase, and everything else you do have made my time here a real wonder. You are one of the main reasons that I enjoyed coming into the lab every day, and you really helped foster such an amazing atmosphere at work that I almost never wanted it to end. Thanks for helping me out when I needed it, and always being down to chat, I can't wait to see you in a tuxedo. Rafael Mirabal, thank you for injecting some much-needed musical diversity into the group, I credit your musical prowess for introducing me to Pink Floyd and quite literally changing my life. You've been an amazing friend to me, and I can't thank you enough for just being you, hopefully you'll get over that one night at Beta. Also, you're a great DM. Luke Vanderzwet, you were my original support system in the Schipper group, and my veritable twin. You helped me process life and see situations from a completely new perspective, thanks for providing me with laughs and long chats over beers, I already miss our classical physics Wednesdays. Tianyu Yang, you were there from the beginning and you really set a great bar for the group. You worked so hard and you showed such dedication that it really made me push myself to be better, and for that I thank you. Mike Emmett, in your short time in the group you really opened my eyes up to how much knowledge there was still out there for me to gain. Your relaxed demeanour and classic trivia gameshows really brought so much

character to the group and it's never been quite the same since you left. Rob Claridge, you are to this day one of the nicest people I have ever met, you are selfless, and genuinely a really kind person. Your personality and your Heavy Metal Fridays were so helpful in creating a workplace that I wanted to be a part of, thank you. Sara Abuadas, you always brought such a liveliness to the lab, and you were always available to talk to about anything. Our chats really helped reduce some of the stress of grad life, thank you. Monika Snowdon, you have been an exceptionally hard worker from the day that you joined our lab, and your work ethic has served to constantly push me to better myself, thank you. Jianan Wang, my fellow Windsorite, after you had been in the lab for a month, I felt like you had been there forever. Having someone to talk about food with was great, and I thank you for your friendship. Sarah Mathers, Windsor gang number 3, your open and positive attitude really brightened up the lab in a time where it was starting to feel a little too dark, thank you. I'll miss talking to you about life and I'll miss the fact that I could always count on you to call out Geoff. Wayne Walter Wang, there was never a dull moment with you around, thank you for bringing some spice into the Schipper group daily life. Thank you to all of the undergraduate students that I have had the pleasure of working with, all of you have helped shape me into the person I am today and I will think back on our time together fondly: Andrew Kukor, Javan Buratynski, Chris Baigent, Yue Melody Shen, Junhao Gigi Hu, Gillian Hawes, George Petrovski, Bill Guo, Cui Ting Chloe Zhao, and Fabio Cuzzucoli.

Howard Siu, you have been a pleasure to work for as a TA. Thank you for entrusting me with extra responsibilities, and for always being willing to be a reference. I'll miss talking to you about your family, I hope that you all have a wonderful life together.

Thank you to all of my committee members who have agreed to come on this journey with me. Dr. Shirley Tang, you have helped me build a solid knowledge on carbon nanotubes, and have contributed to my research as a collaborator, thank you. Dr. Adrian Schwan, you were a real delight to have on my committee, I enjoyed every time I got to talk to you, sober and not so sober. You've always been an outlier in that you have been punctual in your responses and non-judgemental in your feedback, thank you. Dr. Bob Lemieux, thank you for allowing me to use your liquid crystals, books, and instrumentation as if I was one of your own, and for always talking the time to talk to me when we met on campus. Thank you to Dr. Mike Pope for taking your time to read this thesis and be a part of my final steps.

To the love of my life,

Vanessa Bellemore

Table of Contents

List of Figures

List of Tables

List of Schemes

List of Abbreviations

Abbreviation	Definition
5CB	4-cyano-4’-pentylbiphenyl
AD	Arc-discharge
AFM	Atomic force microscopy
ALD	Atomic layer deposition
bipy	2,2’-bipyridine
C_{60}	Buckminsterfullerene
CNTs	Carbon nanotubes
CPU	Central processing unit
CV	Cyclic voltammetry
CVD	Chemical vapour deposition
DBU	1,8-diazabicyclo[5.4.0]undec-7-ene
DCE	Dichloroethane
DCM	Dichloromethane
DDQ	2,3-Dichloro-5,6-dicyano-1,4-benzoquinone
dipytet	3,6-di-2-pyridyl-1,2,4,5-tetrazine
DNA	Deoxyribonucleic acid
DOS	Density of states
EBL	Electron beam lithography
EDXA	Energy dispersive X-ray analysis
E_F	Fermi level
EF	Endohedral fullerene
E_g	Band gap
EMF	Endohedral metallofullerene
eV	Electron volts
Fc	Ferrocene
FET	Field-effect transistor
HER	Hydrogen evolution reaction
HOMA	Harmonic oscillator model of aromaticity
HOMO	Highest occupied molecular orbital
HOR	Hydrogen oxidation reaction
HPLC	High-performance liquid chromatography
HRMS	High resolution mass spectrometry
IPA	Isopropyl alcohol

IR	Infrared
ITO	Indium tin oxide
LA	Laser ablation
LUMO	Lowest unoccupied molecular orbital
MA	Poly(methacrylic acid)
MIBK	Methyl-isobutyl-ketone
MOF	Metal-organic framework
MS	Mass spectrometer
m-SWNTs	Metallic single-walled carbon nanotubes
NICS	Nucleus-independent chemical shift
NMR	Nuclear magnetic resonance
ORR	Oxygen reduction reaction
PAH	Polycyclic (or polynuclear) aromatic hydrocarbon
PANI	Polyaniline
PCBM	Phenyl-C61-butyric acid methyl ester
PC_xBM	Phenyl-C_x-butyric acid methyl ester
Pd/C	Palladium on carbon
PM-IRRAS	Polarized modulation infrared reflection-adsorption spectroscopy
PMMA	Poly(methyl methacrylate)
POM	Polarized optical microscopy
ppm	Parts per million
PVC	Polyvinlychloride
PVD	Physical vapor deposition
pXRD	Powder X-ray diffraction
R&D	Research and development
RBM	Radial breathing mode
Redox	Reduction/oxidation
SDS	Sodium dodecylsulfate
SEM	Scanning electron microscopy
SHE	Standard hydrogen electrode
SSNMR	Solid state nuclear magnetic resonance
SWNTs	Single-walled carbon nanotubes
T-BAG	Tethering by aggregation and growth
TcEP	Thermocapillary-enabled purification
TEM	Transmission electron microscopy
TFA	Trifluoroacetic acid
THF	Tetrahydrofuran
TNT	Trinitrotoluene

TOF	Time-of-flight
V_{DS}	Source-drain potential
V_{GS}	Gate voltage
wt %	Percent by weight
XRD	X-ray diffraction

Chapter 1. π-Conjugated Materials and Their Use in Semiconductors

1.1 Modern Electronics

When you look around today it is easy to be overwhelmed by the sheer number of electronic devices, all capable of tasks that in the recent past seemed to be in the realm of science fiction. The advent of the desktop computer, laptop, and now smartphone have led to the integration of electronics into all facets of life from leisure to productivity. All of the incredible processes that modern electronics are capable of can be traced back to the transistor.

A transistor, at its simplest, is a binary switch which can take either an “on” or “off” state. In practice, they exist as a component of a circuit and are used to modulate the current by either preventing (off) or allowing (on) it to flow. Through the combination of multiple transistors more complex signals can be interpreted, and through the use of billions of transistors, like on modern central processing units (CPUs) (Figure 1),[1] remarkable feats can be accomplished. Transistors are made of semiconducting materials, which possess the inherent ability to switch between a conducting (on) and insulating (off) state.[2]

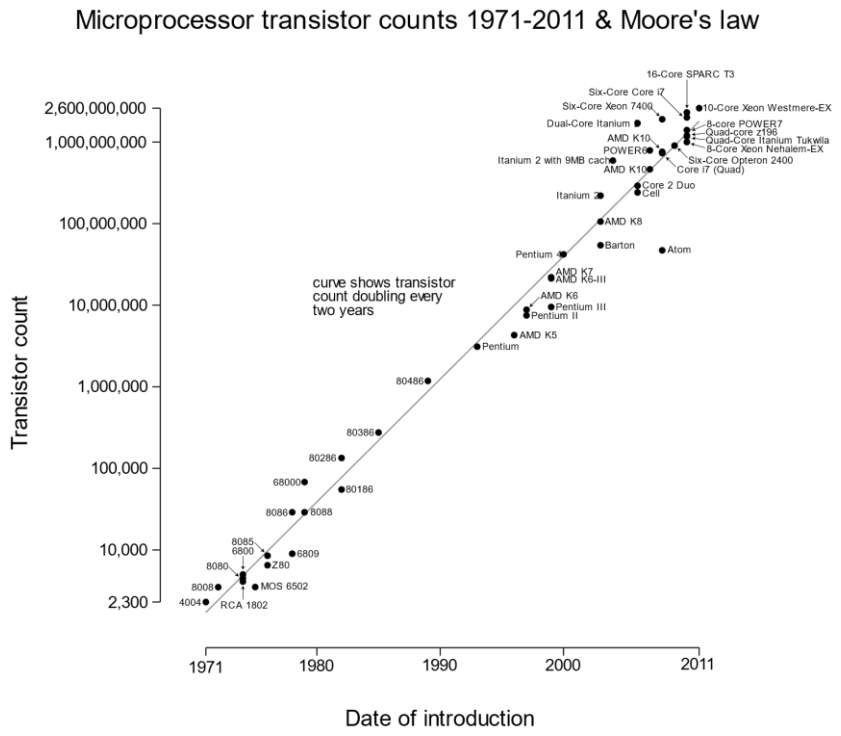

Figure 1. Number of transistors on a CPU over time

1.1.1 Semiconductors, Conductors, and Insulators

There are three categories of electrically conductive materials: conductors, semiconductors, and insulators. All three types are used in our daily lives in completely different applications. Life without even a single group would be unrecognizable to the modern human.

Conductors are typically metals and conduct electrical currents under standard conditions. The most common examples of this are the copper wires that are used to transmit power throughout homes, or the gold/aluminum used to make electrical contacts in electronics.[3,4] Metals act as good conductors because, in a bulk metal, the electrons surrounding the individual metal atoms are delocalized and form an electron cloud that is capable of movement through the stationary metal cations. The electrical resistance of a

metal increases with temperature due to increased electron scattering from vibrations, and as a result, cooling metals improves their conductivity.[5]

Insulators are either incapable of conducting current or require extraneous conditions to do so. Many materials fall into this category including wood, air, wool, most plastics, as well as countless others. Insulators are typically employed for their mechanical properties, and not their electrical properties, but they do find use in some electronics, such as dielectrics in capacitors.[6] The molecular composition of insulating materials generally consists of strong covalent bonds which are incapable of easily breaking or moving electrons around.[7] Despite being called insulators, some of these materials can be made conductive at high temperatures or other harsh external conditions, like high electric fields. Even though they can be made to act as conductors, there is a distinction between insulators and semiconductors despite there not being an exact cut-off point.

Arguably the most interesting of the three as far as electronics are concerned, semiconductors can switch between a conducting state and an insulating state depending on relatively small external forces. This is important because it allows semiconductors to be used in transistors and other electronics that require the ability to switch between multiple states, something conductors and insulators are incapable of. The most easily recognizable of semiconductors is silicon, which is used in all modern electronic devices, but other semiconductors do exist. Germanium,[8] another group 14 element, is also a good semiconductor, as are compounds of group 13 and group 15 elements, such as gallium arsenide (GaAs).[9] In more recent years, a lot of research has gone into the discovery and application of organic-based semiconducting materials which consist of highly conjugated

molecules, polymers, or composites, to complement or replace traditional silicon semiconductors.[10,11,12,13]

1.1.1.1 2D Band Structures of Conductors, Semiconductors, and Insulators

The electronic band structure of a material is a good way to visualize the difference between conductors, semiconductors, and insulators. The band structure of a material is a visual representation of the energy levels within the bulk material. Typical band structure diagrams have three key parts: the conduction band, the valence band, and the fermi level (Figure 2).

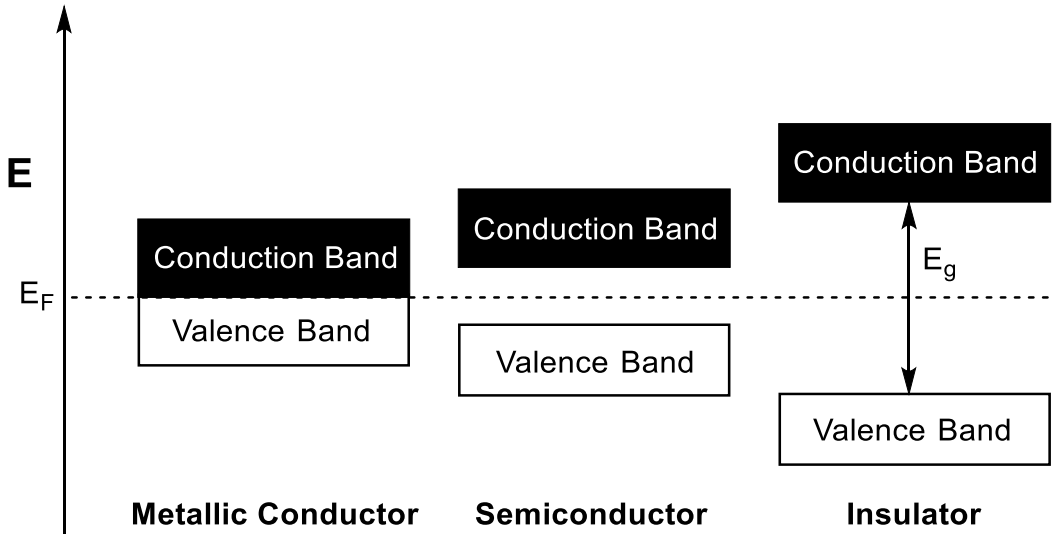

Figure 2. Simplified band structures of metals, semiconductors, and insulators

The valence band of a material represents the highest occupied electron states in that material. The position of the valence band indicates the absolute energy of the electrons in the band. Electrons in the valence band cannot travel freely in most materials, as the valence band is generally filled and thus the electrons have no free states to move to.

The conduction band represents the lowest unoccupied electronic states of the material. The conduction band is so named because if an electron enters the conduction band, it can move freely throughout the material as all the states in the conduction band are empty. In a metal, the conduction band and valence band overlap in energy, such that an electron can move from the valence to conduction band with no external energy requirement. This allows electrons to easily flow throughout the material, which is what makes metals good conductors.

The energy required to promote an electron from the valence band to the conduction band is termed the “band gap” (E_g). The band gap in a conductor is 0 electron volts (eV) because there is no energy requirement for the promotion of electrons. However, the size of the band gap is what distinguishes a semiconductor from an insulator, and further determines the characteristics of semiconducting materials. The cut-off band gap between insulators and semiconductors is not a very well-defined value because it depends on the application of the material, but it is generally accepted as somewhere within the 3 – 4 eV range. If the bandgap of the material is greater than ~3 eV, it is considered an insulator because the energy required to promote an electron to the conduction band is too large for most uses. If it is below ~3 eV it is generally considered a semiconductor.

The Fermi level (E_F) denotes a hypothetical energy level of an electron that has a 50% probability of being occupied at any given time, at thermodynamic equilibrium. This value is important as the position of the Fermi level is what ultimately determines which bands are the valence and conduction bands and determines whether the material is a

conductor or semiconductor/insulator. It also plays a key role in device fabrication, as it determines the barrier to electron or hole injection/extraction.[14]

If the Fermi level lies within any energy band, it means that the band is not fully occupied and thus the material is a conductor. However, if the Fermi level is found between the valence and conduction bands, it indicates that the material is either an insulator or semiconductor. The location of the Fermi level is also important in determining whether a material is a better conductor of electrons or holes. Electron holes, or holes, are quasiparticles that denote a lack of an electron where one would usually exist. If the Fermi level is closer to the conduction band, it means that on average, more electrons will be thermally excited, making the material a conductor of electrons (n-type semiconductor). Conversely, if the Fermi level is closer to the valence band, the material is a conductor of holes (p-type semiconductor).

When assessing the efficacy of a material to be a potent semiconducting material, the band structure is of utmost importance. While the band structure describes the energy required to “turn on” a semiconductor, it does not prescribe how this transition is made. Some materials are capable of thermal excitations, while others undergo photon excitations, and in the case of field-effect transistors an electric field modulates the band structure to make the transition easier.

1.1.1.2 Charge Carrier Mobility

The basic requirement for a semiconducting material to function is for it to be able to easily adopt both an “on” and an “off” state. Besides this fundamental requirement, several other factors play a key role in determining whether a material will be suitable for

use in various electronic devices. One of the most important of these properties is the charge carrier mobility (μ).

The charge carrier mobility of a semiconducting material is a measure of the resistance that a charge carrier (electron or hole) experiences as it travels through the material. The higher the charge carrier mobility, the less resistance is felt by a charge carrier travelling through the material, making for more efficient transport. This is especially important in applications where high current densities are important because it allows for more charge to travel through the material.

Another positive aspect of having a low resistivity in the material is that less heat is produced when charge moves through it. Many electronics are sensitive towards heat, as it adversely impacts the components and can cause severe damage, so it is important that they do not heat up considerably through routine usage. Furthermore, this is doubly important for consumer devices, particularly handheld ones, as heating can cause safety concerns for the user.

Charge carrier mobilities are measured in units of $cm^2\ V^{-1}\ s^{-1}$. The values of mobilities varies drastically depending on the material that is being tested. For example, typical values for crystalline silicon are in the range on 800 $cm^{-2}\ V^{-1}\ s^{-1}$, but many organic semiconductors have mobilities in the 10^{-3} to 1 $cm^{-2}\ V^{-1}\ s^{-1}$ range. The mobilities of such organic materials makes them inapplicable to high-performance transistors but makes them great candidates for use in other prominent devices.

1.1.2 Silicon as a Semiconductor

By far the most widely used semiconductor in the modern era is crystalline silicon. Silicon has been used as the leading semiconductor for decades and as such more

research has been done on silicon-based electronics than any others, and this carries with it several advantages. All modern techniques for fabrication of high-performance electronics have been created with silicon in mind, taking into account the limitations of its physical properties. Because of this, it is easier to continue to work with silicon than it is to find and implement alternative semiconductors. Silicon purification techniques are truly incredible compared to other materials, boasting purities of over 99.9999999%. The high purity of silicon gives near defect-free access to the intrinsic properties of silicon. Silicon is also easily doped with other elements to modulate its properties, allowing it to be used in almost all components necessary to build a functional transistor. Finally, it also forms good contact with other materials that are commonly used in electronics fabrication.

The development around silicon comes about because of its excellent electronic properties and its natural abundance. Silicon boasts good charge carrier mobilities of ~800 cm^{-2} V^{-1} s^{-1} which is greater than many of its competitors. The band gap of silicon is 1.14 eV, which is well within the range for a great semiconducting material. Not only does it have a suitable band gap, but the Fermi level sits at an appropriate level to allow for thermal excitation at room temperature, giving it its intrinsic semiconducting capabilities. Finally, it is a very robust material and can handle high heat and many other harsh conditions which allow it to withstand fabrication processes that other materials cannot handle. These aspects make silicon an excellent semiconducting material to use.

Silicon can easily have its intrinsic properties modulated through simple doping or oxidation. Oxidation of silicon to silicon dioxide (SiO_2) changes it from a great semiconductor, to a good insulator. A way to measure the insulating ability of a material is through its dielectric strength, which is its ability to withstand an electric field. SiO_2 has

a large dielectric strength of 10^7 MV/m, which is a massive increase over the 30 MV/m of silicon. Doping of silicon with boron atoms introduces points in the lattice with electron deficiencies, allowing the material to better conduct positively charged holes, making it a p-type semiconductor. Alternatively, doping with an electron rich element, like phosphorus, introduces sites of increased electron density, improving the conduction of negatively charged electrons. Such modifications are what allow the fabrication of transistors entirely from silicon-based materials, with the sole exception of metal contacts.

Despite the advantages of silicon, there are several inherent drawbacks to the material. Crystalline silicon is highly inflexible and brittle which prevents it from being incorporated into flexible electronics. Additionally, it lacks a direct bandgap, see below, which diminishes its ability to be used in light-based electronics.

In section 1.1.1.1 band structures were introduced, showing a simplified valence band to conduction band transition. However, this only considers the energy required to make the minimum transition from valence to conduction band. In practice, some transitions require a change in momentum of the electron as well as a change in energy; these are called indirect bandgap materials. Silicon is an example of an indirect bandgap material. The bandgap of silicon is generally reported as 1.14 eV, however transition at this energy requires a coupled phonon, or lattice vibration, to supply the momentum for the transition. The practical meaning of this is that an electron cannot be excited at 1.14 eV through a photon absorption, because photons posses no momentum, but requires thermal excitation as well. The direct bandgap of silicon is ~3.5 eV, which puts it into the territory of an insulating material.[15] What this means is that for light-related applications, such as photovoltaics, silicon is a poor substrate because it cannot absorb photons very

efficiently. For this reason, silicon-based solar cells are considerably thick and heavy, however, due to cost, ease of production, and robustness, they are still widely in use.

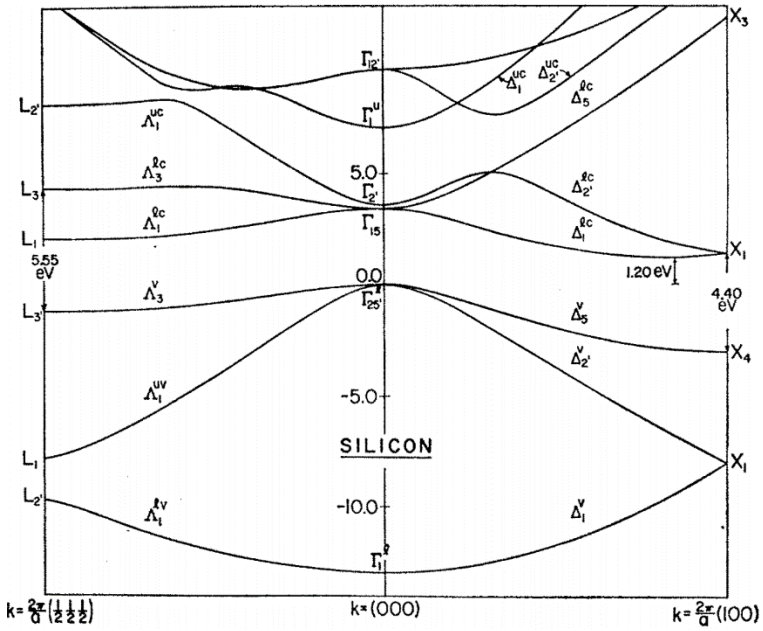

Figure 3. Energy bands of silicon in the [111] and [100] directions of k space[15]

Most of the advancement in transistor technology and computation strength has been a result of making transistors smaller, allowing for more to be incorporated into one CPU. Through a commonly cited guideline known as “Moore’s Law,” the number of transistors on a CPU chip has roughly doubled every two years. This exponential growth is the root cause of the drastic increase in performance that electronics have experienced over the last decades. However, the constant miniaturization of CPUs is approaching its physical limitations due to electron tunneling. Electron tunneling is the ability for electrons to move through a barrier if it is on a sufficiently small scale. An alternative semiconducting material will be required to see improved performance continue in the future.

1.2 Organic Semiconducting Materials

Conductive polymers were first discovered in 1982 with the report of polyaniline (PANI),[16] however, the nature of the conductivity was unknown at the time and largely went unnoticed. It is not understood that polyaniline derives its conductivity from a radical based electron pathway and further doping with ions. Interest in the field of organic conductive polymers did not gain very much traction until the work of Heeger, MacDiarmid, and Shirakawa on polyacetylene, which ultimately garnered them the 2000 Nobel Prize in Chemistry.[17] The push to find new conductive organics and understand the mechanism by which they were capable of conduction led to the discovery of new organic semiconductors. The focus on finding and synthesizing new conductive organics is still present to this day.

Organic materials fall into two broad categories: polymers and small molecules. A polymer is a single molecule that is made up of a large number of small repeating units, achieving weights of 10 – 10,000 kDa, or more. Polymers are widely used for their mechanical properties and include nylon, polyethylene, and polyvinylchloride (PVC). A small molecule is also a single molecule but it has a much smaller molecular weight. They include pharmaceuticals, spices, perfumes, and solvents. The term small molecule is commonly used by polymer chemists to distinguish between polymers and other organic chemicals.

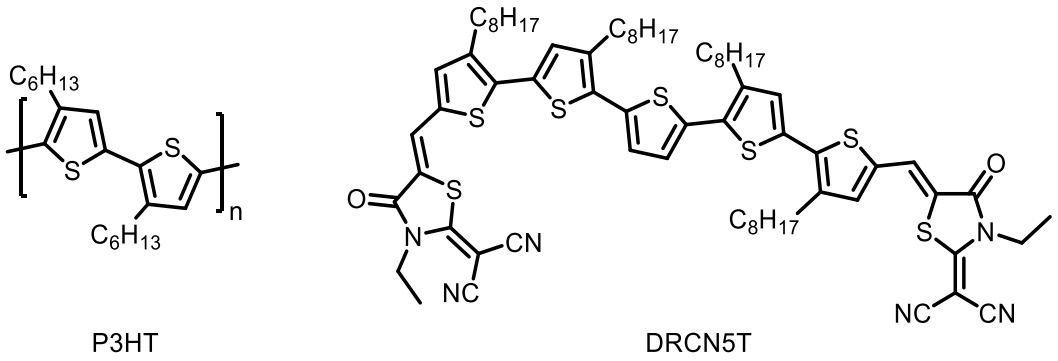

P3HT DRCN5T

Figure 4: Examples of polymeric semiconducting material (P3HT) and small molecule semiconducting material (DRCN5T)[18]

1.2.1 Conjugation and Aromaticity

Atoms undergoing π-bonding adopt an sp^2 orbital hybridization to increase the level of p-orbital overlap with neighbouring atoms. When four contiguous atoms are all sp^2 hybridized, such that there are two adjacent π-bonds, they are considered conjugated. Conjugation describes the combination of these individual π-bonds into a larger π-system, lowering the overall energy of the system.[19]

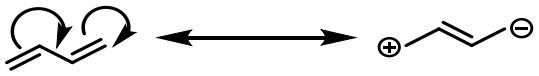

Figure 5. Butadiene resonance structure

Conjugation also allows for the movement of the π-electrons in the conjugated π-system to form resonance structures. This is an equilibrium process and only consists of the breaking and forming of π-bonds, not sigma bonds. Resonance structures formed in this way give insight into the electronic nature of various sites on a molecule, making it possible to discern chemical reactivity and acidity through simple analysis. Conjugation also opens up new reactions including the Diels-Alder reaction,[20] Michael additions,[21] and Aldol reactions,[22] among many others.

The conjugation of a molecule's π-orbitals can also have a direct impact on its stability and reactivity. Conjugation has long been known to stabilize π-bonds by 8 – 17 kJ mol^{-1}, but simple conjugation still leaves alkenes reactive enough to undergo the same addition reactions that isolated alkenes are subject to. However, when the same reactions were first tried on benzene, a molecule then believed to contain several unsaturations, the reactions failed to give any products. Benzene's lack of reactivity puzzled chemists and led to the assumption that it must be more stabilized than many typical unsaturated molecules.[23]

Many structures of benzene were proposed throughout this uncertain time, with Kekulé proposing the correct structure of a cyclohexatriene. However, cyclohexatriene is not a perfect representation of benzene's structure because it has an equivalent cyclohexatriene resonance structure. The combination of these two resonance structures results in all the C-C bond lengths in benzene being equivalent at 1.39 Å, instead of alternating single and double bond lengths as would be the case with cyclohexatriene.[19]

Several methods have been used to obtain experimental and theoretical approximations of the stabilization energy unique to benzene. One such method was through the measurement of the energy required to hydrogenate alkenes. The heat of hydrogenation of cyclohexene was found to be 28.6 kcal mol^{-1} (Figure 6). Through the assumption that benzene is simply cyclohexatriene, the expected heat of hydrogenation of benzene was 85.8 kcal mol^{-1}. However, the heat of hydrogenation of benzene was found to be 49.8 kcal mol^{-1}, a whole 36 kcal mol^{-1} lower than what was predicted. This extra stabilization of benzene has been termed aromatic stabilization energy and is seen in many other compounds. Computational methods that have been used to calculate the

aromatic stabilization energy of benzene have ranged from 25 to 35 kcal mol^{-1} depending on the method used.[24,25,26,27]

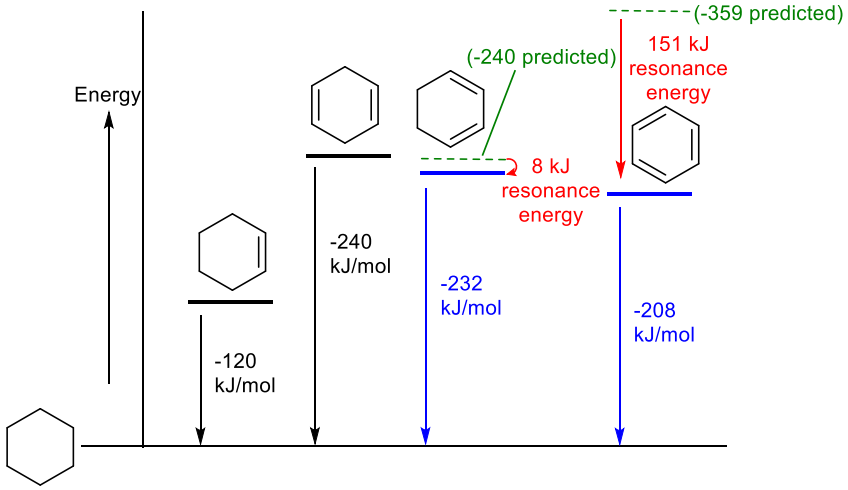

Figure 6. Aromatic stabilization of benzene as predicted by heat of hydrogenation[19]

Erich Hückel devised a set of rules for aromaticity, based on quantum mechanical calculations.[28,29,30] Hückel's rules state that for a molecule to be aromatic it must: have 4n+2 electrons in a conjugated π-system, be planar, be cyclic, and have a continuous ring of p ortibals. Other compounds that fit this criterion but instead have 4n electrons in the conjugated π-system are destabilized and are called anti-aromatic.[19]

1.2.2 HOMO-LUMO to Band Gap

When discussing electronic transitions in organic small molecules, a photon excites an electron from the highest occupied molecular orbital (HOMO) to the lowest unoccupied molecular orbital (LUMO). By tuning the gap between the HOMO and LUMO levels, the electronic properties of an organic material can be modulated. The HOMO-LUMO gap in small molecules is somewhat analogous to the bandgap in bulk materials as it describes the energy required to turn a material into a conductor and thus it defines whether a small

molecule will behave as an insulator, conductor, or semiconductor. Often the two terms are used interchangeably in materials science.

While the HOMO-LUMO gap and bandgap are very similar, they remain two distinct properties. HOMO-LUMO gaps exist only in discrete small molecules that have well-defined molecular orbitals. As a molecule grows in size, and is fully conjugated, the molecular orbitals also grow in density and start to blend into a large band of energy states (Figure 7). The combination of the discrete HOMO and LUMO levels into large bands of energy is what allows organic materials to form good conductive materials. The HOMO levels of a molecule will become the valence band of a resulting bulk material and the LUMO levels will become the conduction band. This can only happen if the material is conjugated throughout the backbone, as that is what allows for easy movement of electrons.[31] For this reason, most organic conductive materials are also known as organic conjugated materials/polymers. However, while transport along a single chain of a large, fully conjugated backbone is fast, practically it is not likely for a charge to travel from one electrode to another along a single molecule. When a charge travels along a single molecule and reaches the end, it must then “hop” to a new chain to continue travelling in the forward direction. Charge hopping between organic polymer chains requires far more energy than that required to move the charge along the backbone of a single molecule, resulting in far lower charge carrier mobilities than in silicon.[32]

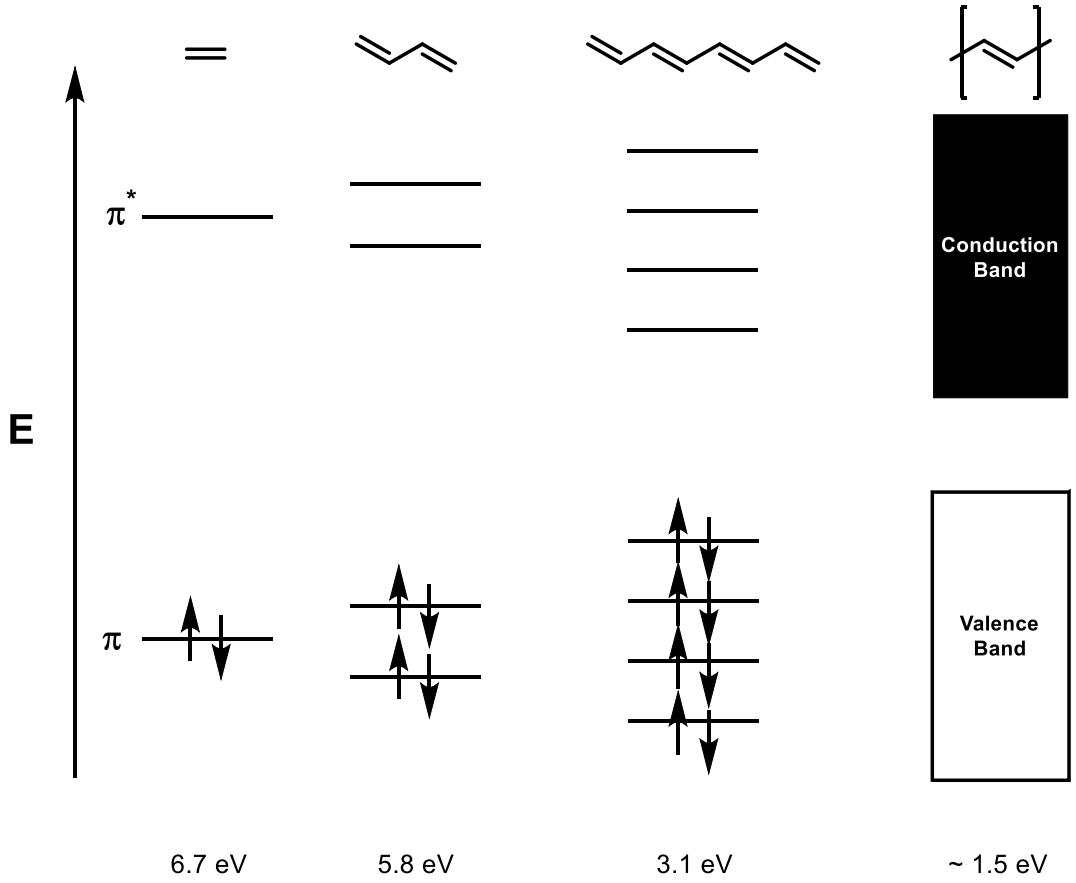

Figure 7. Origin of the band gap in conjugated polymers

The bandgap of an organic polymer is directly related to the HOMO-LUMO gap of the corresponding monomers. This is true for both the energy required to excite the electrons as well as the absolute energy level of the molecular orbitals.[33] Therefore, depending on the structure of the monomers used, the properties of the polymer can be easily altered to fulfill a particular requirement, such as being a good electron donor. The ability to intelligently design materials with targeted properties is one of the major advantages of organic materials.

1.2.3 Modulation of Organic Band Gap

While increasing the conjugation length of a conjugated material can decrease the bandgap, this stops being effective after ~ 8 repeat units.[34] Controlling the band gap of an organic material can be accomplished through several methods: rigidification of the polymer backbone, stabilization of the quinoidal state, incorporating heterocycles, and introducing donor-acceptor motifs.[35,36,37,38] The ability to predict the HOMO-LUMO gap of small molecules based on previously reported syntheses allows for more exact targeting of future properties. Furthermore, because the HOMO-LUMO gap of a small molecule correlates to the bandgap of the resulting polymer, this allows for quick screening of optimal small molecule candidates before committing to polymer synthesis.

1.2.3.1 Rigidification

The ability of an organic molecule to conduct a charge relies on its conjugation, and therefore, on the overlap of contiguous p-orbitals. For many small molecules, like benzene, this is a moot point as they are completely flat, and the overlap is near optimal. However, for many others there are usually sigma bonds that capable of rotation which causes the p-orbital overlap to suffer, especially if steric factors dictate a non-planar geometry.[39] The prevention of this rotation, or rigidification of the conjugated backbone, is one way to decrease the electronic gap of the material.

One way to prevent a loss of planarity is to make sure that the entire backbone consists of multiple connection points. For example, when connecting two benzene units, one can either connect them with a single bond to make biphenyl, or instead fuse the two rings to make naphthalene (Figure 8). The two phenyl rings of biphenyl do not sit coplanar due to the steric effects of the 2 and 2’ hydrogen atoms on the rings, and instead adopts

an equilibrium torsion angle of 44.4°.[40] The significant torsion angle of biphenyl causes a disruption in the conjugation between the two phenyl rings, which would be detrimental to the electronics of a hypothetical polymer. The disruption of conjugation results in a large HOMO-LUMO gap approximated by the UV absorption maximum of 249 nm in methanol.[41]

On the other hand, naphthalene does sit planar, giving it optimal p-obital overlap. Because of the two connection points, and sp^2 hybridized atoms, there is no capability for rotation of the backbone. The improved overlap is apparent in the UV absorption maximum of 285 nm in ethanol,[42] which represents a roughly 0.6 eV decrease in the HOMO-LUMO gap relative to biphenyl. While this strategy seems to perfectly fix the problems with lack of rigidity, it creates an even larger problem in the case of benzene in particular. As you continue to extend the molecule by fusing more linear benzene rings to create anthracene, tetracene, pentacene, etc. the molecules become less stable to the point of transient existence.[27] This family of molecules are known as acenes and will be discussed in more detail later.

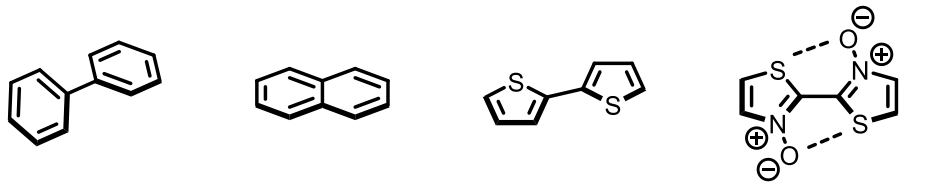

Biphenyl **Napthalene** **Bithiophene** **Bithiazole N-Oxide**

Figure 8: Various molecules depicting the different methods to increase π-orbital overlap

While the strategy of fusing rings does not work well for benzene specifically, it does work well for other monomers. Polymers which have a fused ring backbone are known as

ladder polymers and possess better electronic properties due to their higher p-orbital overlap.[43] The main challenge with conjugated ladder polymers is their synthesis. It can be very difficult to find an appropriate synthetic route to creating conjugated ladder polymers because not only does it require the formation of two bonds, the polymerization must also be very high yielding, in order to produce polymers. For this reason, generally the synthesis involves making small fused ring ladder monomers and coupling them to other monomers through traditional palladium cross couplings. This results in a polymer that is only partially “ladder-like” due to the inclusion of sigma bonds connecting ladder units, but it still has enough of an impact to help create better devices.[44]

Alternatively, instead of directly fusing the backbone to prevent rotation, one can lower the steric demand of the monomers such that they remain planar. The easiest way to do this is to use five-membered rings as the monomers instead of 6-membered rings. For example, 2,2’-bithiophene is easily synthesized through homocoupling and features coplanar thiophene rings (Figure 8).[45] The coplanarity is a result of the lack of steric hindrance as the rings can adopt a conformation where the hydrogen at the 3 and 3’ positions are on opposite sides of the molecule. The UV absorbance maximum for 2,2’-bithiophene is 304 nm,[46] which corresponds to a HOMO-LUMO gap that is even lower than naphthalene. Other five-membered heterocycles also benefit from this lack of steric interaction and therefore make for good monomer candidates.

Another way to ensure planarity of a molecule is to introduce an interaction that promotes a planar conformation. This can be done through the introduction of a substituent on the monomer that interacts with adjacent monomers, creating an effect similar to that of a ladder polymer, but to a much lower degree.[47] Many groups have been

used to imbue polymers with rigidity and they generally take advantage of dipolar interactions between adjacent atoms, especially chalcogen bonding. An example of this type of rigidification has been developed in the Schipper group and relies on the interaction of an oxygen atom on a thiazole subunit interacting with a sulfur atom on an adjacent thiazole (Figure 8).[48] Through the introduction of multiple groups, the effect on the planarity of the resulting molecule can be very pronounced, with a rotation barrier as high as 14.5 kcal mol^{-1} in the case of the N,N'-dioxide.

While planarity helps improve the electronic properties of a molecule, it presents a challenge of reduced solubility. Due to the rigid, planar nature of conjugated organic materials, they are generally very poorly soluble in all solvents, especially as they increase in size.[49] The decrease in solubility is very evident when comparing naphthalene (175 g L^{-1} in hexanes), anthracene (3.7 g L^{-1}), and pentacene which is virtually completely insoluble in all solvents. Poor solubility makes it much more difficult to handle and process a material, making it far less attractive for industrial applications.

To combat solubility problems, long aliphatic chains are added to the molecules, in order to disrupt their crystallinity.[50] Common aliphatic chains used include various straight chain alkanes as well as ethyl hexyl branched alkanes, as the branching of the alkyl chain further disrupts the ability for the molecules to stack closely to one another. These chains, however, also result in a disruption of planarity and therefore a balance between finding a system that is soluble enough for easy use while still being planar enough to possess useful electronic properties is a continual struggle in conjugated polymer synthesis, such that even the branching position of the alkyl chain contributing to the overall device

performance.[51] Fortunately, there are other parameters that can also be modified to aid in the search for materials with useful electronic properties.

1.2.3.2 Stabilization of the Quinoidal State

The conductive state of polymers is described as the quinoidal state. In this form there is complete conjugation along the entire backbone giving it a structure that is analogous to polyacetylene (Figure 9). The quinoidal state is not as stable as the ground state structure due to the loss of aromatic stabilization and so conductive polymers need to overcome an energy barrier to achieve their optimal conductivity.[52] Efforts made to stabilize the quinoidal state will then, in turn improve the conductivity of the resulting polymer.

The reason that the quinoidal state is higher in energy than the ground state is because the aromatic stabilization of each repeat unit is lost. Accessing the quinoidal state requires the breaking of aromaticity in each monomer and thus carries with it an energy penalty. The formation of conjugation along the entire polymer backbone offsets some of this energy cost, but not all of it.

One strategy to decrease the energy cost of entering the quinoidal state is to increase the stabilization achieved in the quinoidal state. To this end, researchers have added fused rings onto the monomers to introduce dienes, in this example thiophene is replaced with benzothiophene (Figure 9). These dienes not only contribute to the overall conjugation of each monomer unit, but also have the added effect of stabilizing the quinoidal state.[53] When entering the quinoidal state, the conjugation along the backbone of the polymer now also has the added effect of introducing aromaticity to the added diene units, offsetting the loss of the aromaticity in the thiophene units, ultimately offsetting the

cost and making the quinoidal state far more stable. This is especially true in the case of poly(isothianaphthene) (Figure 9) because the loss of aromaticity in the thiophene ring is more than offset by the formation of aromaticity in the benzene ring, making the quinoidal state more stabilized than the ground state.[33,54] Many researchers have taken advantage of this effect by using benzene fused heterocycles as their monomers, in order to produce low band gap polymers.

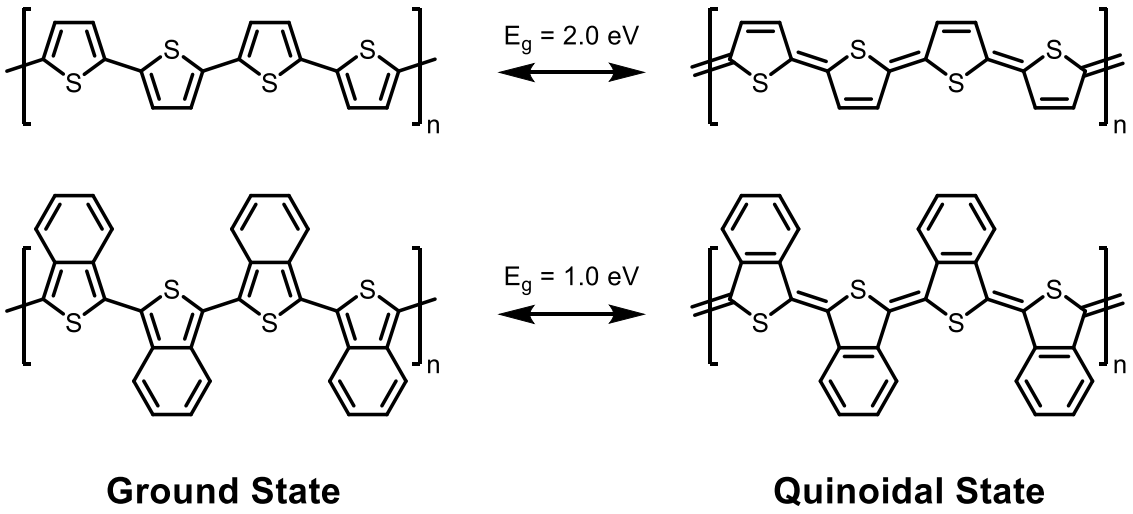

Figure 9: Ground state and quinoidal state of conjugated polymers

1.2.3.3 Heterocyclic Compounds

Heterocyclic compounds dominate the field of conductive polymers and small molecules due to their superior performance relative to their all carbon counterparts. The introduction of heteroatoms into a conjugated system has a direct effect on the resulting HOMO and LUMO levels, and can also play an important role in the planarization of the backbone. The incorporation of heteroatoms into a conjugated system is the most common way to create conjugated organic polymers for use in electronics.[13,55,36,35]

As discussed above in section 1.2.3.1, the size of aromatic rings can drastically affect their planarization. Five-membered ring systems experience less steric repulsion relative to six-membered rings but an all carbon 5-membered ring does not work as a monomer for a conjugated polymer. The closest molecule to an uncharged, aromatic 5-membered all carbon ring is cyclopentadiene. However, cyclopentadiene is extremely unstable and undergoes a Diel-Alder reaction with itself rapidly at room temperature due to its lack of aromaticity and conformationally locked s-cis diene. However, five-membered aromatic heterocycles do not suffer from this problem because they benefit from the aromaticity imparted by the sp^2-hybridized heteroatom, giving the molecules much higher stability.[56] Therefore, heterocyclic aromatic molecules can be used as monomers to synthesize stable and planar conjugated electronic materials.

Heterocycles are also used because they posses drastically different electronic properties depending on the nature of the heteroatom. This will be touched upon in the next section.

1.2.3.4 Donor-Acceptor Motifs

Another great way to modulate the bandgap of a conjugated polymer is to introduce donor-acceptor motifs. That is, using two monomers, one that is electron rich and another that is electron poor, to create the polymer. When doing this, the molecular orbital mixing of the two monomers results in a tightening of the band gap caused by a lowering of the LUMO from the acceptor and a raising of the HOMO from the donor (Figure 10).[36]

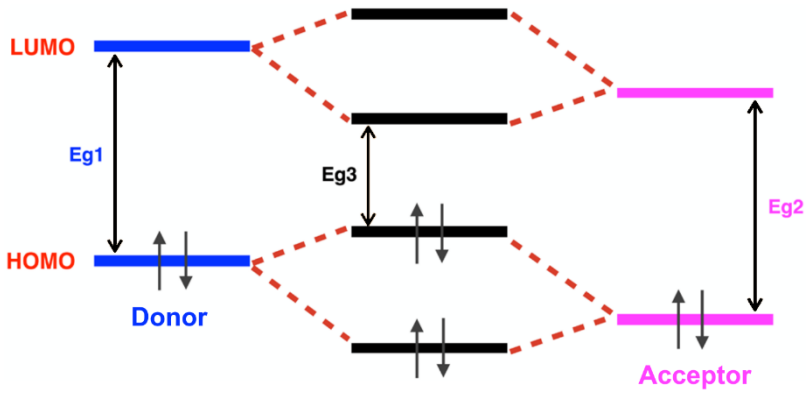

Figure 10: Schematic representation of orbital mixing between a donor (blue) and an acceptor (pink).

Many types of monomers have been used to create donor-acceptor polymers. An early example includes simply combining electron rich thiophene with electron poor pyridine.[57] Since then, the utility of this method has become obvious and donor-acceptor motifs are now ubiquitous in the design of effective conjugated polymers. Many electron poor heterocycles have been utilized including diketopyrrolopyrrole,[58,59] 2,1,3-benzothiadiazole,[60,61,62] isoindigo,[51,63] and other aromatics with electron withdrawing substituents.[64,65] The typical donor of choice is thiophene, or its derivatives.[66,67]

1.3 Carbon Nanotubes

While many conventional conductive organic materials are polymer or small molecule based, several allotropes of carbon have been discovered that additionally make for excellent semiconducting and metallic materials. Carbon nanotubes (CNTs) were discovered in 1991[68] and have been since shown to possess excellent electronic and mechanical properties.[69,70,71] Carbon nanotubes are long, 1-dimensional tubes, made entirely of sp^2-hybridized carbon atoms arranged in six-membered rings with diameters

on the size of nanometers and lengths on the scale of hundreds of nanometers (Figure 11).

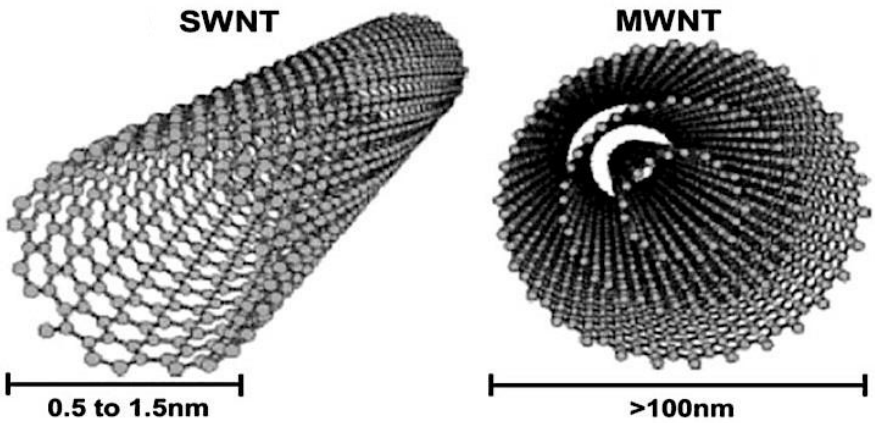

Figure 11: Schematic representation of a single-walled carbon nanotube (SWNT) and a multi-walled carbon nanotube (MWNT)[72]

Carbon nanotubes are generally separated into two main classes: multi-walled carbon nanotubes (MWNTs) and single-walled carbon nanotubes (SWNTs). SWNTs consist of a single nanotube and are used in electronic[73] and mechanical[74] applications. MWNTs consist of many concentric SWNTs of increasing diameter and possess great mechanical properties[75] and make good conductors.[76,77] SWNTs can be either semiconducting (s-SWNTs) or metallic (m-SWNTs), whereas MWNTs are always metallic. In fact, CNTs hold the distinction of being the only organic molecules that are metallically conducting without the need for doping.

Mechanically, both types of carbon nanotubes are used in many structural components that need to be strong and lightweight like tennis racquets, boat hulls, and bicycle frames. The 1D structure of CNTs allows them to act as threads that can be

interwoven to create fibres with incredible strength, while maintaining the lightweight nature of the CNTs.

SWNTs are used in electronic applications including field-effect transistors (FETs),[78,79,80] thin film transistors (TFTs),[81,82,83] sensors,[84,85] biosensors,[86,87] and photovoltaics.[88,89,90] SWNTs have excellent electronic properties including ballistic charge transport,[78] and bandgaps in the range of 0.5 eV – 1.13 eV.[91,92] However, since SWNTs can be either metallic or semiconducting, accidental incorporation of a metallic nanotube into an FET will result in a faulty device.

CNTs are synthesized using one of several high-energy techniques which ultimately result in a mixture of different carbonaceous materials as well as CNTs of different lengths, diameters, and shapes. This is detrimental to their use in electronic devices as the diameter of a SWNT is what determines its semiconducting properties and bandgap. As such, much work continues to be done in finding a method to selectively synthesize one type of SWNT, or to purify a mixture of SWNTs.

1.3.1 Carbon Nanotube Band Structure

The electronic properties of SWNTs can be understood by looking at the band structure of the material. Graphene serves as a great first approximation of the electronic structure of carbon nanotubes due to their similar structure. Graphene is a single, continuous sheet of sp^2-hybridized carbon atoms arranged in six-membered rings. Graphene possesses a completely two-dimensional structure and is fully conjugated in its pristine form. The Fermi level of graphene sits between its π and π^* molecular orbitals, meaning that the HOMO and LUMO levels are represented by the π-system.[93] As

expected, electron transport in graphene is therefore based on the movement of π-electrons.

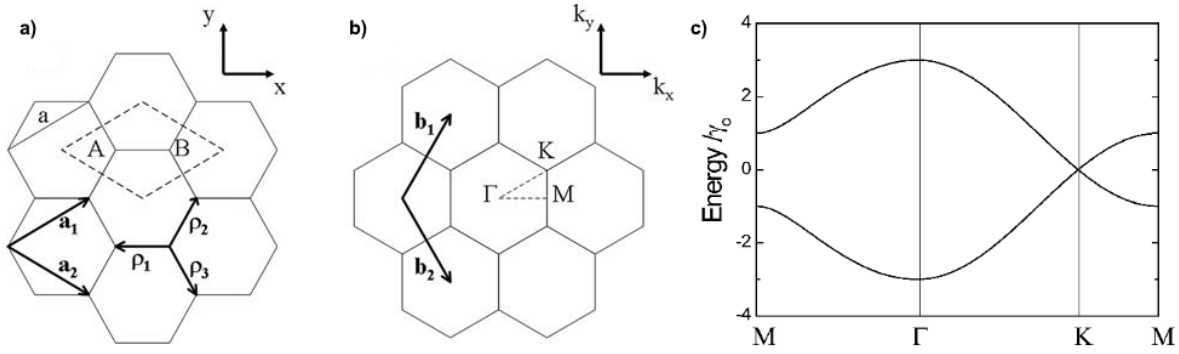

Figure 12: a) Real space representation of a graphene lattice. Unit cell is shown in dashed rhombus with unit vectors a_1 and a_2. b) Reciprocal space representation of a graphene lattice. High symmetry points (Γ, K, M) are shown. c) Energy dispersion of graphene along high-symmetry points.[94]

The band structure of graphene predicts its highly interesting electronic characteristics (Figure 12). The valence and conduction bands of graphene meet at two points denoted “K” points. Both of the K points are on two carbon atoms in the unit cell but even though the conduction and valence band meet at these points, the density of states decreases as the two bands approach the same energy level and ultimately there are zero electronic states at the Fermi level where both bands meet.[95] This means that although there is no bandgap in graphene, it is still a semiconductor because there are no states that would allow for metallic conduction.

Single-walled carbon nanotubes (SWNTs) are also molecules made entirely of sp^2-hybridized carbon atoms arranged in six-membered rings. The difference between graphene and SWNTs is that graphene is a flat, 2D sheet, whereas SWNTs can be seen as a 1D, “rolled up” tubes of graphene. SWNTs can come in many different diameters and chiralities. The type of carbon nanotube is described by its chiral vector, which is

derived from the hypothetical folding of a graphene sheet to give the desired SWNT. The chiral vector is described by the equation: $\boldsymbol{C} = na_1 + ma_2$, where *n* and *m* are integers and a_1 and a_2 are the unit vectors of the graphene lattice (Figure 13). The chiral vector is also commonly represented as a cartesian coordinate system of (*n*, *m*). Some chiral vectors, such as (*n*, *n*) and (*n*, 0), are given the special names armchair and zigzag nanotubes, respectively.

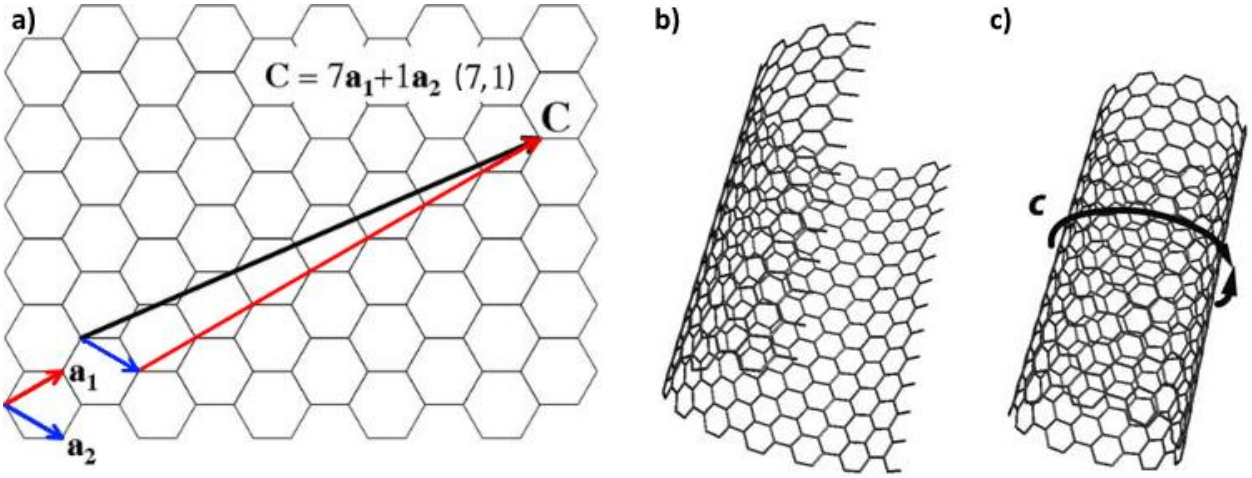

Figure 13: a) Graphene sheet with unit vectors a_1, a_2, chiral vector C, and chiral index (7,1). b) Rolling up graphene sheet. c) Fully formed single-walled carbon nanotube showing chiral vector C.[96]

SWNTs are 1D nanostructures, unlike graphene, and thus have a different band structure. In graphene, there are two wavevectors that describe the wavefunction of an electron in reciprocal space, k_x and k_y, in the x and y direction, respectively. Likewise, for SWNTs there are two wavevectors, $k_\perp$ and $k_\parallel$. Since SWNTs are 1D, they are treated as being infinitely long along the tube axis, and the wavevector $k_\parallel$, which is along the tube axis, can therefore take on any values without restriction. However, since a carbon nanotube has a finite diameter, $k_\perp$, which represents the wavevector perpendicular to the

tube axis, is constrained by a periodic boundary condition: $\boldsymbol{k}_\perp \cdot \boldsymbol{C} = \pi d k_\perp = 2\pi l$, where *d* is the diameter of the nanotube and *l* is an integer.[94]

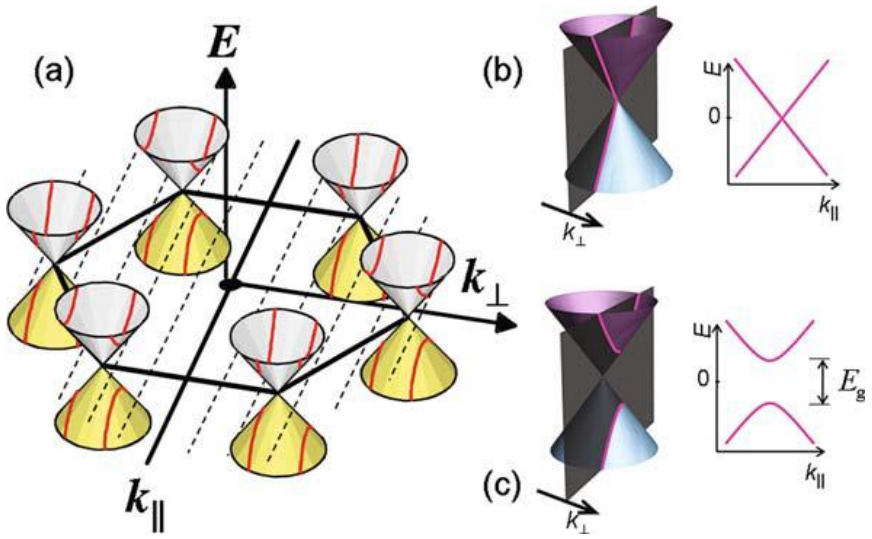

Figure 14: a) A first Brillouin zone of graphene with conic energy dispersions at six K points. The allowed $k_\perp$ states in a SWNT are represented by dashed lines. The band structure of a SWNT is obtained by cross-sections as indicated. Zoom-ins of the energy dispersion near a K point and 1D energy dispersion bands for b) a metallic SWNT and c) a semiconducting SWNT.[94]

The boundary condition placed upon $k_\perp$ leads to the quantization of allowable $k_\perp$ values that differ for SWNTs of different chiralities. This has the ultimate effect of making some chiralities of SWNTs metallic and others semiconducting. Furthermore, because the boundary condition is affected by the diameter, the bandgap of semiconducting SWNTs are also affected by the diameter of the tube. For some SWNTs, $k_\perp$ can take on values such that the K point from the graphene band structure coincides with the $k_\perp$ value, resulting in a zero-bandgap nanotube. Unlike graphene, SWNTs have a non-zero density of states at the Fermi level and are therefore metallic in this configuration. For other diameters, however, $k_\perp$ cannot take a value at the K points, and this results in a non-zero bandgap and a semiconducting nanotube (Figure 14).

SWNTs with wrapping indices of (*n*, *m*) can be categorized into two different groups depending on a value denoted as *p*. *p* is the remainder when the difference between n and m is divided by 3: $n - m = 3q + p$, where *q* is an integer. If $p = 0$, this ensures that at least one value of $k_\perp$ will intersect with a K point. If $p = 1\ or\ 2$, no K points are intersected, and the nanotube is semiconducting in nature. The bandgap of semiconducting nanotubes is inversely proportional to their diameter. For nanotubes of diameter 0.5 nm – 2 nm, the bandgaps are in the range of 0.4 eV – 1.7 eV.[91] These results mean that all armchair nanotubes (n, n) are metallic in nature whereas zigzag SWNTs (n, 0) and nanotubes of other chiralities can be either metallic or semiconducting.[94]

1.3.2 Carbon Nanotubes as Semiconductors

As mentioned previously, SWNTs possess excellent inherent characteristics that allow them to be used in semiconducting devices. The charge carrier mobility of SWNTs is in the range of 10^{-2} – 100,000 $cm^2\ V^{-1}\ s^{-1}$ depending on the particular device architecture,[79,81,97,98] which can be orders of magnitude larger than that of silicon. As seen in the previous section, the band gaps of SWNTs can range from 0.4 eV – 1.7 eV, which is smaller than that of silicon, requiring less energy to undergo switching, and carbon nanotubes possess direct bandgaps, allowing for easy transitions from photon excitation. Finally, CNTs can be modified through direct chemical reaction with other organic molecules, surfactants, polymers, and can even bind to analytes to give changes in electronic properties.[99]

1.3.2.1 Charge Carrier Mobility of Carbon Nanotubes

The high variation in reported charge carrier mobility of CNTs comes about mainly due to the different types of contacts that are made by the CNTs in a given device. The

charge carrier mobility of CNTs is only excellent along the tube axis, where the electrons can easily flow throughout the entire CNT π-system. In fact, when measuring the charge carrier mobility along a single tube with Ti/Au padded palladium source/drain contacts, researchers have been able to achieve ballistic electron transport.[78] Ballistic electron transport is the maximum achievable charge carrier mobility and results when the mean free path of an electron through a material is significantly longer than the material it is traveling through, resulting in no scattering and therefore no resistance. However, only under ideal conditions are charge carrier mobilities so high.

When an electron is traveling along the CNT, it can be scattered by encountering a flaw in the CNT lattice. Electron scattering results in increased resistance and therefore decreased charge carrier mobility. However, unlike other materials, the potential scattering events in SWNTs are reduced to only forward and backward scattering due to their 1D shape, which helps improve charge mobilities.[100]. One of the main sources of decreased charge carrier mobility are static defects along the SWNT. Static defects include vacancies, pentagon-heptagon pairs, foreign atoms, and chemicals deposited on the surface of the CNT. Vacancies can occur in the CNT lattice whereby carbon atoms are missing, resulting in backscattering of electrons. Pentagon-heptagon pairs are another common type of defect along CNTs, which result when two adjacent six-membered rings are fused incorrectly, resulting in a five-membered and seven-membered fused ring system. These defects can be characterized through microscopy[101,102,103] and their effect on the conductance[104] and FET performance[105] of SWNTs has been studied computationally. Foreign atoms can also be incorporated in the CNT during synthesis if not handled properly, or if done intentionally, but this is much harder to directly

observe.[106,107] Finally, chemicals that are deposited onto the surface of CNTs also affect the backscattering of electrons and lower the charge carrier mobility. This last scattering method is especially important as it is what allows CNTs to be used in sensing analyte molecules in their environment.[87]

It is believed to be the case that for CNTs, the scattering due to static defects is minimized, and so phonons are the major cause of scattering events. Phonons are lattice vibrations and cause defects that vary with time, thus are not considered static defects. Phonon scattering increases with temperature and source-drain voltage (V_{DS}) in FETs. When the V_{DS} in a CNTFET device increases, so does the amount of scattering due to phonons, reaching a maximum which causes the FET to reach current saturation. However, in short CNTs, this effect is absent because even under high V_{DS} the mean free path of an electron is still larger than the length of the CNT. Furthermore, researchers have seen differences in scattering between SWNTs that are suspended vs CNTs that are in contact with a substrate. This is likely due to the heat dissipation from the CNT to the substrate, decreasing the number of inelastic collisions.

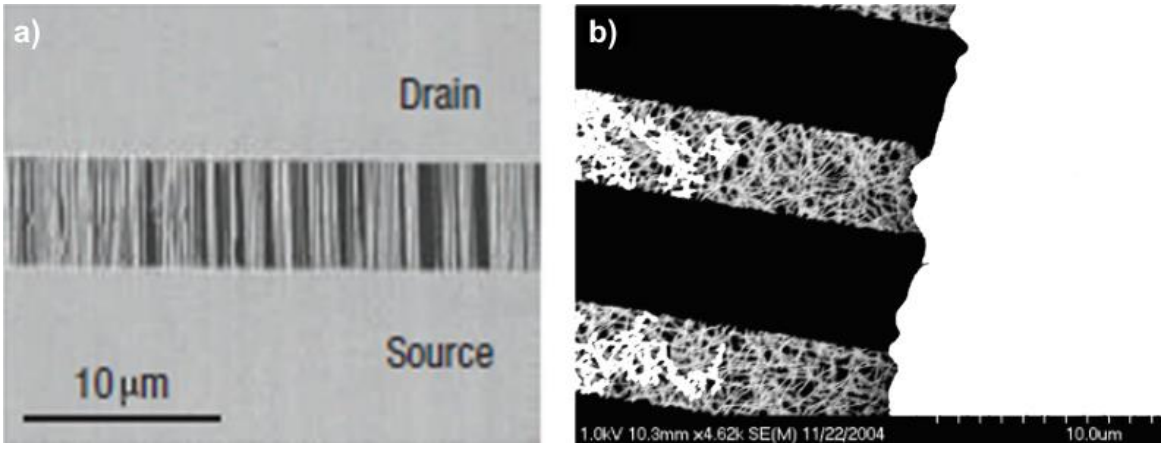

Figure 15: SEM micrographs of a) aligned SWNTs[108] and b) a random network of SWNTs[109] between electrodes.

Finally, the last form of electron scattering is inter-tube electron hopping. In an ideal scenario, electrons flow directly from one electrode, along a CNT, and into the next electrode (Figure 15a). However, in practice, creating a device that has such a perfect layout is very difficult, especially when attempting to incorporate many CNTs into a single device. One runs into the problem that CNTs are not all uniform in length and it is very difficult to selectively deposit them in the desired location and orientation. The strong intertube interaction between SWNTs[110] results in them forming stable bundles, and makes it difficult to deposit nanotubes selectively on a surface (Figure 15b). Most fabrication methods involve either depositing electrodes onto a single SWNT, or depositing a dense layer of SWNTs onto already formed electrodes. In the former, the charge carrier mobility will be excellent because the electrons are taking the most optimal path, which is along a single CNT, but because there is only one CNT, the charge density will be low, severely limiting applications. In the latter, there will be more CNTs allowing for a higher charge density, however the chances that an electron can get from one electrode to the other along a single tube is low. In this case, electrons will travel along a nanotube until they reach the end, and then they will have to hop to an adjacent CNT in order to continue to the electrode. These hopping events have a barrier that is large relative to simply continuing along one CNT, and thus decrease the overall charge carrier mobility.[111]

1.3.2.2 The Band Gap of Carbon Nanotubes

SWNTs can be great semiconductors with small bandgaps depending on their diameter and chirality. The direct bandgap of SWNTs makes them particularly interesting for use in optical-based applications and allows characterization through optical spectroscopic techniques. The various bandgaps of SWNTs make them interesting because theoretically a single diameter can be selected to give an optimal bandgap for a specific application. However, in practice it is very difficult to select for one bandgap which becomes detrimental for many applications. Furthermore, the bandgap and Fermi level of the SWNTs can be directly modulated by an external magnetic field, allowing SWNTs to be used in field-effect transistors, where the generated electric field can turn the transistor on or off.[112]

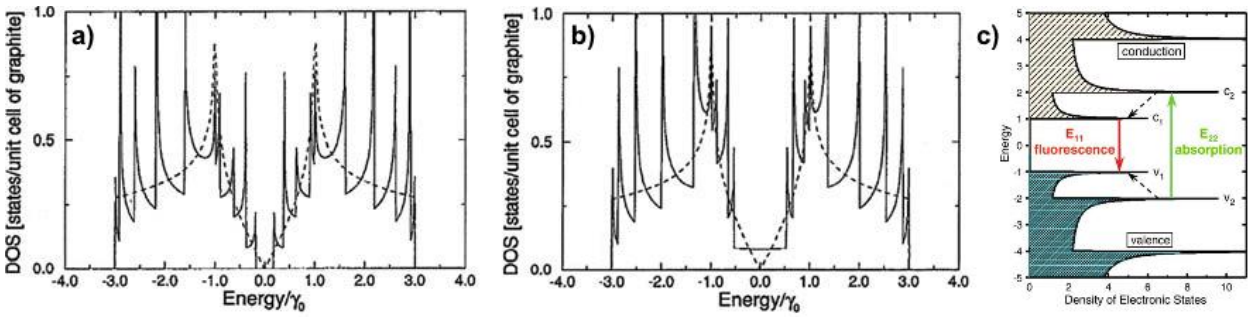

Figure 16: The electronic density of states for a) a (10, 0) semiconducting and b) a (9, 0) metallic SWNT. The dotted lines represent the density of states for graphene.[95] c) A schematic density of states for a semiconducting SWNT. Optical excitations are marked by solid arrows and nonradiative relaxations are marked by dashed arrows.[92]

The 1D structure of SWNTs leads to a very different energy structure than 2D graphene. As can be seen in Figure 16 while the energy structure of graphene (dotted line) and SWNTs are similar, there are many sharp increases in the DOS for SWNTs. These are called van Hove singularities and are a result of the quantization of the

wavevector $k_{\perp}$. The optical properties of SWNTs are a direct result of these van Hove singularities,[113] and even a single SWNT gives rise to sharp absorption spectra due to the sharpness of the DOS of the electronic subbands. The bandgap transition is an excitation from the valence band, v_1, to the conduction band, c_1, and is denoted E_{11}. This is typical of many materials, but in SWNTs there is also another transition that is also available for photon-induced electron excitation. The transition from the valence band, v_2, to the conduction band, c_2, is denoted as the E_{22} transition (Figure 16c). E_{22} absorption is typical of SWNTs and is generally found in the visible light spectrum and allows for the identification of SWNTs based on their optical absorption. Due to the E_{22} and E_{11} absorptions, SWNTs have a wide range of optical absorptions from ~ 0.5 eV – 2.5 eV, for example a (6, 5) SWNT has a calculated E_{11} of 1.13 eV and E_{22} of 2.25 eV.[114]

After undergoing an E_{22} absorption, SWNTs can also undergo an emission from c_1 to v_1. This is a fluorescent emission (E_{11}) and is preceded by relaxation of an electron from c_2 to c_1. The fluorescence is also sharp and easily identifies a SWNT. While an absorption or emission spectrum is not sufficient to determine the exact chirality of a SWNT, the combination of both allows for very accurate assignment. Researchers have made 2D maps of the photoluminescent absorption and emission of various SWNTs and have used these maps as characteristic identifiers for mixtures of CNTs (Figure 17).[115]

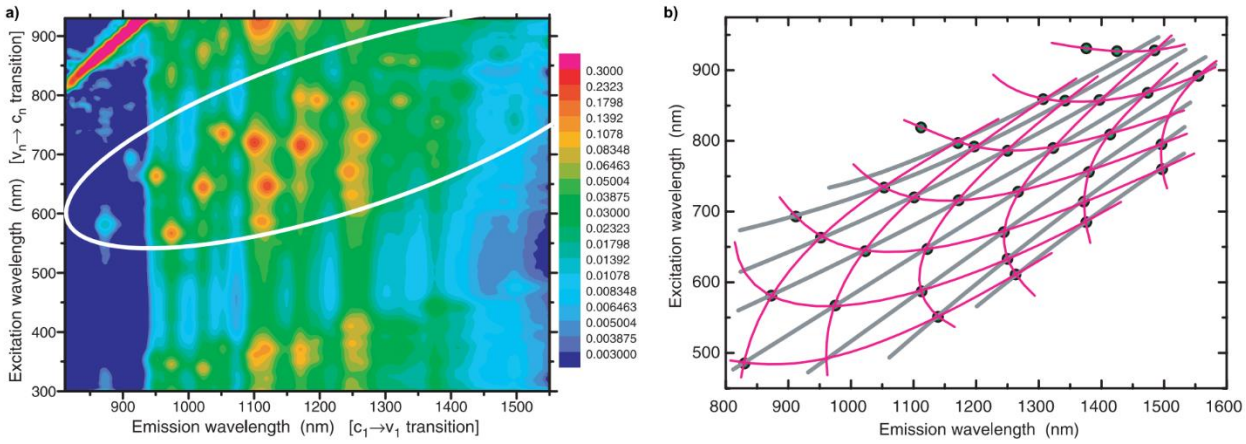

Figure 17: a) Contour plot of fluorescence intensity versus excitation and emission wavelengths for a sample of SWNTs suspended in sodium dodecyl sulfate and deuterium oxide. b) Circles show spectral peak positions from a); lines show perceived patterns in the data.[92]

This method cannot be used for identification of metallic SWNTs as m-SWNTs do not have a bandgap. While m-SWNTs do possess a similar E_{11} absorption (Figure 16b), the electrons that are excited to the conduction band can undergo non-radiative decay to relax back to the valence band, resulting in no fluorescence. Nonetheless the absorption of m-SWNTs can be used to identify them in a sample (Figure 18).

To distinguish between the absorptions of semiconducting SWNTs and metallic SWNTs, the terms S_{11}, S_{22}, and M_{11} are used. S_{11} is used for the E_{11} optical transition in s-SWNTs, while S_{22} is used for the E_{22} transition in s-SWNTs. Additionally, M_{11} denotes the E_{11} transition in m-SWNTs. There is a general trend for these various transitions corresponding to the diameter of the SWNT being probed. For a given diameter, $M_{11} > S_{22} > S_{11}$, which can be seen in a Kataura plot which plots the diameter of metallic and semiconducting SWNTs against their absorptions (Figure 18a).[91]

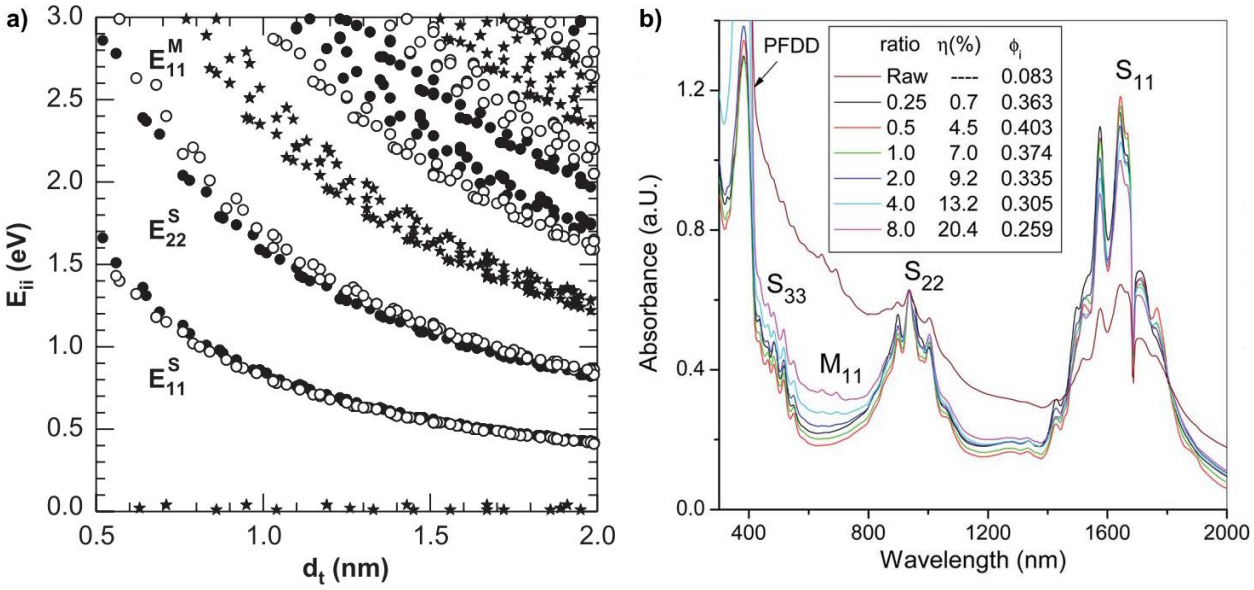

Figure 18: a) Calculated electronic transition energy E_{ii} vs. nanotube diameter d_t for SWNTs, commonly known as a Kataura Plot.[91] b) Absorption spectrum of polymer wrapped SWNTs showing peaks in each of the distinct energy bands.[82]

Another optical spectroscopic technique that is frequently used to characterize CNTs is Raman spectroscopy.[96,116,117,118,119] Raman spectroscopy probes both the electronic structure and the phonon modes of CNTs. This is of double importance because phonons are especially useful when determining the physical properties of a material and can be used as direct probes into the structure of SWNTs. In Raman spectroscopy, a laser is shone onto the target, in this case the SWNTs, resulting in absorption and electron excitation from the valence band to the conduction band. Following excitation, the electron is scattered inelastically through interaction with phonons, and finally relaxes, emitting a photon with energy equal to that of the incident photon less the energy of the phonon. Therefore, Raman spectroscopy gives a direct measure of the energy of phonons in the system.

The Raman spectrum of SWNTs has several key aspects that give a deep insight into their structure.[118] The first region of interest is the radial breathing mode (RBM) region, a low frequency transition seen in the area of ~100 cm^{-1} – 500 cm^{-1} (Figure 19a). This is a mode that is unique among CNTs and is therefore useful for confirming the content of CNTs in a carbonaceous sample. The RBM is named such because it corresponds to the mode of all the carbon atoms moving coherently out of the plane of the tube axis, as if the tube were breathing. The energy required for this transition is therefore quite low and is approximated by the equation: $\omega_{RBM} \sim \frac{C}{d_t}\ \mathrm{cm}^{-1}$, where d_t is the diameter of the nanotube and C is a constant depending on the substrate (248 cm^{-1} for isolated SWNTs on SiO_2).[119] Smaller diameter CNTs undertake more ring strain as a result of radial breathing, which causes them to appear at higher wavenumbers.

The other important features on a CNT Raman spectrum are the G and D bands. The G band, which stands for graphene band, is a band that can be found in graphene as well as CNTs. In graphene the band is found at 1580 cm^{-1}, whereas in CNTs the band is generally split into two bands: G^+ at 1590 cm^{-1} and G^- at 1570 cm^{-1} (Figure 19b). The G^+ feature is sensitive towards doping of the SWNT and shifts downfield when electron donors are present, and upfield if acceptors are present.[120] The G^- feature is indicative of the m-SWNT content in a sample. If a sample possesses m-SWNTs, the G^- band will become unsymmetrical, broad and high in intensity, whereas in a semiconducting sample the G^- band is symmetrical and low in intensity.

The D band is a disorder induced feature that is found at 1360 cm^{-1}. The D band arises from sp^2 hybridized carbon atoms along the carbon nanotube. The D band is a great measure of the number of defects in the CNT, and its intensity reflects this. For a

pristine CNT sample, the D band will be very small, several orders of magnitude smaller than the G band. However, if the sample is modified through chemical means and contains many static defects, the D band can be on par with, or even surpass, the intensity of the G band. This makes the D band an excellent probe of CNT functionalization in reactions where covalent modification of CNTs is desired.

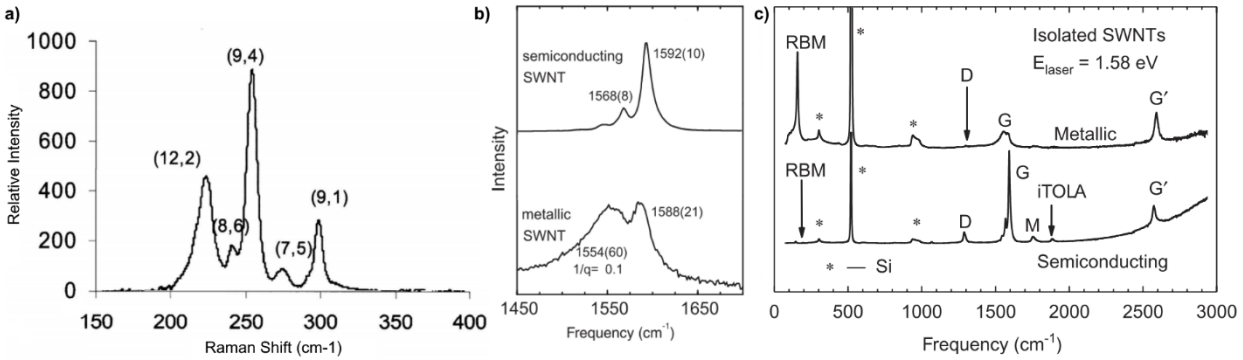

Figure 19: a) Radial breathing mode region of a Raman spectrum showing distinct SWNT signals.[117] **b) Close up on the G-Band of an isolated metallic (bottom) and semiconducting (top) SWNT.**[121] **c) Raman spectrum of an isolated metallic (top) and semiconducting (bottom) SWNT.**[118]

The Fermi level of SWNTs can be shifted through the application of an external magnetic field because the wavevector, $k_{\perp}$, is shifted at both K points, K_1 and K_2 (Figure 20). The shift in $k_{\perp}$, is in the same direction at each K point, and so the bandgap at one K point increases, while at the other it decreases. This effect causes the 1D subbands to no longer be degenerate and has the overall effect of decreasing the bandgap.

The effect of magnetic fields can be seen experimentally by constructing a CNTFET device. When the gate voltage (V_{GS}) is increased, a magnetic field is established, and the field increases in strength with increasing V_{GS}. When measuring the current across a s-SWNT, at 0 V_{GS}, only a small current is found, which corresponds to the natural s-SWNT

Fermi level. As the V_{GS} is increased, and the band gap decreases, more electrons populate the conduction band, and a significant increase in the current is observed. Through a negative bias applied across the gate electrode, the current can be decreased to 0 in s-SWNTs.[83] These characteristics make s-SWNTs excellent candidates for use in FETs.

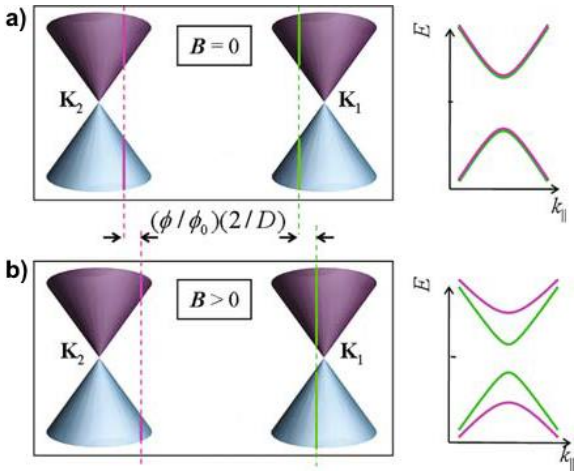

Figure 20: Relative positions of the allowed $k_{\perp}$ states and K points and the resulting 1D subbands of a semiconducting SWNT a) without and b) with an external magnetic field.[94]

However, despite having these great properties, the incorporation of s-SWNTs into FETs is not an easy task. Due to the variety of bandgaps that a mixture of SWNTs can have, the I_{DS}-V_{GS} characteristics of a device can vary wildly.[111] Additionally, if any m-SWNTs are included in the device, the current will be constantly flowing, even when the device should be in the off state, and, if enough of them are present it is impossible for the device to operate as a transistor. Even if all the m-SWTNs are completely removed, having varying bandgaps between the deposited s-SWNTs will cause a similar effect, whereby different transistors on the same device could have different V_{GS} at which they operate optimally. Such a system is untenable to use in commercial high-performance

logic devices as it would require each transistor to be individually tuned, resulting in astronomical cost and time to manufacture even a simple, fully functioning device.

While there remains a number of challenges with using CNTs, even silicon had its shortcomings in its earlier years, which were slowly improved upon until it became the ubiquitous material we know today. Many researchers have been and continue to find ways to improve purity, separation, alignment, and deposition of SWNTs to improve their performance. The state-of-the-art methods that are used for SWNT processing will be discussed later in this thesis.

1.3.2.3 Chemical Modification of Carbon Nanotubes

Another way to impact not only the electronic, but also physical properties of SWNTs, is through chemical modification. As previously mentioned, there are several types of defects that can be found along a CNT. Defects serve as high energy points along the carbon nanotube surface and represent areas for easy modification as aromaticity has already been broken at the defect sites. The functionalization of SWNTs can be done both covalently and non-covalently or by using different chemical linkers in order to modulate their properties.[99,122,123]

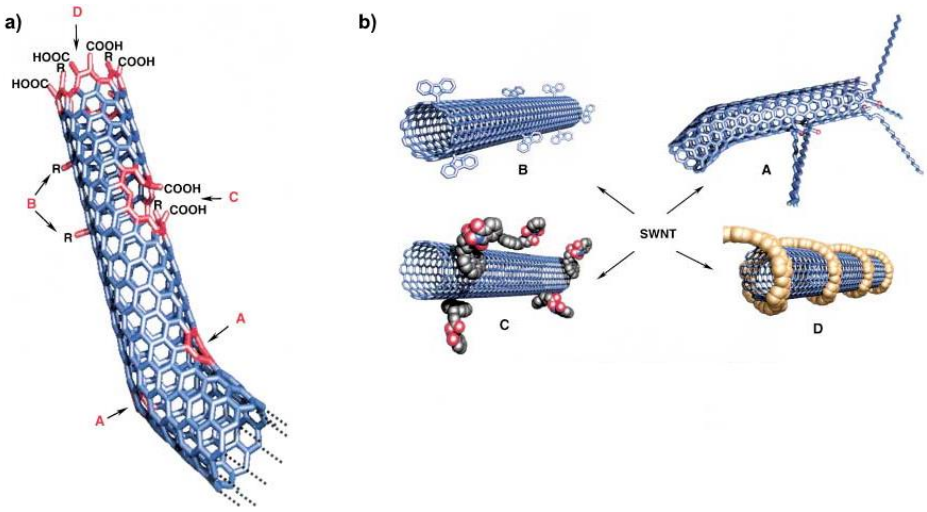

Figure 21: a) Typical SWNT defects: A) 5 and 7-membered rings, B) sp^3-hybridized defects, C) carboxylic acids from oxidative damage, and D) open end of the SWNT terminated with carboxylic acids. b) Functionalization routes for SWNTs: A) defect-group functionalization, B) covalent sidewall functionalization, C) noncovalent exohedral functionalization with surfactants, and D) noncovalent exohedral functionalization with polymers.[99]

Carbon nanotubes do not have perfectly intact endcaps at the ends of tubes, the ends usually contain catalyst particles leftover from their synthesis. Metal catalyst contamination is usually removed through acidic workup with strong oxidizing acids like nitric and sulfuric acid. Oxidative workup removes the metal catalysts but it also oxidizes the ends to pendant carboxylic acid groups.[124] Harsher conditions including heat or sonication in more concentrated acids can cause further oxidation of the CNT backbone through cleavage of C-C bonds, introducing carboxylic acid groups along the CNT.[125]

Carboxylic acid defects along the CNT act as starting points for further chemical modification through simple organic transformations. Carboxylic acids can be converted to acid chlorides with thionyl chloride which allows easy further modification with numerous nucleophiles. Acid chlorides can be converted to amines through a Wolff rearrangement,[126] amides through coupling with amines,[127] or esters through coupling

with alcohols.[128] Additional reactions used to covalently functionalize carbon nanotubes include cycloadditions,[129,130,131] radical addition,[132] as well as many others.

Covalent functionalization has been used to permanently alter the properties of SWNTs. The simplest use of covalent functionalization is to install solubilizing groups onto the SWNT sidewall, allowing for easy solvation of SWNTs in organic and aqueous solvents.[133] The solubilizing groups include carboxylic acids for enhanced water solubility, and esters with long alkyl chains for organic solvent solubility. Conjugation of SWNTs with other molecules of interest, such as fullerenes[134] and metal nanoparticles[135] has given rise to interesting materials. Aryl diazoniums can be used to selectively react with m-SWNTs and alter their electronics to make them s-SWNTs, improving the performance of CNTFETs post-fabrication.[136] The selectivity of this reaction arises from the existence of higher energy electronic states in MWNTs due to the absence of a band gap.[137]

Conversely, non-covalent modification of CNTs can also be desirable if reversibility is required. This type of modification generally takes advantage of the structure of CNTs, including their aromaticity and curvature. The most common methods are wrappings with polymers,[138,82] surfactants,[139,140] and adsorption of small molecules.[141,142]

One of the largest issues with CNTs is their poor solubility in all solvents. Due to strong π-π stacking interactions between CNTs and their long shape which allows for many such interactions to exist, CNTs tend to form bundles when dispersed in solvents. This prevents easy processing of CNTs and limits the types of techniques that can be used to purify them. Non-covalent modification has shown to be an excellent way to overcome this inherent drawback of CNTs as they can be covered in solubilizing

molecules that lead to individualization of the CNTs, without permanently affecting their properties.

Many types of wrappings have been reported to improve the solubility and individualization of carbon nanotubes. One of the most common ways this is accomplished is through the use of surfactants like sodium dodecylsulfate (SDS)[143] among others.[140] These allow for solubilization of CNTs in water, but generally do not have great individualization of the SWNTs.[139]

Polymers have also been used extensively in non-covalent CNT modification. Unlike surfactants, polymers can be easily modified for selective binding to different types of CNTs.[82,144,145] In general, conjugated polymers are used for the binding since they can undergo both van der Waals interactions and π-π stacking interactions with the nanotube. In addition to solubilization, they have also been used not only so solubilization of nanotubes, but also to sort different types of nanotubes to enrich samples.[145,146] However, many polymers are difficult to remove because they form too many interactions with the CNTs which lead to strong binding. The removability of polymer wrappings has been addressed for some polymer systems through chemical removal under specific, mild conditions, but this removal procedure is not broadly applicable.[147]

Small molecules can also be used to coat the surface of CNTs and are often easily removed unlike their polymeric counterparts. The problem with using small molecules arises from the fact that they can be removed too easily from the CNT surface due to their small size and therefore limited interactions with the nanotubes, contrary to polymers which are so large that sufficient interaction is nearly guaranteed. The most common types of molecules employed for this are polycyclic aromatic hydrocarbons (PAHs) since

they can produce significant π-π stacking interactions to allow them to remain on the CNT surface. Pyrene is a frequently used motif for this and is especially useful because pyrene is easily modified to include useful functional groups including alkanes, carboxylic acids, and amines among others.[148,149,150] More recently iptycenes have been used for this type of surface modification because their concave shape is complementary to the CNTs convex shape, improving the π-π stacking overlap.[151,152,153] Iptycenes that are based upon the reaction of acenes and imides are useful because they provide easy functionalization of the imide group.[153] Iptycenes have been used to selectively bind different sizes of CNTs and even for solubilization with functionalized iptycenes.[152,153]

The last major class of molecules that are used in CNT binding are biomolecules.[154,155,156] These molecules are especially important in that they allow CNTs to be used in many bionanotechnological applications including the sensing of biological markers. Due to their polyampholytic character, many proteins can bind directly to CNT surfaces without the need for pre-functionalization of the SWNT surface, or the protein residues. A carbon nanotube that has been coated with proteins can then be used to sense any molecules that bind to the protein, as the slight changes in conformation of the CNT can be sensed through changes in electrical conductivity along it.[157] Polysaccharides can also be used to selectively solubilize smaller diameter SWNTs.[158] Deoxyribonucleic acid (DNA) has been used extensively to wrap CNTs for solubilization[159] and even for purification using ion exchange chromatography in order to selectively enrich s-SWNT samples.[160]

Both covalent and non-covalent modification of CNTs can provide incredible opportunities for the modulation of CNT properties. The issue with CNT solubility can

easily be overcome through both types of modification, and the desirable properties of the pristine CNT can be kept intact if non-covalent functionalization is utilized.

1.3.2.4 Carbon Nanotube Based Field-Effect Transistors

The electronic properties of CNTs make them excellent candidates for use in field-effect transistors. For FETs, SWNTs are the only desirable type of CNT, because MWNTs are metallically conducting. CNTFETs can be created in three different ways: aligned arrays, single nanotubes, and random networks. Aligned arrays consist of many nanotubes that are aligned between the source and drain electrodes. They offer the highest potential charge carrier mobilities and current densities. Single nanotube FETs are largely used to probe the properties of individual chiralities of tubes and other aspects of the FET, like contact or substrate effects. Random networks of CNTs are easy to produce and consist of many CNTs placed down on a substrate with no control over their orientation. They have much lower charge carrier mobilities but are still very effective in flexible electronics and display applications, as well as in sensing applications.

For a semiconductor to be useful in high-performance transistor technologies, such as those used in computers, several benchmarks must be met. The first requirement is a high charge carrier mobility, in the range of silicon (~800 $cm^2\ V^{-1}\ s^{-1}$). The second requirement is a high on/off current ratio (I_{ON}/I_{OFF}), in the range of $>10^4$. Conversely, for a semiconductor to be useful in flexible electronics and displays, they only require a charge carrier mobility in the range of ~1 $cm^2\ V^{-1}\ s^{-1}$, or ~20 $cm^2\ V^{-1}\ s^{-1}$ when they are used in transparent electronics, but still require similar I_{ON}/I_{OFF}. The lower charge carrier mobility requirements are a function of the lower information bandwidth demand of displays and

current flexible electronic devices. As flexible electronics improve, the charge carrier mobilities will have to likewise increase to meet the demand.

As discussed in section 1.3.2.1, the I_{ON}/I_{OFF} of a given FET depends on the ratio of s-SWNTs to m-SWNTs in the device.[161] As the device has more m-SWNTs, there is a larger off-current and this leads to a lower ratio overall. The effect of m-SWNTs can be approximated by Equation (1) for aligned arrays of SWNTs.[111] This means that even for SWNT samples with 99% purity, the average I_{ON}/I_{OFF} will only be 100, which is still far too low for serious use. Furthermore, this only represents an average, meaning that many of the transistors created with such a starting mixture would be completely non-functioning. The drastic effect of m-SWNT contamination on the I_{ON}/I_{OFF} underscores the importance of using very highly enriched s-SWNT starting samples. Methods for generating enriched s-SWNTs will be covered in more detail further on.

$$\frac{1}{\frac{I_{ON}}{I_{OFF}}avg} = 1 - \frac{Purity\ in\ \%}{100} \quad (1)$$

Also discussed in section 1.3.2.1 was the effect of alignment on the charge carrier mobility of a resulting CNTFET. Random networks of SWNTs feature lower charge carrier mobilities in the range of 1 – 100 $cm^2\ V^{-1}\ s^{-1}$, while aligned arrays are in the range of 1,000 – 10,000 $cm^2\ V^{-1}\ s^{-1}$, and single nanotube transistors have been made with charge carrier mobilities that are even higher.[111,78] The charge carrier mobilities of the different configurations relegate random network CNTFETs to flexible electronics, displays, and transparent electronics applications, and allow only aligned arrays to be used in high-performance electronics.

Many interesting FET devices have been created with randomly distributed SWNT networks. Several OLED displays have been demonstrated that feature high I_{ON}/I_{OFF} with much higher charge carrier mobilities than standard solution-processed organic semiconductors.[162,163] Other interesting applications include the ability to create pressure sensors using SWNTs.[164] Due to their flexible nature, SWNTs have been used to create flexible CNTFETs,[98,70] flexible displays,[83] and can even be made through roll-to-roll printing processes.[12] While SWNTs are also stretchable, CNTFETs are not necessarily stretchable since the other components, especially the metal electrodes, are not themselves stretchable.

While CNTFETs generally focus on s-SWNTs, m-SWNTs can also be used in place of the typical metal electrodes. This has been done using SWNT-polymer composites[165] and can be used in flexible organic FETs.[166,167] The major advantage of using SWNTs over metals in these applications is that they can be made transparent and stretchable.[77]

1.3.2.5 Carbon Nanotube Based Sensors

The ability to detect minute amounts of harmful chemicals in an environment or chemicals in a living organism that are predictive for certain conditions are both highly sought after. For example, sensing trinitrotoluene (TNT) or other explosives is very important at airports and other high security areas and has been made possible through organic based chemisensors.[168] SWNTs are useful in these applications because they have a very high surface area which allows for binding to a large number of analyte molecules, and as previously discussed, they can undergo non-covalent surface binding, which allows for reversible binding of analytes. Sensors can operate in two main modes: FET and electrochemical.

Electrochemical sensors depend on catalyzing the reduction/oxidation (redox) of various chemicals of interest. This is done through adsorption of the analyte onto the CNT surface which then catalyzes the electrochemical transition under an externally applied bias. This technique has been used extensively in the sensing of many biomolecules including dopamine, uric acid, serotonin, biomarkers, proteins, DNA, and epinephrine.[86] The detection limits are in the range of 0.1 – 0.001 μM and can be measured using a variety of methods such as differential pulse voltammetry (DPV), cyclic voltammetry (CV), or amperometry. Other non-biological molecules can also be sensed in these types of devices, including hydrogen peroxide.[169] CNT electrochemical sensors can also be made with polymer/SWNT composites or other types of composites, increasing the detection limit and aiding the catalytic electrochemical reaction.[170]

FET sensors are based upon the inherent conductivity of CNTs and the minute changes that occur in the conductivity upon binding with other molecules. The most common way to create a sensor using this approach is to build a CNTFET and then subject the FET to known concentrations of an analyte and measure how the current changes, thus creating a calibration curve so that unknown concentrations can be determined. Using this type of sensor dopamine can be detected in concentrations as low as 0.001 fM.[171] FET-based sensors offer a wider range of application because the SWNT surface can be functionalized to selectively bind to specific molecules. A great example of this is in the case of binding proteins or antibodies directly to a SWNT allowing for detection of biological molecules that bind to them at very low concentrations.[172] Furthermore, the binding molecules do not have to be electrochemically active for them to be detected using this method, allowing CNTFET-sensors to detect molecules like

acetylene gas for ripening of fruits.[173] CNTFET-sensors are sensitive towards m-SWNT impurities because having m-SWNTs in the device increases the off-current. A higher off-current leads to a smaller relative change in current upon binding, resulting in lower detection limits and variability between different devices. For this reason, high purity s-SWNTs should be used.

1.3.2.6 Carbon Nanotube Based Photovoltaics

In the most basic sense, photovoltaic devices rely on absorbing photons to generate current. The photons that can be absorbed depend on the bandgap of the light-absorbing layers in the solar cell. The light is generally absorbed by either silicon in conventional solar cells, or a conjugated organic polymer in thin film, flexible solar cells. These light absorbing materials can absorb various wavelengths of light depending on their bandgaps, but SWNTs on the other hand can be incorporated to absorb infrared (IR) light, increasing the range of wavelengths that are converted to current. Furthermore, the high charge carrier mobility in SWNTs helps to improve charge separation and transport to the electrodes, further improving solar cell efficiency.

Many different types of SWNT-based photovoltaic devices have been produced to date.[174,175] Most of these devices use the SWNTs as a conductive channel to move the current throughout the material, however work in more recent years has focused on using CNTs as the active, light-absorbing, component in photovoltaics. One of the first examples coupled SWNTs as electron acceptors with poly(3-octylthiophene) as the donor, but resulted in poor PCEs of below 1%.[176] Often, the SWNTs are light-absorbing donor materials that are coupled with fullerene acceptor materials, either C_{60} or phenyl-C61-butyric acid methyl ester (PCBM).[177,178] Once again, however, SWNTs are plagued

with m-SWNT impurities, which lead to quenching of excitons and therefore a decrease in overall efficiency of the solar cells and poor PCEs.[175] As a result, the most prominent use of CNTs in photovoltaics is as the conductive electrodes.[179]

1.3.3 Synthesis and Purification of Single-Walled Carbon Nanotubes

As we have seen, that the purity of SWNTs is crucial for their use in nearly all their electronic applications. The synthesis of SWNTs is the source of their impure nature and many efforts have gone into modifying the synthetic methods to make them more selective, to great effect. Likewise, complimentary research has also gone into the purification and sorting of SWNTs post-synthesis in order to further enrich samples to the required high purities.

When SWNTs are synthesized, the resulting product is a mixture of carbon allotropes including SWNTs, MWNTs, fullerenes, graphene, graphite, and amorphous carbon, as well as catalyst impurities. The purity of the product is generally defined by the amount of the sample that contains the allotrope of interest, in this case SWNTs. However, even among the SWNTs there are many different structural parameters including length, diameter, and chirality that must be separated. Purifying the SWNTs from other forms of carbon is a simple process, but further sorting of SWNTs into, for example, m-SWNTs and s-SWNTs, requires more complex processes. For use in high-performance electronic devices, s-SWNT purities well above 99% are required, so scalable and highly selective sorting methods must be developed, both at the synthesis and post-synthesis stage.

Herein, we will discuss the different synthetic methods for making SWNTs and several improvements on those methods, as well as the various post-synthetic sorting methods that are available. The discussion will be limited to the three most prevalent

methods for SWNT synthesis: chemical vapour deposition, arc-discharge, and laser ablation. Also, only several of the most common methods for post-synthesis purification and sorting will be touched upon. The largest emphasis will be placed on the most prevalent techniques.

1.3.3.1 Chemical Vapour Deposition

The most common method for synthesizing carbon nanotubes is chemical vapour deposition (CVD). CVD is simpler, more cost-effective, and produces cleaner CNTs than both arc discharge and laser ablation.[180] A typical CVD setup consists of a tube furnace, an inlet, an outlet, and a holder for the substrate and metal catalysts. A carrier gas (argon or helium), is used to carry both a reducing agent (hydrogen), and a carbon feedstock (carbon monoxide, alcohols, or hydrocarbons) into the tube furnace which is heated at 350 – 1200 °C, resulting in deposition of carbon atoms on the metal catalysts and further reaction to form CNTs. However, the specifics of how the synthesis is performed can have drastic effects on the resulting purity of SWNTs. The most common parameters that are adjusted include the temperature of the chamber, the type of carbon feedstock, the type of metal catalyst, and nature of the growing substrate.

Despite much research, the exact mechanism for carbon nanotube growth in CVD synthesis is still debated. The two prevalent mechanisms are vapour-liquid-solid (VLS) and vapour-solid-solid (VSS). In VLS, the carbon feedstock adsorbs onto the metal catalyst particle which aids in its breakdown into carbon atoms. The carbon then dissolves into the metal particle to form a carbide which diffuses within the metal particle. Finally, solid carbon diffuses to the edge of the metal particle and precipitates onto the surface to begin CNT growth. In VSS, the carbon feedstock first breaks down at the high chambers

temperatures before being adsorbed and diffusing into the metal particle. Finally, the carbon atoms precipitate onto the surface to take part in carbon nanotube growth.[181]

Temperature is one of the easiest to control and most important variables in the synthesis of SWNTs by CVD. The starkest effect of temperature is on MWNT vs SWNT selectivity. At low temperatures MWNTs are favoured, whereas at temperatures as high as 1200 °C SWNTs are heavily favoured and sometimes are nearly exclusively formed depending on other conditions. It is believed that this selectivity comes from a higher energy of formation required to synthesize SWNTs due to their smaller diameters leading to higher strain energies.[180] High temperature CVD has been used to produce SWNTs with over 90% s-SWNT content reliably.[182,183]

The nature of the carbon source is also important in determining the resulting purity and growth rate of the SWNTs, as well as the catalyst lifetime. The most commonly used carbon sources are methane, acetylene, ethane, benzene, ethylene, xylene, carbon monoxide, isobutane, and ethanol.[180] The carbon source chiefly affects the curvature of the nanotube, with linear hydrocarbons tending to form straight, hollow CNTs, whereas cyclic hydrocarbons lead to curved nanotubes. Due to the higher energy of SWNTs relative to MWNTs, SWNTs are more easily synthesized using a carbon feedstock that is more stable at high temperatures. This means that feedstocks like methane and carbon monoxide are historically more often used to make SWNTs, because feedstocks like benzene tend to decompose into other carbonaceous compounds before they can reach a sufficient temperature to form SWNTs, giving a highly impure product. The exception to this rule is ethanol, which since its first use to synthesize SWNTs has become the preferred method for global SWNT production.[184] During the decomposition process,

ethanol releases hydroxide radicals which etch other carbonaceous byproducts and give a largely pure SWNT sample.[185]

SWNTs cannot be grown in any meaningful quantities in CVD without the use of a catalyst. If catalysts are absent, CVD conditions can still produce MWNTs but also result in substantial amounts of other carbon decomposition products. The metal catalyst particles act as nucleation sites for the decomposition of the carbon feedstock and the growth of SWNTs. To produce SWNTs nanometer sized metal particles are generally required, with larger nanoparticles that measure in the tens of nanometers favouring MWNT formation. Transition metals are often used as the catalysts in the CVD synthesis of CNTs, with iron, cobalt, and nickel being the most commonly used.[180] This is because carbon has a high solubility and diffusion rate in these materials at high temperature and it is believed that diffusion is a key step in the mechanism for the formation of SWNTs. Other transition metals have also been extensively employed including molybdenum, copper, and indium, among others.

At first glance, the substrate for CNT growth may not appear to be very important for the resulting purity and selectivity of the CNT products, but the material of the substrate and its surface morphology can have serious affects on the final product. Commonly utilized substrates for SWNT growth include silicon, graphite, quartz, zeolite, and many others. The substrate is not simply a stage which the catalyst nanoparticles are mounted, but rather it can directly impact the resulting CNT product quality. The substrate-catalyst interaction plays a large role in preventing catalyst particle migration and growth during the CVD process, resulting in a narrower distribution of resulting SWNT diameters. Some researchers believe that the oxide substrate may actively be participating in the catalytic

cycle of CNT formation, giving the substrate an even more important role in the overall process. A good representation of the effect that substrates can have can be seen in the work of Chai et. al.[186] in which they tested the efficacy of a cobalt oxide (CoO) catalyst on various substrates at 700 °C and found that the amount of product was severely impacted with alumina producing the most and magnesia producing the least. Further studies show that using the same conditions, molybdenum and iron catalysts produce no product on silica. ST-cut quartz is even capable of growing aligned arrays of CNTs directly on the surface.[187]

So far, the effects that have been discussed only affect the purity of the SWNTs or their tendency to prefer s-SWNT formation over m-SWNT formation, but some systems have been found that preferentially synthesize specific chiralities of SWNTs. (6,5) SWNTs can be selectively produced in high amounts (45%), while the other SWNTs formed in this process are 88% s-SWNTs as well.[188]

Several recent examples have been shown that single CNTs can be used as seeds to grow CNTs of the same chirality. The approach relies on starting with a pure sample, or a single CNT, and growing them in CVD. The newly elongated CNTs are then cut with sonication to increase the number of tubes and decrease their length. The newly cut nanotubes are then subjected to CVD growth again, and the process is repeated.[189] The main problem with this approach is that it requires starting with a pure sample, which can only be purified in small amounts, and grows the pure material at a very slow pace and at a high cost.

CVD is the most widely used method to produce SWNTs on a large scale.[190,191] This is largely due to easy scalability relative to the other methods, and the cheaper

construction and operation of the machinery. Furthermore, CVD is very customizable through the factors listed above, and has resulted in fairly high selectivity and purity of SWNT products. Perhaps the largest drawback of CVD is the incorporation of metallic catalyst contaminations into the resulting SWNTs, which can have serious ramifications in terms of their electronic semiconducting properties and require harsh conditions to remove (Section 1.3.2.3). Thermogravimetric analysis (TGA) of CVD produced SWNTs show residual catalyst as high as 5 percent by weight (wt%) in “super pure” commercial SWNT samples.[192] Despite this, CVD remains the best method for SWNT synthesis.

1.3.3.2 Arc Discharge

Another method that is commonly used to produce SWNTs is arc discharge.[193] Arc discharge (AD) is a low yield, high cost method for SWNT production, but it does have the boon of producing very structurally sound SWNTs with a low number of defects. Despite the prevalence of CVD in large-scale SWNT production, arc discharge systems are also used heavily in both industry and in research labs.

An arc discharge apparatus consists of an anode, a cathode, and a direct current (DC) power supply in a steel chamber. The anode and cathode are generally graphitic carbon and are held at a known distance from one another. The DC power supply supplies a strong current between the two electrodes and they are brought closer together until an inert gas plasma arcs between them, under a low pressure. In this process, the anode is consumed and under the high plasma temperatures (>1700 °C), carbonaceous materials form on the cathode, including CNTs, graphene, fullerenes, and amorphous carbon. The process can be modified to selectively synthesize the different products by adding

catalysts to the electrodes, altering the current/voltage, and changing the carbon source or atmosphere.[194]

The current that is generated between the two electrodes is the main component that allows for the formation of carbon nanomaterials by AD. The most common method of generating the current is through a DC power supply, accounting for almost 90% of all published AD-mediated carbon nanotube synthesis papers. Alternating current (AC) is used very infrequently and results in the deposition of the resulting carbon nanomaterials on the chamber walls instead of on the graphitic cathode, a phenomenon which appears to still be unexplained. The typical range for voltage applied between the electrodes is 15 – 30 V, and must be kept constant to create a stable plasma. The current is generally also fixed to be in the range of 50 – 100 A, but can dip into the teens or go as high as several hundred.[195]

Just like with CVD, arc discharge requires the use of metal catalysts to synthesize SWNTs but not MWNTs. The metals that are used for AD include both single metals and composites, and span across much of the transition metals. The most commonly used metals are iron, nickel, and cobalt, just as in CVD. [194,195] Arc discharge tends to form more MWNTs than CVD which makes catalyst choice very important if the desired product is SWNTs. Due to advancements in AD synthesis, SWNT production can be favoured in AD, but further selectivity, such as diameter or semiconducting vs. metallic tube formation are still being researched. For example, bimetallic nickel catalyst systems were probed for SWNT formation and the concentration of the other metal could be tuned to select for specific SWNT diameters. Fe-W prepared SWNTs are 0.5 nm smaller in diameter than those prepared with just Fe. By introducing CO_2 into the AD system, a plasma is formed

that is capable of selectively etching m-SWNTs, removing them from the resulting product preferentially. Through this method, SWNT samples with ~90% s-SWNT have been produced, as measured by Raman and UV-Vis.[196]

Once again, the carbon source also affects the type of CNTs that are formed as well as their purity. By far the most common source of carbon used in AD is graphite, as it is available in high purities and has excellent conductivity. The problem is that it carries with it a high cost, due to the purity and requirement of catalyst doping. The remainder of carbon sources make up as little as 12% of published AD CNT synthesis papers.[195] Carbon black and coal have been used as carbon sources due to their abundance and low price, but they tend to have far more amorphous carbon impurities and are not ideal at synthesizing SWNTs.

Despite its drawbacks, arc discharge is still popular. With all the advancements that have gone into AD, selectivity in producing s-SWNTs and even preferential diameter synthesis is possible, but the overall purity and uniform synthesis of SWNTs remains a challenge. The biggest advantage that AD has is the production of low-defect nanotubes due to the high defect CNTs being destroyed by reaction with the plasma. However, the cost of running the apparatus at high vacuum and current still inhibits its widespread use.

1.3.3.3 Laser Ablation

The least commonly used of the three main methods for nanotube synthesis is laser ablation (LA). Laser ablation is similar to AD in that a carbon source is targeted with an extremely powerful source of energy, which ultimately yields the desired CNTs. The invention of LA was a direct response to the poor performance of AD methods for synthesizing CNTs.[197] Early LA was capable of synthesizing SWNTs with 90% purity,

making it a very attractive technique.[198] The main problem with it, however, is the high cost and the poor scalability of the method, which have largely left it abandoned in favour of CVD.

A laser ablation setup consists of a furnace, a powerful laser, a graphitic carbon source, a carrier gas, and a water-cooled collector. The furnace chamber is heated, and the laser is then used to focus on the carbon source. The resulting energy causes degradation and evaporation of various carbon species which are carried along the furnace by the carrier gas. The carbon species are then deposited onto a cooled collection site where they react to form carbon nanotubes.[198]

Once again, a catalyst is required for SWNT production, whereas MWNTs are synthesized even in the absence of any metallic catalyst. The SWNTs that are synthesized with LA are typically of higher purity than those obtained from AD. The effective catalysts are the same, with nickel and cobalt being the most used monometallic catalysts and Co/Ni, or Ni/Y bimetallic catalysts also being frequently employed.[195]

Selectivity in resultant SWNT product diameter, chirality, and electronics are very poor when using the LA method. In fact, the most commonly formed nanotubes in laser ablation tend to be (10, 10) m-SWNTs, with about 70% of the overall SWNT mixture being m-SWNTs.[199] Some changes to the synthesis have given rise to increased yields of s-SWNTs, but only to values of around 55%.[200] The diameter of LA-produced SWNTs is largely focused around ~1.36 nm due to the high prevalence of (10, 10) SWNTs. Some researchers have found ways to modulate the diameter of the produced SWNTs, with a simple decrease in the temperature of the reaction chamber causing a similar decrease in the SWNT diameter, albeit at drastically reduced yields.[201]

While laser ablation appeared as a great alternative to AD initially, it has been completely eclipsed by the massive success of CVD. The problems with LA are similar to AD, high cost and poor scalability as LA systems must be run under vacuum and simultaneously at extremely high temperatures, making operation costly, especially when attempting to scale up. Furthermore, the operation of LA results in the consumption of the carbon source, preventing continuous operation.

1.3.3.4 Sorting Metallic and Semiconducting Single-Walled Carbon Nanotubes

The need for purely semiconducting SWNT products is apparent when looking to incorporate CNTs into various electronic devices. As we have seen, CVD allows for some good selectivity when producing SWNT, with synthetic selectivity as high as ~90% s-SWNTs. However, this is still far from being useable in many applications and must be further improved post-synthesis if SWNTs are to be seriously considered as candidates for semiconducting technologies. To this end, many methods have been used in an attempt to separate metallic and semiconducting nanotubes, since their discovery.

Generally, when looking to separate two different chemicals, one must find a property that is different between the two and find a method that can exploit that property. For example, distillation allows for the purification of materials with different boiling points, and silica-gel chromatography allows for separation based on polarity. When looking to extend these ideas to SWNTs, the obvious issue is the similarity in all types of CNTs. All CNTs are comprised of only sp^2-hybridized carbon atoms, boiling does not occur at a reasonable temperature, they lack any serious dipole moments, they have very similar shapes and diameters spanning only a few nanometers, and their lengths are not dependent on any of their other properties.

The most obvious difference between the types of SWNTs is their electronic character, especially when contrasting s-SWNTs and m-SWNTS. The separation of metallic and semiconducting SWNTs should therefore be significantly easier to exploit than sorting based on size or chirality. The difference between m-SWNTs and s-SWNTs manifests itself in a few ways: reactivity, affinity for charges, and their behaviour in an external electromagnetic field.

When comparing the band structure of m-SWNTs and s-SWNTs, the most obvious difference is the absence of a bandgap in the m-SWNTs. The lack of a bandgap means that there exists some non-zero density of states at the Fermi level and directly above and below it. On the other hand, in a s-SWNT the conduction and valence bands are some distance away from the Fermi level. This is extremely important when considering the reactivity of the two with various chemical reagents. If, for example, an incoming reactive molecule is looking to react with a SWNT, the m-SWNTs will provide lower energy states that can accept an electron, and therefore will reduce faster than their semiconducting counterparts. This is exactly the type of reactivity that has been taken advantage of for the enrichment of s-SWNTs.

Among the first chemicals found to react preferentially with m-SWNTs were diazonium salts, in particular 4-bromobenzenediazonium tetrafluoroborate. It was shown that this molecule could, under dilute conditions, react selectively with m-SWNTs, installing an aryl group onto the SWNT sidewall and generating a radical cation SWNT.[132,137] The reaction was observed via UV-VIS spectroscopy and a decrease in the M_{11} bands was seen.[202] Likewise, a scan of the Raman RBM region showed a complete disappearance of the m-SWNT signals, but with retention of the s-SWNTs. The

disappearance of the optical m-SWNT peaks does not mean that they have been removed from the mixture, only that they have had their optical properties altered. The reaction can be reversed when subjected to high heat (300 °C) to give the original CNT RBM Raman spectrum, proving that the reaction can return unaltered SWNTs.[137]

The selective aryl diazonium reaction was exploited by An et. al to create a CNTFET by first building a device with randomly oriented SWNTs containing both m-SWNTs and s-SWNTs.[136] The device was then subjected to repeated reaction with the aryl diazonium, and the off-current dropped drastically, as low as 74% of its original value, while the on-current only dropped by 14%. This preference for m-SWNTs allowed them to create devices with high I_{ON}/I_{OFF} (10^4 – 10^5), however the reaction of the s-SWNTs with the diazonium species seemed to have resulted in a lower charge carrier mobility than expected. Other etchants including methane plasma have also been used to selectively destroy the metallic nature of m-SWNTs.[203] Plasma hydrocarbonation can also be done post-CNTFET fabrication and selectively etches m-SWNTs as well as larger diameter s-SWNTS, leaving a preferential diameter distribution of 1.3 – 1.6 nm.[204]

Selective chemical destruction of m-SWNTs is interesting as it allows for retroactive purification of CNTFETs, it can easily be scaled up with little to no problem, and it is reversible under high temperature conditions. The main issue with the technique is that it is not completely selective, resulting in the decomposition of s-SWNTs as well as m-SWNTs. Destruction of s-SWNTs makes this method significantly weaker in terms of creating an ideal s-SWNT mixture. In fact, it is possible that the extent of s-SWNT reaction is under sampled by optical techniques since they only observe the relative levels of s-SWNTs to m-SWNTs, so even if the m-SWNT peak decreases significantly, the s-SWNTs

may still be lost in the reaction but to a lesser extent. This could be the reason for the diminished nature of the charge carrier mobility seen in the previous example. Finally, selective chemical destruction is not directly a purification method, it simply destroys the m-SWNTS, but the destroyed nanotubes still contaminate the sample. For real purification, chemical modification should be coupled with a purification procedure that can discriminate between modified and unmodified nanotubes.

The dielectric constant difference between semiconducting and metallic SWNTs has been another aspect that has been exploited for their separation. It has been theoretically predicted that s-SWNTs should have a dielectric constant on the order of 5 ε_0 (vacuum permittivity), with m-SWNTs on the order of 1000 ε_0. The dielectric constant of water, and sodium dodecyl sulfate solutions in water, are on the order of ~80 ε_0.[205] Since SWNTs can be solvated through sonication in SDS, and the different types of SWNTs fall on either side of the dielectric constant of SDS solutions, it allows for them to be moved differently under an electric field while in such a solution.

This has been exploited by creating a dielectrophoretic system of SDS suspended SWNTs.[206] When an electric field is generated, the m-SWNTs migrate to the electrodes, leaving the s-SWNTs behind with some m-SWNTs. The Raman spectra of the m-SWNTs produced in this way show a significant reduction in s-SWNTs, sometimes to the point of complete exclusion by Raman. However, this is not a very feasible purification method for SWNTs, due to the fact that it is limited to extremely small (picogram) scale and while it purifies m-SWNTs very well, the remaining s-SWNTs are only partly rid of m-SWNTs.

The electrical conductivity of m-SWNTs can be further exploited by subjecting them to extreme currents, resulting in their heating and ultimately selective destruction.[207] To

prevent the s-SWNTs from meeting a similar fate, a gate voltage is applied that turns off conduction in the s-SWNTs. This has been used to great effect in improving the I_{ON}/I_{OFF} of CNTFETs post-fabrication by two orders of magnitude.[208] This is useful in devices that have a very low density of SWNTs, but as the density increases, m-SWNTs begin to overlap with s-SWNTs and as they are heated, they also heat neighbouring s-SWNTS, causing them to breakdown as well. The resulting effect is a sub-par charge carrier mobility of ~75 $cm^2\ V^{-1}\ s^{-1}$.[209]

A way to prevent the destruction of neighbouring CNTs is to prevent their contact and decrease the heat. These two can both be accomplished using what has been dubbed thermocapillary-enabled purification (TcEP).[210] This method begins with a low density SWNT film on a silicon oxide substrate between two electrodes which is then coated with a molecular resist, in this case α,α,α'-tris(4-hydroxyphenyl)-1-ethyl-4-isopropylbenzene. Next, the m-SWNTs are selectively heated through electrical current, which changes the viscosity of the resist and causes it to move away from the m-SWNTs, creating channels around the m-SWNTs. Then, an oxygen plasma is used to etch away the exposed m-SWNTs and finally, the photoresist is removed. Devices made this way have shown excellent selectivity with over 99.9925% s-SWNT purity, I_{ON}/I_{OFF} in the range of $10^3 – 10^6$, and $\mu > 1000\ cm^2\ V^{-1}\ s^{-1}$.[211] The major drawback in this method is the requirement of a sparse CNT array that is already perfectly aligned between the electrodes, because the channels that are created around m-SWNTs in this method are on the order of 300 nm, meaning any s-SWNTs within 300 nm of an m-SWNT are also removed with this method. However, this can be overcome if this method is coupled with another technique that can provide a sufficiently high starting s-SWNT content.

Chromatographic techniques are, somewhat surprisingly, very good at separating metallic and semiconducting SWNTs. The earliest example of chromatographic SWNT sorting is through the use of ion exchange chromatography (IEX).[212] In the seminal publication, SWNTs were first suspended in an aqueous solution through wrapping with single-stranded DNA. The DNA-SWNTs were subsequently subjected to anionic IEX and separate based on their metallic or semiconducting properties. It is believed that the m-SWNTs elute first on the column because they are far more polarizable than their s-SWNT counterparts, allowing them to effectively screen the negative charges of the DNA phosphate groups, reducing interactions with the stationary phase. However, IEX itself is not exceptional at SWNT sorting and results in maximum ~90% s-SWNT selectivity.[160]

Seeing that IEX was a viable method for SWNT sorting, other chromatographic techniques were developed. The most prominent is the use of SDS eluent on an ally dextran-based size-exclusion gel.[213] Similar to the IEX, m-SWNTs elute much faster than s-SWNTs, likely due to a far greater extent of coating by the SDS surfactant on the m-SWNTs. The s-SWNTs obtained from this method can be cycled and can ultimately give s-SWNTs in purities above 99.9%. Gel chromatography can even be further expanded to sort SWNTs by diameter and even chirality, as will be discussed in the next section. While gel chromatography gives excellent separation of s-SWNTs from a mixture of SWNTs, it requires several cycles to produce high purities.

The last technique to discuss is ultracentrifugation, a technique that is used heavily in the separation of biological and biochemical matter. It relies on a very fast spinning centrifuge to produce a separation based on the density of the materials that are placed inside of a centrifuge tube. When typical biological ultracentrifugation conditions are used,

a constant density medium is used to separate the materials. Unfortunately, for SWNTs this has the problem of convoluting multiple parameters, like diameter and length. This technique can, however, effectively be used to separate bundled SWNTs from individualized SWNTs due to the significant density difference. To be able to get good separation between s-SWNTs and m-SWNTs, polymers that selectively bind to one type over the other must be used. Many polymers have been used for this application, and typically are conjugated polymers.[144,145,214] The selection of polymer can improve the selectivity with some methods showing no remaining m-SWNTs by Raman spectroscopy. Further advancements to ultracentrifugation sorting methods has been made but will be discussed further in the next section. The largest drawback of the method is its small-scale purification, but it does have the benefit of being able to be iterated upon for more rigid purification.

Clearly there is no shortage of methodologies for separating s-SWNTs from m-SWNTs. While some are superior when in terms of purity, others benefit from ease of use and scale. The most optimal way to get highly pure s-SWNTs seems to be to take a sample of already enriched s-SWNTs from a CVD-based synthesis and subjecting it to further purification using one of these methods. If enough purification can be done in this way, then perhaps TcEP or another post-CNTFET fabrication technique can be applied to yield highly effective CNTFETs.

1.3.3.5 Sorting by Diameter or Chirality

No matter how high of a s-SWNT purity that the previously mentioned techniques can obtain, the problem of diameter and chirality sorting remains a roadblock to truly outstanding CNTFET performance. Che et al. made 38 transistors of a single SWNT

bridging two electrodes and measured the transfer characteristics.[161] What was noticed was that among the various s-SWNT transistors they saw largely similar on-off current ratios, but the threshold voltages varied across as much as 20 V. Such a staggering number speaks to the drastic electronic differences even among semiconducting SWNTs. For a proper integrated circuit to be built from SWNTs, millions, if not billions, of such transistors will have to be operating in unison. This cannot be achieved easily if each transistor operates at a different bias, because then each transistor on each integrated circuit will have to be individually probed, making the overall process prohibitively time consuming. To get to the final goal of high-performance CNT-based electronics, purification must go above sorting between s-SWNTs and m-SWNTs, it must also be able to distinguish between diameters and chiralities so that uniform bandgap materials can be made.

Based on Kataura plots, the diameter distribution of s-SWNTs is the number one predictor of their bandgap. Therefore, using a technique that is capable of sorting CNTs based on their diameter should allow for significant refinement of the threshold voltage for CNT-based electronics. As we have seen already, many techniques can be used to sort s-SWNTs from m-SWNTS by taking advantage of the key differences in their interactions with electric charges. However, finding a way to discriminate between different diameters and chiralities of s-SWNTs, which have very similar electronic properties, and only minute differences in diameter, is very difficult. Despite this difficulty, researchers have continued to search for good ways to achieve this, both by expanding upon previous techniques and trying to find new techniques altogether.

It has been shown to be possible to extend gel chromatography to the selection of s-SWNTs based on their diameter by simply increasing the number of columns. This has been useful for selecting nanotubes with diameters lower than 1.4 nm.[213] Alternatively, by combining both IEX and size exclusion gel chromatography in sequence, narrow diameter and even chirality distributions can be obtained. In fact, this method is capable of separating (9, 1) and (6, 5) SWNTs, both of which possess the same diameter.[215] This combinatorial method is great for smaller nanotube (<1.2 nm) but seems to fail at larger diameters despite some effort. Inherently this method still suffers the same drawbacks as discussed previously, but to an even greater extent as it requires even longer columns, taking more time and producing even smaller amounts of product.

Ultracentrifugation can also be improved upon to sort SWNTs based on diameter by using density gradient ultracentrifugation (DGU).[216] In standard ultracentrifugation, the sample of interest is placed in a medium of static density, and then centrifuged to separate materials based on where they fall relative to the medium. In DGU, the wrapped SWNT sample is placed into a medium with a density gradient, such that when the tube is placed into the ultracentrifuge, the SWNT sample is separated throughout the density gradient, allowing for small differences in SWNT density to be discriminated against. Through the use of DGU, s-SWNT purities of 99.9% are obtainable, but more importantly, individual chiralities and diameters are separated as well. The different nanotubes are then removed by syringe from the centrifuge tube and purified from the medium. The separation is easily visualized as the different chiralities of nanotubes appear as different coloured bands, due to their distinct bandgaps. DGU is a great method for sorting SWNTs of different diameters, but it still suffers from the small scale and heavy processing required.

The final method for diameter and chirality enrichment of SWNTs is complexation to π-concave molecules.[217] Sometimes called molecular tweezers, this class of molecules forms particularly strong interactions with SWNTs due to their complimentary size, shape, and ability to form π-π interactions. Early examples include the complexation of iptycene derivatives, allowing for the selective solubilization of certain diameters of SWNTs. It is predicted that by changing the size of the iptycene tweezer that the selectivity should change. More recent examples include the use of chiral, porphyrin based molecular tweezers, which have been capable of selectively binding to SWNTs based on chirality, diameter, and even roll-up angle. These methods are excellent, dependant on if the molecular tweezer can be easily synthesized and/or reused, as it enables SWNTs to be sorted on a larger scale due to the ease of scaling solution processes.

1.3.4 Summary of Carbon Nanotube Based Electronics

Carbon nanotubes have been a topic of intense research for decades now and the progress that has been made towards their application is staggering. However, when compared to other similar materials that emerged around the same time, CNTs seem to suffer from many more roadblocks. While CNTs have excellent inherent electronic properties, they require a high level of purification in order for those properties to be realized. However, CNTs can still be incorporated into many electronic devices with little issue thanks to the advances that have been made in cleaner synthesis and purification.

Other technologies that tend to compete with SWNTs are semiconducting organics and inorganic semiconductors, like silicon. These two alternatives are used for vastly different applications than one another, whereas SWNTs can be used in place of both. For example, semiconducting organic polymers are incapable of ever achieving the

charge carrier mobilities that are required for use in computers, but they are great when used in flexible electronics, or photovoltaics. Silicon is the gold standard of transistor technology but fails when it comes to flexible electronics and is ill-suited for use in solar cells, despite its widespread current use. SWNTs can be seen as a replacement for both sides of the spectrum: high performance transistor technologies that require high charge carrier mobility, and lower performance flexible electronics, as well as everything in between. Their inherent properties make them the perfect candidate to replace nearly all other semiconducting technologies but are currently held back by their demanding purification.

1.4 Fullerenes

In 1985, the first carbon nanomaterials, fullerenes, were discovered,[218] which was punctuated with a Nobel Prize in 1996 awarded to the founders. Fullerenes kickstarted the now massive field of nanotechnology and garner interest to this day due to their electronic and optical properties. They share many similar traits to their carbon nanotube cousins, with some referring to CNTs as a subset of the fullerene family. Fullerenes are roughly spherical or ellipsoidal in shape and comprise entirely of sp^2-hybridized carbon atoms, much like CNTs. However, fullerenes lack the 1D shape of CNTs, and so they possess a localized electronic structure described by HOMOs and LUMOs instead of conduction and valence bands. As such, fullerenes have poor solubility in many solvents, and possess similar electronic properties to CNTs due to their extensive π-conjugation. However, fullerenes experience low intermolecular interactions with other fullerenes making them somewhat soluble in aromatic solvents like toluene and chlorinated aromatics.[219] Fullerenes exist with different shapes, sizes, and physical properties.

The most stable member of the fullerene family is the spherical C_{60}, also called Buckminsterfullerene,[220] from which the family gets its name. The molecule was named after the famous American architect Richard Buckminster Fuller, who was known for his geodesic dome structures. The second most commonly found fullerene synthesized by traditional methods is C_{70}. Unlike C_{60}, C_{70} is ellipsoidal in shape and has two very distinct regions, the curved ends and the flatter middle. Higher fullerenes, that is those with a higher number of carbon atoms, also exist but are made in far smaller quantities by most contemporary methods, and can exist in spherical and ellipsoidal shapes (Figure 22). Furthermore, some of the higher fullerenes can be chiral, and even exist in many different isomers.

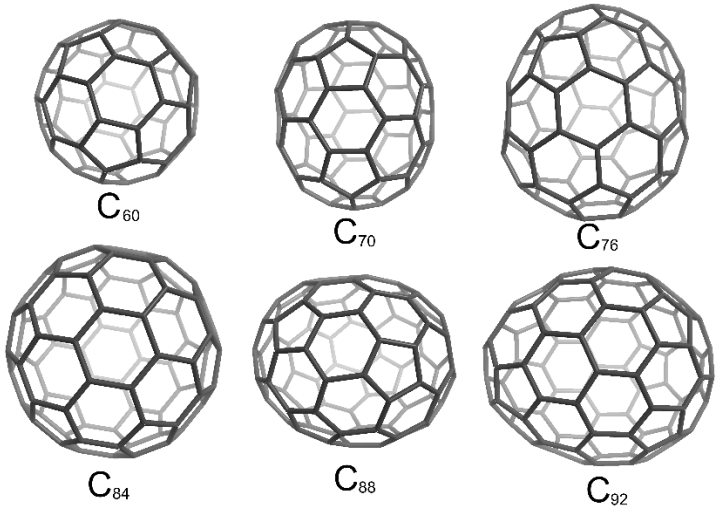

Figure 22: Fullerenes sized C_{60} to C_{92} showing only one isomer of each.

In this section we will be discussing the many properties, types, and applications of fullerenes. We will begin by giving a more in-depth discussion about the two main types of fullerenes and a general overview of the higher fullerenes and endohedral fullerenes.

We will then discuss the most common synthesis methods and purification techniques. Finally, an overview of fullerene-based applications will round out the section.

1.4.1 Types of Fullerenes

1.4.1.1 Buckminsterfullerene – C_{60}

Harold Kroto, Richard Smalley, and Robery Curl were awarded the 1996 Nobel Prize in Chemistry for their synthesis and identification of C_{60} as Buckminsterfullerene. The molecule is spherical in shape with a diameter of about 7 Å and is comprised of contiguous sp^2-hybridized carbon atoms. It shares a shape with common soccer balls, in that the carbon atoms are arranged in pentagons surrounded on each side by hexagons. Every carbon atom in C_{60} is identical,[221] but the bond lengths are not. Bonds between two six-membered rings ([6, 6]) are 139.1 pm, whereas those between a five and six-membered ring ([5, 6]) are 145.5 pm. This bond length difference alludes to the lower double bond character of [5, 6] bonds than [6, 6] bonds, and the lower aromatic character of fullerenes relative to graphene. This is further exemplified by the increased pryamidization angle and s-character of the sp^2-hybridized orbitals in fullerene.[222,223]

C_{60} was first synthesized using a high-power laser targeted at a graphite disk in a helium environment.[218] However, this simple procedure results in the formation of a black soot, similar to that of activated carbon. The researchers coupled the outlet of the reactor to a time-of-flight (TOF) mass spectrometer (MS) and were able to monitor the formation of C_{60} in real time, as the pressure of helium in the chamber was increased. The methods used to synthesize fullerenes will be discussed more in detail in a following section.

The electronic structure of C_{60} is interesting in that it possesses 60 π-electrons, a triply degenerate LUMO, and a quintuply degenerate HOMO (Figure 23).[223] The LUMO

of C_{60} is very low-lying, making it a great candidate for reduction, and its electrochemistry has been studied extensively. Due to the triply degenerate LUMO, C_{60} is capable of accepting six electrons to form the charged C_{60}^{6-} fulleride, as well as all the other fullerides in between. Electrochemical reduction occurs in toluene-acetonitrile at -10 °C, starting with a first reduction potential ($E_{1/2}$) at -0.98 V, followed by -1.37 V, -1.87 V, -2.35 V, -2.85 V, and -3.26 V vs ferrocene (Fc/Fc^+). All anions are stable, and the reductions are reversible on the time-scale of the experiment.[224] While C_{60} is excellent as an electron acceptor, it is a very poor electron donor and requires a high bias to be oxidized to C_{60}^+. The first oxidation occurs at +1.26 V vs Fc/Fc^+, giving a HOMO-LUMO gap of 2.32 eV for C_{60}.[225] It is important to note that these redox values are highly dependant on solvent and can shift by as much as 0.2 V.[224]

The HOMO-LUMO gap of C_{60} coincides with a green light absorbance (Figure 23) which makes a fullerene solution appear pink in colour due to the absorbance maximum around 540 nm with decreased absorbance in the blue and red regions of the visible light spectrum.[226] However, this absorption feature is quite small relative to the two larger absorption features with maxima around 350 nm and 300 nm. The HOMO-LUMO transition in C_{60} occurs between two h-orbitals, specifically from the h_u molecular orbital to the t_{1u} molecular orbital, which are split due to the icosahedral symmetry of the molecule. Such a transition that preserves parity is forbidden by the Laporte Selection Rule and results in a very weak absorption. There is evidence to suggest that upon excitation of an electron, the C_{60} molecule may undergo a Jahn-Teller effect to further split the energy levels of its molecular orbitals.[227] On the other hand, the large absorbances in the near-UV region of the spectrum correspond to the excitation of an

electron from the h_u molecular orbital to the t_{1g} molecular orbital. The change in parity makes the transition allowed and results in the large absorbance.

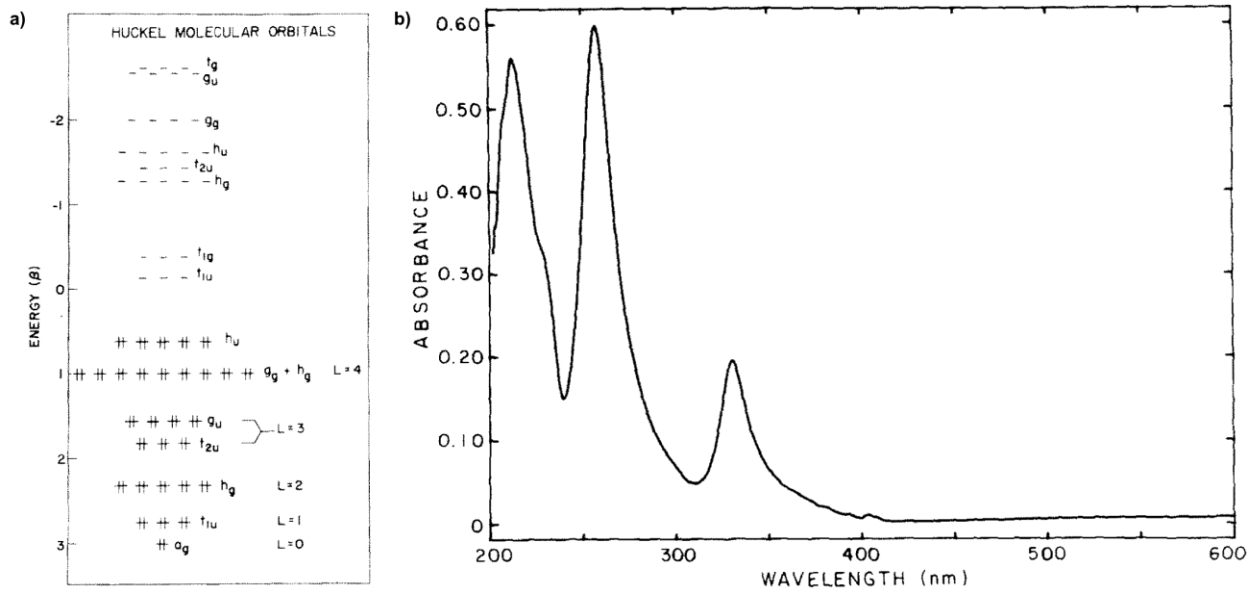

Figure 23: a) Calculated Huckel molecular orbitals of C_{60}.[223] b) UV-Vis absorption spectrum of C_{60}.[226]

In the ground state, fullerenes are not conductors of electrical current, but they can be made into conductors, and even superconductors, through reduction.[227] Because the fullerene HOMO is filled and the LUMO is completely empty, there are no charge carriers available. When C_{60} undergoes reduction, the HOMO now acts as a conduction band and results in a metallically conductive material. Many researchers have taken advantage of this effect by doping fullerenes with alkali metals, reducing them and introducing metal atoms into the fulleride lattice.[222,228,229,230] The doping has the effect of not only adding electrons to the LUMO of C_{60}, thus making it an inherent metallic conductor, but the metal atoms increase the electronic coupling between fullerides, enabling them to become superconductors at low temperatures (<40 K).[228] The superconducting effect is observed in M_3C_{60} fullerides and varies based on the metal dopant.

The electronic properties of C_{60}, coupled with its remarkable symmetry, and use in molecular machines[231,232] have kept fullerenes in the spotlight since their discovery. C_{60} has been the main driver behind plastic solar cell technology and will be discussed in more detail further in the thesis. The superiority of C_{60} among other fullerenes stems from its higher stability, resulting in an improved yield using the synthetic methods of choice.

1.4.1.2 Fullerene C_{70}

When C_{60} was synthesized and identified in 1985, another significant peak was observed on the TOF-MS corresponding to a formula of C_{70}. The structure was later identified as another member of the fullerene family, containing all sp^2-hybridized carbon atoms, but these carbon atoms are not all identical like in C_{60}. In fact, C_{70} shares a structure with C_{60}, except an extra row of 10 carbon atoms are inserted into the centre of the structure. The elongated shape of C_{70} creates two distinct regions: the curved ends and the flatter middle. This also results in five different types of carbon atoms throughout the C_{70} molecule.[221] The differences in the structure have significant ramifications on the chemical reactivity of C_{70} and provide an avenue for the separation of C_{60} from C_{70}.

The electrochemistry of C_{70} is remarkably similar to that of C_{60}. C_{70} undergoes six reversible reductions from C_{70} to C_{70}^{6-}, with the first reduction occurring at -0.98 V and subsequent reductions at -1.38 V, -1.84 V, -2.25 V, -2.74 V, and -3.14 V vs Fc/Fc^+.[233] The reduction potentials are almost identical to that of C_{60}, and even the oxidation of C_{70} occurs at 1.20 V, giving C_{70} an electrochemical HOMO-LUMO gap of 2.22 V, slightly smaller than C_{60}. These results indicate that C_{70} is also an excellent electron acceptor and could be used in applications which require a donor-acceptor system.

What makes C_{70} stand out when compared to C_{60} is its UV-Vis absorption spectrum. Fullerene C_{70} appears orange in solution and has a much higher absorbance than C_{60} in the visible region. C_{70} features a broad absorption band with a maximum at 470 nm, along with several maxima between 300 nm and 400 nm, and finally two large absorbances with maxima at 210 nm and 245 nm (Figure 24).[226] The lack of icosahedral symmetry in C_{70} results in drastically different molecular orbitals than in C_{60}. The LUMO is no longer a triply degenerate state but is instead only doubly degenerate, with the LUMO + 1 being close enough in energy to still undergo easy transition for the sake of light absorption and reduction. C_{70} is much better at absorbing visible light than C_{60} and, depending on the solvent, or film, the difference can be extremely profound. For example, solutions in n-hexane show that C_{70} has a molar extinction coefficient about two orders of magnitude larger than that of C_{60}.[234]

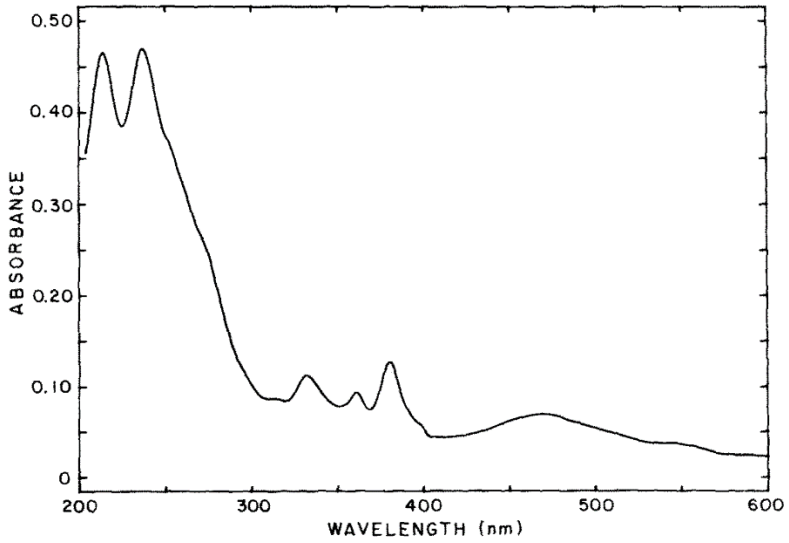

Figure 24: UV-Vis absorption spectrum of C_{70}.

Due to their extremely similar redox properties, C_{60} and C_{70} have seen use in the same types of applications. In this competition, C_{70} has the advantage over C_{60} for use in

solar cells due to its increased absorption of visible light, and near identical HOMO and LUMO levels.[235] However, C_{60} generally performs better in terms of charge carrier mobility, outperforming C_{70} by two orders of magnitude. C_{70} was also expected to produce the same type of superconductive fullerides that C_{60} can, but while the M_3C_{70} fullerides can be synthesized, they fail to produce a superconductive state. The use of C_{70} has largely been hampered by its relative paucity as a result of synthesis methods and purification techniques. As such, C_{70} is generally sold at higher prices and lower purities than C_{60}, which undercuts its improved solar cell performance.

1.4.1.3 The Higher Fullerenes

The family of fullerenes does not end at C_{70} but continues into far larger molecules, including fullerenes with over 300 carbon atoms that have been detected by TOF-MS.[236] These fullerenes that are larger than C_{70} are commonly referred to as the "higher fullerenes." While one might be led to believe that they would share almost identical properties as C_{60} and C_{70}, this is not the case. The electrochemistry of the higher fullerenes can be very different, and their ability to exist as different isomers further differentiates their properties even among higher fullerenes with the same number of carbon atoms.[237,238] When fullerenes are synthesized, the higher fullerenes generally make up the smallest amount of the resulting fullerene soot, and so they can be difficult to study properly. This is especially true as the fullerenes grow larger, and as a result most of the research surrounding the higher fullerenes is limited to fullerenes under 90 carbons in size. Herein, a brief overview of the chemical properties of the fullerenes C_{76}, C_{78}, and C_{84} will be presented.

The electrochemistry of C_{60} and C_{70} is characterized both by their facile multiple reductions, and a single difficult oxidation. The higher fullerenes are capable of undergoing similar reductions, but are also capable of undergoing easier oxidation, making them good at accepting and donating electrons. For example, C_{76} can undergo six reductions with the first reduction taking place at -0.83 V and can also undergo reversible oxidation at 0.81 V vs Fc/Fc^+.[237] That means the electrochemical HOMO-LUMO gap of C_{76} is only 1.64 eV, much smaller than that of C_{60} and C_{70}. Fullerene C_{76} also features a second reversible oxidation at 1.30 V vs Fc/Fc^+. These features are common amongst C_{78} and C_{84} as well, with both showing facile, reversible reduction and oxidation with HOMO-LUMO gaps similar to that of C_{76}.[238] These results make higher fullerenes interesting in applications that require cationic generation, where C_{60} and C_{70} cannot easily be used.

Another interesting feature of the higher fullerenes is their ability to form multiple isomers with different symmetries. C_{78} possesses two such isomers that have been isolated and characterized by nuclear magnetic resonance (NMR).[239] The two isomers are denoted C_{2v}-C_{78} and D_3-C_{78} to identify that they differ in their symmetry. The change in symmetry group has a profound effect on the electrochemistry of the two C_{78} isomers because it directly impacts the formation of molecular orbitals. The oxidation potential of C_{2v}-C_{78} is 0.95 V vs Fc/Fc^+, but it is only 0.70 V for D_3-C_{78}, whereas their reduction potentials are the same. The consequence is that D_3-C_{78} possesses the smallest electrochemical gap of fullerenes discussed to this point of only 1.47 eV, however, fullerene C_{2v}-C_{78} is the largest of these higher fullerenes at 1.72 eV.[237]

Similarly, the UV-Vis absorption of the higher fullerenes is interesting in its own right. Due to their smaller HOMO-LUMO gaps, the onset of absorption in the higher fullerenes is at much higher wavelengths when compared to C_{60} (Figure 25).[236] C_{76} has absorption as high as 850 nm, and absorbs continually into the UV region. The magnitude of the absorption is higher than that of C_{60} in much of the visible region and very similar results can be seen for both C_{78} isomers. Interestingly, the two isomers of C_{78} have very distinct absorption spectra, with C_{2v}-C_{78} having maxima at 700 nm, 630 nm, 530 nm, and 410 nm in the visible region, and molar extinction coefficients comparable to C_{70}. Meanwhile D_3-C_{78} has a much weaker absorption but features an absorption maximum as high as 810 nm.

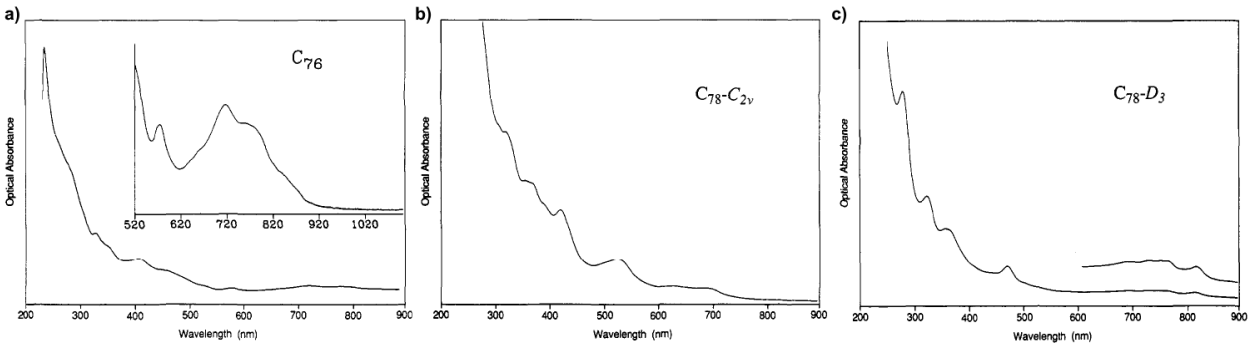

Figure 25: UV-Vis absorption spectra of higher fullerenes in hexanes.

While the higher fullerenes present some very intriguing properties, they have not been as thoroughly studied as C_{60} and C_{70} even though the absorption spectra of the higher fullerenes makes them a potential upgrade from C_{60} for photovoltaic devices. The largest roadblock in studying and implementing the higher fullerenes in new technologies is their cost. The higher fullerenes are more difficult to purify than C_{60} and C_{70}, resulting in a very high price tag and low purities, precluding their detailed study. Furthermore, the

tendency for them to form isomers with drastically different properties, which are very difficult to separate, makes them even harder to use effectively.

1.4.1.4 Endohedral Fullerenes

The last class of fullerenes that we will be discussing are fullerenes with an atom or molecule inside of their shell. Endohedral fullerenes (EFs) are described by the formula $X@C_n$, where X is the species inside the fullerene of size C_n.[240,241,242] The first endohedral fullerene synthesized and characterized was $Sc_3N@C_{80}$, which is the most abundant fullerene after C_{60} and C_{70}.[243] EFs can either contain metals, in which case they are called endohedral metallofullerenes (EMFs),[242] or they can contain non-metals.[244] Due to the sheer number of different endohedral fullerene derivatives, only a cursory summary of their properties will be presented here.

The endohedral metallofullerenes are by far the most common as their synthesis only requires an introduction of metals into the graphite source during synthesis, along with nitrogen in the atmosphere to form metal nitrides (Figure 26). This synthetic method allows for high yields of the resulting endohedral fullerenes. However, if one is looking to install a single nitrogen atom into a fullerene,[245] ion bombardment is necessary, resulting in incredibly low yields (10^{-4} %). Other molecules have also been installed through the use of organic chemistry to “cut open” and “stitch up” the fullerene, but this also requires many steps and has a very low yield.[244] As such, the most commonly studied endohedral fullerenes are the EMFs.

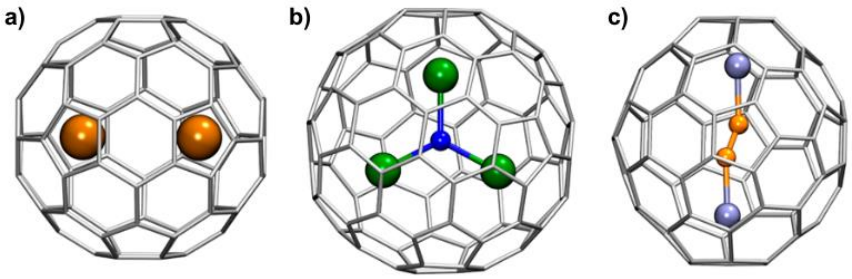

Figure 26: Types of endohedral metallofullerenes including a) metallofullerene $La_2@C_{80}$-I_h, b) nitride cluster fullerene $Y_3N@C_{88}$-D_2, c) carbide cluster fullerene $Ti_2C_2@C_{78}$-D_{3h}.[242]

Due to the high electron affinity of fullerenes,[246] it was believed that endohedral metallofullerenes would exhibit anionic fullerene character, which is what was observed. $Sc_3N@C_{78}$ exhibits MO levels which show electron transfer from the metal atoms to the fullerenes, as well as weak coordination of the metal to the fullerene via the π-system.[247] The charging of the fullerene directly impacts the stability of the fullerene isomer. In the case of C_{80}, the I_h symmetrical form was calculated to be the least stable neutral species, however as $Sc_3N@C_{80}$ (6- oxidation state for the fullerene) the I_h isomer is the most stable.[248] This effect allows for the synthesis of many isomers that are normally inaccessible.

One of the most drastic differences between fullerenes and endohedral metallofullerenes is their electrochemistry. Due to the anionic nature of the EMFs, they generally undergo oxidation at much lower potentials, but are still capable of undergoing several reductions as well. For example, $Y@C_{82}$ exhibits its first oxidation at 0.10 V and its first reduction at -0.34 V vs Fc/Fc^+, for an electrochemical gap of only 0.44 eV.[249] These results are fairly consistent for all EMFs with only a single metal atom inside the fullerene cage, but they are not the case for the nitride-based EMFs. $Sc_3N@C_{80}$ exhibits redox

properties very similar to that of normal fullerenes with an oxidation at 0.97 V and reduction at -1.26 V vs Fc/Fc^{+}.[250] The large variation in ease of oxidation, reduction, and the differences in the HOMO-LUMO gap amongst the EMFs, coupled with the sheer number of known EMFs, makes them interesting for testing in device applications.[242]

Endohedral fullerenes are a really intriguing concept in theory: a molecular container that stores other chemical species. They have some properties that make their continued study a meaningful endeavour as they can be used for applications involving medical imaging. However, even more so than the higher fullerenes, most of the EFs are either incredibly expensive or completely unavailable for purchase, and even among the EFs that are for sale many are prohibitively expensive for anything but small-scale research. For the endohedral fullerenes to see a real growth in interest and use, new methods for selective synthesis or purification of many different types must be devised.

1.4.2 Synthesis of Fullerenes

The synthesis of fullerenes is very similar to that of carbon nanotubes. The first synthesis of fullerenes was through laser evaporation of graphite,[218] but while this provided the world with a taste of what fullerenes had to offer, it suffered from terribly low yields which were largely only useful for detection and theoretical study. It was not long before new methods for fullerene synthesis emerged which allows for larger quantities to become available for more demanding chemical research.

The first method to offer a serious improvement over laser evaporation provided access to around 100 mg of C_{60} over a full day's operation.[251] This method involves resistive heating of a pure graphite rod to the point of evaporation, followed by extraction of the resulting fullerene soot with benzene to extract the fullerene products. While this

method for fullerene production is extremely important in a historical sense, on the practical production side, it has become obsolete. The largest problem with resistive heating is that it requires extreme conditions (>1200 °C, 1 kbar) for a low yield, with only 1% of the soot produced containing fullerenes. Along with the low yield of fullerenes in general, this method is particularly poor at producing higher fullerenes. Currently, the two most common methods for fullerene production include pyrolysis and arc discharge.

1.4.2.1 Pyrolysis Synthesis of Fullerenes

Since the early days of fullerene research, many theoretical claims were made that fullerenes may be formed in the presence of a flame that produces carbon soot. The use of a hydrocarbon feedstock into a high temperature flame results in the formation of a soot, that depending on the atmospheric environment, can be rich in fullerene content.[226] This method can be used to produce large amounts of fullerenes, and more importantly it can be run in a continuous fashion very easily, collecting the fullerene soot automatically without need to stop the machine and wait for it to cool. The method relies on a low-pressure chamber, a flame, a hydrocarbon feedstock, an oxygen gas source, and an inert carrier gas (Figure 27).

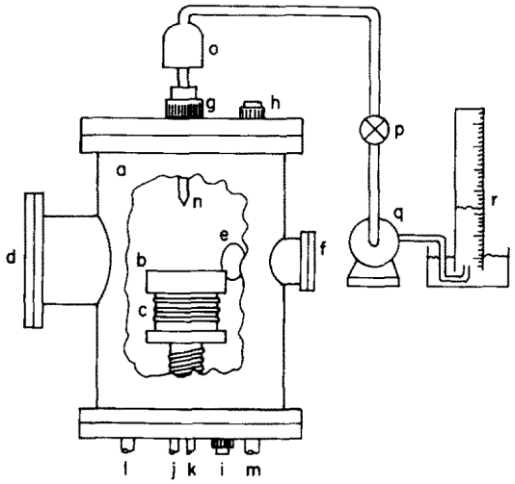

Figure 27: Typical combustion chamber for fullerene synthesis: a) low-pressure steel chamber, b) copper burner plate, c) water cooling coil, d – f) windows, g – i) gas feedthroughs, j) annular-flame feed tube, k) core-flame feed tube, l) and m) exhaust tubes, n) sampling probes, o) filter, p) valve, q) vacuum pump, r) gas meter.[252]

The standard setup for a pyrolysis chamber consists of a steel chamber with a burner, oxygen, argon, and carbon feeds, a vacuum pump, and generally also contains water cooling coils.[253] The system can be designed in such a way that the fullerene soot is collected in a secondary chamber, adjacent to the sooting flame, which allows for continuous operation if the second chamber has a valve for fullerene collection.[190]

The nature of the carbon feedstock can be rather important. The first feed to be used was benzene which resulted in yields as high as 3 g of fullerene for each kilogram of benzene.[226,254] Furthermore, the C_{70}/C_{60} ratio could be modified from 0.26 – 5.7, giving it an advantage over other techniques which predominantly produce C_{60}. However, due to the health concerns surrounding benzene, other aromatic alternatives have been studied as suitable replacements. It has been shown that many aromatic precursors can be used including cyclopentadiene, triphenylene, pyrene, and even metallocycles such as ferrocene.[255] The two candidates that have emerged as the best feedstocks are toluene and tetralin.[256,257]

While the feedstock is important, it is also very important that the feedstock be premixed with oxygen and an argon carrier gas. The ratio of C/O in the feedstock has been shown to have a drastic impact not only on the fullerene yield, but also on the types of fullerenes that are produced.[256] Also, an increase in the oxygen content of the flame de facto increases the temperature of the burner, so the C/O ratio impacts multiple

variables and is one of the most important factors that leads to quality fullerene production. At lower chamber pressures (20 – 100 Torr), the optimal C/O ratio tends to be around unity. In benzene flames under optimal conditions this gives around 3.6 % conversion of the carbon feedstock to soot, and about 7.2 % of the soot contains fullerenes, with a C_{60}/C_{70} ratio of 0.59. Meanwhile, under a toluene flame at 40 Torr, a C/O ratio of near unity gives only 2 % soot yield, but as high as 37 % fullerene content in the soot. Higher C/O ratios tend to improve the total soot yield, but drastically decrease the fullerene content of the soot, with a maximum of fullerene production around 1.15 %. The higher C/O ratio also favours the formation of higher fullerenes, decreasing the content of C_{60} in the resulting fullerene soot.

Temperature also plays a major role in the formation of soot and the content of fullerenes in the soot. The optimal temperature of the flame appears to be around 1800 K, with some error due to the velocity of the gas feed and the C/O ratio. Theoretical calculations on the effect of temperature show that higher flame temperatures (2,300 K) show fullerene content as high as 28 %, but they produce nearly no soot.[256] The lower temperatures are not conducive to high fullerene content, but produce far more soot, and so 1800 K produces the optimal fullerene content.

Pyrolysis has proven to be an excellent method for fullerene production and is used by some companies for industrial production.[190] Using combustion protocols previously discussed, Frontier Carbon Corporation was able to produce as much as 400 kg of fullerenes per year in 2002, and 40 ton/year in 2003 using a toluene feedstock. Based on their optimal yield conditions, the ratio of their fullerenes are C_{60} (60%), C_{70} (25%), and

higher fullerenes (15%). This is significantly different than the fullerenes that are obtained from the other most commonly performed synthesis: arc discharge.

1.4.2.2 Arc Discharge Synthesis of Fullerenes

Arc discharge is the other prevailing synthetic route for fullerenes. As was discussed in the SWNT discussion, arc discharge involves the induction of a plasma arc between two graphitic electrodes, vaporizing the anode and depositing soot onto the cathode and chamber walls. However, the conditions of fullerene synthesis are generally quite different than those required for SWNTs, but both can be fabricated in the same setup if desired.[258] The major distinction between fullerene and SWNT arc discharge synthesis is that fullerenes are made catalyst free, from pure graphite electrodes.

The main advantage of arc discharge is that it is easier to set up than a pyrolysis system and the graphitic electrode can be doped to give other carbon nanomaterials. Not only can catalysts be added to create SWNTs,[259] but metals can be incorporated to form endohedral fullerenes as well.[242] The yields of fullerenes in arc reactors are generally higher than that of a pyrolysis reactor, with as high as 23 wt% of the graphite being converted to soot and 2–4 wt% of the graphite ultimately yielding fullerenes.[260] The yield of arc discharge is therefore up to four times greater than pyrolysis. It has also been shown that the resulting fullerene dispersion is far more uniform than in pyrolysis, with a C_{60}/C_{70} ratio of 5.06, regardless of conditions, with only about 2 % higher fullerene content.[261] The content of higher fullerenes can be drastically increased by addition of 1 % boron to the graphitic electrode.[262]

There are, however, several drawbacks of using arc reactors to produce fullerenes, several of which have been overcome.[263] The first issue is the buildup of deposited soot

onto the cathode, which results in unproductive carbon consumption. This has been remedied through the reversal of electrode voltages, resulting in the burning of the carbon deposited on the cathode. The second drawback is that the fullerene soot is deposited onto the walls of the chamber and must be scraped off manually, after waiting for the chamber to cool. Controlled gas flows have been used to constantly remove the deposited soot so that the arc can be run semi-continuously and the soot is much easier to obtain once the process is complete. The third drawback is the need to constantly remove and replace the spent graphitic electrodes. The use of automated robotic arms has solved this issue but while this is acceptable in an industrial setting, it is considerably more challenging to do on a research scale.[191] The final major drawback of arc reactors is their immense energy input requirement.[257] This is an inherent feature of the arc discharge process and cannot be significantly changed.

Arc reactors have been used to produce fullerenes on an industrial scale since the 90s. With a fully automated arc reactor setup capable of producing up to 11 wt% fullerene soot with 76 mm diameter graphite electrodes, MER Corp. has created a very competitive fullerene production method.[191] While the arc discharge synthesis of fullerenes produces near zero gaseous carbon emissions during the process, a thorough review of the overall energy costs show that arc reactors require about five times as much energy as the pyrolysis method, making it more environmentally impactful.[257]

1.4.3 Fullerene Purification

Due to the polydisperse nature of fullerene synthesis, the resulting soot requires heavy purification before high quality fullerenes can be isolated (Figure 28). The first step of the purification is a straightforward extraction of the fullerenes from the as produced

soot. For this, a Soxhlet of boiling toluene is used, dissolving the fullerene material with a cut-off of around C_{100}.[236] If even larger fullerenes are desired, the soot can be further extracted with chlorinated aromatics, like chlorobenzene. With the fullerene soot extracted, and all the amorphous carbon, ash, and miscellaneous aromatics removed, the different fullerenes must to be isolated from one another.

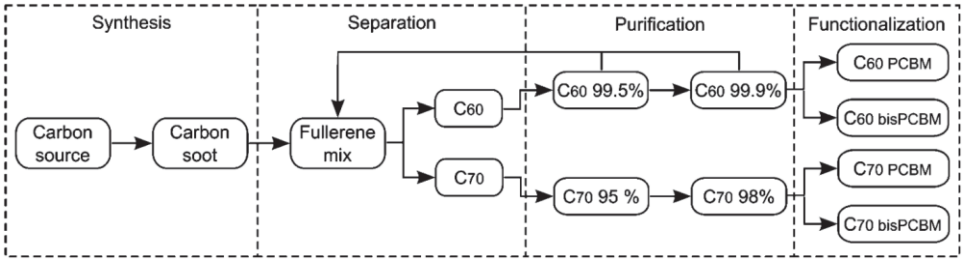

Figure 28: Typical process flow of fullerenes.[257]

The purification of a single type of fullerene is a challenge due to their almost identical structures. The first separation methods involved flash chromatography through alumina with a hexanes eluent.[264] Such chromatographic separation resulted in appallingly low yields and were replaced with reverse phase C_{18} high-performance liquid chromatography (HPLC).[239] While the introduction of HPLC was a welcome improvement, the quantities that were isolable using it remained small, but were enough for significantly more accessible materials for research purposes.

The most significant improvement to the purification of fullerenes was the introduction of the COSMOSIL Buckyprep HPLC column.[265,266] The stationary phase consists of a pyrene molecule with a propyl spacer. The Buckyprep columns offer the ability to separate up to 35 times more fullerene material than C_{18} HPLC stationary phases and have

become the leading method for fullerene separation. This method for fullerene purification will be discussed in more detail in Chapter 3.

1.4.4 Fullerene Solar Cells

Fullerenes have been used in an incredibly wide array of applications ranging from biological to electronic. They have been incorporated in sensors,[267] medical techniques,[268] molecular machines,[269] and FETs.[270] However, their incorporation into solar cells has overshadowed all their other uses.[271,272,273,274,275] The small size of fullerenes allows them to be incorporated into flexible, thin film solar cells, which are attractive for their light weight, and easy roll-to-roll printing manufacturing process.

The operation of a photovoltaic solar cell involves the absorption of a photon, the generation of charge carriers, the dissociation of charge carriers, and finally a generation of current, and it requires both a donor material and an acceptor material (Figure 29).[276] The energy levels of the donor and acceptor are tuned such that the HOMO and LUMO of the donor are slightly higher than that of the acceptor, while ensuring that their HOMO-LUMO gaps fall within the visible light spectrum. A photon of light from the sun will excite an electron in the donor material (or the acceptor) and the resulting exciton (electron-hole pair) will migrate towards a donor-acceptor material interface. When the exciton reaches a neighbouring acceptor, the electron will be donated from the LUMO of the donor to the lower-lying LUMO of the acceptor, generating an ionic pair. Finally, the electron and hole will separate and propagate through their respective material (donor for the hole and acceptor for the electron) until they reach the electrodes, generating a current.

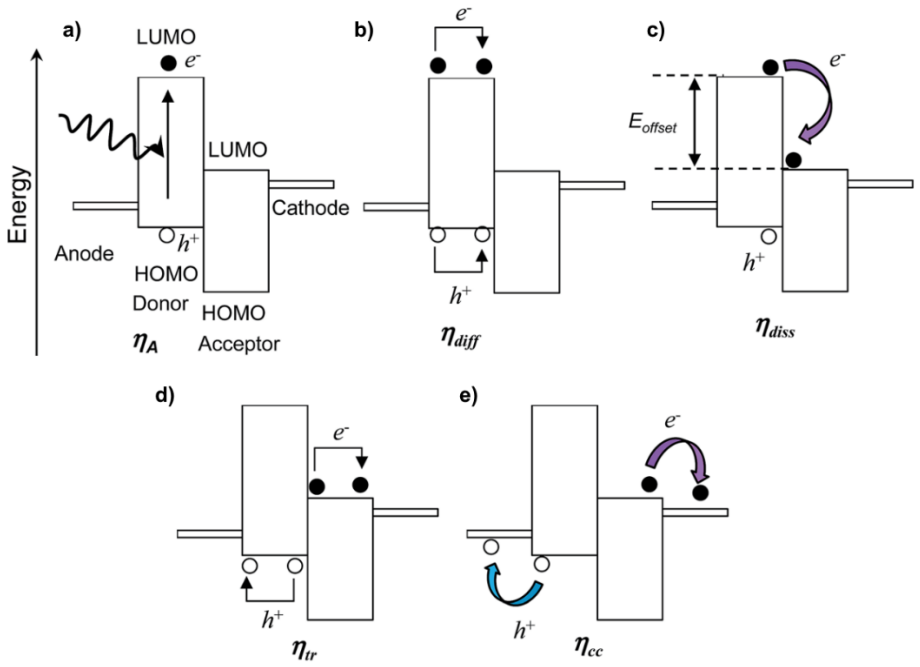

Figure 29: The process of converting incident light to electric current: a) light absorption and photogeneration of an exciton, b) exciton diffusion to the donor/acceptor interface, c) exciton dissociation, d) transport to the photoactive layer/electrode interface, e) collection of charges by the electrodes, transferring the current to an external circuit. e^- and h^+ represent an electron and hole, respectively.[276]

Due to the stringent requirements of energy match between the donor and acceptor materials, as well as the necessity to have a material that is both stable and has a sufficiently fast charge separation, many materials have been studied as candidates for both donors and acceptors. Electron rich conjugated organic polymers serve as great donor materials. They can be tuned through organic synthesis and are easy to process due to their solubility and flexibility. The most commonly used donor material in organic photovoltaics is poly-3-hexylthiophene (P3HT).

As was discussed previously, fullerenes are excellent electron acceptors, with C_{60} and C_{70} capable of undergoing six single-electron reductions.[277] Their tendency to accept electrons, coupled with their visible spectrum absorbance, and their low-lying HOMO and

LUMO levels, made them excellent candidates for use as acceptors in photovoltaics. Furthermore, their tendency to accept electrons is several orders of magnitude faster than their back transfer, making them excellent at separating charges in photovoltaics.[278] The main problem with using fullerenes in photovoltaics arises from their low solubility in organic solvents and, as a direct consequence, their poor mixing with organic polymers. The solubility of fullerenes can easily be improved through their derivatization via [2+1] cycloaddition to give the phenyl-C_x-butyric acid methyl ester (PC_xBM) derivatives. Not only are PCBMs soluble in chlorobenzene, they also exhibit far better crystal packing, which gives them higher charge carrier mobilities than pristine fullerenes.[279] Field effect transistors based on PCBMs have shown charge carrier mobilities as high as 0.21 $cm^2 V^{-1} s^{-1}$.[270]

$PC_{61}BM$ was the standard acceptor material in photovoltaics for a long time. It has been used in many devices, achieving power conversion efficiencies (PCE) over 7%. However, $PC_{71}BM$ works much better as the acceptor material, with PCEs over 8% in multiple devices.[276] The improvements have been attributed to the increased absorption of $PC_{71}BM$ in the visible region of the electromagnetic spectrum, giving devices with $PC_{71}BM$ a higher current generation.[235] $PC_{84}BM$ has also been trialed in photovoltaics and computations on the higher fullerenes have been carried out to probe their potential. While the higher fullerenes exhibit potentially useful HOMO-LUMO levels, the high degree of difficulty of separation hinders their use. The higher fullerenes already possess multiple isomers, but upon functionalization, this issue is exacerbated as each isomer can be functionalized multiple times and in multiple locations. The computational study

determined that each of the resulting fullerene derivatives would exhibit different electronic properties, resulting in an inhomogeneous material and low performance.[280]

The synthesis of the fullerene derivatives requires several steps and purification, exacerbating the problem of high fullerene cost. Despite this, the performance of fullerenes as acceptors has let them remain as the premier acceptor in photovoltaics. For fullerene photovoltaic devices to see widespread commercial success, the cost of fullerenes must be lowered substantially. Improvements made towards the industrial scale synthesis of fullerenes was the first step to decreasing their cost, however, in order for their costs to reduce even further, the purification of fullerenes must be significantly improved upon.

Chapter 2. Nanotube Interactions with π-Concave Materials

2.1 Common π-Concave Binding Motifs for Single-Walled Carbon Nanotubes

The shape of carbon nanotubes is one of their interesting properties, with the outside of a carbon nanotube consisting of a fully conjugated π-convex system. Due to the conjugated nature of carbon nanotubes they undergo significant π- π binding to other π-systems including pyrene[148,281,282] and perylene.[139,283] In fact, the binding of SWNTs to pyrene is commonly used to create CNT-based sensors through the coating of the SWNT surface with pyrene.[142]

While the π- π interactions of pyrene and other flat aromatic compounds with SWNTs has been widely used for immobilization, newer developments have included the use of π-concave aromatic systems to bind to the π-convex SWNTs.[217] π-concave systems undergo stronger binding to SWNTs due to their complementary shape giving them a larger π-surface area with better contact. Several different π-concave motifs have been used for this type of binding to varying degrees of success. Due to their shape, π-concave systems are often referred to as tweezers, molecular tweezers, and nanotweezers.

The problem is that up until recently a good method to determine the binding strength has not existed.[284] As a result, discussing the binding efficacy of π-concave molecules to SWNTs is not easy when consulting the literature, making it difficult to determine the exact parameters that improve nanotube binding. Compounding this is the fact that not much

work has been done in the field of π-concave hosts for SWNTs. Nonetheless several motifs have been proven to bind well to the SWNTs and they will be discussed here, along with the applications they have been used for.

2.1.1 Iptycene Binding to SWNTs

One of the most commonly used motifs for SWNT binding are iptycenes. The family gets its name from the simplest iptycene, triptycene (Scheme 1). The iptycenes feature a bicyclo[2.2.2]octane core with a phenyl ring fused to each of the ethylene units and can be extended or combined to create a vast array of different structures.[285,286] The two most important features of the iptycenes are their bent shape and aromatic structure. This results in an overall π-concave shape, even though the bend in the molecule breaks the overall π-conjugation. The most common method to make iptycenes involves a Diels-Alder reaction between a benzyne and an acene, installing the requisite bend of iptycenes.[285]

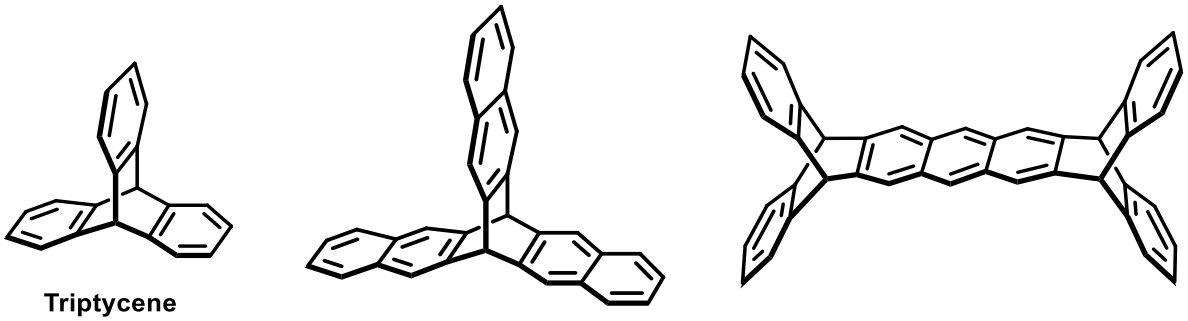

Scheme 1. The iptycene family

The most common use for π-concave binding to SWNTs is for solubilization, which has been accomplished to great effect using numerous iptycene-based systems. The first of these was a report by Sheng-Zhen Zu et al. using triptycene molecules bearing ethylene glycol linkers and adamantyl end groups.[287] By placing SWNTs into an aqueous

solution of the triptycene derivative and cyclodextrin, the SWNTs became solubilized. This occurs through binding of the triptycene to the SWNT sidewalls through π-π interactions and the cyclodextrin forms a complex around the adamantyl end groups, solubilizing the SWNTs. Due to the small size of the individual iptycene molecules relative to the SWNTs, the solubilization of the SWNTs requires the binding of multiple triptycenes with each SWNT. The design of triptycene based hosts for SWNT solubilization has been iterated upon multiple times, improving the degree of solubility and removing the need for cyclodextrin.[141,152] In addition to simply solubilizing SWNTs, the researchers saw a preferential diameter selectivity of the solvated nanotubes with nanotubes 1 nm or smaller in diameter being preferentially solvated.[141]

Other researchers have looked at using larger iptycenes to bind to SWNTs, in particular, Tromp et al. synthesized pentacene-based iptycenes for use as SWNT nanotweezers.[153] Similar to the triptycene work, the pentacene-based iptycene was used for solubilizing SWNTs, and similar to the triptycene case diameter selectivity was observed, but unlike with the tyiptycene SWNTs up to 1.3 nm in diameter showed a 10-fold increase in solution relative to larger diameters. These results suggest that the size of the iptycene can be directly correlated to the diameter selectivity of the resulting binding. Computational work was done to further understand these results and predict selectivity but the conclusions of the work are suspect as they contradict the empirical data, likely due to them ignoring solvent effects on binding.[151]

Chiral iptycenes were synthesized by Marquis et al. for the purpose of selective solubilization of chiral nanotubes.[288] They were shown to very effectively solubilize SWNTs in the range of 0.8 – 1.0 nm in diameter, and on top of that, a significant selectivity

for SWNTs with a larger helical angle was observed. Unfortunately, due to the lengthy synthesis there was insufficient material to determine the effective chiral separation of one type of nanotube.

2.1.2 π-Extended Tetrathiafulvalene

Tetrathiafulvalene is a sulfur-based heterocyclic compound that has been studied for its use in electronics due to its electron rich nature (Scheme 2). 2-[9-(1,3-dithiol-2-ylidene)anthracen-10(9H)-ylidene]-1,3-dithiole (exTTF), sometimes referred to as π-extended tetrathiafulvalene, has likewise been studied for its electron rich nature and interesting shape. Much like triptycene, the benzene rings on exTTF are puckered around the central ring (Scheme 2), creating a π-concave surface, which is useful for binding to π-convex systems, like SWNTs.

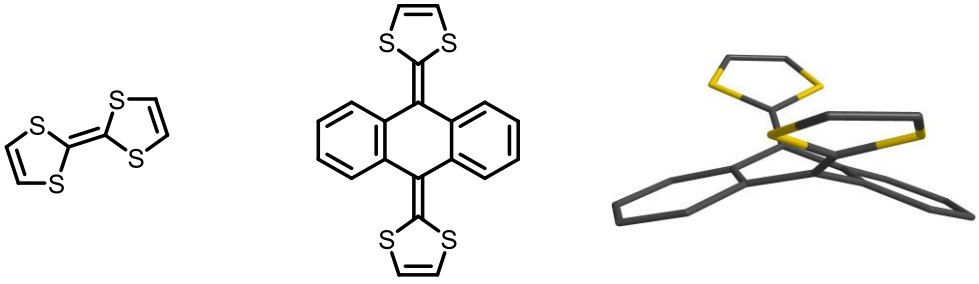

Tetrathiafulvalene **ExTTF**

Scheme 2: Tetrathiafulvalene and π-extended tetrathiafulvalene.

While tetrathiafulvalene possesses the proper shape for binding to SWNTs, they have not been shown to bind well enough on their own despite the potential electron donor-acceptor synergy. Previous studies have shown that they can bind to SWNTs if the exTTF unit is attached to a pyrene to aid in the binding by increasing the total π-surface area.[289] To improve the binding of exTTF, two exTTF units were tethered together with a

m-phthalic ester spacer, creating a larger molecule with two SWNT binding sites. The resulting nanotweezers show great binding to SWNTs along with some selectivity in solubilization, but more importantly this work revealed that exTTF units that form guest-host complexes with SWNTs are also capable of undergoing full charge separation upon photoexcitation.[290] Through the process the exTTF molecule undergoes an oxidation with the SWNTs being reduced, and the lifetime of the charge separated state is 160 ps. Charge transport has interesting implications for solar cell technologies using SWNTs for electron transport and exTTF as the light harvester.

2.1.3 Porphyrin Nanotweezers

Porphyrins are the last major motif used for SWNT binding that will be discussed here, and are interesting π-hosts for SWNTs because they are excellent light harvesters and can be derivatized quite easily. Porphyrins are planar π-systems but can be made into π-concave nanotweezers through the use of a spacer that connects two porphyrin rings (Scheme 3).

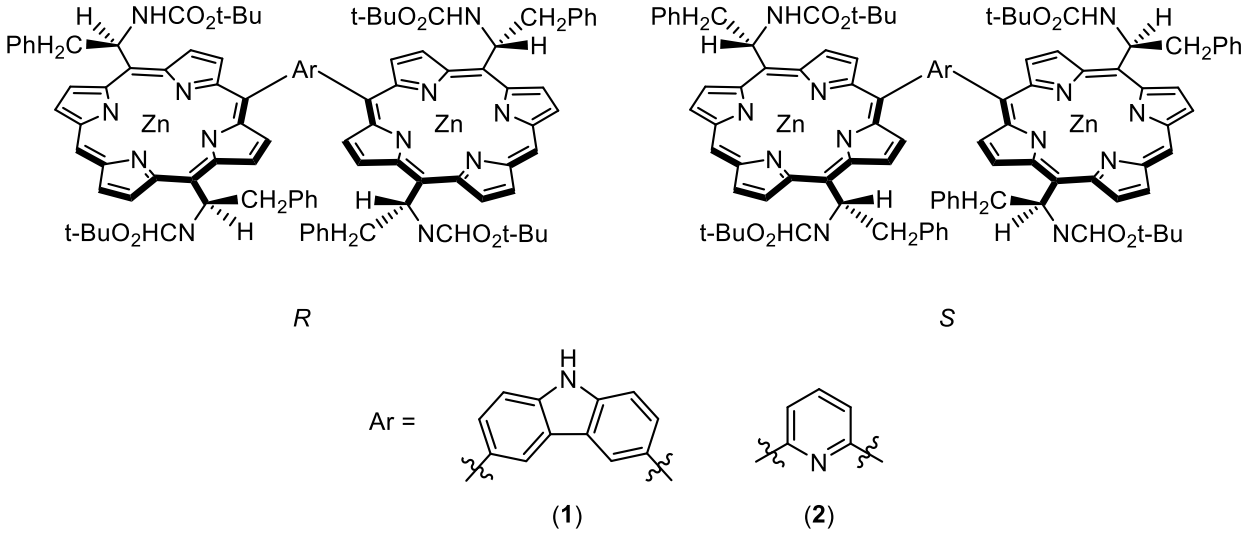

Scheme 3. Porphyrin-based chiral nanotweezers for SWNT binding.

It is very difficult to get chiral separation of SWNTs through many of the conventional separation methodologies used to sort diameters of tubes, but Komatsu's group has pioneered the use of chiral porphyrin nanotweezers which have shown very promising results in chiral separation of SWNTs.[291] The nanotweezers in Scheme 3 were used to produce highly enriched chiral samples of both (7, 5) and (6, 5) nanotubes as evidenced by circular dichroism. Depending on the spacer used, the type of nanotube that was solubilized changed, giving the researchers better control over the exact nature of the resulting nanotube solution. The carbazole spacer produces a larger space between the porphyrins and also creates a tighter biting angle, which creates a nanotweezer that binds to nanotubes based on their diameter and chirality. On the other hand, the pyridine spacer creates a smaller separation between porphyrins and increase the bite angle, such that the nanotweezers are no longer sensitive to the diameter of the nanotubes, and instead interact based on the roll-up angle of the nanotube. This separation method remains one of the best ways to obtain enantiomerically enriched nanotubes despite its low selectivity relative to separation methods for other organic molecules, underlining the difficulty of chiral nanotube separation.

2.2 Current Methods for Aligning Carbon Nanotubes

As has been briefly discussed, the alignment of carbon nanotubes greatly impacts their performance in electronic devices and for that reason many methods have been devised to align carbon nanotubes effectively. The alignment of CNTs is however no menial task due to their nanoscale size and the strong intertube interactions which cause them to bundle, preventing alignment. Several methods have been created that address

the challenge of nanotube alignment to various degrees and they will be discussed in detail here.

The first method used to align carbon nanotubes was through cutting of a carbon nanotube-polymer resin composite.[292] Using this method, Ajayan et al. were able to take random dispersions of raw CNTs in a polymer resin and align them to an incredible degree simply by cutting the polymer resin into thin slices ranging from 50 nm to 1 μm in thickness, using a diamond knife. No cross-sections of nanotubes were observed, which seems to indicate that the perpendicular tubes were either removed entirely or were aligned by the knife into the plane of the polymer. This approach is very straight-forward and requires minimal specialty hardware but is also severely limited by the fact that the resulting nanotubes are trapped within an insolating polymer resin. Perhaps this method could be extended to the use of semiconducting polymer matrixes to improve its applicability.

Another common method for nanotube alignment is through their controlled growth on glass, leading to a highly dense “forest” of vertically aligned carbon nanotubes.[293] This is accomplished through sputtering of a thin film of nickel onto the glass surface, followed by CVD growth with ethylene gas at 666 °C. The nickel layer acts as the catalyst and leads to the vertical growth of the nanotubes, but the ends of the nanotubes are then capped with nickel nanoparticles as a result. Vertically aligned carbon nanotubes are not directly applicable to FET applications as they currently exist, but the researchers discuss their utility in field-emission displays, which have been made obsolete by the prevalence of liquid crystal displays (LCDs).

Researchers at IBM created a method for nanotube alignment by taking advantage of their shape anisotropy and through chemical modification of the nanotube walls.[294,295] The original process was done by functionalizing the walls of the nanotubes with hydroxamic acid functional groups, which selectively bind to HfO_2 surfaces, and then depositing the nanotubes onto a patterned HfO_2 surface. The surface was patterned in such a way that channels that were small in width were created such that the width of the channel was smaller than the length of the nanotubes, forcing them into alignment by virtue of their size (Figure 30). However, this method requires covalent chemical modification of the SWNT surface, permanently altering their electronics, and it results in a very low density of deposited CNTs. To combat both of these problems the experiments were modified such that the trenches were covalently functionalized with a cationic hydroxamic acid, and the SWNTs were wrapped with SDS, an anionic surfactant. Since the hydroxamic acid selectively functionalizes HfO_2 over SiO_2, the deposition of the SDS-wrapped SWNTs was selective inside of the HfO_2 trenches. Furthermore, the functionalization of the HfO_2 directly, drastically improved the density of the SWNTs on the surface. However, the main drawback of this method is that the channel width has to be exceptionally small (70 nm) in order to get optimal alignment of the nanotubes, which requires electron beam lithography, an expensive and time-consuming process.

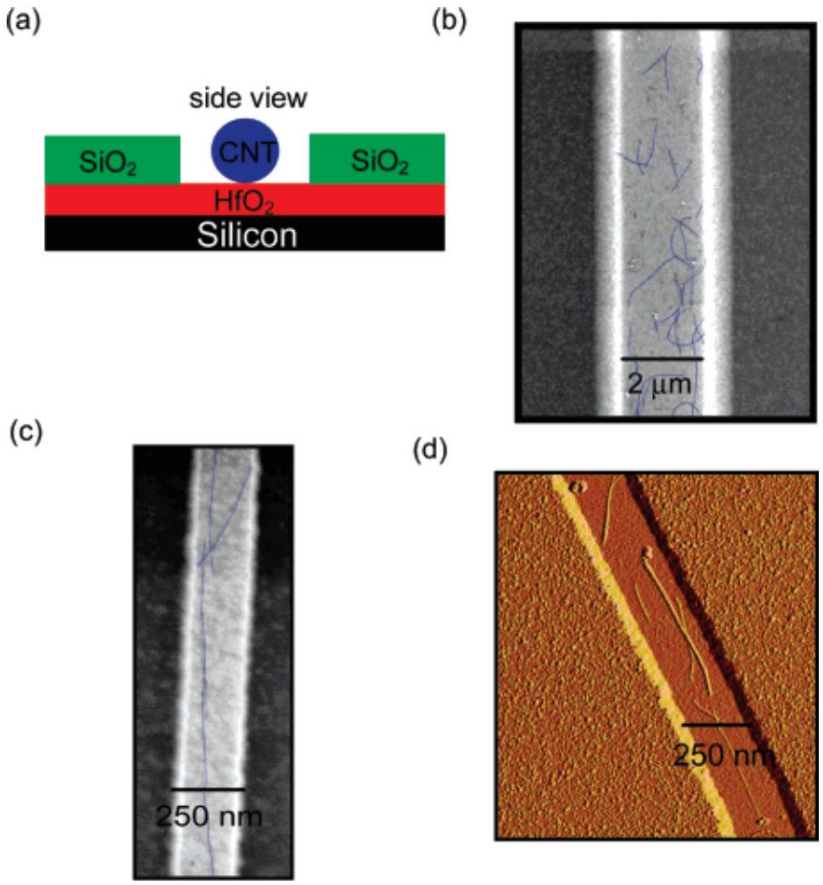

Figure 30: a) Schematic of the side view of the patterned substrates. b) SEM image of functionalized SWNTs assembled in a 2 µm HfO_2 bottomed trench. c) and d) SEM and AFM image, respectively, of 250 nm trenches with aligned functionalized SWNTs.[294]

Another approach is to deposit a nanotube suspension onto a rapidly spinning substrate, thus aligning the nanotubes radially as they are moved along the surface.[81,296] This was accomplished by Bao's group through the use of a syringe pump to slowly deposit drops of nanotube suspensions, but it requires that the surface be functionalized so that the nanotubes remain on the surface in appreciable quantities. They attempted functionalization with both amine-terminated and phenyl-terminated silanes, determining that the polar amine groups adhered the spincoated nanotubes more effectively, displaying a density 5 – 10 times greater (Figure 31). The researchers also observed a

significant selectivity for s-SWNT deposition on the amine-terminated surface and m-SWNTs on the phenyl-terminated surface, further proving the utility of this method. The problem with spincoating for nanotube alignment is that the resulting bulk alignment is radial, not uniform in one direction. This is an issue because current transistor manufacturing techniques are not optimized for this type of alignment, making it non-ideal.

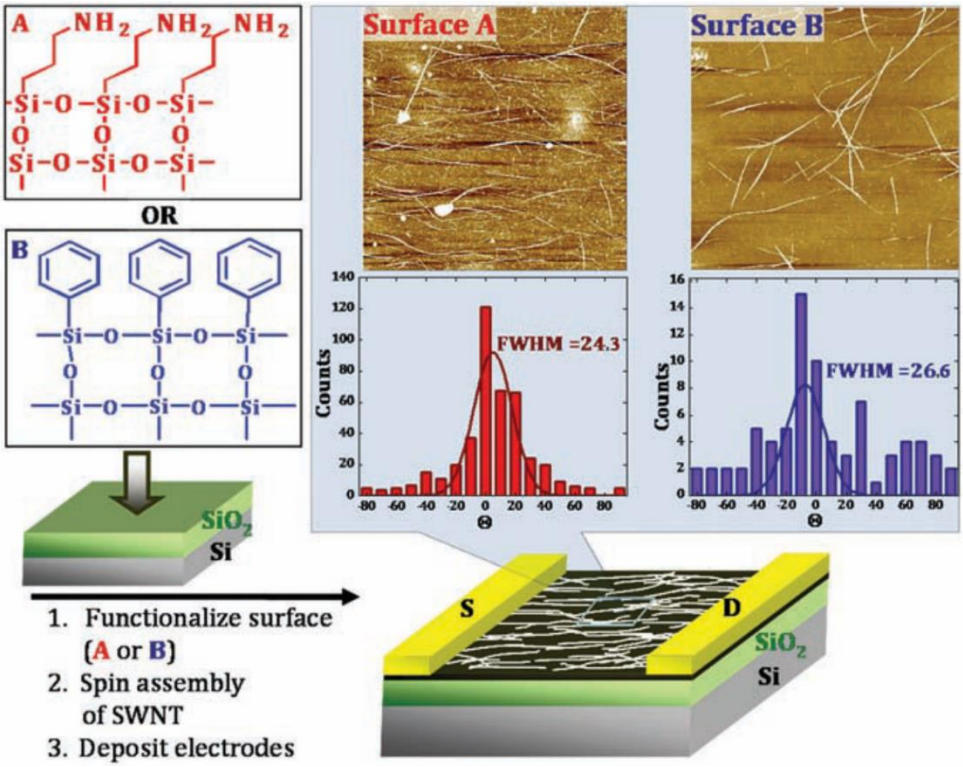

Figure 31: Schematic of the SWNT TFT fabrication and structure using spincoating on amine-terminated (A) and phenyl-terminated (B) silicon.[81]

A great way to study the electronics of individual nanotubes was demonstrated by Yuzvinsky et al. through the combination of lithography and spincoating.[297] The researchers devised a method whereby CNTs could be deposited onto electron-beam activated poly(methylmethacrylate), controlling the exact location of the nanotube

deposition based on the areas that had been developed (Figure 32). The deposition and alignment of the nanotubes is delivered through spincoating, but the positional control is provided by the EBL, giving this method a high degree of control over the placement of the nanotubes. This is very effective for eventually creating devices out of individual nanotubes for detailed testing, but the low density coupled with the drawbacks of spincoating and EBL render this method incapable of creating large arrays of aligned nanotubes.

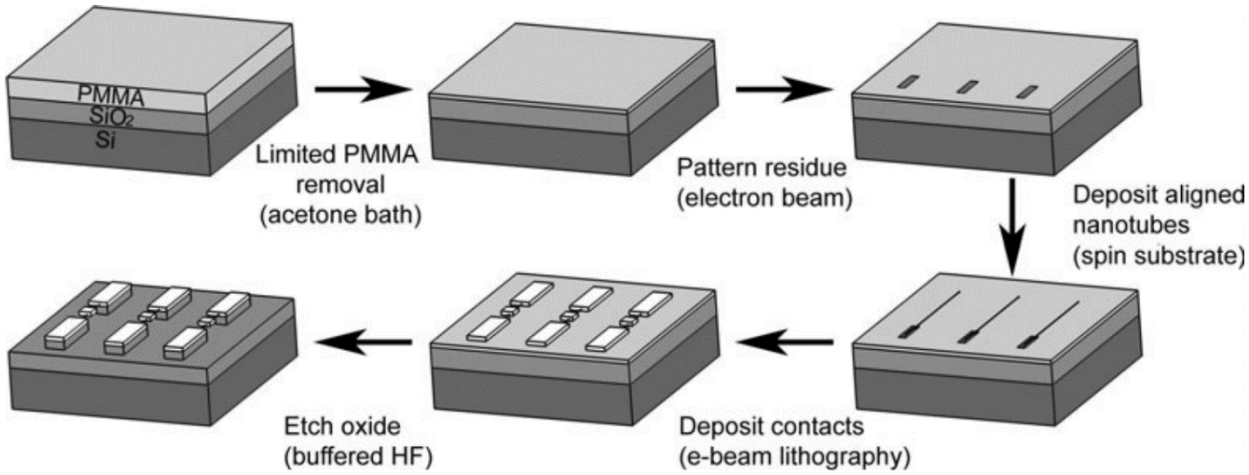

Figure 32: Fabrication process of patterned PMMA surface for controlled and aligned SWNT deposition.[297]

Gopalan's group has devised a method for large-scale deposition of highly aligned nanotubes based on the Langmuir-Blodgett film fabrication technique.[298] The method relies on dispersing SWNTs into chloroform, and then taking the resulting ink and dropping it into a Langmuir-Blodgett trough, allowing the chloroform to slowly evaporate while simultaneously pulling a substrate of choice up through the edge of the chloroform drop (Figure 33). This has the effect of aligning the nanotubes onto the substrate perpendicular to the direction that it is being pulled in, due to the shape anisotropy of the

nanotubes and the constant pressure from the Langmuir-Blodgett trough barriers. The resulting density and alignment are both excellent and some positional control is possible by varying the speed that the substrate is being pulled at, and by varying when the SWNT drops are added to the trough. Cao et al. use a similar approach, relying on a Langmuir-Schaeffer method for their nanotube deposition instead, and achieve even higher densities, approaching complete surface coverage.[299] The significant drawbacks of these methods are that they lack precise control over nanotube deposition, and more importantly, are done in water.

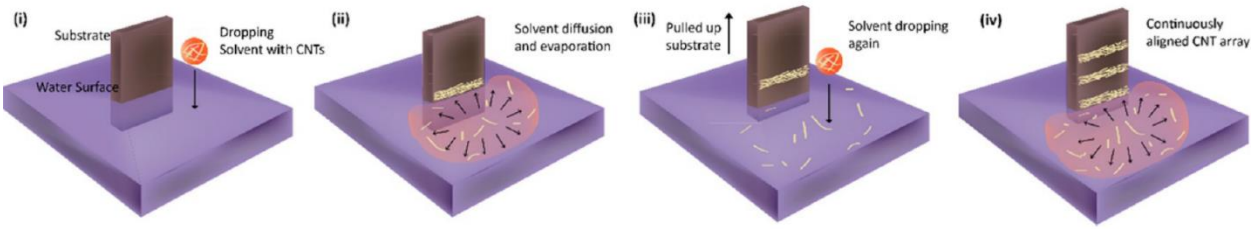

Figure 33: Schematic illustration of the iterative process used to fabricate aligned SWNTs driven by the spreading and evaporation of controlled doses of organic solvent at the air/water interface.[298]

Finally, the last major method for aligning carbon nanotubes is through the controlled growth on specially prepared substrates. Kang et al. showed that by placing iron catalysts on a stable temperature cut quartz wafer along the [2110] direction, the resulting surface could be subjected to CVD conditions to grow SWNTs parallel to the surface. The SWNTs grown this way exhibit near perfect alignment as well as high densities (Figure 34), making them prime candidates for FET fabrication. However, the major issue with this technique is that the SWNTs that are synthesized are about equal parts semiconducting and metallic, resulting in very poor on/off ratios of about 2. Che et al. have improved the CVD method such that the resulting nanotubes are 97.6% s-SWNTs, but this still only

results in an on/off ratio of 42.[161] Due to the low on/off ratio, this technique has to be coupled with other post-processing techniques to remove the m-SWNTs present in the sample.

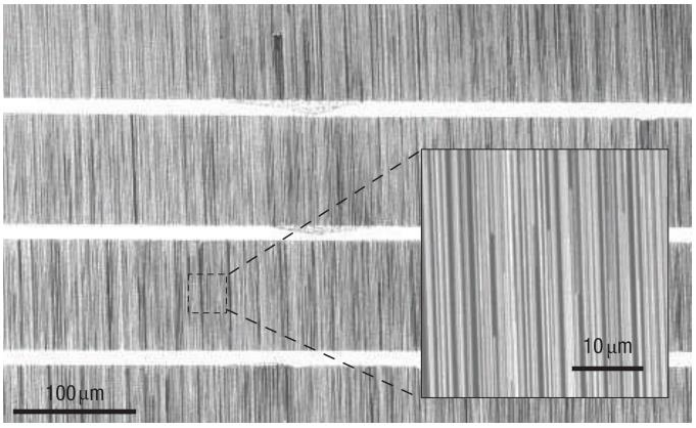

Figure 34: Aligned arrays of SWNTs grown on a cut quartz substrate. The bright horizontal stripes correspond to the regions of iron catalyst.[108]

Clearly, there are many potential options for aligning SWNTs to various degrees, all with their own benefits and drawbacks. The commonality between most of these methods, however, is their incapability to select for the electronic nature of the aligned nanotubes, be that the diameter, or simply semiconducting vs. metallic SWNTs. This means that they have to be coupled with SWNT sorting methods that we have discussed previously, increasing the complexity, time, and cost of the overall process. Therefore, a technique that could affect the alignment and sorting of nanotubes in one step is highly desirable, especially if it allows for selective placement of the resulting nanotubes.

2.3 Simultaneous Sorting and Alignment of Single Walled Carbon Nanotubes Using an Alignment Relay Technique

Due to the need for good methods for both aligning and sorting carbon nanotubes for their use in transistor technologies, we were determined to create a new method that could achieve both in one step. Inspiration was drawn from the π-concave design of typical nanotweezers used to solubilize and sort SWNTs, and we envisioned a method that would use the already established binding of iptycenes to SWNTs in order to impart diameter and potentially chiral selectivity. The problem with using iptycenes for alignment is two-fold: iptycenes do not naturally possess any alignment properties, and for SWNTs to be usefully aligned they must be deposited onto a surface. The second point is an issue only because iptycenes have solely been used to bind to SWNTs in solution, surface binding would require several important modifications. To overcome the issue of iptycene alignment a method for transferring the alignment properties of other materials, specifically liquid crystals, onto the iptycenes was planned. To then be able to align nanotubes on a substrate surface, it would be imperative to synthesize an iptycene derivative that is capable of covalently functionalizing a surface, while maintaining its alignment. Once the triptycenes are aligned they should be able to bind to SWNTs, such that the SWNTs are forced into alignment with the triptycenes themselves. We dubbed this passing on of alignment information from liquid crystals, to triptycene, and finally to SWNTs, the Alignment Relay Technique (ART).

2.3.1 Liquid Crystals

Liquid crystals are molecules that can take on a phase of matter between that of a crystalline solid and an isotropic liquid which possesses the properties of both phases. Liquid crystal phases characteristically have orientational order, as well as the potential

for positional order, depending on the particular liquid crystal phase in which the molecule exists. We were originally interested in liquid crystals because of their inherent order and their ability to be very easily aligned over long distances through external factors including magnetic fields,[300] electric fields,[301] polarized light,[302] and rubbed poly-imide coated surfaces.[303]

There are two main families of liquid crystals: thermotropic and lyotropic. Lyotropic liquid crystals are molecules that exhibit liquid crystal phases based on their concentration in a given solvent. The most common example of lyotropic liquid crystals are phospholipids which organize into bilayers to form cell walls in animals. Conversely, thermotropic liquid crystals exhibit liquid crystal phases at different temperatures, like conventional phase transitions, and are commonly used in displays and other electronics. Thermotropic liquid crystals interested us because their liquid crystal phases are easily maintained through simple temperature control. Moreover, thermotropic liquid crystals can be forced into alignment in the plane of a substrate surface, as is the case in liquid crystal displays.[304] Thermotropic liquid crystals are generally designed in such a way as to create some type of shape anisotropy and dipole moment along the molecule, which promotes their self-assembly and the formation of liquid crystal phases.

Among thermotropic liquid crystals there are two major categories: calamitic and discotic (Figure 35). Discotic liquid crystals, as the name implies, are disc-shaped and generally consist of a symmetrical aromatic core with alkyl chains on the periphery. The aromatic cores promote binding between neighbouring molecules and the long alkyl chains aid in the assembly of aromatic cores, which typically results in columnar packing. Calamitic liquid crystals are instead rod-shaped and generally consist of a rigid aromatic

core with flexible alkyl side chains and a polar head group. The rigid core ensures that the dipole moment is fixed and ensures that the anisotropy of the molecule is large enough to promote preferential packing, while the polar and non-polar sides of the molecule further promote favourable packing orientations. Both types of thermotropic liquid crystals are capable forming many phases that have varying degrees of order from simple orientationally ordered phases to positionally ordered, tilted, twisted, bent, and chiral phases.[305]

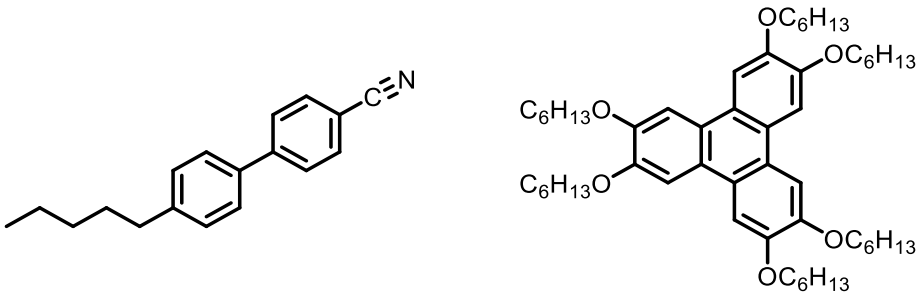

Calamitic Liquid Crystal **Discotic Liquid Crystal**

Figure 35: Examples of calamitic and discotic liquid crystals

We were drawn to calamitic liquid crystals due to reports of their use in the alignment of other materials,[306] particularly the effect that they have on triptycene.[307] Due to the shape of triptycene it lacks the ability to pack tightly, which creates pockets of internal free volume within the crystal structure. The internal free volume acts as a vacuum and guest molecules can be pulled into these areas in order to minimize the internal free volume of the system. This is usually accomplished by the incorporation of solvent molecules, but it was discovered that the rod-shaped calamitic liquid crystal 4-cyano-4'-pentylbiphenyl (5CB) is also capable of occupying the internal free volume pockets. More importantly, when 5CB is under the effect of external alignment it transfers the alignment

to the triptycene molecules due to the packing structure (Figure 36). This was confirmed with polarized UV-Vis spectroscopy and it stood out to us as the ideal method for introducing alignment into our triptycenes, so that we could ultimately align our SWNTs.

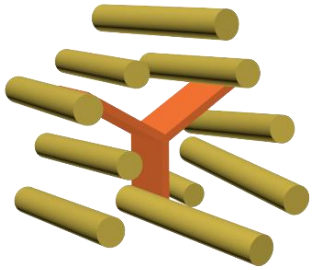

Figure 36: Triptycene alignment in calamitic liquid crystal.

2.3.2 Functionalization of Metal-Oxide Surfaces

Once we had determined a method for the alignment of triptycene, we had to find a suitable method to tether the molecule onto a substrate surface. There are many functional groups that are capable of forming covalent bonds to a plethora of substrates from glass to silica and metal oxides.[308] Our goal was to find a functional group that would be capable of binding the oxide layer of silicon so that our methodology could be directly applied to transistor fabrication. We also anticipated that having the ability to functionalize a transparent substrate would allow for us to use polarized optical microscopy (POM) to observe the liquid crystal phase of the system, to ensure that the alignment of the liquid crystals is not perturbed by the triptycenes. The functional group also had to be able to form multiple covalent bonds, in order to prevent rotation of the triptycene upon binding to the surface. The ideal functional group would have to be easy to install at a late stage in the synthesis, be itself easy to synthesize, or be commercially available.

The obvious choice was to use silanes as they are effective at binding to silicon oxide surfaces. Silanes can form up to three covalent bonds with surfaces when starting with the trichlorosilane or the triethoxylsilane, and bind exceptionally to other silicon-based surfaces, as well as alumina and titanium oxide. However, the installation of silanes onto triptycene would not be very easy and would first require preactivation of the triptycene through bromination or the synthesis of a silane-based dienophile, which tend to be quite poor coupling partners in Diels-Alder reactions.

We then turned our attention to phosphonates as potential anchors because phosphonates and phosphonic acids have been used to covalently functionalize surfaces including silicon oxide,[309,310] indium tin oxide (ITO),[311] other metal oxides, and even metal nanoparticles.[308,312] Phosphonates are capable of forming up to two covalent bonds and either one hydrogen bond or one dative bond depending on the Lewis acidity of the surface (Scheme 4).[312] In some instances, three covalent bonds are believed to form as well. These qualities made us further consider phosphonates as a viable route.

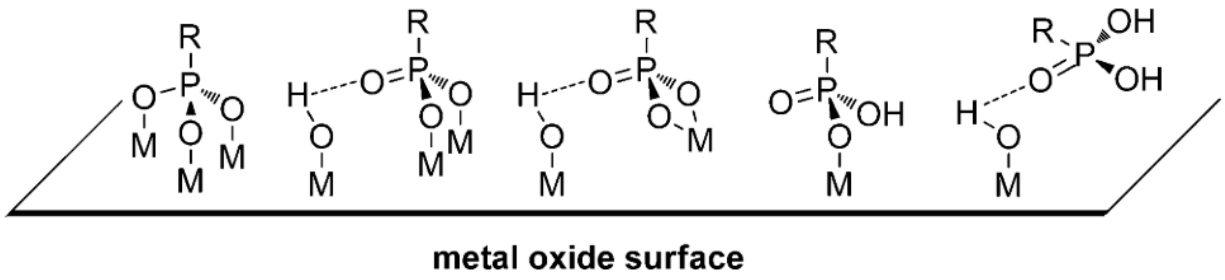

Scheme 4: Binding modes of phosphonic acids to metal oxide surfaces.[312]

Fortuitously, there have been studies that utilize phosphonic acids to functionalize the dielectric in organic semiconductors to improve the performance of the device,[313] and to coat ITO electrodes to improve wettability.[314] Phosphonic acids tend to form

monolayers on the surface of these substrates and in the case of organic FETs they create a layer that aids in the deposition and contact between the organic semiconductor and the dielectric/electrodes. In pentacene organic TFTs, the phosphonic acid layer had an impressive impact on the device performance: 60x increase in the charge carrier mobility, decreasing the threshold voltage by 0.8 V and improving the I_{ON}/I_{OFF} by four orders of magnitude. Interestingly, the same treatment was tested with pristine C_{60} and the resulting devices could achieve charge carrier mobilities as high as 3.7 cm^{-2} V^{-1} s^{-1}. These results interested us in testing phosphonic acids as the anchoring group for our triptycenes because not only have they proven to be useful in the functionalization of many important surfaces, but they could also have a positive effect on the resulting SWNT TFTs.

Lastly, a synthetic method for the direct installation of phosphonates was required to solidify their use in our alignment method. We devised a synthesis to introduce the phosphonates through a Diels-Alder reaction between the two commercially available molecules bis(diethoxyphosphoryl)acetylene and anthracene (Scheme 5). This would install two phosphonate groups that could form up to six bonds to a surface, while simultaneously creating the iptycene backbone which is required for both SWNT binding and alignment relay from the liquid crystals. The side-effect of this method, however, is that the resulting iptycene **1**, lacks the third aromatic ring seen in triptycene, potentially altering the packing detrimentally as far as liquid crystal alignment is concerned.

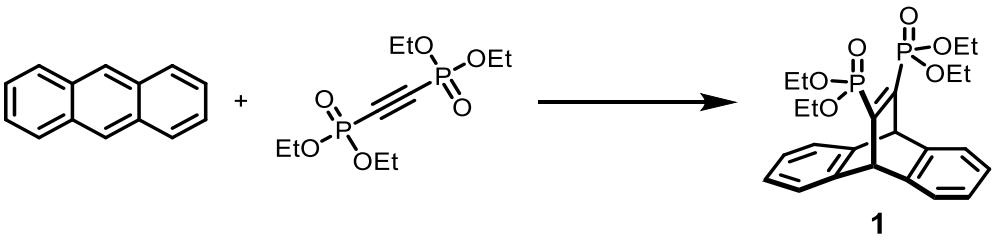

Scheme 5. Diels-Alder route to phosphonate iptycene 1.

2.3.3 First Attempts at the Alignment Relay Technique

With our target molecule identified, studies into our hypothesized SWNT alignment methodology started, first with the synthesis of our target molecule (**1**). The Diels-Alder reaction proceeded at 160 °C in toluene over five days to give the product phosphonate iptycene at a 50 % yield. While the yield was low, the material was used to conduct alignment experiments to confirm its use before further optimization of the synthesis was performed. The surfaces that we chose to test the functionalization of with **1** were SiO_2 and TiO_2, the former due to its ubiquitous use in electronics and the latter because it is a transparent electrode which allows for observation of the surface with optical microscopy.

First, an optimization of the binding conditions was performed, but instead of using **1** for the optimization, phenylphosphonic acid was used as an inexpensive substitute. The initial functionalization studies were focused on silicon as there is more literature on silicon cleaning and functionalization than there is for ITO. Several methods were used to clean the silicon oxide surface, summarized in Table 1. Among the cleaning methods were organic cleaning at room temperature and high temperature, as well as both basic and acidic oxidizing conditions. Each of the cleaned substrates was then subjected to further testing through the functionalization conditions seen in Table 2.

Name	Conditions
Organic Clean I	1) 10 min sonication in THF 2) 10 min sonication in acetone 3) 10 min sonication in H_2O
Organic Clean II	1) DCE, Δ, 10 min 2) 10 min sonication in acetone 3) MeOH, Δ, 10 min
Standard Clean I	1) 10 min sonication in acetone 2) 10 min sonication in H_2O 3) 5:1:1 $H_2O/H_2O_{2(30\%)}/NH_4OH_{(30\%)}$ 10 min at 80 ^oC
Piranha Clean	1) 10 min sonication in acetone 2) Dry throroughly with N_2 3) 3:1 $H_2SO_{4(conc.)}/H_2O_{2(30\%)}$ 45 min, 100 °C

Table 1: Conditions tested for the cleaning of silicon oxide before attempted functionalization with phenylphosphonic acid.

Trial Number	Concentration of phenylphosphonic acid	Temperature
1	1 mM	25 ^oC
2	1 mM	60 ^oC
3	1 mM	100 ^oC
4	1 M	25 ^oC
5	1 M	60 ^oC
6	1 M	100 ^oC
7	1 M	120 ^oC
8	100 mM	60 ^oC
9	10 mM	60 ^oC

Table 2: Conditions tested for the functionalization of cleaned silicon oxide surface with phenylphosphonic acid. The reaction was run in THF for 18h by completely submerging the silicon oxide substrate.

While many different cleaning and functionalization conditions were screened, it was difficult to determine the extent of coating of the silicon oxide layer. A common method

for assessing the elemental composition of surfaces is x-ray photoelectron spectroscopy (XPS), which uses x-rays to eject electrons from the atoms of a surface and measures the energy of the photo-emitted electrons. The energies of the emitted electrons are very characteristic of the surface atoms and can even be attributed to individual orbitals. XPS was used to test the functionalization of our silicon surface by monitoring the phosphorus and carbon peaks. At first the data seemed to suggest that 60 °C at 1mM was the most effective based on the percentage of phosphorus found in the XPS signal but this was quickly discarded because the silicon that was used in the functionalization was doped with phosphorus, throwing all the results into question. Indeed, the cleaned silicon surface with no functionalization gave a phosphorus peak almost identical to those obtained from the functionalization experiments.

In an attempt to remedy the problem, boron-doped silicon was used instead, but the phosphorus signal in the XPS still remained equally strong in the blank sample. This result was unexpected, but it was noticed that while the phosphorus peak was unreliable, the carbon peak appeared to fluctuate drastically between samples, and that the blank always had less carbon than the functionalized surfaces. Based on this observation, the data was revisited but this time with a focus on the carbon abundance on the surfaces and it was found that the higher temperature samples produced surfaces with the highest carbon content. The reaction worked best at 140 °C, and so **1** was used in the functionalization of a piranha cleaned silicon surface in a capped glass tube in THF with a concentration of 1 M at 140 °C for 18h, which afforded a surface with the highest carbon content seen in any of the functionalization reactions. The functionalization was confirmed to work on ITO as well.

Throughout these trials it was apparent that the surface modification had taken place through a qualitative change in the surface wetting behavior of the solvents used during the washing procedure post-functionalization. Surprisingly, when the functionalization of silicon oxide with **1** was done at room temperature, the surface also exhibited the same change in wetting behavior as it did at 140 °C. The XPS data suggests that functionalization indeed does occur with the phosphonates at room temperature, and perhaps the large increase in carbon at high temperatures is due to the formation of multilayers, or decomposition of carbonaceous organics. The fact that **1** could functionalize SiO_2 at room temperature was encouraging, because it meant that it would be easier to work with.

5CB was chosen as the liquid crystal for the alignment of **1** due to its ability to form a nematic liquid crystal phase at room temperature, which we found to be an effective temperature for functionalization, and its effective use in the alignment of triptycene.[307] The alignment relay technique relies on taking the alignment of a rubbed polyimide liquid crystal alignment layer and using that to pass on the alignment to the liquid crystal 5CB, then to **1**, and finally to the SWNTs that will be deposited onto the surface. In this case, 2 wt% of **1** was dissolved in 5CB so that when the 5CB was aligned on the polyimide layer, the alignment was also transferred onto **1**. At this point SiO_2 was placed on the polyimide layer, creating contact between phosphonate **1** and SiO_2, allowing covalent functionalization to take place while **1** is still under the effect of alignment from the liquid crystals. After 18h, the SiO_2 was removed and washed with dichloromethane to give a **1**-functionalized surface that, ostensibly, had been aligned. The orientation of **1** was fixed because it would have formed numerous covalent bonds to the SiO_2 surface, precluding

rotation. After the alignment-controlled functionalization, XPS data and wetting characteristics evidenced proper covalent modification of the SiO_2 surface.

While it was apparent that the functionalization was successful, a method to determine the alignment of the resulting surface was needed. Two potential methods for determining the alignment of **1**-functionalized SiO_2 were identified: polarization modulation infrared reflection-adsorption spectroscopy (PM-IRRAS), and directional contact angle measurements. First, vertical water contact angle measurements were taken on **1**-functionalized SiO_2 in two different directions with the expectation that the if **1** were aligned, the contact angle would be different in the perpendicular directions due to the anisotropy of the molecule. However, the results showed a contact angle of 35 ° in both directions which did not indicate alignment. So next, the surface was subjected to PM-IRRAS following a procedure laid out by Gliboff et al.[315] In their work, they were able to use the technique to determine the tilt angle of phosphonates on indium zinc oxide. When similar measurements were taken on **1**-functionalized SiO_2, the silicon substrate proved to be ineffective at reflecting the infrared light. The poor reflection coupled with the small amount of sample on the substrate gave no detectable signal. Even in ideal circumstances, the signal obtained by others is weak due to the small number of surface-bound molecules. Similarly, ITO does not reflect infrared light well either, so we had to determine another method to observe the alignment of **1**.

Instead of trying to observe the alignment of such a small molecule through indirect means, we thought that deposition of SWNTs onto the surface would provide a clear probe into the alignment of **1**. SWNTs are large enough to be directly imaged through atomic force microscopy (AFM) so if nanotubes that are deposited on a **1**-functionalized

surface were aligned, it would be evidence that **1** is also aligned. In order to use the nanotubes as an indication of the alignment of **1**, conditions for nanotube deposition were screened. However, when AFM measurements of the resulting surface was obtained, no nanotube deposition was observed under any of the conditions that were tested. Ultimately, it appeared as though either the **1**-functionalized surface was not aligned, or that **1** was incapable of proper binding to SWNTs in the solid phase.

2.3.4 Designing a New Iptycene for the Alignment Relay Technique

Due to the failure of **1** as an adequate alignment agent in the original alignment relay technique experiments, it was concluded that a new iptycene would have to be synthesized for the ART to work. The original report of triptycene alignment in a liquid crystal solution claimed that the alignment was due to the internal free volume of the triptycene unit.[307] The installation of the phosphonate groups directly onto anthracene may have broken up the 3D structure that creates the internal free volume in triptycene, and as a result it is possible that **1** lacks any ability to be aligned in a liquid crystal (Scheme 6). Furthermore, there is also less π-surface area on **1**, making it potentially weaker at binding with SWNTs.

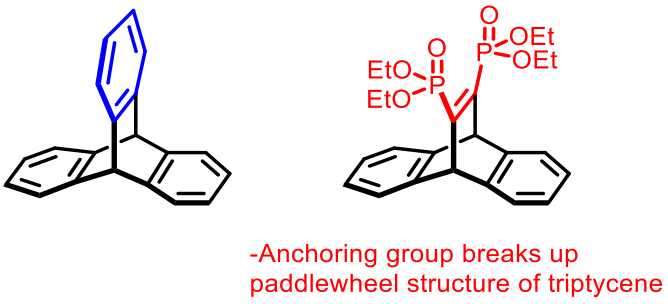

Scheme 6: Loss of paddlewheel structure in original iptycene design.

In order to remedy these problems, a new target molecule (**2**) was devised which contains multiple intact triptycene units in conjunction with phosphonate anchoring groups (Scheme 7). The two triptycene cores create a large π-concave surface area which should allow for excellent SWNT binding, while also creating plenty of internal free volume for the calamitic liquid crystals to occupy, improving the alignment of **2** in 5CB. Finally, the phosphonate groups were preserved as they had proven effective at functionalizing both ITO and SiO_2 in previous experiments with both phenyl phosphonic acid and **1**.

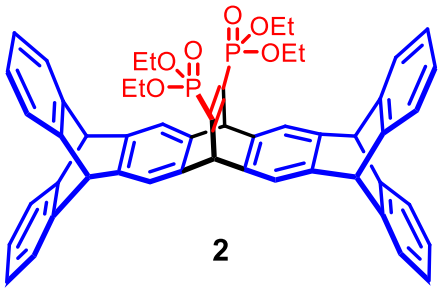

2

-Anchoring Group
-Triptycene Core for SWNT Binding
-Large Internal Free Volume for Alignment

Scheme 7: Larger iptycene design for SWNT alignment.

2.3.4.1 Synthesis of Extended Iptycene (2) for use in the Alignment Relay Technique

While **2** had never been synthesized before, the precursor molecule had been reported by Hart et al. making it an attractive synthetic target.[285] However, attempts to reproduce Hart's synthesis proved to be unfruitful, with many of the steps failing under the reported conditions, and so the conditions had to be reworked to provide an optimal route to our target molecule. The overall synthetic scheme can be seen in Scheme 8.

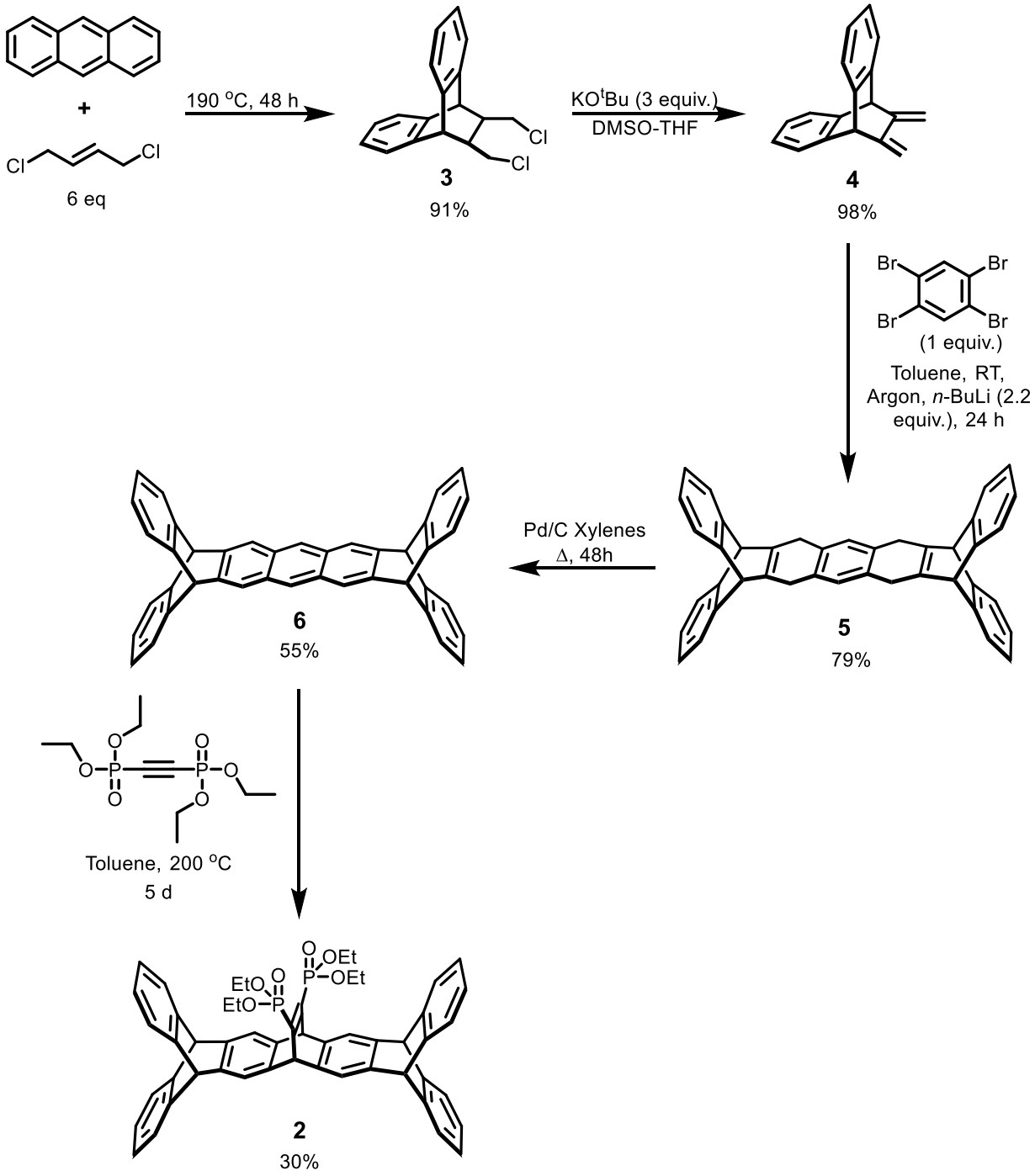

Scheme 8: Reaction scheme for the synthesis of iptycene 2.

The first step in the reaction sequence involves a Diels-Alder reaction between anthracene and trans-1,4-dichlorobutene to give Diels-Alder adduct **3**. The reaction

results in a black solution with some precipitate formation upon cooling to room temperature. The original report called for purification of the mixture by passing it through an alumina plug to remove the black byproducts, however this did not adequately remove the byproducts and a mixture of starting materials, product, and black byproducts were recovered. Attempts to remove the black byproducts on silica gel proved effective, but unfortunately the excess dichlorobutene and unreacted anthracene eluted with product **3** and further separations were ineffective. The amount of dichlorobutene used in the reaction was reduced to one equivalent and the reaction was run in toluene in order to reduce the amount of dichlorobutene left over after the reaction. However, this caused yield to suffer drastically and much of the dichlorobutene and anthracene was left unreacted, and once again inseparable from the product. Finally, the reaction was run neat with six equivalents of dichlorobutene and the reaction was followed by NMR to determine that after two days, there was complete consumption of anthracene. Instead of relying on chromatography to remove the excess dichlorobutene, it was removed through vacuum distillation, with the pure, clear distillate being reused in subsequent reactions. The remaining black oil was purified using silica gel chromatography to give **3** as a pure white solid.

A double elimination reaction of **3** gave **4** in nearly quantitative yields with no trouble. The elimination reaction worked so well that it was attempted on the crude reaction product of the first Diels-Alder in order to bypass the need for purification of **3**. The elimination of the crude mixture resulted in the characteristic colour change for the elimination reaction, but upon workup and isolation, only **3** with some remaining

dichlorobutene was recovered. It is likely that the dichlorobutene reacted with the base faster than **3** could, preventing the desired elimination reaction.

The synthesis of the non-aromatized iptycene core (**5**) was achieved through a Diels-Alder reaction between 1,2,4,5-tetrabromobenzene and diene **4**. 1,2,4,5-tetrabromobenzene was converted to a benzyne in situ through the dropwise addition of *n*-BuLi resulting in **5** precipitating from the solution. Product **5** was then aromatized in refluxing xylenes over 5 % palladium on carbon (Pd/C) and recrystallized from acetone to give the product in 55 % yield. The aromatization was revisited in order to improve the yield, but further reactions with Pd/C in different quantities, temperature, and solvents did not improve the yield. Fortunately, switching oxidizing agent to 2,3-dichloro-5,6-dicyano-1,4-benzoquinone (DDQ) was responsible for increasing the yield to 88 % and is now the preferred method for oxidation of extended iptycenes in our lab.

The final step was a last Diels-Alder reaction between extended iptycene **5** and bis(diethoxyphosphoryl)acetylene. The first conditions tested were the same as those used to create the original phosphonate iptycene **1**, but it failed to produce significant quantities of desired product **2**. Luckily, the starting materials were not consumed in the reaction and simply increasing the temperature was enough to push the reaction forward and obtain pure **2** through silica gel flash chromatography. Both starting materials were also purified and recovered for recycling in future reactions.

2.3.4.2 Testing the Liquid Crystal Alignment of 5CB Doped with Iptycene 2

Before testing the alignment relay technique with extended iptycene **2**, a study was conducted to determine the effect of **2** on the alignment of 5CB while under the effects of a rubbed polyimide liquid crystal alignment layer. The concern was that the dissolution of

2 into the 5CB nematic liquid crystal phase might disrupt the orientational order of the phase or change the phase transition temperatures. The easiest way to determine if this is the case is to look at the solution under crossed polarizers in a polarized optical microscope, which required the alignment to be conducted on a transparent substrate. The rubbed polyimide alignment layer itself is transparent so ITO was chosen as the functionalization substrate over SiO_2 because the former is transparent.

A polarized optical microscope is quite simple in construction and only differs from a regular optical microscope by the inclusion a heating stage for the sample, and two polarized lenses, one placed before the sample and the other placed after it. In simpler POMs the lenses are fixed in a perpendicular direction, in others the lenses can be rotated to different angles. The basic operating position of a POM is with the lenses perpendicular such that any light that goes through the first polarized lens is completely blocked when it goes to the second lens (Figure 37). Therefore, when placing a standard isotropic liquid in a POM, the image is completely black because it refracts the light in every direction equally, thus not changing the polarization of the light.

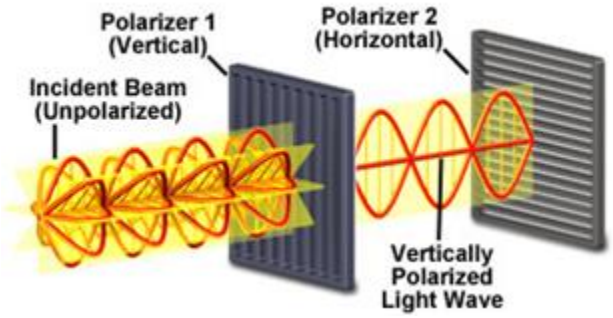

Figure 37: Example of light passing through crossed polarizers.

When a liquid crystal is placed between the crossed polarizers light can pass through the second polarizer due to the birefringence of liquid crystal materials. For example, calamitic liquid crystals, like 5CB, are rod shaped and so have one long axis and one short axis, which leads to a molecule with very high shape anisotropy. When the liquid crystals form their short-range domains of orientational order, they act as birefringent materials, meaning that they refract the light differently in two directions. This causes plane-polarized light to be refracted in such a way that it is no longer plane polarized, and therefore some of the light can pass through a second, perpendicular polarizer. The birefringence of liquid crystals causes unique patterns to be observed based on the local alignment of the liquid crystals in a sample, with some areas appearing dark, others light, and the rest will be varying shades and colours. The type of image is indicative of the liquid crystal phase which allows for accurate identification of the liquid crystal phase that is formed (Figure 38). The transition temperature for each of the liquid phase can be determined by observing the changes in POM structure while changing the temperature of the heating stage. The colours and shapes of the resulting image are the result of defects in the alignment of the liquid crystal, so when there are no defects, the image appears as a single, solid colour (Figure 38a).

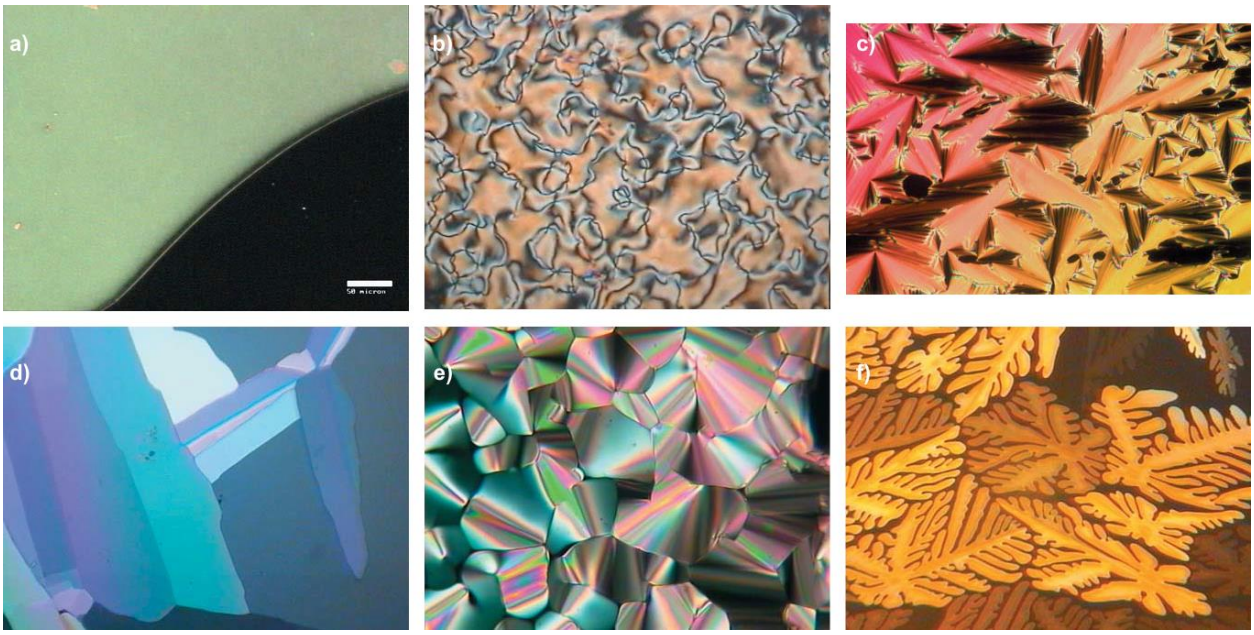

Figure 38: Example POM images of various liquid crystals: a) aligned nematic phase (light green), b) Schlieren texture of a nematic phase, c) fan-shaped texture of a smectic A phase, d) mosaic texture of a smectic B phase, e) pseudo focal conic fan-shaped texture of a discotic columnar phase, and f) dendritic growth of a banana B_1 phase.[316]

When looking at 5CB under crossed polarizers at room temperature, one expects to see the typical Schlieren texture of a nematic liquid crystal, similar to Figure 38b, and once aligned the image should become a smooth, single colour, like in Figure 38a. The 5CB/**2** solution had to be tested to ensure that the incorporation of 2 wt% of **2** would not disrupt the liquid crystal phase stability of the 5CB liquid crystal. First, the solution was observed between two glass slides, and the heating stage was heated to 40 °C such that the 5CB entered the isotropic liquid phase and the image went black. The stage was allowed to cool slowly until the Schlieren structure that is characteristic of a nematic liquid crystal started to become visible at 35 °C, as expected of 5CB, indicating that there was no destabilization of the nematic liquid crystal phase.

Once the stability of the liquid crystal phase in the 5CB/**2** solution was confirmed, it was important to ensure that the alignment of 5CB would not be disturbed by the presence of **2**. Before this, however, pure 5CB was used as a standard to ensure that the alignment layers were functioning properly. The first alignment attempts were a failure, with aligned streaks being seen throughout the sample, which were attributed to scratches on the alignment layer surface (Figure 39a). Upon selection of unblemished alignment layers, the 5CB standard showed alignment immediately upon cooling from the isotropic liquid phase into a solid yellow colour (Figure 39b).

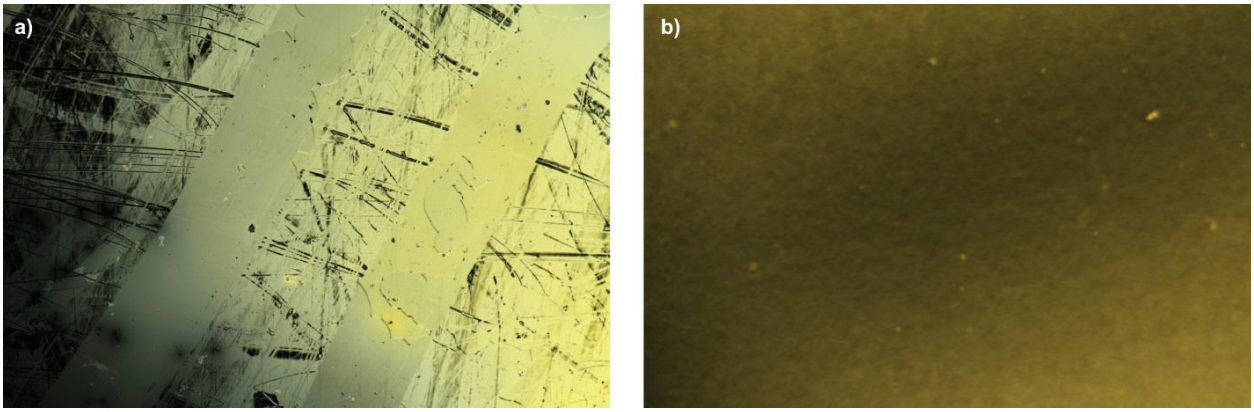

Figure 39: POM images of 5CB standard under the effects of alignment. a) Exhibiting defects due to scratched alignment layer, b) proper alignment.

With the alignment of 5CB on the rubbed polyimide alignment layer confirmed, the 5CB/**2** solution was examined. For this, the 5CB/**2** solution was placed between ITO and the rubbed polyimide alignment layer, with the ITO surface on the bottom, and the stage was heated to 40 °C. However, upon cooling, instead of forming a solid colour quickly, a defect-rich pattern emerged immediately (Figure 40a). The small, aligned regions slowly merged over time into larger regions of order, that showed only a small number of Schlieren defects (Figure 40b, c, and d). After about fifteen minutes, the alignment was

completed (Figure 40e) and confirmation that **2** would not interfere with the overall liquid crystal alignment was received, and therefore **2** could be potentially useable in the alignment relay technique.

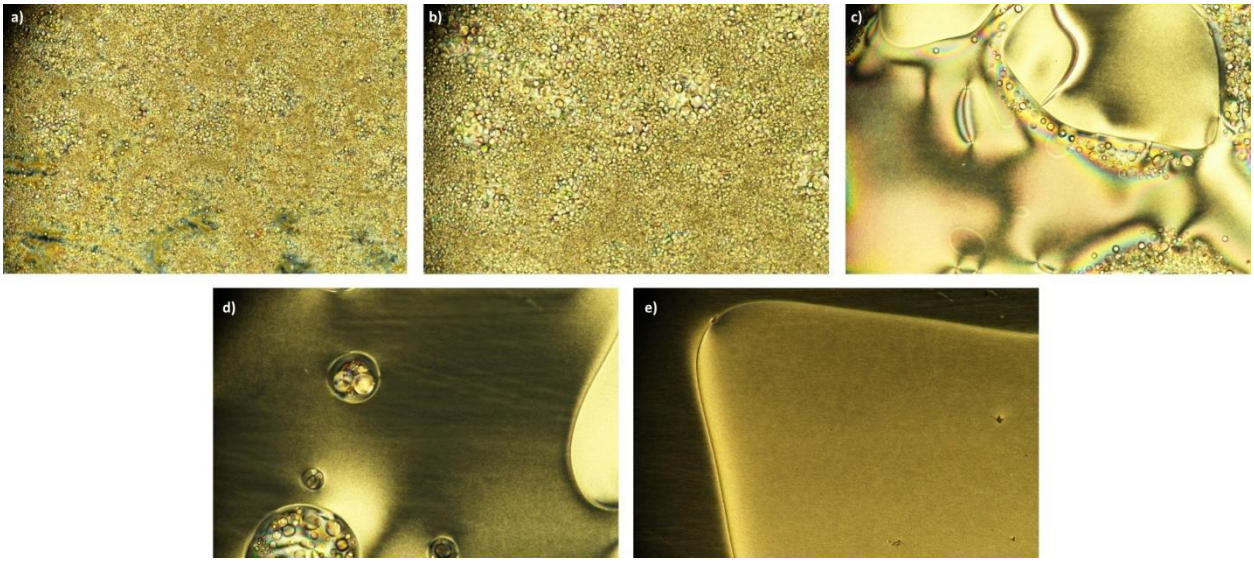

Figure 40: POM images of 5CB/2 solution between an alignment layer and ITO upon slow cooling from 40 °C exhibiting a) defect-rich pattern, b) increase in size of ordered regions, c) large aligned regions with Schlieren defects, d) almost completely aligned liquid crystal with several areas with defects, and e) well-aligned 5CB/2 solution.

2.3.4.3 Alignment Relay Technique Trials

With the alignment of the 5CB/**2** solution confirmed, it was time to test it with the alignment relay technique. The piranha cleaning method that was found to work best for phenyl phosphonic acid and **1** was also used to clean the ITO and SiO_2 for these trials. A solution of 2 wt% **2** in 5CB was heated past 40 °C and a drop of the solution was pipetted onto a liquid crystal alignment layer and allowed to cool to room temperature, after which a 10 x 10 mm slide of cleaned ITO was placed on top of it. The slides were pressed together such that the drop was spread out across the surface of the ITO, and they were left to react for a day. The ITO was then separated from the alignment layer and was

rinsed with dichloromethane (DCM) to remove all unreacted **2** and all the 5CB. At this point, the ITO surface is covalently functionalized with an aligned array of **2** and is ready for SWNT deposition.

At first, SWNT deposition times had to be screened, with the **2**-functionalized ITO slide being left in an aqueous suspension of surfactant wrapped SWNTs. Originally, the deposition times that were being tested ranged in the minutes to hours, and the surfaces were then dried with a stream of N_2. However, the AFM images of the resulting surfaces showed no nanotube deposition when compared to the cleaned ITO standard (Figure 41a). When the deposition time was increased to 24 h, the AFM images started to show some nanotube deposition, and the small number of nanotubes found on the surface were aligned in the same direction (Figure 41b). With such promising results, longer deposition times were attempted, and it was found that after two days the **2**-functionalized surface had a good density of well-aligned SWNTs deposited onto it (Figure 41c).

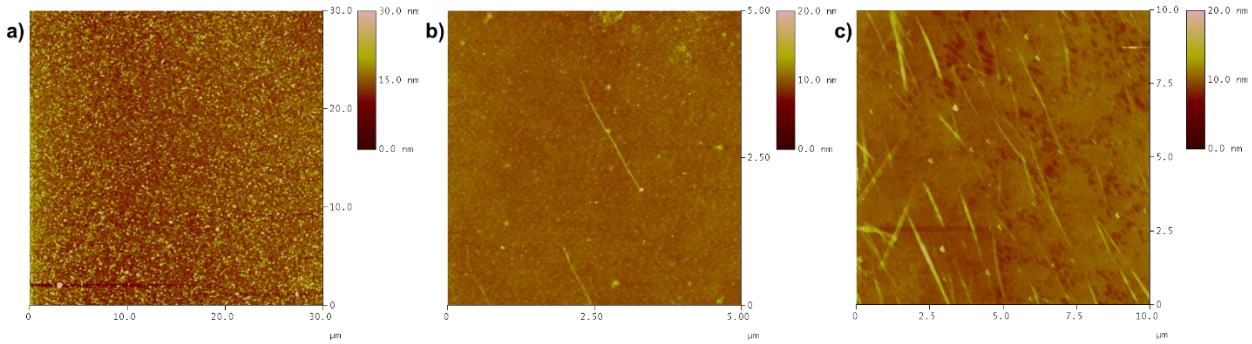

Figure 41: AFM images of a) piranha cleaned ITO, b) after one day nanotube deposition time, c) after two days of deposition time.

The results required validation to confirm that it was indeed the liquid crystal alignment was being relayed to the SWNTs. To do this, we decided to run an experiment where there was a break in the alignment relay by removing the liquid crystals such that

2 was not under the effect of alignment when it functionalized the ITO surface. First, benzonitrile was used as a replacement for 5CB because it is a small molecule with the same shape but lacks liquid crystal phases, and therefore provides no alignment. The resulting **2**-functionalized surface therefore possesses no alignment and should not align the nanotubes that are deposited on the surface. Another control experiment was also run with 5CB at 50 °C such that 5CB was in the isotropic liquid phase, losing all alignment properties. After the deposition of nanotubes on the surfaces, AFM images showed that nanotubes were completely absent from both control experiment surfaces (Figure 42).

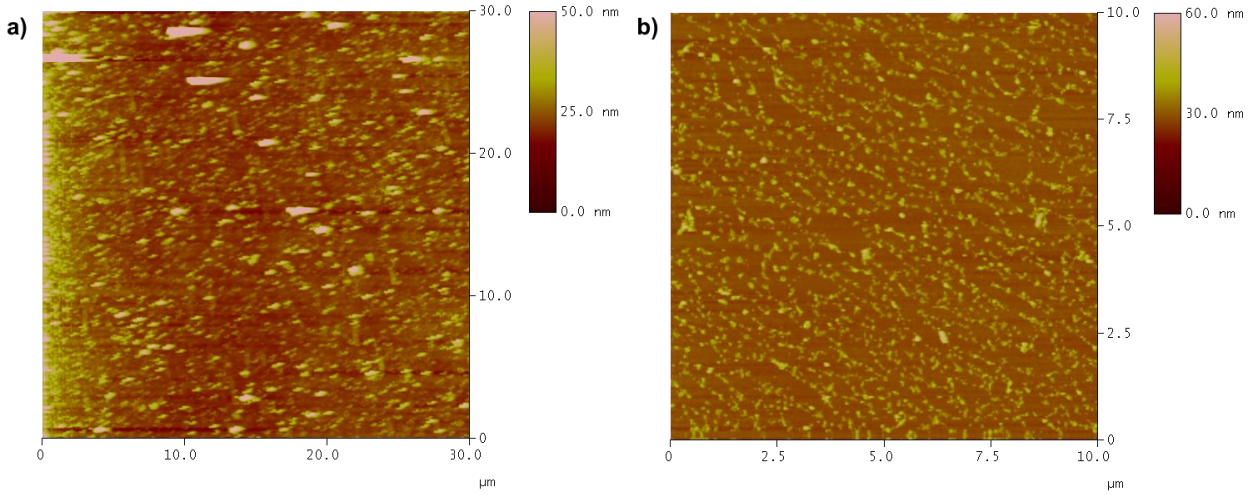

Figure 42: AFM images of control experiments a) with benzonitrile, b) with 5CB above clearing point.

The reason for this result was not immediately obvious, but upon further investigation it became clear that the nanotubes do not deposit onto the unaligned surface because there is a lack of π-π interactions between the surface and the nanotubes. In an aligned surface, the nanotubes can find domains where they undergo π-π interactions along the entire length of the nanotube, allowing them to stay on the surface during deposition and cleaning. Previous studies have shown that carbon nanotubes are resistant to deposition

on non-polar surfaces,[317] so we believe that without the alignment of **2** providing sufficient π-π stacking interactions, the nanotubes do not have the required binding energy to stay on the surface and are either not deposited at all or are easily removed during post-deposition washing process (Figure 43).

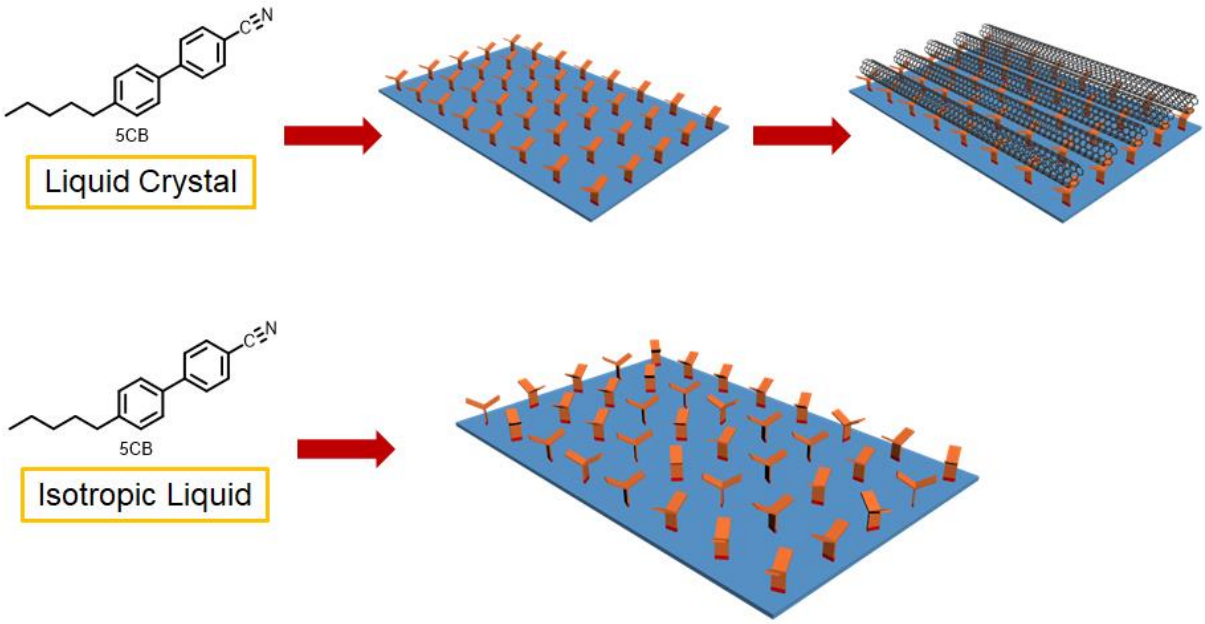

Figure 43: Schematic representing the alignment of 2 on ITO under the effects of liquid crystal alignment and in the absence of alignment. The aligned surface allows for easy deposition of nanotubes.

2.3.4.4 AFM and Raman Studies of the Alignment and Sorting of the ART

The alignment relay technique was envisioned to be able to not only align carbon nanotubes but also sort them due to the shape of the iptycene nanotweezers. With the observation of alignment exhibited by the nanotubes deposited on **2**-functionalized ITO, we needed to quantify the alignment and determine if there was any sorting of the nanotubes.

First, AFM was used to quantify the alignment of the nanotubes found on the ITO surface. The statistical analysis of the alignment was done through AFM study of several images amounting to about 200 nanotubes. Most of the nanotubes were aligned along the same director with some outliers, and the standard deviation of the alignment was 23 ° with 90% of the nanotubes within 37 ° of the average alignment (Figure 44). This is quite astounding considering the methodology used required no specialized equipment, like lithography, and can be done over a large area. Using AFM, the density of the nanotubes was found to be 0.39 μm^{-2}.

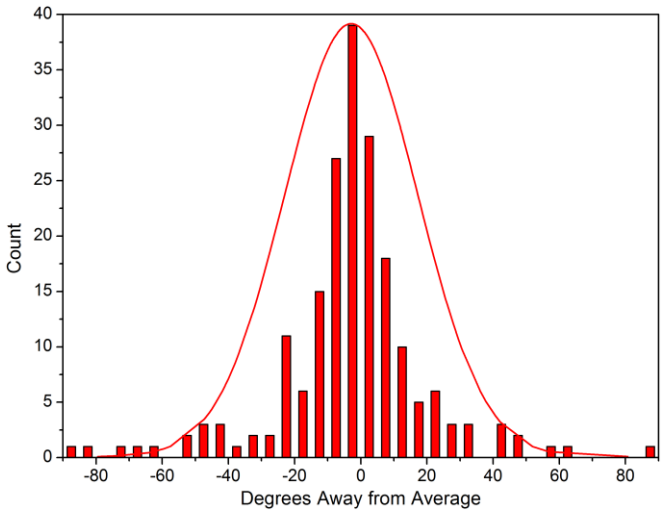

Figure 44: Histogram of the alignment of nanotubes deposited on an aligned 2-functionalized ITO surface. Alignment of each nanotube is shown as the deviation from the average alignment of the total sample.

Through the AFM alignment measurements, it became apparent that the nanotubes were of exceptionally long lengths compared to what was expected. The average length of the as-purchased nanotube suspension was 1.00 µm, but upon further AFM analysis of ART-deposited nanotubes on ITO, the average length was determined to be 1.83 µm (Figure 45). This was surprising, as length was not one of the parameters that was

expected to be effectively sorted by the ART. We believe that the cause of the preferential binding to longer nanotubes is because the longer nanotubes are capable of forming more π-π interactions than the shorter nanotubes, giving them a higher binding energy to the surface. This result implies that the binding mechanism is likely reversible and thermodynamically favours longer nanotubes, in fact the reversibility of the ART has been exploited in other work done in the Schipper group through the introduction of simple sonication during the deposition step.[318]

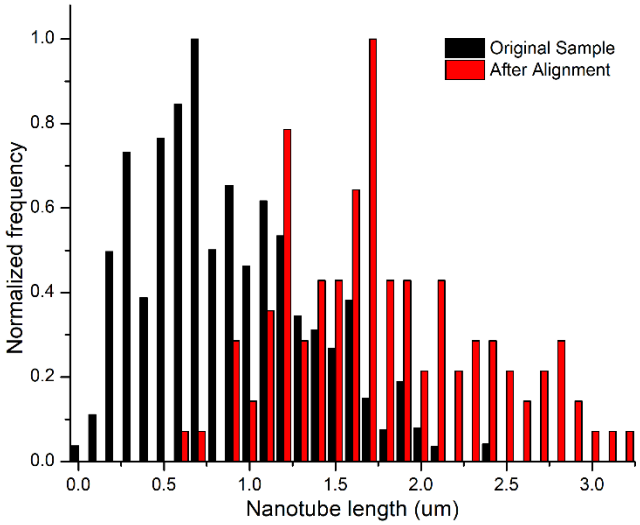

Figure 45: Length data of nanotubes from the original as-purchased sample (black) and ART-deposited nanotubes (red).

The AFM micrographs were also used to determine the diameter sorting of the resulting nanotubes, however when height measurements were taken, they varied drastically (several nanometers) along the length of a single nanotube. This variation is likely due to the proprietary surfactant wrapping on the nanotubes being inhomogeneously distributed along the nanotube surface. To overcome this issue, we turned to Raman spectroscopy to determine the diameter of the nanotubes instead. Raman spectroscopy has the advantage of not being sensitive to the surfactant and it is

capable of observing large areas, resulting in a much larger sample size. However, the drawback is that Raman spectroscopy requires a surface that is capable of reflecting the incident laser towards the detector, and due to ITO being transparent it could not be used in the Raman studies.

We switched surfaces from ITO to SiO_2 for the purposes of Raman spectroscopy because SiO_2 is good at reflecting the incident laser light, but this meant that the ART had to be optimized on silicon first. Luckily, the process worked about the same as on ITO, with a reaction time of one day and a deposition time of two days, and the resulting surface showed a standard deviation of alignment of 33 °, average length of 1.53 µm, and density of 0.57 μm^{-2}. With an ART-deposited nanotube sample ready on SiO_2, Raman studies were made available.

The Raman studies were conducted with a 632 nm excitation laser on a vibration-resistant stage. The radial breathing mode region of the Raman spectrum was of interest because it gives direct insight into the diameters of the nanotubes. First, a standard sample was prepared by piranha cleaning a SiO_2 surface, and then dropcasting the as-purchased, surfactant wrapped carbon nanotubes onto the surface and allowing the solvent to evaporate, depositing a thick film of CNTs. The Raman spectrum of the standard sample showed a strong signal for three chiralities of nanotubes corresponding to diameters of 1.25 nm, 1.44 nm, and 1.59 nm (Figure 46). When the Raman studies were conducted on ART-deposited nanotubes on SiO_2, several scans of different areas had to be combined, due to the low number of nanotubes on the surface. The results show that there is a drastic preference for larger diameter nanotubes, with the 1.25 nm nanotubes almost completely selected out of the sample, and the 1.59 nm nanotubes

becoming the most abundant (Figure 46). An unknown peak appeared at 232 cm^{-1} which was believed to correspond to **2**, as its structure is similar enough to a CNT that it may possess a phonon that is like that of a CNT radial breathing mode. The Raman spectrum of freshly prepared **2**-functionalized SiO_2 contained only the peak at 232 cm^{-1}, verifying that it belongs to **2**.

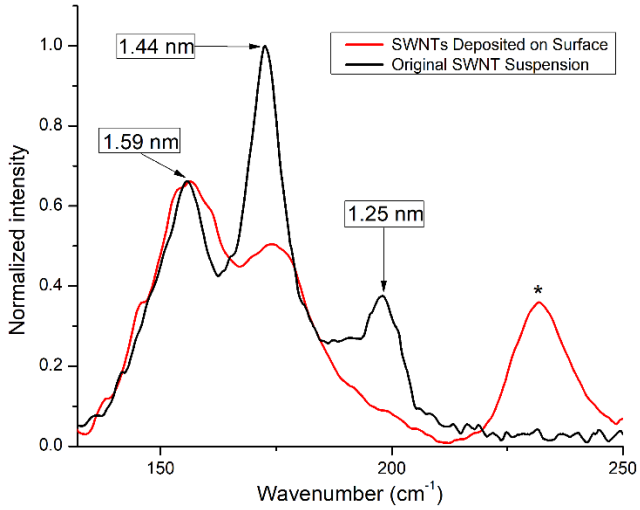

Figure 46: Radial breathing mode region of the Raman spectrum of a) the as-purchased nanotube sample dropcast on SiO_2, b) ART-deposited nanotubes on SiO_2. The peak marked with a * indicates the signal from extended iptycene 2.

With these results, we were able to confirm that not only does the alignment relay technique effectively align carbon nanotubes and sort them by length, but it also has a significant effect on the diameter sorting as well. Furthermore, because phosphonate monolayers have been incorporated into other FETs, it bodes well for the direct incorporation of ART into future CNTFET fabrication processes. The ART is amenable to large area depositions through the use of larger alignment layers and does not require any expensive instrumentation or tedious work. The main reason for creating the ART however, was to have a technique that is capable of further modifications that allow for

judicious targeting of preferred CNT properties through rational alterations of key parameters.

2.3.5 Testing Other Liquid Crystals in the ART

One of the easiest parameters to change in the alignment relay technique is the liquid crystal. The first liquid crystal that was tested was 5CB for ease of use reasons: it is a room temperature nematic liquid crystal that is very easy to align and is still liquid enough to dissolve other materials. With 5CB working so well, we wanted to try a higher clearing point nematic liquid crystal and a smectic A (SmA) phase liquid crystal to see what effects they might have on the overall control of the ART.

Our intention was that the higher clearing point would allow for a faster reaction between **2** and the substrate, decreasing the overall time of the ART. Additionally, a faster reaction time may also increase the density of **2** on the surface, and perhaps also improve the nanotube deposition. To test this hypothesis we tried to use a proprietary MERCK liquid crystal, denoted here as **LcMRK**, with a clearing point of 70 °C. The liquid crystal alignment portion of the ART was done on a heating stage which was first heated past 70 °C and then held at 65 °C for one day using a **LcMRK/2** solution. After deposition, AFM microscopy of the surface showed deposition of what appears to be triangular shaped crystals, but no nanotubes (Figure 47). The crystals are likely **LcMRK** that crystallized onto the surface and were not washed off during the rinsing procedure. However, further cleaning was unable to completely remove the crystals from the surface, and even after extended sonication in organic solvents nanotube deposition was still not observed. Perhaps another liquid crystal with a lower clearing temperature, or different structure would be easier to completely remove from the surface post-functionalization.

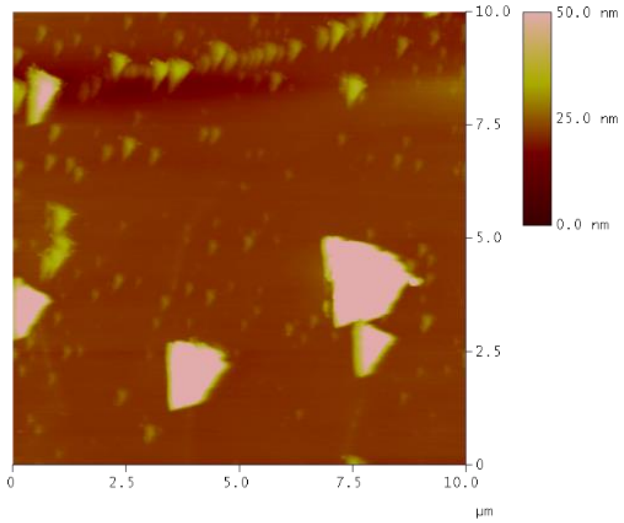

Figure 47: AFM micrograph of 2-functionalized ITO surface after ART-deposition with LcMRK as the liquid crystal.

Fortunately, the results obtained when switching to 4'-octyl-4-biphenylcarbonitrile (8CB) were far more promising. 8CB is an analogue of 5CB with an octyl chain instead of a pentyl chain (Scheme 9), but the small change in structure has a profound effect on the order of the liquid crystal phase. 5CB is a nematic liquid crystal, meaning it is the lowest ordered liquid crystal phase which exhibits only orientational order, and on the other hand, 8CB is a room temperature smectic A liquid crystal, a more ordered phase. SmA phases exhibit improved orientational order over nematic phases and they also possess lamellar positional order as well (Scheme 9). We were expecting that the increase in orientation and the added positional order would improve the order of **2** on the surface, thus providing an increase in the alignment of the deposited nanotubes. 8CB was the liquid crystal of choice because, like 5CB, it is commercially available, well studied, and is in the SmA phase at room temperature.

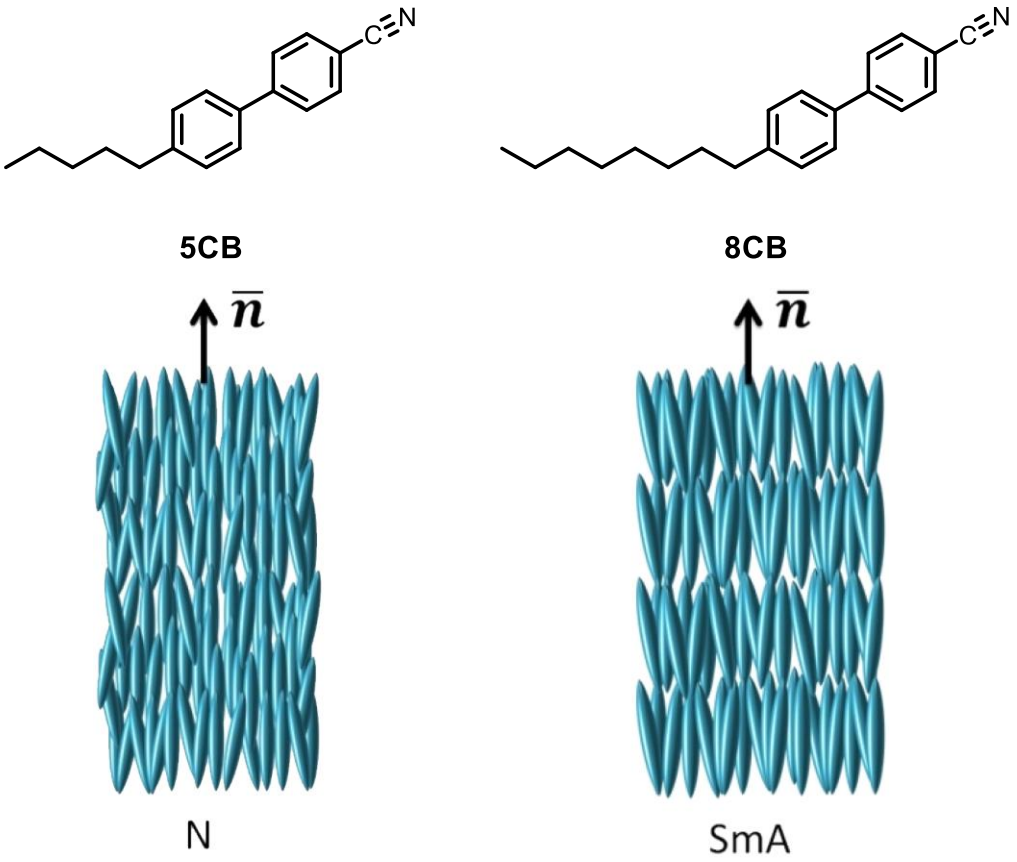

Scheme 9: 5CB and 8CB showing the order of their liquid crystal phases.

When performing the ART with 8CB it becomes crucial to heat the 8CB/**2** mixture past the clearing point to make 8CB less viscous, allowing for full dissolution of **2**. 8CB was incorporated into the ART using ITO as the substrate with a reaction time of one day and deposition time of two days, as in the original ART procedure. The ART-deposited nanotubes showed alignment, but more interestingly, it became immediately apparent that the length of the nanotubes was considerably shorter than when the ART is done with 5CB. A detailed statistical analysis of ~ 1,800 nanotubes over an area of 2,200 μm^{-2} revealed that the standard deviation of alignment was 30 °, the density of the nanotubes was 0.81 nanotubes μm^{-2}, and the average length of the nanotubes was 0.81 µm. These

results are in stark contrast to the 5CB parameters of 1.83 μm, 0.39 nantotubes μm^{-2}, and a standard deviation of alignment of 23°.

The plainest difference between the two ART experiments is that the length sorting is completely reversed. When 5CB was used, the ART-deposited nanotubes were on average 0.83 μm longer than the as-purchased sample, conversely 8CB ART-deposited nanotubes were 0.29 μm shorter on average than the standard sample. This means that with the simple change of the liquid crystal from a room temperature nematic to a room temperature SmA, the ART-deposited nanotubes show a > 1 μm shift in the length sorting. On top of profound swing in length sorting, the nanotubes were also about twice as densely deposited on the 8CB ART-surface.

We hypothesize that the length sorting difference and increase in density is directly due to the improved order in the SmA phase. Up to this point the **2**-functionalized surface has been depicted in its ideal condition with perfect alignment and perfect positional order (Figure 48), however the reality is likely far from this idealized depiction. Far more likely is that **2** is not perfectly aligned or positioned, and in the case of 5CB, **2** would be aligned fairly well, but would possess no positional order whatsoever. When using 8CB, the alignment should be improved, and **2** would also possess positional order. We think that the positional order of 8CB, and therefore of **2**, is the reason for both the increase in density and preference for shorter nanotubes. The rationale for the original length sorting observed in 5CB was that the nanotubes of longer length were able to undergo enough interactions along their length to bind to the surface, whereas the shorter nanotubes were not and were washed off. When extending this idea to 8CB, we see instead that the shorter nanotubes must be now capable of forming enough π-π interactions to bind to the

surface. For this to be true, there must be a fundamental change in the alignment of **2** on the substrate. It is likely that the change to 8CB has imparted positional order onto **2**, creating more domains where **2** is aligned both orientationally and positionally. This would increase the density of the nanotubes on the surface and because the as-purchased nanotubes were highly abundant in shorter nanotubes, the resulting 8CB ART-deposited nanotubes are shorter and more densely packed.

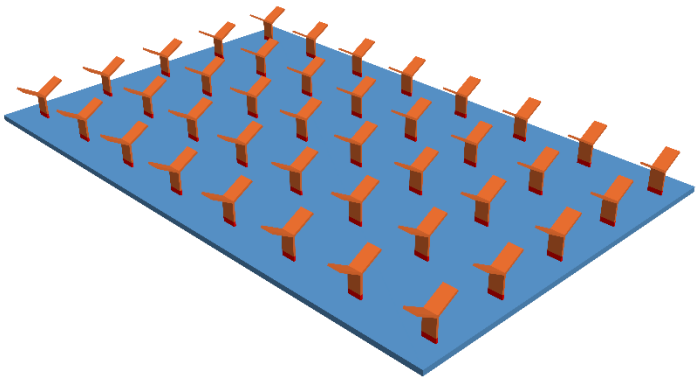

Figure 48: Idealized schematic of an aligned array of iptycenes covalently functionalized on a surface.

The other interesting aspect was that the average alignment was actually lower in the 8CB samples when compared to the 5CB samples, despite the higher order of SmA phases. The result was confusing but when the 8CB ART alignment was done on SiO_2, it also had a standard deviation of alignment of 30°, and in fact, every time the 8CB ART was performed, the standard deviation of alignment was very close to 30°. This is different from the 5CB ART which varies in the alignment from 23 ° to 42 ° from sample to sample, with no intentional change in conditions or preparation. We attribute this to the higher orientational order parameter of 8CB, in that it is far more consistent whereas 5CB has a lower degree of order, but more randomness so it can occasionally create a highly aligned surface or a poorly aligned surface.

Once we finished the 8CB ART AFM studies, we switched substrates to SiO_2 to undertake Raman spectroscopy studies. The reaction conditions used for the 5CB ART on SiO_2 resulted in very poor density of deposited nanotubes, which was attributed to lower reactivity of phosphonates with silicon oxide than with ITO. The functionalization reaction creates ethanol as a byproduct, so in an attempt to improve reactivity the reaction was tested under vacuum conditions to drive off the ethanol and push the reaction forward. The functionalization was run in a vacuum oven at room temperature under alignment conditions with varying reaction times from three hours to two weeks. Unfortunately, reaction times lower than one day still did not show any nanotube deposition, and the longer reactions appear to have transferred some film onto the surface (Figure 49).

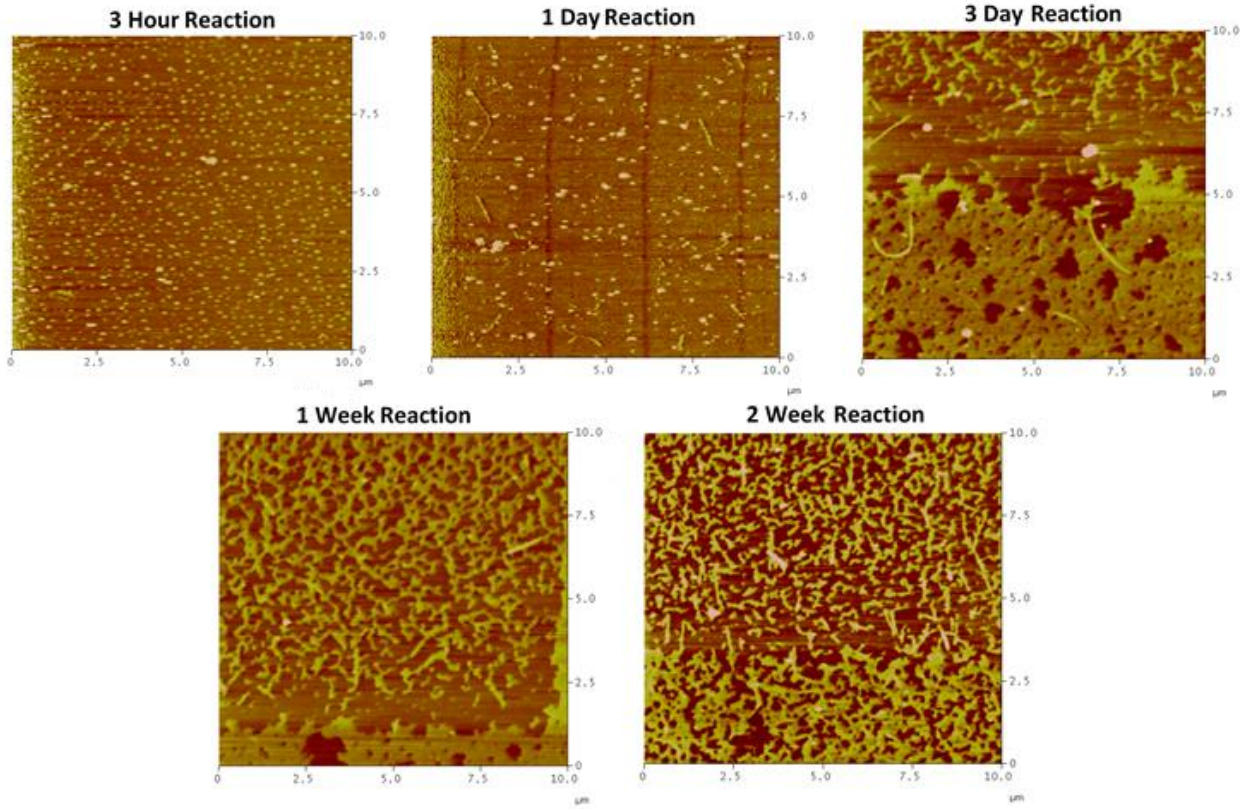

Figure 49: AFM micrographs of SiO_2 functionalization under vacuum.

The identity of the film was unknown, but we thought that it might be a thick, dense film of CNTs. So, the ART was performed under vacuum deposition again, but instead of using the CNT suspension in the deposition step, a surfactant solution of the same concentration without any nanotubes in it was used. Even with the nanotubes absent from the ART, the same film formed indicating that the film originated from something else. Seeing as the film was not the result of **2**, the only remaining potential source of the film was the polyimide coating of the alignment layer, or the surfactant itself. Since the surfactant is likely very easy to wash off in the typical washing procedure, we believe that under vacuum conditions there is a partial transfer of the polymer from the alignment layer onto the SiO_2 surface. This transfer is not observed under atmospheric pressure, so it appears that the vacuum accelerates the transfer. The film transfer precluded further investigation of vacuum reactions, but vacuum reactions can be revisited if another alignment mechanism for the liquid crystals is used, such as magnetic fields.

Instead of relying on vacuum reactions, the reaction time was increased, although this is not ideal because an increase in the ART time makes it less viable for adaptation to use in electronics. Fortunately, after two days of reaction the 8CB ART worked very well on SiO_2, with the resulting nanotubes exhibiting a density of 1.72 nanotubes μm^{-2}, an average length of 0.68 µm, and a standard deviation of alignment of 30°. The results are even more striking than on ITO with the density tripling versus the 5CB ART on SiO_2.

With a properly ART-functionalized SiO_2 surface Raman spectroscopy studies were once again accessible. It was expected that the change in liquid crystal would not have

any impact in the diameter sorting of the nanotubes because the diameter selectivity is believed to be a result of the size and shape of the π-concave iptycene host. In fact, that is exactly what happened: the diameter of the 8CB ART-deposited nanotubes was the same as the 5CB ART-deposited nanotubes. The larger diameter nanotubes were enriched and the smaller diameter nanotubes were selected out of the sample in the same way as previously demonstrated. The 8CB results were very satisfying because they show that a small change in the ART can have a large impact on the resulting surface, and furthermore, the parameters can be targeted independently of one another, giving a high level of control over the final nanotube surface.

Finally, various nanotube deposition times were screened to determine whether there would be a significant difference in the parameters of the deposited nanotubes. It was expected that an increase in density of the nanotubes and perhaps even an improvement in the alignment would be observed, as nanotubes were dynamically exchanged with one another over the course of the longer deposition time. However, the results were quite random and no correlation in diameter, length, density, or alignment was observed as a function of deposition time. As such, one day remains the optimal deposition time for the alignment relay technique.

2.3.6 Alignment Relay Technique on Hafnium Oxide

Over the last few years, hafnium oxide has become an increasingly important component of FETs. As the size of transistors has decreased, there has been a drive to find more powerful dielectrics than SiO_2 to act as the gate dielectric. Hafnium oxide has become the leading dielectric to replace silicon dioxide, so it is important for us to find a way to adapt the ART to include functionalization of hafnium oxide.

The first attempt at using hafnium oxide as the substrate in the ART was done using 8CB, with the same conditions that are used for SiO_2. Unfortunately, under these conditions, no deposition was observed, and after increasing the reaction time to three days of reaction and two days of deposition, minimal CNT deposition was observed with a density of 0.02 nanotubes μm^{-2}, albeit with an incredible degree of alignment with a standard deviation of only 12° (Figure 50). These results suggest that the degree of functionalization of hafnium oxide with **2** was very low, and it led to us trying to find an alternative anchoring group that would react better with hafnium oxide.

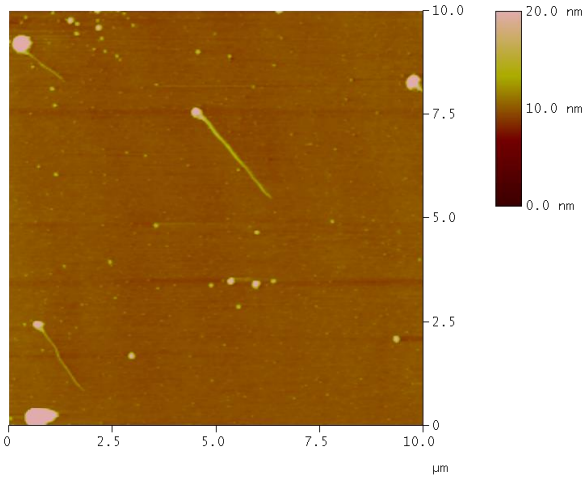

Figure 50: AFM image of ART-deposited nanotubes on hafnium oxide.

2.3.6.1 Synthesis of Iptycene with Hydroxamic Acid Anchoring Group

In the search for a more optimal binding group we came across a report by a research group from IBM who had used hydroxamic acids to selectively functionalize a hafnium oxide surface over a silicon oxide surface.[294,295] Hydroxamic acids are commonly used as ligands for transition metal catalysis and exist in both keto and enol tautomeric forms (Figure 51).[319] They are easily deprotonated to give the hydroxamate which is capable of

forming two covalent bonds with metal oxide surfaces, and their selectivity for hafnium oxide made the inclusion of hydroxamic acids on our iptycene particularly intriguing.

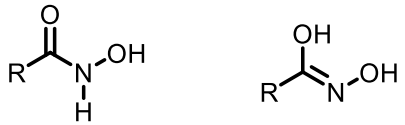

Keto **Enol**

Figure 51: Keto and enol tautomers of a hydroxamic acid.

We envisioned a synthetic route involving the installation of diesters onto our iptycene through a Diels-Alder reaction, followed by conversion of the esters to the desired hydroxamic acids. The installation of the esters is straightforward and only requires a Diels-Alder reaction with dimethyl acetyelenedicarboxylate (DMAD). Alternatively, DMAD could first be converted to the hydroxamic acid and then be used in a Diels-Alder reaction, directly installing the hydroxamic acids. Both routes were tested using anthracene as the substrate, so as to not consume our extended iptycene **6** (Scheme 10).

Route 1 offers the most convergent synthesis, requiring no step after the formation of the iptycene and was therefore initially more attractive, however attempts to convert DMAD to the hydroxamic acid were not successful. The reactions involved first reacting hydroxyl amine hydrochloride with potassium hydroxide in cold methanol, followed by precipitation and removal the formed potassium chloride, in order to obtain free hydroxylamine. The hydroxylamine solution was stirred for five minutes and then added to a stirring solution of DMAD in methanol. The first pass at the reaction resulted in a very violent reaction so subsequent attempts were done with dropwise addition of the hydroxylamine solution to DMAD. Once the addition was complete, further potassium

hydroxide was added until a pH of 10 was achieved, followed by stirring for 18 h after which the mixture turned orange. Upon acidification a light orange precipitate formed but the ^{1}H NMR contained no signals, lacking the characteristic hydroxamic acid peaks. The violent reaction that was observed lead to speculation that a potential Michael-addition could be competing with the aminolysis reaction, adding extra hydroxylamines to the DMAD. Further attempts with various bases and reaction conditions still failed to yield a product that could be characterized as **7**, so route 1 was abandoned in favour of route 2.

Route 1:

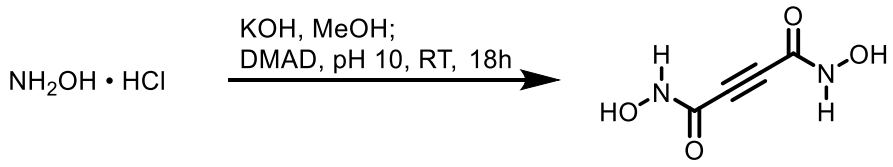

7

Route 2:

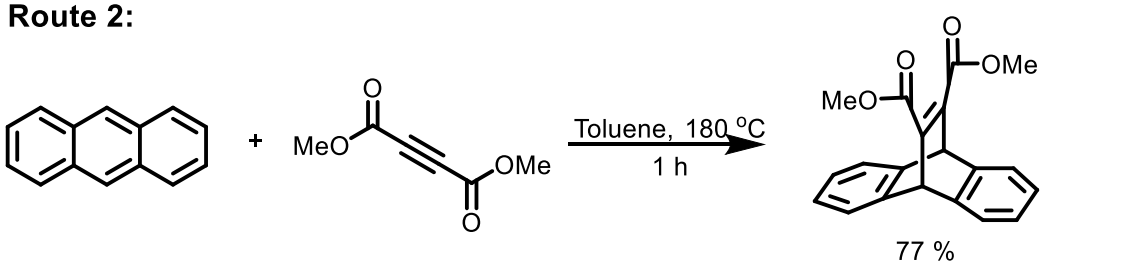

77 %

8

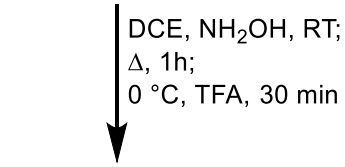

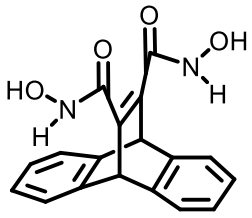

(10 %)

9

Scheme 10: Installation of hydroxamic acid anchoring groups onto anthracene.

While route 2 is not as efficient, it was possible that the conversion of the esters to the hydroxamic acids may have proceeded cleaner after the Diels-Alder. We used anthracene as the starting material for the model reaction with DMAD and the Diels-Alder gave product diester **8** in a 77 % yield after isolation by column chromatography on silica gel, however the conversion of the esters to the hydroxamic acid still proved to be challenging. Originally, the same conditions as route 1 were used but once again the resulting precipitate did not show any product signals in the proton NMR. The process was repeated several times with alterations in solvent, temperature and base to no avail. Finally, conditions were found that seemingly gave the desired product, albeit in very low yield. A solution of hydroxylamine hydrochloride in dichloroethane (DCE) was added to a stirring solution of **8** in DCE at room temperature. Cold triethyl amine was added slowly and the reaction mixture was refluxed for one hour, cooled on ice, and acidified with trifluoroacetic acid (TFA) to give a white precipitate in a 10 % yield. The precipitate was collected, and NMR analysis shows the expected product peaks, with the absence of the methyl peaks, however the hydroxamic acid amine peak was also missing. It is possible that the hydroxamic acid peak was undergoing rapid exchange in the deuterated water (D_2O) NMR solvent, and thus was not observable on the NMR timescale, but due to the incomplete proton spectrum, the identity of **9** has never been fully confirmed.

The covalent functionalization of a surface requires a very small amount of material, so despite the low yield that was seen in the anthracene trials, if the reaction could easily be extended to the synthesis of **11** we could still attempt to use it in the ART. Using the

best conditions obtained with the anthracene trials, the synthesis hydroxamic acid functionalized extended iptycene **11** was attempted (Scheme 11). The Diels-Alder reaction between **6** and DMAD was far slower than with anthracene and required two days of reaction time to give even modest yields, but otherwise worked as expected. The conversion of the esters to the hydroxamic acids, however, resulted in some new problems. After running the reaction a white precipitate was once again formed and collected, however unlike in the anthracene trials, this precipitate was entirely insoluble in deuterated water, and attempts to solvate **11** in non-polar organic solvents, polar organic solvents, and both acidic and basic aqueous mixtures all failed. A final attempt was made to solvate the white precipitate in heated 8CB and 5CB, but this also failed, and because the ART requires that the iptycene be soluble in the liquid crystal, the installation of hydroxamic acids onto the iptycenes was abandoned.

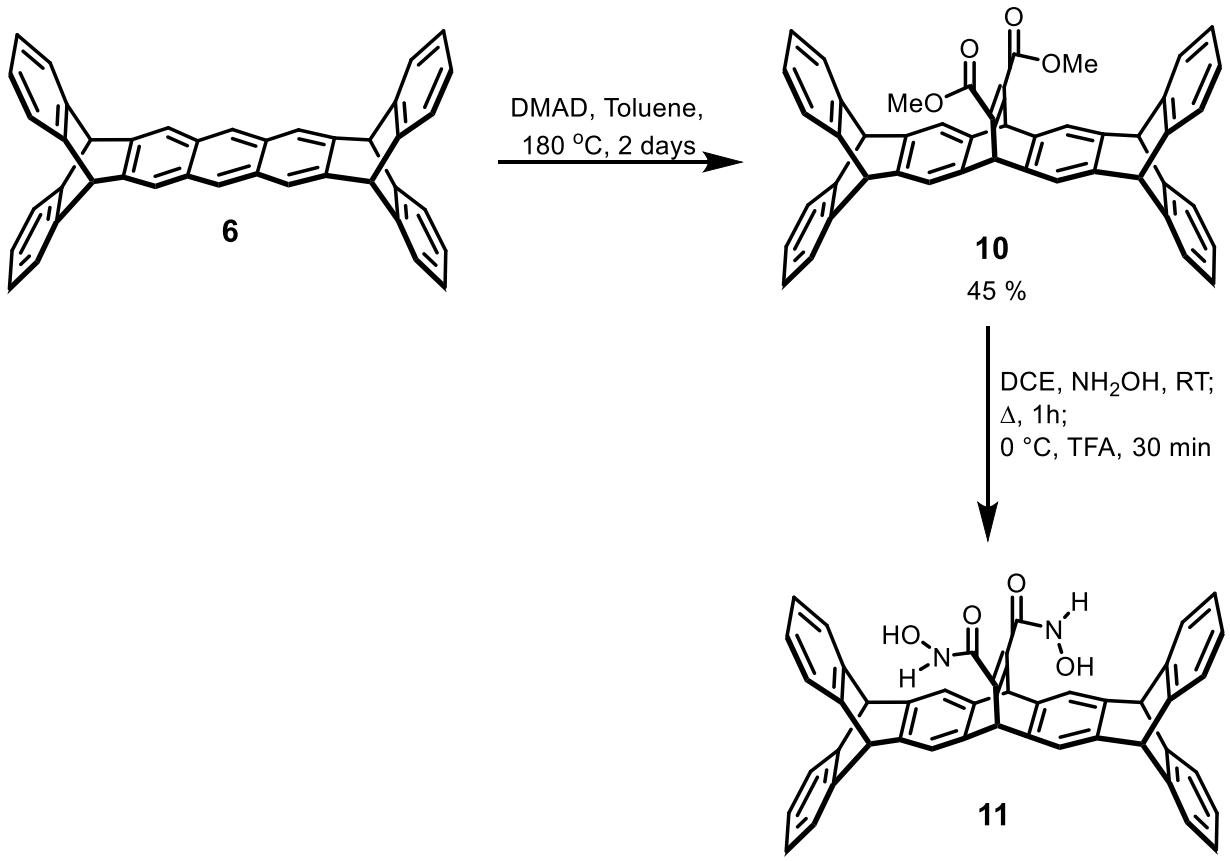

Scheme 11: Installation of hydroxamic acid groups onto extended iptycene.

Moving forward the hydroxamic acids could be derivatized to improve solubility. For example, an alkyl substituted hydroxyl amine can be used as a starting material in place of hydroxylamine hydrochloride, introducing a flexible solubilizing group and reducing the polarity of the molecule. There are several potential problems with this route, one being that the inclusion of large flexible alkyl chains may impede the approach of the iptycene onto the surface and hinder the resulting covalent bonds, making the product incapable of forming effective covalent bonds to the hafnium oxide surface. Furthermore, the alkyl chains may cause a disruption in the liquid crystal alignment, altering the liquid crystal phase or simply impeding the alignment and dense packing of the iptycene on the

functionalized surface. Despite these potential issues, the inclusion of even short alkyl chains may be of interest moving forward.

2.3.7 Using Lithographic Techniques to Enhance the Alignment Relay Technique

Lithographic techniques are heavily relied upon for the installation of nanoscopic features in the fabrication of functional nanomaterials, due to the excellent nanometer-scale resolution that they can achieve.[320,321,322,323] We were interested in coupling the alignment and deposition capabilities of the ART with the nanoscale control of lithography to see if we could further improve the effects of the ART. We had envisioned creating a surface with sub-micron sized trenches with the hopes that these would act as boundaries that would prevent nanotubes from adopting angles that deviate too far away from the intended angle. Furthermore, we originally wanted to couple this with a demonstration of the selective deposition of nanotubes with the hydroxylamine iptycene, so a surface with regions of HfO_2 and SiO_2 was the original target.

There are several ways that one can go about creating a surface that has regularly patterned trenches, and because we were targeting trenches with widths in the range of 70 – 300 nm, we had to rely on electron beam lithography (EBL). If the feature size is above one micron, UV lithographic techniques can be used instead, making the process much faster and less costly. The EBL machine that used had a spot size as small as 2.9 nm under optimal conditions and could therefore be easily relied upon to create the trenches that were required.

The route to creating the trenched surface required several key decisions to be made in terms of the exact methods used for each step: there were two potential routes that

were considered which can be seen in Scheme 12 and Scheme 13, route 1 features six steps while route 2 requires seven. The shorter process makes route 1 more enticing but further consideration of each step lead to route 2 being the chosen path forward.

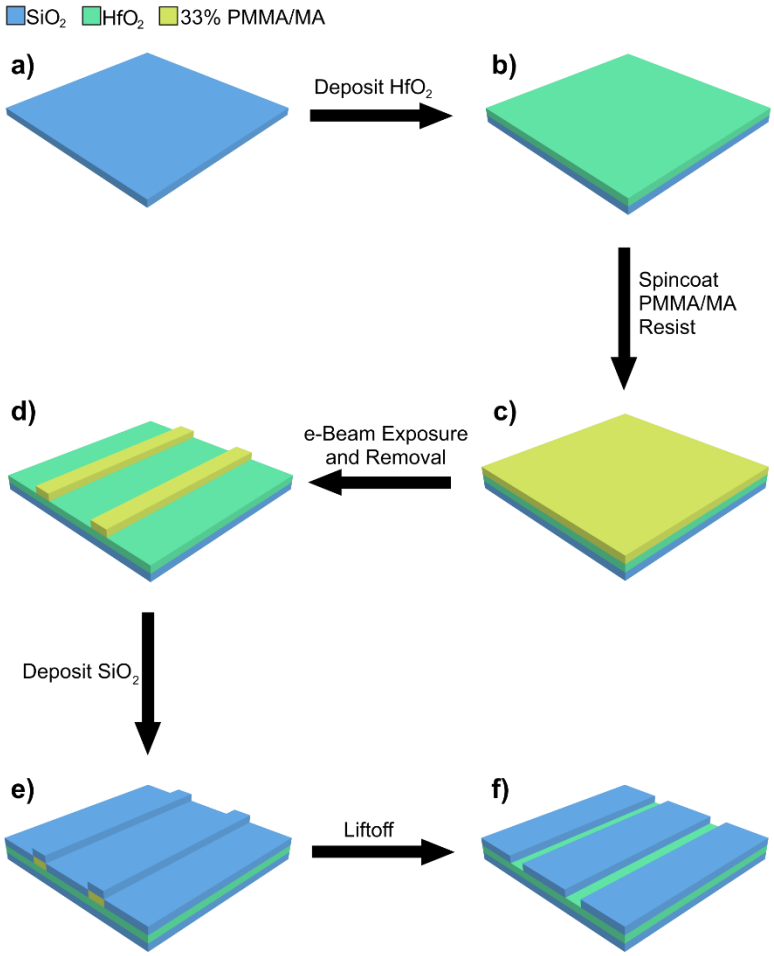

Scheme 12. Route 1 for creating trenched surface, featuring liftoff procedure.

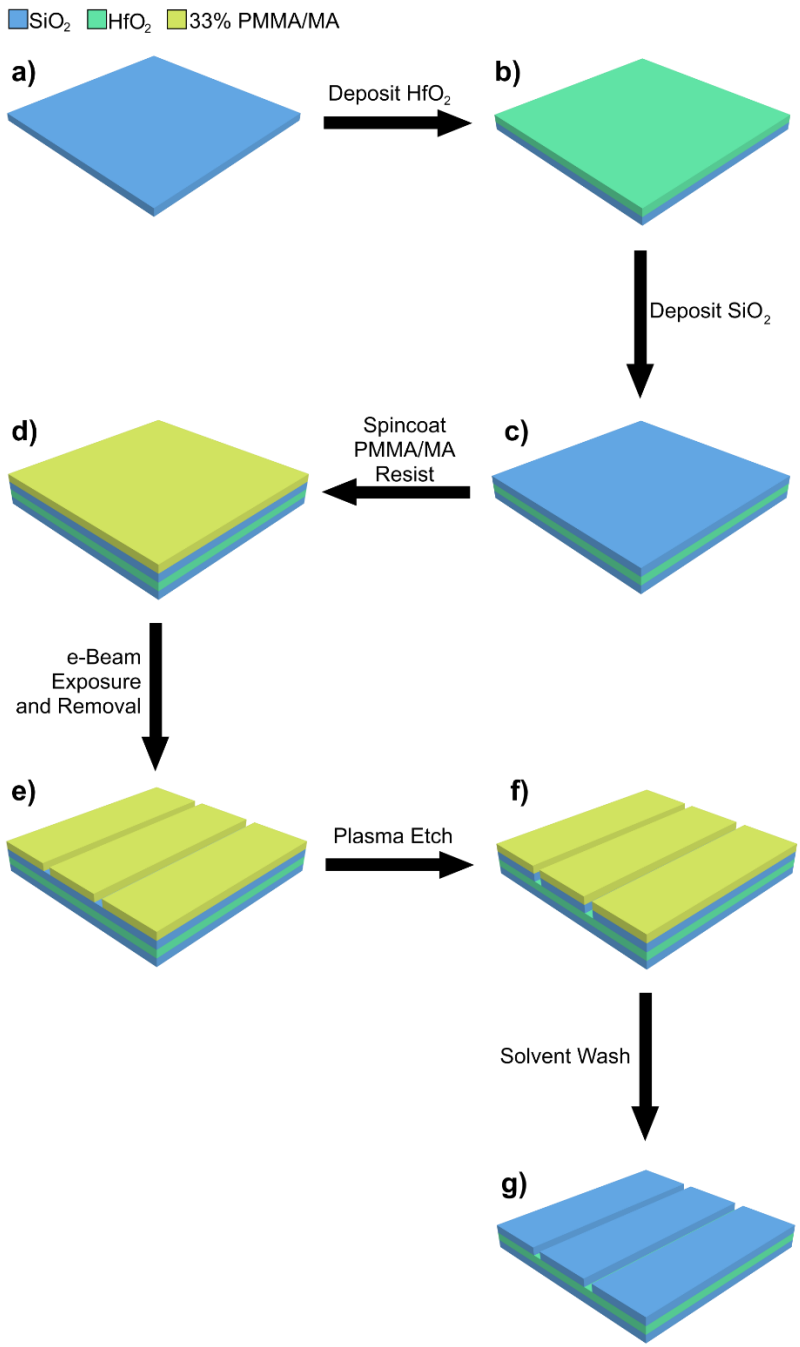

Scheme 13. Route 2 for creating trenched surface, featuring plasma etch.

The key difference between the two is the specifics around how the trenches are made. In route 1 the trenches in the top silicon layer are made indirectly by EBL: the electron beam sensitizes the resist (Scheme 12d) and following removal of the sensitized

areas and deposition of silicon oxide (Scheme 12e), the resist is completely removed in a liftoff procedure which also removes the excess silicon oxide (Scheme 12f). In this approach, during the sensitization step the electron beam would be targeting the area that ultimately becomes the SiO_2 plateaus in the final surface (Scheme 12f). Because the size of the trenches is on the scale of nanometers, and the size of the plateaus is on the scale of microns, the total surface area that the electron beam would have to target is at least one order of magnitude larger in this case. This route would therefore take several days to manufacture a desirable surface with an area of approximately 10 mm x 10 mm.

Furthermore, liftoff procedures are generally not as clean because the removed substrate is still present in the solution as it is being removed and these particles can adsorb to the surface, resulting in a dirty, ununiform surface. The anisotropic nature of the trenches also makes liftoff quite challenging because in order for the liftoff process to work well, the etching solvent has to be able to access and dissolve the resist. In our case, the only open surface for the solvent to react with the resist would be from the outside edges and would require the solvent to travel all along the narrow trench to remove the resist, making it likely that the trenches would be well formed around the outside of the surface, but raises the question of whether or not they would effectively be formed towards the middle. For these reasons we decided against using route 1, and instead turned our attention to route 2.

Route 2 creates the trenches in an opposite manner to how route 1 creates them. A complete layer of silicon oxide is first deposited onto the hafnium oxide and this is then further coated with an e-beam resist (Scheme 13b-d). The resist is then etched using EBL to create the areas that will ultimately become the trenches (Scheme 13e), covering a far

smaller area and therefore reducing the overall exposure time significantly. The exposed silicon is then removed through plasma etching (Scheme 13f), and because the resist is resistant to the plasma etch, it protects the silicon beneath it from being removed. Finally, the resist can be removed easily with organic solvents, because it is the top layer, to give the desired surface (Scheme 13g). Thus, all of the main problems that were present in route 1 are alleviated with route 2, even though the overall process requires an additional step.

A silicon wafer was purchased from the University of Waterloo Quantum NanoFab Facility for use as the base substrate, and all manipulation of the substrate was done in the Quantum NanoFab Facility cleanroom to prevent contamination with small particles. The silicon wafer was first cleaned using a piranha solution to create a robust silicon oxide layer and remove any contaminating organics. The cleaned surface was then loaded into an atomic layer deposition (ALD) chamber and a ~ 50 nm layer of hafnium oxide was deposited to cover the entire silicon oxide substrate. The substrate was again cleaned and then placed into a physical vapor deposition (PVD) chamber where a silicon oxide target was resistively heated to evaporation in order to cover the substrate with a ~ 10 nm thick layer of silicon oxide. The substrate was again subjected to piranha submersion to both clean the substrate and oxidize the silicon oxide layer fully to silicon dioxide. The substrate finally then diced into 10 mm x 10 mm square pieces that would be useable in the EBL process.

For the electron beam to have any effect on the substrate, it first had to be coated with an electron beam resist. A copolymer of poly(methyl methacrylate) (PMMA) and poly(methacrylic acid) (MA) was used as the resist. The copolymer PMMA/MA contains

33% of MA and was preferable to simple PMMA due to the significantly higher electron beam sensitivity, better contrast, and higher resolution which was necessary for the small lines that were desired in this process. Upon excitation with an electron beam, the polymer resist undergoes depolymerization in the incident area, making it easy to remove with organic solvents, in the case of this copolymer, the developing solvent of choice is a 1:3 mixture of methyl-isobutyl-ketone (MIBK) and isopropanol (IPA). This mixture is strong enough to dissolve the exposed resist, but weak enough that it does not significantly dissolve or disturb the unexposed resist on the timescale of development (~1 minute). The unexposed copolymer can easily be completely removed through sonication in acetone.

The resist-coated surface was then exposed to an electron beam at multiple doses to determine the optimal dosage required to obtain the lines that we wanted, this is commonly called a dose test. The test revealed an optimal dosage capable of generating the appropriate line width with the lowest time and energy, and without causing the lines to become thicker than desired. With the appropriate dose determined, a second 10 nm x 10 nm surface was using the same procedure, and through the use of EBL the surface was split into three distinct regions, one with 70 nm wide trenches, one with 100 nm wide trenches, and the final with 300 nm wide trenches. The trenches in each region are separated by 3 µm, and the three regions are separated by 0.5 mm.

After development of the resist layer, the exposed SiO_2 layer was etched in a fluoride plasma. The dry etch was done on an Oxford Instruments ICP380 using CHF_3 as the plasma precursor for a length of ~6 seconds to etch the ~50 nm SiO_2 layer down to the HfO_2 layer underneath. CHF_3 was chosen as the etchant because of the affinity of silicon

towards fluoride, which results in a more selective etching process. The goal was to be able to only remove the SiO_2 layer, while leaving the HfO_2 intact (Scheme 13f).

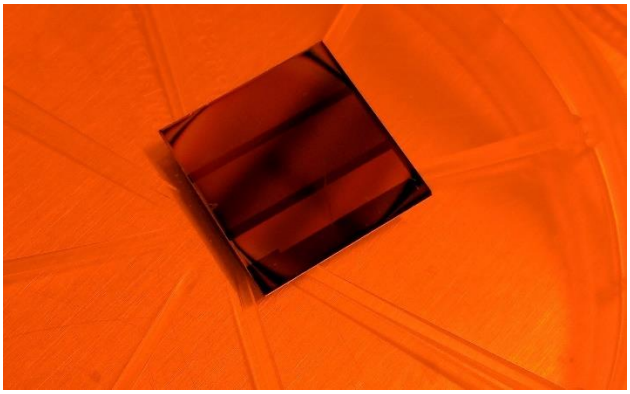

Figure 52: Photograph of the substrate after nanofabrication showing three regions of trenches.

Once the etching process was completed the excess resist was removed in an acetone bath to give the desired surface (Scheme 13g). The trenches in the surface could be easily seen by eye (Figure 52). One of the regions of trenches is smaller than the others because the exposure time was so long that the facility was closing, and the experiment had to be stopped early. Nonetheless, the trenches were still intact and plentiful enough to carry forward to the experimental steps.

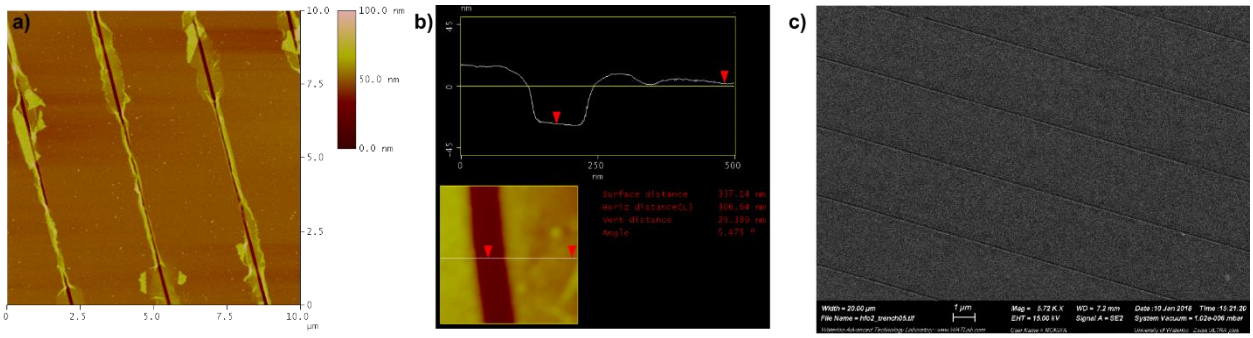

Figure 53: Verification of the trenched surface using AFM (a, b) and SEM (c).

The integrity of the trenches was verified through AFM and scanning electron microscopy (SEM) (Figure 53). AFM analysis shows that the trenches are present along the surface with what appears to be some residual resist along the edges of the trenches. The depth of the trenches was confirmed to be ~30 nm with AFM. Also notable is that the trenches are not completely uniform in their width, likely due to either imperfections in the EBL process or in the development of the resist after exposure. SEM displays the same characteristics as the AFM, and also shows several defects along the length of the trenches such as disconnects and slight shifts in their position. These disconnects are a feature of the EBL process, as when the beam reaches the edge of the exposure window it becomes less precise, and when the stage is moved to continue the exposure it can result in slight discontinuities. Overall, despite the small imperfections, the structure of the surface turned out as originally planned.

With the synthesis of **11** resulting in failure, we no longer had a molecule that was capable of functionalizing HfO_2 effectively and selectively, but we had been creating both **11** and the surface simultaneously. So, with the trenched surface created, a new use for it had to be imagined. The first step was to characterize the surface to ensure that the trenches were indeed HfO_2, and to do this we turned to SEM and used the same machine to do an energy dispersive X-ray analysis (EDXA). The operating principle of EDXA is as follows: an electron of sufficient energy bombards a surface completely removing an electron from one of the inner electron shells of an atom, an electron from a higher energy shell then relaxes to occupy the now vacant site, releasing an amount of energy that is characteristic for each atom, and works especially well for heavier atoms with a large number of electrons. The energy that is emitted in the electron relaxation process is then

graphed to give a spectrum of all atoms in the surveyed sample, which can be integrated to give an accurate chemical composition. EDXA should therefore be capable of surveying the surface for Hf and Si, both of which should provide strong signals, depending on the region surveyed. However, when the EDXA experiments were run, it was observed that in both the trenches and on the plateaus only Si was present, with no Hf appearing anywhere on the sample (Figure 54). The results indicate that the HfO_2 layer was likely also etched in the fluoride plasma step of the process due to the small thickness of the HfO_2 and SiO_2 layers. If HfO_2 trenches are desired, the HfO_2 layer should be increased in thickness significantly to avoid this issue from occurring again. However, because **11** was not successfully synthesized, this result was a boon. It allowed us to use the surface under the typical ART conditions and observe what effect the trenches would have on nanotube deposition and alignment, both with and without the use of a liquid crystal alignment layer. The results of these experiments are still pending.

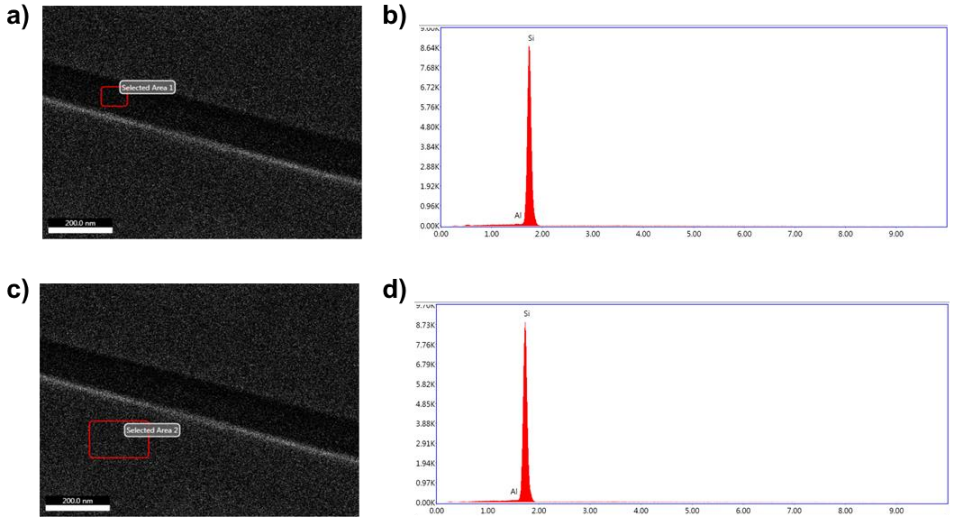

Figure 54: EDXA showing the composition of the trenches (a, b) and the plateaus (c, d).

2.3.8 Synthesis of a Larger Iptycene for Use in the Alignment Relay Technique

Up to this point the ART has been modified changing the liquid crystal, altering the anchoring group, and through processing of the substrate, but perhaps the most obvious choice is altering the size of the iptycene molecular tweezer. The size of the iptycene can both be increased or can be made asymmetrical and even chiral (Scheme 14). The idea is that the size and shape complementarity between the π-concave iptycene host and the π-convex nanotube guest would provide optimal binding to specific nanotubes over others.[151]

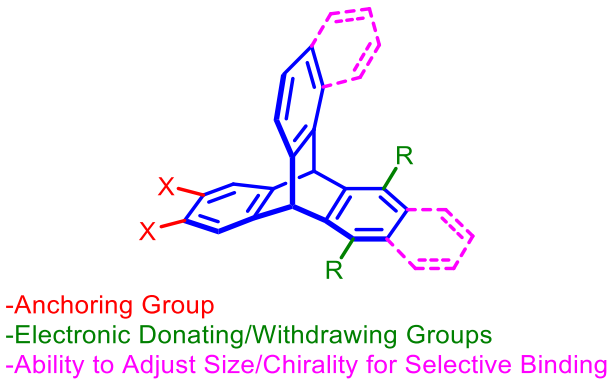

Scheme 14: Iptycene design parameters.

The synthesis of a larger iptycene nanotweezers seemed immediately obvious to us as a simple extension of the synthesis of extended iptycene **2**, in this case using pentacene instead of anthracene (Scheme 15). The only other difference between the two routes was the incorporation of DDQ into the oxidation step to give **15**, as it had already been shown to work better in the previous synthesis. The price of pentacene is very high, and because pentacene was being used as a starting material in this synthesis, we decided to synthesize it ourselves, so all the pentacene used in this synthetic route was made in our lab. Furthermore, the Diels-Alder reaction between

anthracene/pentacene and cis-1,4-dichlorobutene had been unreliable, with the same procedure resulting in very poor conversions. It appears as though this is due to a breakdown of the dichlorobutene starting material over time, with some samples that were purchased from Sigma-Aldrich appearing as clear liquids but others showing a yellow immiscible liquid contaminant. This was somewhat of an issue when synthesizing our original iptycene **2**, but it became a serious problem in the synthesis of **16**.

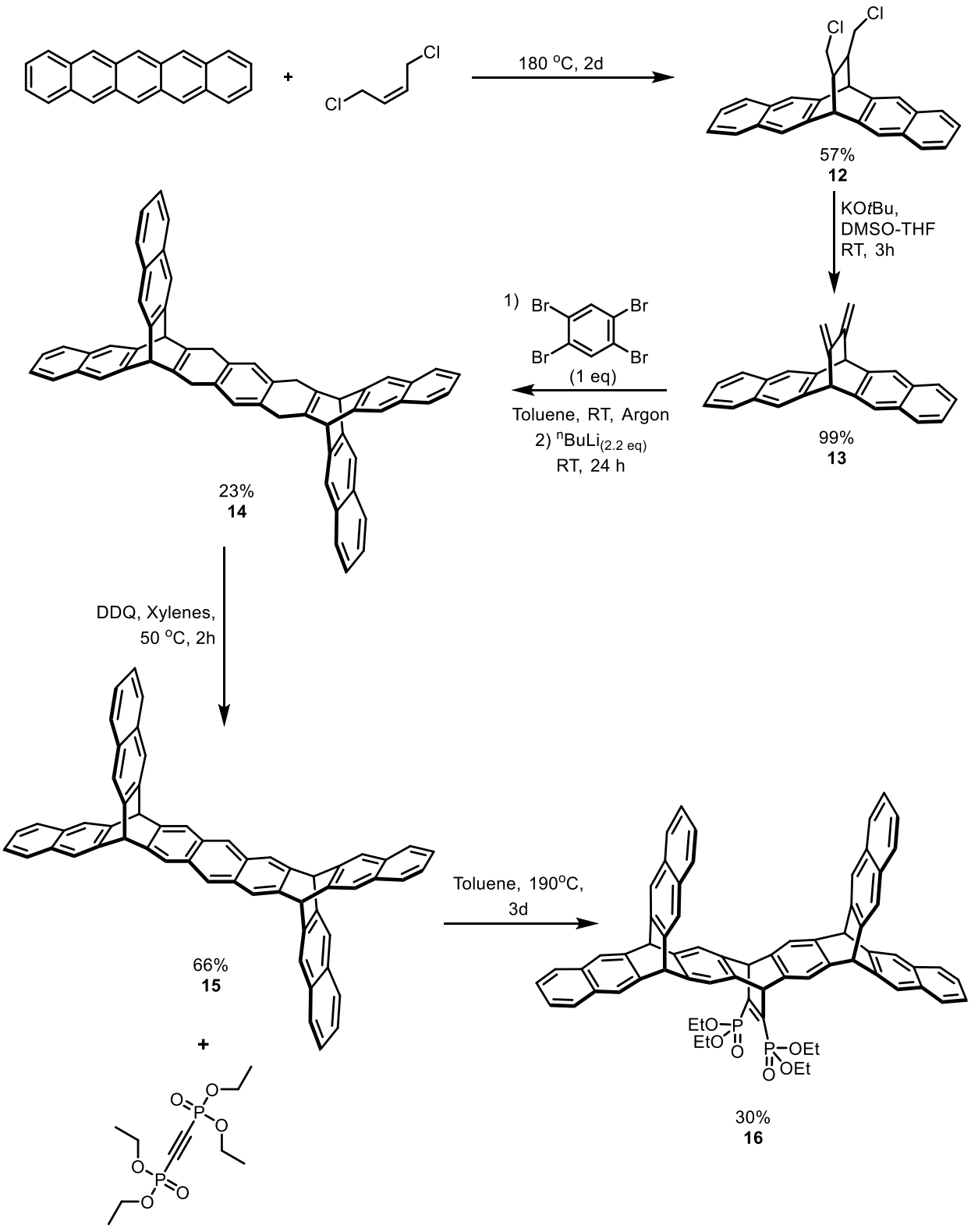

Scheme 15: Synthesis of Large Iptycene 16.

The reaction between pentacene and dichlorobutene to give **12** was attempted over a dozen times using various reaction conditions because several problems were encountered with the original conditions. The first trial saw the use of toluene as the reaction solvent, but the reaction proceeded in very poor yields, inconducive to further synthesis. The reaction was then done neat in excess dichlorobutene but upon heating overnight, the liquid dichlorobutene starting material was gone and the reaction mixture was transformed into a single solid, dark brown mass. The solid was placed in boiling toluene but failed to dissolve, and the material extracted from the solid showed a ^{1}H NMR that was completely different than both starting materials and the expected product, void of the characteristic bridge-head carbon peak seen in iptycenes. We speculated that the reagents may be undergoing some type of radical reaction and so the reaction was run in the dark, and in an inert atmosphere, but the same insoluble solid mass was obtained. At this point we suspected that the dichlorobutene starting material may be contaminated and began to synthesize our own.

The synthesis of cis-1,4-dichlorobutene has been reported in the literature from the starting materials cis-1,4-butenediol and thionyl chloride (Scheme 16). The synthesis is reportedly done in an ice bath, ensuring that the temperature remains below 10 °C, however when the reaction was attempted following these conditions, only a small amount of product was obtained, and the reaction mixture changed colours to a dark blue, instead of the expected colourless. It was assumed that the reaction had heated up upon addition of thionyl chloride and so the reaction was rerun in a dry ice/acetone bath to ensure proper cooling was maintained. After distillation of the reaction mixture, a large amount of clear liquid was obtained, which was assumed to be the desired product. ^{1}H

NMR characterization revealed that it was not the desired product, but another small molecule with a very similar structure, and no product was present in the reaction mixture either. The next trial saw the reaction mixture heated to 60 °C with pyridine as the nucleophilic catalyst, as it appeared that heat may in fact be necessary. After distillation, the product was obtained in 79 % yield, revealing that indeed heat is required for the reaction to proceed. It appears likely that the distillation step is not only isolating the product, but may actually be encouraging the reaction as well.

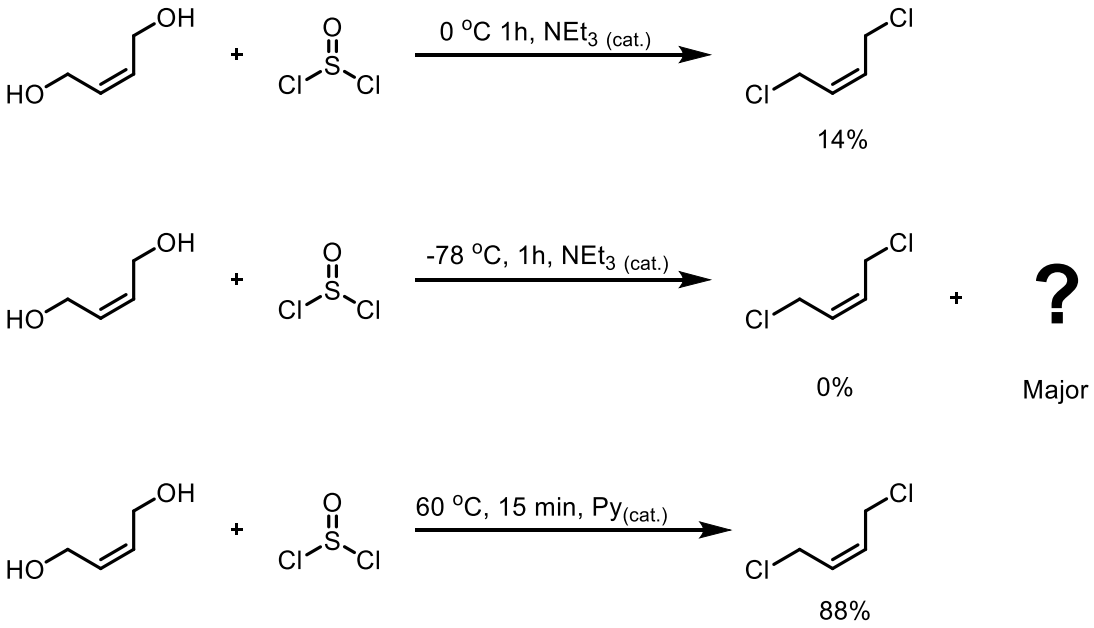

Scheme 16: Synthesis of cis-1,4-dichlorobutene.

Using the freshly distilled dichlorobutene, the Diels-Alder reaction with pentacene was attempted, but unfortunately the same issues were once again observed, with the reaction mixture completely solidifying into a brown mass. We decided to check if the temperature of the reaction may be too high, but when the reaction is run even at 140 °C, no reaction occurs even over the course of several days. Running the reaction with a fresh batch of pentacene yielded some of the desired product, and so it seemed as though

perhaps the pentacene was also contaminated, preventing the reaction, but even with both pentacene and dichlorobutene freshly made and purified, the solidification was still a problem. It was discovered that the most reliable way to prevent solidification of the reaction mixture was to add the reactants neat, and then sonicate the sample to break up any of the solid pentacene before finally heating the reaction mixture. Using this approach, **12** was obtained in 57 % yield and the reaction was successfully reproducible. These results lead us to believe that the pentacene aggregates are likely undergoing a polymerization reaction with the dichlorobutene upon heavy heating, but when they are broken down to increase the surface area, the Diels-Alder reaction is faster. Even under these conditions, some dark brown solid is still formed but is easily removed in the ensuing purification.

With **16** synthesized, we incorporated it into the ART using 8CB as the liquid crystal and both ITO and SiO_2 as substrates. The results showed good alignment and length selectivity, as is expected of the alignment relay technique, however, the length sorting was even more skewed towards smaller nanotubes (Figure 54), somewhat unexpectedly. On both ITO and SiO_2 an average length of 0.54 μm and 0.58 μm, respectively, was observed. This result is interesting because it's about half of the average length of the original sample and is even 0.20 – 0.30 μm shorter than the shortest trials using 8CB and **2**. Coupled with the length sorting was a high density of 1.41 and 0.81 nanotubes μm^{-2} on ITO and SiO_2, respectively. These results are also interesting because they are opposite of what is usually seen, with ITO having a much higher density than SiO_2 in other experiments. The inversion of density is unexpected because it has been determined that SiO_2 is functionalized more slowly than ITO using phosphonate **2**, so it would stand to

reason that the density of **2** on ITO would be higher than on SiO_2 and therefore, the density of nanotubes should be greater as well. However, the opposite results are observed with **2**, but the expected result is seen with **16**, meaning that there is likely more at play than simply the rate of reaction.

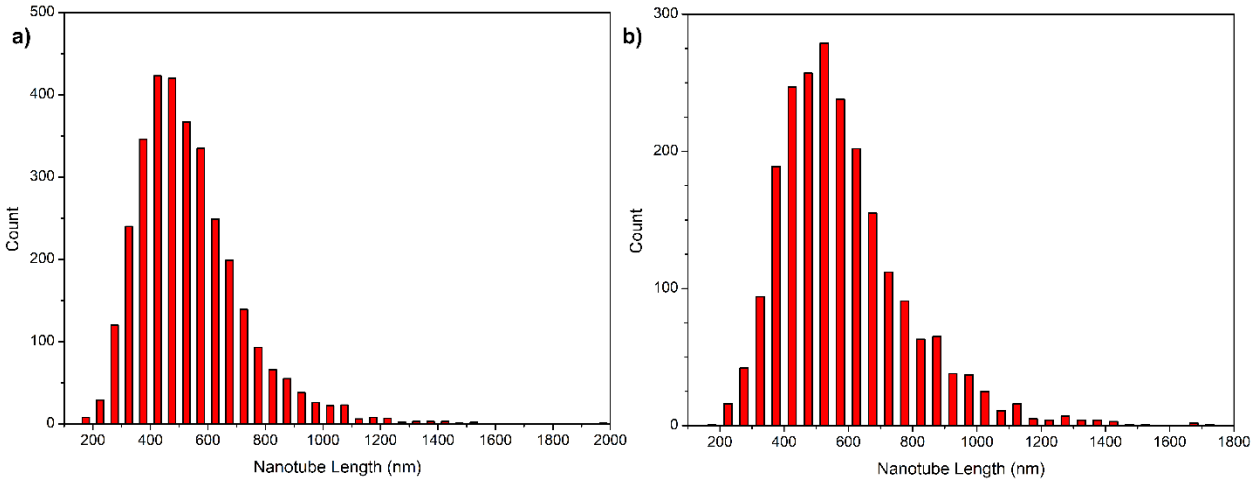

Figure 54: Length distribution of ART-deposited nanotubes using 16 and 8CB on a) ITO and b) SiO_2.

The alignment on both surfaces was about the same as with **2**, exhibiting standard deviations of 33° and 29° for ITO and SiO_2, respectively (Figure 55). There was very little of note about the alignment that differed from the previous ART experiments except that for SiO_2, the alignment data suggested a slightly bimodal, wide pattern instead of the sharper distribution that is usually seen. The ITO distribution was very similar to those seen previously.

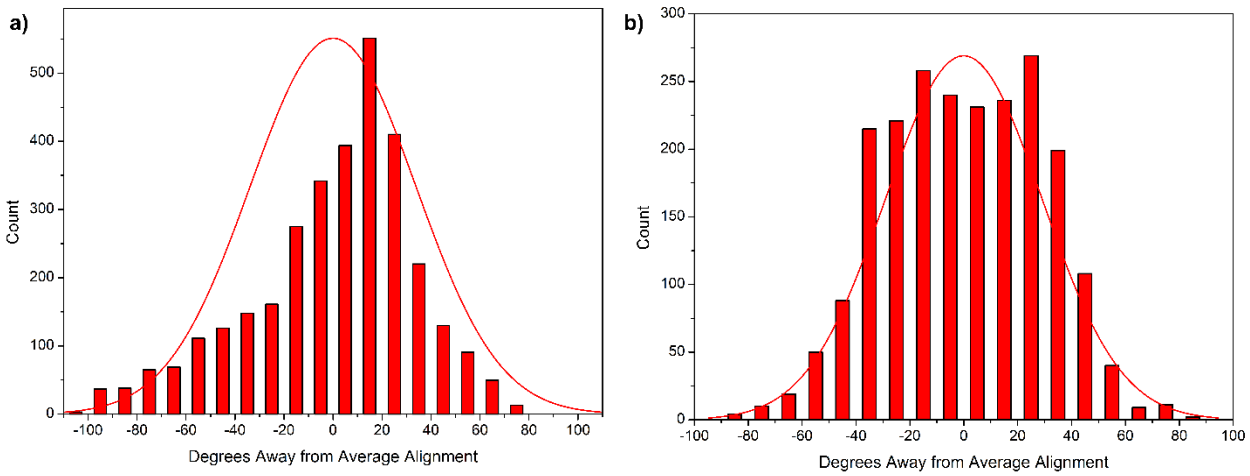

Figure 55: Alignment distribution of ART-deposited nanotubes using 16 and 8CB on a) ITO and b) SiO_2.

The most important experiment was determining the diameter of the ART deposited nanotubes via Raman spectroscopy as the diameter selectivity was the main goal of switching between **2** and **16**. The diameter selectivity of **16** turned out to be mostly similar to **2**, with the only major difference being the inclusion of a large peak at 141 cm^{-1} (1.76 nm diameter) and the increased prominence of the shoulder peak at 150 cm^{-1} (1.65 nm diameter) (Figure 56). Like with **2**, the 175 cm^{-1} (1.44 nm diameter) peak, which is the most abundant in the original sample, is now overshadowed by the 155 cm^{-1} (1.59 nm diameter) peak representing a preference for larger diameter nanotubes. However, the inclusion of the 141 cm^{-1} peak indicates selectivity for even larger diameter nanotubes in **16**, as this peak represents the largest nanotubes present in the as purchased sample. Furthermore, the 141 cm^{-1} peak in the as purchased sample has very low intensity, accounting for a very small percentage of the nanotubes in the overall sample. In particular, when comparing the 156 cm^{-1} peak to the 141 cm^{-1} peak, the latter has a relative intensity of 27 %, however after being subjected to the ART the relative intensity changes. When using **2** as the molecular tweezer, the relative abundance of the largest

diameter nanotubes actually drops to only 18 %, but when using the larger **16** it increases to 58 % relative intensity, more than double that of the original sample. This data confirms our hypothesis that the larger size of **16** provides further bias towards the deposition of very large diameter nanotubes. To further examine the extent of this preference, a sample of larger diameter nanotubes should be tested in the future.

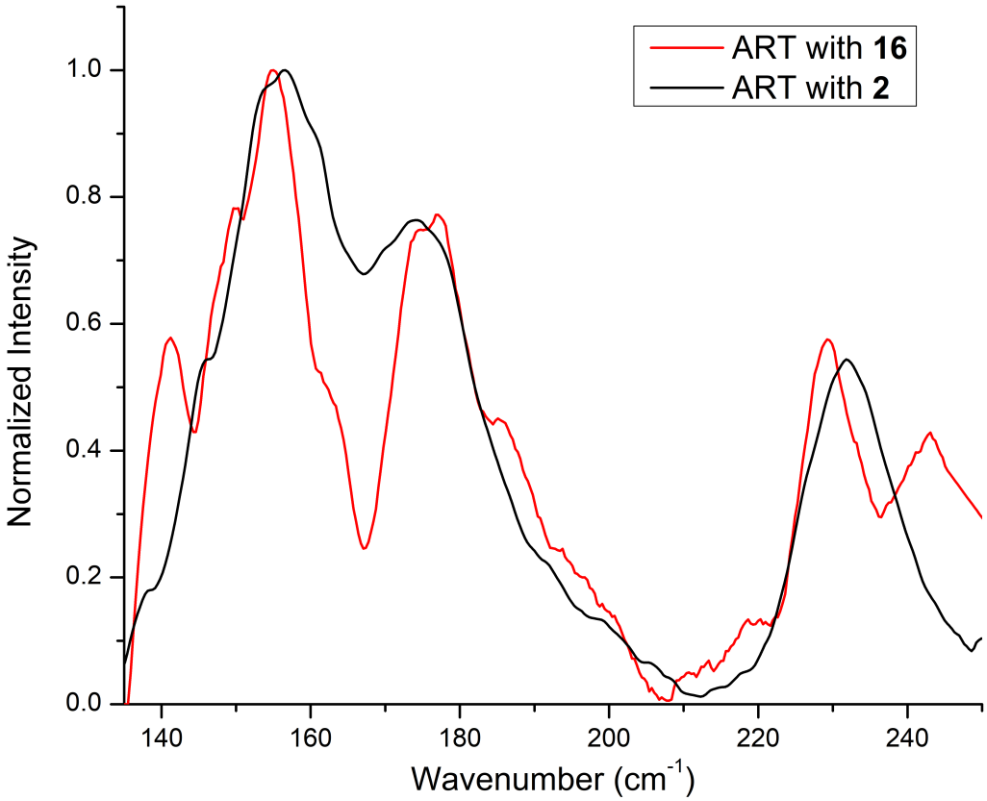

Figure 56: Comparison of diameter selectivity of ART on SiO_2 with 8CB with molecular tweezers 16 (red) and 2 (black).

The final feature of note on the Raman spectrum are the two peaks at 229 cm^{-1} and 243 cm^{-1}. These peaks are attributed to the vibrations of **16** in the same vein that the peak at 231 cm^{-1} is attributed to **2**. Interestingly, the larger **16** has a slightly lower wavenumber shift, which may be a predictor of its larger diameter in much the same way that the RBM shifts predict the diameters of nanotubes.

2.4 Using π-Concave Iptycene Hosts to Improve Carbon Nanotube Based Biosensors

As was discussed in Section 1.3.2.5, carbon nanotubes can be used to create sensors for various chemicals and biological markers. The goal has been to incorporate small CNT-based devices as the first step at the point of care in order to make quick diagnoses instead of relying on the traditional methods that require samples to be sent away to other facilities and can take weeks to process. CNT-based biosensors offer the potential for immediate diagnosis and can be used to survey a wide array of chemicals to a very high degree of accuracy, *vide supra*. However, there remain a few challenges that prevent the direct use of CNT-based biosensors in this way.

Current sensors are based around either direct binding of biologicals to the CNT surface, or through the coating of the CNT surface with functionalized pyrene molecules that are themselves able to bind to the analytes of choice, and both methods have their own drawbacks. When the biologicals, such as antibodies, are directly bound to the CNT surface, they do not coat the CNT enough to prevent other materials from binding to the CNT and thus the signal from non-specific binding is too large to create a useful device out of these systems, expect under ideal, laboratory research conditions. Alternatively, if pyrene is used to anchor the antibody to the CNTs, the coverage is higher, but there is still significant non-specific binding and the pyrene binding to the CNTs is weak enough that they can be displaced during sample analyzation, leading to more non-specific binding. The goal of such applications is to be able to subject the device to blood that is taken directly from a patient without need for significant manipulation, but currently these tests result in far too much non-specific binding and displacement to be useful.

Partnering with the expertise of the Tang group at the University of Waterloo, we were interested in seeing if our π-concave iptycene design would allow for a stronger binding of the antibodies onto the surface of the CNTs, or if we could even use the iptycenes as a way to passivate the surface such that non-specific binding could be eradicated completely.

2.4.1 First Attempts at Nanotube Binding

We devised a simple molecule to test the binding affinity of iptycenes with SWNTs under the conditions that were used by the Tang group. **2** was not used to test the binding because it requires a lengthy synthesis and instead an iptycene that was both simple to make and would be capable of binding to the SWNT was created instead. Since **1** had been previously synthesized it was used in the initial testing, the larger derivative, **17**, was also synthesized and tested (Scheme 17).

The synthesis of **17** was straight forward and followed the same one-step synthesis as **1**, however upon purification of the material, the ^{1}H and ^{13}C NMR spectra showed more peaks than were expected, and these excess peaks were very similar to those expected of the desired product. The ratio of the aromatic peaks in **17** to the bridge head and aliphatic peaks in the ^{1}H NMR was weighted too heavily in the direction of the aromatic peaks. Furthermore, there were other peaks that appeared in the same region as the bridgehead peak, which lead us to conclude that two Diels-Alder products, **17** and **18**, were created in a 5.5:1 ratio (Scheme 17). The materials were inseparable upon further column chromatography, but it was believed that they would both be capable of interacting with the SWNTs due to their similar shapes, and so the mixture was handed to our collaborators.

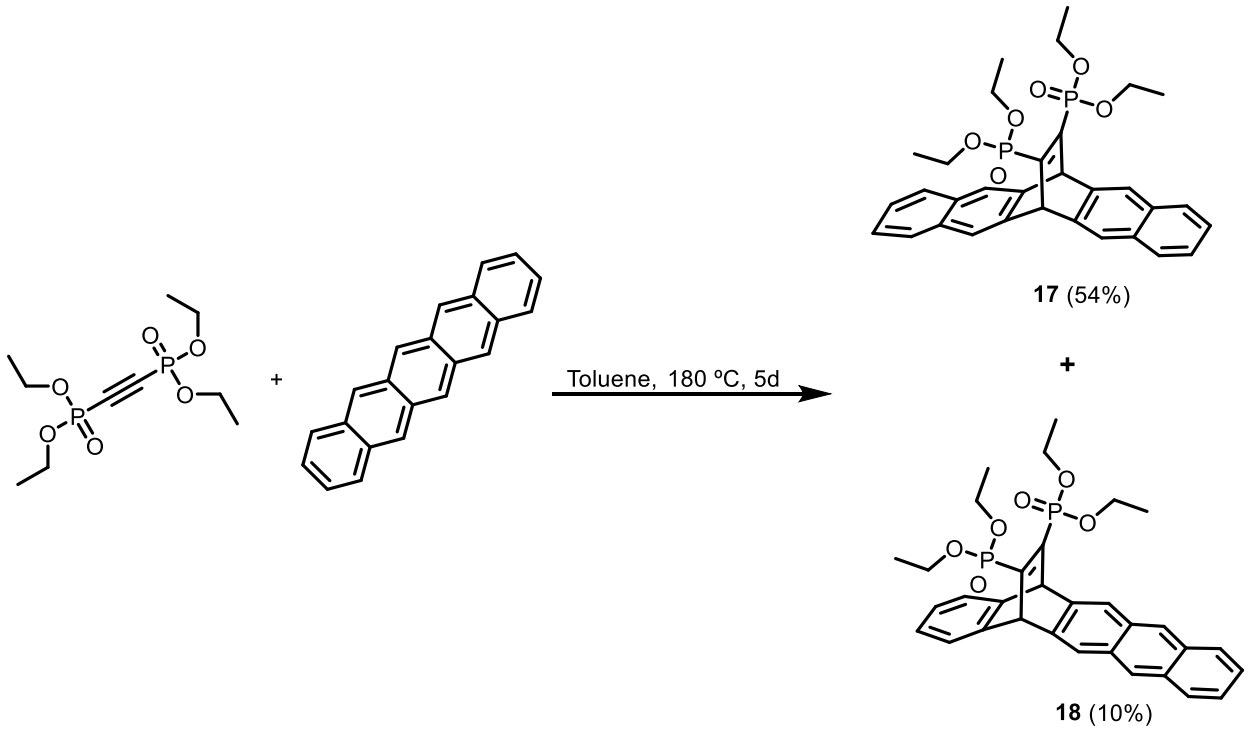

Scheme 17: Synthesis of pentacene-based phosphonate iptycene.

The aromaticity of pentacene as well as the selectivity of the Diels-Alder reaction with pentacene has been previously studied computationally. The central ring exhibits the highest degree of aromaticity with the aromaticity of the rings decreasing further from the central ring, as predicted by nucleus-independent chemical shift (NICS) and harmonic oscillator model of aromaticity (HOMA) calculations.[27] Aromaticity is a stabilizing effect and so one would tend to expect the central ring, the one that is the most aromatic, to also be the least reactive position when breaking aromaticity. However, here we clearly see a 5:1 preference for the central ring to undergo the Diels-Alder reaction. While this perhaps seems strange intuitively, it is indeed the trend that is borne out by theoretical and practical experiments. The activation energy barrier for the central ring in a Diels-Alder reaction with acetylene is ~23 kcal mol^{-1}, while the outermost rings have an

activation energy of ~33 kcal mol^{-1}, and the final two rings are around 26 kcal mol^{-1}. The preference for the central ring in these experiments is clear, but also the secondary ring has an activation energy barrier difference that is still close enough to be competitive, especially at high temperatures, as is evidenced by the formation of **18**. This preference may be due to the increased HOMO coefficient on the central ring relative to the outer rings.

The initial tests showed improved results with mixture **17**/**18** over that of the typical pyrene system that was used in Tang's groups, however further testing required that the antibodies be conjugated to the molecules. Typically, this conjugation is done by the formation of amide bonds through a reaction between the amino groups of the antibody and a reactive succinimidyl ester, which is found on the pyrene that is generally used. Before attempting to install the succinimidyl ester onto molecules **17** and **18**, an experiment was carried out to determine if the phosphonate would be reactive towards the amines under the buffer conditions, forming phosphoramide bonds. However, all reactions were unsuccessful, and it became clear that a new functional group would have to be installed in order to move forward with the project.

2.5 Conclusions and Future Work

The goal of the Alignment Relay Technique was to design a bottom-up method for the simultaneous sorting and alignment of SWNTs that could easily be tuned to provide ultimate control over nanotube deposition. To this end we have proven that firstly the ART succeeds in its goal of simultaneous alignment and sorting of nanotubes based on length and diameter. Furthermore, we have shown that small changes in the nature of the liquid crystal used can target profound differences in the resulting length and density of the

nanotubes. Larger molecular tweezers can be used to further discriminate based on nanotube diameter, without affecting the other parameters. It has also been shown that sonication during the deposition step can be used to improve both alignment and sorting based on the reversibility of the binding events.

The future of the ART is promising, with many avenues still available for further research. One of the large questions remaining is how ordered the actual iptycene is on the functionalized surface, and if any techniques can be used to elucidate this fundamental property, it may drastically improve our understanding of the ART. Other factors in the ART have yet to be tested including the introduction of a chiral iptycene in order to determine whether the method could be amenable to chiral selectivity, and the synthesis of electron rich/poor iptycene derivatives which may further improve selectivity when starting from a mixture of metallic/semiconducting nanotubes. Further research into the effects of other liquid crystal phases and temperatures could provide a means to decrease the amount of time required for the ART while also targeting other deposition parameters. The effect of confinement on the nanotubes based on the nanolithography experiments has yet to be fully explored and remains an interesting path because it could result in a method that no longer requires an external liquid crystal alignment layer. Other work could focus on the use of magnetic fields or other methods for liquid crystal alignment. Clearly, the ART still has much room for further improvement and thus it remains an important cornerstone for the research being done in the Schipper group.

In the case of using the iptycene molecules for nanotube biosensors, it has become clear that other anchoring groups must be used instead. The phosphonates are not ideal as they lack the ability to easily facilitate further transformation. Attempts at incorporating

maleimide esters which are typically used for this type of chemistry have failed, but other methods including thiol-ene click or thiol-maleimide click have presented themselves as potential alternatives that require further exploration.

Chapter 3. Fullerene Interactions with π-Concave Materials

3.1 Common Motifs Used for Fullerene Binding

The field of hosts for fullerenes is much older and richer than that of SWNT binding. In the past, selective binding had been used as a way to selectively isolate different fullerenes from one another, since their purification is so challenging. As has been discussed previously, separating the higher fullerenes from C_{60} and C_{70} is fairly straight forward, but purifying C_{60} from C_{70} can still be challenging and expensive. Since C_{60} and C_{70} are the most commonly used fullerenes, complexation methods for purification are very attractive as they allow for larger scale separation and, depending on the host, can be cheap and recyclable. Much like with SWNTs there are a number of common motifs that are commonly utilized for fullerene complexation, and they have several advantages or disadvantages relative to one another.

The fullerene-host complexes are generally easily characterized through UV-Vis absorption spectroscopy, and so a Job plot can be used to assess the binding constants of these complexes. This has allowed for a very detailed study of various binding motifs, architectures, and functional groups to be probed systematically, giving a better understanding of what works best for fullerene complexation. Herein, we will give an overview of the most common types of binding motifs, and the effect that structure and substitution play in the role of π-concave fullerene host design. For a more comprehensive breakdown please see our review on the subject.[217]

3.1.1 Porphyrin Hosts for Fullerenes

Porphyrin binding to fullerenes has been long taken advantage of for use in HPLC chromatographic separation of various fullerenes, and has since been used heavily in fullerene binding.[324] The binding between fullerene and porphyrin is good because of the π-π interactions and the metal-fullerene interaction, but it is still rather weak for a single porphyrin ring interacting with a fullerene due to the lack of shape matching. To circumvent this issue, Aida, Saigo et al. created a class of porphyrin cage compounds that are capable of completely encompassing a fullerene molecule, thus drastically improving the binding affinity (Figure 57).[325]

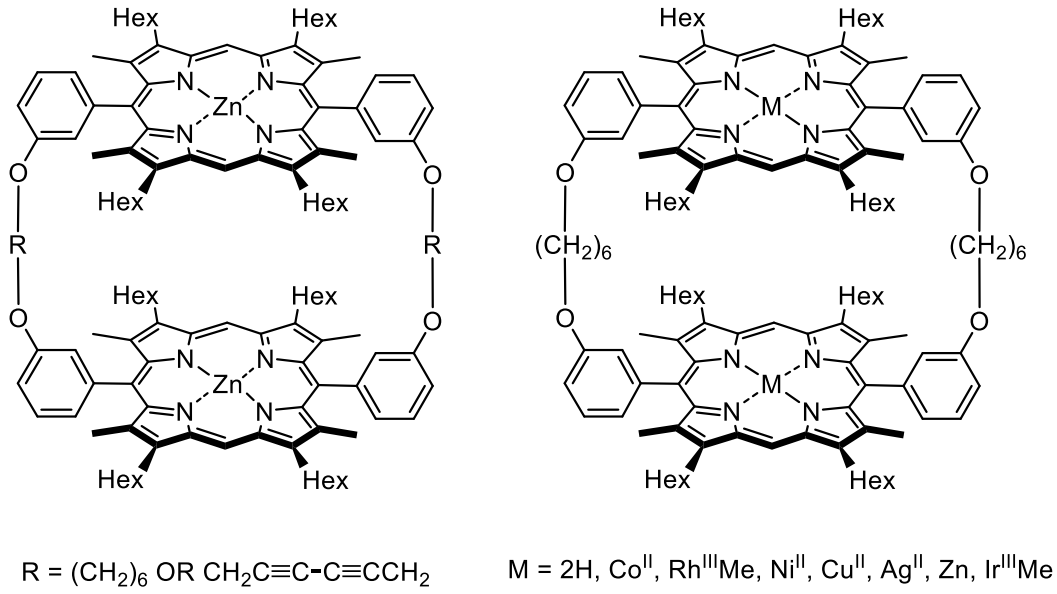

R = $(CH_2)_6$ OR $CH_2C{\equiv}C\text{-}C{\equiv}CCH_2$ M = 2H, Co^{II}, $Rh^{III}Me$, Ni^{II}, Cu^{II}, Ag^{II}, Zn, $Ir^{III}Me$

Figure 57. Various porphyrin hosts designed to test the effects of rigidity and metal coordination on the complexation of fullerene guests.

Initial studies focused on using zinc porphyrins to bind to C_{60} in solution, with the linkers that connected the two porphyrin rings varying between flexible hexamethylene chains and rigid diacetylenes. The crystal structure of the porphyrin cage-fullerene complex show that the hexamethylene chains contract to allow for better binding to the

fullerene guests, with a binding constant of 6.7 x 10^5 M^{-1} in benzene. However, the diacetylene spacer exhibited no spectral changes upon addition of fullerene to the solution, indicating that no binding had taken place. In this case, it appears as though the spacer may be locked into a position that is not optimal for fullerene binding and so the rigidity is detrimental to the binding affinity.

The next investigations were on the effect that the metal had on fullerene binding.[326,327] It had been observed that the distance between the zinc in the porphyrin ring and the carbon atoms in the fullerene were closer than the van der Waals radii, indicating that there is definitely some interaction between the metal and the fullerene guest. Of the metals tested (Figure 57) the Rh^{III} and Ir^{III} centers exhibited the starkest increase in binding affinity. The rhodium-porphyrins possess association constants of 2.5 x 10^7 M^{-1} for C_{60} and 10^8 M^{-1} for C_{70}, and the iridium-porphyrins show remarkable association constants above the limit of detection in benzene and had to instead be measured in 1,2-dichlorobenzene, ultimately yielding an association constant of 1.3 x 10^8 M^{-1} in 1,2-dichlorobenzene, about three orders of magnitude higher than the rhodium counterparts in like solvent. The incredibly high association constant has been attributed to η^2 binding to the C-C double bonds in fullerene. As was discussed previously, fullerenes show a low aromaticity and behave partially as isolated double bonds, which likely promotes η^2 binding to iridium and rhodium.

These porphyrin cage compounds can be used to effectively purify C_{60}/C_{70} mixtures effectively and easily, with the zinc-porphyrin cage compound purifying a 35/65 mixture of C_{60}/C_{70} to >99% C_{70}. This is accomplished through complexation in benzene, isolation of the complex, and decomplexation through addition of 2,2'-bipyridine (bipy). Purification

can also be extended to chiral higher fullerenes, as evidenced by the purification of C_{76}.[328] Through the use of a chiral porphyrin cage molecule (Figure 58), the researchers were able to complex the fullerene, isolate the complexes with size exclusion chromatography, and induce decomplexation via silica gel chromatography to obtain (-)-C_{76} in 7% ee. While this may not sound very impressive, it is still much higher than can be obtained over cycled chiral HPLC runs.

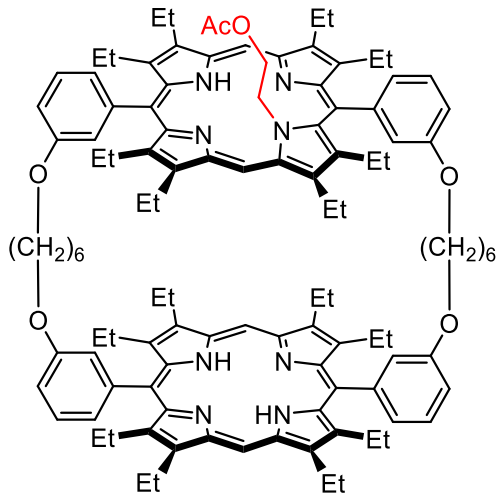

Figure 58: Chiral porphyrin cage molecule for chiral separation of C_{76}.

3.1.2 Corrannulene-Based Fullerene Hosts

As we have seen with SWNT-host design, shape complementarity is very important in creating a good host molecule. In 1965, a bowl-shaped molecule called corannulene was synthesized (Figure 59), this was decades before the discovery of fullerene but has since been dubbed as a “buckybowl” due to the perfect shape complementarity. Corannulene is a fragment of a fullerene containing only one 5-membered ring and five 6-membered rings, and it retains its aromaticity despite its seriously puckered bowl shape, with a bowl depth of 0.87 Å.

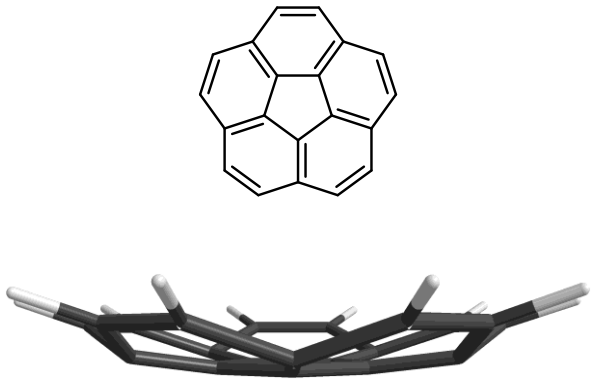

Figure 59: Corannulene with its puckered bowl shape.

After the discovery of fullerenes, corannulene became a popular candidate for studies on fullerene binding, but all attempts to isolate a complex failed. The co-crystallization of the two molecules was non-trivial but was eventually accomplished,[329] however there has never been a report of the direct observation of a complex formation in solution. This is likely due to a very weak interaction between the corannulene and fullerene, which is rather unexpected due to the excellent π-concave-π-convex matching. Attempts were made to alter corannulene by adding additional benzene rings to increase the π-surface area in order to promote complex formation. Dibenzo[a,q]corannulene was synthesized for this purpose and while co-crystals were able to be grown, there still lacked any evidence for solution-based complexes.[330]

A different route was taken to create the first ever binding complex between a fullerene and a curved polycyclic aromatic hydrocarbon. Mizyed et al. took advantage of the electron poor nature of fullerenes by incorporating heteroatoms onto the periphery of corannulene, in hopes that the heteroatoms could undergo n→π interactions with the fullerenes and that the added electron density in the corannulene would also strengthen the π-π interaction.[331] They were able to successfully demonstrate a solution complex

with their thiolated corannulenes and chlorinated corannulenes, with association constants of ~400 M^{-1} and ~200 M^{-1}, respectively (Figure 60).

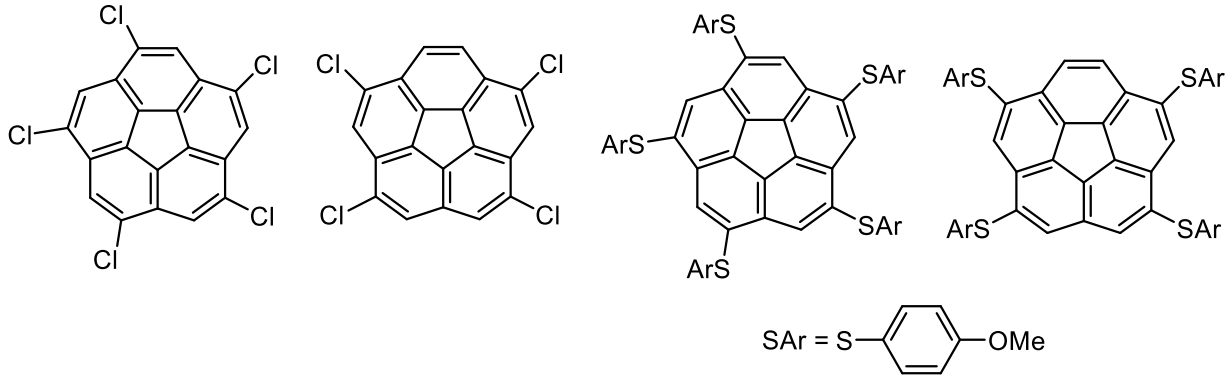

Figure 60: First heteroaromatic corannulenes.

Two groups independently identified pentabenzo-azacorannulene as an interesting candidate for fullerene binding due to its increased π-surface area and the direct incorporation of an electron rich pyrrole at the center of the molecule (Figure 61).[332,333] They both approached the synthesis differently and ultimately ended up with slightly different molecules, but the properties were both very similar. The bowl depth of the inner core is slightly deeper than corannulene at 0.90 – 0.92 Å, and the oxidation potential is over 1.30 V lower than that of corannulene indicating that the azacorannulenes are far more electron rich. The resulting binding affinity was 6.2 x 10^4 M^{-1} in toluene, proving that the incorporation of electron rich heteroaromatic moieties can drastically impact fullerene binding when coupled with shape complementarity.

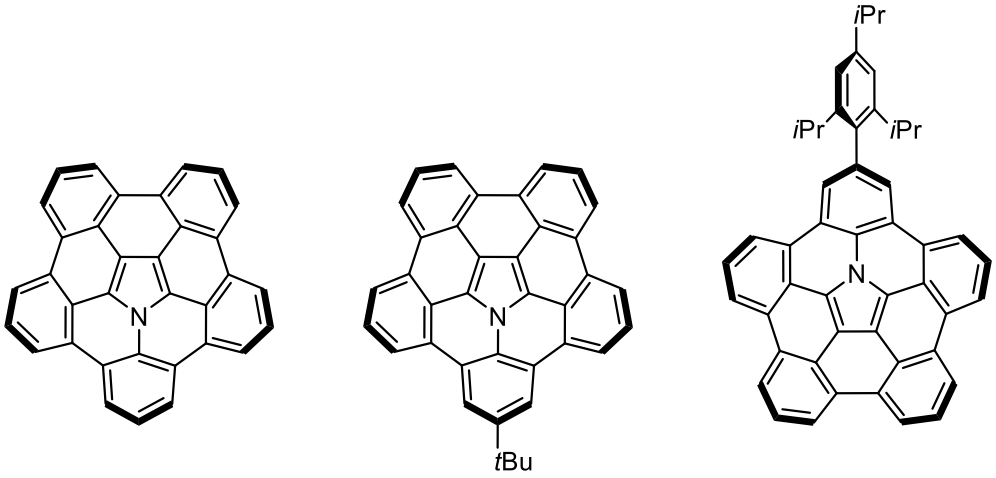

Figure 61: Pentabenzo-azacorannulene and its two synthesized derivatives.

The last major advancement in corannulene hosts for fullerenes has been the invention of so-called “buckycatchers,” molecular tweezers based around corannulene subunits. Buckycatchers were pioneered by Sygula’s group and generally feature two corannulenes attached by a bent spacer (Figure 62).[334,335,336,337] This has the effect of improving the π-surface area that interacts with the fullerene, while also retaining the shape complementary nature of corannulene. Based on the different spacers used, and the bending angles that they instill onto the molecule, the association constants range from 2.7 x 10^3 M^{-1} to 8.5 x 10^4 M^{-1} in toluene. This is in direct contrast to corannulene which on its own does not even form a stable complex with fullerenes in solution.

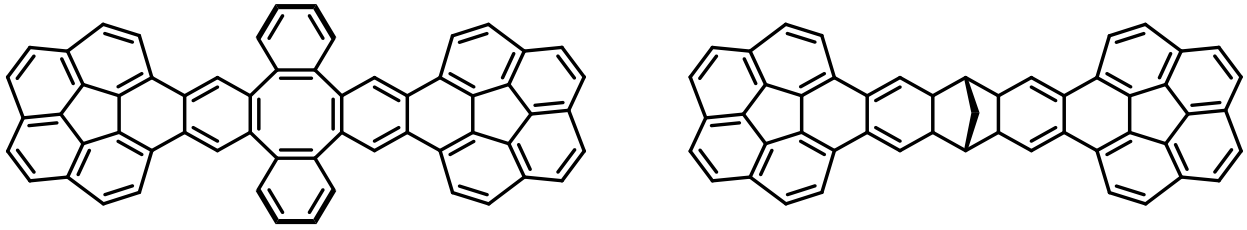

Figure 62: Two buckycatchers synthesized by Sygula’s group.

3.1.3 π-Extended Tetrathiafulvalene

As we saw earlier when discussing SWNTs, exTTF is an electron rich, bent, aromatic molecule that has great shape complementarity with the π-convex shape of CNTs and fullerenes. This work was pioneered by Pérez et al. using exTTF molecular tweezers consisting of two exTTF subunits with a meta-phthalic ester spacer (Figure 63).[338] The binding constants of this π-concave host with C_{60} was measured to be 2.98 x 10^3 M^{-1} in chlorobenzene.

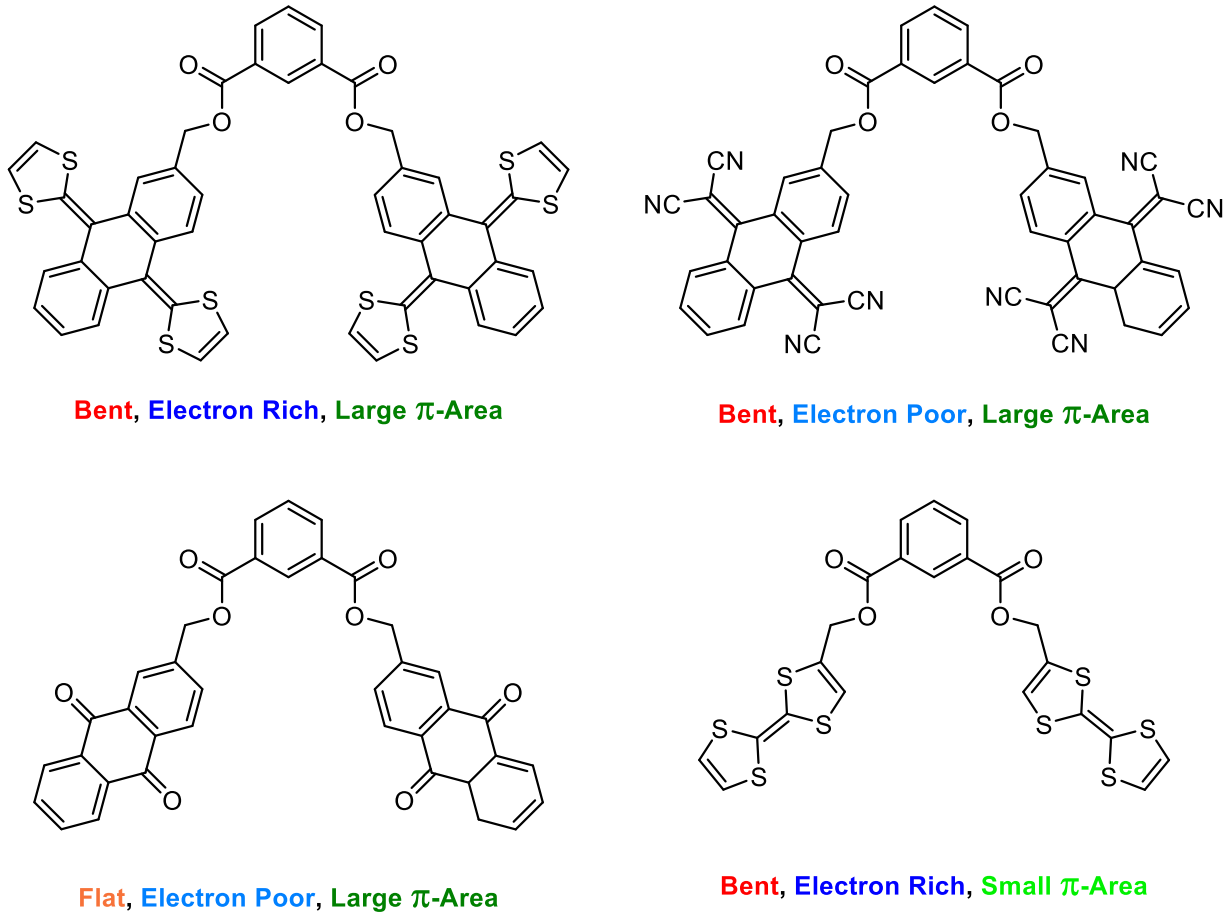

Figure 63: Series of tweezers used to probe the effects of different binding sites and substitutions on fullerene binding.

Perhaps the most insightful experiment done with exTTF hosts for fullerenes was one which probed the effects of π-surface area, shape complementarity, and electron rich/poor hosts.[339] The researchers started by synthesizing a series of exTTF-based hosts with different backbones, binding sites, and substitutions (Figure 63). The results demonstrate that the original exTTF tweezer, which is electron rich, bent, and has an extended π-surface area has the largest binding constant to C_{60}. The electron poor tetracyano derivative exhibits about half the effective binding, while the planar anthraquinone derivative has even lower binding than the tetracyano tweezers. This result indicates that while the electronic effects are powerful, the shape complimentary π-concave π-convex interactions are more important in similar systems. Finally, the TTF (non-π extended tetrathiafulvalene) derivative shows no binding in solution which provides evidence that π-surface area is the most important aspect of all when it comes to binding to fullerenes.

3.1.4 Summary of Important Parameters for Effective Fullerene Binding

The results of the preceding experiments, along with others not covered here, indicate that there are several key factors that can be used to create an effective host for fullerenes. The important factors that determine effective binding to fullerenes are:

1. van der Waals and π-π interactions are the most important contributor to fullerene host-guest interactions.
2. π-concave to π-convex shape complementarity improve the effective π-surface area of the host.
3. Electron rich hosts bind more favorably with fullerenes.
4. Heteratomic hosts increase binding with fullerenes, likely due to n→π interactions.

5. Metal atoms can bind very strongly to fullerenes through η^2 bonds to the C-C double bonds, drastically improving the binding affinity.
6. Rigid hosts have much stronger binding than flexible hosts if they are of optimal size.
7. Flexible hosts can more easily bind to fullerenes, making them simpler to design.[217]

3.2 Purification of Fullerenes Through the Use of an Iptycene-Functionalized Silica Gel Flash Chromatography

The purification of fullerenes to a high degree and in large quantities remains the largest challenge to their widespread application, and to this point we have discussed to some length the most common ways of purifying them. The easiest way is to extract fullerenes from the as-produced soot is through simple extraction with toluene, but this generally gives a mixture of C_{60}, C_{70}, and a small quantity of higher fullerenes. Taking this mixture and purifying it further is the hardest step but can be accomplished to a high degree of purity using either HPLC or selective complexation.

Selective complexation was discussed briefly in the previous section in the context of porphyrin cages, but it was first discovered and demonstrated with a family of molecules called calixarenes.[340] Calixarenes are macrocyclic structures of phenol connected at their meta-sites which are capable of forming a cone-like structure due to the hydrogen bonding of the phenolic units. By placing *p*-*t*Bu-calix[8]arene into a solution of C_{60} in toluene, the C_{60} is quickly complexed, and this complex can then be crystalized, and recovered, followed by decomplexation of the C_{60} in chloroform. This process must be repeated several times to obtain C_{60} in purities above 99.5%, and while this method

was useful historically, it is no longer used due to the labour intensive process and repetitions required to obtain the desired pure fullerene. Furthermore, this method is not very effective at purifying C_{70} and has not been shown to work at all for higher fullerenes, making it far less attractive than other options.

An easier method for selective complexation was first discovered by Hirsch et al.[341] and further explored by Nagata et al.[342] This technique involves the simple addition of 1,8-diazabicyclo[5.4.0]undec-7-ene (DBU) to a solution of fullerenes in 1,2,4-trimethylbenzene. A rapid single electron transfer occurs from DBU to a fullerene acceptor, and results in formation of a ($[DBU]^+$-$[C_x]^-$) complex, and because the higher fullerenes have a higher electron affinity, they are selectively complexed first, leaving C_{60} free in solution. After five hours, the complexes were filtered off to give C_{60} in high purities (>99%) and high yields (~88%). This method was shown to be easily scalable to over kilograms of material but is only capable of easy purification of C_{60} and has not been shown to be adaptable to the purification of C_{70} or the higher fullerenes.

By far the most commonly used and commercially relevant method for fullerene purification is HPLC. Early purifications relied on simple reverse phase HPLC but have since been improved by incorporating specially functionalized silica gels that include aromatics to improve interactions between the fullerenes and the stationary phase. The most commonly used of these HPLC stationary phases is the COSMOSIL Buckyprep (Figure 64) which contains a pyrene unit capable of forming π-π interactions with the fullerenes in the mobile phase. HPLC on this column allows for the purification of several milligrams of fullerenes over the course of several runs. What is unique about HPLC is that it not only purifies C_{60} from C_{70} but can also be used to purify higher fullerenes and

endohedral fullerenes, albeit in small quantities. Other stationary phases are also in use, including one featuring a phenothiazinyl group, which is especially effective at separating metalloendohedral fullerenes (Figure 64). The advent of pyrene-phase HPLC has been a boon in the purification and sales of fullerenes and continues to be the leading method of purification.

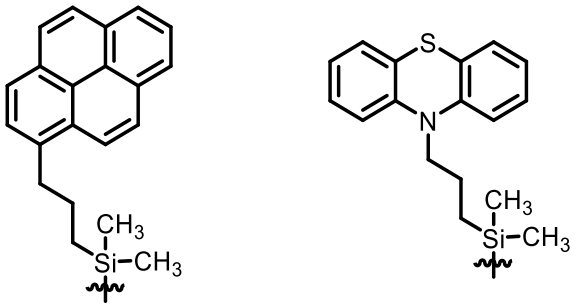

Figure 64: COSMOSIL Buckyprep (left) and Buckyprep-M (right) stationary phases.

Despite the broad applicability of the Cosmosil Buckyprep HPLC columns, they still suffer from two major problems: price and scale. The problem with price is an inherent issue when dealing with HPLC, as HPLC columns are expensive and they also require an expensive instrument to run the separation. In the case of the Buckyprep columns, a 25 cm column with a 28 mm inner diameter costs over 40,000 USD and the matching guard column adds another 12,000 USD. These columns are capable of injection volumes around 2 mL resulting in ~99% pure C_{60} and C_{70} and can be cycled again to improve the purity. The reason for the small injection volumes, and the need to use HPLC altogether, is that the pyrene stationary phase does not form strong enough interactions with the fullerenes for larger scale purification.

The obvious alternative to HPLC purification is simple flash chromatographic separation, which most organic chemistry labs rely on for the isolation and purification of their novel organic molecules. Flash chromatography is simple and only requires glassware and silica gel that can be found in all standard synthetic organic laboratories. It works well for most organic molecules because the retention on silica gel is long enough to provide a meaningful separation of materials based on polarity matching with the stationary phase. So far, it has been impossible to extend flash chromatography to the fullerenes due to their poor interaction with stationary phases, even the specially designed pyrene phase is only strong enough to allow for small scale separation through HPLC. We envisioned a new type of stationary phase that would take advantage of shape complementary π-concave-π-convex interactions with fullerenes in order to lead to longer retention times. If such a system could be created, we thought that it may be possible to scale up fullerene purification using simple flash chromatography.

We turned our attention to the typical systems that had been used as host molecules for fullerenes, but they generally required lengthy syntheses and were not directly amenable to silica gel functionalization. Instead, we envisioned an iptycene system, akin to the one that we used for the alignment relay technique. Iptycenes have a bent, π-concave shape and should therefore be great candidates for strong interactions with fullerenes, and we already had confirmation of their binding power with SWNTs. It has already been clearly demonstrated that even pyrene silica gel phases form sufficient interactions for HPLC separation, so we hypothesized that the addition of the shape complementarity with an iptycene-functionalized silica gel may increase the interactions enough to enable flash chromatographic separation (Figure 65).

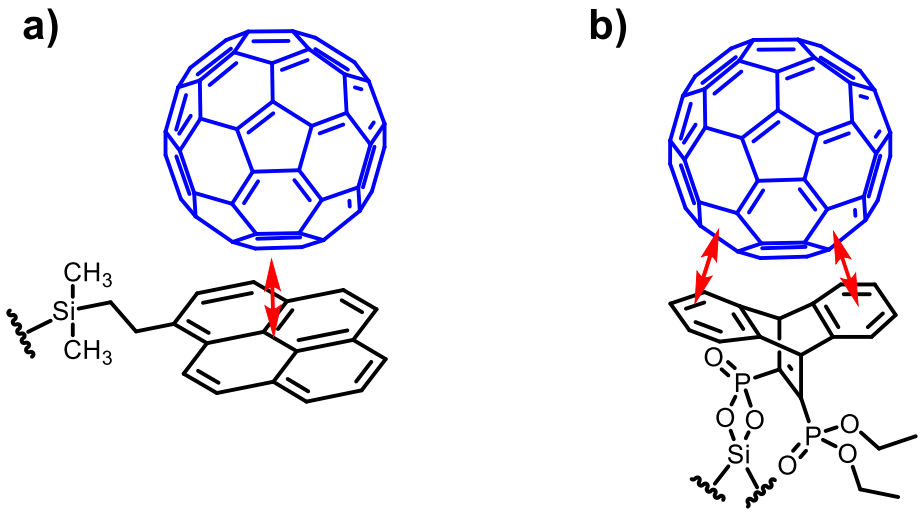

Figure 65: Schematic diagram showing a) shape mismatch between fullerene and state of the art Buckyprep stationary phase, b) shape complementarity between fullerene and hypothetical iptycene-based stationary phase.

3.2.1 Design, Synthesis, and Testing of Anthracene-Based Iptycene for Fullerene Purification

The initial idea was to use the same type of iptycene that we used in the ART and test its efficacy in fullerene separation, and we believed that **1** would be effective at functionalizing silica gel based on previous reports of silica gel functionalization with phosphonic acids.[343] With **1** already synthesized, it was important to determine a method for the functionalization of silica gel using our molecule.

The functionalization was done in refluxing tetrahydrofuran (THF) as a starting point. When the silica gel was filtered off and the filtrate reduced down under vacuum, it was noticed that all of iptycene **1** was still remaining in the filtrate and the mass of the silica gel was virtually unchanged. This was taken as an indication that the functionalization was not proceeding as expected and the literature was explored for further guidance. A common method to functionalize silicon oxide with phosphonates is called the “tethering by aggregation and growth” (T-BAG) method. In this method, the

phosphonate is first physisorbed onto the silicon oxide surface by submerging it in a THF solution of the phosphonate and slowly evaporating the THF. The physisorbed phosphonate is then heated in a vacuum oven at 140 °C to push the functionalization by driving off the ethanolic byproduct.

The T-BAG method was adopted to our silica gel functionalization strategy by first placing **1** and silica gel into a round bottom flask with acetonitrile and refluxing the suspension for four hours. The acetonitrile was then removed under reduced pressure on a rotary evaporator, in the same way that one would dry-load silica gel for flash chromatography. The **1**-physisorbed silica gel was transferred to a beaker and then placed into a vacuum oven and heated at 140 °C for four hours, after which the silica gel was removed from the oven and washed with dichloromethane to remove any unreacted **1**. The **1** that was recovered was re-characterized and found to be pure and was used in subsequent functionalizations. The obtained **1**-functionalized silica gel was yellow-orange in colour.

Next, the amount of **1** used in the functionalization was optimized in order to achieve maximum loading on the silica gel. In order to measure the loading of the silica gel ^{29}Si solid state nuclear magnetic resonance (SSNMR) was used. When taking the ^{29}Si SSNMR spectrum under magic angle spinning conditions, the spectrum consists of two peaks around -110 ppm (Figure 66). The leftmost peak around -100 ppm corresponds to silicon atoms which contain one hydroxyl group, while the peak at about -110 ppm comes from the resonance of silicon atoms with no free hydroxyl groups.[343] There is also sometimes a peak around -90 ppm that corresponds to silicon atoms with two hydroxyl groups, but this is much smaller in magnitude and depending on the silica gel used may

not be present at all. As the silica gel undergoes functionalization, the hydroxyl groups become silyl ether linkages, and therefore the peak around -100 ppm decreases in magnitude relative to the peak at -110 ppm.

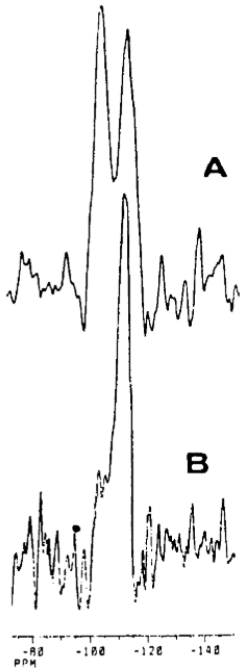

Figure 66: Typical ^{29}Si magic angle spinning SSNMR spectra showing the effect of phosphorylation on the signal at -103 ppm. A) Aldrich silica gel, B) after reaction with phenylphosphonic acid.[343]

Compound **1** contains four potential covalent bond forming sites on the molecule, so it was important to first get an approximate loading before turning to SSNMR for the final verification, as ^{29}Si SSNMR experiments take a long time to perform. This was easily accomplished by doing the silica gel functionalization step at various loadings of **1**, ranging from 0.25 equiv. to 4 equiv. In this case, equivalents were based on the number of free silanol groups per mole of the silica gel, which was estimated based on the specification sheet provided to us by SiliCycle, but due to the imprecise nature of the calculations, we converted the equivalents to a w/w% instead. As can be seen in Figure

67, the peak corresponding to the silanol groups was still very present with 7 w/w% loading of **1**, but when doubled to 14 w/w% the peak nearly vanished, and with 28 w/w% loading there is no discernable silanol peak remaining.

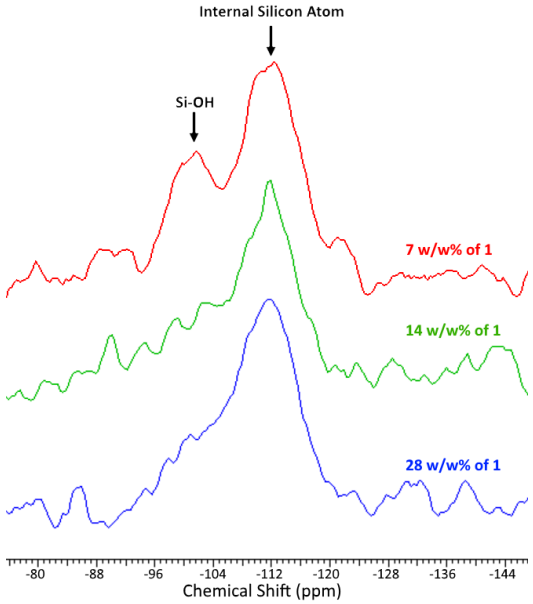

Figure 67: ^{29}Si SSNMR of 1-functionalized silica gel at varying loadings.

With the appropriate loading determined a batch large enough to carry out a real separation was synthesized. A 12 g column was used for the first separation tests and the separation was run on a CombiFlash Rf+ system so that the elution of fullerenes could be monitored by UV-Vis spectroscopy. The sample used was a 90:10 C_{60}/C_{70} mixture, denoted “fullerite,” which is a common ratio seen in fullerene soot after the higher fullerenes have been removed. Two milligrams of fullerite were dissolved in toluene and dry loaded onto silica gel to undergo separation. First, a control experiment was conducted using unfunctionalized silica gel with hexanes as the eluent in order to obtain a baseline elution time for comparison, and the fullerite eluted at 6 minutes as one single peak, indicating no separation on standard silica gel, as expected. The **1**-functionalized

silica gel was then tested on the same system to see if any resolution of the C_{60} and C_{70} peaks could be observed, but again only one peak eluted at 6 minutes (Figure 68). The lack of increase in retention time indicated that there was a need to further improve the interactions between the stationary phase and the fullerenes.

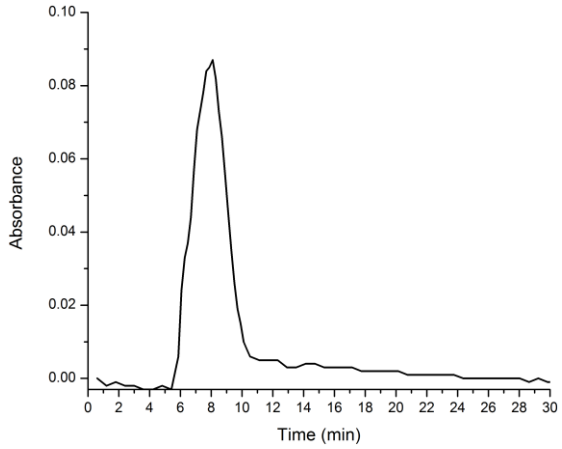

Figure 68: UV-Vis chromatogram of C_{60}/C_{70} mixture being eluted on a flash column with 1-functionalied silica gel as the stationary phase and hexanes as the mobile phase.

3.2.2 Design, Synthesis, and Testing of Pentacene-Based Iptycene for Fullerene Purification

While **1**-functionalized silica gel failed at separating the fullerite mixture, it likely worked as well as the Buckyprep system would have in the same experiment. The better shape matching of **1** would give it a better π-orbital overlap with the fullerenes and it would also increase the level of van der Waals interactions, the two most important design parameters for fullerene hosts. We hypothesized that using the pentacene-based iptycenes **17** and **18** (Scheme 17) would provide even more π-surface area while still maintaining the same degree of shape complementarity, thus potentially increasing retention times. A mixture of **17** and **18** was used due to separation issues, see above.

The **17**/**18** mixture was used to functionalize silica gel in an analogous way to **1**, turning the silica gel orange upon functionalization. The separation of fullerite was performed again in pure hexanes and an unprecedented increase in retention time was observed. The fullerenes did not start to elute in pure hexanes until ~35 minutes into the run and a second peak eluted at ~90 minutes (Figure 69). The results were encouraging and so the solvent system was changed to incorporate more toluene, increasing the speed of the elution. In a 3:1 hexanes/toluene eluent system, the two peaks eluted at ~30 minutes and ~55 minutes. In the extreme case of a pure toluene eluent system, the fullerenes eluted at 6 minutes, but two peaks could be observed, overlapping with one another.

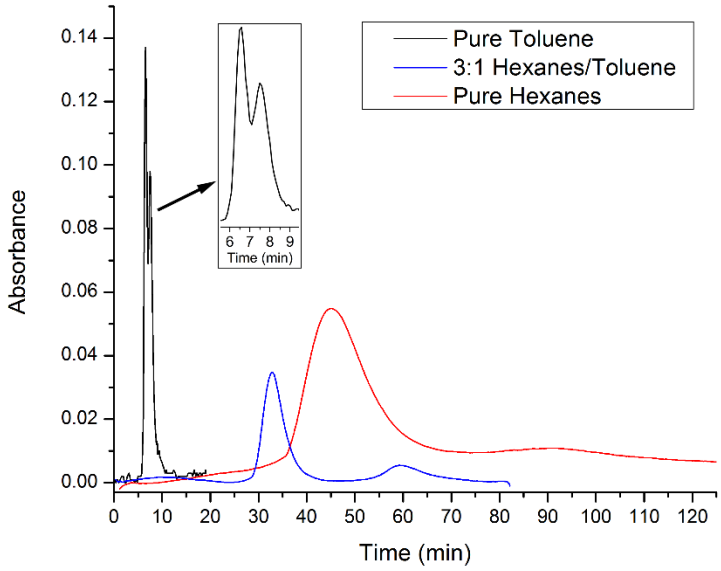

Figure 69: UV-Vis chromatograms of a C_{60}/C_{70} mixture being eluted on a flash column with 17/18-functionalized silica gel using various eluent systems.

The two eluted peaks were collected separately, and the solvent was removed under reduced pressure, with the first peak appearing pink in solution and the second peak appearing orange, indicating that they were C_{60} and C_{70}, respectively. The separation

returned 24 mg of C_{60} and C_{70} combined. To confirm their identities further, the UV-Vis spectrum of each sample was obtained (Figure 70). Both matched well with literature spectra, indicating that they were indeed separated and reasonably pure fullerenes.

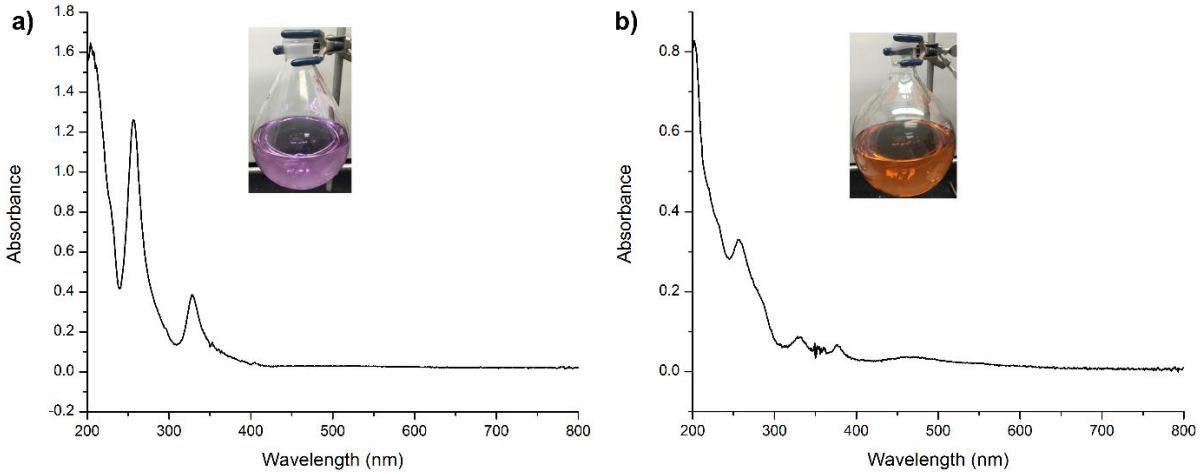

Figure 70: UV-Vis spectra of a) C_{60}, the first elution peak, and b) C_{70}, the second elution peak. Inset pictures of the flasks show colour of toluene solution with each sample.

With these results we showed that our **17**/**18**-functionalized silica gel is capable of separating fullerenes via flash chromatography, a feat that is difficult to achieve.[344] This has major implications for the future of fullerene purification because it will allow for the cheap, effective, and high scale purification of fullerenes with simple technology. However, the major issue that arose during this work was that the **17**/**18**-functionalized silica gel began to degrade over the course of several runs and the efficacy of the separation became weaker and weaker, until eventually it was incapable of separating C_{60} from C_{70} after ten runs. The likely mechanism for this degradation is reaction of the phosphonates with water present in the mobile phase, hydrolysing the phosphonate and thus removing the iptycenes from the silica gel. If this is indeed the case, the “purified” samples of fullerenes will be contaminated by the iptycenes and will then require a

secondary pass through a standard silica gel column to remove the iptycene. The phosphonates were chosen for their convenience in synthesis and commercial availability, but it is clear that a different group will have to be used if one wishes to use this method in industry, ideally incorporating a silane connector as is commonly employed. Despite this drawback, the proof that fullerenes can be purified on such a large scale, with a simple technique, is a great boon in the field of fullerene research.

3.3 Conclusion and Future Work

The use of an iptycene-based stationary phase for fullerene separation has yielded results that far surpass those of any other fullerene chromatographic purification method. However, as noted, the stationary phase is not entirely inert towards the chromatographic conditions and readily deteriorates throughout the course of several uses. The next steps should focus foremost on developing an iptycene with an anchoring group capable of withstanding repeated use as a stationary phase. The most ideal of these anchoring groups would be a chlorosilane as this is the typical industry standard and has proven to be very robust. Other potential ways to solve this issue include the use of coupling the iptycene to prefunctionalized silica gel, allowing for a wide variety of iptycene anchoring groups to be utilized.

The other improvement that could be made to the separation medium is to make it even more effective at retaining the fullerenes. This can be accomplished one of several ways, but the most straightforward would likely be bromination of the iptycene or incorporation of nitrogen or sulfur heteroatoms into the iptycene. As has been seen in other fullerene binding materials, the inclusion of these heteroatoms significantly increases binding affinity and could further improve the efficacy of the resulting separation

material. This could allow for even larger scale purification of the fullerenes, potentially allowing for hundreds of miligrams to be separated using standard laboratory flash columns. However, the importance of a durable stationary phase is paramount due to the possibility of the iptycenes contaminating the otherwise pure fullerene samples.

Chapter 4. Heteroaromatic-Based Metal-Organic Framework

4.1 Metal-Organic Frameworks

Metal-organic frameworks (MOFs) are extended 2D or 3D arrays of organic molecules and metals (Figure 71).[345] They are similar to a crystal in that they have a repeating, periodic structure, but are generally formed through the coordination chemistry between some organic moiety and a metal atom, or metal cluster. MOFs are interesting materials because they are supramolecular structures that generally consist of a highly porous structure,[346] which when coupled with the incorporation of transition metals allows MOFs to be used in super capacitors,[347] heterogeneous catalysis,[348,349,350] as a separation media,[351,352,353] as templates for carbon nanomaterial growth,[354] and for selective adsorption of hosts.[355,356,357]

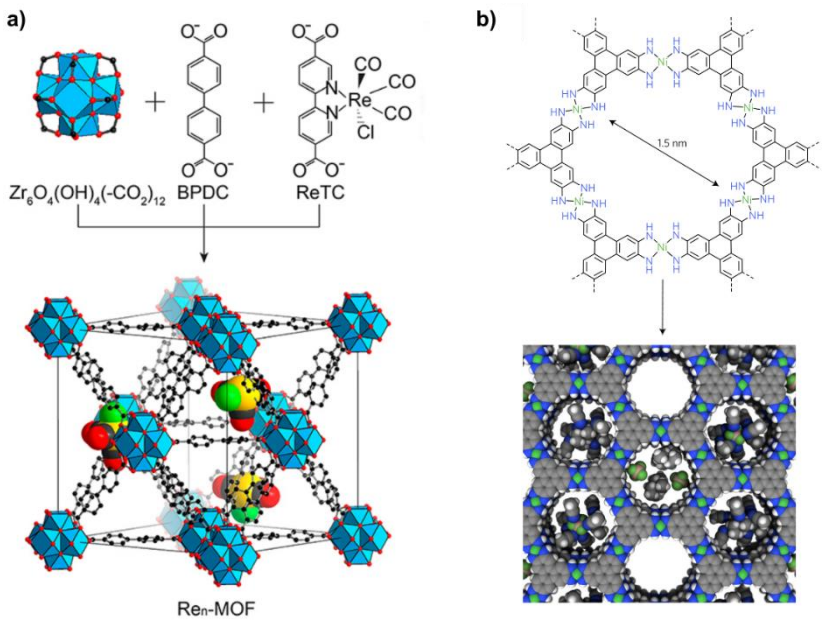

Figure 71: MOF structures of a) 3D[358] and b) 2D MOFs.[347]

In the past, MOFs had been described as co-ordination polymers and their synthesis reflects this. Generally, MOFs are made by the introduction of either a metal precursor to a suitable ligand building block, or vice versa. The reactions can be done at a wide variety of temperatures (room temperature to 200 °C), various pH levels, concentrations, and with different solvent polarities, much like a standard organic reaction.[345] However, unlike a standard polymer, MOFs require monomers that can connect in an array instead of a line, and this is where the ligand design becomes an important aspect of MOF synthesis. The most common types of MOF monomers contain carboxylate or nitrogen chelating groups. [347,352,359,360,361] In some cases the monomers possess more than two chelating sites in order to promote a network structure and MOF formation,[347] but in other cases the metal centres can bind to many monomers in different orientations, giving rise to the MOF structure.[348] MOFs are insoluble in most, if not all, solvents which can make their characterization difficult because solution techniques can not be used. Generally, the goal of MOF synthesis is to create a material that is either of sufficient quality to obtain a single crystal X-ray diffraction for easy characterization, or if that is not possible, a powdered X-ray diffraction along with other supporting characterization experiments is required.

Charge transport in MOFs is central to many of their applications, especially their use as electrocatalysts, and the movement of charge can broadly take place one of two ways depending on the structure of the MOF. In one instance, where the MOF has low porosity or has an insulating organic backbone, the charges are localized at redox centres and hop between them on the surface, with little or no overall change in the bulk.[362] Alternatively, if the MOF has a planar aromatic organic component it can delocalize the charge throughout the MOF structure, allowing for the entire MOF to act as a more

effective catalyst, but requiring the intake of counterions which can impede the adsorption of the analyte.[363] More specifically, one can target other charge transfer mechanisms like through-bond donor-acceptor charge transfer, similar to what is seen in a lot of conjugated organic polymers.[364,365] The design of MOFs is therefore challenging because there are many factors at play including porosity, the nature of the metal centre, the electronics of the ligand, the counterions present, and the inclusion of other dopants, along with the overall structure and assembly of the MOF. For these reasons, MOFs can be used in many applications and there is constant improvement seen in the field, with much room left to perfect MOF technologies.

4.1.1 MOFs as Electrocatalysts in Fuel Cells

One of the most promising applications of MOFs is their ability to be used as heterogeneous electrocatalysts, which have interested researchers for their potential use in fuel cells for energy storage.[366] A fuel cell is the common name for an electrochemical cell that converts the chemical energy of a fuel and oxidant into an electrical current. In most common cases the fuel in a fuel cell is hydrogen gas and the oxidant is oxygen gas, creating a simple by-product of water during fuel cell operation (Figure 72).[367] This is advantageous over current fossil fuels because hydrogen is a carbon-free fuel and creates only water as a by-product, and hydrogen is a readily abundant fuel, unlike fossil fuels.

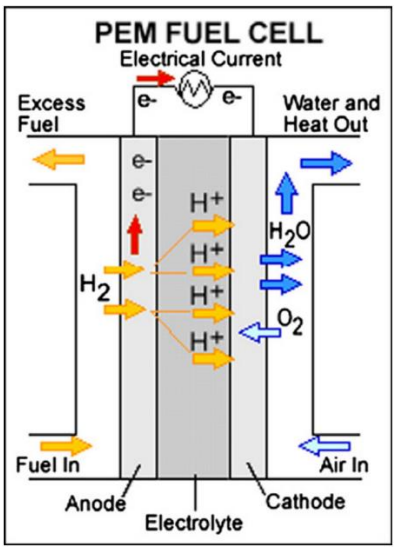

Figure 72: Schematic representation of a polymer electrolyte membrane fuel cell. Hydrogen gas is used as the fuel source and oxygen from the air is used as the oxidant, with water as the by-product.[367]

The continuous operation of fuel cells requires the constant supply of the hydrogen fuel which is difficult to accomplish in a mobile technology, like cars, where fuel cells would ideally be used. Hydrogen is a gas at ambient pressure, and it has an energy density that is far too low for practical application, meaning that it must be heavily compressed or cooled for use in automobiles. However, both compression and cryogenic cooling have their own inherent costs, which raise the price of the fuel cells to unacceptable levels.[368] For this reason, the storage of hydrogen gas in a dense form at ambient pressure has been an area of active research for some time. Solid support materials can be used to adsorb hydrogen gas and store it safely during transportation, significantly reducing safety concerns, and MOFs have demonstrated excellent capabilities for hydrogen storage. [356]

The production of hydrogen gas for use as a fuel can be done through the hydrogen evolution reaction (HER), which takes water and breaks it down into hydrogen gas and

an oxygen-containing by-product.[369] While advancements in the HER are important for clean generation of hydrogen gas, it is not a process that is directly involved in the fuel cell itself. The more important reaction is the dissociation of the resulting hydrogen gas to two protons through electrocatalytic oxidation, sometimes called the hydrogen oxidation reaction (HOR) (Figure 72 left side). The HOR is accomplished by a platinum electrode in most state-of-the-art fuel cell systems, but other precious metals have shown promise to potentially replace platinum under alkaline conditions.[370] The HOR produces protons that are capable of passing through the electrolyte membrane to undergo reaction with oxygen at the other electrode, completing the cell. The platinum electrodes used for HOR work well and so much of the research around fuel cells focusses on the other side of the cell.

The other half of the cell is based on the reduction of oxygen to complete the redox cycle. The electrons liberated in the HOR flow through the external circuit to the cathode where they are used to reduce oxygen from an incoming stream of air in what is called the oxygen reduction reaction (ORR) (Figure 72, right side). The ORR is a subject of constant and thorough investigation because it is the part of the fuel cell that still has much room for improvement.[371] The current problem with the ORR are three-fold: energy is lost as heat from resistance, an overpotential is seen in all experimental setups, and mass transfer of protons and oxygen to the cathode is slow (Figure 73).[371]

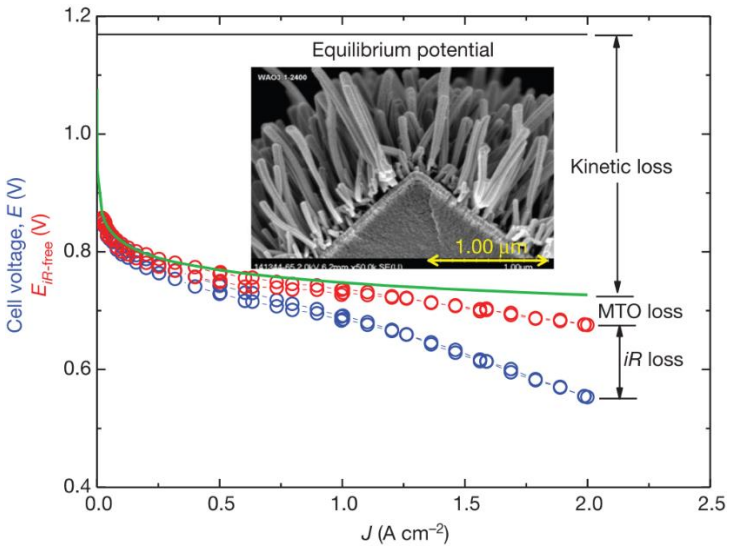

Figure 73: Fuel-cell polarization curve showing overpotential due to kinetic loss, mass transport overpotential (MTO), and losses to heat as a function of current density.[371]

The theoretical potential that a hydrogen fuel cell delivers is 1.23 V based on the half cell potentials, but platinum cathodes offer poor results with a potential of 0.51 V and a current density of only 1.25 mA cm^{-2}.[367] This has led to the development of many new types of cathodes based on other materials, including non-precious metal catalysts[366] and MOFs.[354] MOFs have been shown to be excellent catalysts for this work due to their high porosity, allowing for faster diffusion, and their ability to stay efficient over a much longer life cycle than platinum electrodes. Because of this, MOF-based electrodes have produced fuel cell potentials of ~0.8 V at current densities as high as 6 mA cm^{-2} and 96% retention of current density over a course of 25 h of continuous application.[354] Other MOFs have shown onset potentials as high as 1.06 V, with no degradation after 50,000 cycles.[372] While the use of MOFs as fuel cell cathodes is a relatively new development, the results have been promising and there are still many avenues available for future improvements, including doping, structural tuning, and structural nano-engineering.[373]

4.1.2 MOFs as Electrocatalysts for CO_2 Reduction

The other large area of MOF electrocatalyst research focuses on their use in CO_2 reduction. The goal of CO_2 reduction is to take the largely abundant waste product of fossil fuel burning and convert it to value added chemicals that can be used in consumer products. For example, by capturing CO_2 and reducing it, one can create carbon monoxide, formic acid, methane, methanol, ethylene, and ethanol, among other products, a combined market of hundreds of billions of dollars.[374] The most direct route to converting CO_2 to a value added chemical is to convert it to methanol and this can be done using current industrial processes but requires high temperatures and pressures while only resulting in low methanol yields.[375]

The electrochemical reduction of CO_2 has emerged as a convenient and effective way of converting CO_2 into value-added chemicals using heterogeneous catalysis and renewable electrical energy sources.[376,377] One of the bonuses of using electrocatalysts to reduce CO_2 is that the H_2 reductant can be supplied directly as water. The electrochemical reduction of CO_2 is at a minimum a two-electron process but depending on the desired target product can involve twelve or more electrons (Table 3). Due to the many electrons required for the higher order reductions, as well as the different reactions that are available during CO_2 reduction, it can be difficult to target specific products. This is coupled with the problem that all of the reduction potentials are not only close to each other but are also very close in energy to the reversible hydrogen electrode equilibrium potential. This means that the CO_2 reduction process is in direct competition with the HER which makes it necessary to find a catalyst that not only is effective at CO_2 reduction but is slow at the HER.

Reaction	E^0 (V vs RHE)[a)]
$2H^+ + 2e^- \rightarrow H_2$	0
$CO_2 + 2H^+ + 2e^- \rightarrow CO + H_2O$	−0.11
$CO_2 + 2H^+ + 2e^- \rightarrow HCOOH$	−0.21
$CO_2 + 4H^+ + 4e^- \rightarrow HCHO + H_2O$	−0.10
$CO_2 + 6H^+ + 6e^- \rightarrow CH_3OH + H_2O$	0.03
$CO_2 + 8H^+ + 8e^- \rightarrow CH_4 + 2H_2O$	0.17
$2CO_2 + 8H^+ + 8e^- \rightarrow CH_3COOH + 2H_2O$	−0.26
$2CO_2 + 12H^+ + 12e^- \rightarrow C_2H_4 + 4H_2O$	0.07
$2CO_2 + 12H^+ + 12e^- \rightarrow C_2H_5OH + 3H_2O$	0.09
$3CO_2 + 18H^+ + 18e^- \rightarrow 1\text{-}C_3H_7OH + 5H_2O$	0.09

[a)]The equilibrium potential at 25 °C and 100 kPa, and with proton activity of 1 mol L^{-1}.

Table 3: Standard potentials for electrochemical reduction of CO_2.[376]

The activity of various metals has been roughly mapped out in the case of CO_2 reduction.[378] The research suggests that metals can be grouped into: 1) CO production with Au, Ag, Zn, Pd, and Ga metal; 2) formate production with Pb, Hg, In, Sn, Cd, and Tl metal; 3) hydrogen evolution with Ni, Fe, Pt, and Ti metal; 4) higher order carbon products with copper metal. In this case, copper is unique in that it is capable of effectively catalyzing several processes including methane, ethylene, ethanol, propanol, and other $C_{>2}$ products. However, copper also has historically suffered from poor selectivity and larger over potentials than other metals.

Instead of relying on atomic metals as electrocatalysts, researchers have branched out research into several directions, most notably to us MOFs. Since MOFs can be synthesized from a wide array of different metal and ligand combinations, there have been many heterogeneous electrocatalyst MOFs that are used for CO_2 reduction. One interesting feature of MOF-based electrolytes is that there are many examples of non-precious metals being used effectively in CO_2 reductions, with both iron and cobalt-based porphyrin MOFs capable of effectively reducing CO_2 to CO.[379,380] What is interesting with

these results is that iron is usually only effective at hydrogen evolution, but when inserted into the porphyrin-MOF, its reactivity completely changes to favour CO_2 reduction. Likewise, cobalt is not typically seen as a CO_2 reduction catalyst, but once again performs exceptionally well in the porphyrin-MOF system.

Perhaps even more interesting is the effect that MOF incorporation has on the electrocatalytic behaviour of copper. As noted above, copper tends to suffer from very poor selectivity in CO_2 reduction, producing many products, albeit with generally great efficiencies. However, by creating a copper-based MOF system with rubeanic acid organic linkers, Hinogami et al. were able to create an electrocatalytic system capable of producing formic acid in purities above 99%, while also increasing the reaction rate 13-fold.[381] The increase in reaction rate is believed to be due to increase in surface area, and therefore active catalytic sites, over the standard copper metal electrode. Similar results were also seen in thin-film copper-MOFs which were capable of producing oxalic acid in over 90% purity through CO_2 reduction.[382] Notably, the difference between these two copper-MOFs was the change in organic linker: in the case of formic acid formation, rubeanic acid, a sulfur and nitrogen containing molecule was used, while in the case of oxalic acid formation, benzene-1,3,5-tricarboxylic acid was used as the linker. These seemingly small changes had the effect of completely altering the reaction product from a C_1 to a C_2 product, highlighting how important the nature of the linker is.

With so many possibilities in terms of structure and MOF design, the future of MOFs holds great potential, but further improvement in CO_2 reduction electrocatalysis requires several key thresholds to be met. The faradaic efficiency of ideal electrocatalysts should be over 90%, which means that side reactions and other sources of loss must be

mitigated. A small overpotential (more positive than -0.6 V) and a high energy density > 200 mA cm^{-2} need to also be achievable. Finally, all of this must also be obtainable during constant operation over a month or longer. This last condition is still the most challenging as many MOFs tend to breakdown during continuous operation.

4.2 1,4,6,9-tetra(pyridine-2-yl)pyridazino[4,5-*g*]phthalazine Copper Metal-Organic Framework System

4.2.1 Synthesis of 1,4,6,9-tetra(pyridine-2-yl)pyridazino[4,5-*g*]phthalazine

During our previous work with fullerene separation we had attempted to synthesize several other stationary phases that could improve the efficacy of the separation. One idea that we pursued was the installation of nitrogen heteroaromatics into the backbone of the separation material, however this proved challenging as not many acene-type molecules exist that contain nitrogen heteroatoms. Serendipitously, another member of our research group was working on an unrelated project which required the use of 3,6-di-2-pyridyl-1,2,4,5-tetrazine (dipytet). Dipytet is an interesting molecule consisting of a tetrazine core and two pyridyl substituents that is very useful as a Diels-Alder reactant. In particular, it is capable of undergoing a Diels-Alder reaction followed by a retro Diels-Alder to convert certain endoxides to benzofurans (Scheme 18). The ultimate Diels-Alder in this case gives both benzofuran and an analogue of dipytet where the central 1,2,4,5-tetrazine ring has been converted to a pyridazine.

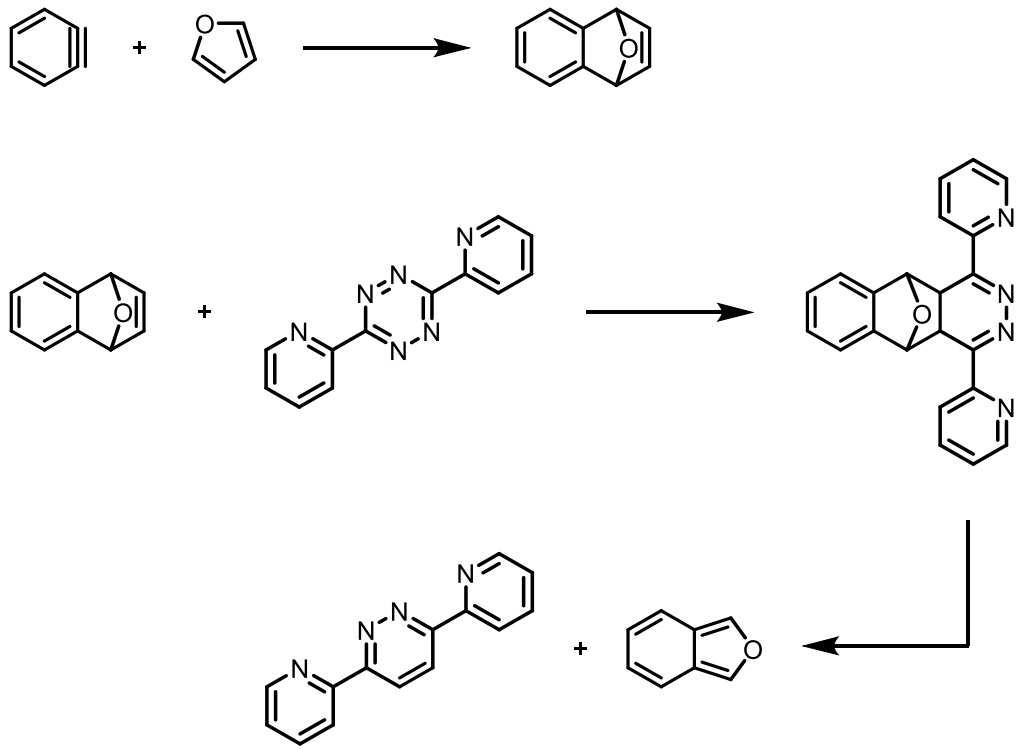

Scheme 18: The use of dipytet as a Diels-Alder reactant.

Dipytet is a good diene in the Diels-Alder reaction and we thought that we may be able to use this to our advantage in designing a potential azaacene. The retro Diels-Alder shown in Scheme 18 only occurs because the conjugation of the endoxide allows for the formation of benzofuran as the product of the Diels-Alder. If instead a simple dienophile is used, there is no driving force for the retro Diels-Alder to occur, so one can potentially use dipytet as an effective reactant for the installation of a pyridazine ring. We envisioned using a non-conjugated diene to undergo two separate Diels-Alder reactions with two equivalents of dipytet, building an extended carbon backbone, that could potentially be aromatized in subsequent steps. To do this 1,4-cyclohexadiene was used as the diene so that the resulting molecule would be straight and resemble very closely an acene (Scheme 19). Originally, it was thought that the synthesis would require a second step in

order to complete the aromatization of the azaacene, but delightfully the conditions provided the fully aromatized product as an orange solid.

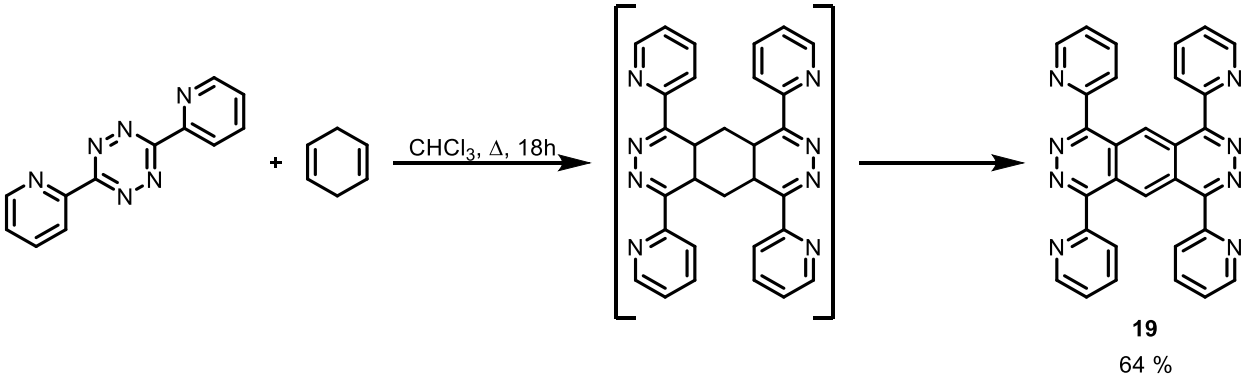

Scheme 19: Synthesis of 1,4,6,9-tetra(pyridine-2-yl)pyridazino[4,5-*g*]phthalazine.

As was stated, the original purpose of synthesizing **19** was to test it for fullerene purification, and it was planned that the introduction of the nitrogen atoms into the backbone of the acene would cause it to become electron deficient enough to undergo an inverse-demand Diels-Alder reaction with strained or electron rich dienophiles. The goal was to be able to install an anchoring group through Diels-Alder, similar to the synthesis of **17**/**18**. This was tested by reacting **19** with norbornene, norbornadiene, and vinylene carbonate. Unfortunately, none of the reactions showed any consumption of the starting materials as monitored by TLC, even at temperatures as high as 180 °C over the course of four days. Even with the addition of catalytic, substoichiometric, and excess p-toluene sulfonic acid to make **19** more electron poor, no reaction was observed.

The failure of the Diels-Alder reaction left us with **19** without any concrete plan with what to do with it. However, it is quite apparent when looking at the molecule that it

contains several domains that could potentially act as chelation sites towards metals. This got us thinking that perhaps it might make a good organic linker to form a new MOF, so we began to investigate this possibility.

4.3 1,4,6,9-tetra(pyridine-2-yl)pyridazino[4,5-*g*]phthalazine in the Synthesis of Novel Metal-Organic Frameworks

First, conditions for the synthesis of MOFs using **19** as an organic linker were tested, with the overarching goal of creating a MOF that would have interesting properties for either gas storage, electrocatalysis, or as a super capacitor. It was thought that due to the fully aromatic, planar azaacene backbone on **19** it might lend itself to better charge transport, aiding in electrocatalysis. Furthermore, because of the potential for free rotation of the pyridyl substituents, several potential MOF structures could be formed (Scheme 20). These structures are simplifications but show that for square planar metal centres there are already at least two different binding modes that are plausible. Binding mode **a** (Scheme 20) shows what can be considered a linear coordination polymer, but could also lead to π-stacking between the linear chains to form sheets,[347] and binding mode **b** (Scheme 20) depicts a way for the structure to propagate into two-dimensions. Tetrahedral or octahedral metal centres would lead to even more potential binding modes, perhaps even leading to chiral structures, leading us to believe that this was an avenue worth exploration.

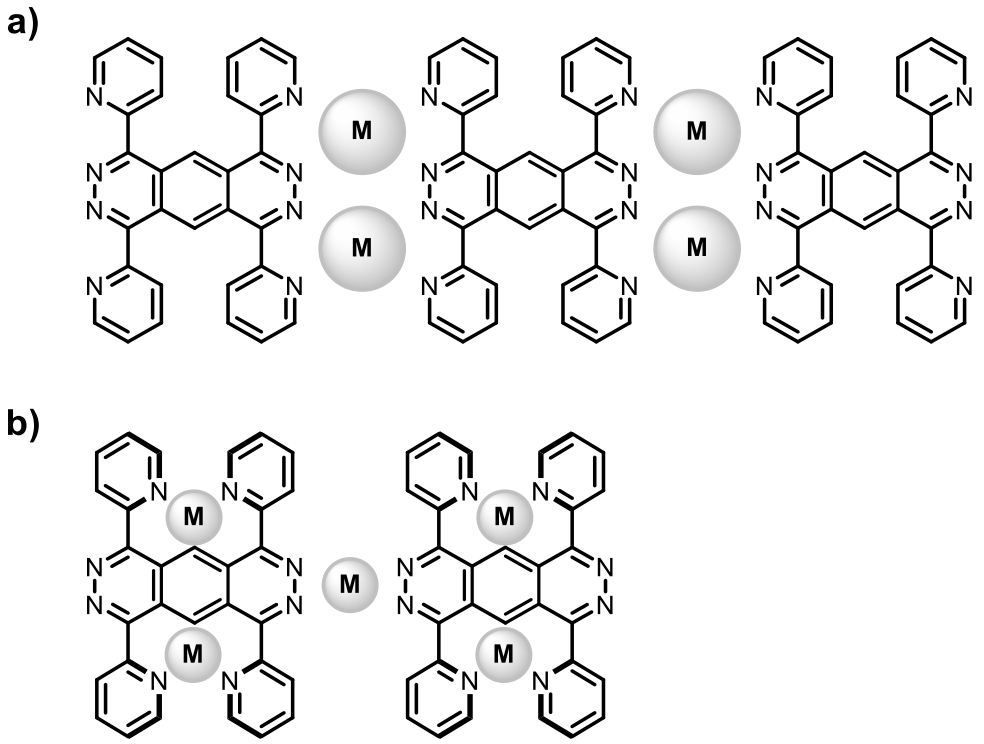

Scheme 20: Two possible binding modes for MOF formation with 19.

The thought of a nitrogen heteroaromatic-based MOF was intriguing because nitrogen heterocycles have been shown to enhance the effective electrocatalytic activity of various metal electrodes in both their native[383] and protonated forms.[384,385,386] The exact mechanism for this is still debated but it appears as though the redox capabilities of most nitrogen heterocycles aids in overall process. Some nitrogen heterocycles have reversible redox windows near the HER and CO_2 reduction potentials, which has lead scientists to believe that it aids in the shuttling of protons, hydrides, and electrons throughout the system.[387]

4.3.1 Synthesis of 1,4,6,9-tetra(pyridine-2-yl)pyridazino[4,5-*g*]phthalazine-Based Metal Organic Frameworks

Our first goal was to determine whether or not **19** would be an effective organic linker in MOF formation. To test this, we screened metals, solvents, and temperatures until we

got evidence of MOF formation, and then began testing other metals under the same conditions to see which metals were capable of forming a MOF with **19**. The first hit that we got was $NiSO_4 \cdot 6H_2O$ in dimethylformamide (DMF), at 120 °C for 18 h. This reaction yielded a green precipitate that was completely insoluble in polar organic solvents, non-polar organic solvents, and water. The highly crystalline nature of MOFs tends to render them insoluble, so it was assumed that this was an indication that the MOF formation was working and the effect of stoichiometry on the reaction was tested.

Ligand Equiv.	Metal Equiv.	Mass Obtained
4	1	1 mg
3	1	1 mg
2	1	0 mg
1	1	5 mg
1	2	16 mg
1	3	15 mg
1	4	54 mg

Table 4: Effects of stoichiometry on MOF formation.

Since the product was insoluble, the precipitate was simply washed with water and acetone to remove any unreacted metal and **19**, and then the insoluble fraction was weighed to get a crude measurement of the “yield” of the MOF. Based on the binding

modes in Scheme 20, conditions were tested in which the limiting reagent was **19** in a 1:4 ratio, up to conditions where **19** was in a 4:1 excess using 25 mg of the ligand in each trial (Table 4). When **19** is in excess little to no insoluble material precipitates during the reaction. On the contrary, as $NiSO_4$ increases in abundance, more and more insoluble product is formed.

The next step was to see which other metals could form insoluble fractions under these conditions. The results of the metal screening are summarized in Table 5. Because the exact structures of the MOFs were unknown at this point, the determination of a percent yield was not possible. Instead, a crude conversion calculation whereby the mass of the precipitate was divided by the combined masses of the reactants was used. Only five metals gave over 50% conversion: nickel, copper, palladium, silver, and ruthenium, all of which are in the (II) oxidation state except for silver, which was silver (I). The results are interesting because nickel and palladium are in the same group, as are copper and silver, and they are all very well studied in catalysis. Ruthenium is the odd result because it is a d^8 metal and iron gave no product at all, making ruthenium the only second row transition metal to form a MOF with **19** that its first-row analogue does not. Ruthenium is also well studied as a catalyst in organic chemistry and is famously used in ring-opening and ring-closing metathesis reactions.

The results indicate that the nature of the metal atom is not the only important factor, the counterion drastically impacts the conversion. In the case of nickel, the sulfate counterion gives over a two-fold increase in conversion when compared to nickel acetate. Copper is a better indication of this effect with copper sulfate reaching a conversion of 72 %, but acetate, chloride, and carbonate all fail to reach even 30 % conversion. This

indicates that the sulfate ion somehow either facilitates the MOF formation or produces a more stable MOF structure than the other counterions. However, the heavier metals all show good conversion without the need for the sulfate counterion. Palladium chloride forms a MOF at appreciable conversion, whereas copper chloride has poor conversion, which may indicate a size complementary relationship between the metal and the ligand that is responsible for effective MOF formation. The potential formation of copper MOFs was of interest because of copper's high activity in electrocatalysis. All the MOFs that were synthesized failed to solvate in any organic solvents or water, even at high temperatures making further characterization difficult initially.

Metal	Conversion (%)
$NiSO_4$	69
$Ni(CH_3CO_2)_2$	28
$CuSO_4$	72
$Cu(CH_3CO_2)_2$	26
$CuCO_3$	28
$CuCl_2$	24
$SnCl_2$	0
$Pd(CH_3CO_2)_2$	38
$PdCl_2$	56
$FeCl_3$	0
$Zn(CH_3CO_2)_2$	12
$CoCl_2$	14
$RhCl_3$	4
$IrCl_3$	0
$AgNO_3$	65
$(Ph_3P)_3RuCl_2$	62

Table 5: Conversion of starting materials in MOF formation with various metals.

4.3.2 Attempts at Creating Soluble MOFs

With so many potential MOFs created, the next step was their characterization, and the most direct and effective way to characterize a MOF fully is to subject it to a single-crystal X-ray diffraction (XRD) experiment. Unfortunately, the sample particles were not large enough for single-crystal analysis so instead efforts were turned towards devising a method to make the products soluble such that they could be recrystallized to give single-crystals that were large enough for characterization.

Copper sulfate was used as the model system due to its high conversion, and the reaction which formed the copper precipitate was run several times with varied reaction conditions in an effort to garner a large, single crystal. The objective was to lower the reaction rate such that either the larger crystals formed naturally, or so that the reaction could be stopped early while the MOFs were still small enough to be soluble. Firstly, the reaction was run at lower temperatures including 100 °C, 80 °C, and 60 °C, but there was no consumption of starting materials at these temperatures, even after two days of reaction time. Secondly, different solvent systems were tested to see if they would provide for either a slower reaction rate, or perhaps the MOF would have poorer solubility and precipitate earlier such that it could then be dissolved and recrystallized in a better solvent. The problem was that most solvents are not effective at solubilizing both **19** and $CuSO_4$ so we had to rely on solvent mixtures, varying the amount of DMF and both THF and acetonitrile. This method still gave us an insoluble product that was just as insoluble in pure DMF, with the side-effect of lowered conversion. Thirdly, the concentration was varied from the original 0.064 M with respect to the combined starting materials half as concentrated, five times more dilute, and ten more dilute. When diluted in half, the

reaction still gave the insoluble precipitate at reduced conversion, but at higher dilutions, the precipitate did not form even after two days of reaction time.

The failure of the previous methods led to a different approach at retarding the reaction rate. It was hypothesized that adding a secondary ligand that is incapable of forming a MOF, but still capable of chelating with the metal, would directly compete with **19**, and thus reduce the rate of MOF formation. 2,2'-Bipyridine was chosen as the ligand in hopes that it would have a binding strength similar to that of **19** so that the binding would be reversible enough to still allow for MOF formation and by increasing the concentration of bipy, the rate of MOF formation could be slowed even further. It was hypothesized that the mechanism for this rate modulation would be analogous to that of atom-transfer radical polymerization (ATRP). The reaction would begin with the formation of a small "MOF" through reaction of **19** and $CuSO_4$ (Scheme 21), and that this actively growing MOF could then at any point be capped by chelation with bipy instead of **19**, effectively deactivating the MOF towards further growth as bipy lacks the necessary number of binding sites. Eventually, the bipy ligands would be reversibly replaced with **19**, activating the MOF towards further growth once again. The MOF growth would self-terminate at the point of precipitation, but the goal would be to stop the reaction before this point and obtain a bipy-terminated MOF.

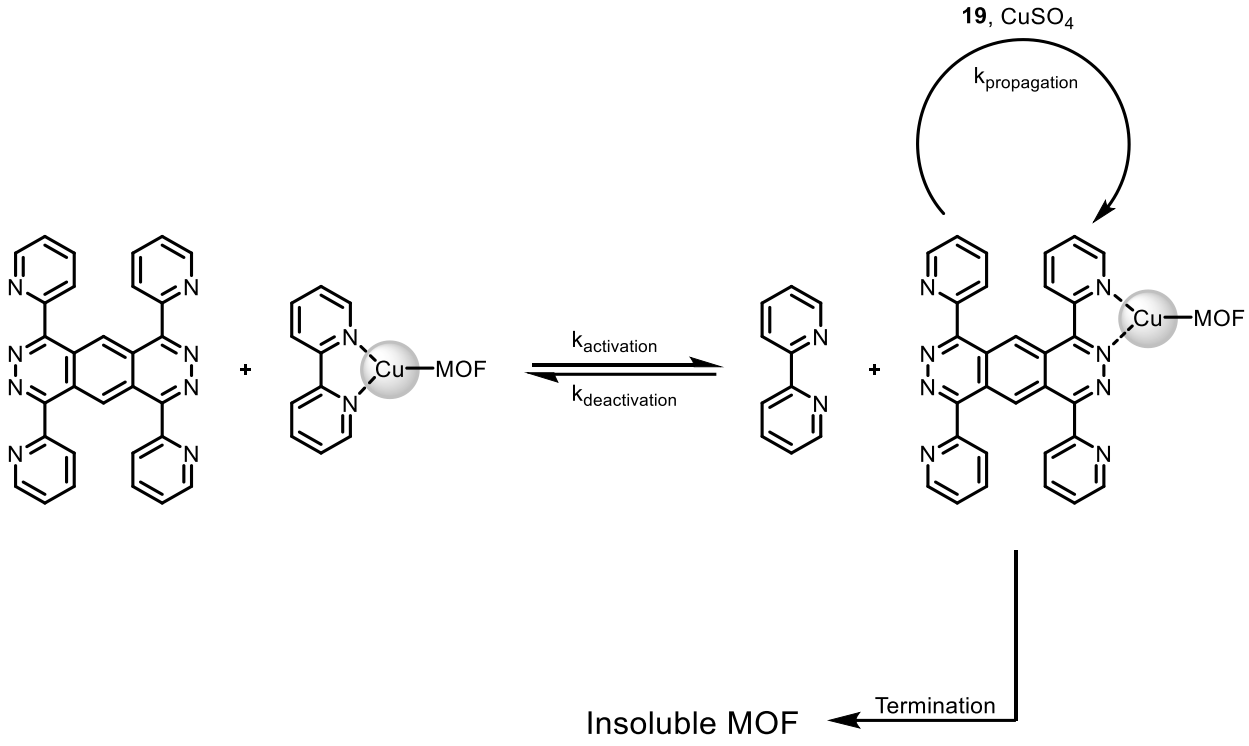

Scheme 21: Proposed mechanism for reducing MOF growth rate.

The competition reaction was attempted under several conditions in order to find conditions such that the rate of deactivation was faster than activation, while keeping the rates close in magnitude. The first experiment involved simply a 1:1 ratio of bipy and **19** but it still resulted in quick precipitation of the product without any obvious signs of inhibition, nor were there any soluble products when tested throughout the reaction time. The amount of bipy was subsequently increased by double and then five-fold. When doubled there was no observed difference, but upon five-fold increase there was a new product formed, however it appears as though this is simply some kind of copper bipy system and not a MOF at all. Further work on this method may yield favourable results but will take serious fine-tuning to determine the appropriate ratios and concentration for an effective partial inhibition of MOF growth.

4.4 Characterization of 1,4,6,9-tetra(pyridine-2-yl)pyridazino[4,5-*g*]phthalazine-Based MOFs

After the synthesis of a soluble MOF failed, attention was instead turned towards characterizing the solid material using other characterization techniques. Several techniques are available to characterize insoluble solids and the main techniques that we decided to take advantage of are: powder X-ray diffraction (pXRD), cyclic voltammetry, transmission electron microscopy (TEM), and energy dispersive X-ray analysis. Through the combination of these techniques, a general formula and structure for the MOF can be established, and its redox properties can be understood.

4.4.1 Cyclic Voltammetry Characterization of 1,4,6,9-tetra(pyridine-2-yl)pyridazino[4,5-*g*]phthalazine-Based MOFs and Their Precursors

The first step that was taken in the determination of the product was cyclic voltammetry with a goal of ensuring that the product was redox active before taking characterization further as the other techniques are quite costly. The redox activity of the product gives insight into whether it behaves as an electron donor or acceptor and the change between starting material and product can further give evidence to suggest that a new material has been successfully made.

A typical CV setup involves a working electrode, reference electrode, counter electrode, solvent, analyte, electrolyte, and the solvent is generally sparged with N_2 to remove any oxygen. The removal of oxygen is important when trying to discern the inherent redox characteristics of a material because if oxygen is present it can be reduced either by the electrode, or in this case, by the electrocatalyst, giving a strong signal that may overlap with the analyte. Along the same lines, water is also excluded from the cell for these measurements. However, because the MOF products are insoluble, they are

not amenable to this type of measurement which requires that the analyte be soluble in the solvent.

The CV experiment of insoluble materials and heterogeneous catalysts is generally done by adsorbing them onto the surface of a glassy carbon electrode. Glassy carbon is used due to its porous nature which enables it to better adhere the catalyst particles, and the absorption of MOFs onto glassy carbon electrodes can be done in two ways. In the first method the MOF is placed into a volatile, dry solvent and sonicated to break it down into small particles, then the suspension is dropcast onto the electrode surface, allowing the solvent to evaporate. The process is repeated until enough MOF has been deposited to obtain the desired measurements. Alternatively, the process can be done in the same way but with the addition of porous carbon black to the suspension before dropcasting it onto the electrode. The addition of carbon black to the suspension aids in adhesion to the carbon electrode.

The five MOFs that were synthesized in highest conversions were tested to see their redox properties. They were all prepared using a simple dropcasting method, without using carbon black as an additive, but unfortunately all but the copper MOF were unable to adsorb properly to the glassy carbon electrode and could be seen visibly falling off during testing. The other four systems were then once again dropcasted but with the aid of carbon black. Silver, nickel, and palladium still fell off of the electrode, but the ruthenium MOF managed to adhere, however the signal obtained from it was very weak and was quickly masked by the slow leaching of oxygen back into the cell. Further testing is required for the ruthenium system.

The copper MOF adhered properly to the glassy carbon electrode and generated a proper CV curve (Figure 74). The cell was nitrogen-purged, with dry acetonitrile as the solvent, and tetrabutylammonium hexafluorophosphate as the electrolyte. The reference electrode was Ag/AgCl and the open-circuit potential was measured to be +0.365 V. Three reversible reduction peaks can be seen at +0.127 V, -0.097 V, and -0.369 V, which seem to indicate that the MOF is an electron accepting material, but it also gives some insight into the potential sites that are accepting the electrons. The copper is in the (II) oxidation state in the precursor and is unlikely to change through the synthesis due to the neutral nature of **19**. Therefore, one would expect to see a $Cu^{II} \rightarrow Cu^{I}$ reduction peak, and perhaps a $Cu^{I} \rightarrow Cu^{0}$ reduction peak in the material, however three distinct peaks are observed. Furthermore, they are all sequentially harder to reduce, leading us to believe that it may be the aromatic cores of **19** that are being reduced. **19** contains an azaacene core which is electron deficient due to the incorporation of the pyridazine groups, and the pendant pyridine groups are also electron deficient. In the case of many pyridine-type nitrogen heteroaromatics, reductive pathways are well known, and this is very apparent in the case of $Ru(bipy)_3$, where the three 2,2'-bipyridyl ligands each undergo a reversible reduction in a relatively small potential window, while the oxidation of Ru^{III}/Ru^{II} is at a very highly positive voltage and there is no observable Ru^{II}/Ru^{I} reduction peak.[388]

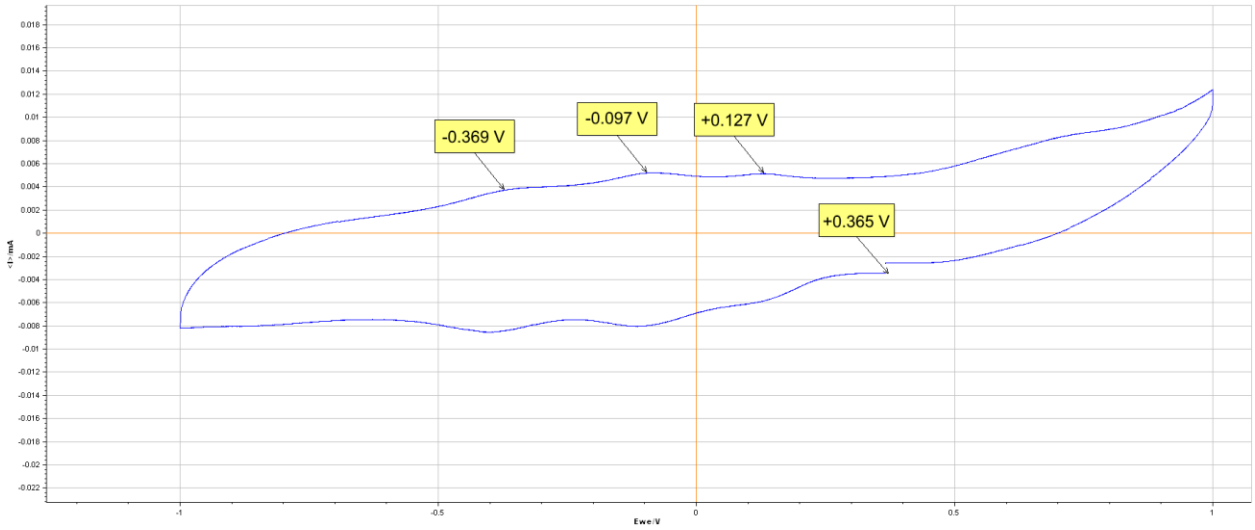

Figure 74: Cyclic voltammetry curve of $CuSO_4$-based MOF

The CV shown in Figure 74 have an open-circuit voltage equivalent to that of the Ag/AgCl reference electrode, which makes comparison to other literature values somewhat inconvenient and so the peaks have been converted to their potentials with respect to the standard hydrogen electrode (SHE) in Table 6. Along with the redox peaks observed in our experiments, the redox potentials for copper have been added to the table for easy comparison. The table shows that the copper reduction peaks all occur at very different potentials than what was observed for our MOF product, indicating that it is the aromatics that are undergoing the reductions. This is further evidence that the material formed is indeed a MOF created through reaction of **19** and $CuSO_4$ as it experiences no solubility but has taken on the redox properties of **19** as a ligand. The results indicate that either **19** can undergo three separate reductions itself, or that there are three **19** ligands per metal.

Species	Potential Vs. SHE
Cu^{I}/Cu^{0}	+0.520
Cu^{II}/Cu^{0}	+0.337
Ag/AgCl	+0.197
Cu^{II}/Cu^{I}	+0.159
MOF Reduction 1	-0.041
MOF Reduction 2	-0.265
MOF Reduction 3	-0.537

Table 6: Reduction potentials versus standard hydrogen electrode.

The assumptions that the redox properties were due to the aromatics were validated by the CV of **19** (Figure 75), as two reversible redox peaks were observed. This indicates that the ligand itself is redox active, and based on the reduction potentials of the MOF product, the peaks seen are very likely due to the **19** ligand, not the copper centres.

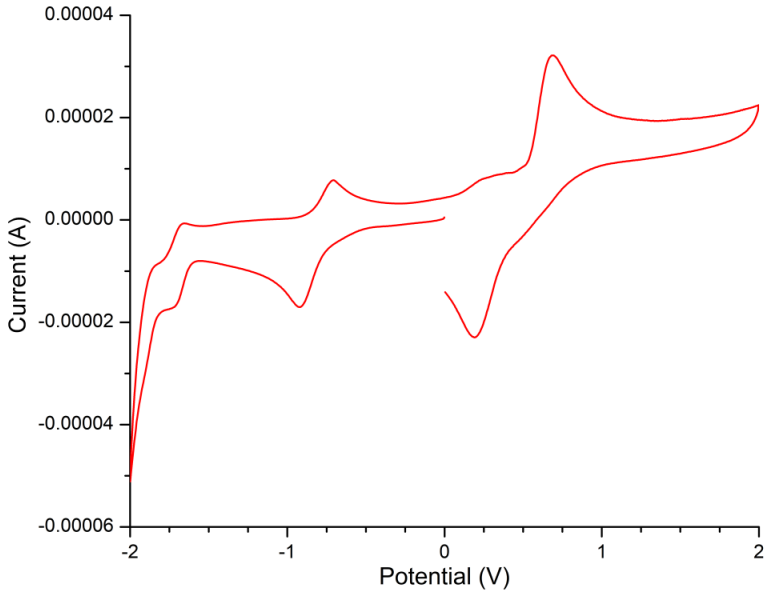

Figure 75: Cyclic voltammogram of 19 in acetonitrile.

4.4.2 Powder X-Ray Diffraction of 1,4,6,9-tetra(pyridine-2-yl)pyridazino[4,5-*g*]phthalazine-Based MOF

While the cyclic voltammetry experiments gave us some evidence of MOF formation, it lacked to provide us with any deeper understanding of the structure. We turned to powder X-ray diffraction to glean some structural insight. The pXRD pattern can be seen in Figure 75.

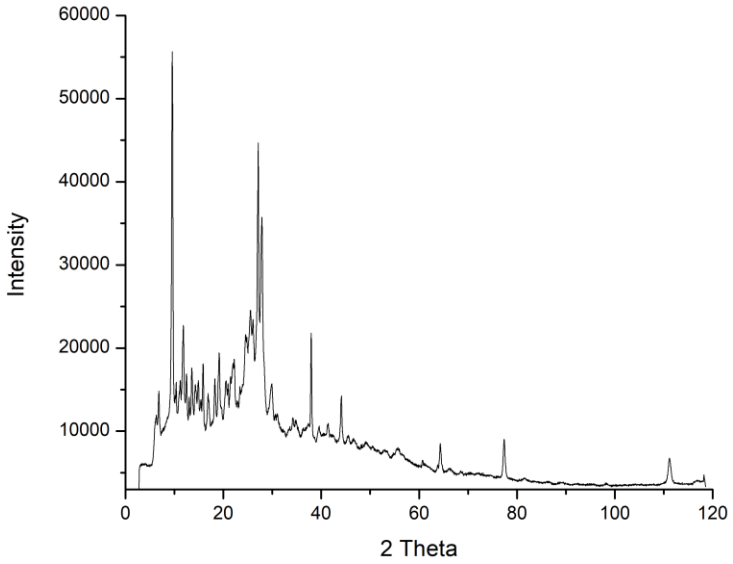

Figure 75: pXRD spectrum of $CuSO_4$-based MOF

The pXRD spectrum of the synthesized $CuSO_4$-based MOF indicates that the material is crystalline in nature, which is what is expected of a well-ordered structure, like a metal-organic framework, and serves as further evidence of the formation of a MOF. However, further details were not easily extracted from the data due to its difference from other compounds available in the database. Comparisons to a simulated spectrum would help confirm the expected structure, but since the structure was unknown, simulations could not be run.

4.4.3 Transmission Electron Microscopy and Energy Dispersive X-Ray Analysis of 1,4,6,9-tetra(pyridine-2-yl)pyridazino[4,5-*g*]phthalazine-Copper MOF

Transmission electron microscopy was turned to in an attempt to determine if the morphology of the material could be directly observed. Many MOF structures are heavily porous, but that is not necessarily the case and understanding the porosity of our newly synthesized material would help in determining which applications it could be further tested for. The TEM images of the copper-based MOF reveal that the material forms crystals on the scale of ~100 nm, and appears to form a macroporous solid, with no micropores directly observed (Figure 76).

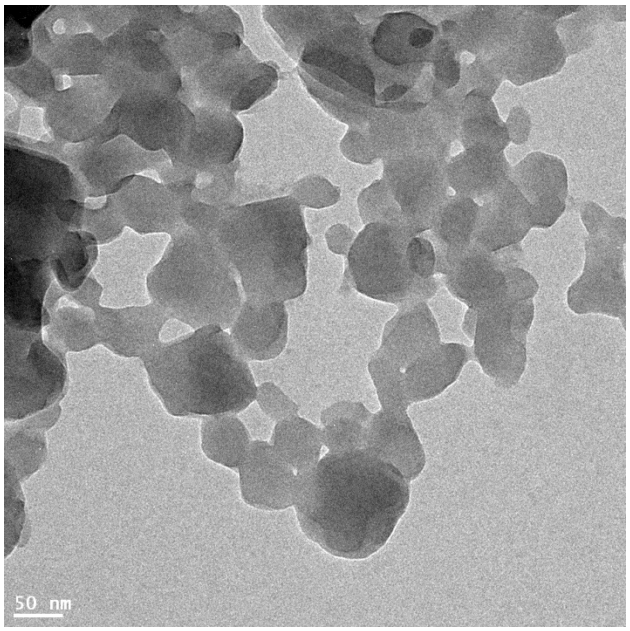

Figure 76: Transmission electron micrograph of 1,4,6,9-tetra(pyridine-2-yl)pyridazino[4,5-*g*]phthalazine-Copper MOF

To determine a formula for the MOF, EDXA was performed on the sample on a nickel grid, so that the typical copper grid would not interfere with the measurements. The EDXA was repeated on several regions and the average was taken to establish a formula of

$Cu_9C_{30}H_{18}O_7N_8S_5$. The formula indicates that the structures that were predicted in Scheme 20 are not accurate due to the overabundance of copper (9 Copper to 1 **19**). The results seem to indicate the formation of a copper cluster, perhaps bridged by sulfur or oxygen atoms, as has been seen in the past with copper(II) and multidentate nitrogen ligands,[389] and in biological systems.[390]

4.4.4 Testing CO_2 Reduction Capabilities of 1,4,6,9-tetra(pyridine-2-yl)pyridazino[4,5-*g*]phthalazine-Copper MOF

The MOF system was tested for its efficacy towards CO_2 reduction based on previous reports of copper electrocatalytic systems. The reduction was done in an electrocatalytic cell with 0.1 M $KHCO_3$ as the aqueous electrolyte, and with a constant stream of CO_2 being fed into the solution, and a potential of -1.4 V vs Ag/AgCl. The MOF was affixed to a glassy carbon electrode by first creating an ink in Nafion® 117 solution, followed by dropcasting onto the freshly polished electrode surface. The gaseous products of the reaction were monitored by gas chromatography and the liquid products were observed with ^1H NMR.

The products formed by the MOF when subjected to CO_2 reduction conditions were 88.5 % H_2, 0.79 % CO, and minute quantities of formic acid. The heavy formation of H_2 indicates that the speed of the HER on the electrocatalytic surface was far faster than the higher order carbon products, making the catalyst largely ineffective at CO_2 reduction. While these results are far from ideal, the other MOF systems that were synthesized could likewise be tested to determine their efficacy, particularly the other copper-based systems which feature various other counterions, perhaps fundamentally changing the reactivity of the MOF catalytic centres.

4.5 Conclusion and Future Work

Compound **19** has interested us in its potential to be used in MOF-based applications due to its many chelation sites. We have been able to show that there is indeed some MOF formation using copper sulfate and other metal compounds, but we have been unable to fully characterize the material due to its insoluble nature. The $CuSO_4$-based MOF was promising as an electrocatalyst due to its inclusion of copper centres, however the results show that the hydrogen evolution reaction was significantly faster than any other reduction pathways, making it ineffective for our intended use. There are several options moving forward for this group of MOFs. Firstly, the other MOFs can be tested using similar methods to determine if they possess any interesting reduction products, especially the other copper containing MOFs. Secondly, the medium that the reduction tests were conducted in can be modified, the pH can be altered, or the buffer can be changed as well in order to determine if that will give rise to any difference in observed product formation. Thirdly, the synthesis can be tuned by the incorporation of larger metal clusters instead of the single atom inorganic precursors used, this can drastically affect the resulting structure and may create a more porous structure, potentially altering the rates of product formation. Finally, the MOFs can instead be tested for their use as gas storage media instead of as electrocatalysts, as their porous nature may be useful for such applications.

Conclusion

We have been able to develop several interesting research projects based on the shape complementary nature of carbon nanomaterials and iptycenes. Shape complementarity enables many interesting applications that cannot be accessed through simple π-π interactions with flat aromatic molecules and π-convex carbon nanomaterials. We have demonstrated the utility of this through the work reported in this dissertation, and much work still remains on further improving these methods.

Through the interaction of SWNTs and iptycenes we have been able to develop the Alignment Relay Technique, enabling the simultaneous sorting and alignment of SWNTs when deposited onto a functionalized surface. The alignment is quite impressive when combined with the diameter and length sorting capabilities of the method. We have further been able to prove that by simple alterations in the ART parameters, the sorting and alignment of the resulting deposited nanotubes can be altered. By changing the 5CB liquid crystal to the more ordered 8CB, we have shown a threefold increase in density coupled with a decrease in the average length of the deposited nanotubes, all while retaining the diameter sorting. Further experiments have demonstrated the ability for the iptycene nanotweezers to impact the diameter sorting of the deposited nanotubes, while maintaining the alignment and length sorting. These results indicate that, upon further optimization, the ART will be able to selectively deposit nanotubes of a desired type based on the careful choice of the deposition parameters. Future work involves testing the trenched surface's ability to align the liquid crystals and aid in the alignment of the nanotubes. The design of new iptycenes which include electron withdrawing/donating groups and various heteroatoms could aid in the alignment and selectivity of the

methodology, perhaps allowing for the sorting of nanotubes by electronic type as well. New anchoring groups may be installed in order to functionalized new surfaces of interest, specifically allowing for the functionalization of hafnium oxide, as well as increasing the rate of the functionalization. Other post-deposition techniques may be employed, as has been seen in the success of post-deposition sonication of the nanotubes. The deposition of the nanotubes may also be optimized, testing various concentrations of nanotubes, as well as testing new methods like drop casting, in order to decrease the time required for the ART. Finally, other liquid crystal alignment methods can also be tested to not only determine their efficacy at improving the alignment of the nanotubes, but also to potentially improve the scalability of the ART. The Alignment Relay Technique has proven to be an interesting new methodology for depositing nanotubes, with a high future potential for application.

The use of π-convex-π-concave interactions has further been proven through the implementation of iptycene-functionalized silica gel for the separation of fullerenes. Our method shows unprecedented separation using simple flash chromatographic techniques, which is in direct contrast with the current state of the art which relies on HPLC for small scale purification. We have demonstrated that using our iptycene-functionalized silica gel it is possible to purify the same amount of material, but with a method that is used in synthetic laboratories around the world. Despite the high efficacy of this method, there remains the problem of silica gel degradation. Future work should focus first on implementing a more robust silica gel functionalization, ideally through the use of chlorosilane anchoring groups. After this, the effectiveness of the methodology can be further tested on higher fullerenes and endohedral fullerenes as well, as their

separation, even with current HPLC methodology, remains challenging. To further improve separation, while decreasing retention times, heteroatoms such as halogens, nitrogen, and sulfur can be added to the iptycene to improve their binding affinity to the fullerenes. Finally, binding affinity studies should be conducted to quantify the binding. This new methodology not only exemplifies how powerful shape complementarity can be, but also enables the simple separation of fullerenes.

Our newly synthesized pyridazinophthalazine molecule has shown potential for use in MOF formation. Currently, we have been able to show that the ligand system may be forming MOFs with several metals, and have even been able to demonstrate that the copper-MOF can be used effectively in hydrogen evolution, indicating its conductive, electrocatalytic nature. However, due to the poor conversion of CO_2 to other useful carbon analogues, further optimization is required. Future work should focus on testing the electrocatalytic potential of the other MOFs that were synthesized to determine if they have any useful application in CO_2 electrocatalytic reduction. Furthermore, as the structure of the MOF has been determined to be microporous, it should be tested as a gas storage medium. Finally, other synthetic techniques should be tested, including metal clusters and potential incorporation of co-ligands. While current studies have failed to yield desired results, they have shown that the pyridazinophthalazine system has the potential to be used as a catalyst for MOF formation, and perhaps may also be useful in the creation of organometallic homogeneous catalysts.

As synthetic chemists, our ability to create new iptycene molecules has allowed us to create elegant solutions to difficult problems in other scientific fields and it is our ability to create new materials that has allowed for continued development of these techniques.

In my work I have produced a new method for the simultaneous sorting and alignment of carbon nanotubes, have iterated upon this method, have incorporated iptycenes into biosensors, have created a method for purifying fullerenes using flash chromatography, and have created a new ligand for MOF formation. Due to the Schipper group's background in synthetic organic chemistry, the future of these research projects is very promising, as they each have the potential for significant improvements, and even offer branching off points for new projects. Thank you for taking the time to read this summation of my thesis work.

Supporting Information

Table of Contents

1. General Experimental Considerations

1.1 Solvents and Reagents

Unless otherwise stated, all reactions were run open to air and without drying or preparing the solvents in any other way. All solvents used in synthesis were HPLC grade, and solvents used for column chromatography were reagent grade. All starting materials and other chemicals/substrates were purchased from Sigma-Aldrich except for: bis(diethoxyphosphoryl)acetylene (purchased from STREM Chemicals Inc.), IsoNanotubes-S 90% purity (NanoIntegris Inc.), rubbed polyimide coated glass substrates (Instec Inc.), SiliaSphere® 20 µm silica gel (SiliCycle Inc.), SiliaFlash® P60 40 – 63 µm silica gel (SiliCycle Inc.), pentacene was synthesized in our lab, and trans-1,4-dichloro-2-butene was synthesized in our lab. All chemicals were used without further purification unless stated.

1.2 Equipment

^{1}H NMR measurements were taken with a Brüker AVANCE 300 (300 MHz) δ or Brüker AC300 (300 MHz) δ NMR spectrometers, with chloroform as the internal standard. ^{13}C NMR measurements were taken with Brüker AVANCE300 (75.5 MHz) δ or Brüker AVANCE500 (125.8 MHz) δ NMR spectrometers, with deuterated chloroform as the internal standard. ^{31}P NMR measurements were taken with a Brüker AC300 (121.4 MHz) δ NMR spectrometers, with phosphonic acid in water as the external reference. ^{29}Si SSNMR measurements were taken with a Brüker AVANCE500 (99.3 MHz) δ NMR spectrometer, with magic angle spinning and using tetramethylsilane as the internal standard. The following abbreviations are used for NMR peak multiplicities: s, singlet; d, doublet; t, triplet; dd, doublet of doublets; m, multiplet; br, broad. Chemical shifts are reported in parts per million (ppm) relative to chloroform (δ 7.26) for ^{1}H NMR, chloroform

(δ 77.0) for ^{13}C NMR, phosphoric acid in water (δ 0.00) for ^{31}P NMR, and tetramethyl silane (δ 0.00) for ^{29}Si NMR.

High resolution mass spectrometry (HRMS) was conducted via electrospray ionization (ESI) measured on a Thermo Scientific Q Exactive™ Plus Hybrid Quadrupole-Orbitrap™ at the University of Waterloo Mass Spectrometry Facility.

Ultraviolet-visible absorption spectra were measured with a Perkin Elmer Lambda 35 UV/Vis spectrophotometer in solution phase with chloroform as the solvent and were corrected for background signal with a solvent filled cuvette.

Atomic force microscopy measurements were taken using a Veeco Dimension 3100 in tapping mode at WATLab.

X-ray photoelectron spectroscopy experiments were performed on a VGS ESCALab 250 Imaging ESCA at WATLab.

Secondary-ion mass spectrometry experiments were performed on an IONTOF SIMS-5 at WATLab.

Scanning electron microscopy was performed on a FEI Quanta Feg 250 ESEM with EDX at WATLab.

Transmission electron microscopy was performed on a JEOL 1200EX TEMSCAN with X-ray microanalysis system on both copper and nickel grids. The experiments were performed at the Canadian Centre for Electron Microscopy at McMaster University.

Atomic layer deposition of hafnium oxide films was done on an Oxford PlasmaLab 100 FlexAL ALD system at the Quantum NanoFab.

Physical vapour deposition of silicon oxide was performed on a Intlvac Nanochrome II instrument at the Quantum NanoFab.

Electron beam lithography was performed on a JEOL JBX-6300FS Electron Beam Lithography System with a 100 kV accelerating voltage at the Quantum NanoFab.

Plasma etch of silicon and hafnium oxides was done with an Oxford Instruments ICP380 system, using CF_4, at the Quantum NanoFab.

Spin coating of e-beam resist was done on a Brewer Science CEE 200X spinner on a 1300X vacuum hotplate at the Quantum NanoFab.

All silicon wafers were diced into 10 mm x 10 mm squares using the DISCO DAD3240 dicing saw with a sapphire edged blade at the Quantum NanoFab.

Flash chromatography was performed on a CombiFlash® Rf+ and CombiFlash® Rf systems with in-line UV-Vis spectrometer and, in some cases, with an in-line atomic-pressure chemical ionization mass spectrometer.

PMIRRAS, Contact Angle, Raman

2. Synthesis

2.1 Synthesis of tetraethyl (9,10-dihydro-9,10-ethenoanthracene-11,12-diyl)bis(phosphonate) (1)

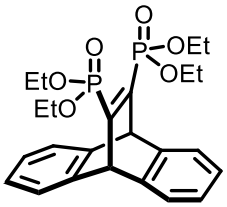

To a 25 mL thick-walled, glass pressure tube was added anthracene (0.897 g, 5.03 mmol), bis(diethoxyphosphoryl)acetylene (0.500 g, 1.68 mmol), and 20 mL of dry toluene.

A magnetic stir bar was added to the mixture and the glass tube was sealed with a Teflon™ screw cap that had the treads wrapped in Teflon™ tape. The resulting mixture was heated with stirring at 160 °C in a sand bath for five days. The solution was allowed to cool, was then filtered and the filtrate was concentrated by rotary evaporator. The resulting residue was purified by flash chromatography on silica gel using ethyl acetate as the mobile phase to give yellow oil **1** in 50 % yield. R_f = 0.15 (ethyl acetate). ^{1}H NMR in $CDCl_3$ (δ 7.26 ppm) at room temperature: 7.36 ppm (m, 4H), 7.00 ppm (m, 4H), 5.79 ppm (t, 2H, J = 6.4 Hz coupling to ^{31}P), 4.01 ppm (m, 8H), 1.24 ppm (t, 12H, J = 7.4 Hz). ^{31}P NMR in $CDCl_3$ at room temperature with phosphoric acid in water as the external reference (δ 0.00 ppm): 14.34 ppm. Spectral data matched literature values reported by Acheson.[391]

2.2 Synthesis of tetraethyl (5,7,9,14,16,18-hexahydro-5,18:9,14-bis([1,2]benzeno)-7,16-ethenoheptacene-25,26-diyl)bis(phosphonate) (2)

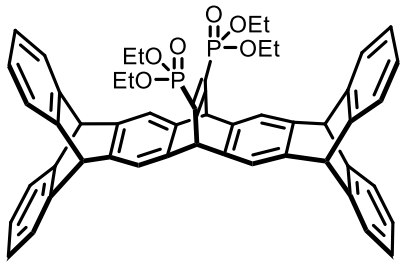

Bis(diethoxylphosphoryl)acetylene (0.317 g, 1.06), **6** (0.563 g, 1.06 mmol), and 10 mL of toluene were added to a 25 mL microwave tube equipped with a magnetic stir bar. The microwave tube was capped, and the solution was heated with stirring at 200 °C in a sand bath for five days. The resulting solution was purified by flash chromatography on silica gel using ethyl acetate as the eluent system to give the product as a white solid in a 30

% yield. R_f = 0.1 (ethyl acetate). m/z (calc.) = 829.28479, m/z (found) = 829.28363. ^{1}H NMR in $CDCl_3$ (δ 7.26 ppm) at room temperature: 7.30 ppm (m, 8H) 7.21 ppm (m, 4H), 6.95 ppm (m, 4H), 6.83 ppm (m, 4H), 5.57 ppm (t, 2H, J = 6.9 Hz coupling to ^{31}P), 5.24 ppm (s, 4H), 3.94 ppm (br. m, 8H), 1.13 ppm (t, J = 12H, 7.4 Hz). ^{13}C NMR in $CDCl_3$ (δ 77.0 ppm) at room temperature: 154.3 – 151.7 ppm (dd, J = 9.7 Hz, 192.6 Hz), 145.5 ppm, 145.3 ppm, 142.9 ppm, 141.1 ppm, 125.1 ppm, 123.6 ppm, 123.5 ppm, 119.7 ppm, 62.6 ppm (t, J = 3.3 Hz), 55.4 ppm (t, J = 11.9 Hz), 54.0 ppm, 16.2 ppm (t, J = 3.3 Hz). ^{31}P NMR in $CDCl_3$ at room temperature relative to phosphoric acid in water (δ 0.00): 15.13 ppm.

2.3 Synthesis of 11,12-bis(chloromethyl)-9,10-dihydro-9,10-ethanoanthracene (3)

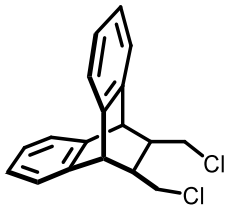

To a 25 mL thick-walled, glass pressure tube was added anthracene (4 g, 22.44 mmol), trans-1,4-dichlorobut-2-ene (12.5 mL, 118.3 mmol), and a magnetic stir bar. The tube was then sealed with a Teflon™ screw cap with Teflon™ tape around the threads, and the mixture was heated with stirring at 200 °C for two days in a sand bath. The black mixture was allowed to cool and was then filtered to remove any unreacted anthracene. The filtrate was purified by vacuum distillation at 110 °C to collect trans-1,4-dichlorobut-2-ene distillate as a clear liquid. The remaining brown solid was purified by flash chromatography on silica gel using 10% ethyl acetate in hexanes as the mobile phase to

give the product as a white solid in a 91% yield. ^{1}H NMR in $CDCl_3$ (δ 7.26 ppm) at room temperature: 7.34 ppm (m, 4H), 7.18 ppm (m, 4H), 4.46 ppm (s, 2H), 3.32 ppm (dd, 2H, J = 5.3 Hz, 10.6 Hz), 2.99 ppm (dd, 2H, J = 9.5 Hz, 11.1 Hz), 1.77 ppm (m, 2H). Spectral data matched literature values reported by Hart.[285]

2.4 Synthesis of 11,12-dimethylene-9,10-dihydro-9,10-ethanoanthracene (4)

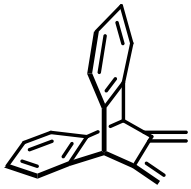

To a 100 mL round bottom flask was added **3** (2.423 g, 7.99 mmol), potassium tert-butoxide (2.693 g, 24 mmol), 8 mL of tetrahydrofuran, 32 mL of dimethyl sulfoxide and a magnetic stir bar. The mixture was stirred at room temperature for 18 h and changed colour to dark green nearly instantly. The solution was poured into 200 mL of ice-water and turned yellow. The water was extracted with ether and the resulting organic phase was washed with brine, dried over sodium sulphate, and concentrated on a rotary evaporator. The solid was recrystallized from hexanes to give the product as a white solid in 98 % yield. ^{1}H NMR in $CDCl_3$ (δ 7.26 ppm) at room temperature: 7.32 ppm (m, 4H), 7.11 ppm (m, 4H), 5.29 ppm (s, 2H), 5.13 ppm (s, 2H), 4.87 ppm (s, 2H). Spectral data matched literature values reported by Hart.[285]

2.5 Synthesis of 5,6,8,9,14,15,17,18-octahydro-5,18:9,14-bis([1,2]benzeno)heptacene (5)

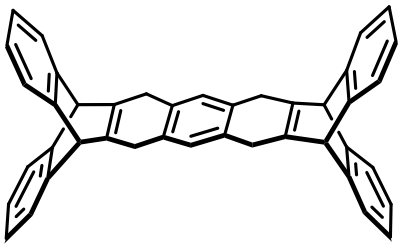

A flame dried 250 mL round bottom flask was kept under and argon atmosphere and charged with a magnetic stir bar, **4** (1.841 g, 7.99 mmol) and 1,2,4,5-tetrabromobenzene (1.511 g, 3.83 mmol), 100 mL of dry toluene. To the stirring, room temperature solution was added n-butyl lithium (2.5 M in hexanes, 4.22 mL) dropwise over one hour. The reaction mixture was stirred at room temperature for 18 h and was then quenched with slow addition of isopropyl alcohol. The mixture was then poured onto water and left to sit for 30 minutes as a white precipitate formed. The solid was collected by filtration and recrystallized from 1,2-dichloroethane to give the desired product as a white solid in 79% yield. ^{1}H NMR in $CDCl_3$ (δ 7.26 ppm) at room temperature: 7.29 ppm (m, 8H), 6.95 ppm (m, 8H), 6.80 ppm (s, 2H), 4.85 ppm (s, 4H), 3.56 ppm (s, 8H). Spectral data matched literature values reported by Hart.[285]

2.6 Synthesis of 5,9,14,18-tetrahydro-5,18:9,14-bis([1,2]benzeno)heptacene (6)

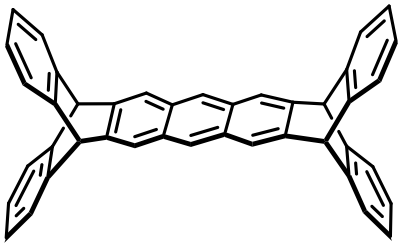

5 (0.150 g, 0.28 mmol), 10% palladium on carbon (0.017 g), and 15 mL of xylenes were added to a 50 mL flask equipped with a magnetic stir bar. The solution was heated under a reflux condenser with stirring at 160 °C for two days. The resulting mixture was filtered while hot and the black precipitate was washed with dichloromethane. The yellow filtrate was concentrated under reduced pressure to give a yellow-white solid. The solid was purified by flash chromatography on silica gel using 10% dichloromethane in hexanes as the eluent system to give the product as a white solid in a 55% yield. Rf = 0.2 (1:4 DCM:Hexanes). ^{1}H NMR in $CDCl_3$ (δ 7.26 ppm) at room temperature: 8.07 ppm (s, 2H), 7.81 ppm (s, 4H), 7.42 ppm (m, 8H), 7.03 ppm (m, 8H), 5.50 ppm (s, 4H). Spectral data matched literature values reported by Hart.[285]

2.7 Synthesis of N^1,N^4-dihydroxybut-2-ynediamide (7)

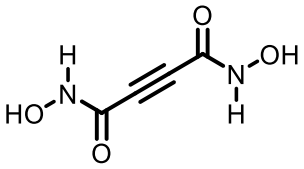

Separate solutions of hydroxylamine hydrochloride (2.000 g, 31.01 mmol) in 25 mL of methanol and potassium hydroxide (3.230 g, 57.57 mmol) in 25 mL of methanol were prepared, and both were cooled in an ice bath. The potassium hydroxide solution was added to the hydroxylamine hydrochloride solution with stirring, and the resulting solution was allowed to stand for five minutes in an ice bath, precipitating potassium chloride. The precipitate was removed by filtration and the filtrate was very slowly added to dimethyl acetylenedicarboxylate (0.88 mL, 7.18 mmol) in a 50 mL round bottom flask equipped with a magnetic stir bar, at room temperature. Additional potassium hydroxide was added to the solution until the pH ~10 as measured by universal pH indicator strips. The solution

was stirred at room temperature for 18 h. Initially the solution turned dark red, but over the course of the reaction it turned orange and a precipitate formed. The mixture was concentrated on a rotary evaporator, and the residue was then dissolved in H_2O and acidified with 2M HCl to give a light orange solution. The product was extracted with ethyl acetate (3 x 50 mL), dried over magnesium sulfate, and concentrated on a rotary evaporator. However, ^{1}H NMR analysis indicated that the product peaks associated with the hydroxamic acid were not present.

2.8 Synthesis of dimethyl 9,10-dihydro-9,10-ethenoanthracene-11,12-dicarboxylate (8)

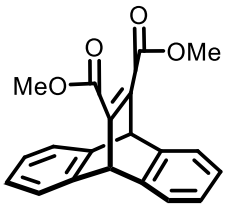

Anthracene (0.250 g, 1.40 mmol) and dimethyl acetylenedicarboxylate (0.216 mL, 1.76 mmol) were placed in a 2 mL microwave tube which was purged with N_2, and heated with magnetic stirring at 180 °C for one hour. The anthracene fully dissolved upon reaching temperature, and the colour of the solution changed from light yellow to dark orange/brown. The solution was cooled to 100 °C and poured into methanol, and the precipitate was recrystallized in methanol to give the product in a 76 % yield. ^{1}H NMR in $CDCl_3$ (δ 7.26 ppm) at room temperature: 7.37 ppm (dd, 4H, J = 3.2 Hz, 5.3 Hz), 7.01 ppm (dd, 4H, J = 3.2 Hz, 5.3 Hz), 5.47 ppm (s, 2H), 3.79 ppm (s, 6H). Spectral data matched literature values reported by Wheeler et al.[392]

2.9 Synthesis of N^{11},N^{12}-dihydroxy-9,10-dihydro-9,10-ethenoanthracene-11,12-dicarboxamide (9)

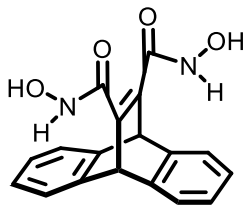

Hydroxylamine hydrochloride (0.503 g, 7.24 mmol) was added to a solution of **8** (1.000 g, 3.12 mmol) in 25 mL of dichloroethane in a 50 mL round bottom flask at room temperature. The mixture was cooled to 10 °C, stirred with a magnetic stir bar, and triethyl amine (0.734 g, 7.24 mmol) was added. The reaction mixture was refluxed for one hour and then cooled to 0 °C. Trifluoroacetic acid (1.780 g, 15.61 mmol) was added and the mixture was stirred at 0 °C for 30 minutes. The resulting precipitate was collected by filtration, washed with dichloroethane and dried open to air.

2.10 Synthesis of dimethyl 5,7,9,14,16,18-hexahydro-5,18:9,14-bis([1,2]benzeno)-7,16-ethenoheptacene-25,26-dicarboxylate (10)

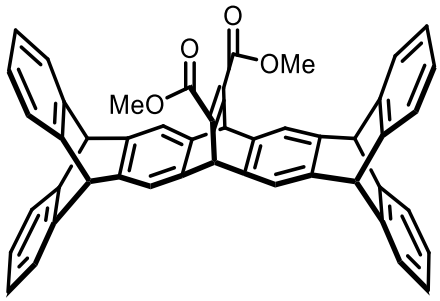

Dimethyl acetylenedicarboxylate (2.0 mL, 16.27 mmol), **6** (0.585 g, 1.10 mmol), a magnetic stir bar, and 2 mL of toluene were added to a 25 mL microwave tube. The vial was capped and heated at 180 °C with stirring for three days. Reaction progress can be monitored by ^{1}H NMR by comparing bridgehead carbon peaks: product at 5.25 ppm, **6** at

5.51 ppm, and if **6** is not properly purified a peak at 5.45 ppm will appear and belongs to **5**. The resulting mixture was concentrated on a rotary evaporator and recrystallized from acetone to remove some of the excess starting material and the precipitate was then purified by flash chromatography on silica gel using a gradient of 20 % - 50 % ethyl acetate in hexanes as the mobile phase. The product was further purified by recrystallization form methanol to give the product as a white solid. m/z (calc.) = 673.23734, m/z (found) = 673.23699. ^{1}H NMR in acetone-d_6 (δ 2.05 ppm) at room temperature: 7.25 ppm (s, 4H), 7.22 ppm (dd, 4H, J = 3.2 Hz, 4.8 Hz), 7.13 ppm (dd, 4H, J = 3.2 Hz, 4.8 Hz), 6.86 ppm (dd, 4H, J = 3.7 Hz, 5.3 Hz), 6.75 ppm (dd, 4H, J = 3.2 Hz, 5.3 Hz), 5.17 (s, 6H), 3.59 (s, 6H). ^{13}C NMR in acetone-d6 (δ 29.92 ppm) at room temperature: 166.5 ppm, 148.4 ppm, 146.8 ppm, 146.6 ppm, 144.0 ppm, 142.6 ppm, 125.8 ppm, 124.4 ppm, 120.5 ppm, 54.4 ppm, 52.9 ppm, 52.4 ppm.

2.11 Synthesis of N^{25},N^{26}-dihydroxy-5,7,9,14,16,18-hexahydro-5,18:9,14-bis([1,2]benzeno)-7,16-ethenoheptacene-25,26-dicarboxamide (11)

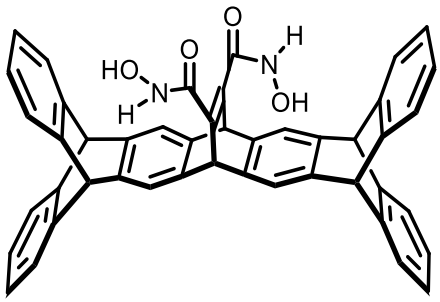

A solution of hydroxylamine hydrochloride (0.021 g, 0.30 mmol) and triethyl amine (0.030 g, 0.30 mmol) in 1.2 mL of methanol was stirred for 30 minutes at room temperature in a 5 mL microwave tube. **10** (0.050 g, 0.07 mmol) was then added and the mixture was refluxed for eight hours, after which a white precipitate formed and was collected. The

precipitate was washed with excess methanol and allowed to dry in air. Attempts were made to get the precipitate into deuterated solvents but no signal was ever seen in the NMR spectra.

2.12 Synthesis of 15,16-bis(chloromethyl)-6,13-dihydro-6,13-ethanopentacene (12)

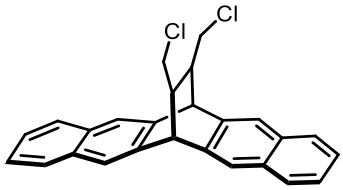

Freshly prepared pentacene (2.00 g, 7.19 mmol), freshly prepared trans-1,4-dichloro-2-butene (22 mL, 198.90 mmol), and a magnetic stir bar were added to a 48 mL thick-walled, glass pressure tube. The mixture was sonicated for one minute and the tube was purged with argon gas before being capped with a Teflon™ screw cap with Teflon™ tape around the threads. The tube was placed in a sand bath where it was heated with stirring at 180 °C for 36 hours. The resulting brown mixture was distilled under vacuum at 60 °C to remove the trans-1,4-dichloro-2-butene as a colourless liquid and the remaining brown, viscous mass was purified via flash chromatography on silica gel with a gradient of 0 % - 5 % ethyl acetate in hexanes as the mobile phase. R_f = 0.45 in 10 % ethyl acetate in hexanes. m/z (calc.) = 403.10148, m/z (found) = 403.10139. ^{1}H NMR in $CDCl_3$ (δ 7.26 ppm) at room temperature: 7.81 ppm (m, 8H), 7.44 ppm (m, 4H), 4.81 ppm (s, 2H), 3.55 ppm (dd, 2H, J = 4.4 Hz, 10.5 Hz), 3.00 ppm (t, 2H, J = 10.5 Hz), 2.66 ppm (m, 2H). ^{13}C NMR in $CDCl_3$ (δ 77.0 ppm) at room temperature: 140.1 ppm, 137.1 ppm, 132.6 ppm,

132.5 ppm, 127.6 ppm, 125.8 ppm, 125.7 ppm, 124.2 ppm, 122.2 ppm, 46.4 ppm, 44.2 ppm, 44.1 ppm.

2.13 Synthesis of 15,16-dimethylene-6,13-dihydro-6,13-ethanopentacene (13)

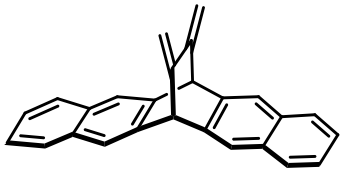

To a 25 mL microwave vial was added **12** (1.00 g, 2.48 mmol), potassium *t*-butoxide (1.530 g, 13.64 mmol), 4 mL of tetrahydrofuran, 16 mL of dimethylformamide, and a magnetic stir bar. The mixture was stirred at room temperature for three hours and the resulting brown solution was poured into ice water. A saturated aqueous solution of ammonium chloride was added to the ice water until pH 7 was achieved. The aqueous suspension was extracted with ethyl acetate (4 x 50 mL), the organic extractions were combined and washed with deionized water (2 x 50 mL) and brine (2 x 50 mL). The organic layer was dried over magnesium sulfate and concentrated on rotary evaporator to give the product in 99 % yield. m/z (calc.) = 331.14813, m/z (found) = 331.14795. ^{1}H NMR in $CDCl_3$ (δ 7.26 ppm) at room temperature: 7.78 ppm (s, 4H), 7.76 ppm (dd, 4H, J = 3.4 Hz, 6.4 Hz), 7.38 ppm (dd, 4H, J = 3.4 Hz, 6.1 Hz), 5.37 ppm (s, 2H), 5.24 ppm (s, 2H), 5.12 ppm (s, 2H). ^{13}C NMR in $CDCl_3$ (δ 77.0 ppm) at room temperature: 143.9 ppm, 139.3 ppm, 132.6 ppm, 127.6 ppm, 125.6 ppm, 121.6 ppm, 106.0 ppm, 55.0 ppm.

2.14 Synthesis of 6,7,9,10,17,18,20,21-octahydro-6,21:10,17-bis([2,3]naphthaleno)nonacene (14)

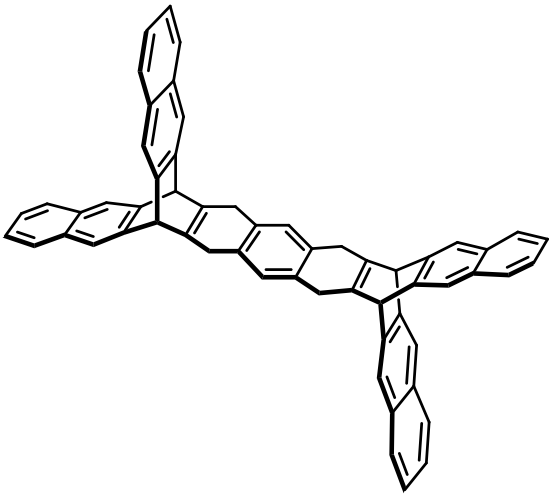

To a flame dried, argon purged 100 mL round bottom flask was added **13** (1.00 g, 3.03 mmol), 1,2,4,5-tetrabromobenzene (0.596 g, 1.51 mmol), 35 mL of dry toluene, and a magnetic stir bar. To this stirring mixture was added 3 mL of 1.3 M *n*-butyl lithium in hexanes dropwise, over the course of an hour. The resulting mixture was quenched with 5 mL of isopropanol, poured into ice water and extracted with ethyl acetate (2 x 50 mL). The combined organic layers were washed with brine (2 x 50 mL), dried over magnesium sulfate, and concentrated on a rotary evaporator. The resulting oil was purified by flash chromatography on silica gel using a gradient of 0 % - 10 % ethyl acetate in hexanes to give the product in 23 % yield. Due to the difficulty in purification, the product was used for the subsequent reaction despite poor purity. R_f = 0.62 (20% ethyl acetate in hexanes). ^{1}H NMR in $CDCl_3$ (δ 7.26 ppm) at room temperature: 7.75 ppm (s, 10H), 7.75 ppm (dd, 8H, J = 3.4 Hz, 6.4 Hz), 7.41 ppm (dd, 8H, J = 3.2 Hz, 6.1 Hz), 5.03 ppm, (s, 4H), 3.50 ppm (s, 8H).

2.15 Synthesis of 6,10,17,21-tetrahydro-6,21:10,17-bis([2,3]naphthaleno)nonacene (15)

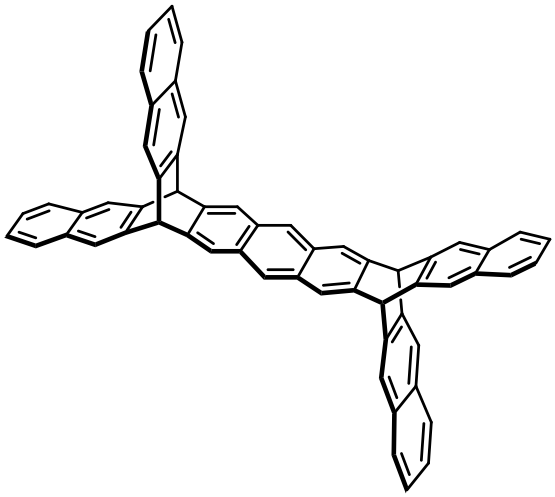

A 20 mL microwave vial was charged with **14** (0.100 g, 0.14 mmol), 2,3-dichloro-5,6-dicyano-1,4-benzoquinone (0.065 g, 0.29 mmol), 5 mL of xylenes, and a magnetic stir bar. The vial was heated with stirring at 50 °C for two hours, then the reaction mixture was concentrated on rotary evaporator and purified by flash chromatography on silica gel with a gradient of 0 % - 10 % ethyl acetate in hexanes as the mobile phase. The product was obtained in a 66 % yield. R_f = 0.51 (20 % ethyl acetate in hexanes). ^{1}H NMR in $CDCl_3$ (δ 7.26 ppm) at room temperature: 7.93 ppm (s, 4H), 7.89 ppm (s, 8H), 7.76 ppm (dd, 8H, J = 3.4 Hz, 6.1 Hz), 7.63 ppm (s, 4H), 7.41 ppm (dd, 8H, J = 3.2 Hz, 6.1 Hz), 5.73 ppm (s, 4H). ^{13}C NMR in $CDCl_3$ (δ 77.0 ppm) at room temperature: 142.5 ppm, 140.3 ppm, 132.1 ppm, 131.7 ppm, 127.5 ppm, 125.9 ppm, 122.2 ppm, 121.5 ppm, 120.9 ppm, 53.1 ppm.

2.16 Synthesis of tetraethyl (6,8,10,17,19,21-hexahydro-6,21:10,17-bis([2,3]naphthaleno)-8,19-ethenononacene-31,32-diyl)bis(phosphonate) (16)

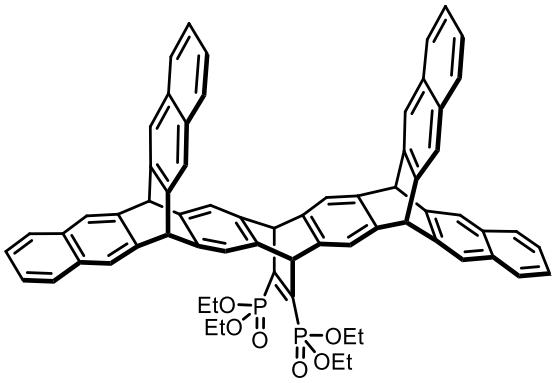

A 5 mL microwave vial was charged with **15** (0.05 g, 0.07 mmol), bis(diethoxylphosphoryl)acetylene (0.026 g, 0.09 mmol), 3 mL of toluene, and a magnetic stir bar. The microwave tube was capped and heated with stirring at 190 °C for three days. The resulting solution was concentrated on a rotary evaporator and purified by flash chromatography on silica gel using ethyl acetate as the mobile phase to give the product in a 30 % yield. ^{1}H NMR in $CDCl_3$ (δ 7.26 ppm) at room temperature: 7.91 ppm (s, 4H), 7.88 ppm (s, 8H), 7.76 ppm (dd, 8H, J = 3.2 Hz, 6.1 Hz), 7.61 ppm (s, 4H), 7.40 ppm (dd, 8H, J = 3.4 Hz, 6.4 Hz), 5.72 ppm (s, 4H), 4.15 ppm (q, 8H, J = 7.3 Hz), 1.27 ppm (t, 12H, J = 7.1 Hz). ^{13}C NMR in $CDCl_3$ (δ 77.0 ppm) at room temperature: 140.4 ppm, 132.1 ppm, 131.8 ppm, 131.7 ppm, 127.5 ppm, 125.9 ppm, 122.3 ppm, 121.6 ppm, 120.9 ppm, 64.1 ppm (t, J = 3.0 Hz), 53.2 ppm, 29.7 ppm, 16.1 ppm (t, J = 3.2 Hz). ^{31}P NMR in $CDCl_3$ at room temperature relative to phosphoric acid in water (δ 0.00): -9.38 ppm.

2.17 Synthesis of tetraethyl (6,13-dihydro-6,13-ethenopentacene-15,16-diyl)bis(phosphonate) (17) and tetraethyl (5,14-dihydro-5,14-ethenopentacene-15,16-diyl)bis(phosphonate) (18)

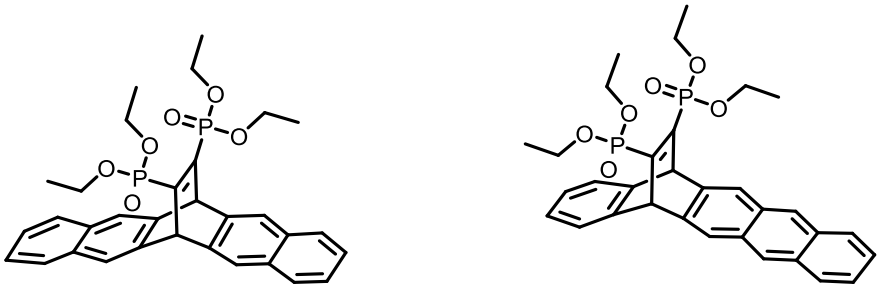

A 25 mL thick-walled, glass pressure tube was charged with pentacene (1.132 g, 4.07 mmol), bis(diethoxylphosphoryl)acetylene (1.213 g, 4.07 mmol), 20 mL of toluene, and a magnetic stir bar. The glass tube was capped with a Teflon™ screw cap with Teflon™ tape wrapped around its threads, and was then heated with stirring in a sand bath to 180 °C for five days. The mixture was cooled and filtered, and the filtrate was collected, concentrated on a rotary evaporator, and purified by flash chromatography on silica gel with ethyl acetate as the mobile phase to give an oily, yellow, inseparable mixture of isomers (**17** and **18** in a 5.5:1 ratio respectively) in an overall 64% yield. R_f = 0.15 (ethyl acetate). Spectral data for isomer **17**: ^{1}H NMR in $CDCl_3$ (δ 7.26 ppm) at room temperature: 7.83 ppm (s, 4H), 7.74 ppm (m, 4H), 7.42 ppm (m, 4H), 6.00 ppm (t, 2H, J = 6.6 Hz), 4.04 ppm (br m, 8H), 1.25 ppm (t, 12H, J = 7.1 Hz). ^{13}C NMR in $CDCl_3$ (δ 77.0 ppm) at room temperature: 151.5 ppm (dd, 8.6 Hz, J = 189.7 Hz), 139.2 ppm, 131.9 ppm, 127.6 ppm, 126.0 ppm, 122.3 ppm, 62.6 ppm (t, J = 2.9 Hz), 54.3 ppm (t, J = 11.5 Hz), 16.2 ppm (t, J = 2.9 Hz). ^{31}P NMR in $CDCl_3$ at room temperature relative to phosphoric acid in water (δ 0.00): 14.34 ppm. m/z (calc.) = 829.28424, m/z (found) = 829.28363. Spectral data for isomer **18**: ^{1}H NMR in $CDCl_3$ (δ 7.26 ppm) at room temperature: 8.28 ppm (s, 2H), 7.94 ppm (m, 2H), 7.90 ppm (s, 2H), 7.42 ppm (m, 4H)*, 7.10 ppm (m, 2H), 5.90 ppm (t, 2H, J

= 6.9 Hz), 4.03 (br m, 8H)*, 1.25 (t, 12H)*. ^{13}C NMR in $CDCl_3$ (δ 77.0 ppm) at room temperature: 151.5 ppm (dd, 8.6 Hz, J = 189.7 Hz)*, 142.2 ppm, 138.6 ppm, 131.9 ppm*, 130.2 ppm, 128.0 ppm, 125.9 ppm*, 125.2 ppm, 123.9 ppm, 121.8 ppm, 62.5 ppm (t, J = 2.9 Hz)*, 54.3 ppm (t, J = 11.5 Hz)*, 16.2 ppm (t, J = 2.9 Hz)*. ^{31}P NMR in $CDCl_3$ at room temperature relative to phosphoric acid in water (δ 0.00): 14.30 ppm*. Peaks labelled with an asterisk (*) are either partially or completely overlapped with those of **17**.

2.18 Synthesis of 1,4,6,9-tetra(pyridine-2-yl)pyridazino[4,5-*g*]phthalazine (19)

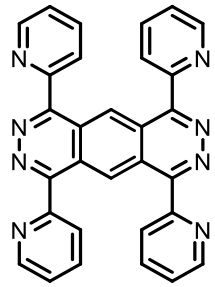

A 25 mL round bottom flask was charged with 3,6-di-2-pyridyl-1,2,4,5-tetrazine (1.00 g, 4.23 mmol), 1,4-cyclohexadiene (0.20 mL, 2.11 mmol), 15 mL of chloroform, and a magnetic stir bar. The solution was stirred at 70 °C for 18 h, and turned orange. The solution was cooled, concentrated on a rotary evaporator, and purified by flash chromatography on silica gel with 40 % ethyl acetate in hexanes as the mobile phase to give the product as orange, needle crystals in a 64 % yield. R_f = 0.5 (40% ethyl acetate in hexanes). ^{1}H NMR in $CDCl_3$ (δ 7.26 ppm) at room temperature: 8.56 ppm (m, 6H), 8.04 ppm (d, 4H, J = 8.0 Hz), 7.75 ppm (dd, 4H, J = 7.4 Hz), 7.34 ppm (dd, 4H, J = 4.8 Hz). ^{13}C NMR in $CDCl_3$ (δ 77.0 ppm) at room temperature: 148.3 ppm, 147.5 ppm, 146.6 ppm, 136.7 ppm, 124.8 ppm, 121.2 ppm.

2.19 Synthesis of Copper-1,4,6,9-tetra(pyridine-2-yl)pyridazino[4,5-*g*]phthalazine Metal Organic Framework

A 5 mL microwave tube was charged with **19** (0.025 g, 0.05 mmol), copper sulfate pentahydrate (0.051 g, 0.20 mmol), 2 mL of dimethylformamide, and a magnetic stir bar. The microwave tube was capped and heated with stirring at 120 °C for 18 h. The reaction mixture was cooled to room temperature, filtered, and the precipitate was washed with deionized water and acetone and then allowed to dry in the air.

2.20 Synthesis of cis-1,4-dichloro-2-butene

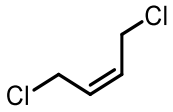

A 250 mL flame dried, round bottom flask was charged with cis-2-butene-1,4-diol (75 mL, 0.91 mol), pyridine (1.5 mL, 18.6 mmol), and a magnetic stir bar. The flask was equipped with a reflux condenser, heated with stirring to 60 °C, and thionyl chloride (93 mL, 3.1 mol) was added dropwise over the course of 40 minutes, turning the solution black. The solution was allowed to react for an additional 15 minutes. The flask was then equipped with a vacuum distillation apparatus and heated to 85 °C until a clear liquid began to collect, giving the product in 88 % yield. ^{1}H NMR in $CDCl_3$ (δ 7.26 ppm) at room temperature: 5.81 ppm (t, 2H, J = 6.4 Hz), 4.11 ppm (d, 4H, J = 6.4 Hz). Spectral data matched literature values.

3. Substrate Functionalization

3.1 Alignment Relay Technique with 4-cyano-4'-pentylbiphenyl and tetraethyl (5,7,9,14,16,18-hexahydro-5,18:9,14-bis([1,2]benzeno)-7,16-ethenoheptacene-25,26-diyl)bis(phosphonate) (2) on indium tin oxide

A 25 mm x 25 mm indium tin oxide coated glass slide was cleaned through sonication in isopropanol for 10 minutes and dried with a stream of nitrogen gas before being submerged in a piranha solution* (3:1 $H_2SO_{4(conc.)}$:$H_2O_{2(30\ \%)}$) heated at 100 °C for 30 minutes. The slide was removed from the piranha solution, rinsed with miliQ water, and dried under a stream of nitrogen gas. The slides were used immediately after being cleaned.

To a 20 mL glass scintillation vial was added **2** (2.5 mg, 0.003 mmol), 4-cyano-4'-pentylbiphenyl (50 mg, 0.20 mmol), and 10 mL of chloroform. The resulting solution was heated to 40 °C and evaporated under reduced pressure to give a solution of **2** in 5CB. A drop of the solution was pulled up into the tip of a glass Pasteur pipette and deposited onto the centre of a rubbed polyimide-coated glass slide. The cleaned ITO slide was then placed onto the rubbed polyimide slide and pressed down with tweezers, such that the drop on the surface spread out into a thin film, covering the entire surface of the slides. The pressed slides were left to react at room temperature for 24 h, after which the slides were separated and washed with chloroform. The washings were collected and reused in further functionalization reactions.

The resulting **2**-functionalized ITO surface was submerged in a 25 mL suspension of single-walled carbon nanotubes (surfactant-wrapped, 90% semiconducting, 0.01 mg/mL) for 48 h. The ITO slide was then removed from the suspension, washed with miliQ water,

and dried under a stream of nitrogen gas. This procedure gives a SWNT-deposited surface in which the SWNTs are aligned and sorted by length.

**Piranha solution is dangerous and requires proper training and safety precautions during use.*

3.2 Alignment Relay Technique with 4-cyano-4'-pentylbiphenyl and tetraethyl (5,7,9,14,16,18-hexahydro-5,18:9,14-bis([1,2]benzeno)-7,16-ethenoheptacene-25,26-diyl)bis(phosphonate) (2) on Silicon Dioxide

The same procedure used in 3.1 was performed on the native oxide layer of a 10 mm x 10 mm silicon slide. This procedure gives a SWNT-deposited surface in which the SWNTs are aligned and sorted by length and diameter.

3.3 Alignment Relay Technique with 4-cyano-4'-octylbiphenyl and tetraethyl (5,7,9,14,16,18-hexahydro-5,18:9,14-bis([1,2]benzeno)-7,16-ethenoheptacene-25,26-diyl)bis(phosphonate) (2) on Indium Tin Oxide

The same procedure used in 3.1 was performed, instead using 4-cyano-4'-octylbiphenyl as the liquid crystal. This procedure gives a SWNT-deposited surface in which the SWNTs are aligned and sorted by length.

3.4 Alignment Relay Technique with 4-cyano-4'-octylbiphenyl and tetraethyl (5,7,9,14,16,18-hexahydro-5,18:9,14-bis([1,2]benzeno)-7,16-ethenoheptacene-25,26-diyl)bis(phosphonate) (2) on Silicon Dioxide

The same procedure used in 3.1 was performed on the native oxide layer of a 10 mm x 10 mm silicon slide, using 4-cyano-4'-octylbiphenyl as the liquid crystal, and allowing the

functionalization to occur for two days. This procedure gives a SWNT-deposited surface in which the SWNTs are aligned and sorted by length and diameter.

3.5 Functionalization of Silica Gel with Phosphonates tetraethyl (6,13-dihydro-6,13-ethenopentacene-15,16-diyl)bis(phosphonate) (17) and tetraethyl (5,14-dihydro-5,14-ethenopentacene-15,16-diyl)bis(phosphonate) (18)

To a 250 mL round bottom flask was added SiliaSphere® 20 µm silica gel (12 g), a mixture of **17**/**18** (6.99 g, 12.13 mmol), a magnetic stir bar, and 75 mL of acetonitrile. The resulting slurry was heated at reflux with stirring for four hours, cooled, and concentrated on a rotary evaporator. The dried silica gel was transferred to a 150 mL beaker and placed in a vacuum oven at 140 °C for four hours. The resulting silica gel was orange in colour and was washed with dichloromethane to remove and unreacted **17**/**18**. The functionalization of the resulting silica gel was verified by ^{29}Si SSNMR, with TMS as the internal standard.

4. Cyclic Voltammetry and Differential Pulse Voltammetry

4.1 Cyclic Voltammetry and Differential Pulse Voltammetry Measurements of 1,4,6,9-tetra(pyridine-2-yl)pyridazino[4,5-*g*]phthalazine (19)

To a flame-dried 5 mL glass beaker was added 2 mL of dry acetonitrile, 5 mg of **19**, and tetrabutylammonium hexafluorophosphate (0.077 mg, 0.20 mmol). The beaker was fitted with a holed cap and a platinum reference electrode, counter electrode, working electrode were placed into the solution. A stream of nitrogen gas was bubbled through the solution through a syringe for 5 minutes before measurements were taken. The scans were conducted between +2 and -2 A at a scan rate of 100 mV/s.

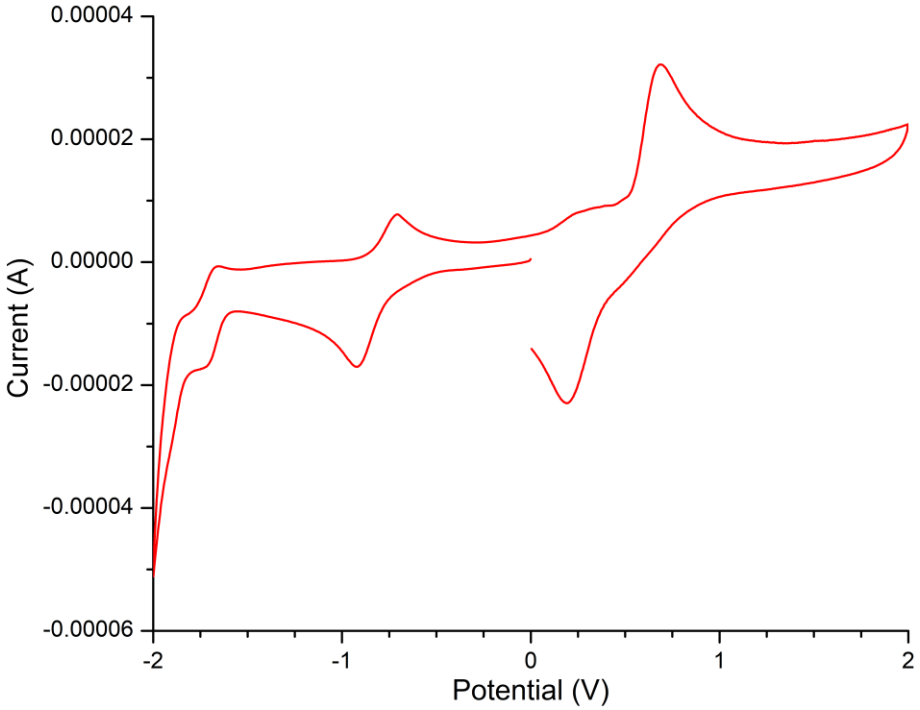

Figure S1: Cyclic voltammogram of 19.

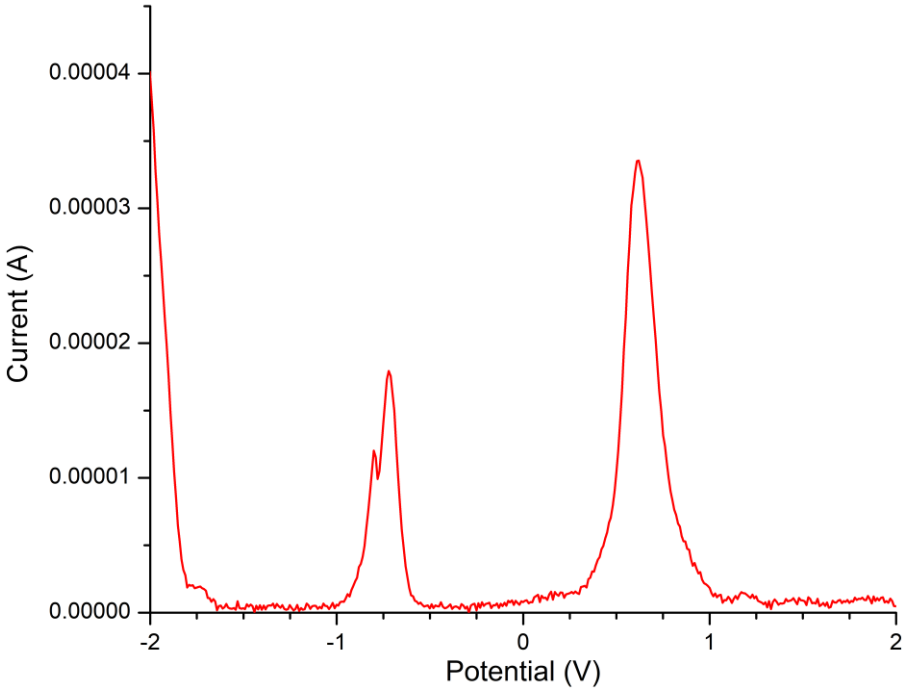

Figure S2: Differential pulse voltammogram of 19 in the positive direction.

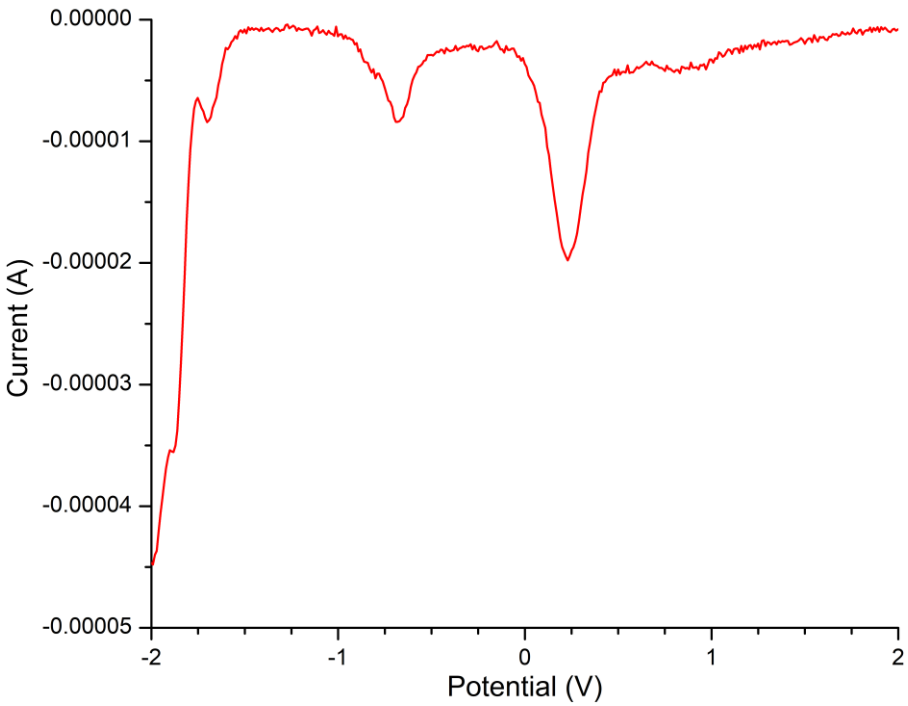

Figure S3: Differential pulse voltammogram of 19 in the negative direction.

4.2 Cyclic Voltammetry and Differential Pulse Voltammetry Measurements of Copper-1,4,6,9-tetra(pyridine-2-yl)pyridazino[4,5-*g*]phthalazine Metal Organic Framework

To a 25 mL flame-dried scintillation vial was added 10 mg of the metal-organic framework and 10 mL of dry acetonitrile. The vial was capped and sonicated for ten minutes to disperse the MOF throughout the solvent. A glassy carbon electrode was polished using aluminum oxide polishing compound and the dispersion was deposited onto the electrode using a micropipette, 20 µL at a time, the acetonitrile was allowed to evaporate, and the process was repeated ten times to deposit a small layer of the MOF onto the electrode. To a flame-dried 5 mL glass beaker was added 2 mL of dry acetonitrile and tetrabutylammonium hexafluorophosphate (0.077 mg, 0.20 mmol). The beaker was fitted with a holed cap and an aqueous silver/silver chloride reference electrode, platinum counter electrode, and MOF-covered glassy carbon electrode were placed into the

solution through the cap. A stream of nitrogen gas was bubbled through the solution through a syringe for 5 minutes before measurements were taken. The scans were conducted between +2 and -2 A at a scan rate of 50 mV/s.

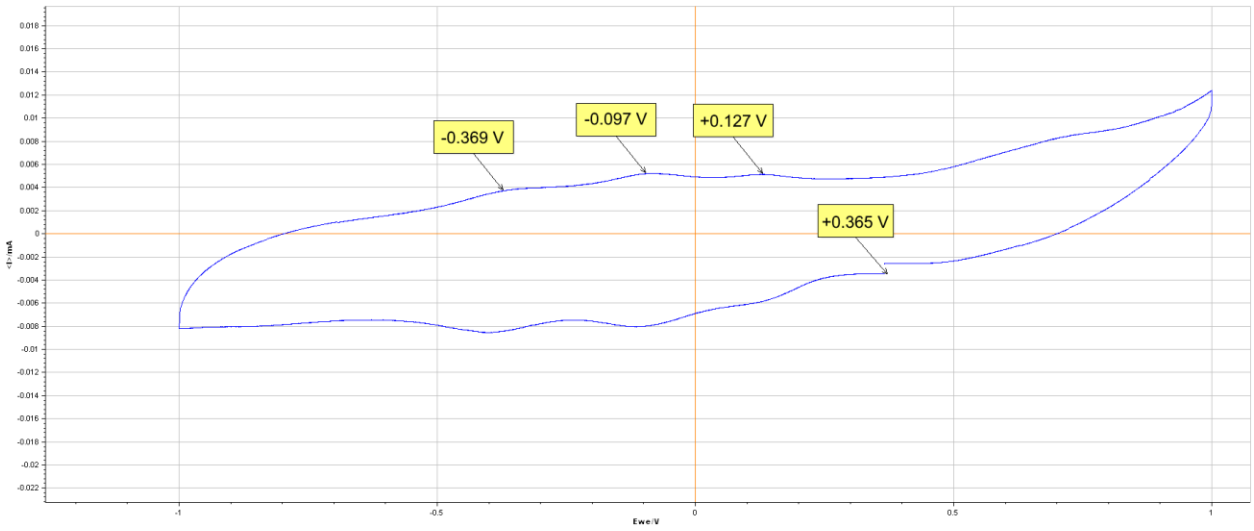

Figure S4: Cyclic voltammogram of Copper-1,4,6,9-tetra(pyridine-2-yl)pyridazino[4,5-*g*]phthalazine Metal Organic Framework.

5. Transmission Electron Microscopy

5.1 Transmission Electron Micrographs of Copper-1,4,6,9-tetra(pyridine-2-yl)pyridazino[4,5-*g*]phthalazine Metal Organic Framework

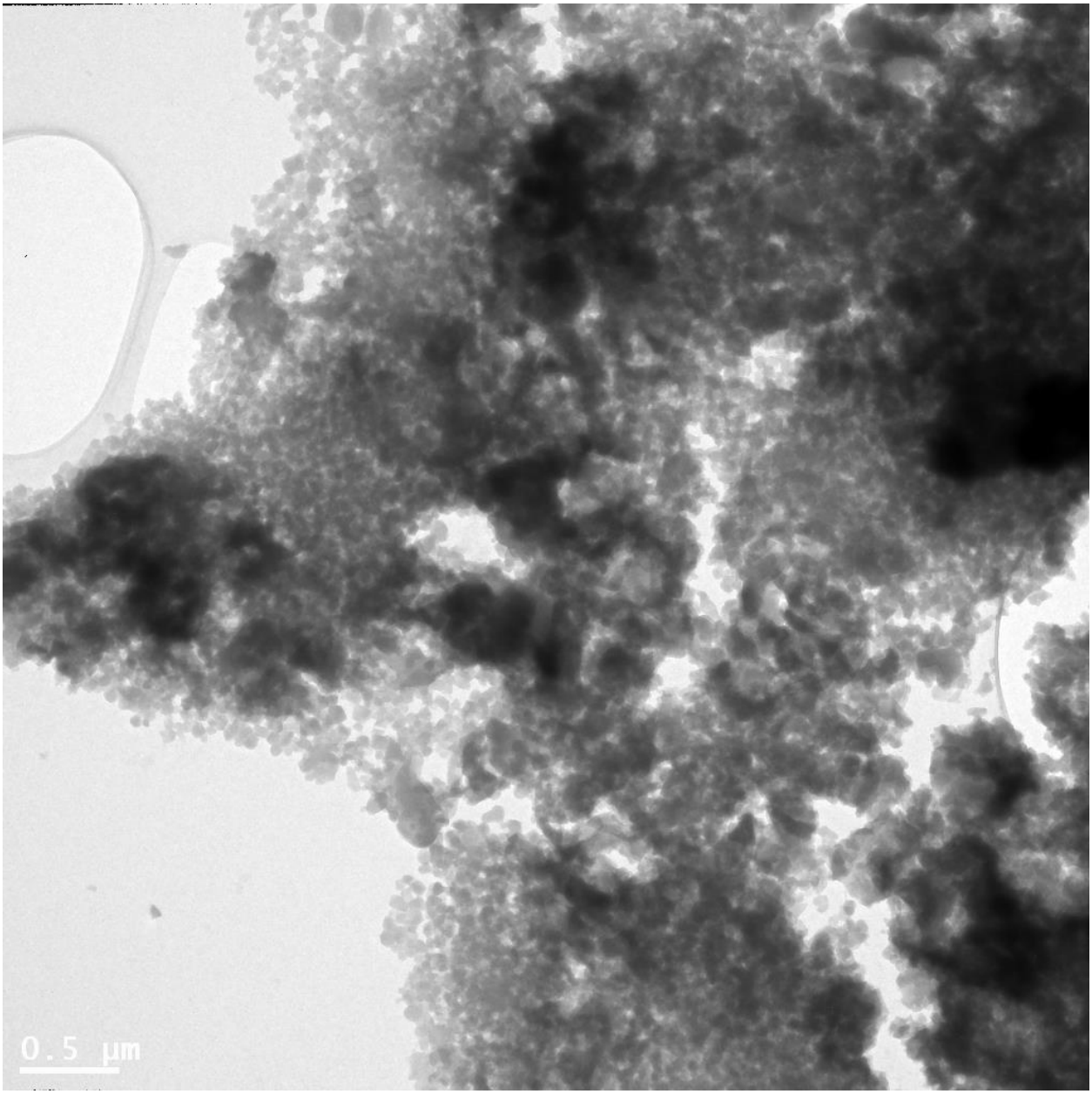

Figure S5: TEM of MOF on copper grid at 5 µm x 5 µm scale.

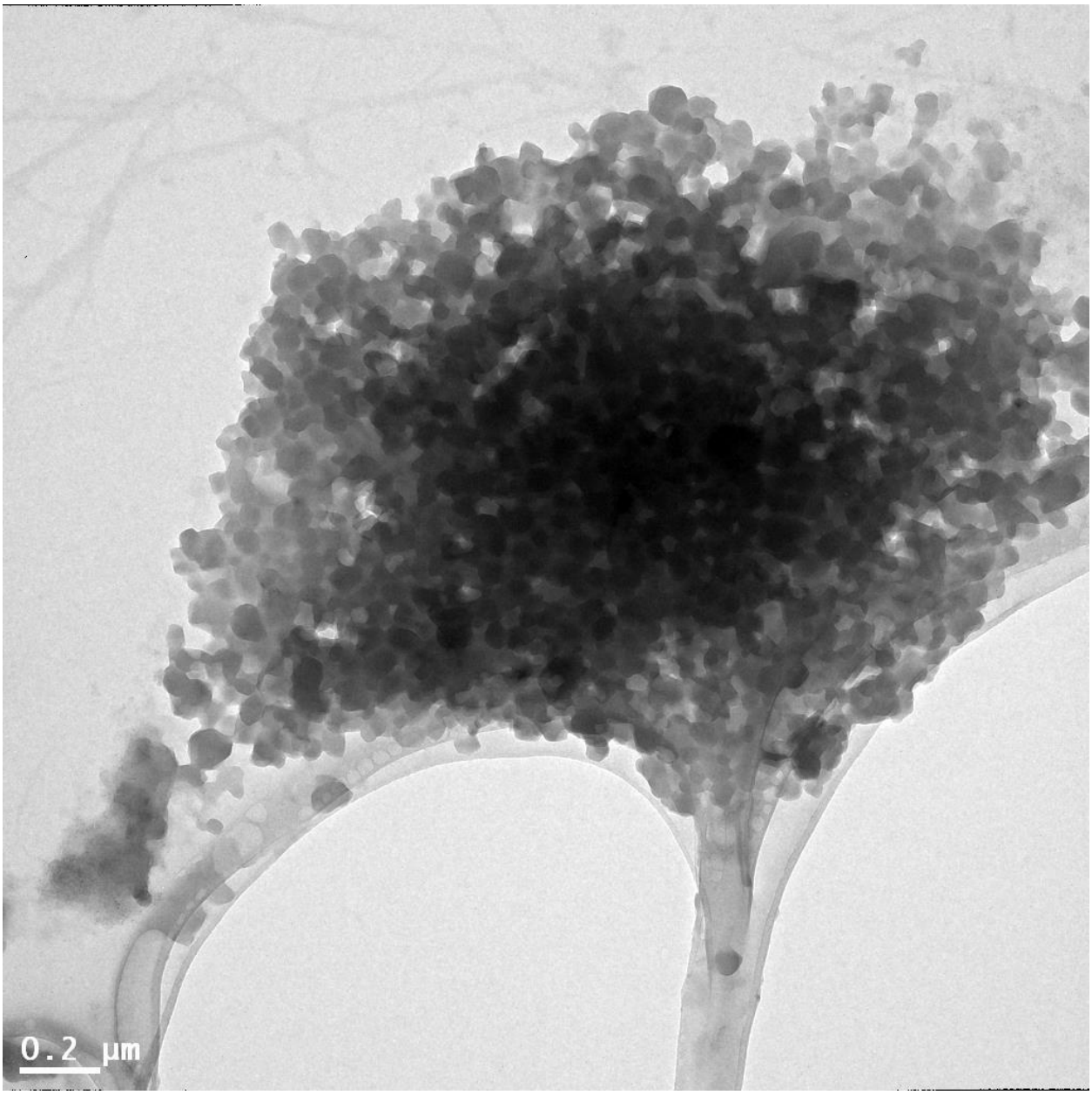

S6: TEM of MOF on copper grid at 2 µm x 2 µm scale.

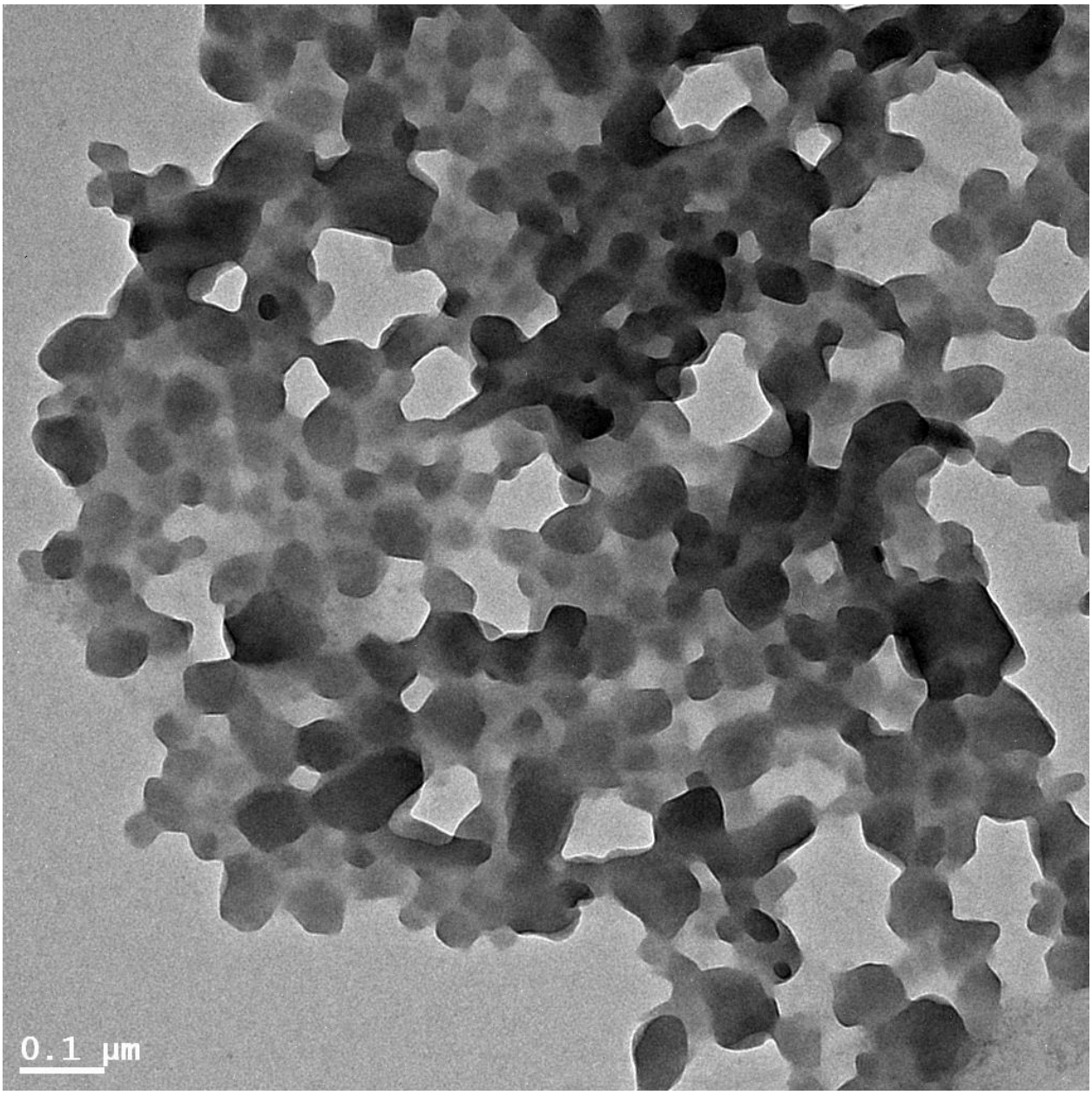

S7: TEM of MOF on copper grid at 1 µm x 1 µm scale.

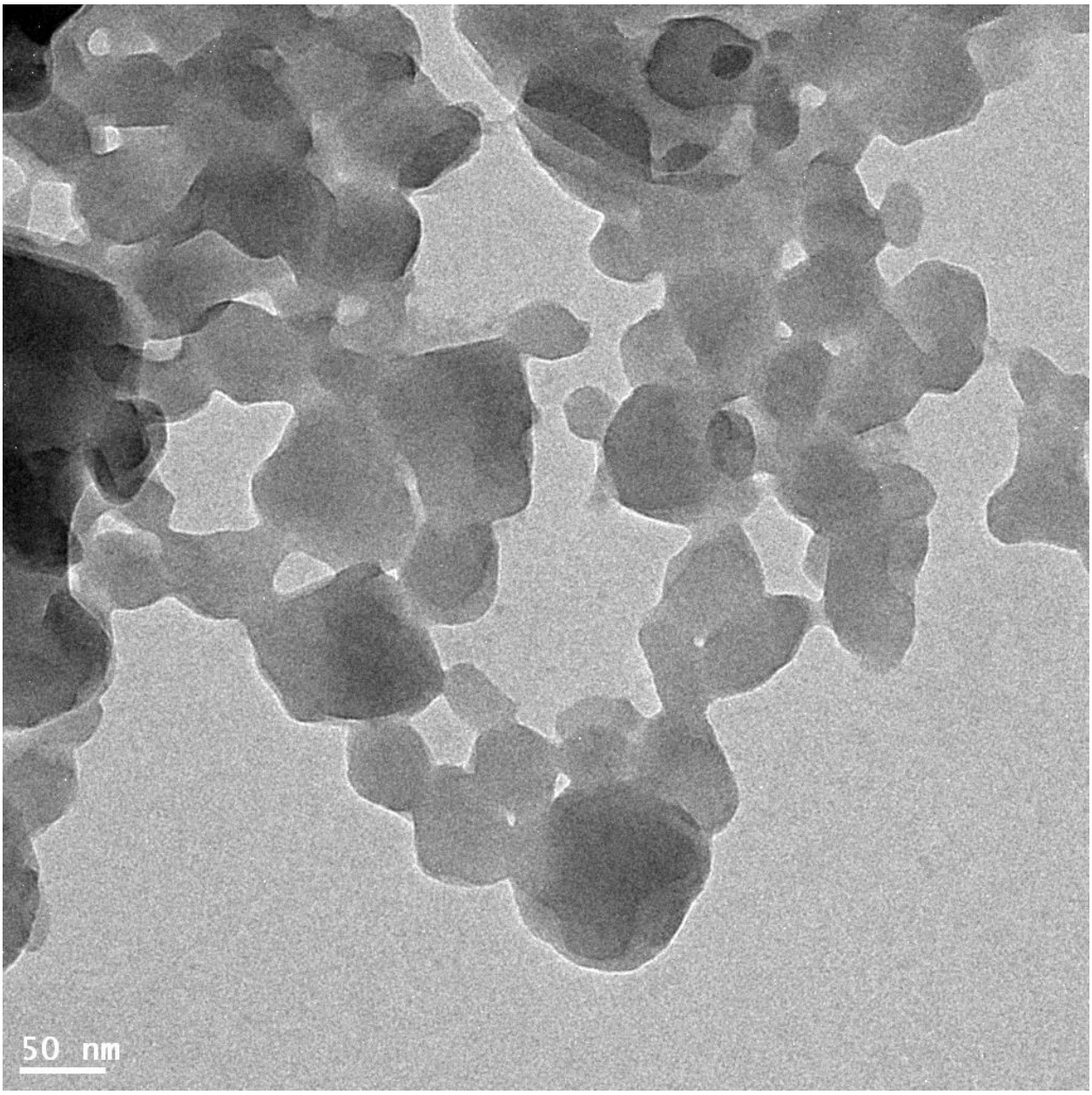

S8: TEM of MOF on copper grid at 500 nm x 500 nm scale.

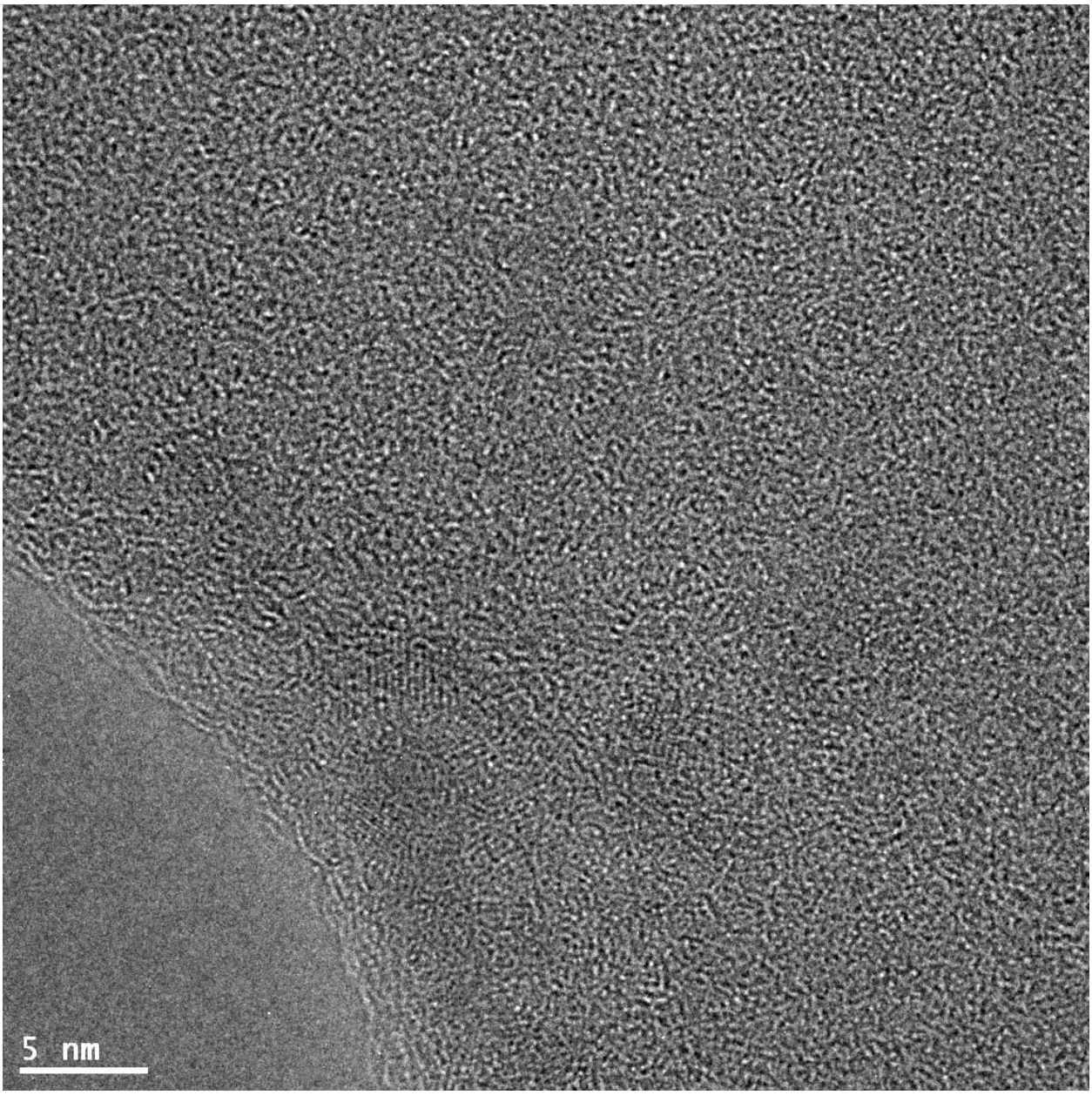

S9: TEM of MOF on copper grid at 50 nm x 50 nm scale.

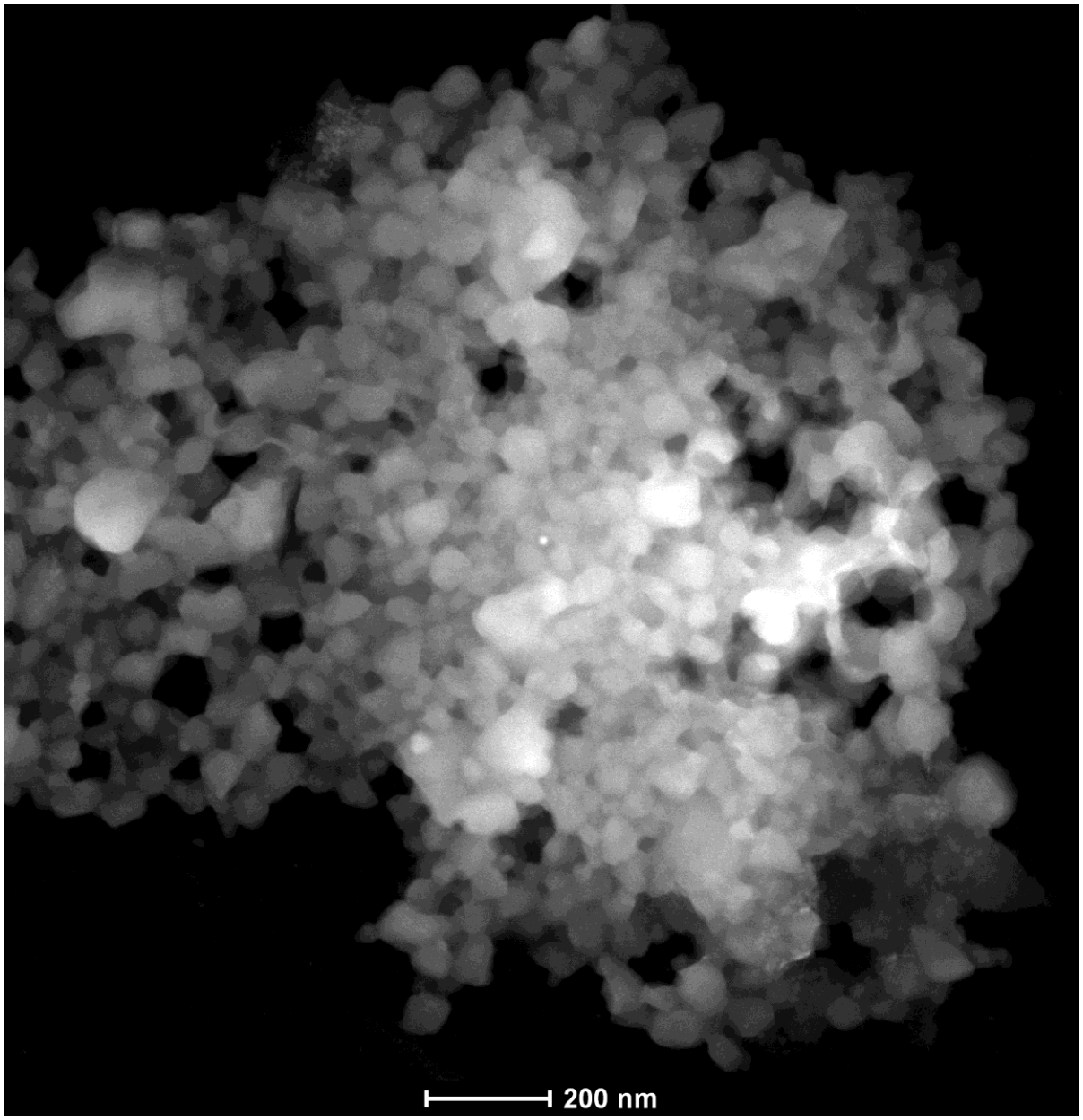

S10: TEM of MOF on nickel grid at 2 µm x 2 µm scale.

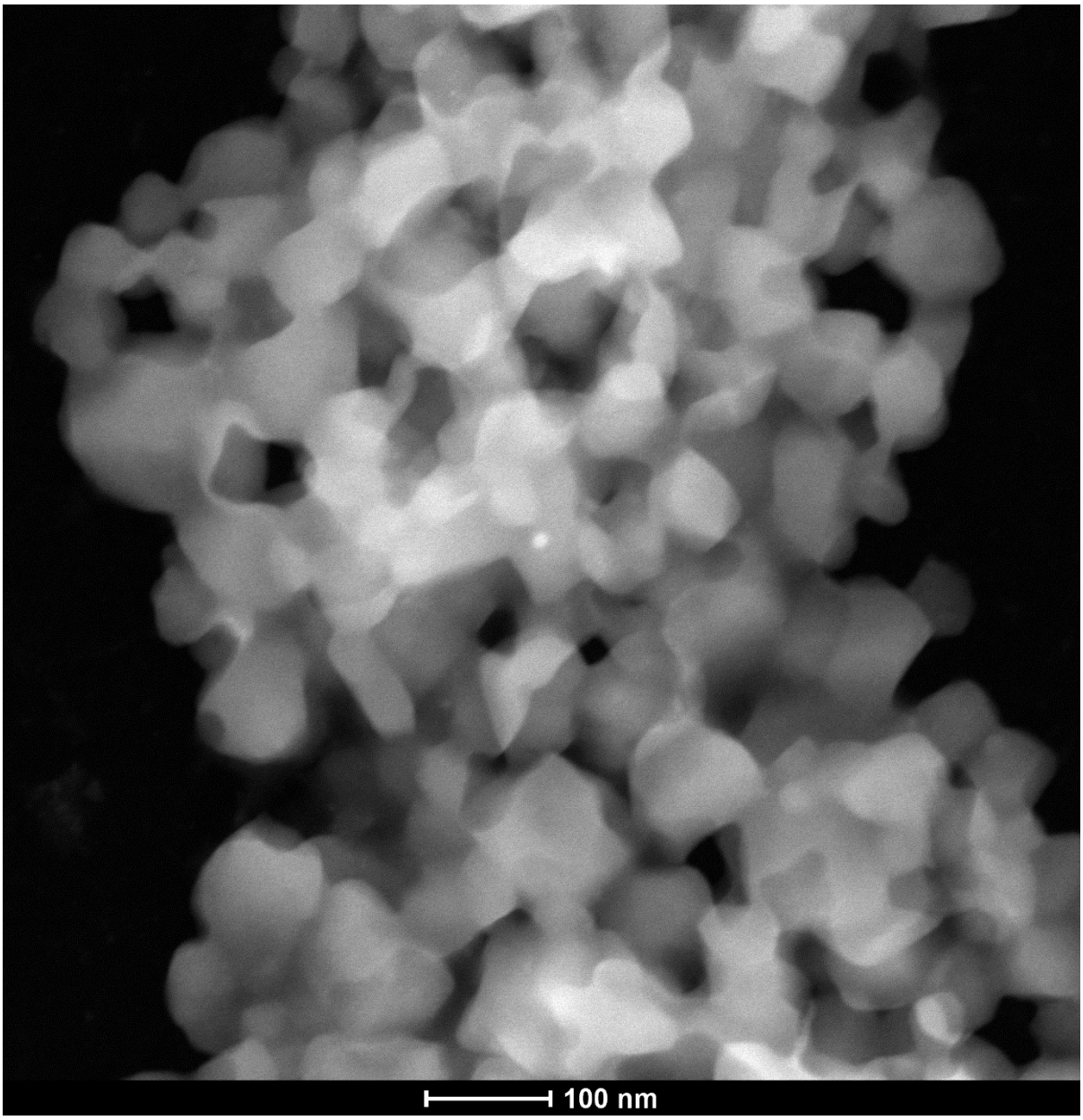

S11: TEM of MOF on nickel grid at 1 μm x 1 μm scale.

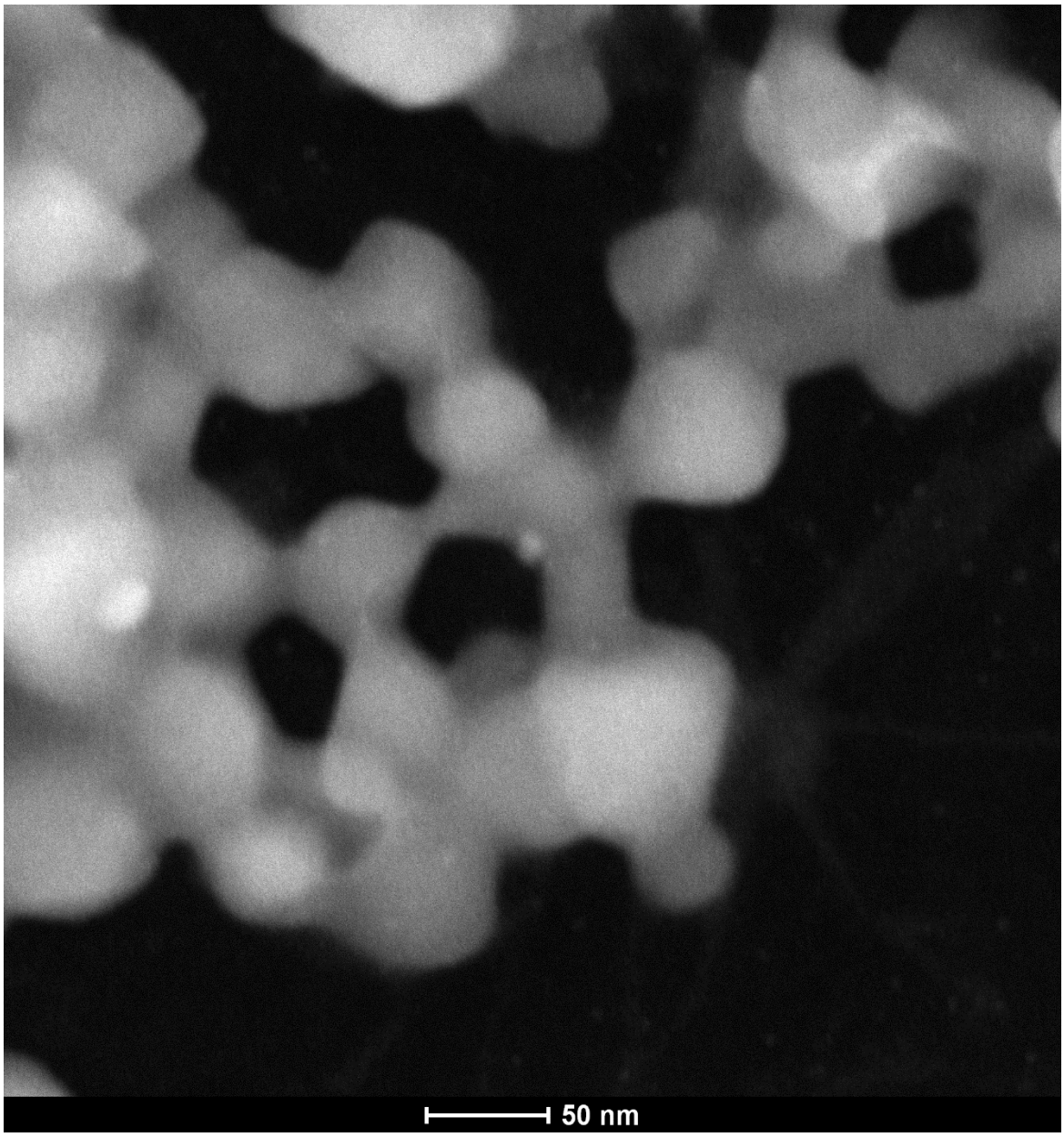

S12: TEM of MOF on nickel grid at 500 nm x 500 nm scale.

6. Scanning Electron Microscopy

6.1 Scanning Electron Micrographs of Patterned Silicon Oxide Surface

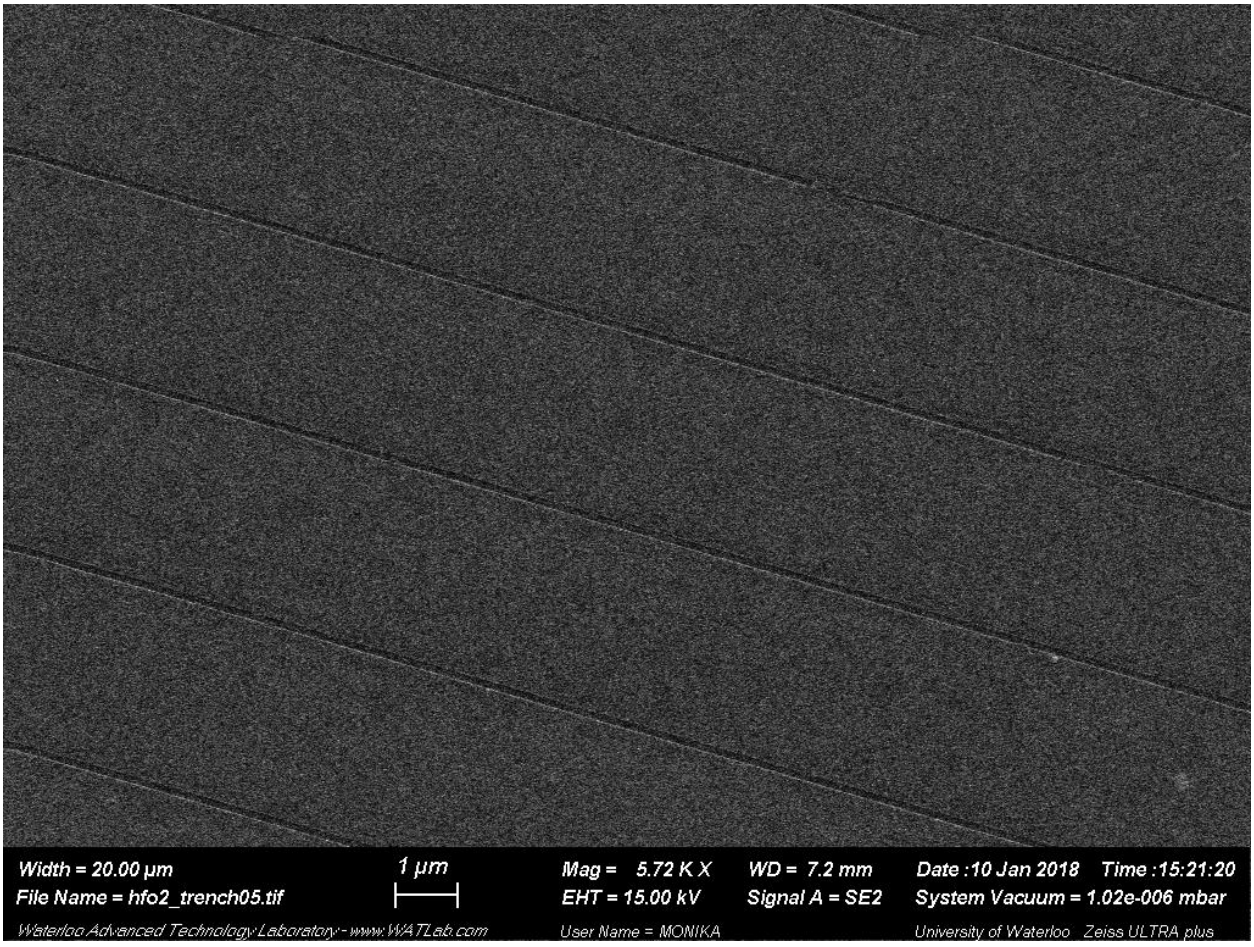

S13: SEM of patterned silicon oxide surface at a 20 µm x 20 µm scale.

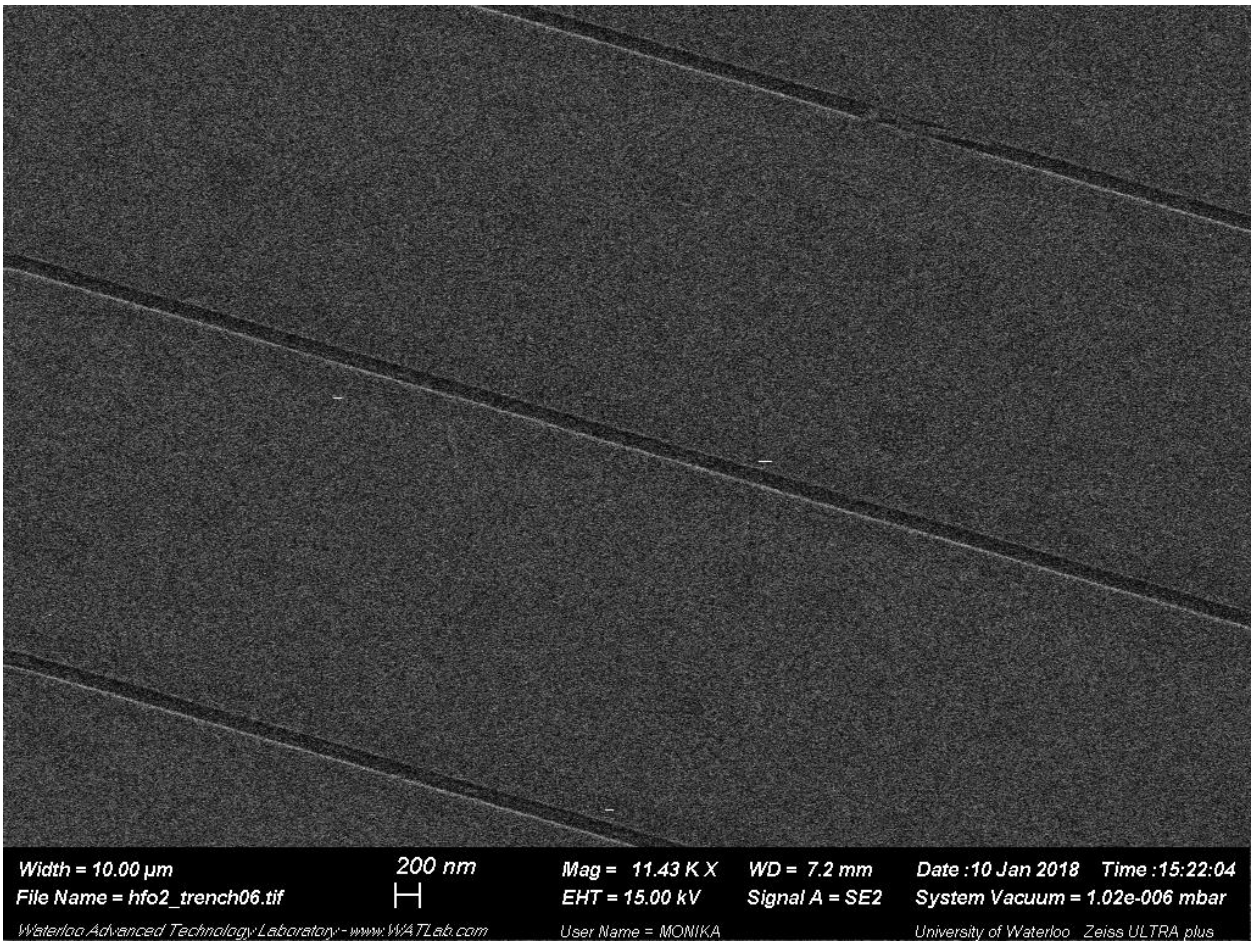

S14: SEM of patterned silicon oxide surface at a 10 µm x 10 µm scale.

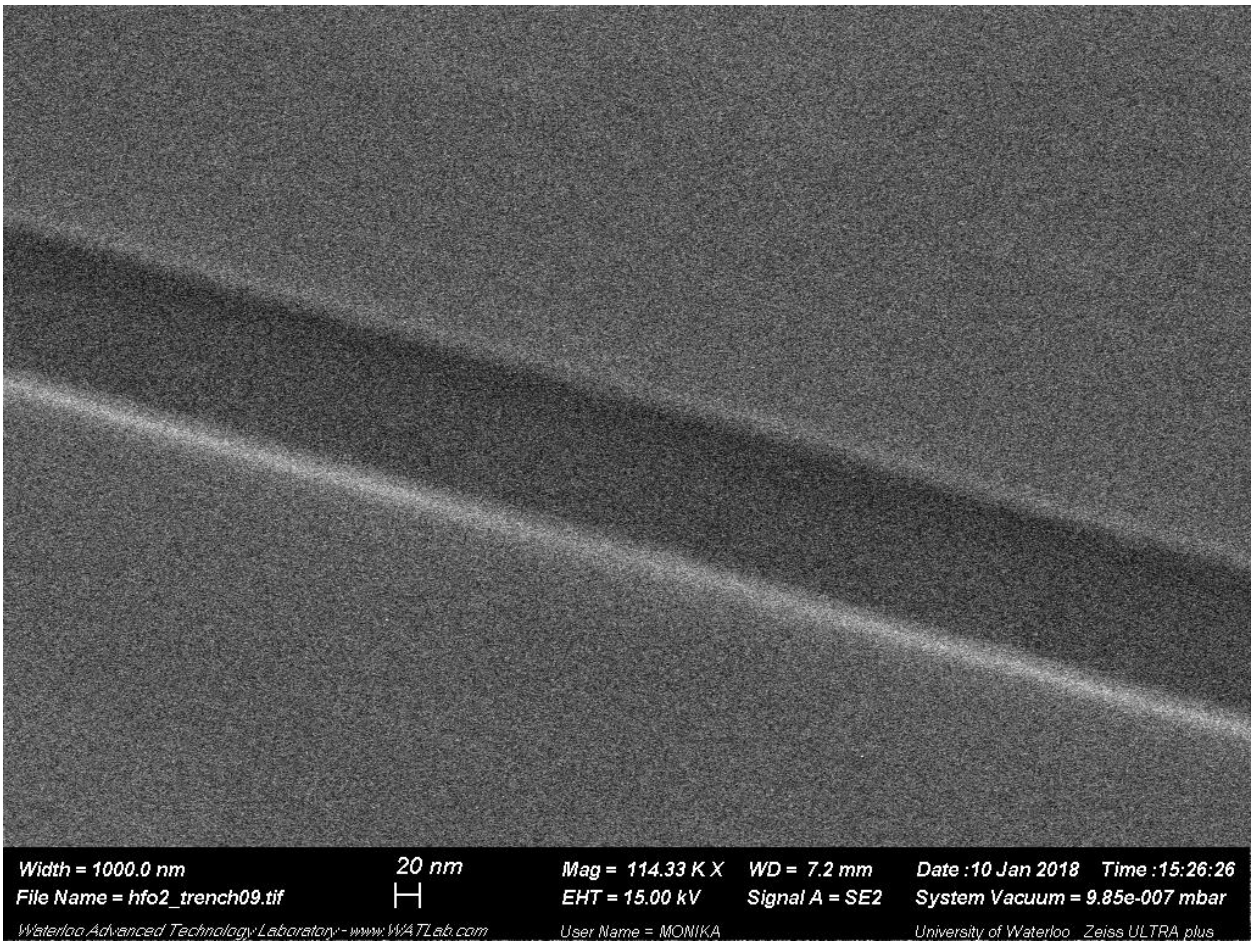

S15: SEM of patterned silicon oxide surface at a 1 µm x 1 µm scale

7. Energy Dispersive X-Ray Analysis

7.1 Energy Dispersive X-Ray Analysis of Patterned Silicon Oxide Surface

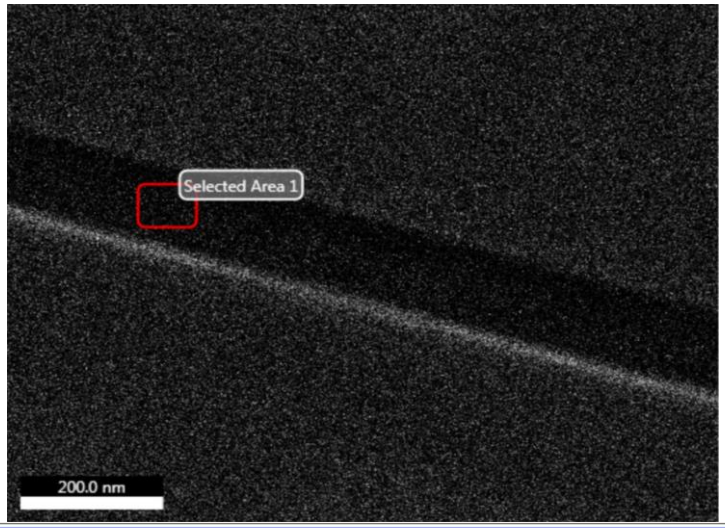

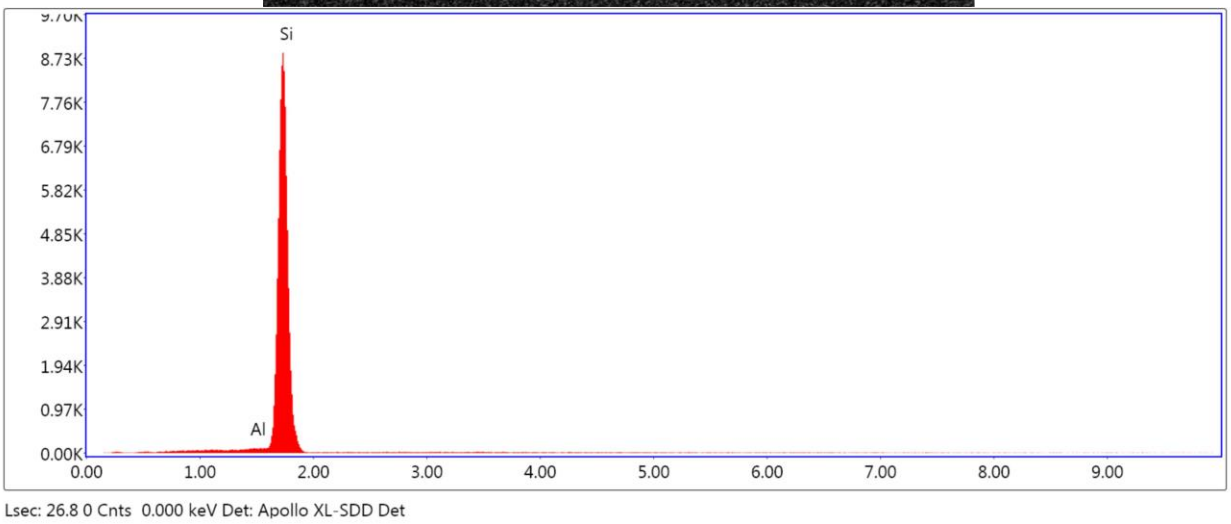

Element	Weight %	Atomic %	Net Int.	Error %	Kratio	Z	R	A	F
AlK	1.09	1.13	37.35	9.86	0.01	0.98	0.99	0.96	1.08
SiK	98.91	98.87	3,115.82	1.75	0.98	1	1	0.99	1

S16: EDXA of the trench region of a patterned silicon oxide surface

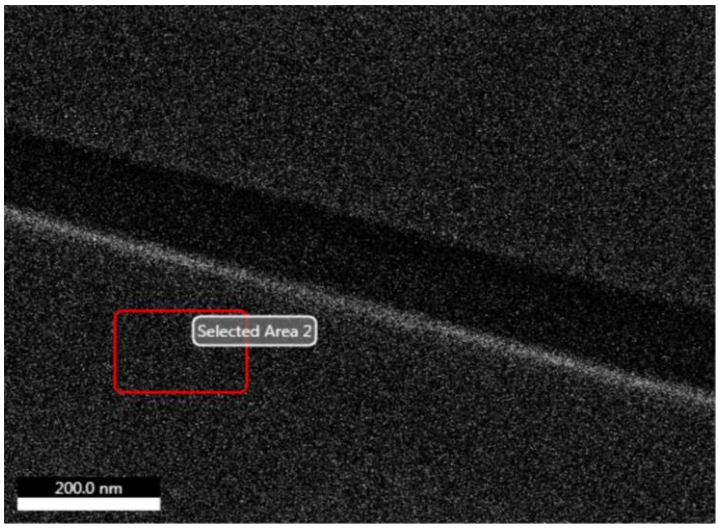

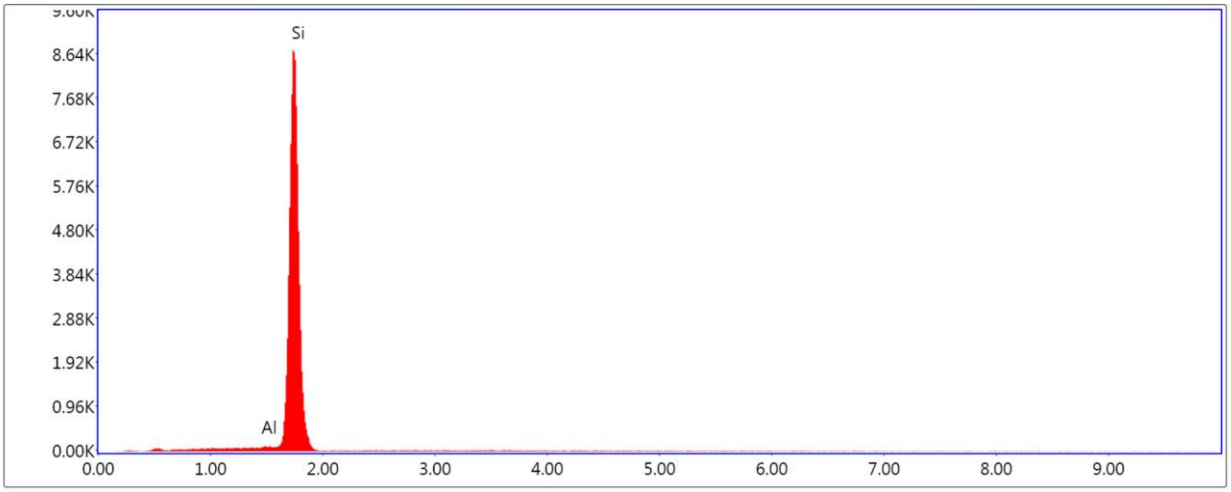

Element	Weight %	Atomic %	Net Int.	Error %	Kratio	Z	R	A	F
AlK	1.08	1.12	37.03	9.72	0.01	0.98	0.99	0.96	1.08
SiK	98.92	98.88	3,101.43	1.75	0.98	1	1	0.99	1

S17: EDXA of the plateau region of a patterned silicon oxide surface

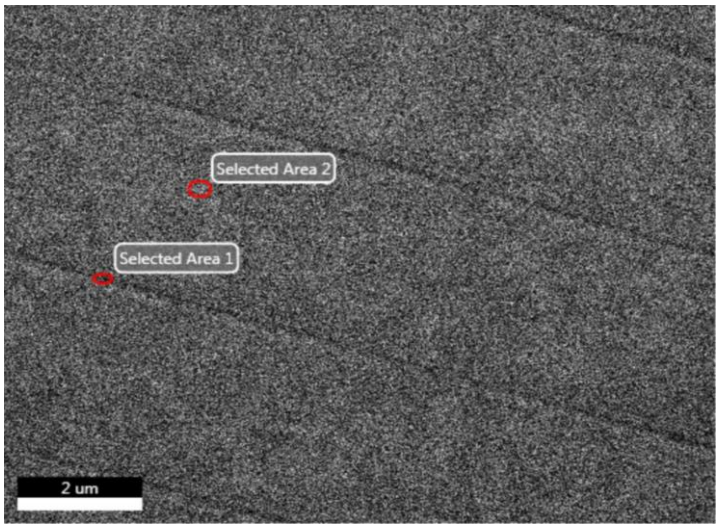

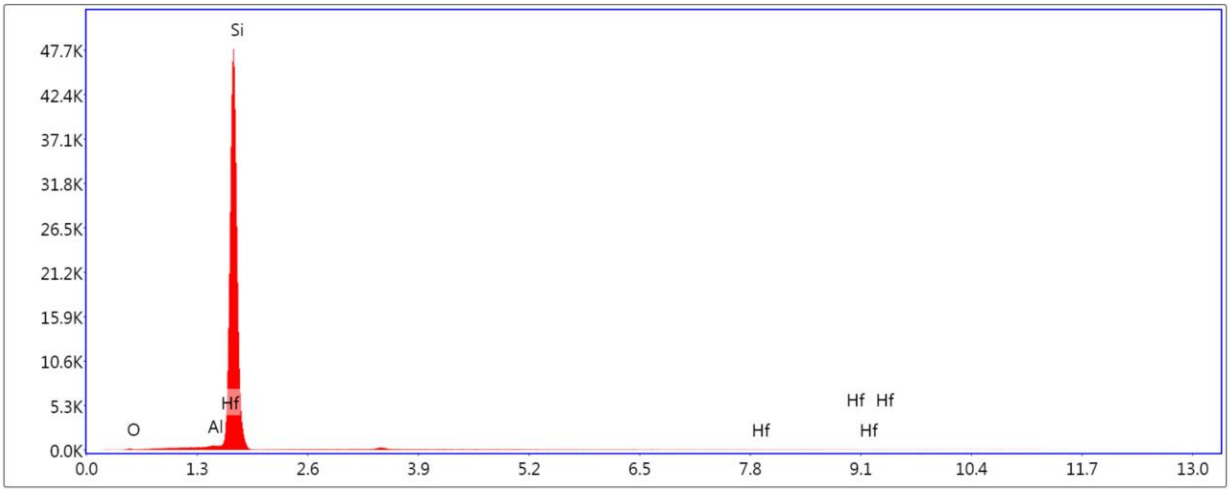

Lsec: 23.6 0 Cnts 0.000 keV Det: Apollo XL-SDD Det

Element	Weight %	Atomic %	Net Int.	Error %	Kratio	Z	R	A	F
O K	0.82	1.44	19.65	23.16	0.00	1.1	0.95	0.2	1
AlK	0.73	0.76	146.13	5.92	0.01	0.98	0.99	0.94	1.07
SiK	97.88	97.71	18,916.08	1.34	0.96	1	1	0.98	1
HfL	0.57	0.09	9.68	56.72	0.00	0.61	1.2	1.05	1.25

S18: EDXA of the trench region of a patterned silicon oxide surface

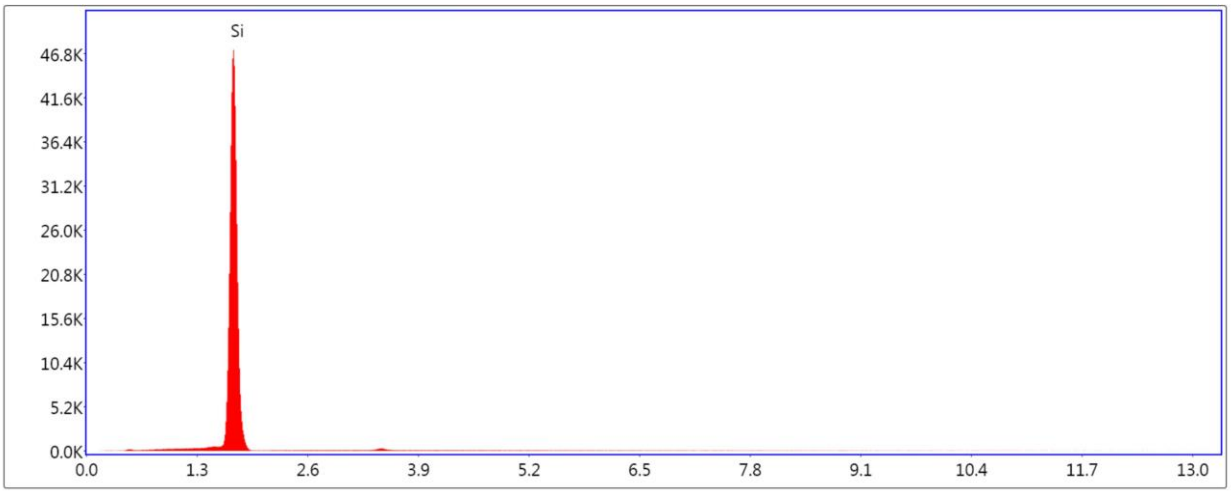

Element	Weight %	Atomic %	Net Int.	Error %	Kratio	Z	R	A	F
SiK	100.00	100.00	19,227.41	1.11	1.00	1	1	1	1

S19: EDXA of the plateau region of a patterned silicon oxide surface

7.2 Energy Dispersive X-Ray of Copper-1,4,6,9-tetra(pyridine-2-yl)pyridazino[4,5-*g*]phthalazine Metal Organic Framework

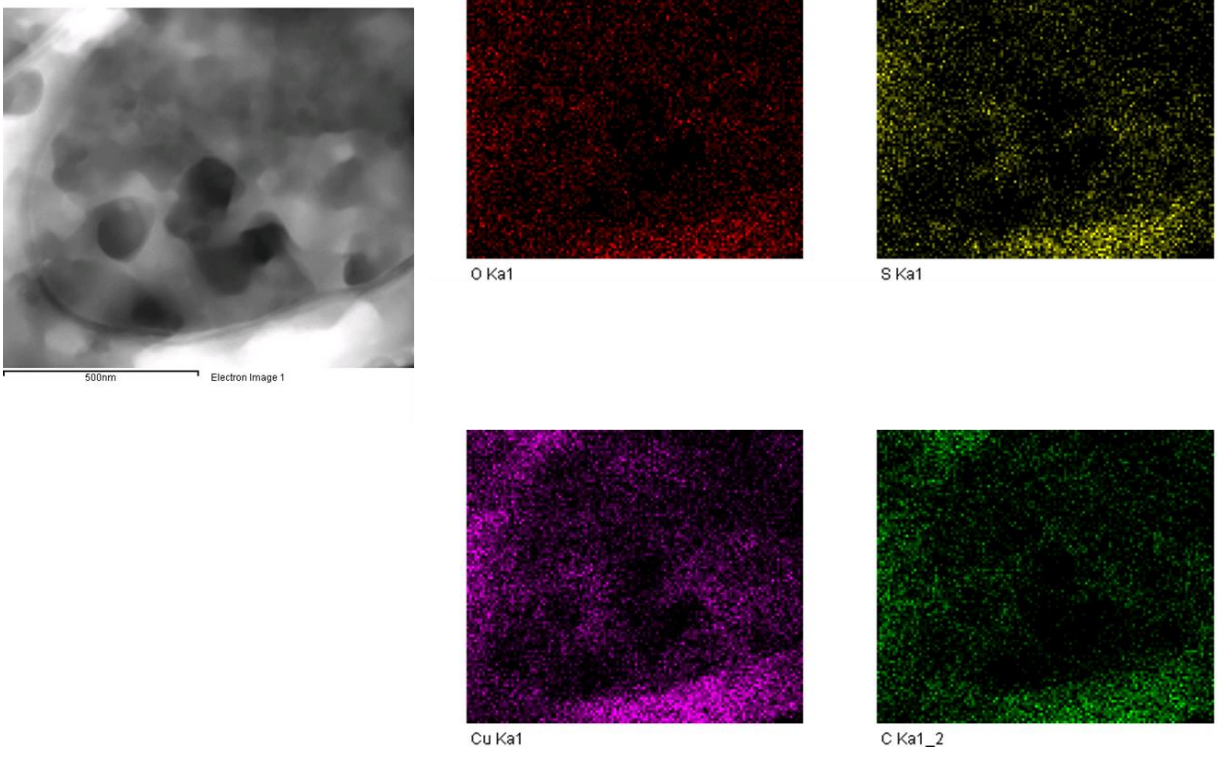

S20: Elemental map of MOF at 1 µm x 1 µm scale with oxygen in red, sulfur in yellow, copper in pink, and carbon in green

Spectrum processing :

Peaks possibly omitted : 1.745, 6.371, 9.751, 11.549 keV

Quantitation method : Cliff Lorimer thin ratio section.

Processing option : All elements analyzed (Normalised)

Number of iterations = 1

Standardless

Element	Weight%	Atomic%
C K	27.25	56.65
O K	7.61	11.88
S K	15.24	11.86
Cu K	49.90	19.61
Totals	100.00	

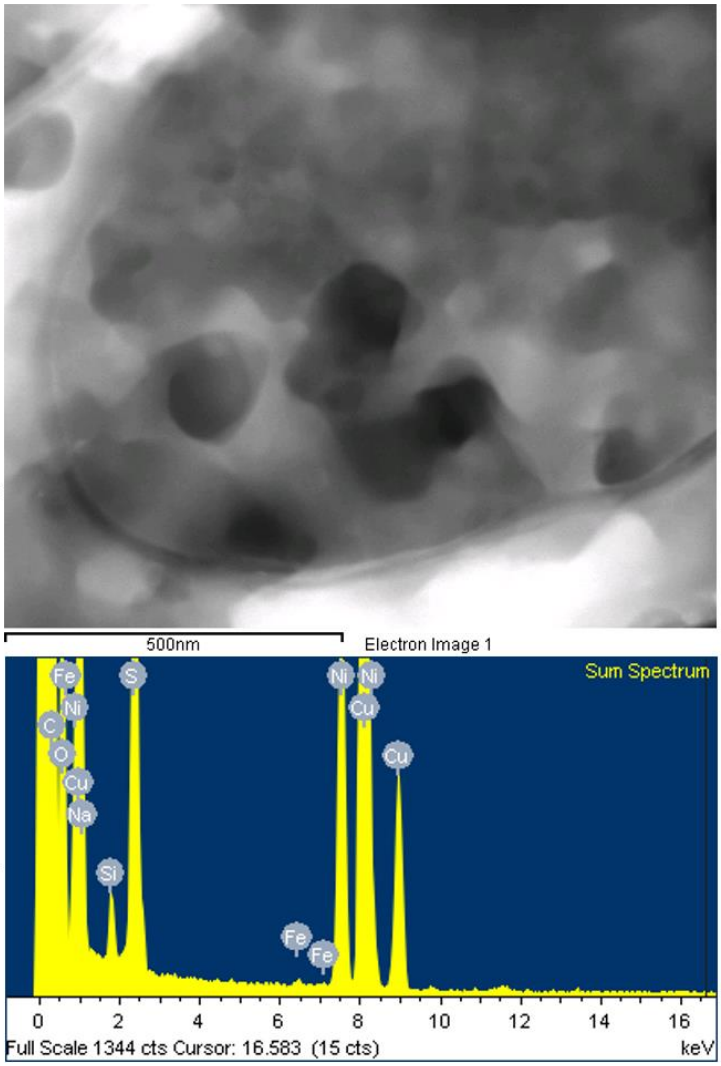

S21: EDXA of MOF, area 1

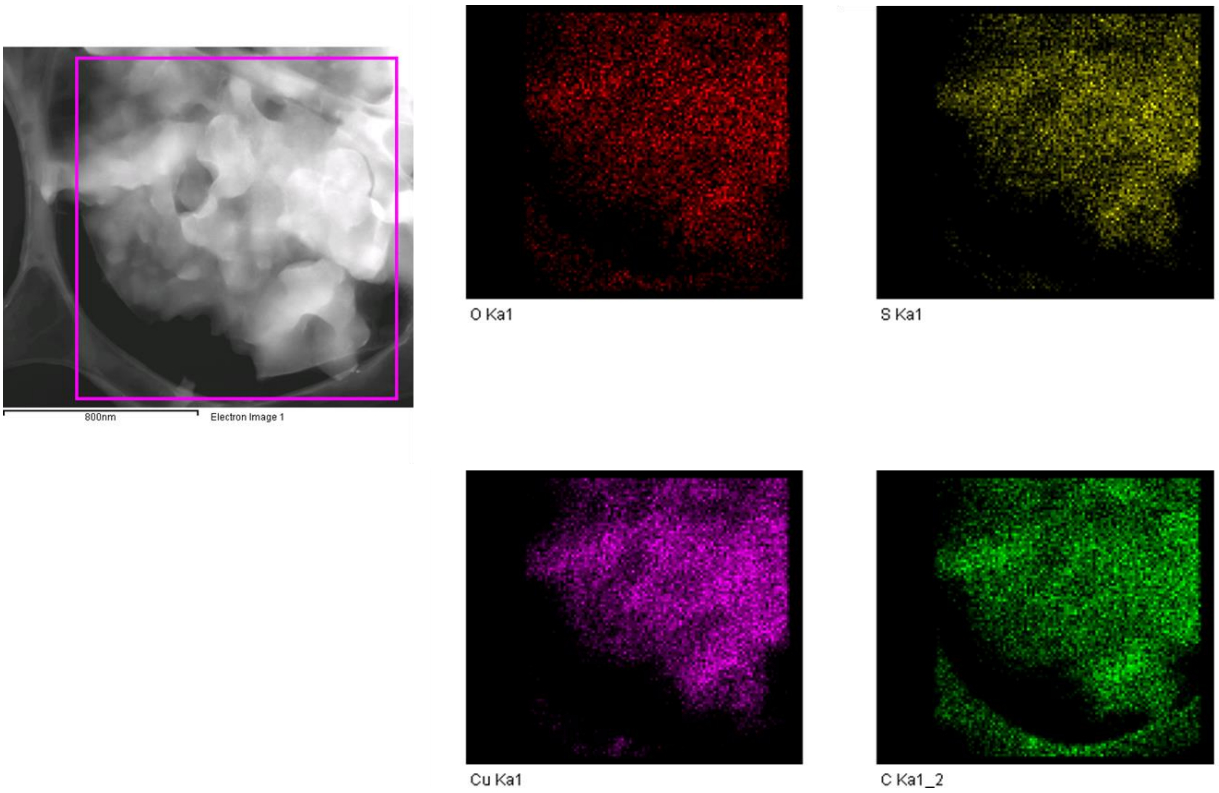

S22: Elemental map of MOF at 1.6 µm x 1.6 µm scale with oxygen in red, sulfur in yellow, copper in pink, and carbon in green

Spectrum processing :

Peaks possibly omitted : 1.747, 6.398, 9.689, 11.429, 11.480 keV

Quantitation method : Cliff Lorimer thin ratio section.

Processing option : All elements analyzed (Normalised)

Number of iterations = 1

Standardless

Element	Weight%	Atomic%
C K	33.26	62.87
O K	8.01	11.37
S K	13.62	9.64
Cu K	45.12	16.12
Totals	100.00	

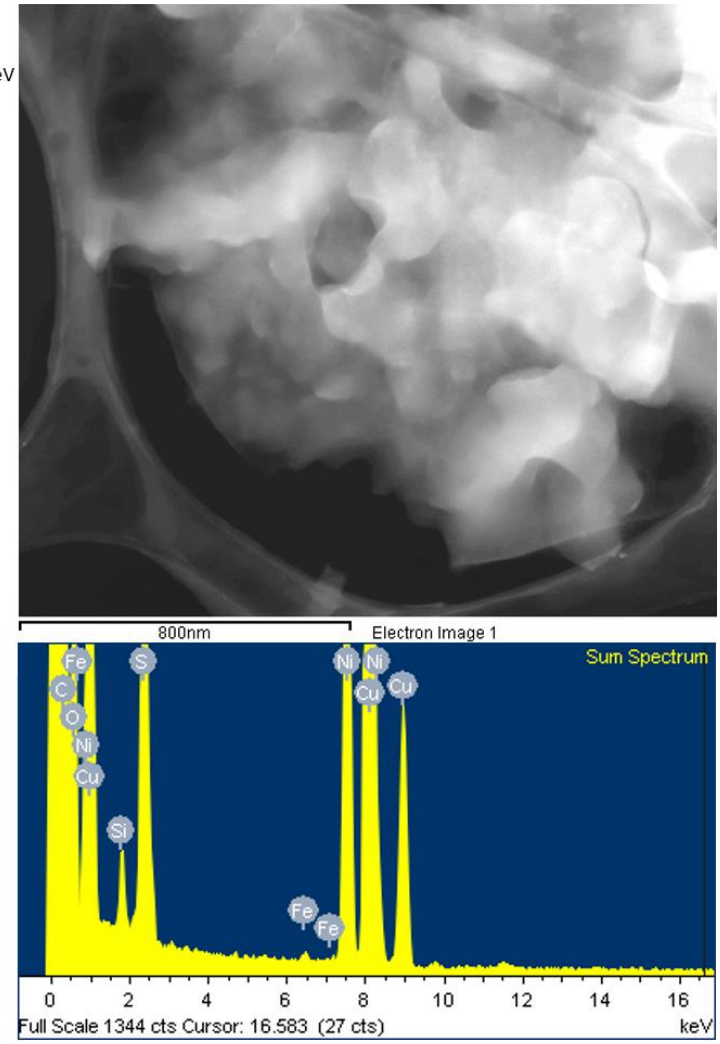

S23: EDXA of MOF, area 2

Spectrum processing :

No peaks omitted

Quantitation method : Cliff Lorimer thin ratio section.

Processing option : All elements analyzed (Normalised)

Number of iterations = 1

Standardless

Element	Weight%	Atomic%
C K	27.62	55.22
O K	11.24	16.88
S K	12.93	9.68
Cu K	48.21	18.22
Totals	100.00	

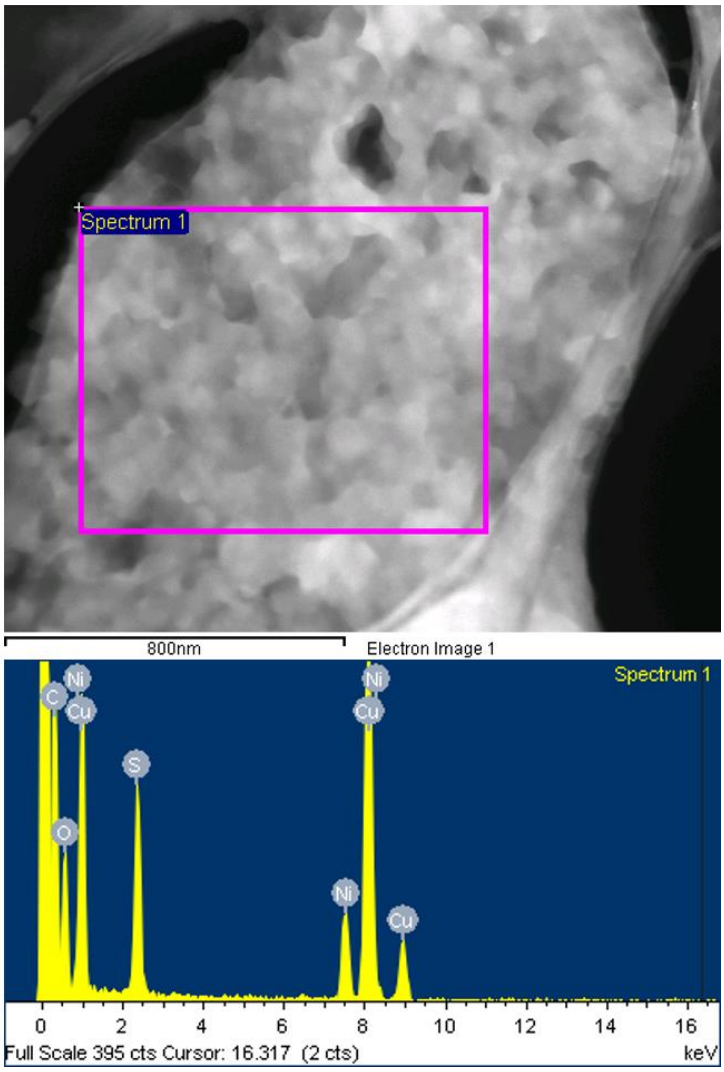

S24: EDXA of MOF, area 3

Spectrum processing :

No peaks omitted

Quantitation method : Cliff Lorimer thin ratio section.

Processing option : All elements analyzed (Normalised)

Number of iterations = 1

Standardless

Element	Weight%	Atomic%
C K	30.31	57.52
O K	12.11	17.26
S K	12.98	9.22
Cu K	44.60	16.00
Totals	100.00	

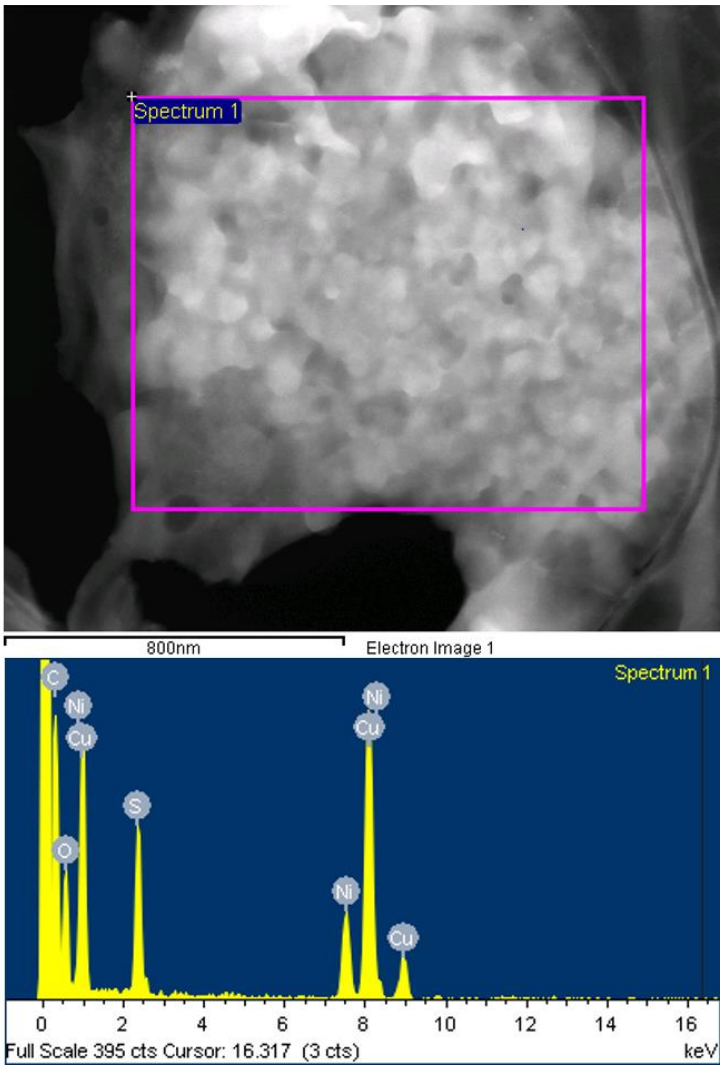

S25: EDXA of MOF, area 4

Spectrum processing :

No peaks omitted

Quantitation method : Cliff Lorimer thin ratio section.

Processing option : All elements analyzed (Normalised)

Number of iterations = 1

Standardless

Element	Weight%	Atomic%
C K	28.03	58.14
O K	6.99	10.89
S K	14.25	11.07
Cu K	50.73	19.89
Totals	100.00	

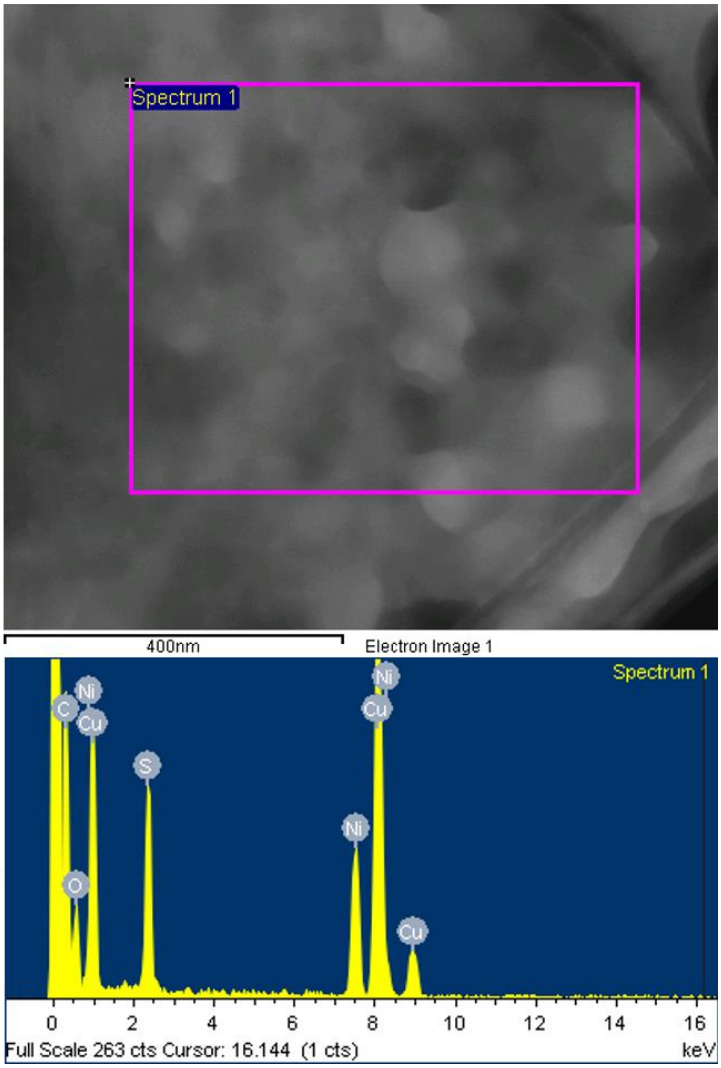

S26: EDXA of MOF, area 5

Spectrum processing :

No peaks omitted

Quantitation method : Cliff Lorimer thin ratio section.

Processing option : All elements analyzed (Normalised)

Number of iterations = 1

Standardless

Element	Weight%	Atomic%
C K	30.61	58.56
O K	10.55	15.15
S K	14.11	10.11
Cu K	44.73	16.18
Totals	100.00	

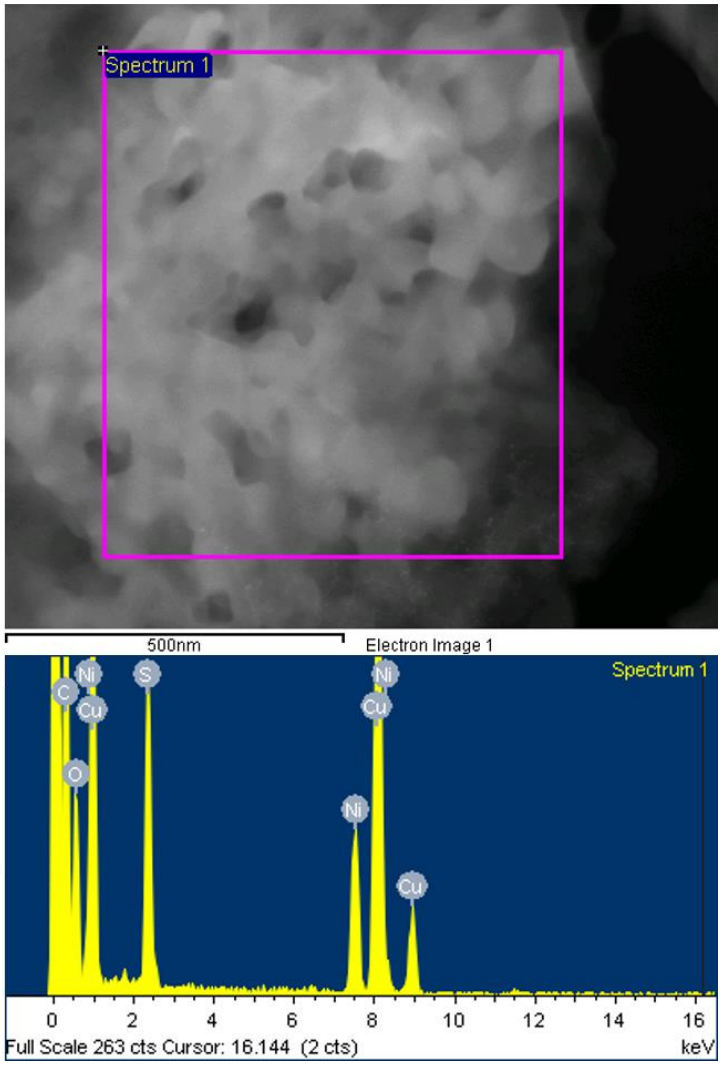

S27: EDXA of MOF, area 6

Spectrum processing :

No peaks omitted

Quantitation method : Cliff Lorimer thin ratio section.

Processing option : All elements analyzed (Normalised)

Number of iterations = 1

Standardless

Element	Weight%	Atomic%
C K	27.62	57.19
O K	7.94	12.35
S K	13.64	10.58
Cu K	50.79	19.88
Totals	100.00	

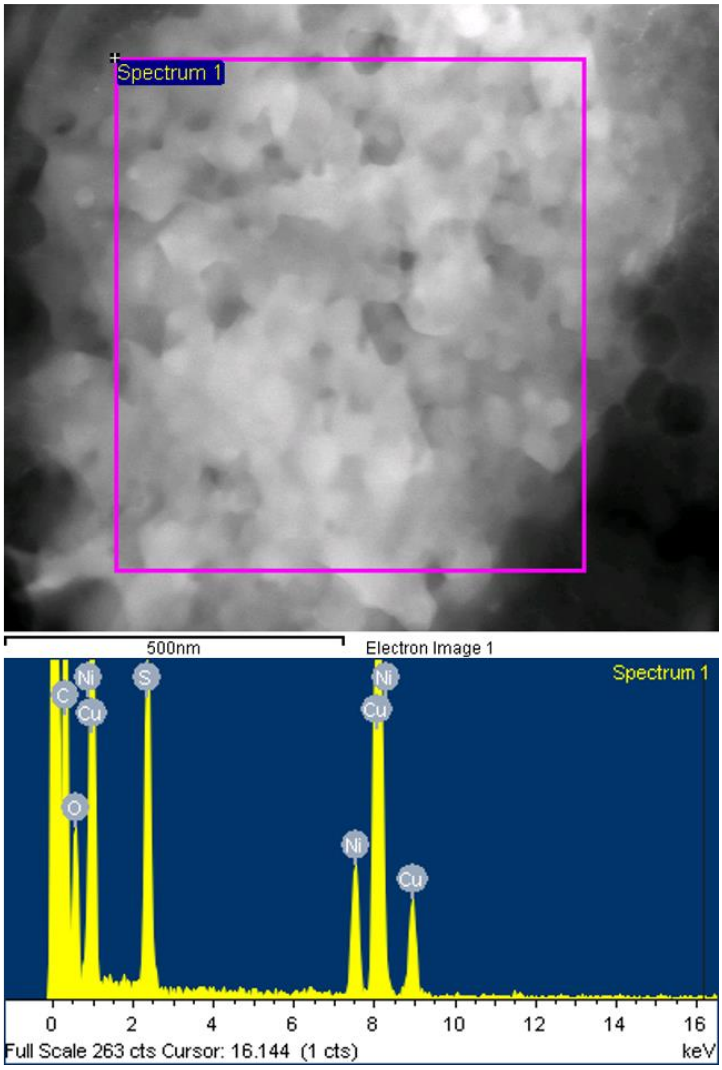

S28: EDXA of MOF, area 7

8. Atomic Force Microscopy

8.1 Atomic Force Micrographs of ART-Deposited SWNTs on an Indium Tin Oxide Surface with 4-cyano-4'-pentylbiphenyl and tetraethyl (5,7,9,14,16,18-hexahydro-5,18:9,14-bis([1,2]benzeno)-7,16-ethenoheptacene-25,26-diyl)bis(phosphonate) (2)

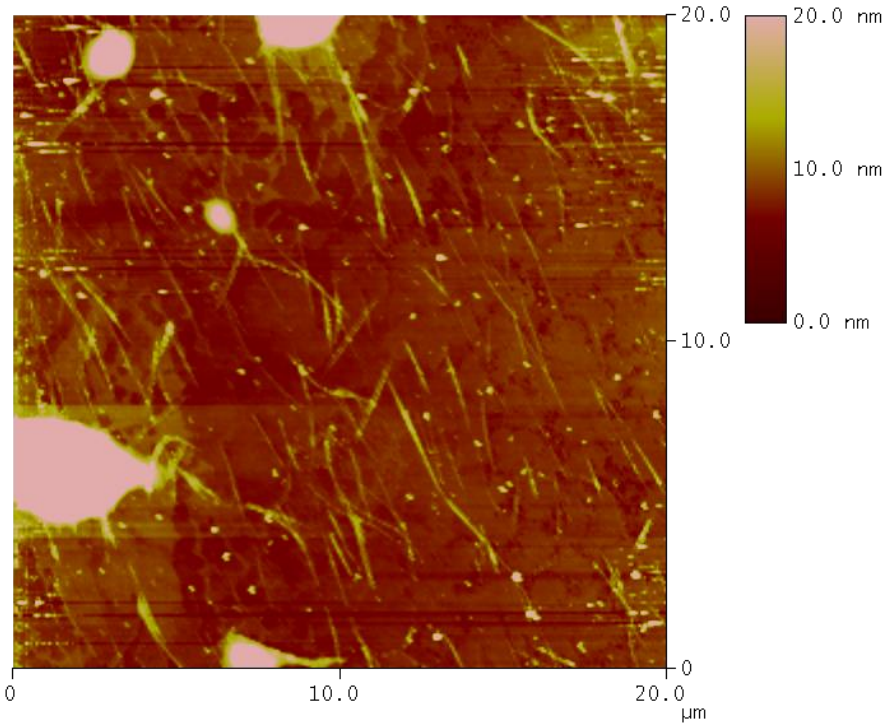

S29: AFM of SWNTs on ITO with 5CB and 2, area 1

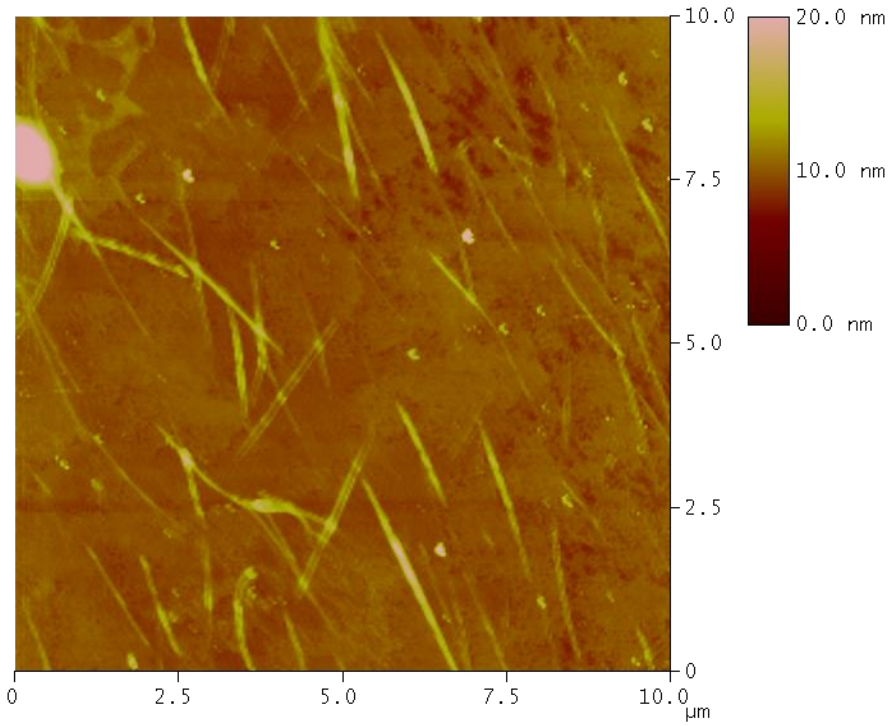

S30: AFM of SWNTs on ITO with 5CB and 2, area 2

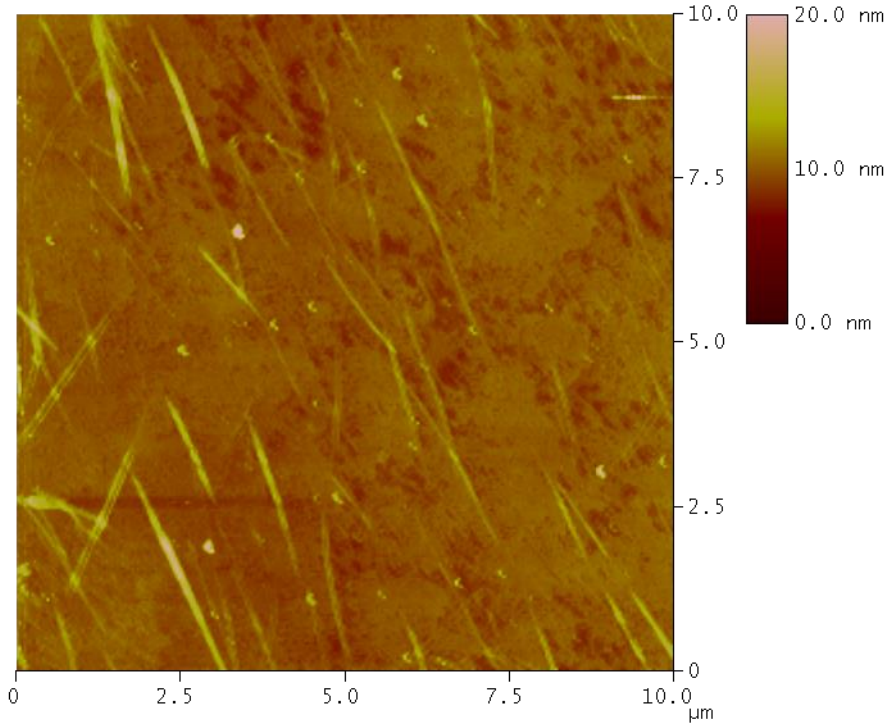

S31: AFM of SWNTs on ITO with 5CB and 2, area 3

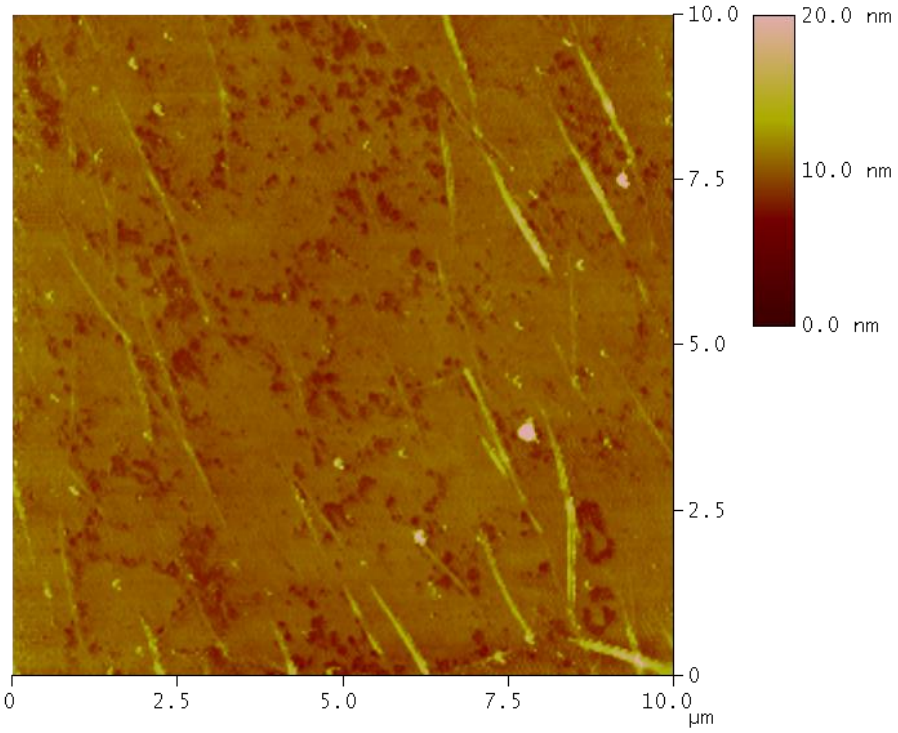

S32: AFM of SWNTs on ITO with 5CB and 2, area 4

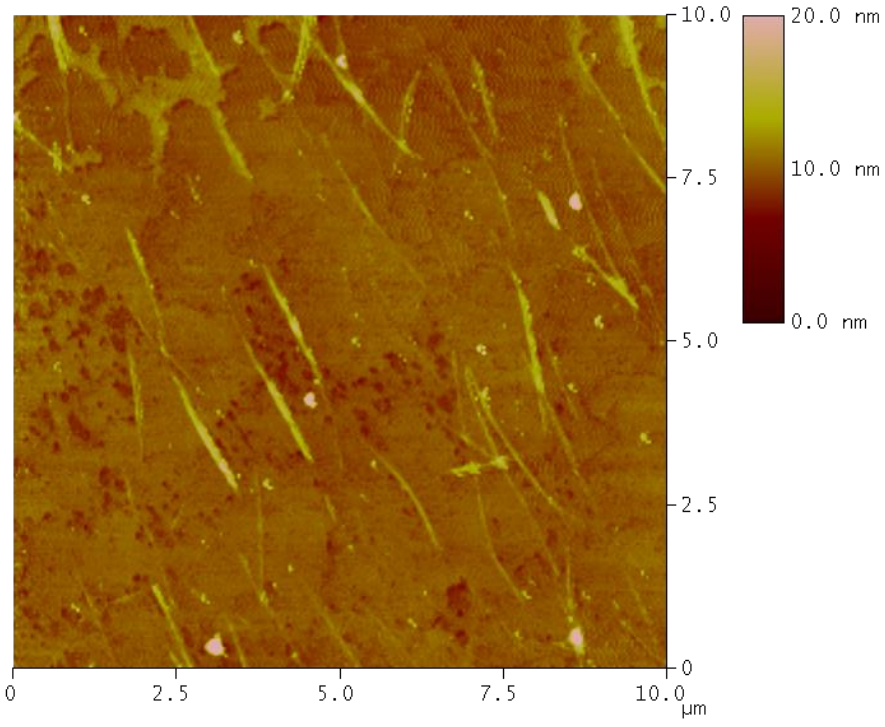

S33: AFM of SWNTs on ITO with 5CB and 2, area 5

8.2 Atomic Force Micrographs of ART-Deposited SWNTs on a Silicon Dioxide Surface with 4-cyano-4'-pentylbiphenyl and tetraethyl (5,7,9,14,16,18-hexahydro-5,18:9,14-bis([1,2]benzeno)-7,16-ethenoheptacene-25,26-diyl)bis(phosphonate) (2)

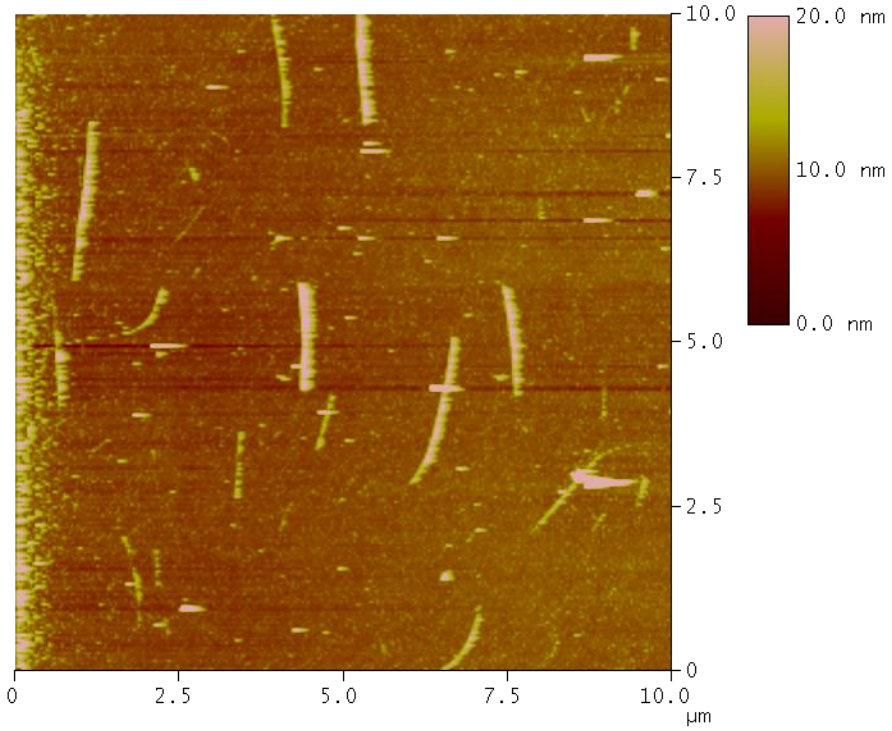

S34: AFM of SWNTs on SiO_2 with 5CB and 2, area 1

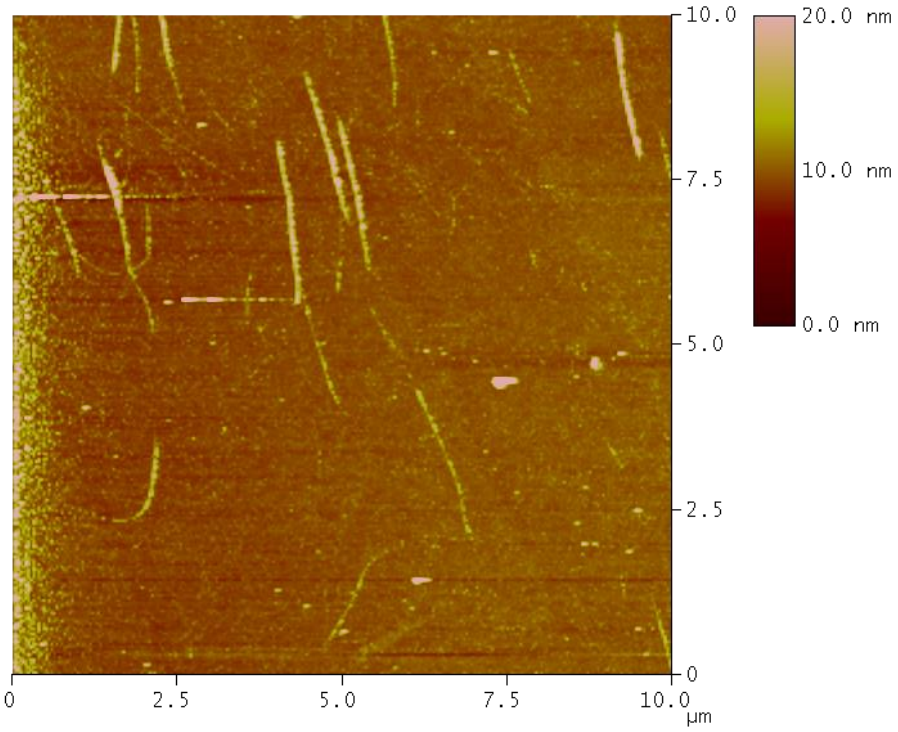

S35: AFM of SWNTs on SiO_2 with 5CB and 2, area 2

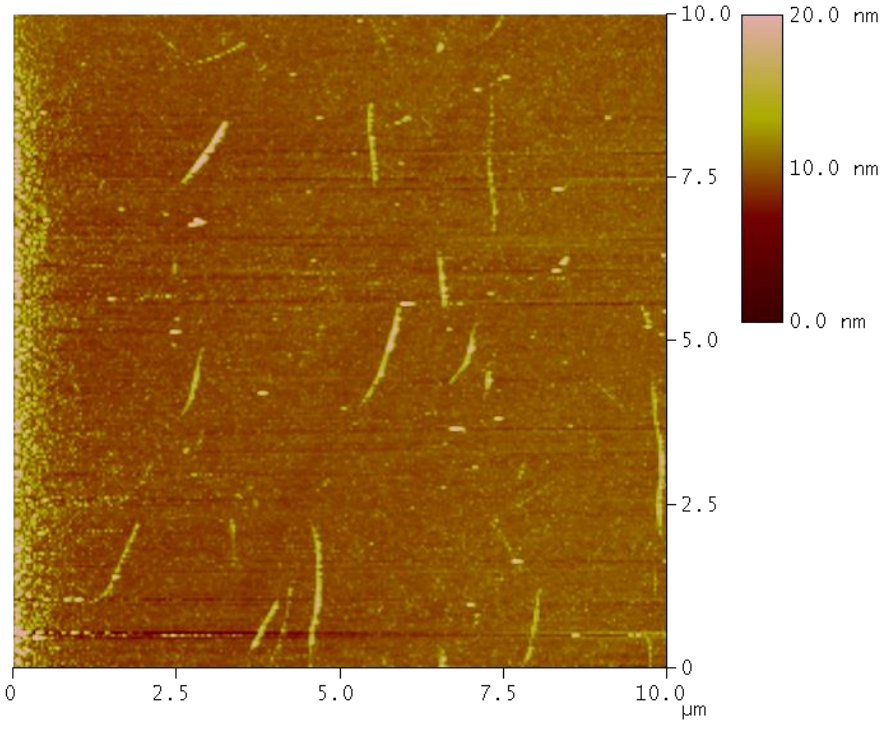

S36: AFM of SWNTs on SiO_2 with 5CB and 2, area 3

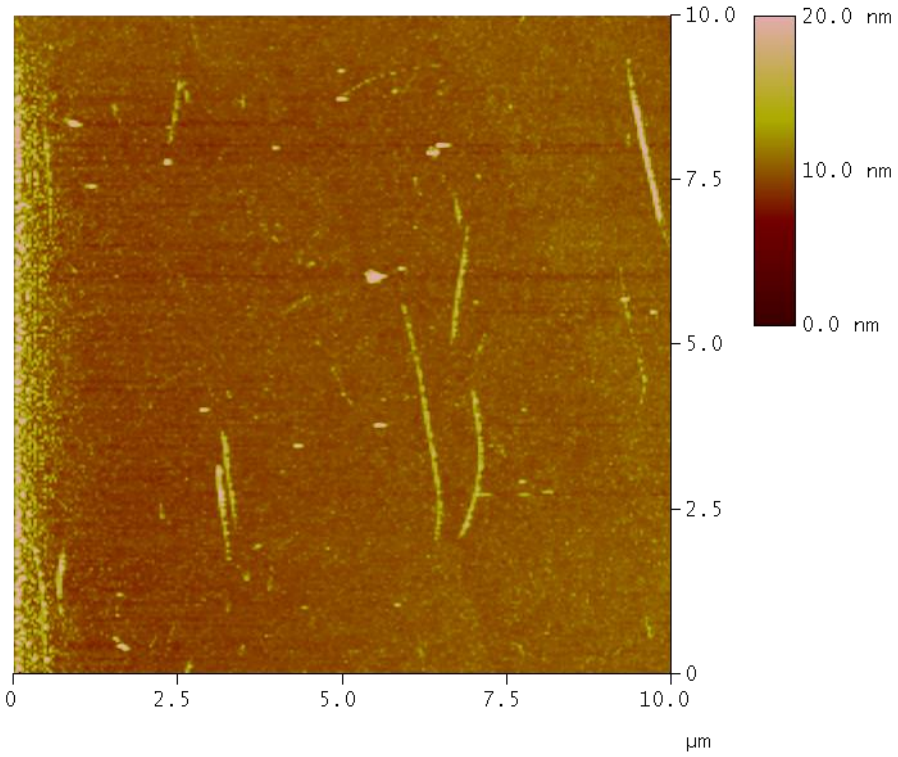

S37: AFM of SWNTs on SiO_2 with 5CB and 2, area 4

8.3 Atomic Force Micrographs of ART-Deposited SWNTs on an Indium Tin Oxide Surface with 4-cyano-4'-octylbiphenyl and tetraethyl (5,7,9,14,16,18-hexahydro-5,18:9,14-bis([1,2]benzeno)-7,16-ethenoheptacene-25,26-diyl)bis(phosphonate) (2)

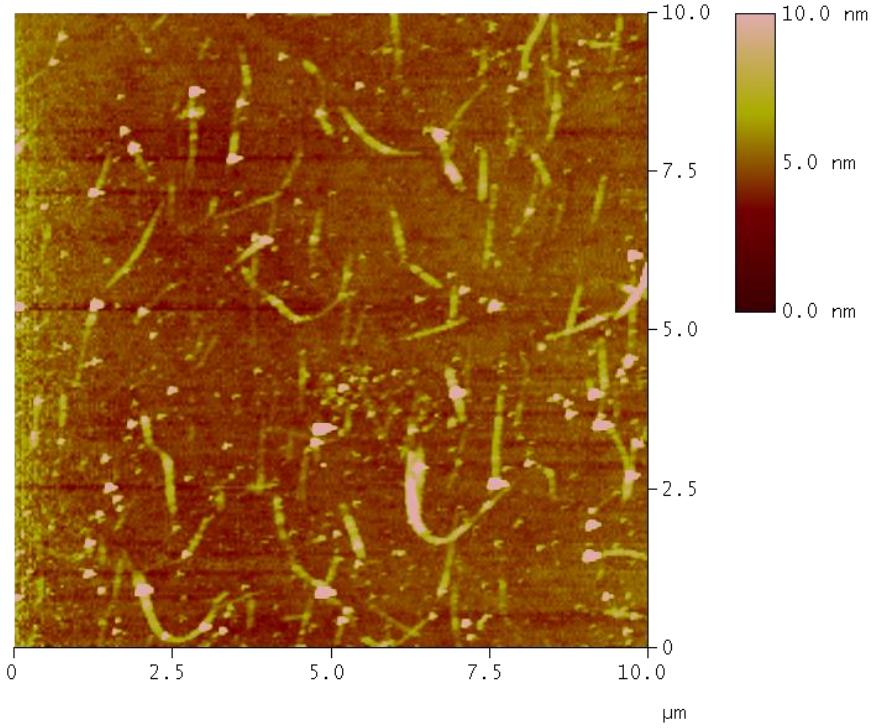

S38: AFM of SWNTs on ITO with 8CB and 2, area 1

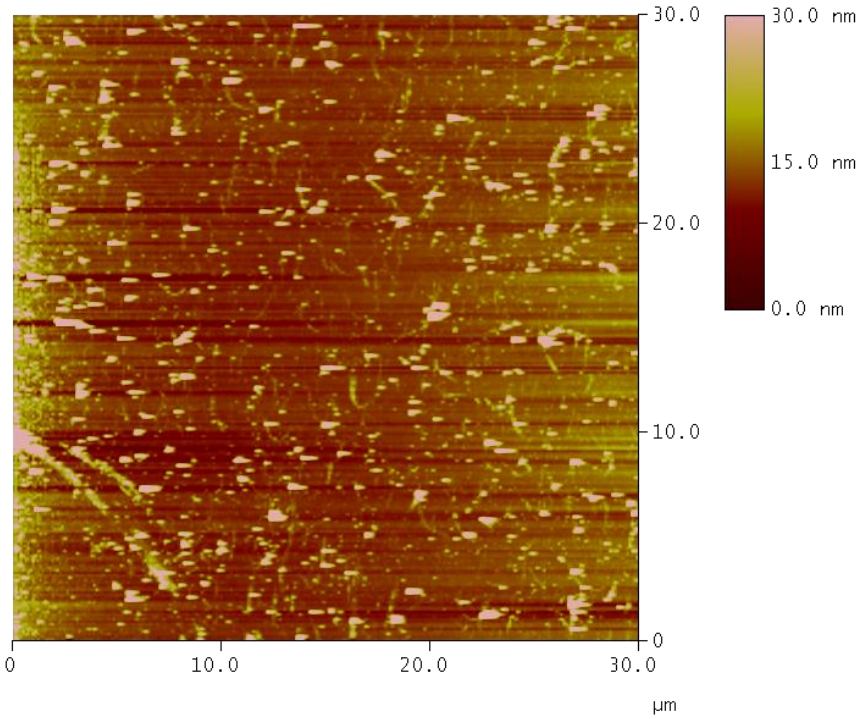

S39: AFM of SWNTs on ITO with 8CB and 2, area 2

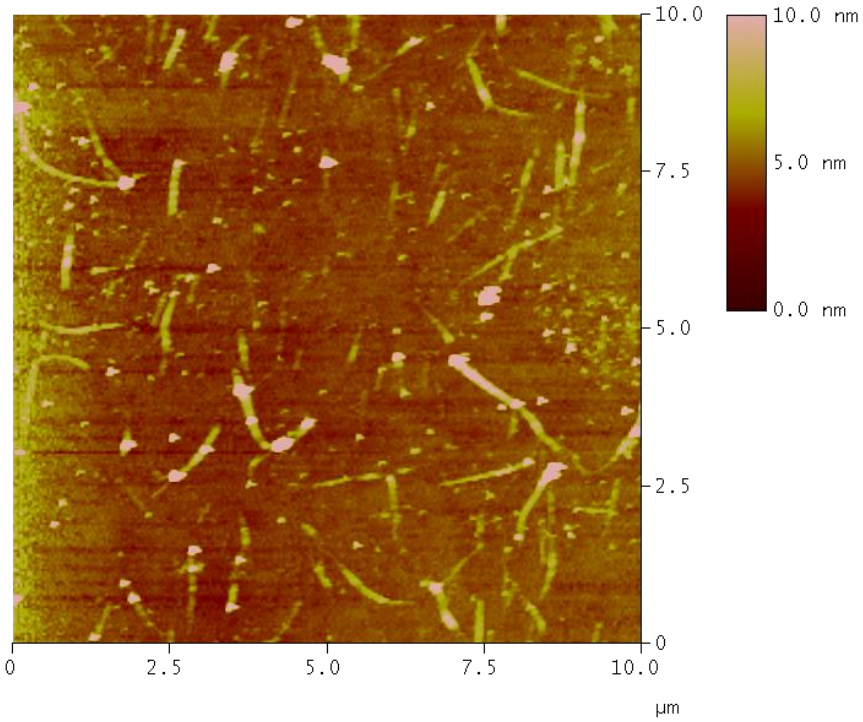

S40: AFM of SWNTs on ITO with 8CB and 2, area 3

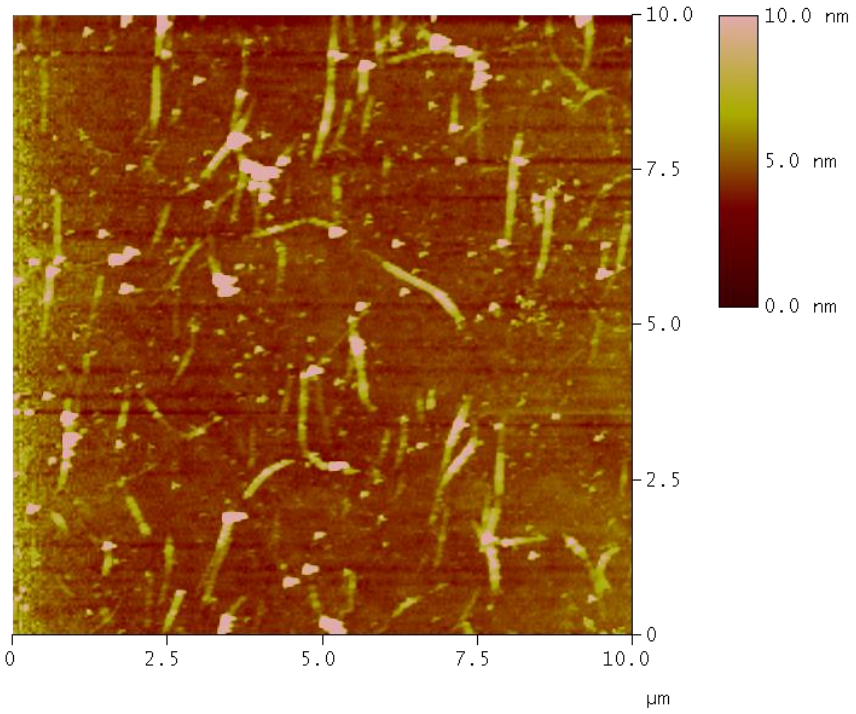

S41: AFM of SWNTs on ITO with 8CB and 2, area 4

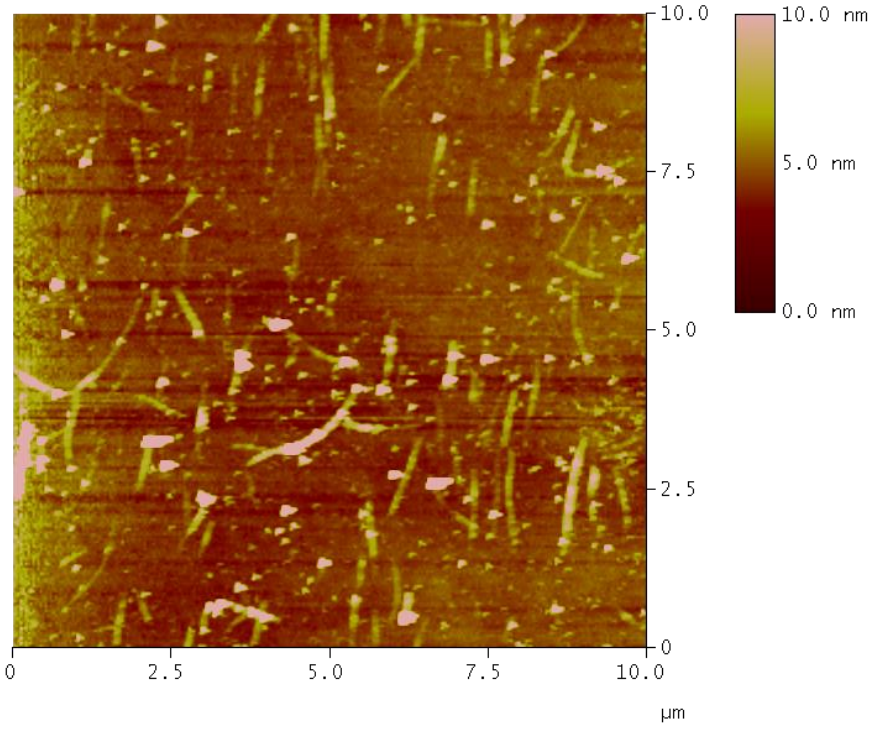

S42: AFM of SWNTs on ITO with 8CB and 2, area 5

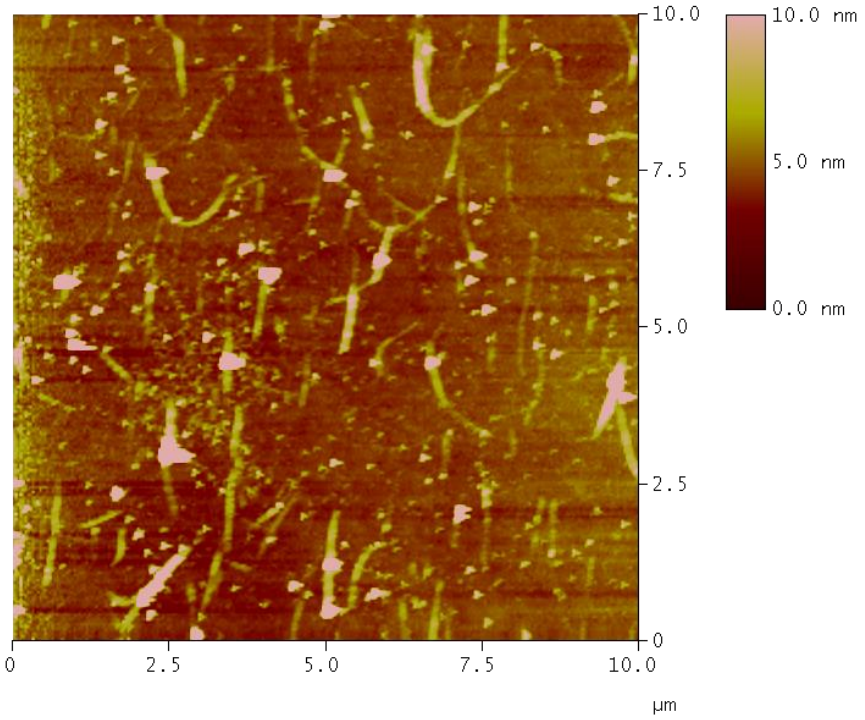

S43: AFM of SWNTs on ITO with 8CB and 2, area 6

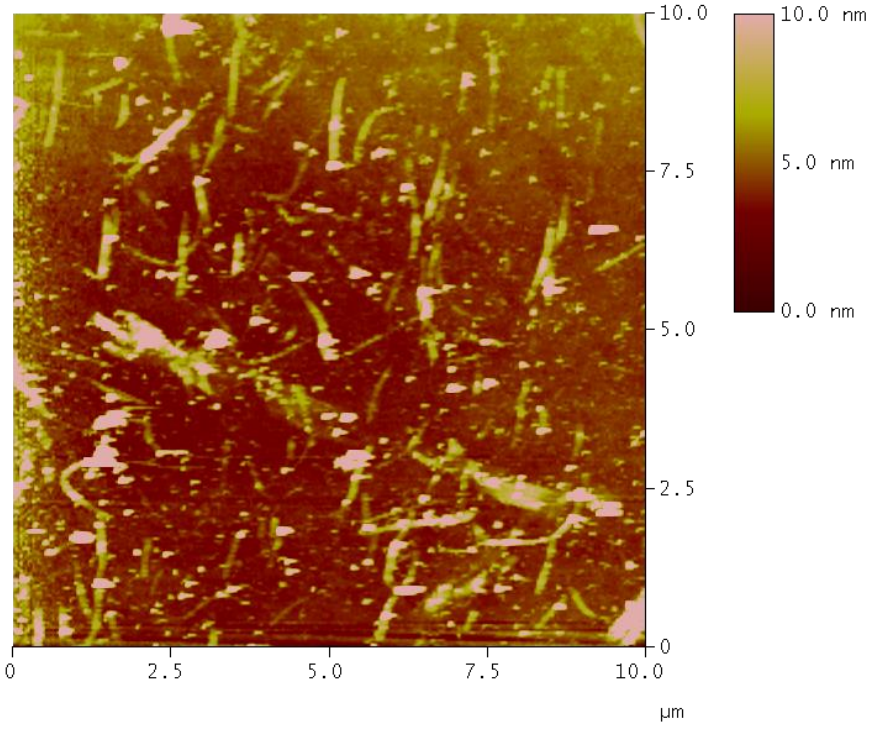

S44: AFM of SWNTs on ITO with 8CB and 2, area 7

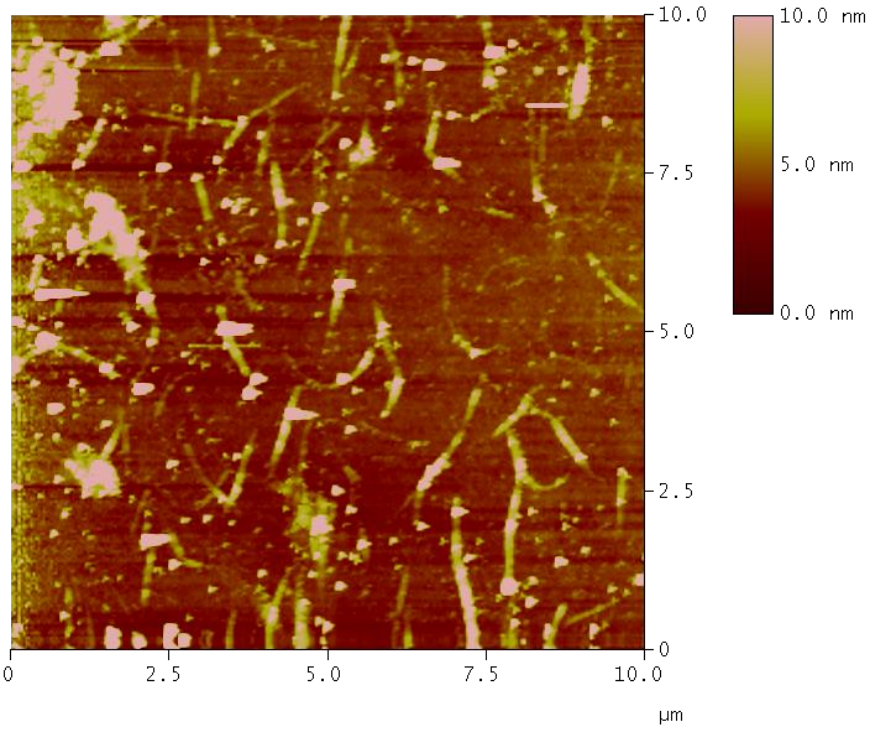

S45: AFM of SWNTs on ITO with 8CB and 2, area 8

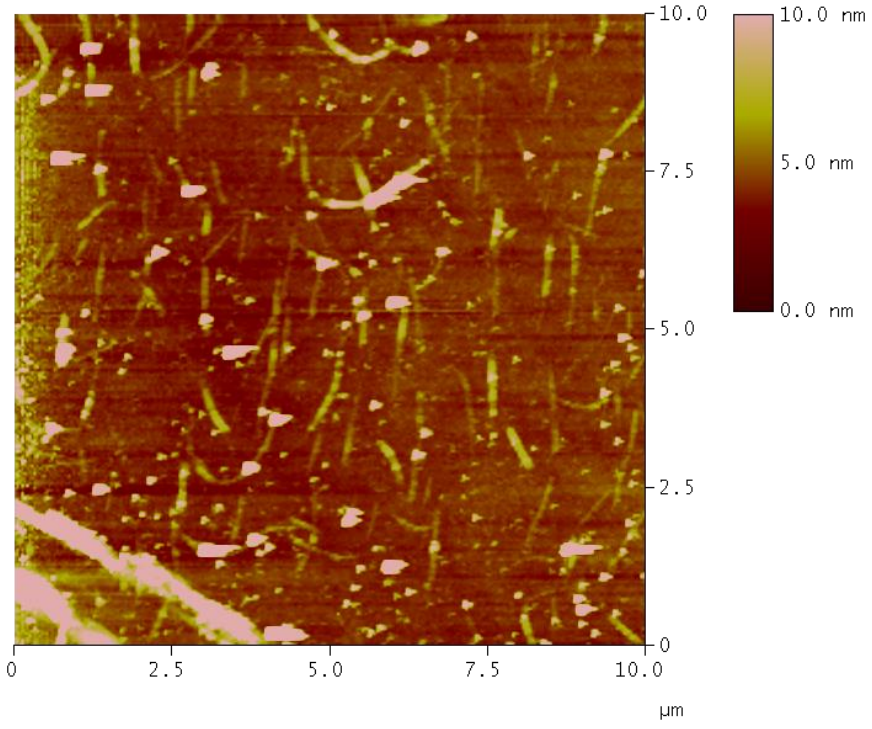

S46: AFM of SWNTs on ITO with 8CB and 2, area 9

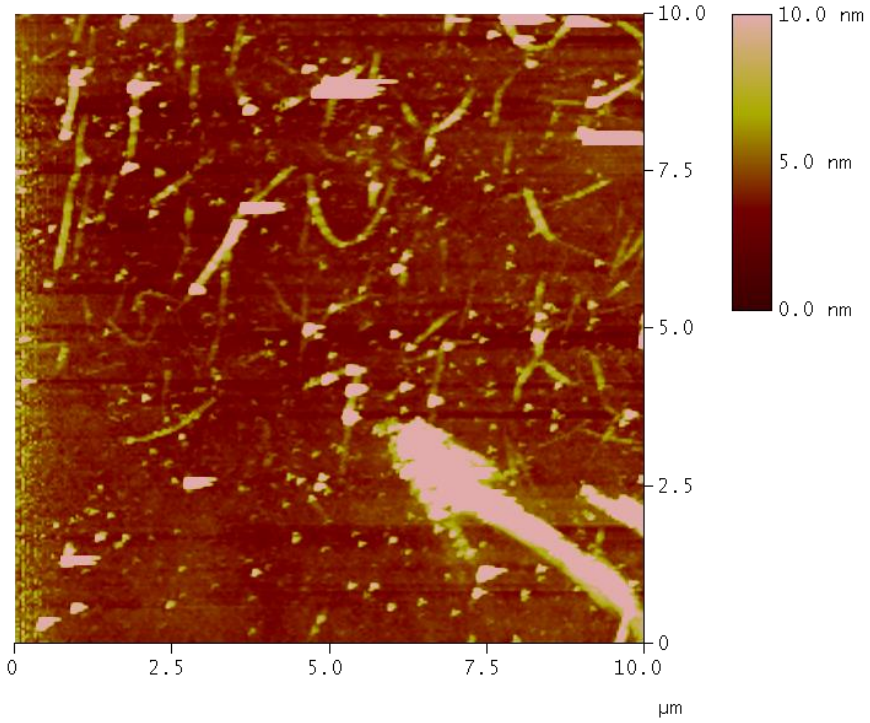

S47: AFM of SWNTs on ITO with 8CB and 2, area 10

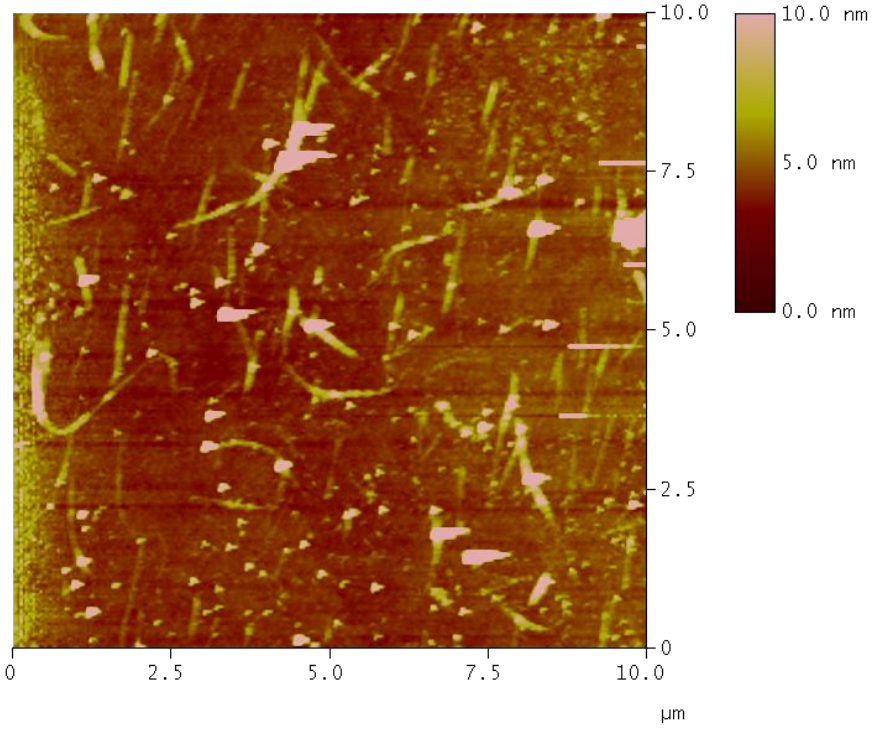

S48: AFM of SWNTs on ITO with 8CB and 2, area 11

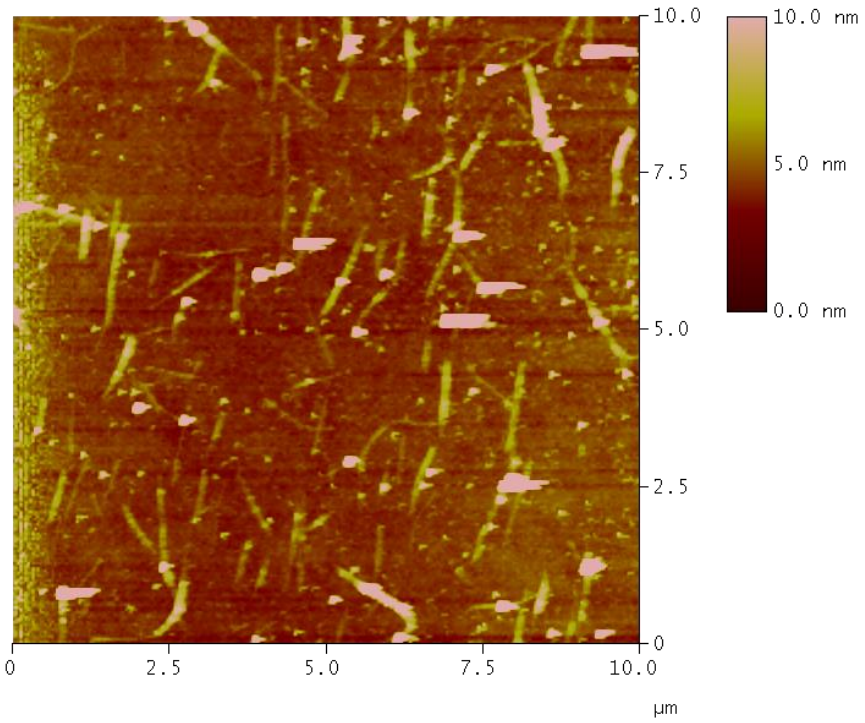

S49: AFM of SWNTs on ITO with 8CB and 2, area 12

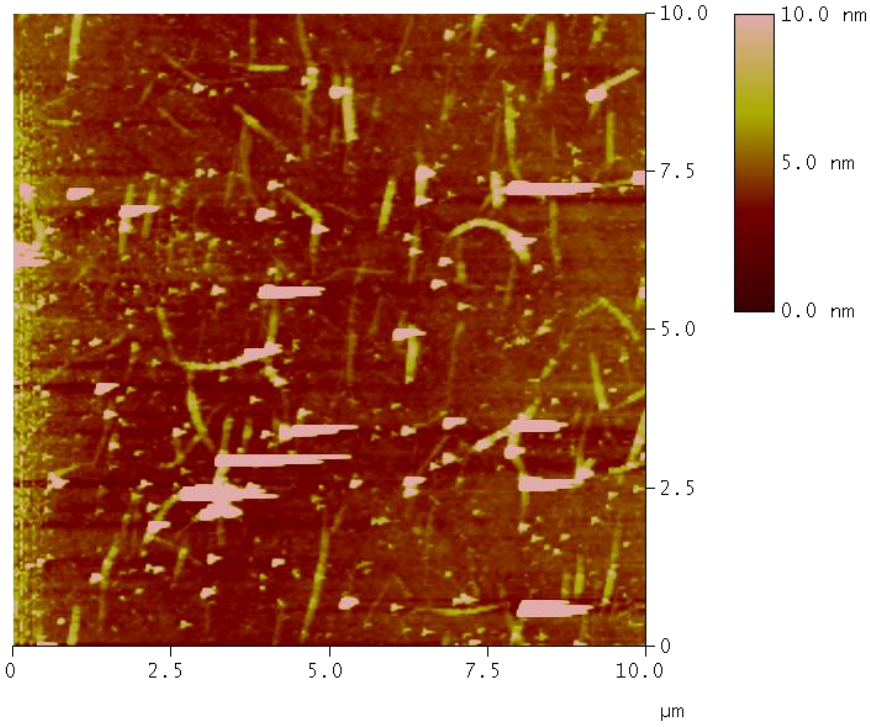

S50: AFM of SWNTs on ITO with 8CB and 2, area 13

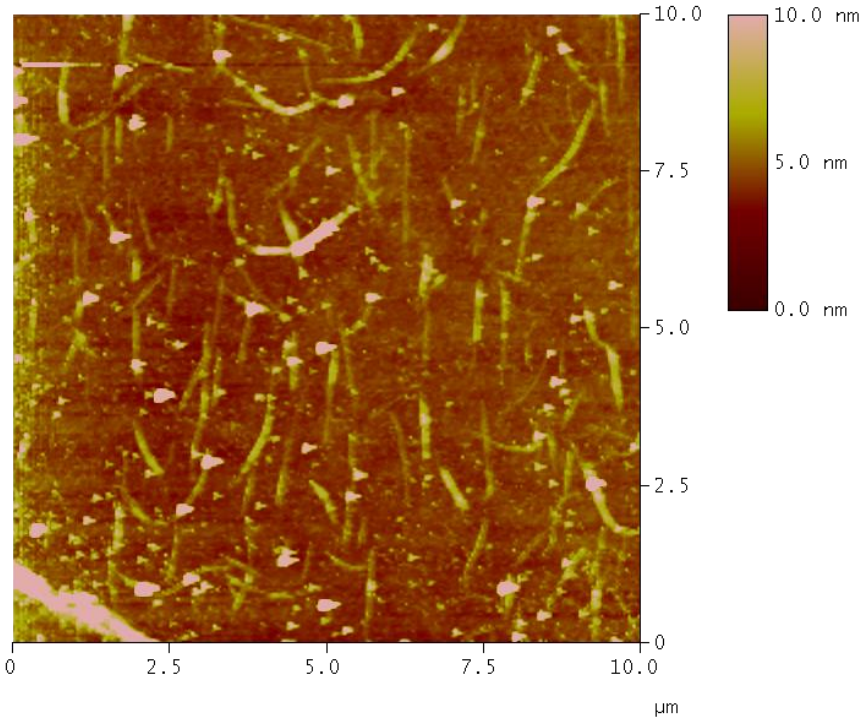

S51: AFM of SWNTs on ITO with 8CB and 2, area 14

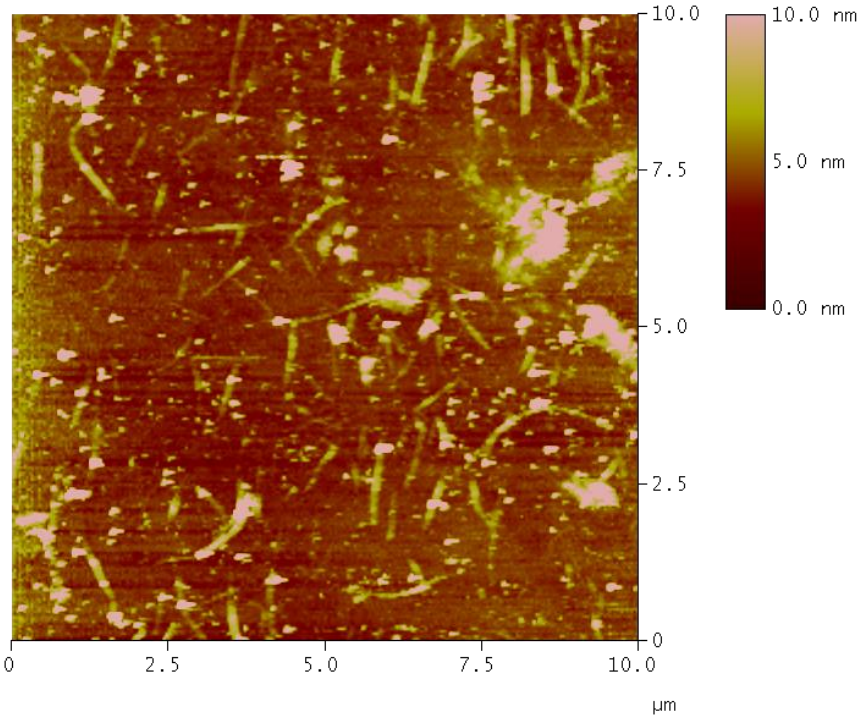

S52: AFM of SWNTs on ITO with 8CB and 2, area 15

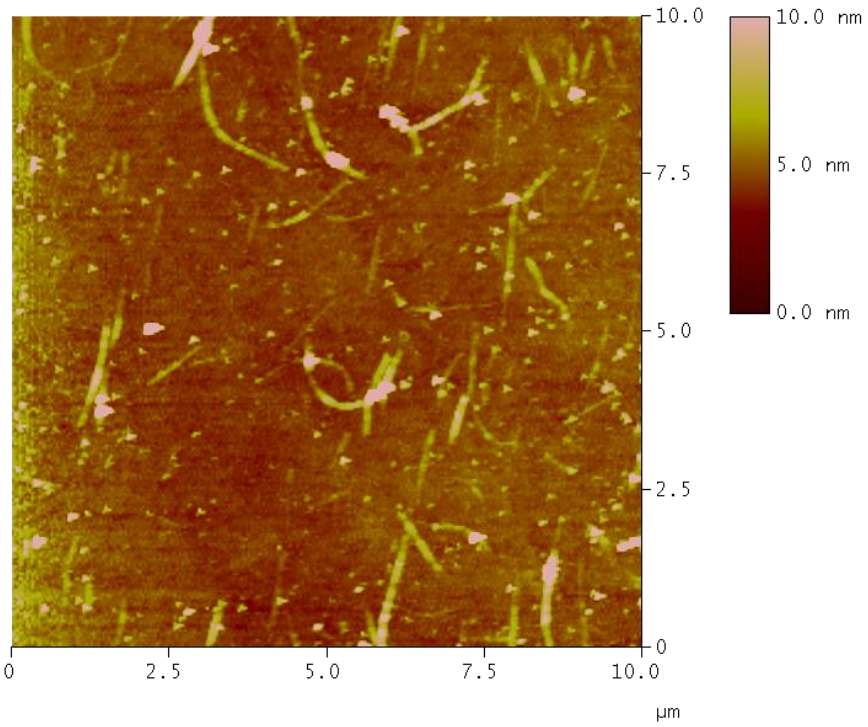

S53: AFM of SWNTs on ITO with 8CB and 2, area 16

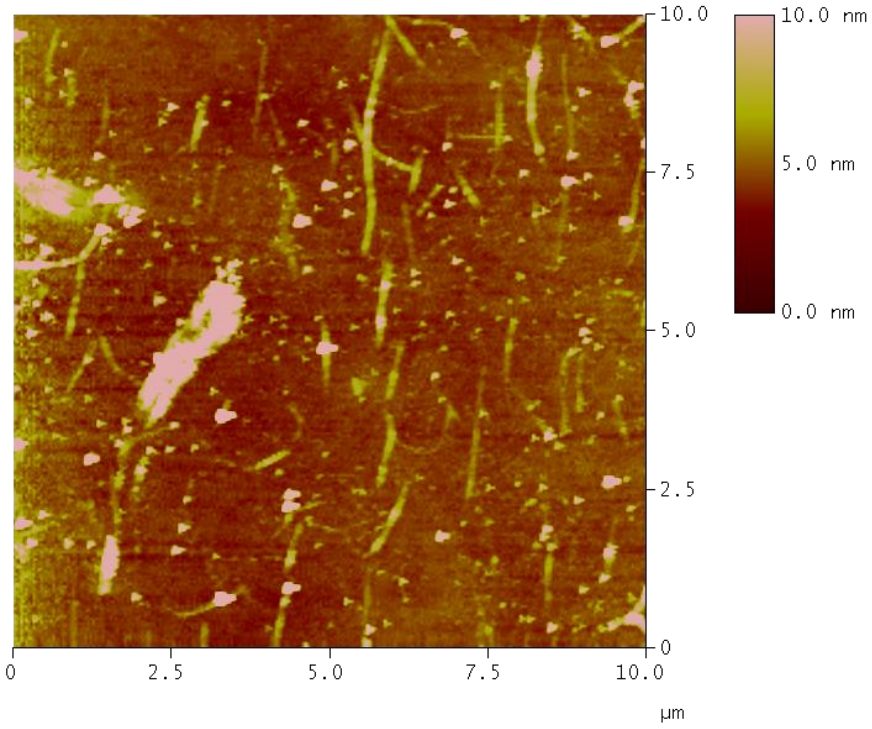

S54: AFM of SWNTs on ITO with 8CB and 2, area 17

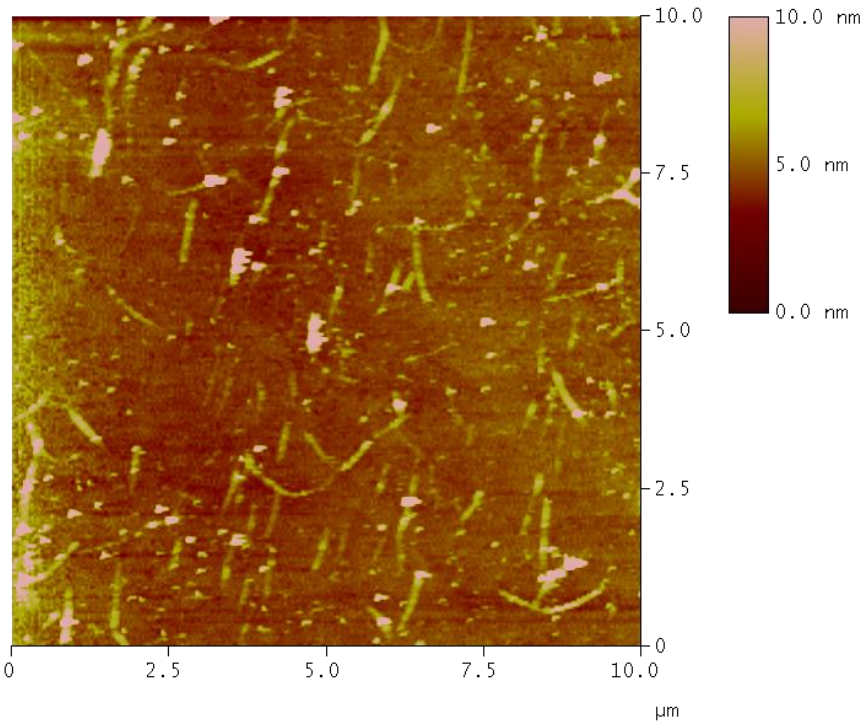

S55: AFM of SWNTs on ITO with 8CB and 2, area 18

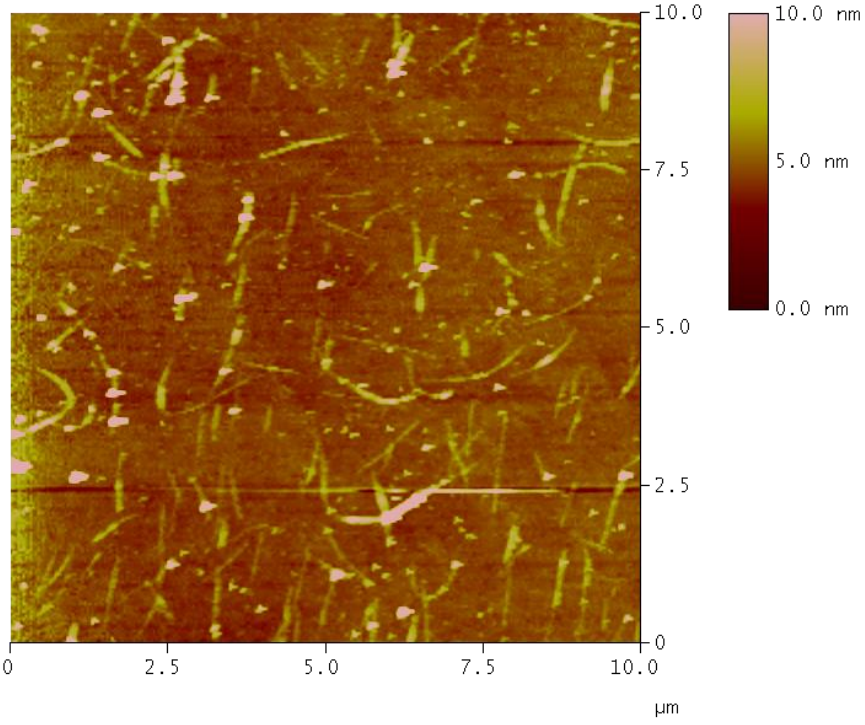

S56: AFM of SWNTs on ITO with 8CB and 2, area 19

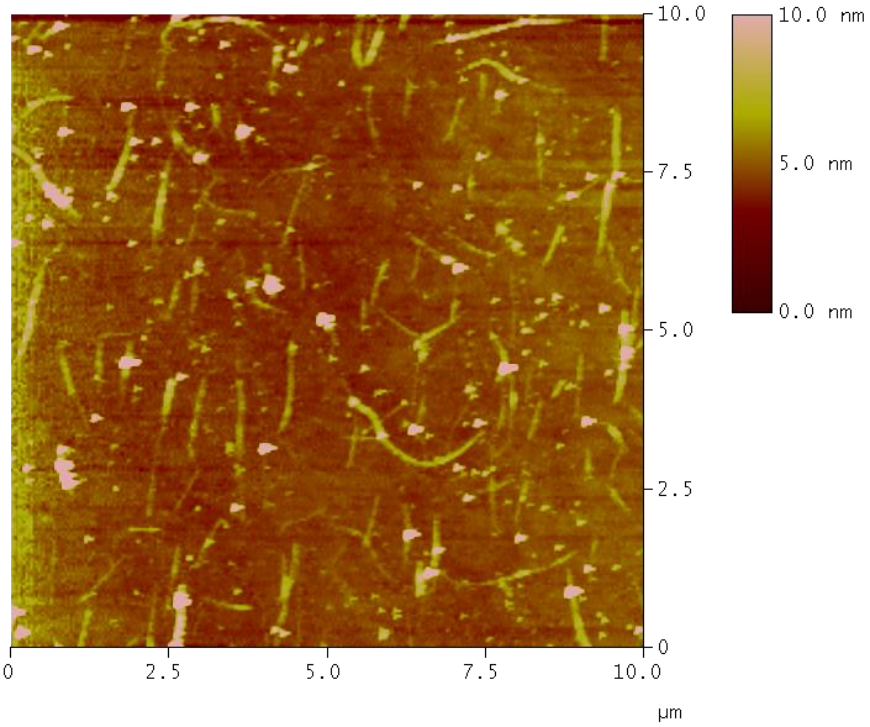

S57: AFM of SWNTs on ITO with 8CB and 2, area 20

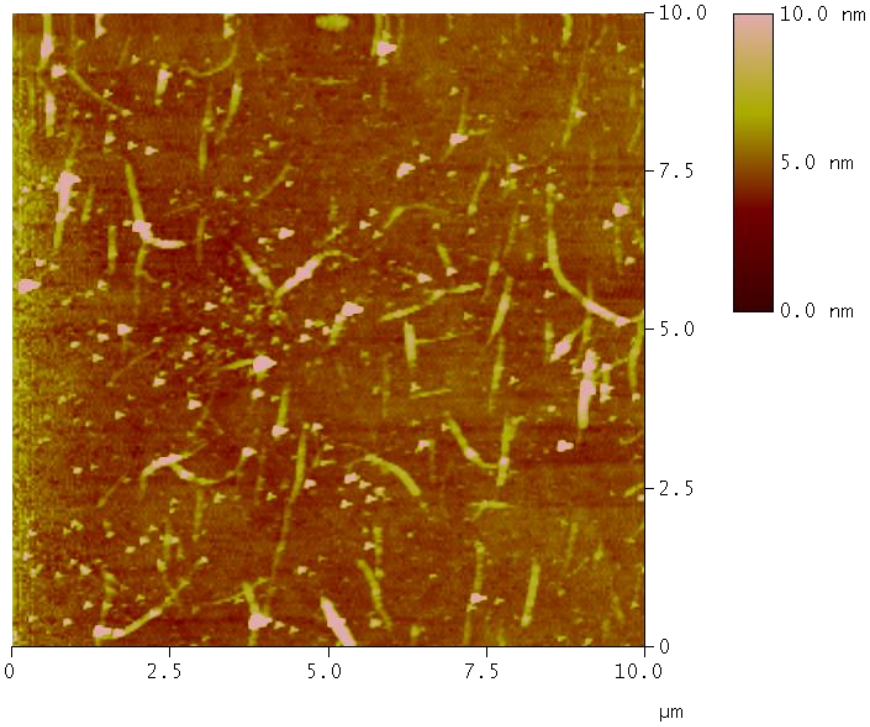

S58: AFM of SWNTs on ITO with 8CB and 2, area 21

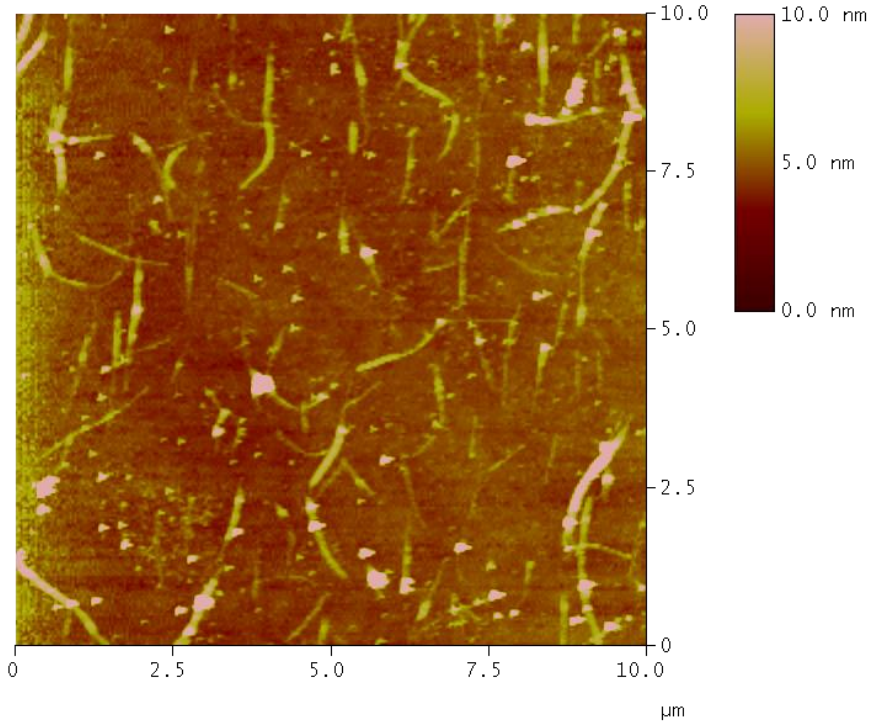

S59: AFM of SWNTs on ITO with 8CB and 2, area 22

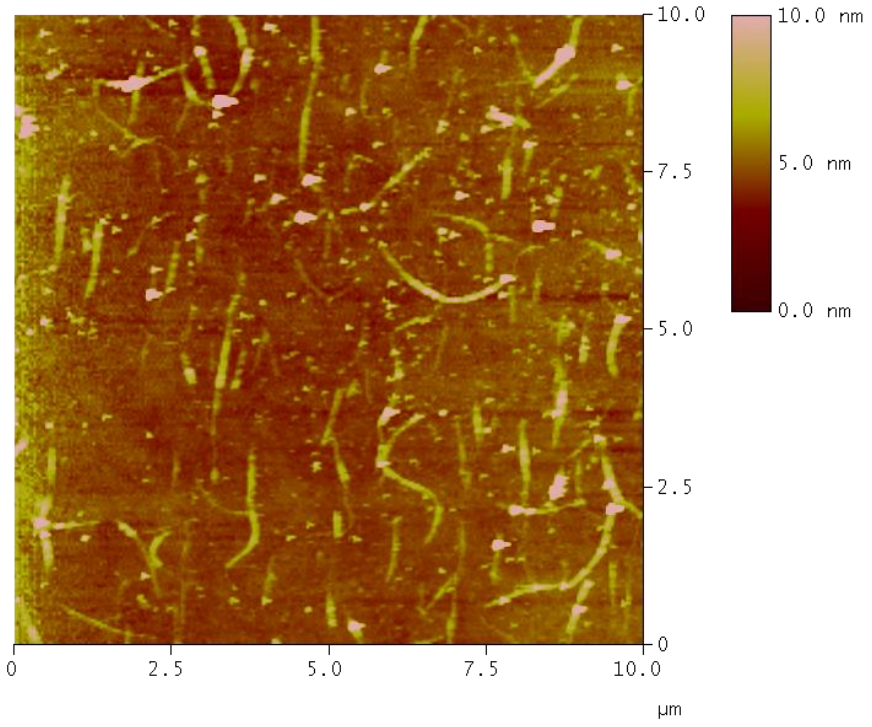

S60: AFM of SWNTs on ITO with 8CB and 2, area 23

8.4 Atomic Force Micrographs of ART-Deposited SWNTs on a Silicon Dioxide Surface with 4-cyano-4'-octylbiphenyl and tetraethyl (5,7,9,14,16,18-hexahydro-5,18:9,14-bis([1,2]benzeno)-7,16-ethenoheptacene-25,26-diyl)bis(phosphonate) (2)

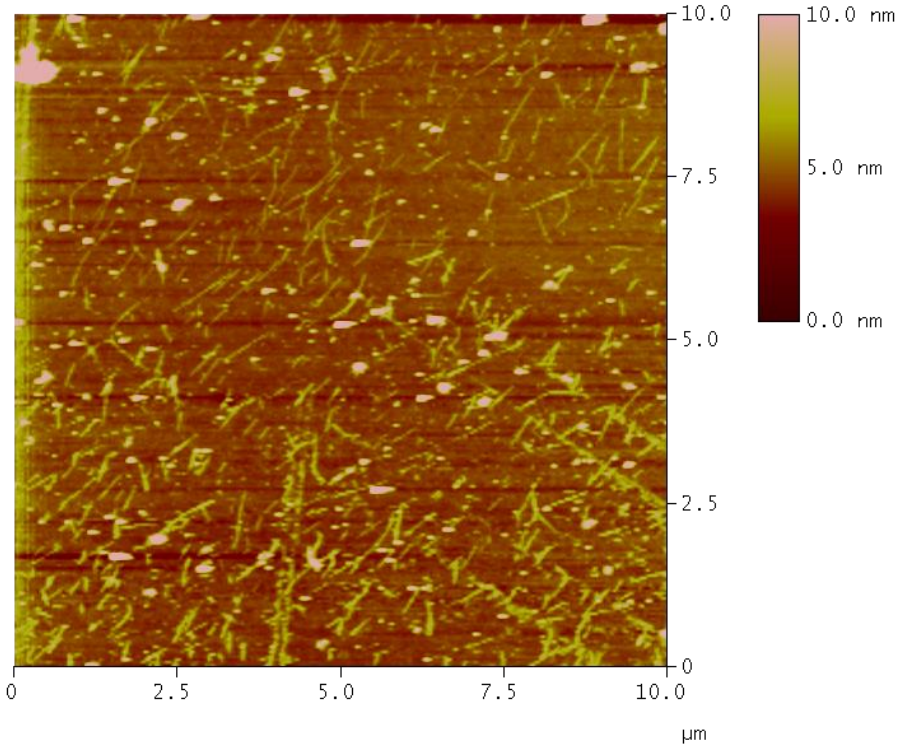

S61: AFM of SWNTs on SiO_2 with 8CB and 2, area 1

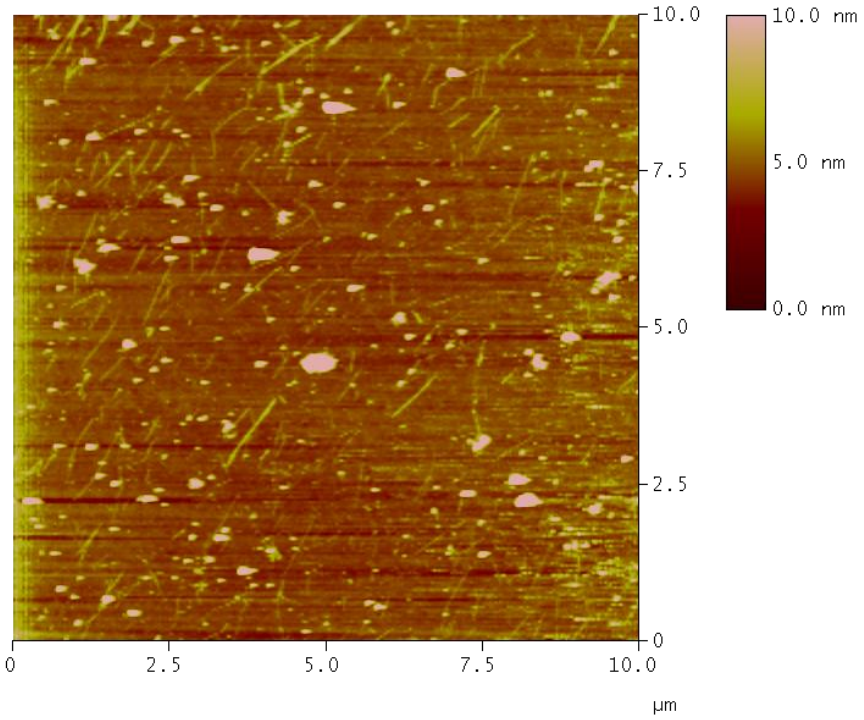

S62: AFM of SWNTs on SiO_2 with 8CB and 2, area 2

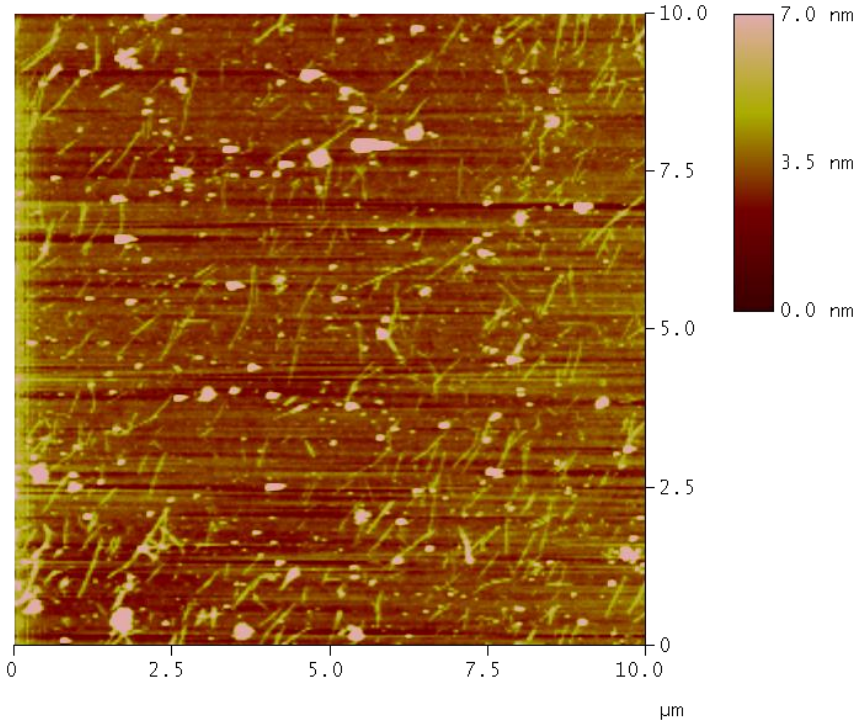

S63: AFM of SWNTs on SiO_2 with 8CB and 2, area 3

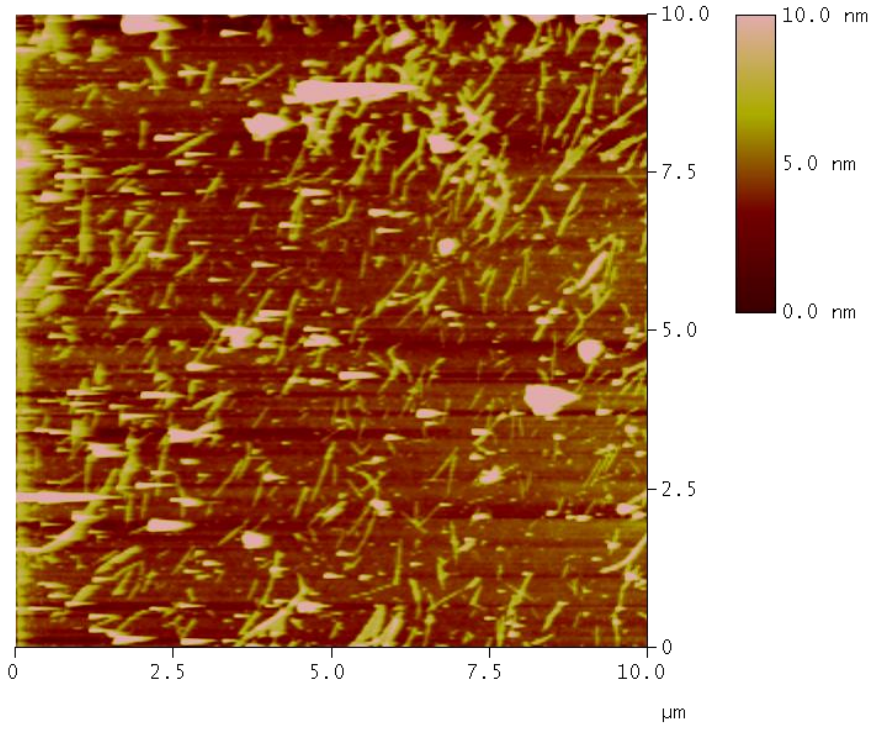

S64: AFM of SWNTs on SiO_2 with 8CB and 2, area 4

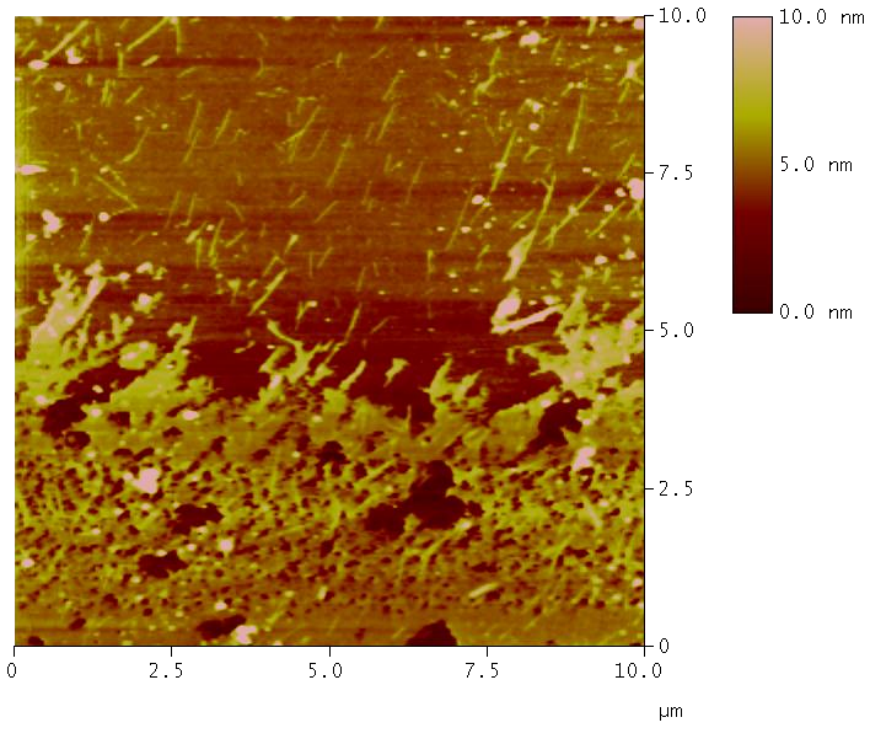

S65: AFM of SWNTs on SiO_2 with 8CB and 2, area 5

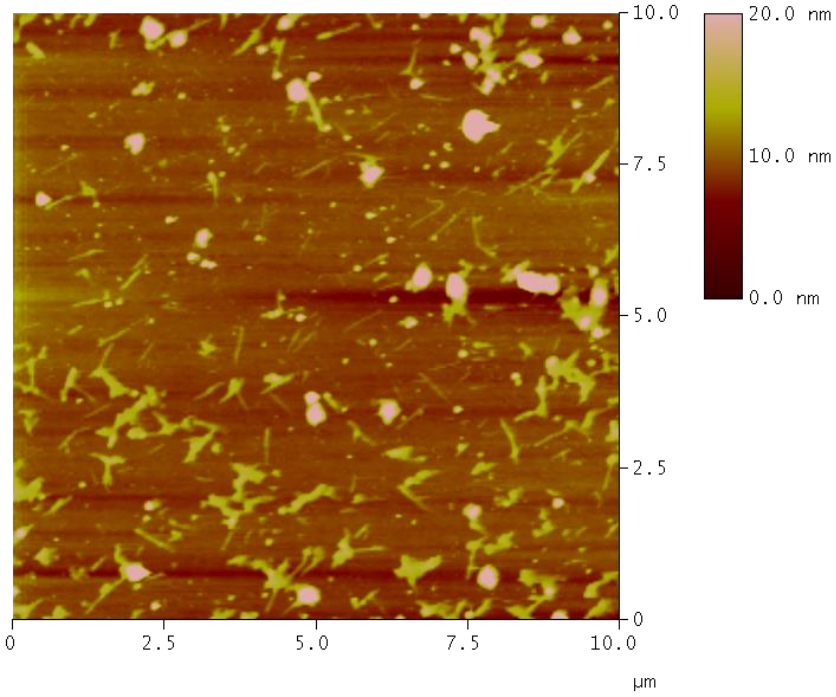

S66: AFM of SWNTs on SiO_2 with 8CB and 2, area 6

8.5 Atomic Force Micrographs of ART-Deposited SWNTs on an Indium Tin Oxide Surface with 4-cyano-4'-octylbiphenyl and tetraethyl (6,8,10,17,19,21-hexahydro-6,21:10,17-bis([2,3]naphthaleno)-8,19-ethenononacene-31,32-diyl)bis(phosphonate) (16)

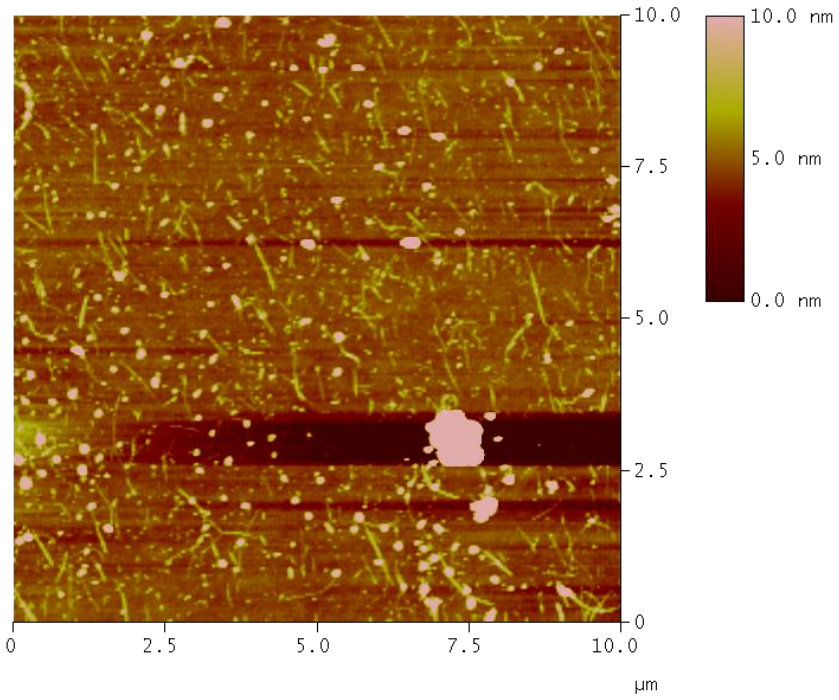

S67: AFM of SWNTs on ITO with 8CB and 16, area 1

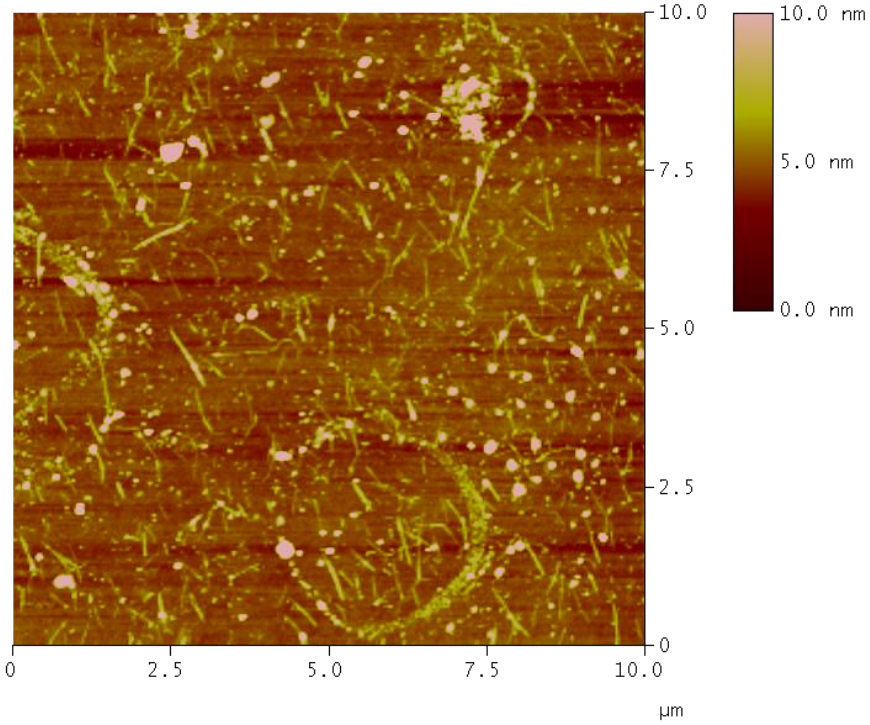

S68: AFM of SWNTs on ITO with 8CB and 16, area 2

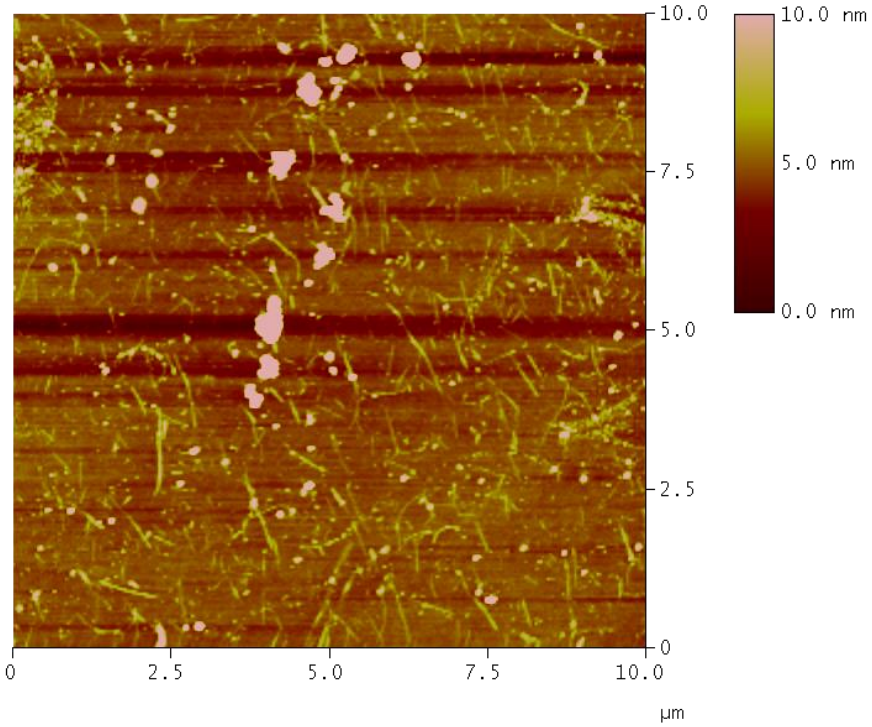

S69: AFM of SWNTs on ITO with 8CB and 16, area 3

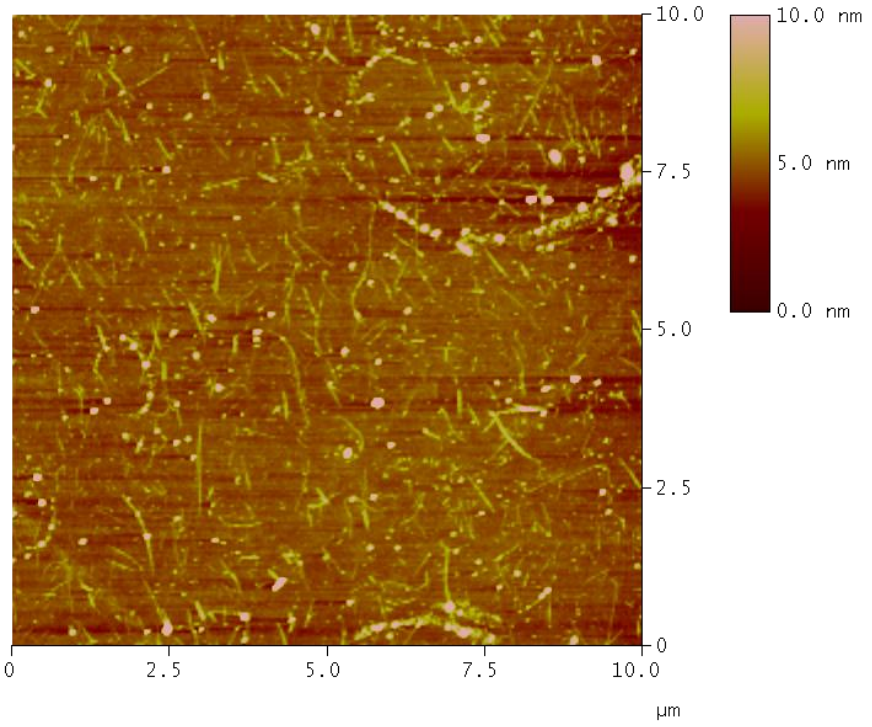

S70: AFM of SWNTs on ITO with 8CB and 16, area 4

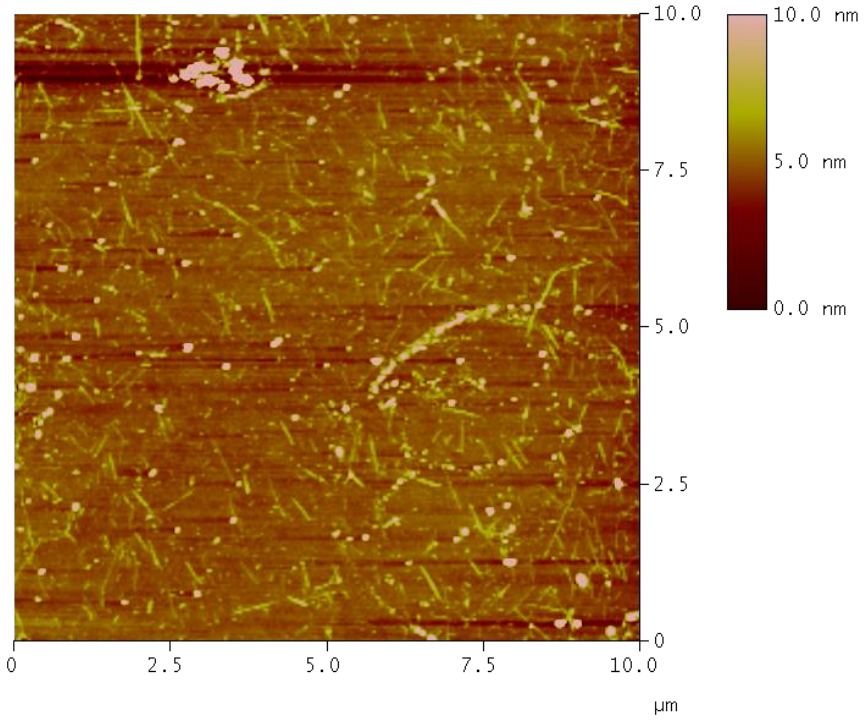

S71: AFM of SWNTs on ITO with 8CB and 16, area 5

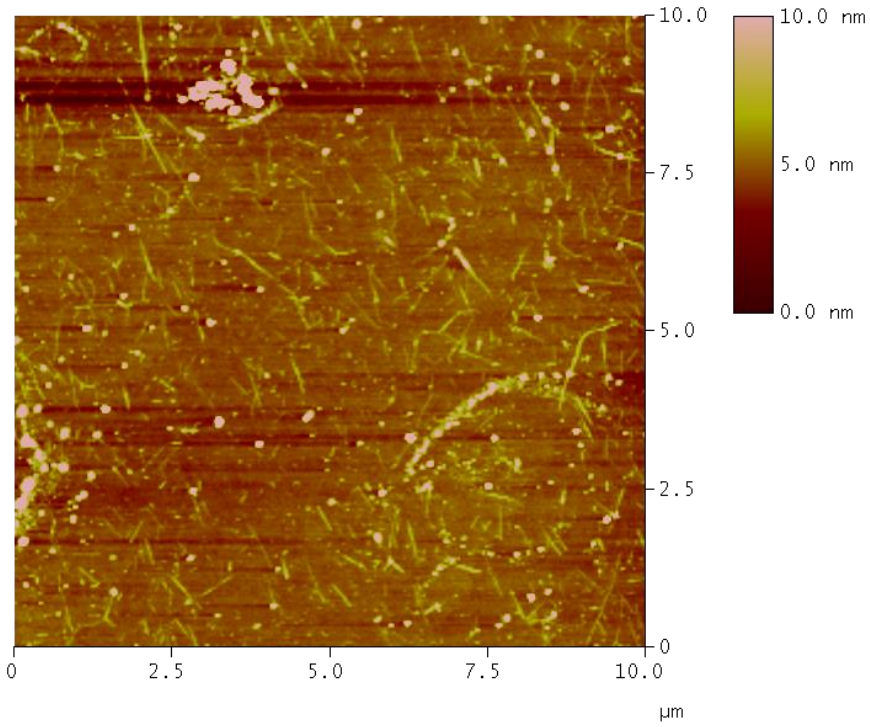

S72: AFM of SWNTs on ITO with 8CB and 16, area 6

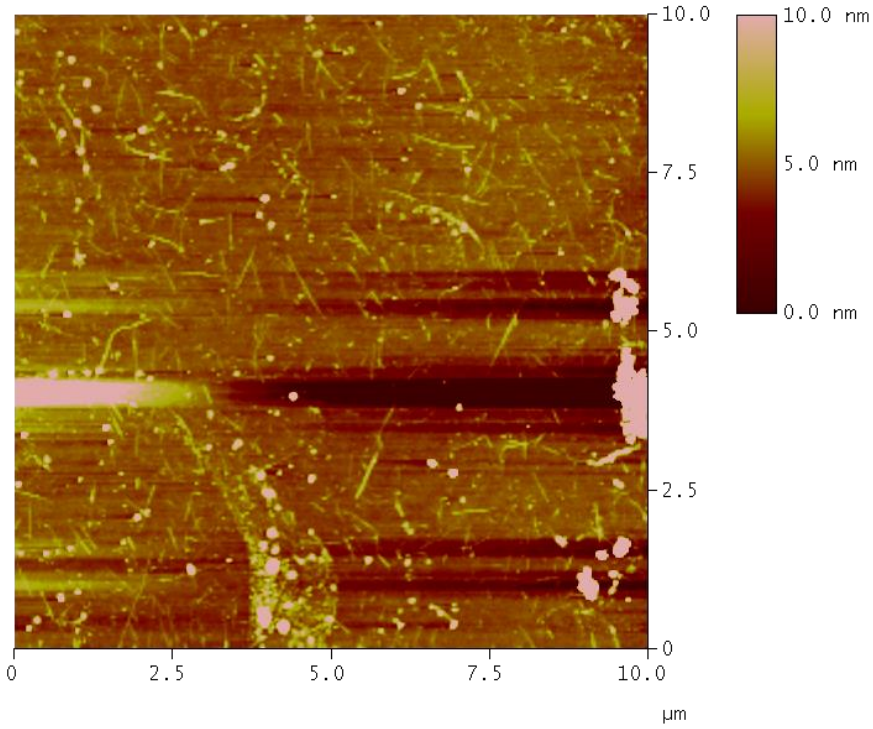

S73: AFM of SWNTs on ITO with 8CB and 16, area 7

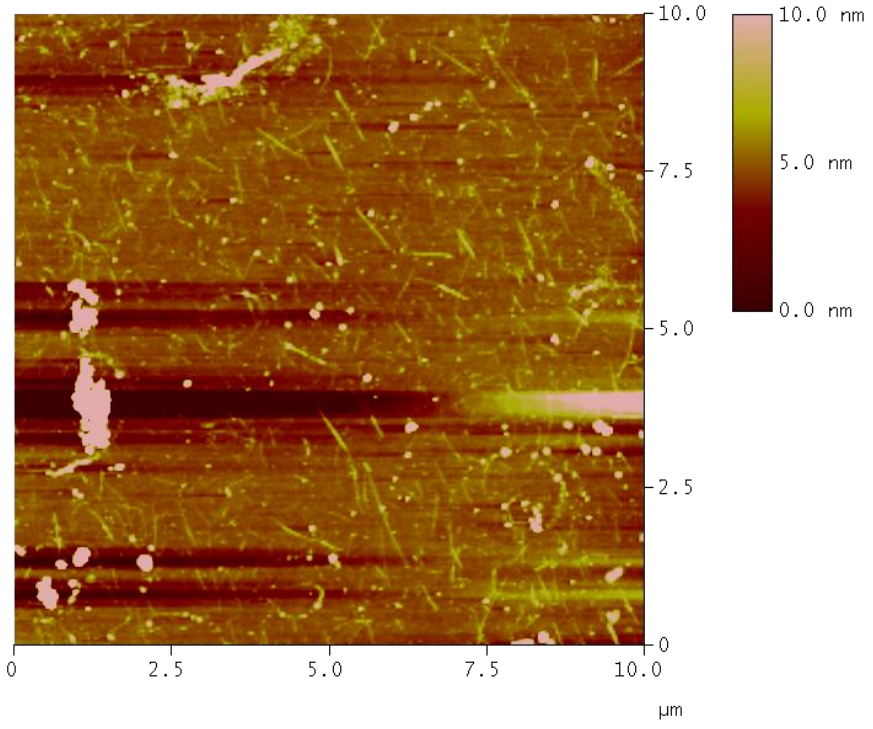

S74: AFM of SWNTs on ITO with 8CB and 16, area 8

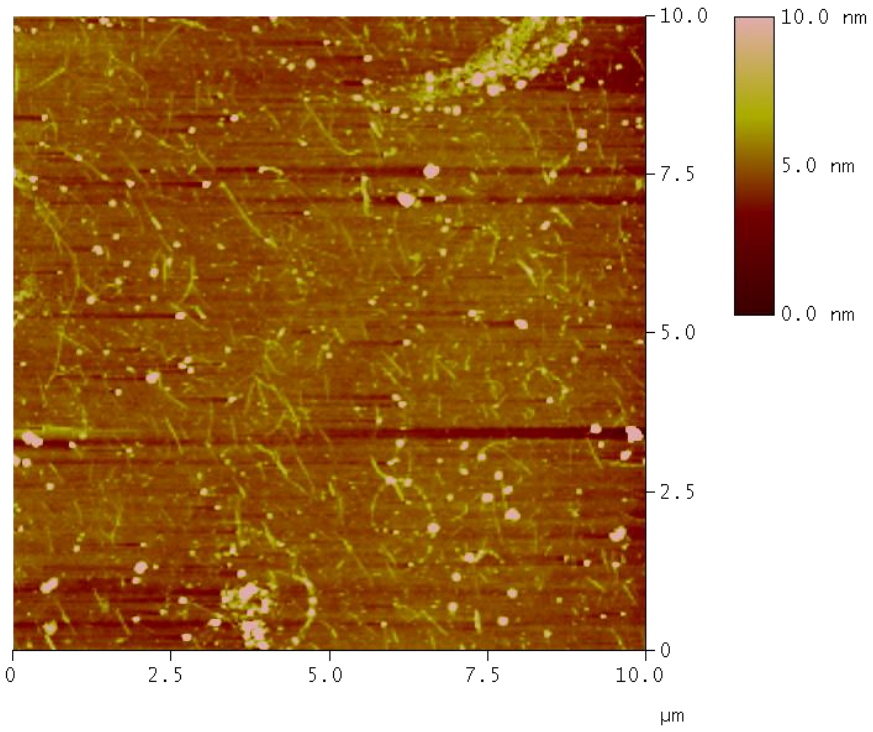

S75: AFM of SWNTs on ITO with 8CB and 16, area 9

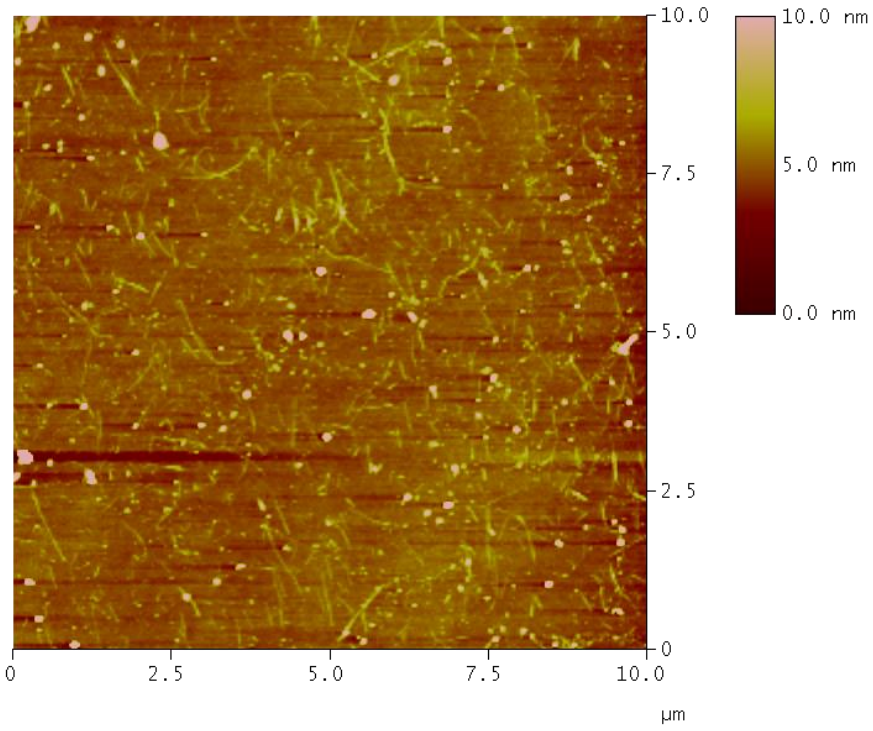

S76: AFM of SWNTs on ITO with 8CB and 16, area 10

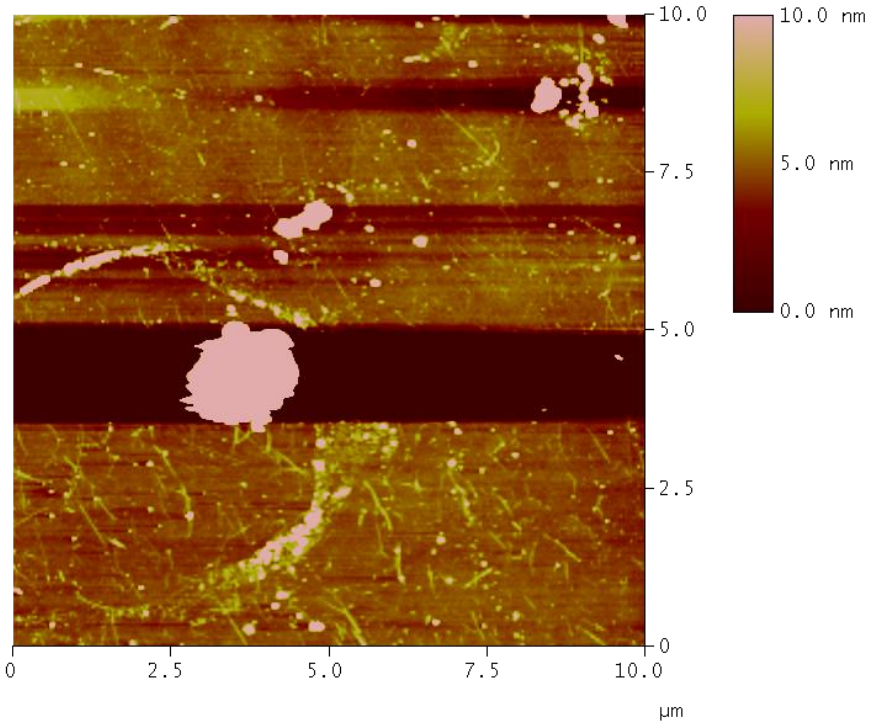

S77: AFM of SWNTs on ITO with 8CB and 16, area 11

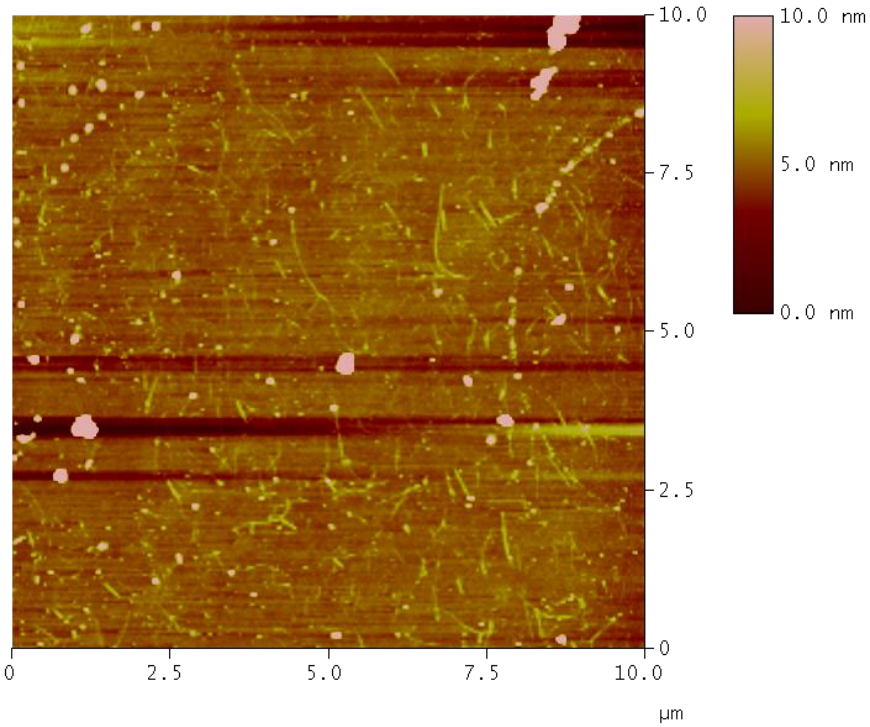

S78: AFM of SWNTs on ITO with 8CB and 16, area 12

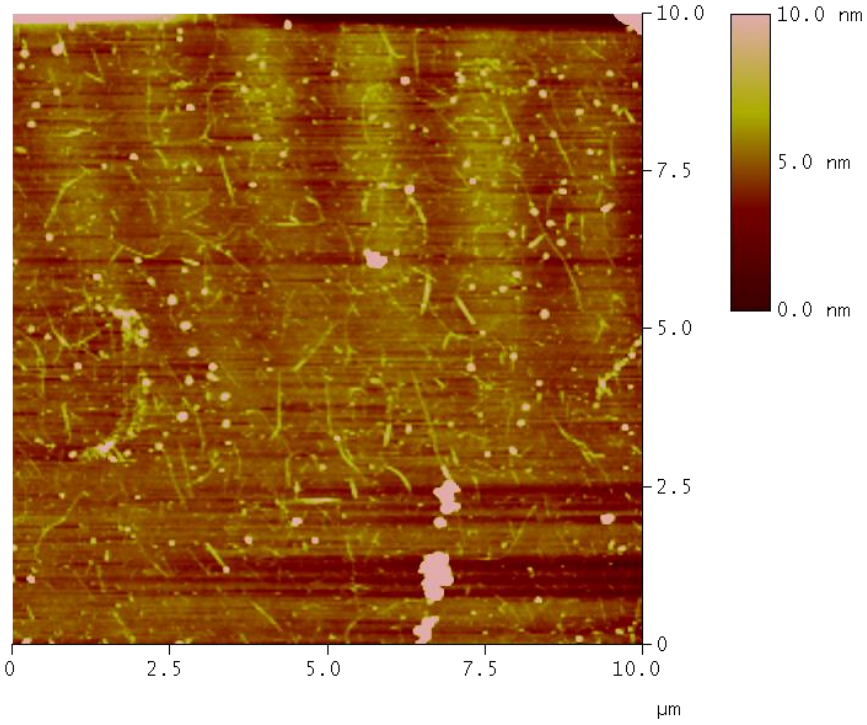

S79: AFM of SWNTs on ITO with 8CB and 16, area 13

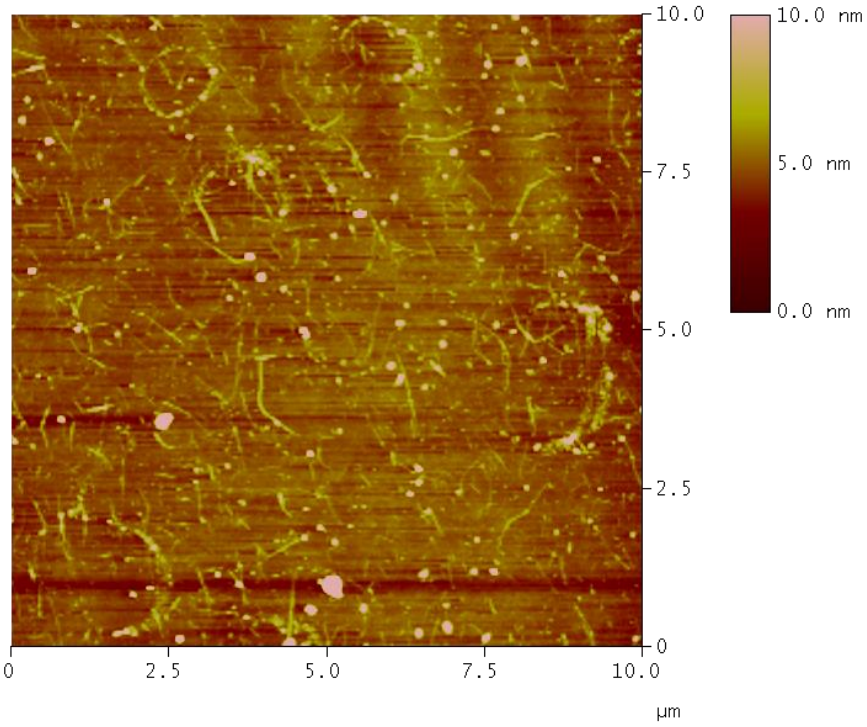

S80: AFM of SWNTs on ITO with 8CB and 16, area 14

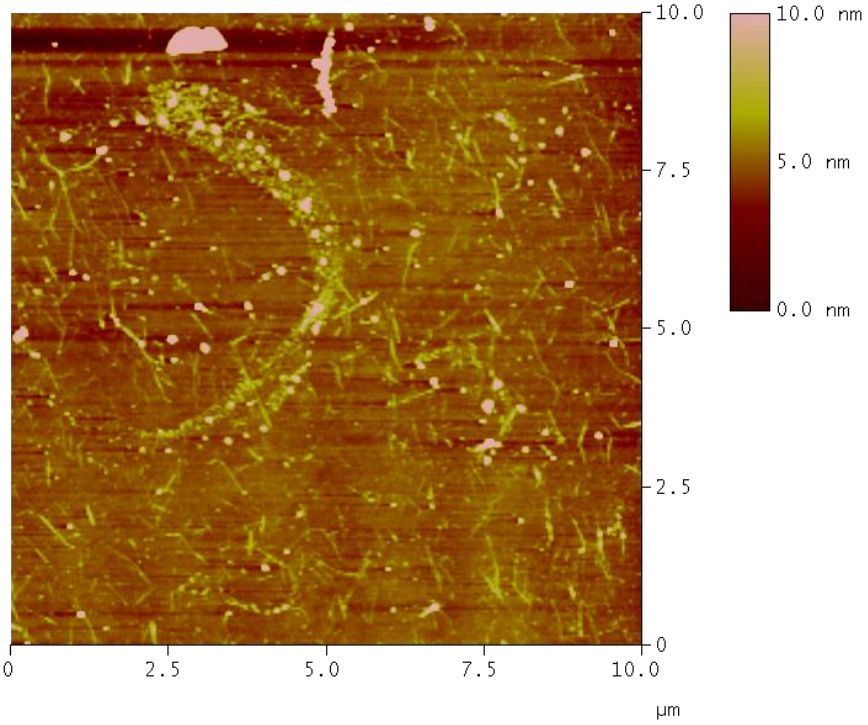

S81: AFM of SWNTs on ITO with 8CB and 16, area 15

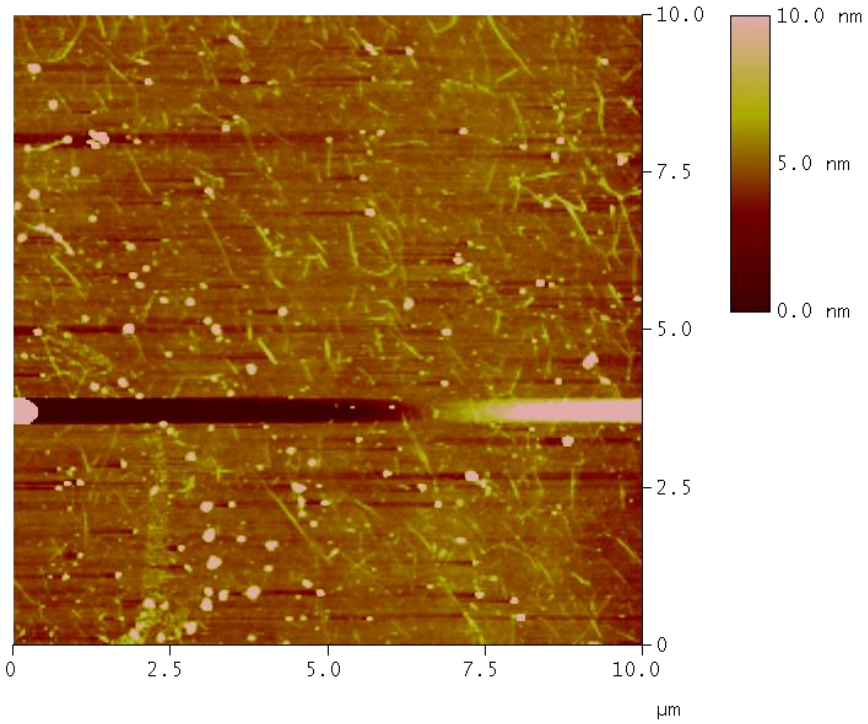

S82: AFM of SWNTs on ITO with 8CB and 16, area 16

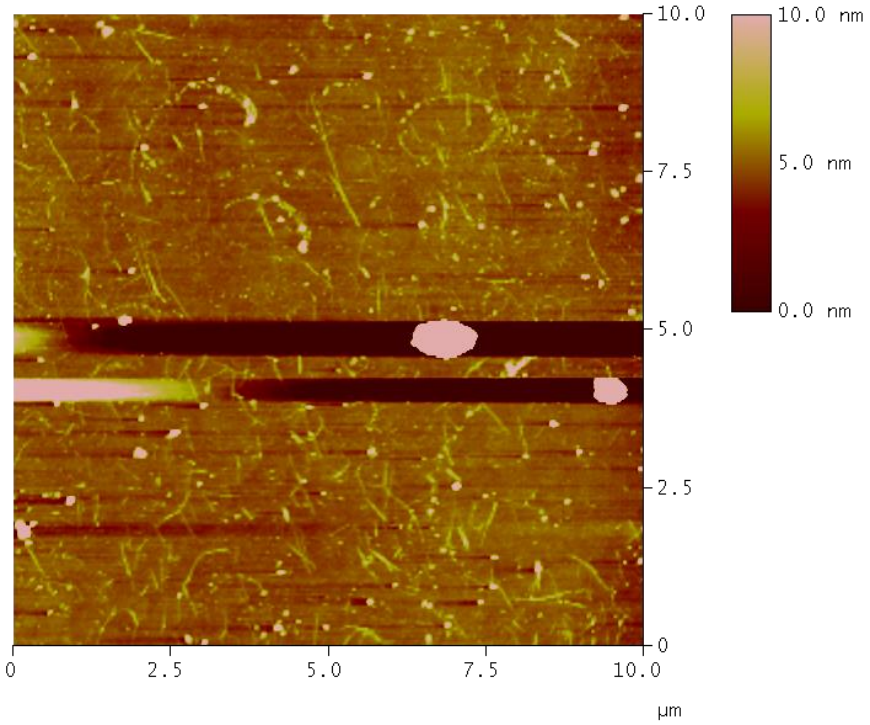

S83: AFM of SWNTs on ITO with 8CB and 16, area 17

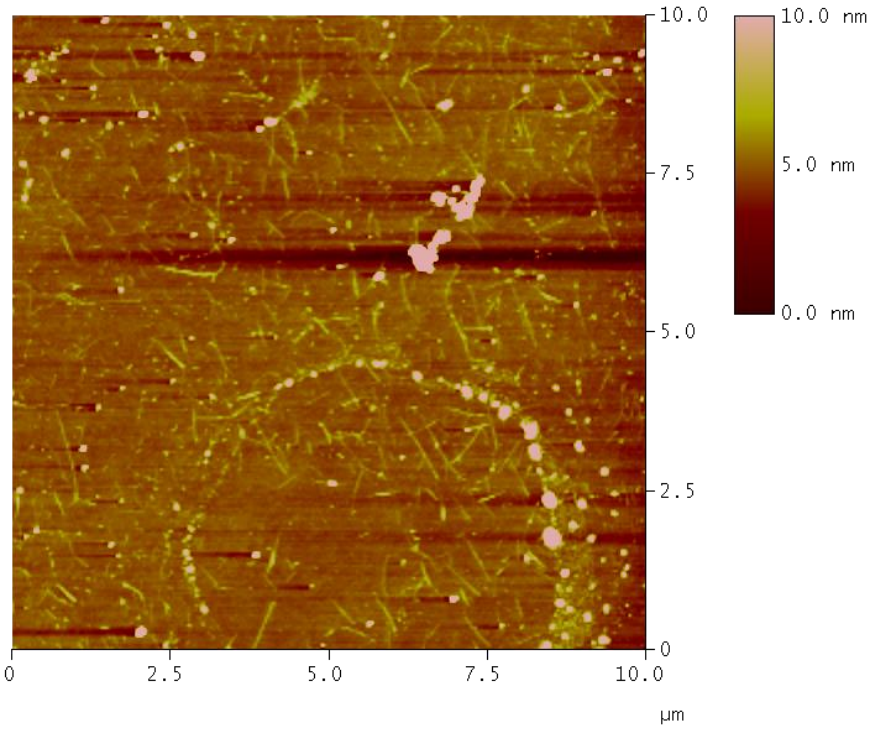

S84: AFM of SWNTs on ITO with 8CB and 16, area 18

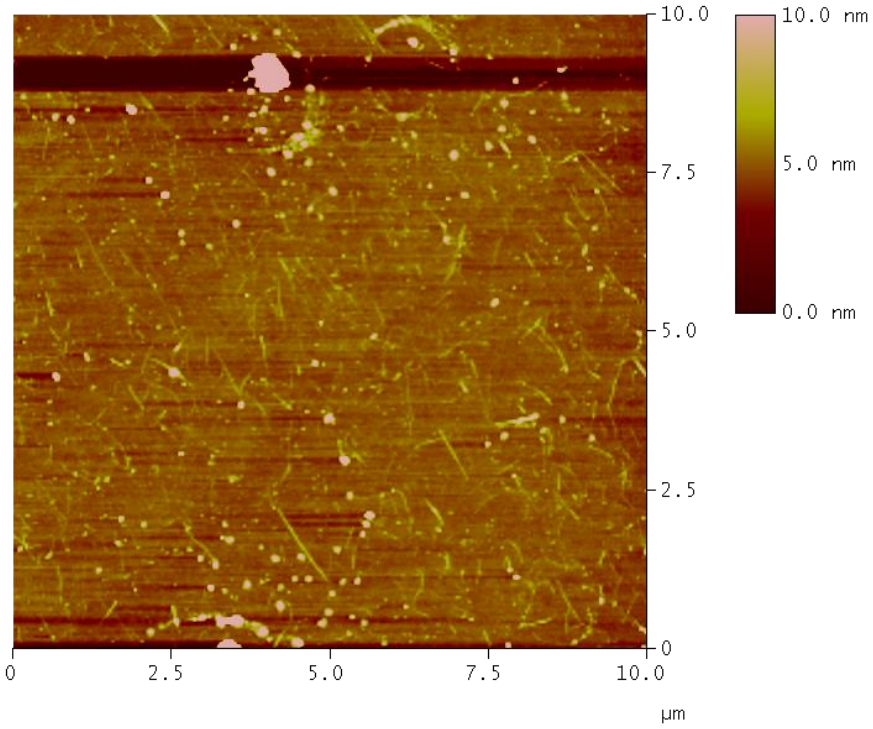

S85: AFM of SWNTs on ITO with 8CB and 16, area 19

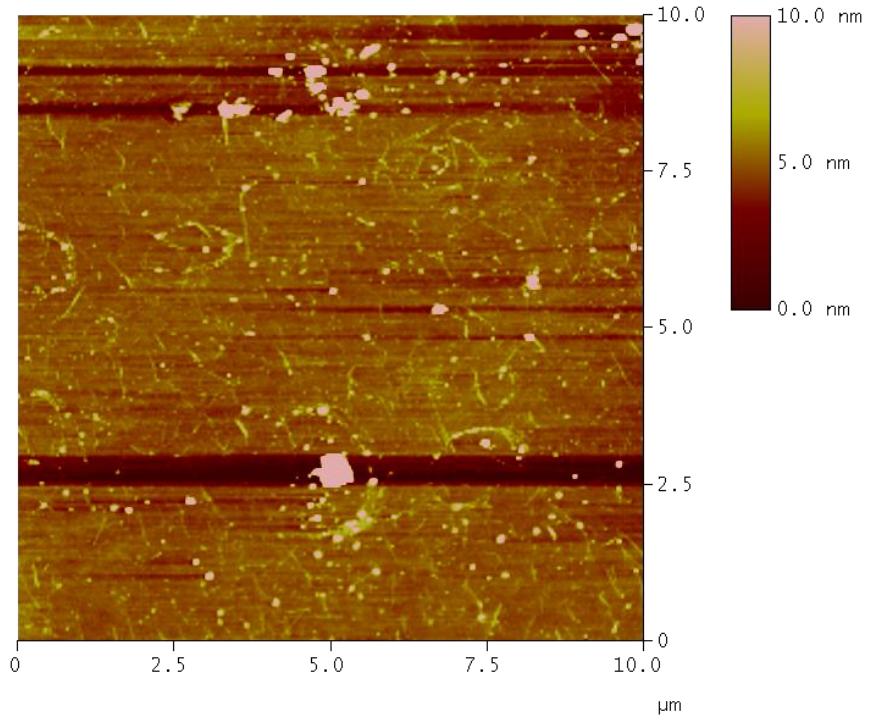

S86: AFM of SWNTs on ITO with 8CB and 16, area 20

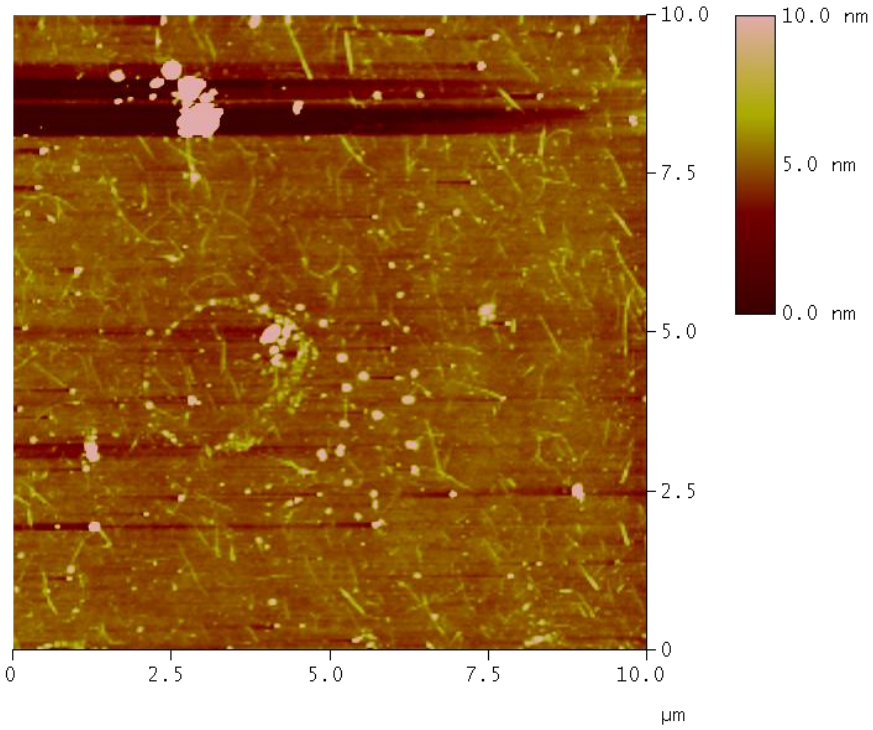

S87: AFM of SWNTs on ITO with 8CB and 16, area 21

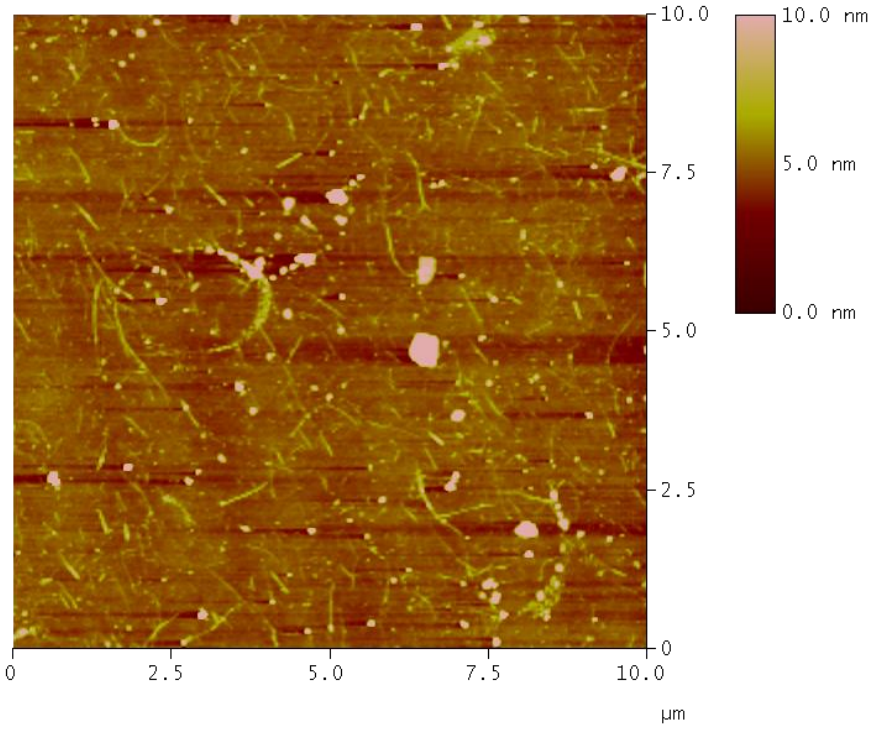

S88: AFM of SWNTs on ITO with 8CB and 16, area 22

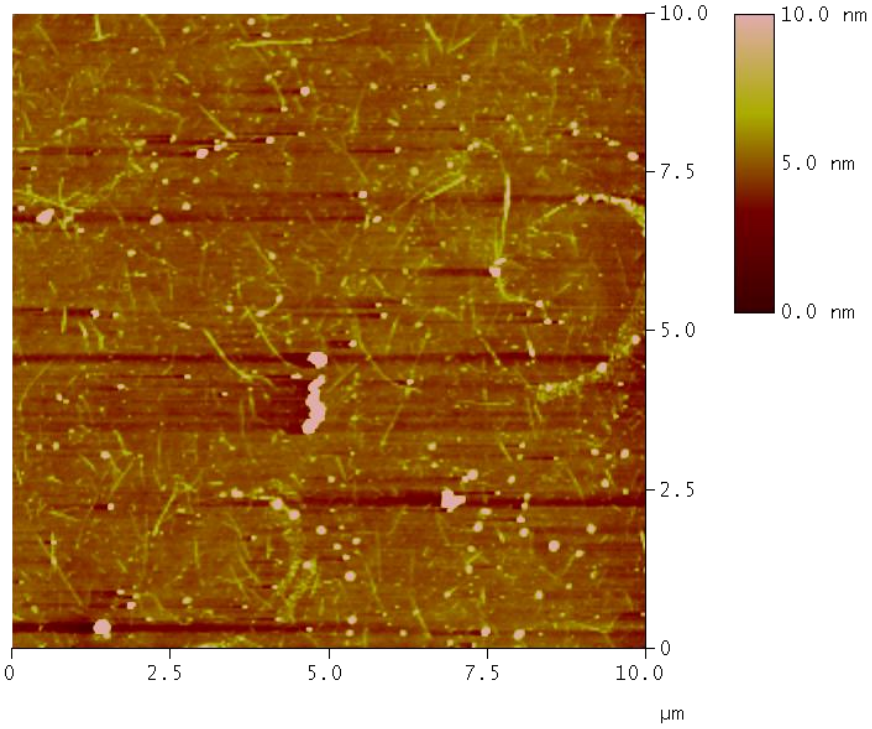

S89: AFM of SWNTs on ITO with 8CB and 16, area 23

8.6 Atomic Force Micrographs of ART-Deposited SWNTs on a Silicon Dioxide Surface with 4-cyano-4'-octylbiphenyl and tetraethyl (6,8,10,17,19,21-hexahydro-6,21:10,17-bis([2,3]naphthaleno)-8,19-ethenononacene-31,32-diyl)bis(phosphonate) (16)

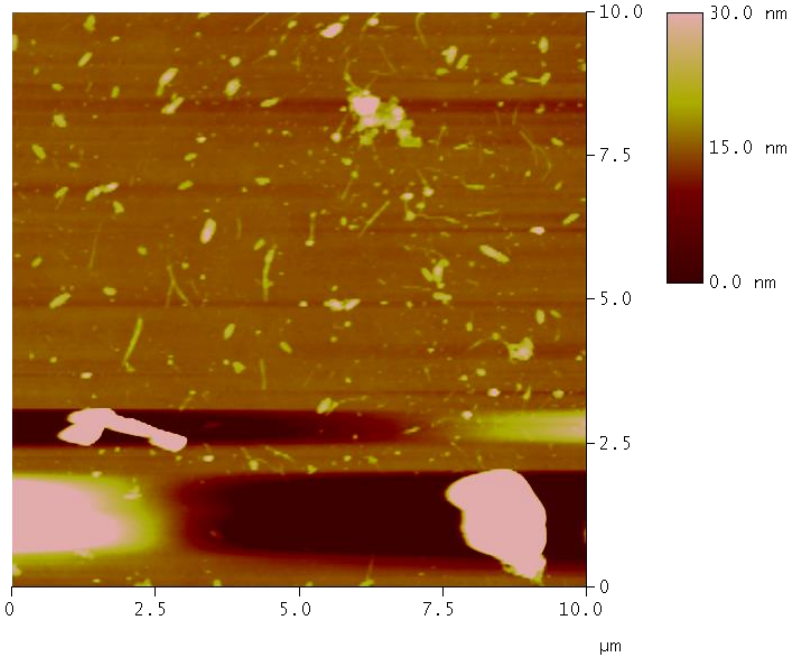

S90: AFM of SWNTs on SiO_2 with 8CB and 16, area 1

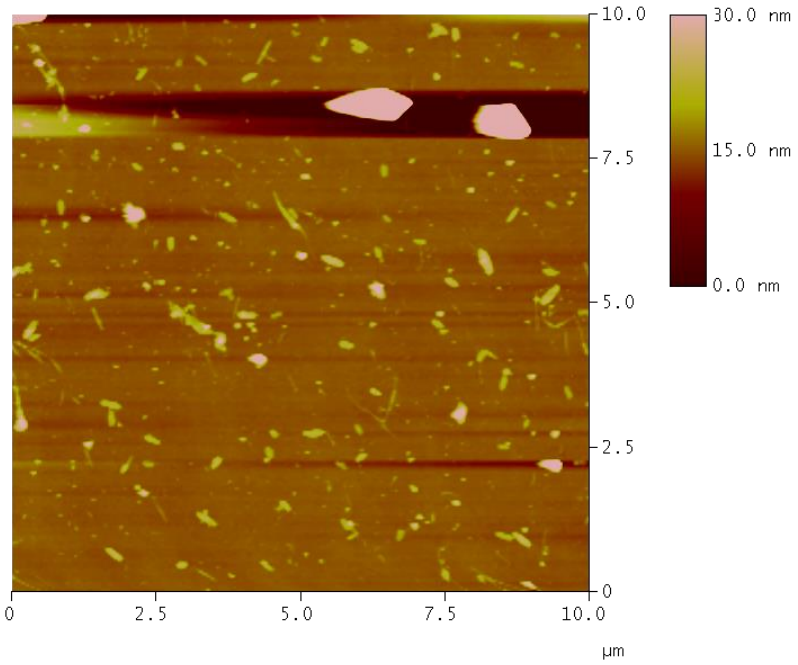

S91: AFM of SWNTs on SiO_2 with 8CB and 16, area 2

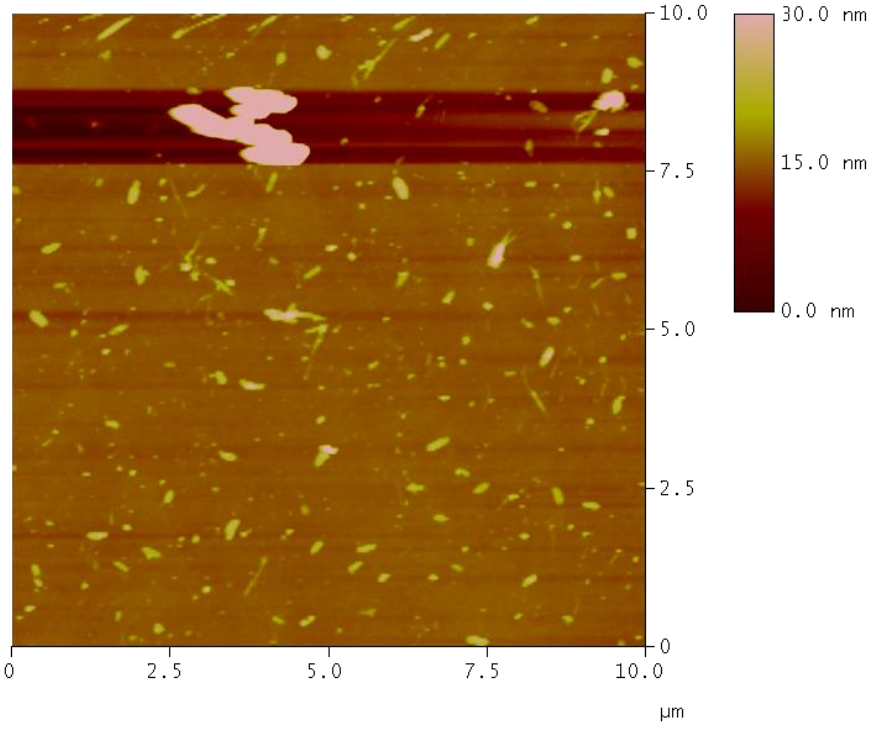

S92: AFM of SWNTs on SiO_2 with 8CB and 16, area 3

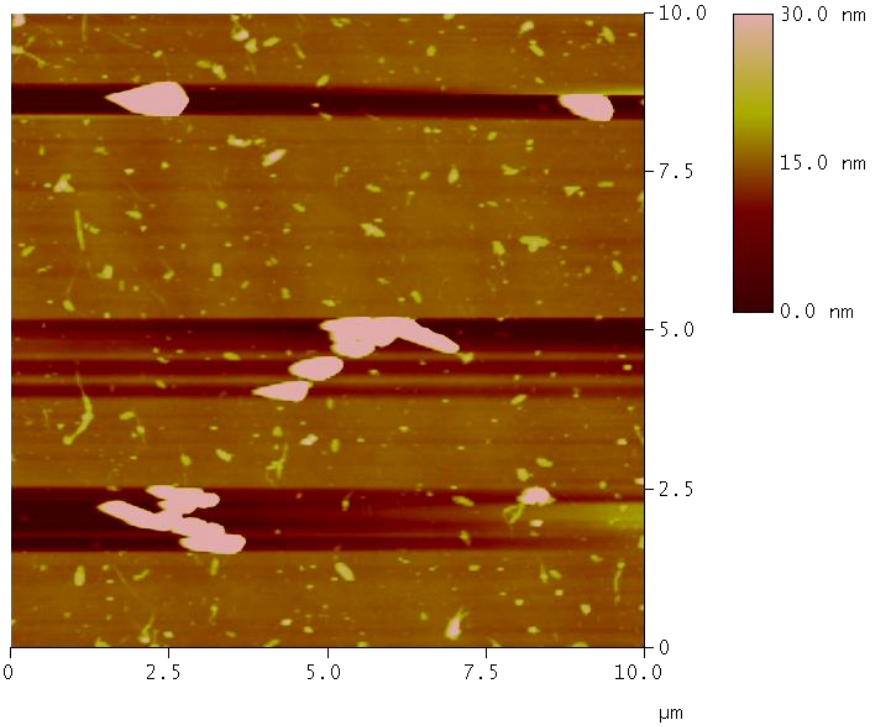

S93: AFM of SWNTs on SiO_2 with 8CB and 16, area 4

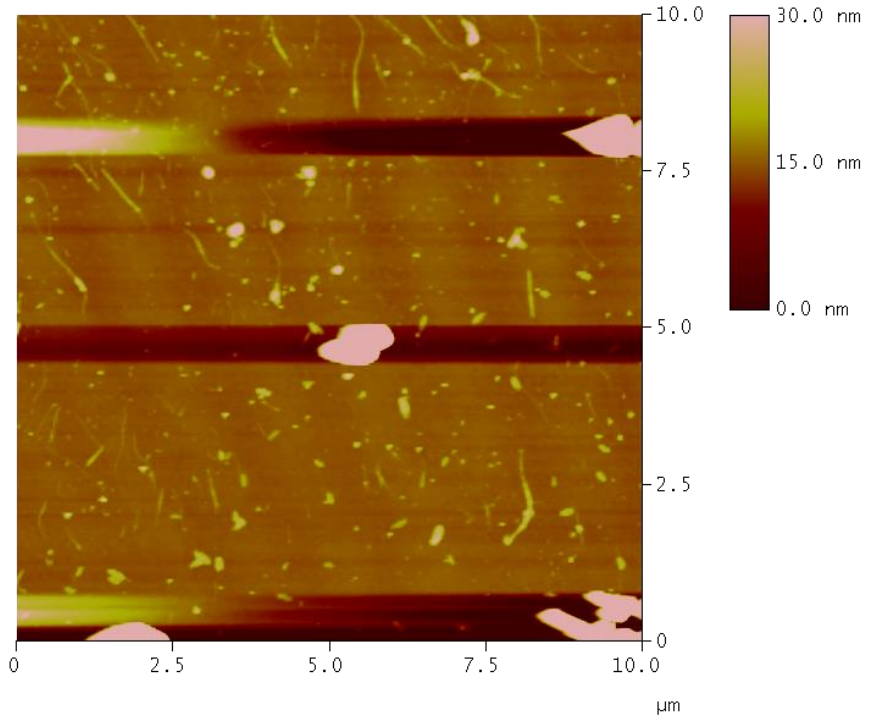

S94: AFM of SWNTs on SiO_2 with 8CB and 16, area 5

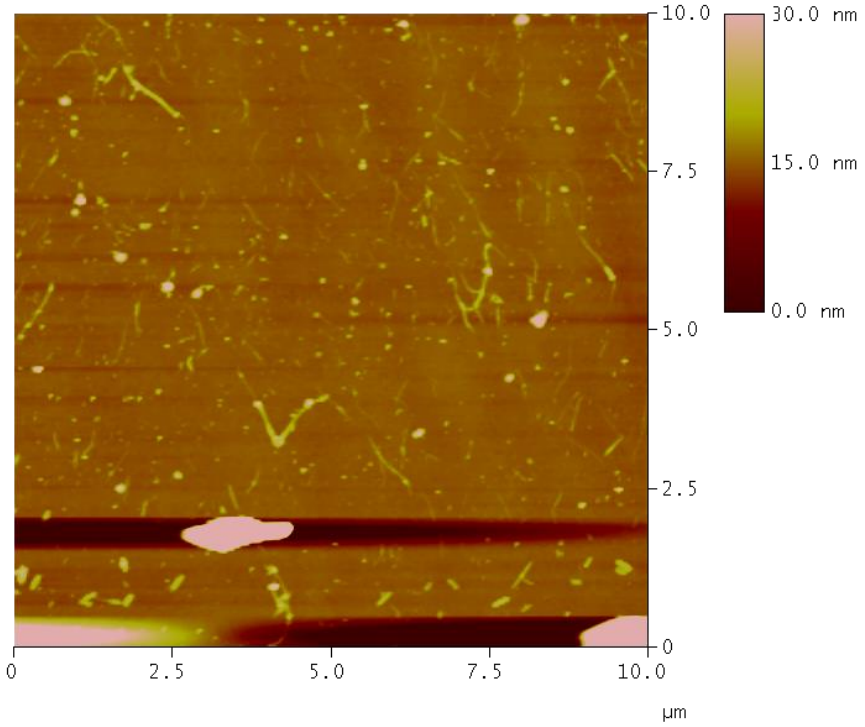

S95: AFM of SWNTs on SiO_2 with 8CB and 16, area 6

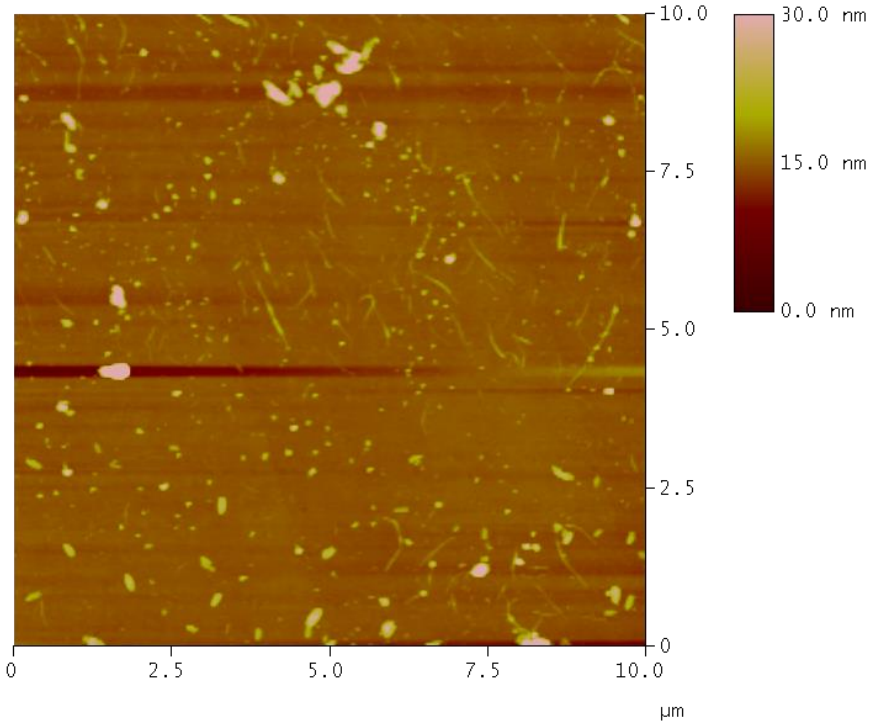

S96: AFM of SWNTs on SiO_2 with 8CB and 16, area 7

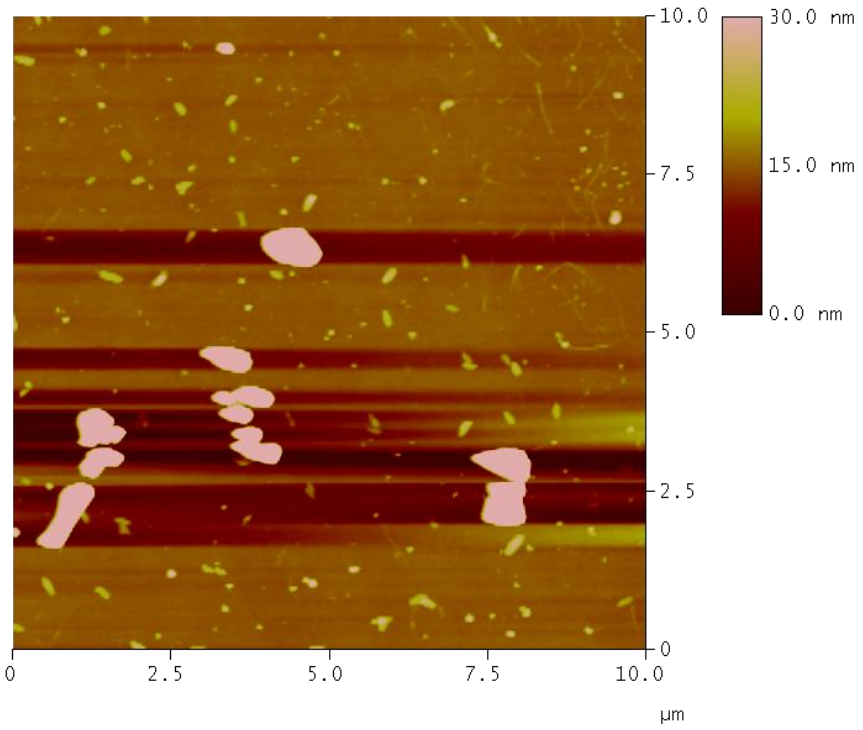

S97: AFM of SWNTs on SiO_2 with 8CB and 16, area 8

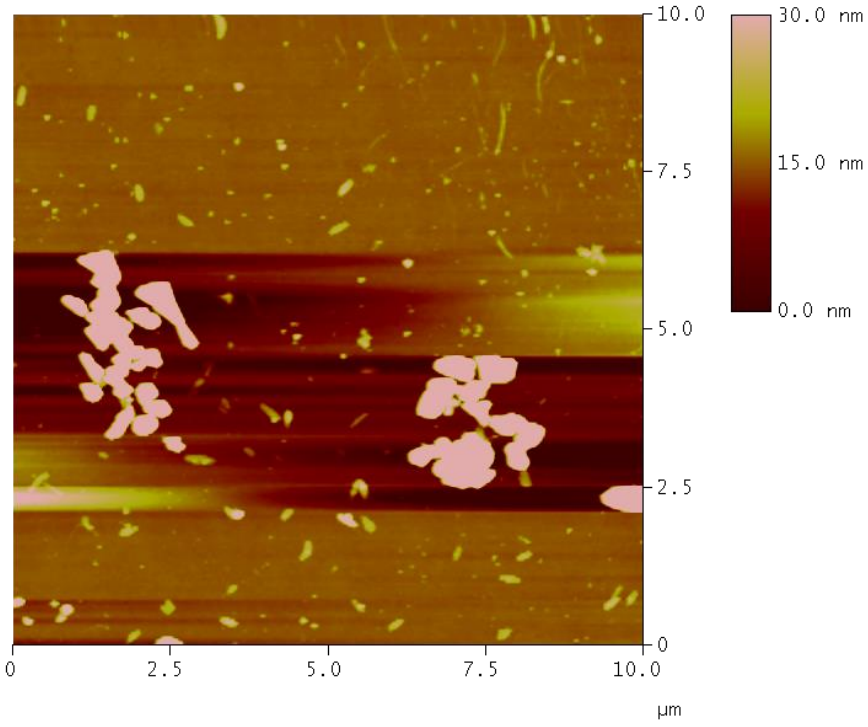

S98: AFM of SWNTs on SiO_2 with 8CB and 16, area 9

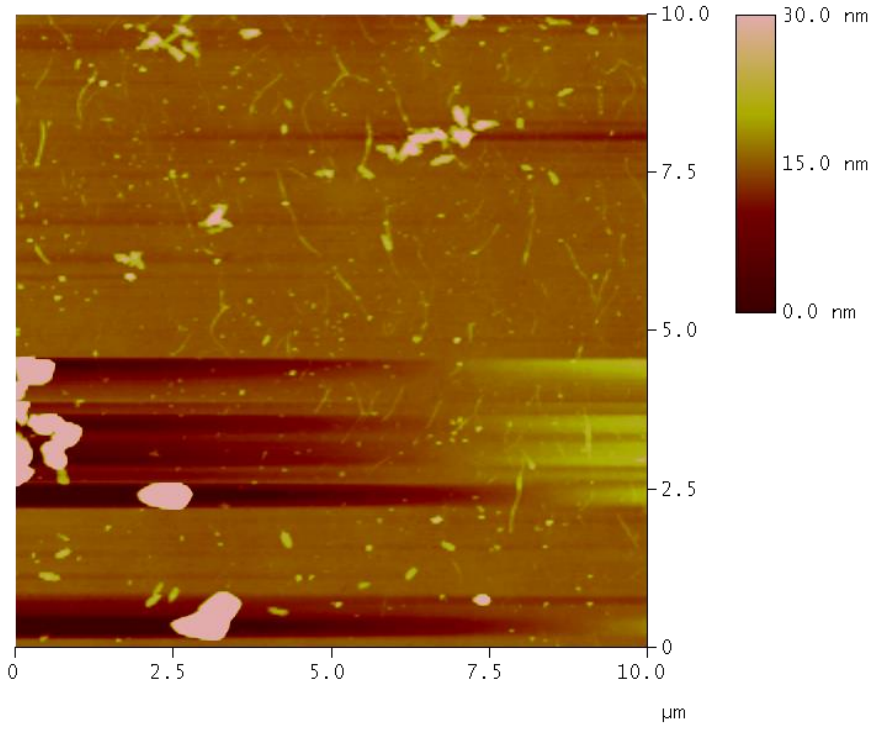

S99: AFM of SWNTs on SiO_2 with 8CB and 16, area 10

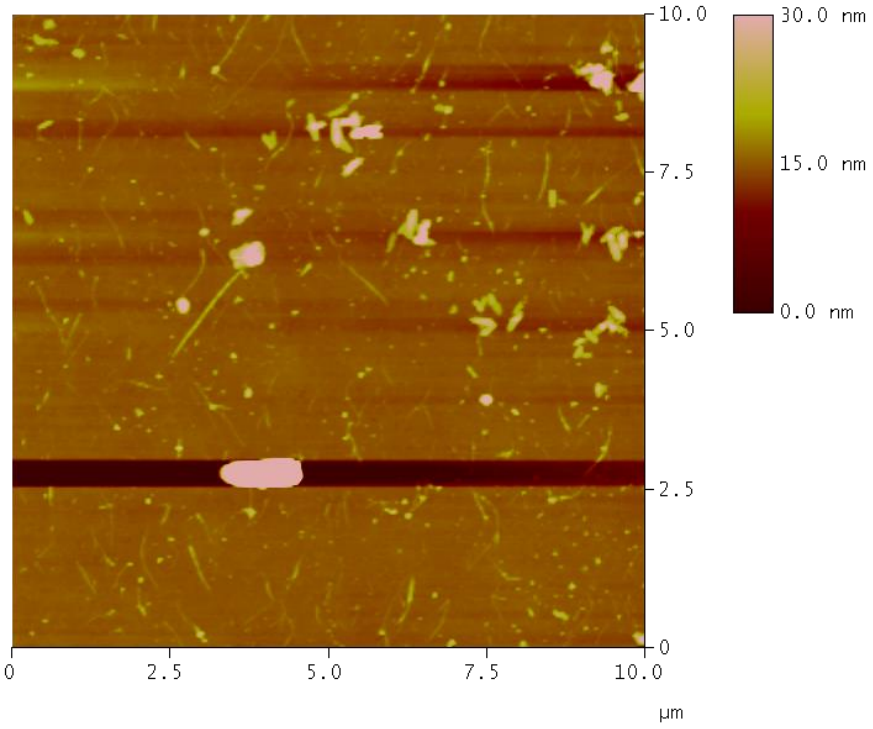

S100: AFM of SWNTs on SiO_2 with 8CB and 16, area 11

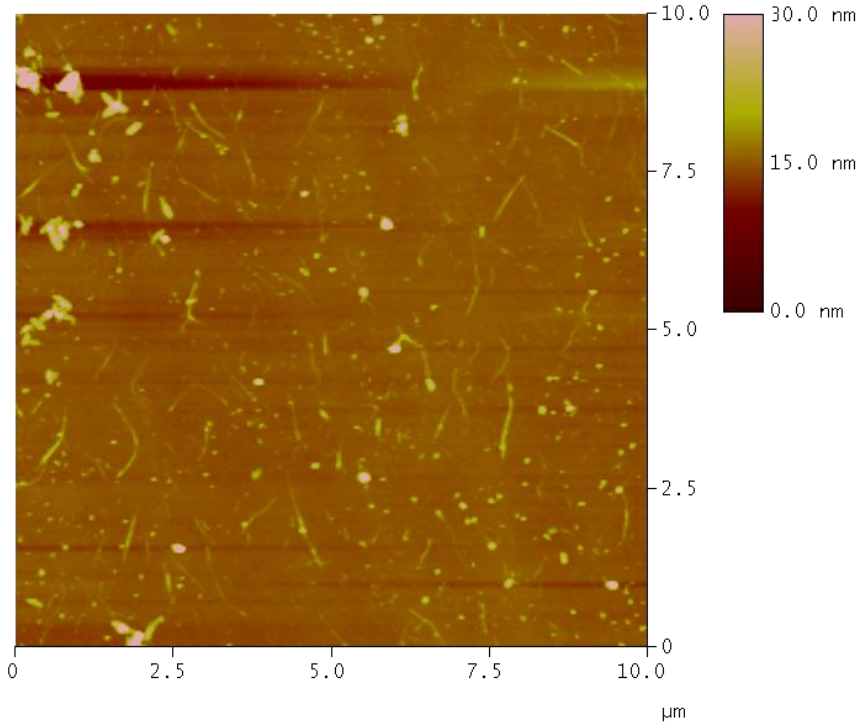

S101: AFM of SWNTs on SiO_2 with 8CB and 16, area 12

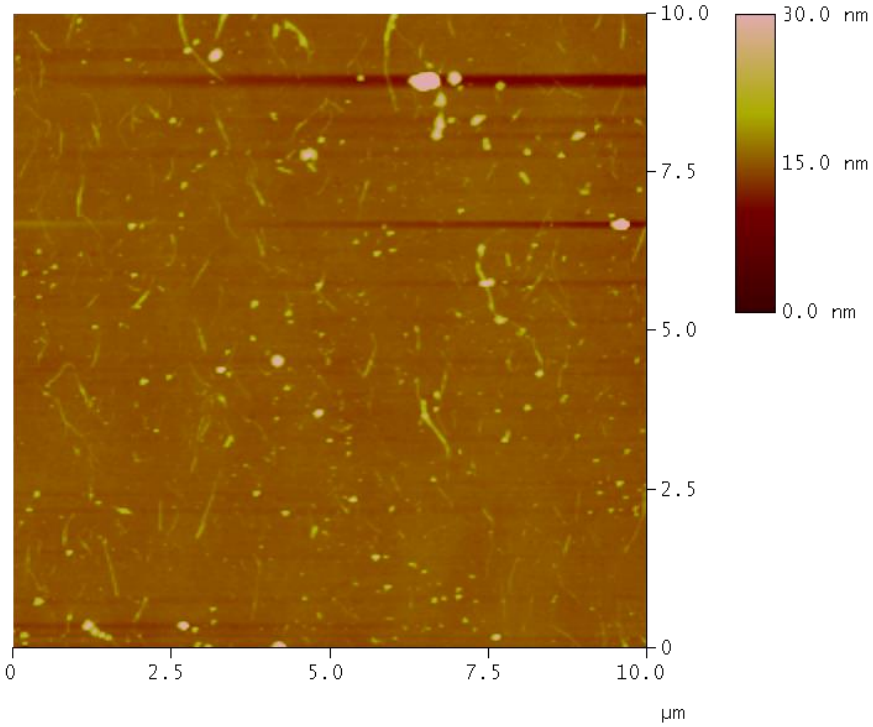

S102: AFM of SWNTs on SiO_2 with 8CB and 16, area 13

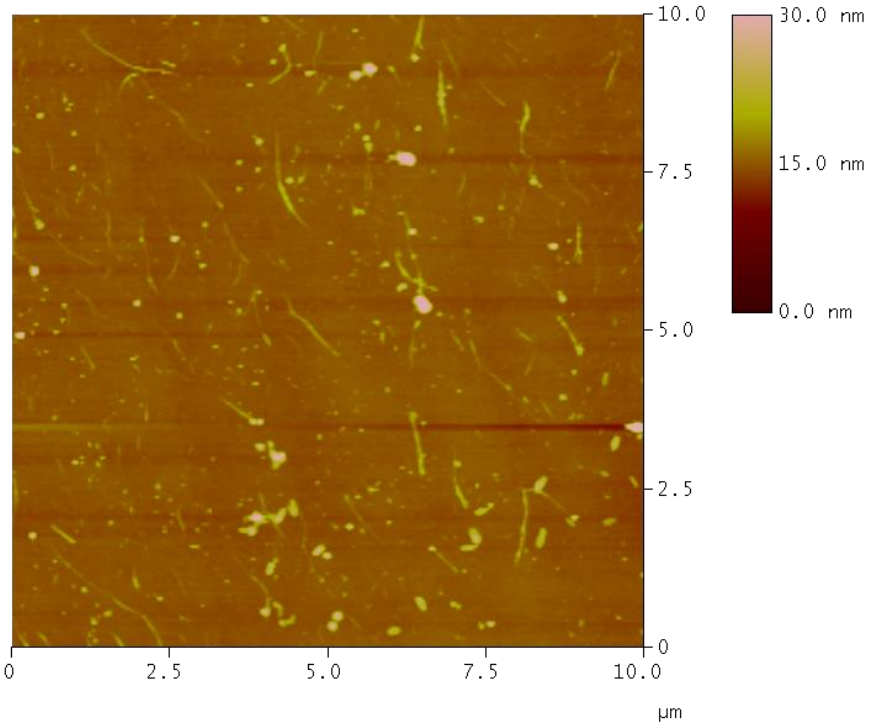

S103: AFM of SWNTs on SiO_2 with 8CB and 16, area 14

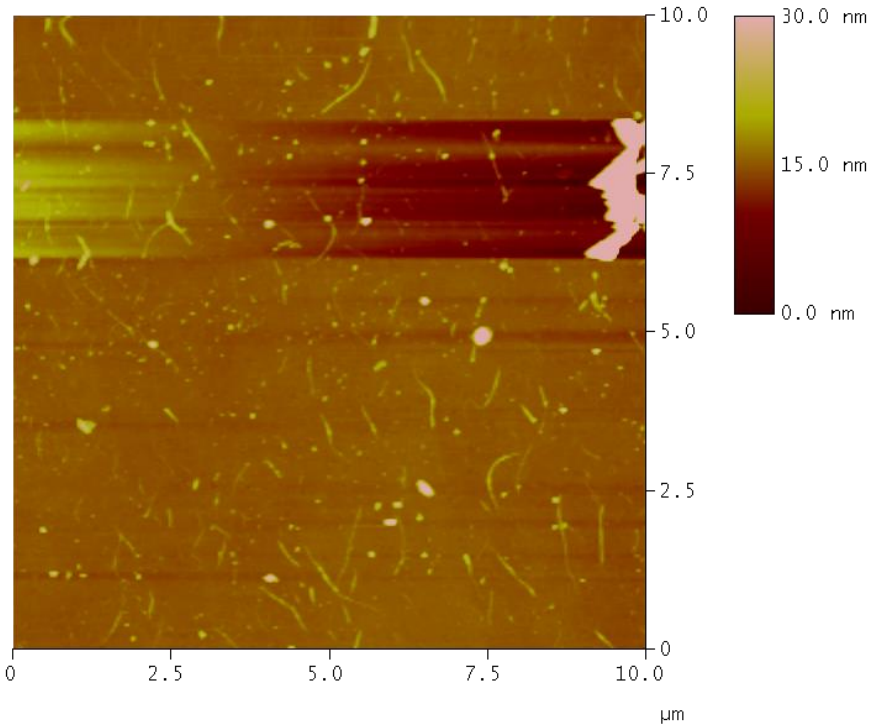

S104: AFM of SWNTs on SiO_2 with 8CB and 16, area 15

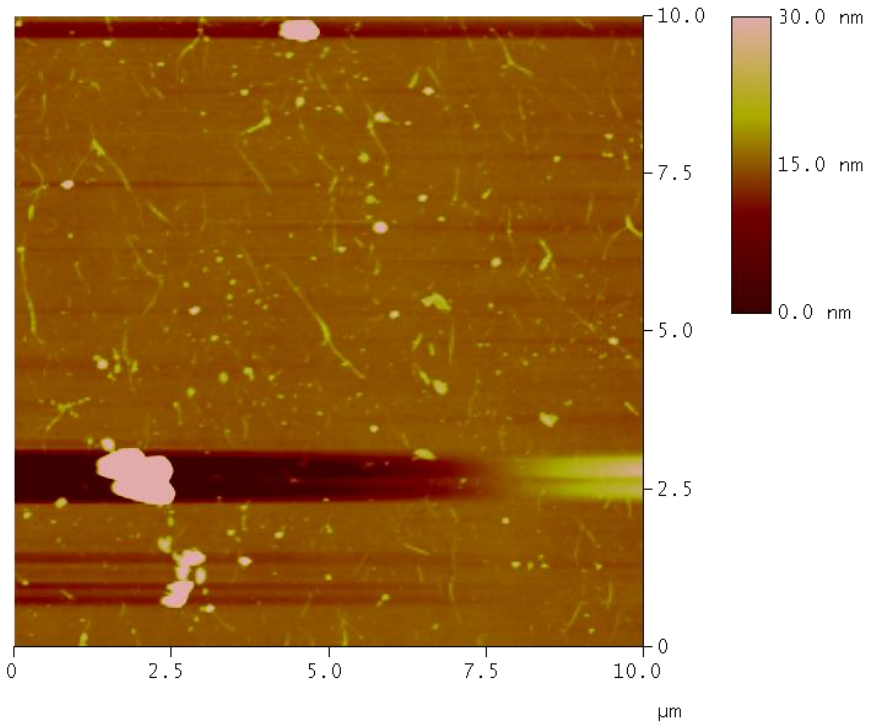

S105: AFM of SWNTs on SiO_2 with 8CB and 16, area 16

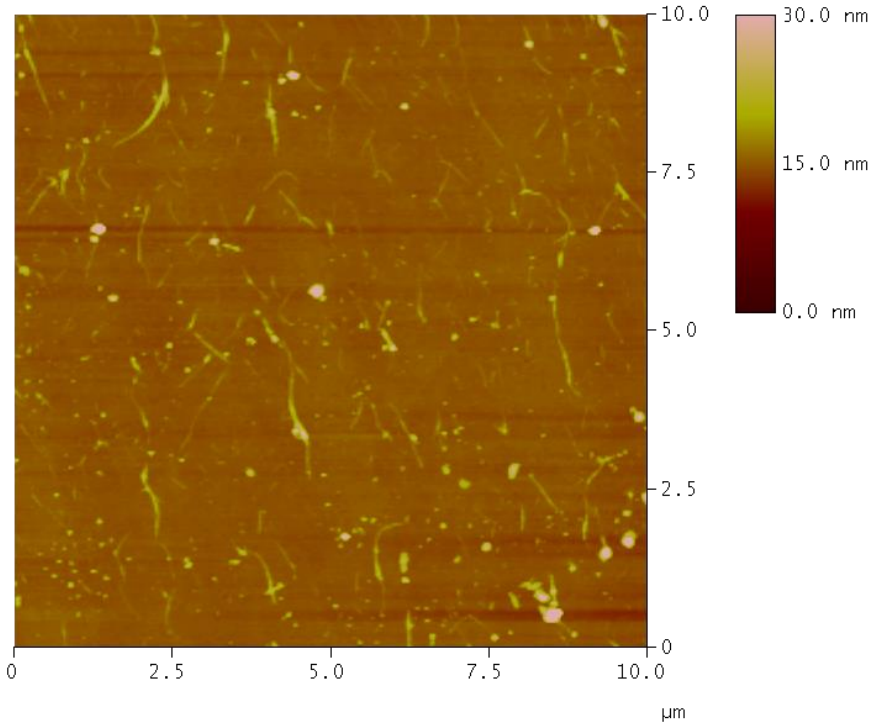

S106: AFM of SWNTs on SiO_2 with 8CB and 16, area 17

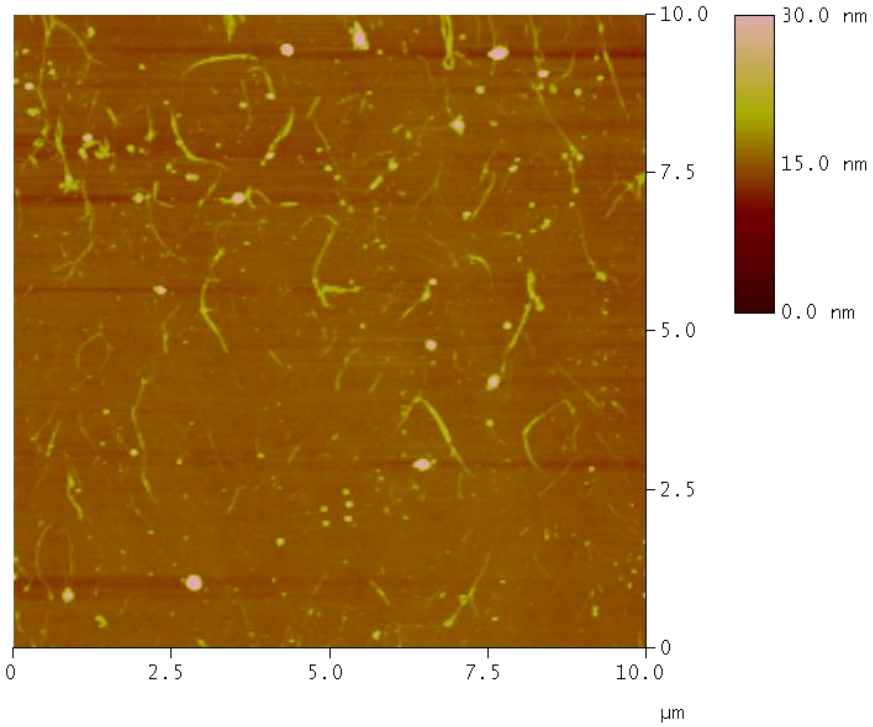

S107: AFM of SWNTs on SiO_2 with 8CB and 16, area 18

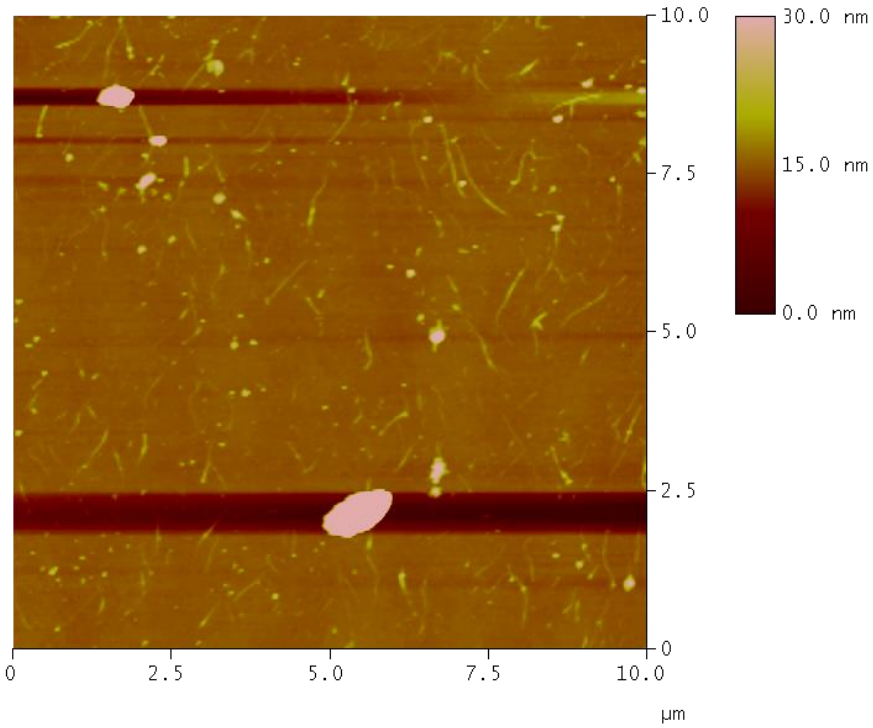

S108: AFM of SWNTs on SiO_2 with 8CB and 16, area 19

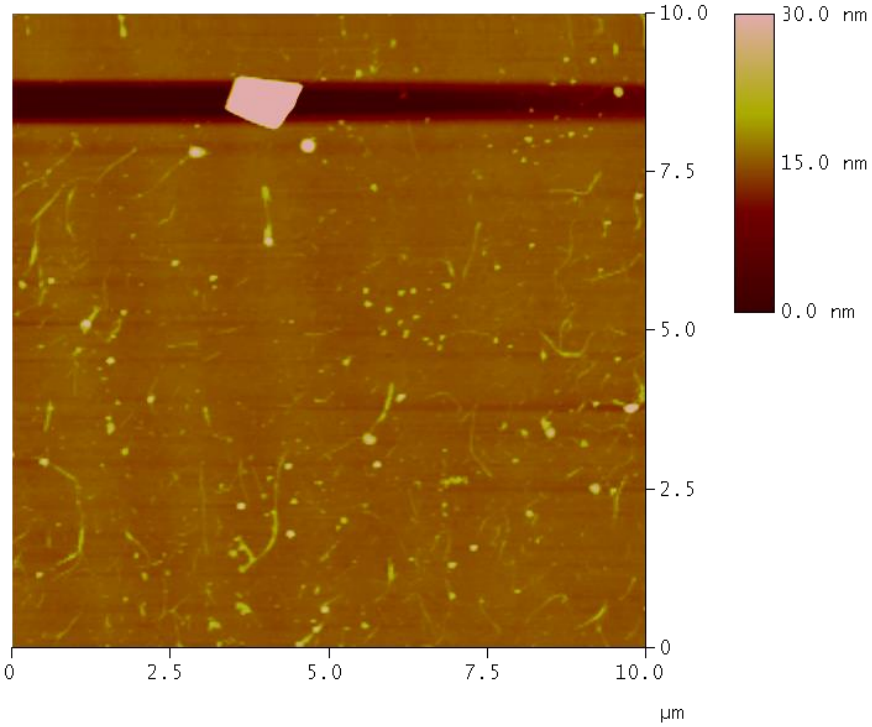

S109: AFM of SWNTs on SiO_2 with 8CB and 16, area 20

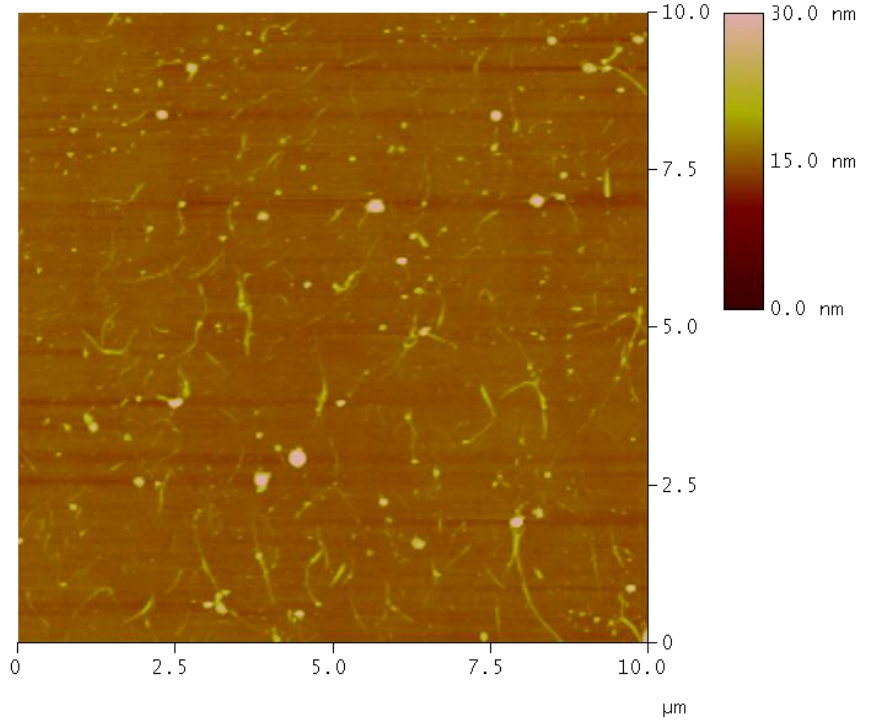

S110: AFM of SWNTs on SiO_2 with 8CB and 16, area 21

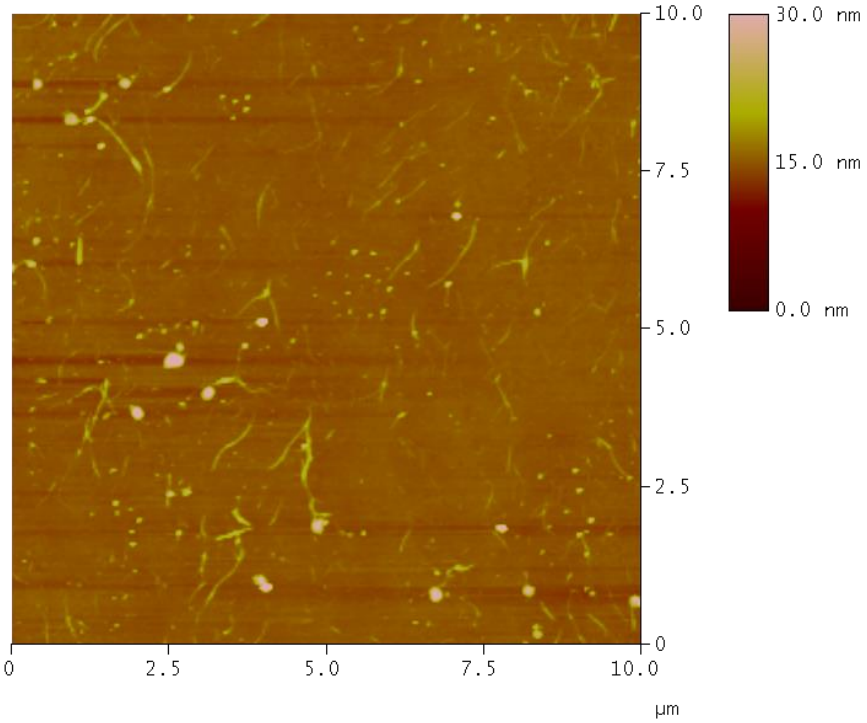

S111: AFM of SWNTs on SiO_2 with 8CB and 16, area 22

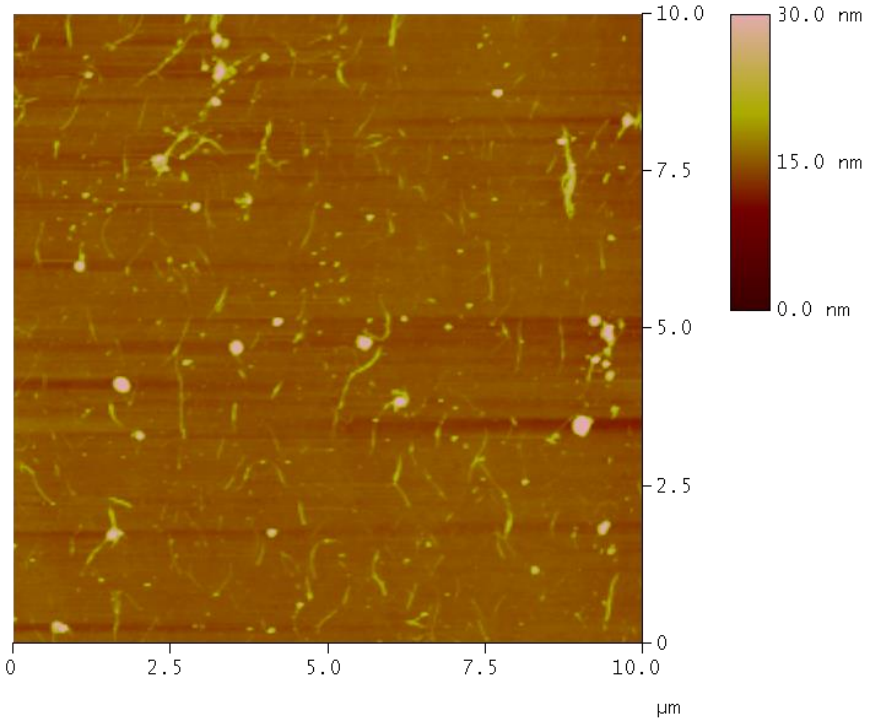

S112: AFM of SWNTs on SiO_2 with 8CB and 16, area 23

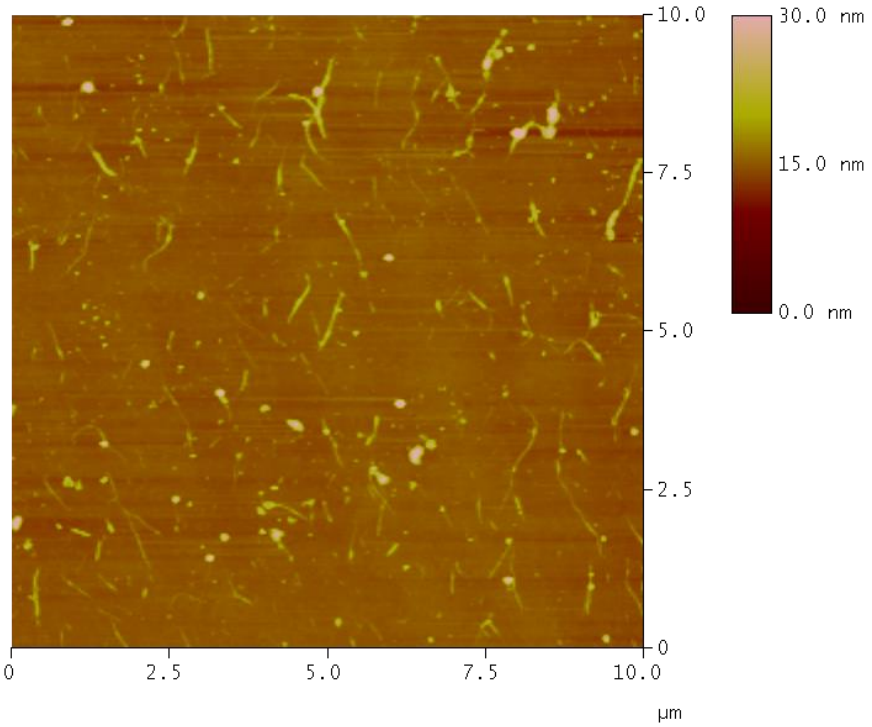

S113: AFM of SWNTs on SiO_2 with 8CB and 16, area 24

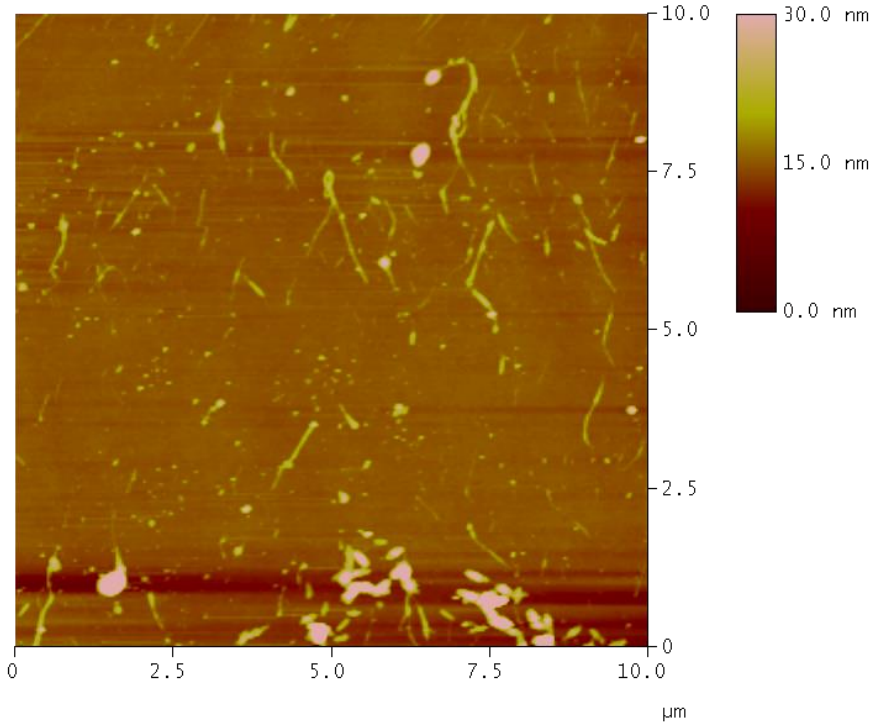

S114: AFM of SWNTs on SiO_2 with 8CB and 16, area 25

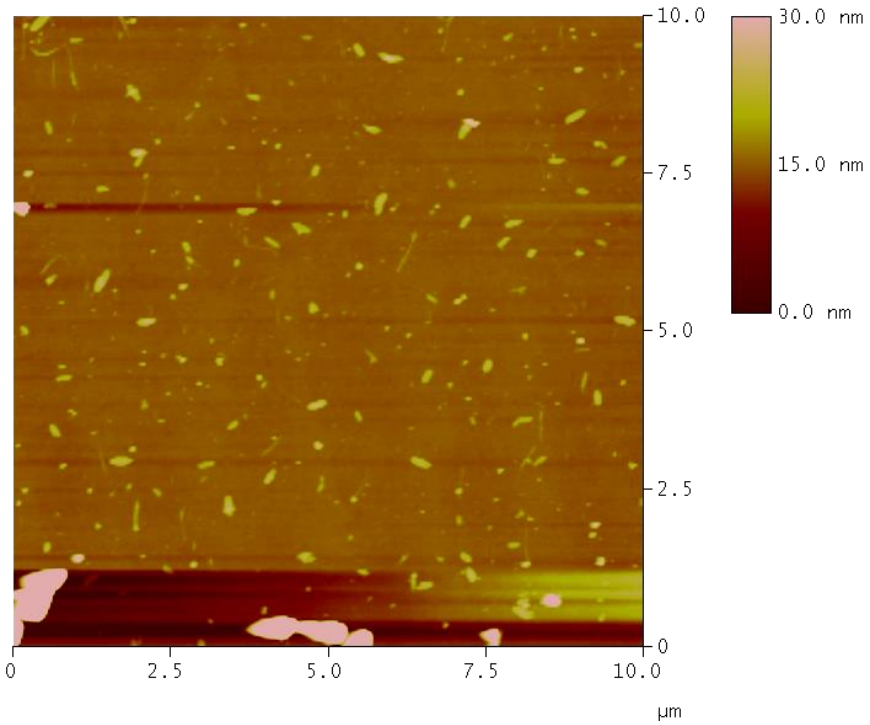

S115: AFM of SWNTs on SiO_2 with 8CB and 16, area 26

8.7 Atomic Force Micrographs of Patterned Silicon Oxide Surface

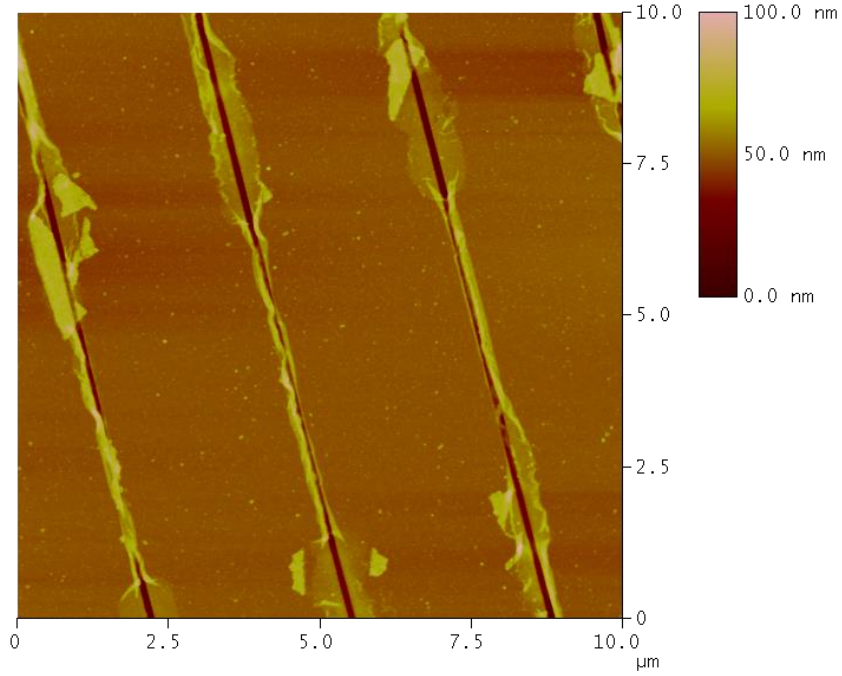

S116: AFM of patterned SiO_2 surface

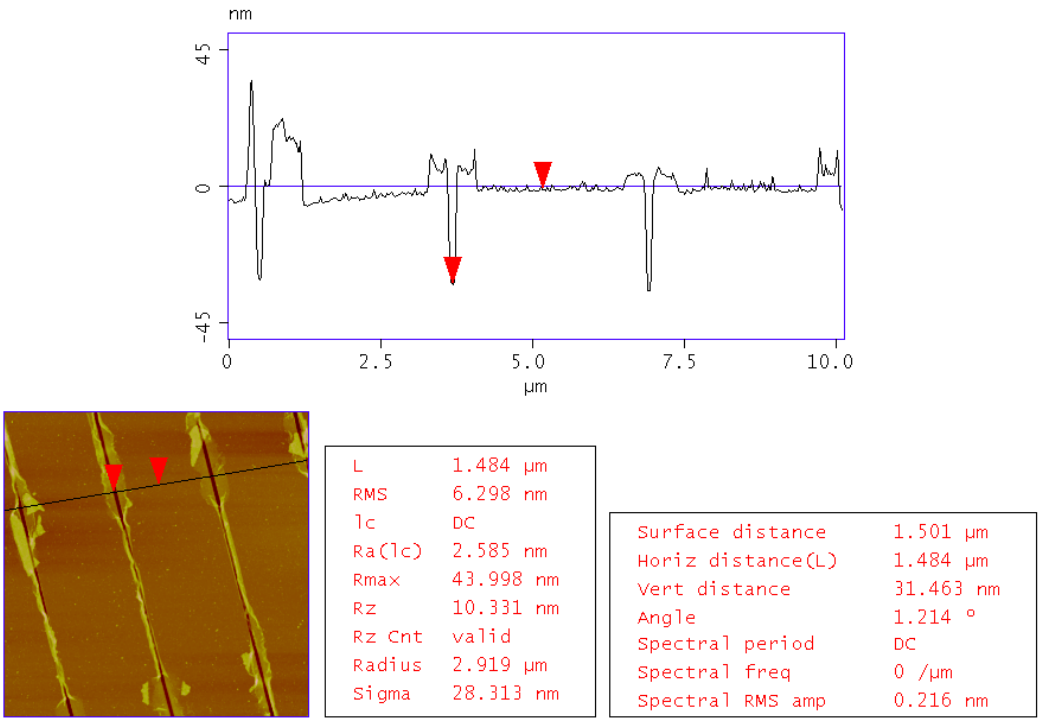

S117: Height profile of patterned SiO_2 surface

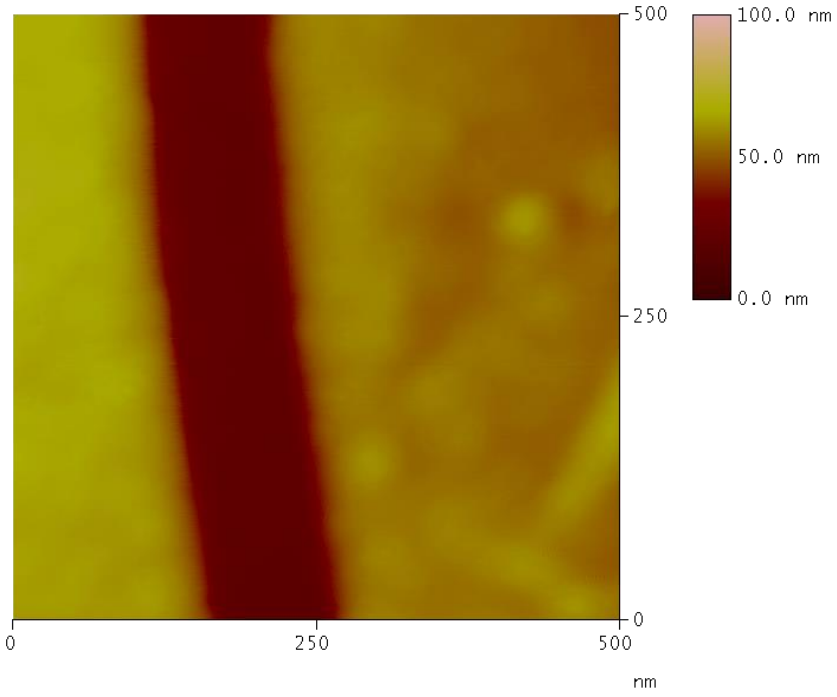

S118: Close-up of trench on patterned SiO_2 surface

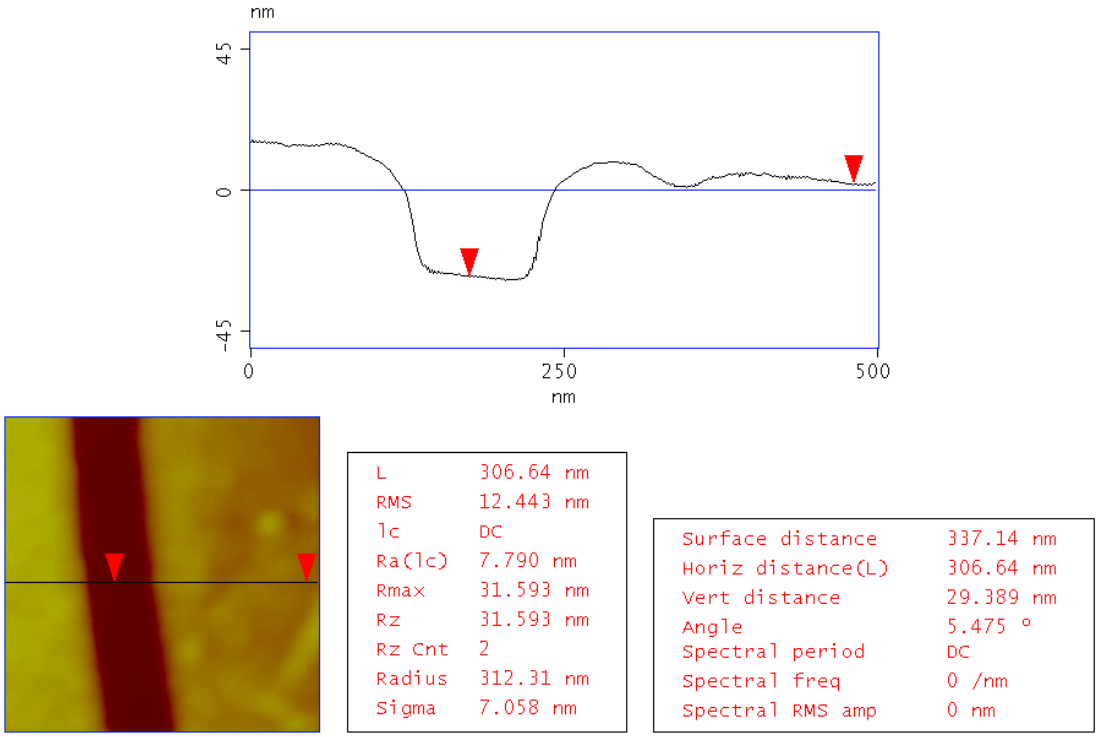

S119: Height profile of close-up patterned SiO_2 surface

9. X-Ray Photoelectron Spectroscopy

9.1 X-Ray Photoelectron Spectra of Silicon Dioxide Surfaces Functionalized with tetraethyl (9,10-dihydro-9,10-ethenoanthracene-11,12-diyl)bis(phosphonate) (1)

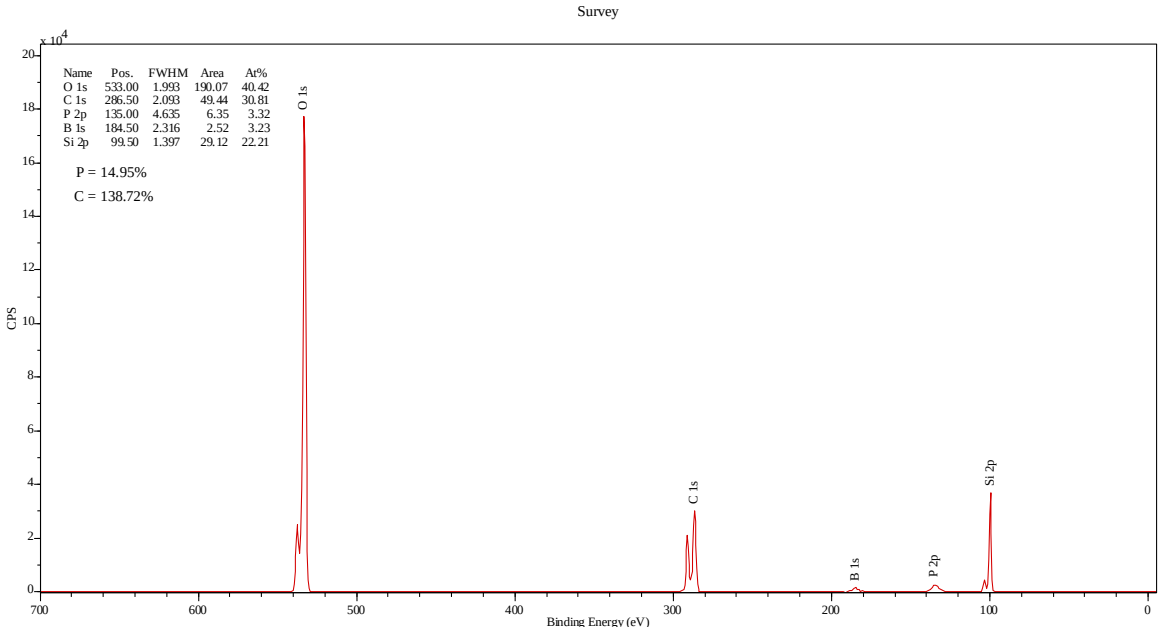

S120: XPS spectrum of 1 on piranha cleaned SiO_2 in THF at 140 °C

9.2 X-Ray Photoelectron Spectra of Silicon Dioxide Surfaces Functionalized with Phenylphosphonic Acid

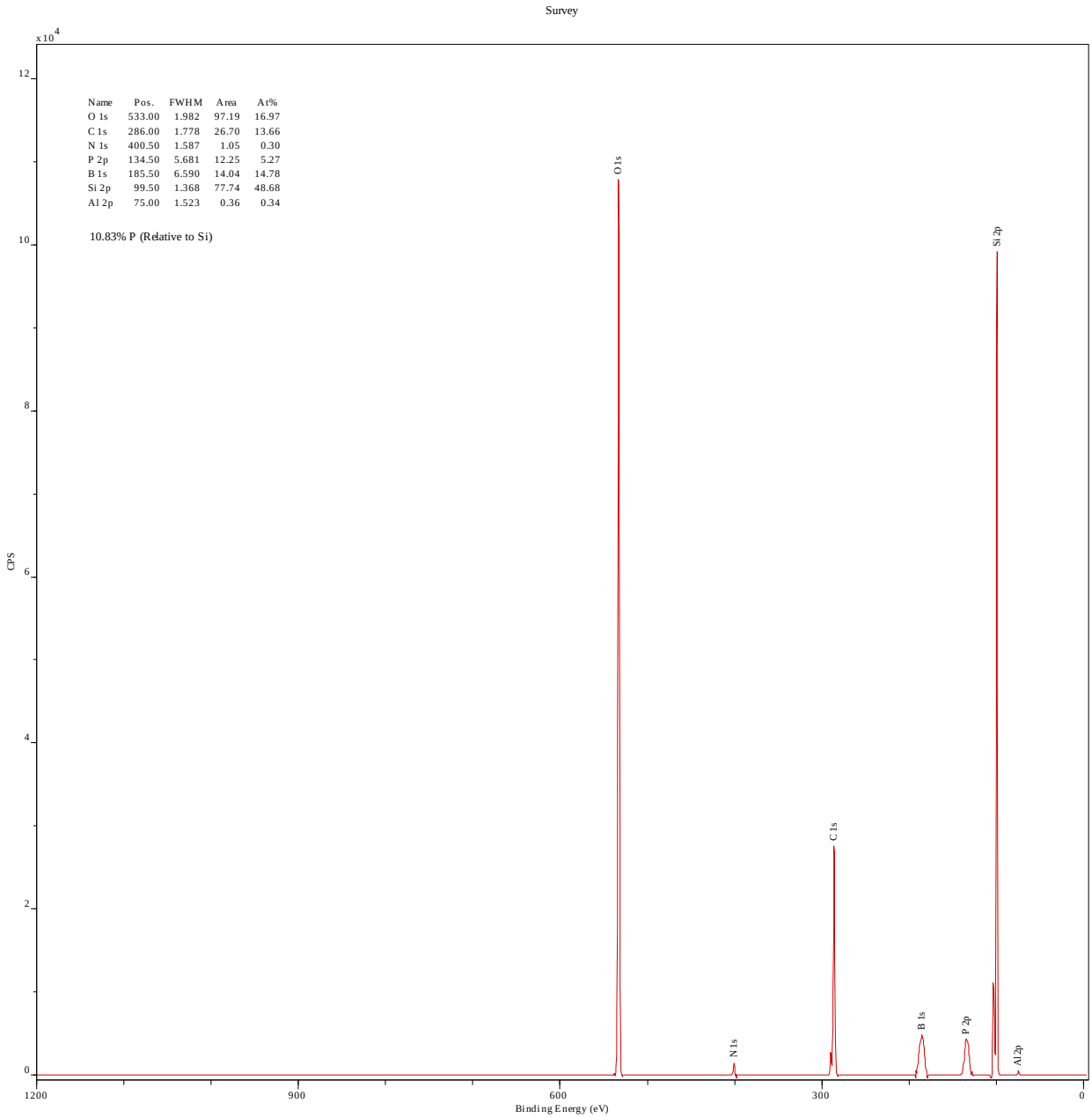

S121: XPS spectrum of phenylphosphonic acid on P-doped SiO_2

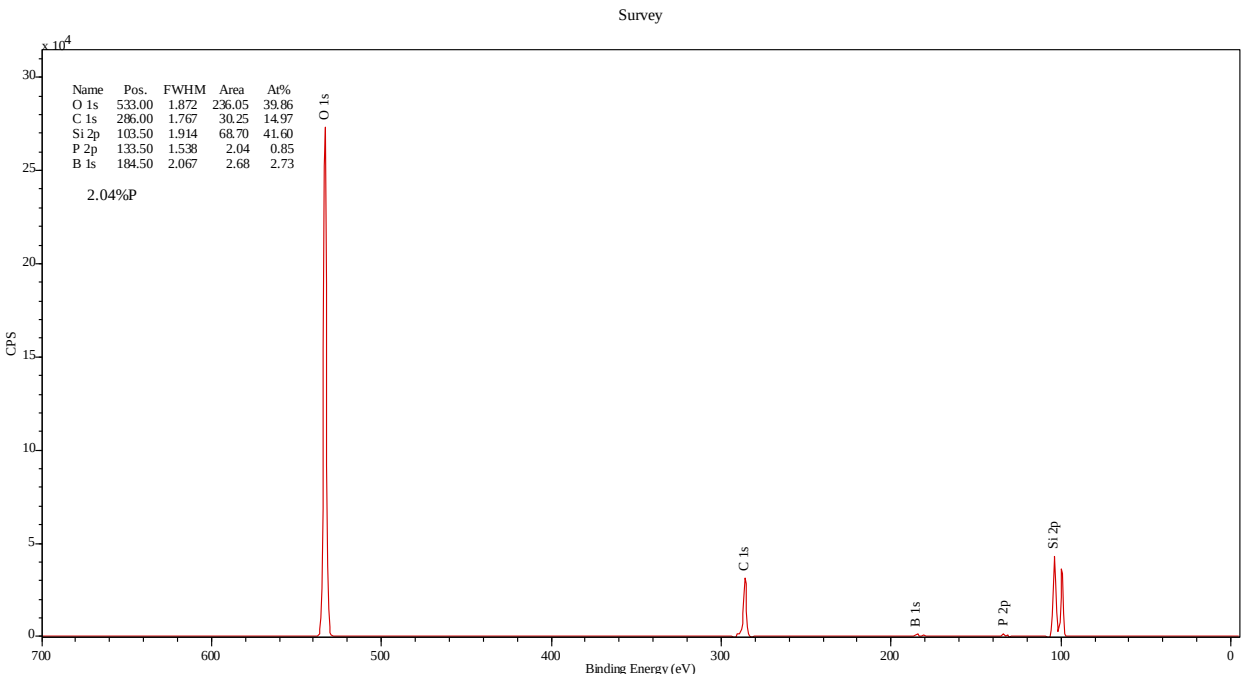

S122: XPS spectrum of phenylphosphonic acid on organic solvent washed SiO_2 in THF at 60 °C

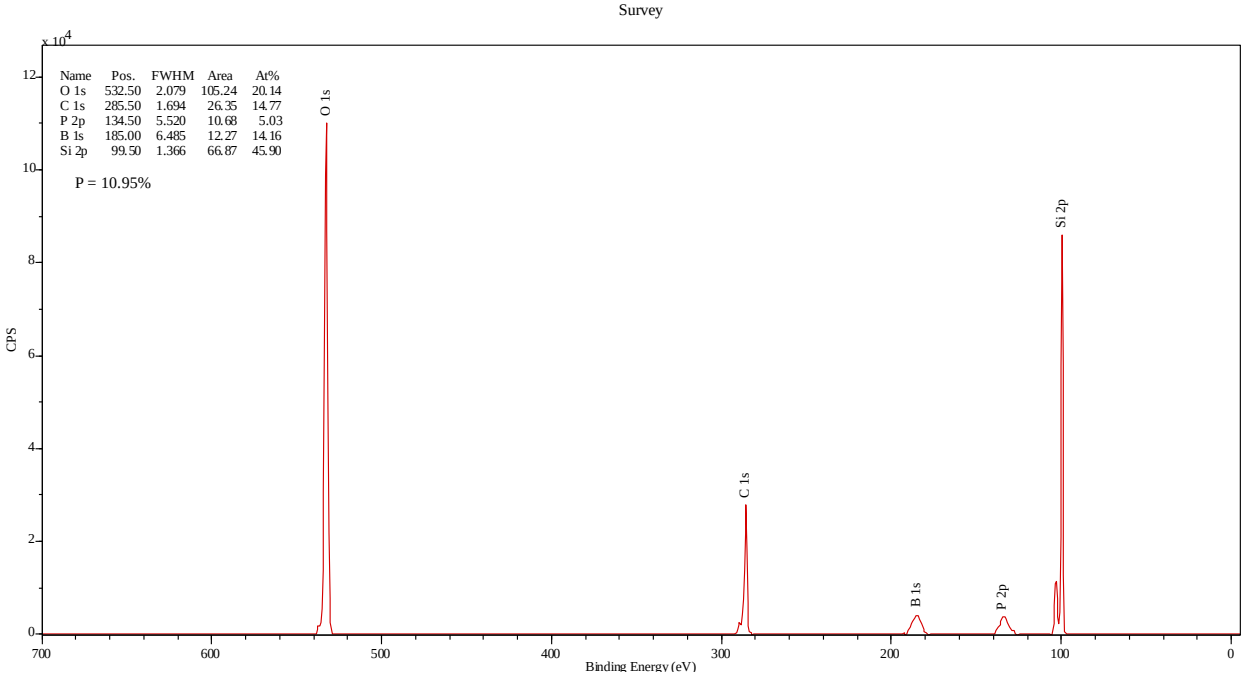

S123: XPS spectrum of phenylphosphonic acid on piranha cleaned SiO_2 at 140 °C

9.3 X-Ray Photoelectron Spectra of Silicon Dioxide Surfaces Functionalized with Diethyl Phenylphosphonate

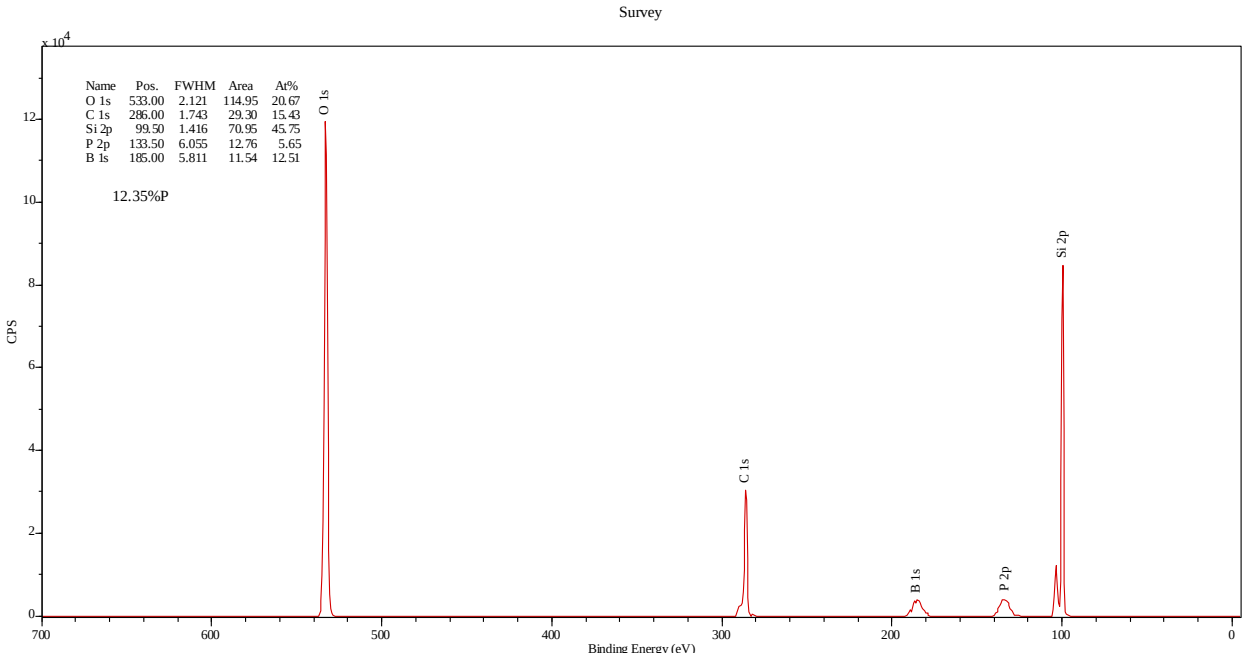

S124: XPS spectrum of diethyl phenylphosphonate on organic solvent washed SiO_2 in THF at 60 °C

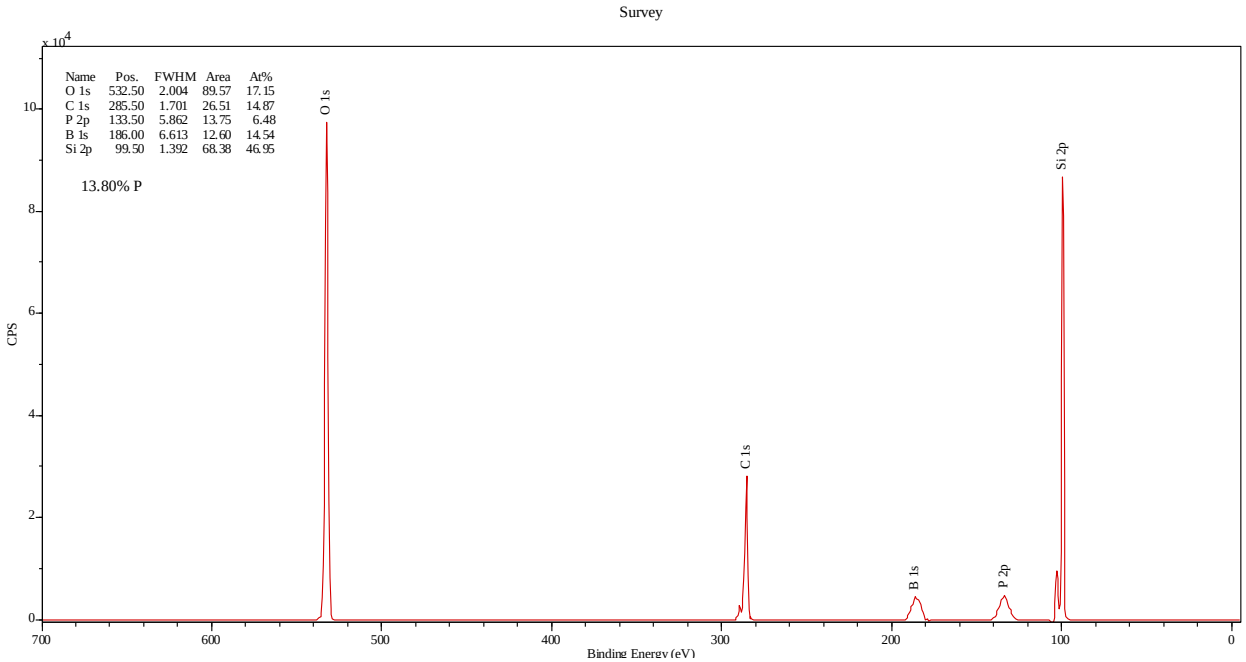

S125: XPS spectrum of diethyl phenylphosphonate on piranha cleaned SiO_2in THF at 140 °C

10. UV-Visible Absorption Spectroscopy

10.1 UV-Visible Spectra of Fullerenes Purified Using Phosphonate Functionalized Silica Gel

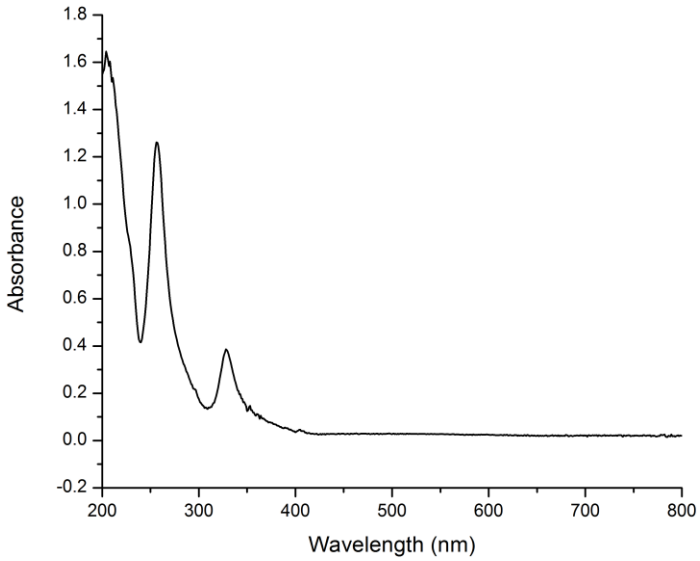

S126: UV-Vis spectrum of C_{60} purified with phosphonate functionalized silica gel

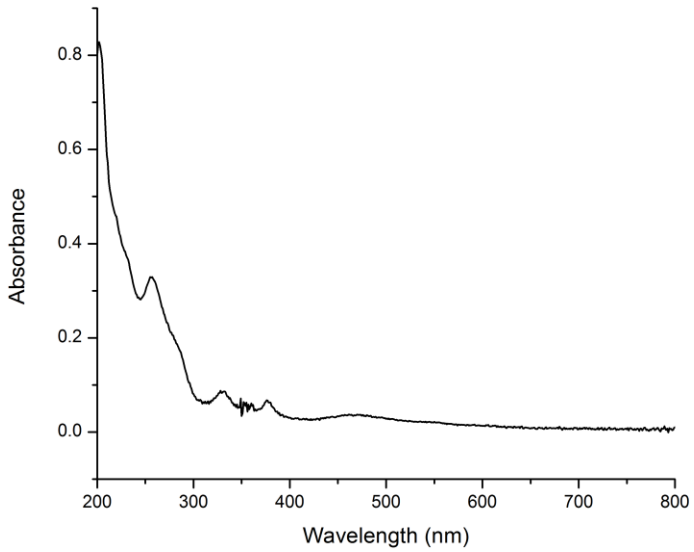

S127: UV-Vis spectrum of C_{70} purified with phosphonate functionalized silica gel

11. Raman Spectroscopy

11.1 Raman Spectra of as Purchased SWNTs Deposited onto Silicon Dioxide

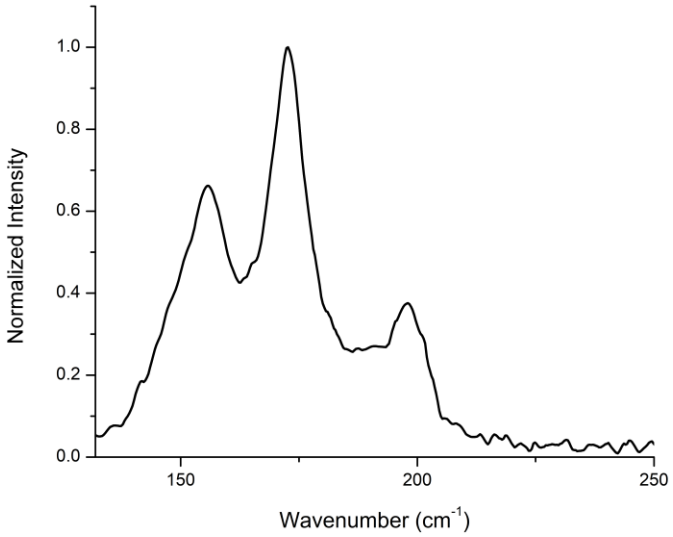

S128: Raman spectrum of the RBM region of as purchased SWNTs deposited onto SiO_2 with excitation at 633 nm

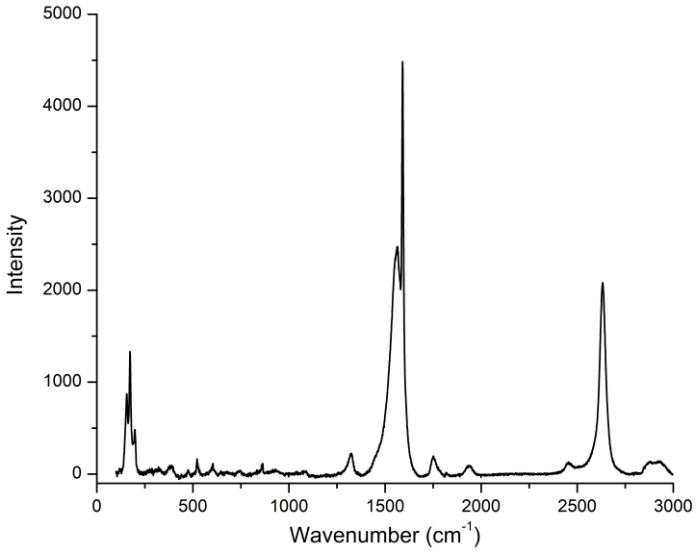

S129: Raman spectrum of as purchased SWNTs deposited onto SiO_2 with excitation at 633 nm

11.2 Raman Spectra of Alignment Relay Technique SWNTs Deposited onto Silicon Dioxide Using 4-cyano-4'-pentylbiphenyl and tetraethyl (5,7,9,14,16,18-hexahydro-5,18:9,14-bis([1,2]benzeno)-7,16-ethenoheptacene-25,26-diyl)bis(phosphonate) (2)

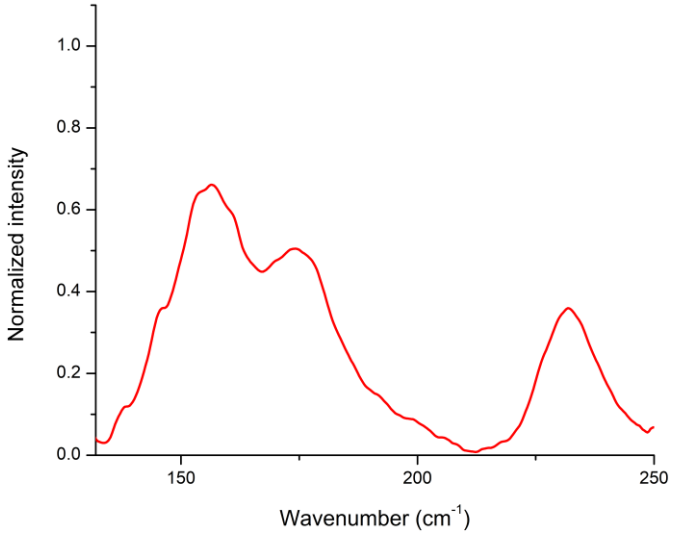

S130: RBM region of as purchased SWNTs on SiO_2, excitation at 633 nm

11.3 Raman Spectra of Alignment Relay Technique SWNTs Deposited onto Silicon Dioxide Using 4-cyano-4'-octylbiphenyl and tetraethyl (5,7,9,14,16,18-hexahydro-5,18:9,14-bis([1,2]benzeno)-7,16-ethenoheptacene-25,26-diyl)bis(phosphonate) (2)

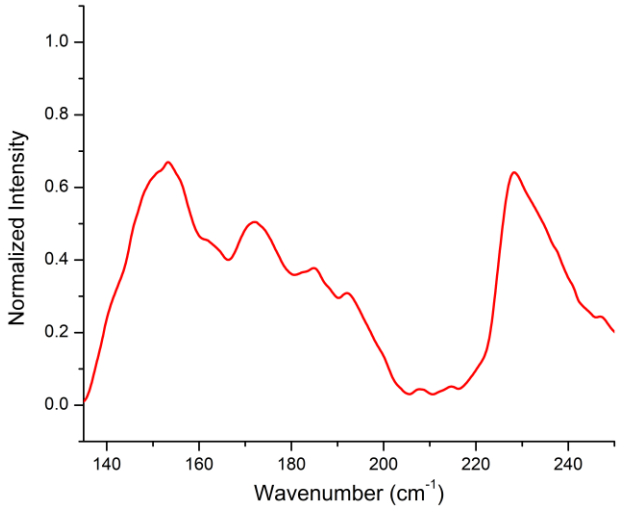

S131: RBM region of ART deposited SWNTs on SiO_2 with 5CB and 2, excitation at 633 nm. One day nanotube deposition time.

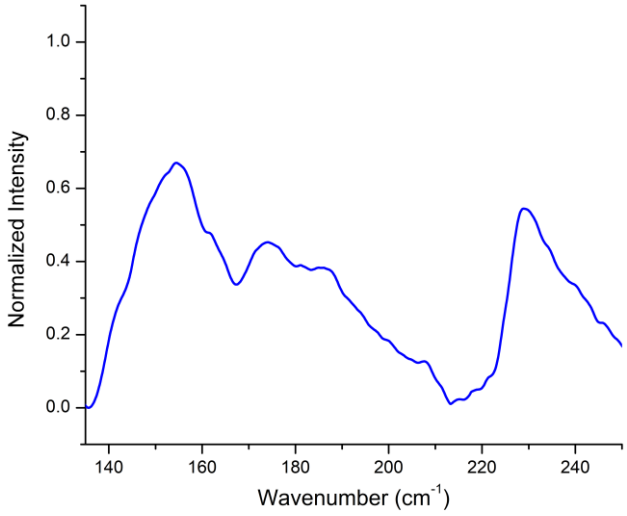

S132: RBM region of ART deposited SWNTs on SiO_2 with 5CB and 2, excitation at 633 nm. Two day nanotube deposition time.

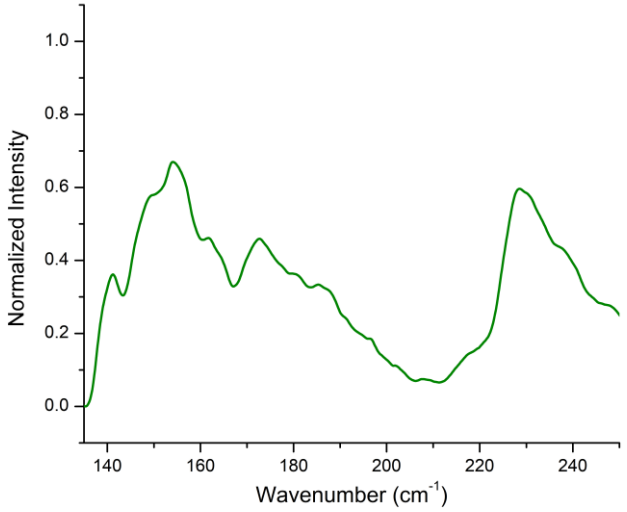

S133: RBM region of ART deposited SWNTs on SiO_2 with 5CB and 2, excitation at 633 nm. Four day nanotube deposition time.

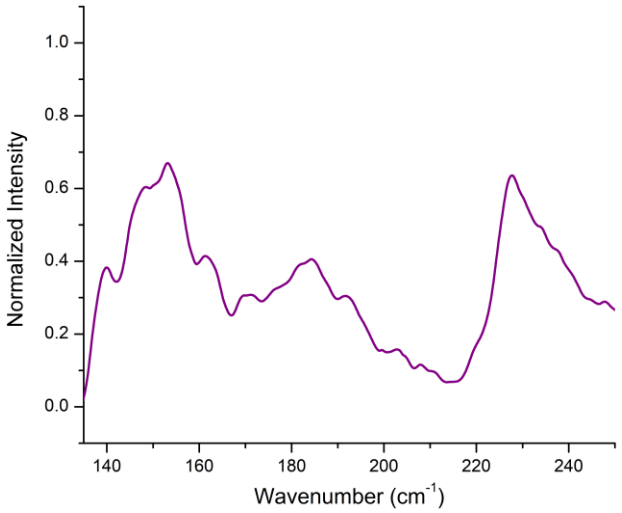

S134: RBM region of ART deposited SWNTs on SiO_2 with 5CB and 2, excitation at 633 nm. Two week nanotube deposition time.

11.4 Raman Spectra of Alignment Relay Technique SWNTs Deposited onto Silicon Dioxide Using 4-cyano-4'-octylbiphenyl and tetraethyl (6,8,10,17,19,21-hexahydro-6,21:10,17-bis([2,3]naphthaleno)-8,19-ethenononacene-31,32-diyl)bis(phosphonate) (16)

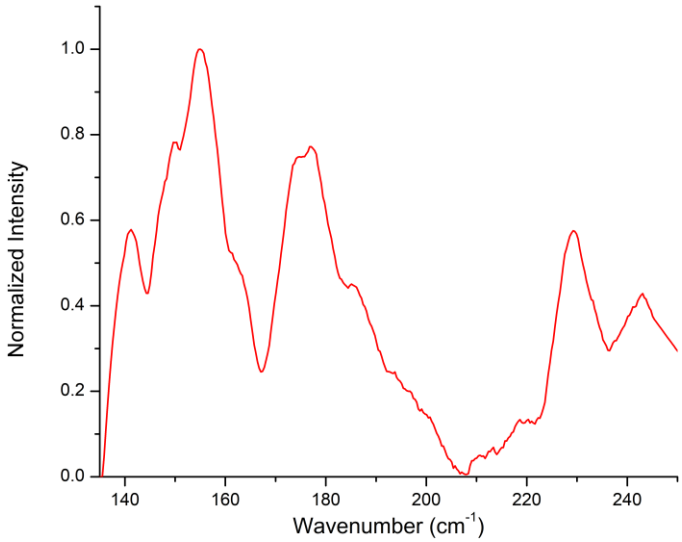

S135: RBM region of ART deposited SWNTs on SiO_2 with 8CB and 16, excitation at 633 nm.

12. Secondary Ion Mass Spectroscopy

12.1 Secondary Ion Mass Spectra of tetraethyl ((9s,10s)-9,10-dihydro-9,10-ethenoanthracene-11,12-diyl)bis(phosphonate) (1) Functionalized Silicon Dioxide

SIMS data is too large to attach to this document but an excel sheet of the data can be obtained from the Schipper group.

13. NMR Spectra

13.1 ^{1}H NMR of tetraethyl (9,10-dihydro-9,10-ethenoanthracene-11,12-diyl)bis(phosphonate) (1)

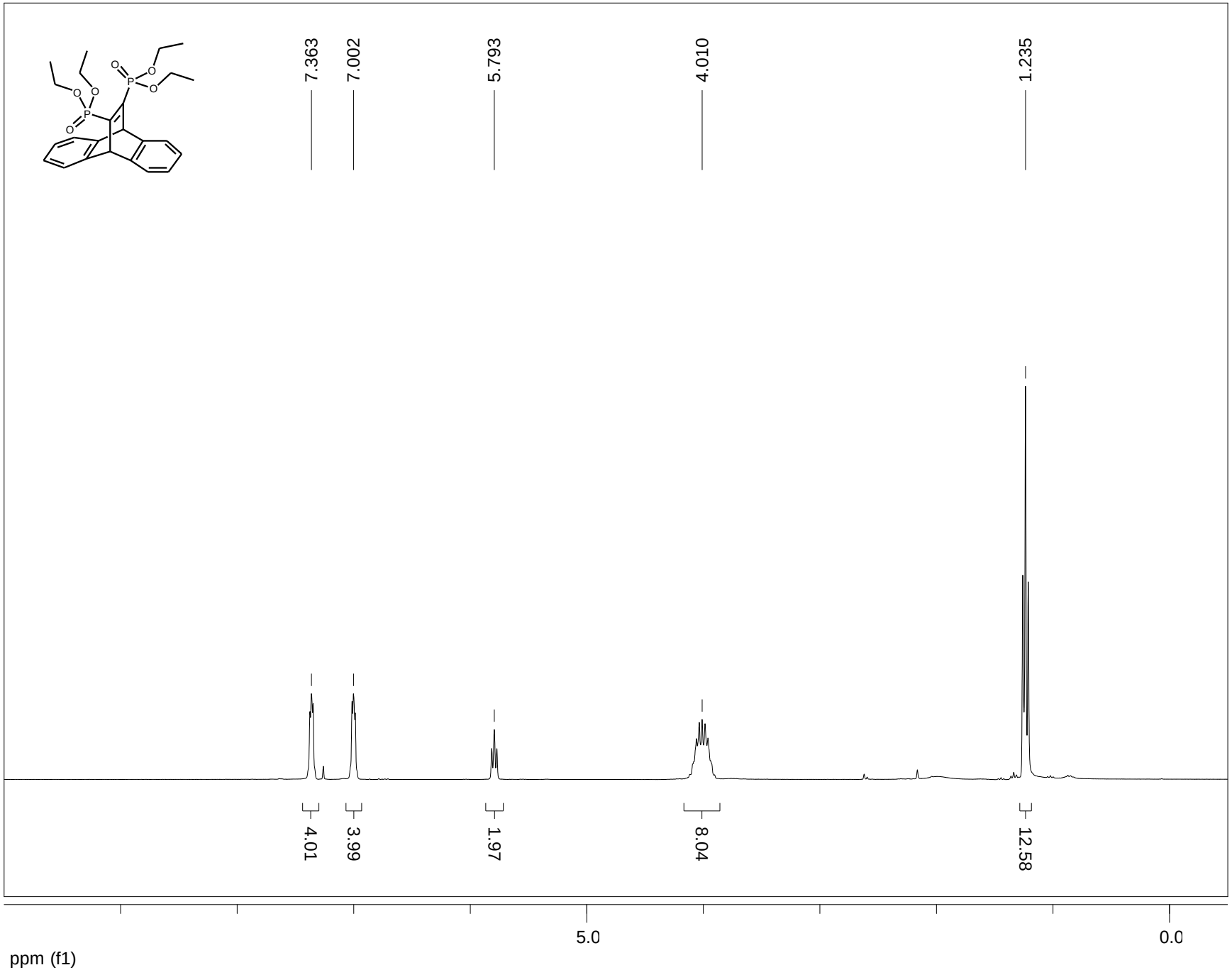

13.2 ^{31}P NMR of tetraethyl (9,10-dihydro-9,10-ethenoanthracene-11,12-diyl)bis(phosphonate) (1)

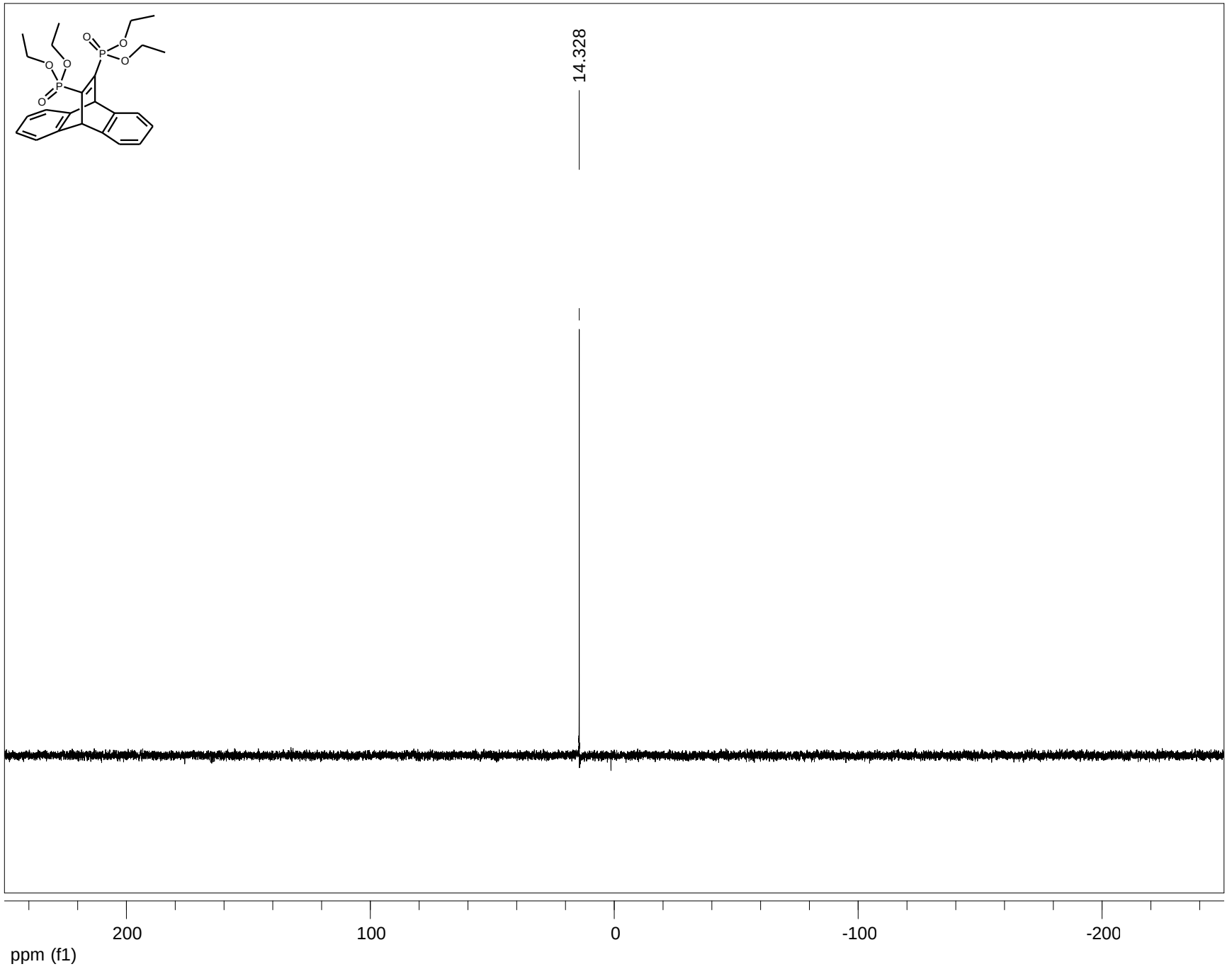

13.3 ^{1}H NMR of tetraethyl (5,7,9,14,16,18-hexahydro-5,18:9,14-bis([1,2]benzeno)-7,16-ethenoheptacene-25,26-diyl)bis(phosphonate) (2)

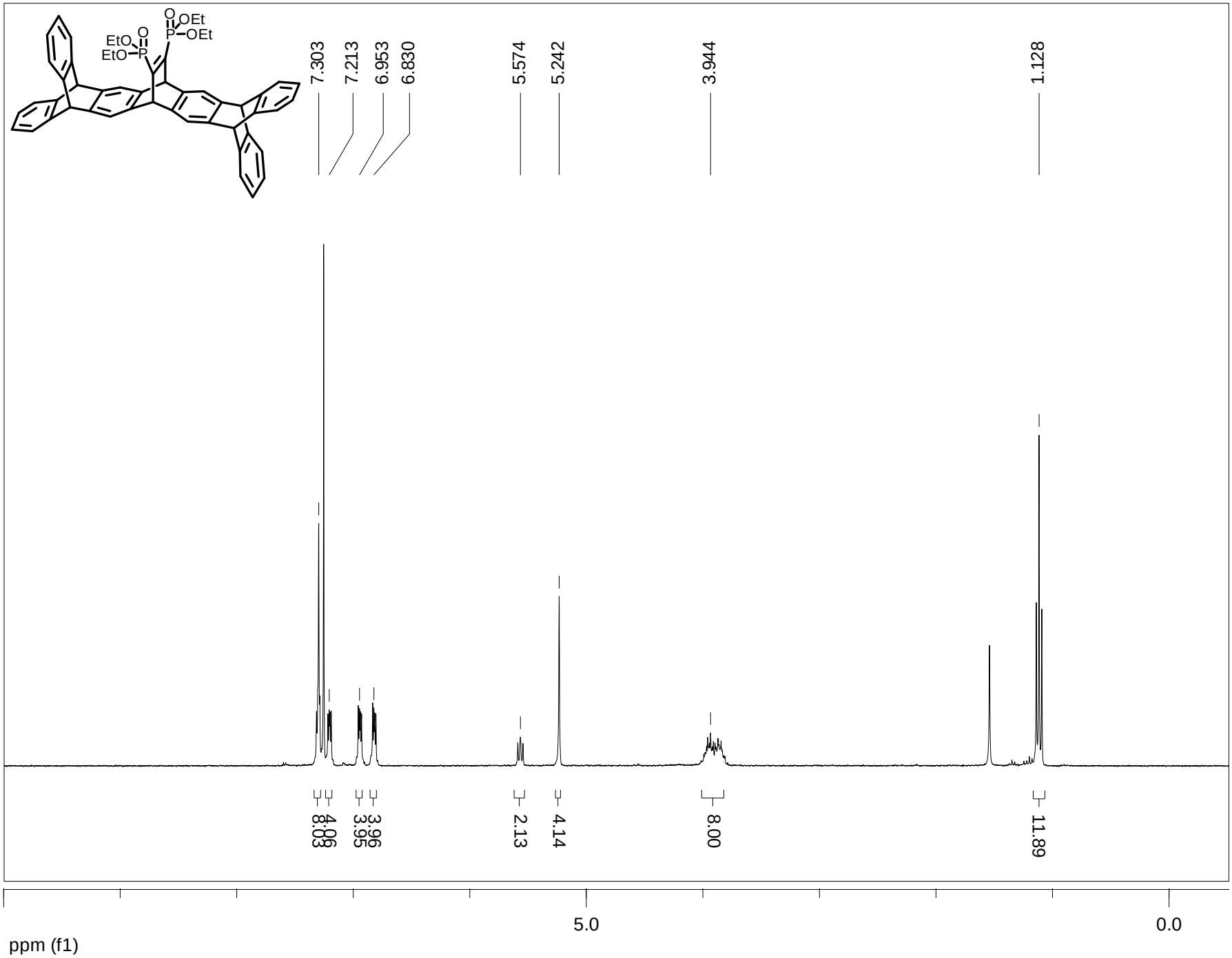

13.3 ^{31}P NMR of tetraethyl (5,7,9,14,16,18-hexahydro-5,18:9,14-bis([1,2]benzeno)-7,16-ethenoheptacene-25,26-diyl)bis(phosphonate) (2)

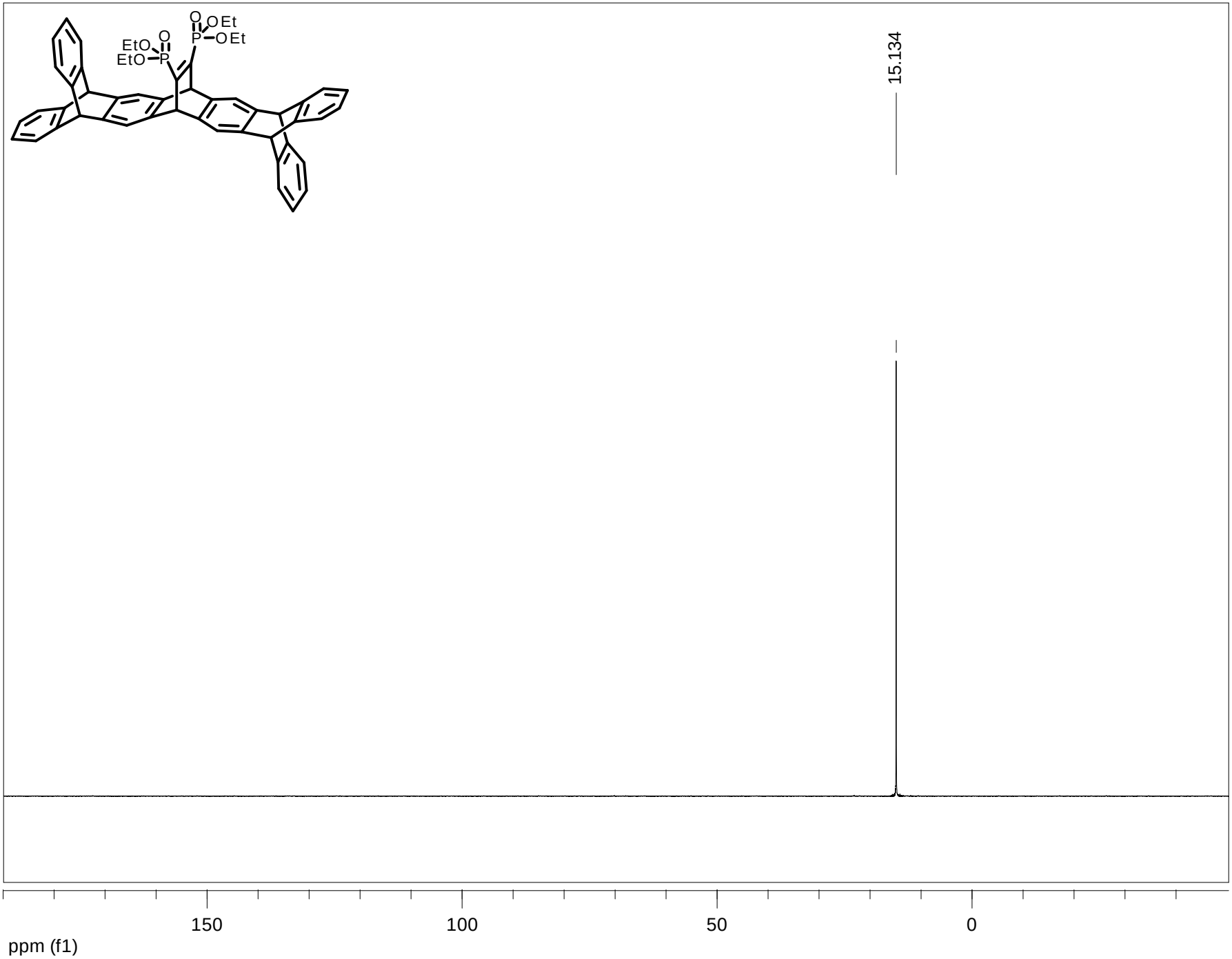

13.4 ^{13}C NMR of tetraethyl (5,7,9,14,16,18-hexahydro-5,18:9,14-bis([1,2]benzeno)-7,16-ethenoheptacene-25,26-diyl)bis(phosphonate) (2)

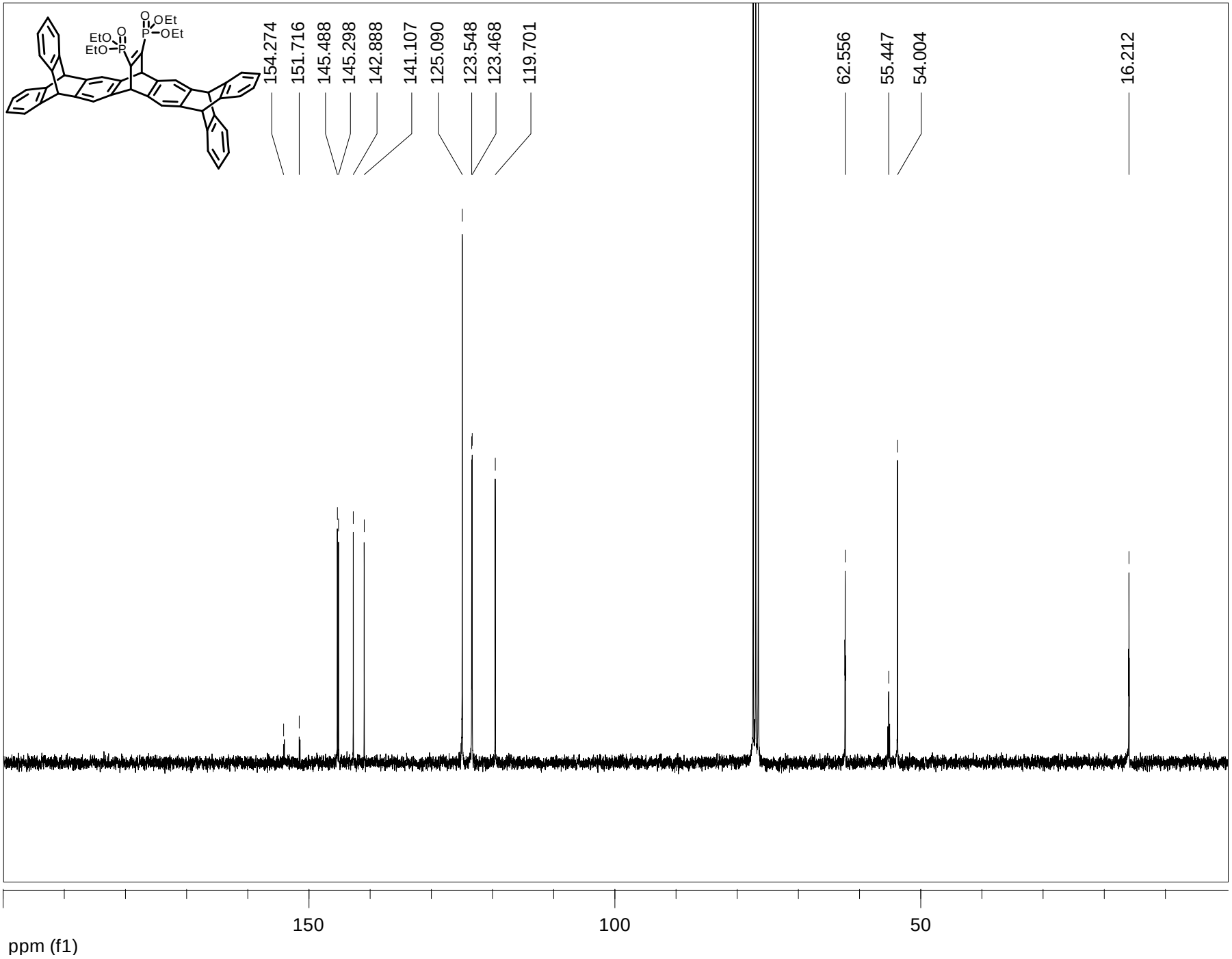

13.5 ^{1}H NMR of dimethyl 5,7,9,14,16,18-hexahydro-5,18:9,14-bis([1,2]benzeno)-7,16-ethenoheptacene-25,26-dicarboxylate (10)

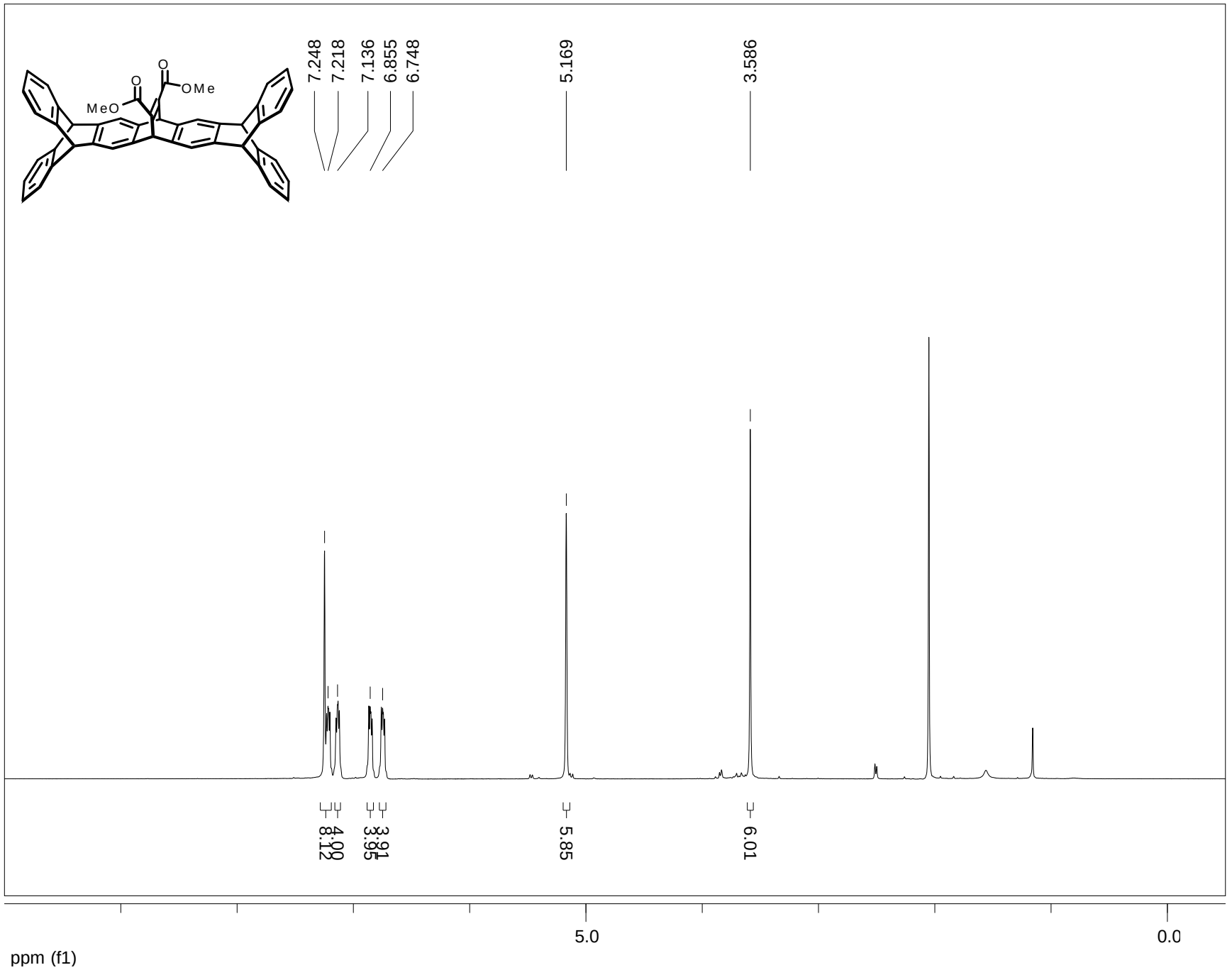

13.6 ^{1}H NMR of 15,16-bis(chloromethyl)-6,13-dihydro-6,13-ethanopentacene (12)

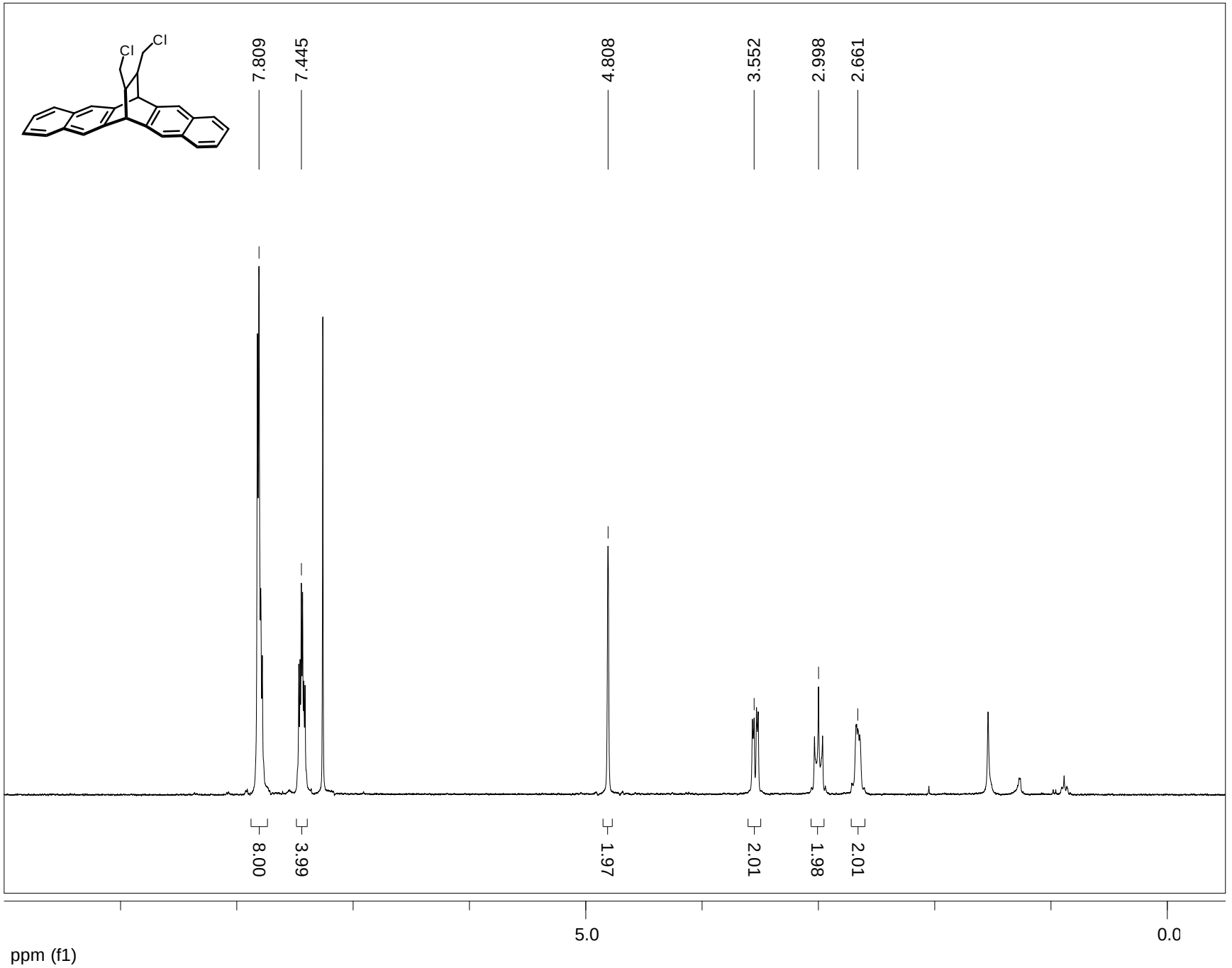

13.7 ^{13}C NMR of 15,16-bis(chloromethyl)-6,13-dihydro-6,13-ethanopentacene (12)

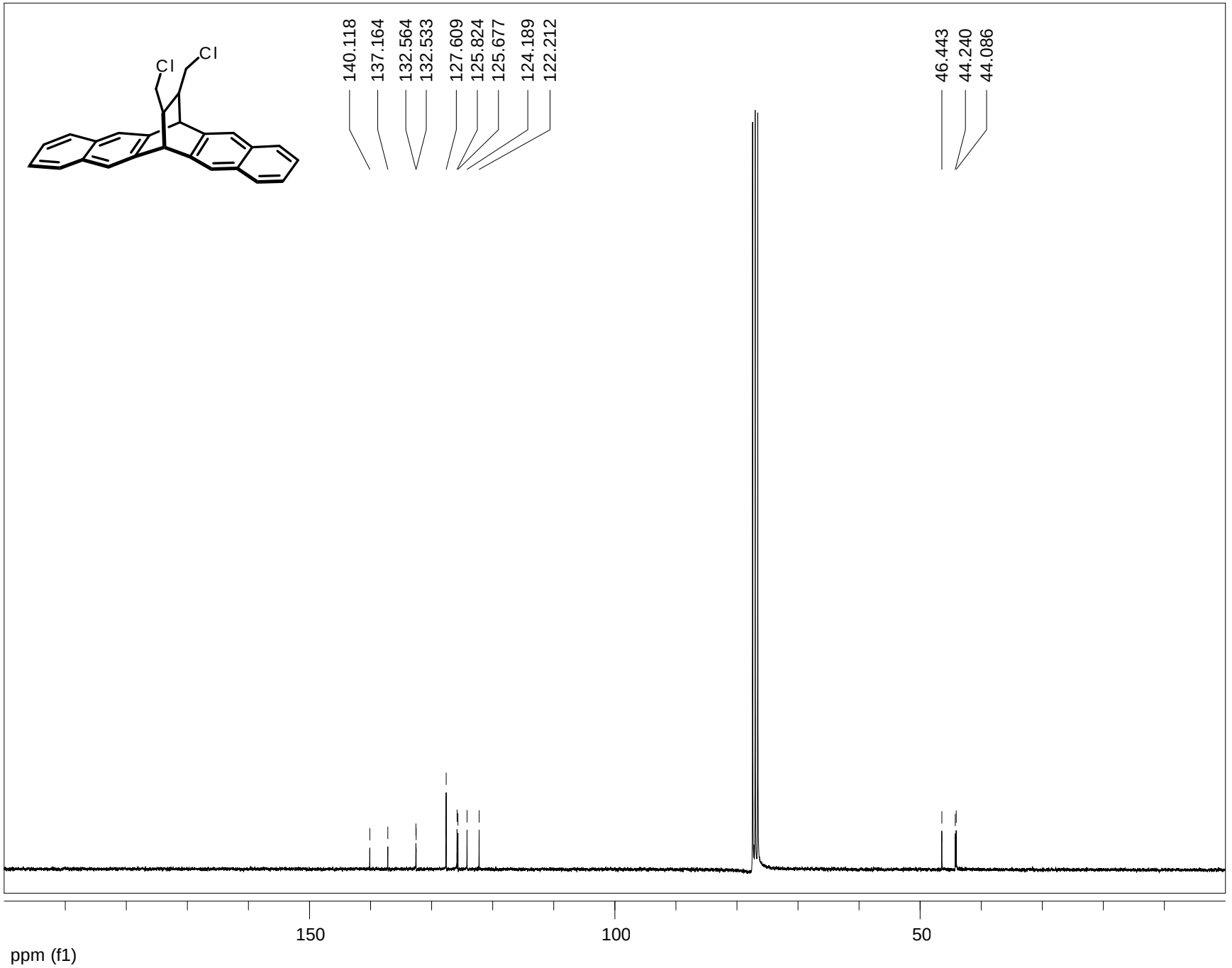

13.8 ^{1}H NMR of 15,16-dimethylene-6,13-dihydro-6,13-ethanopentacene (13)

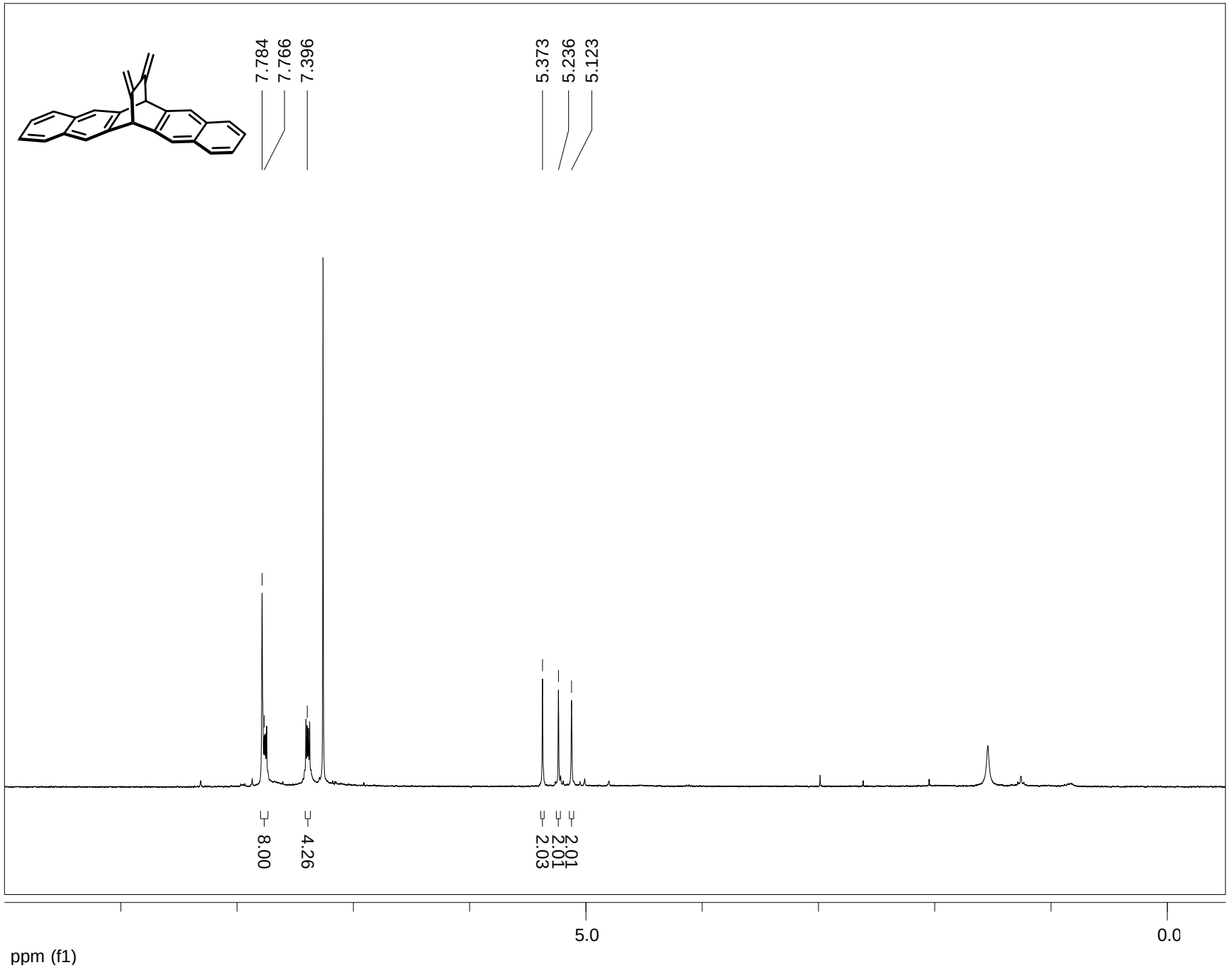

13.9 ^{13}C NMR of 15,16-dimethylene-6,13-dihydro-6,13-ethanopentacene (13)

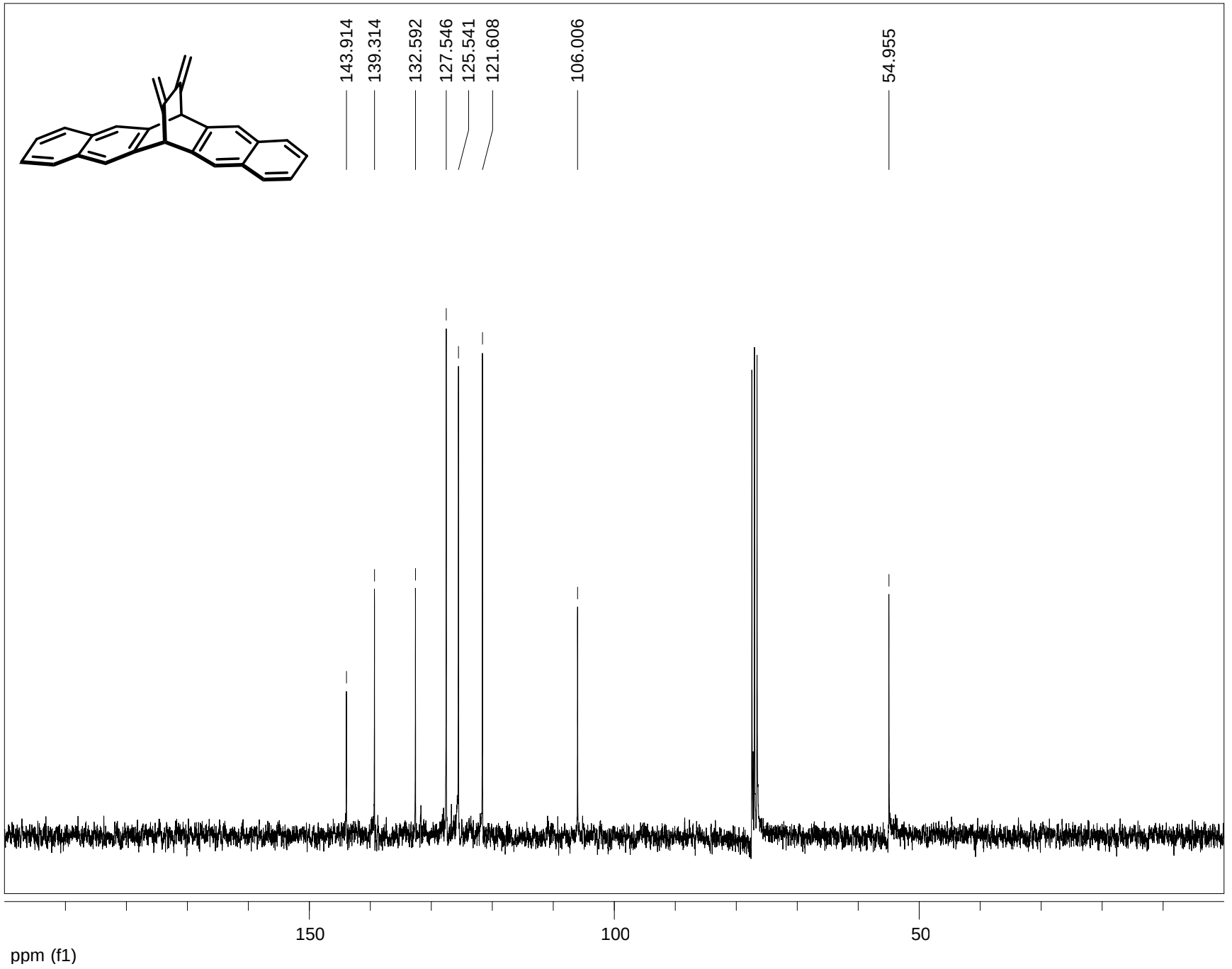

13.10 ^{1}H NMR of 6,7,9,10,17,18,20,21-octahydro-6,21:10,17-bis([2,3]naphthaleno)nonacene (14)

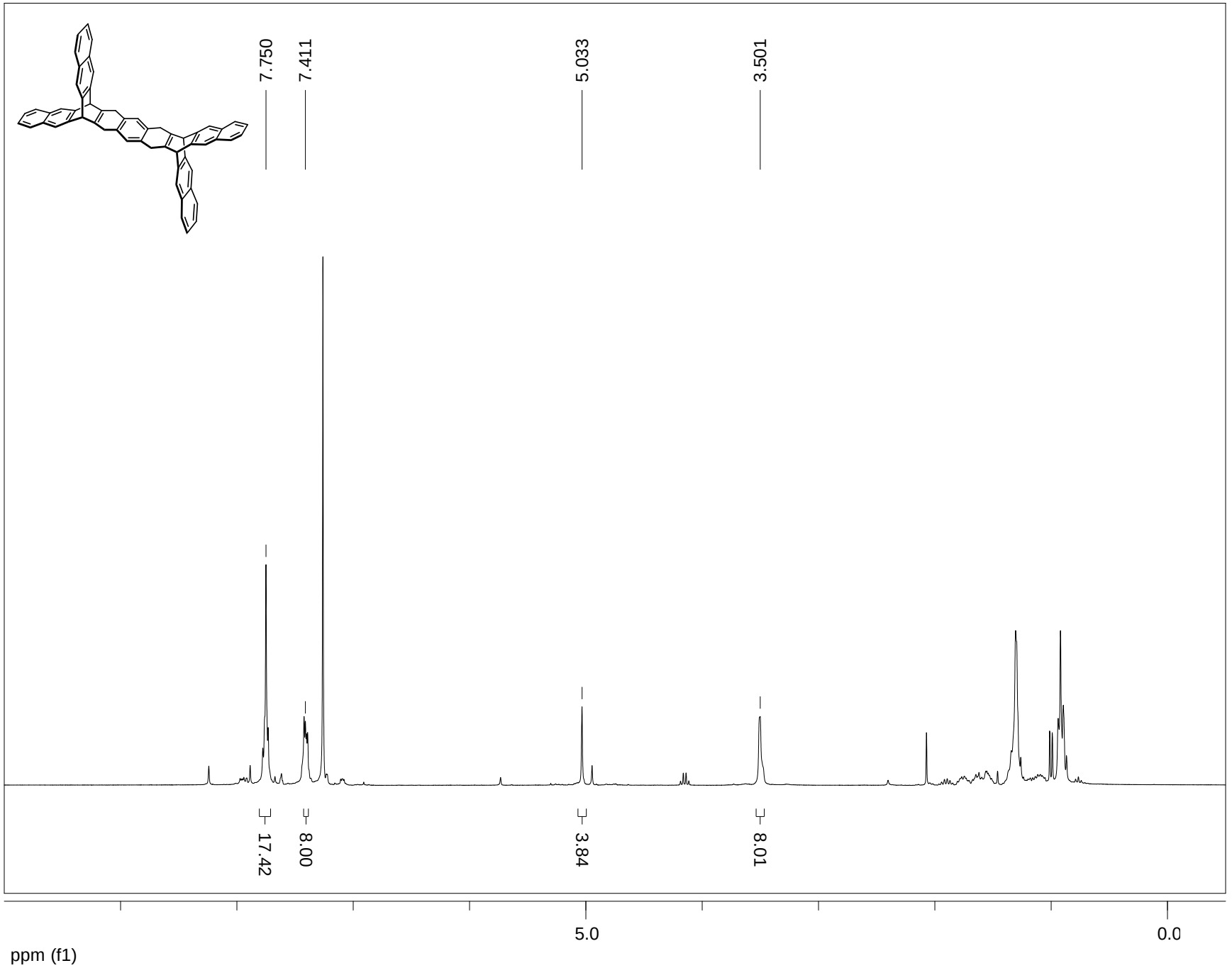

13.11 ^{1}H NMR of 6,10,17,21-tetrahydro-6,21:10,17-bis([2,3]naphthaleno)nonacene (15)

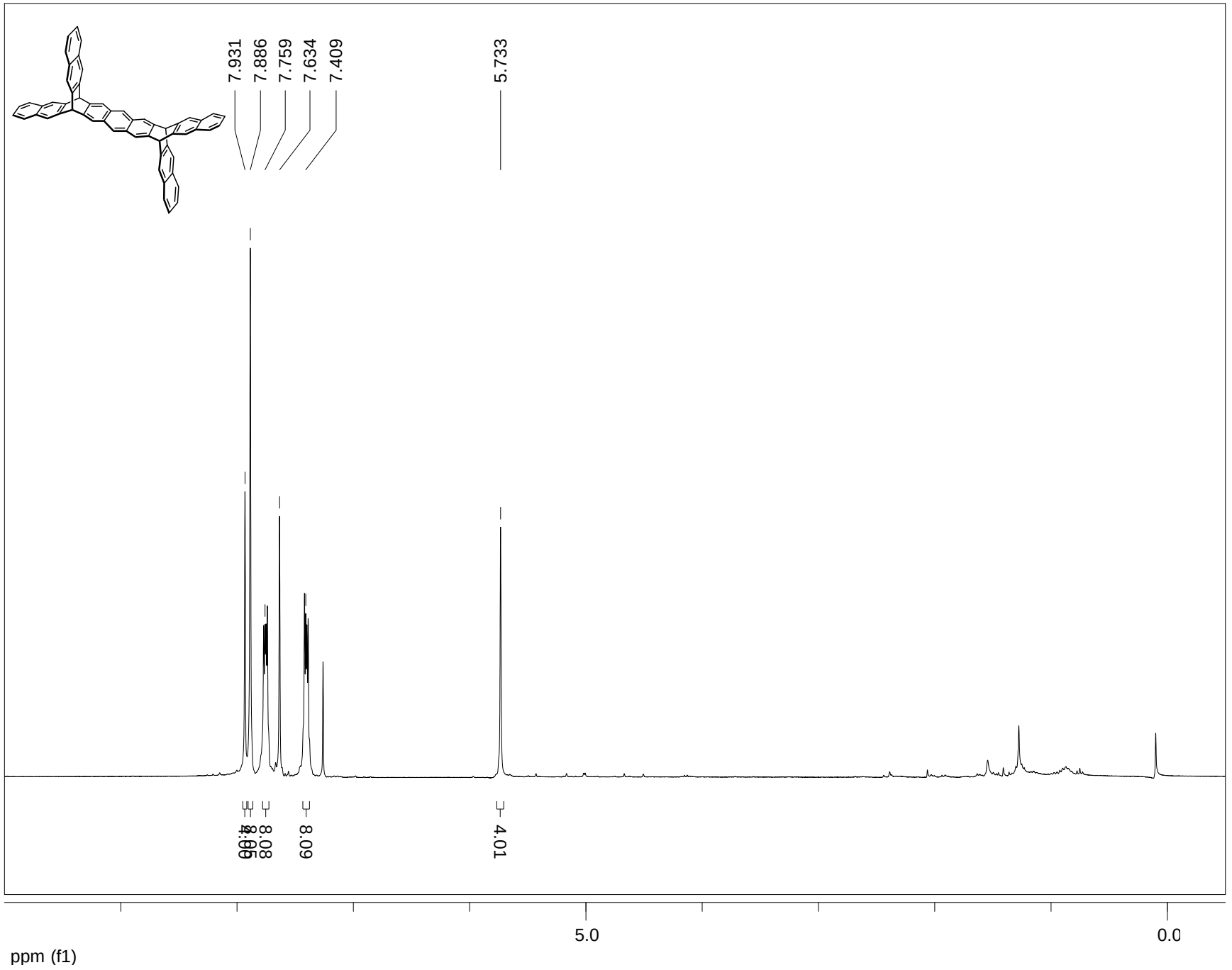

13.12 ^{13}C NMR of 6,10,17,21-tetrahydro-6,21:10,17-bis([2,3]naphthaleno)nonacene (15)

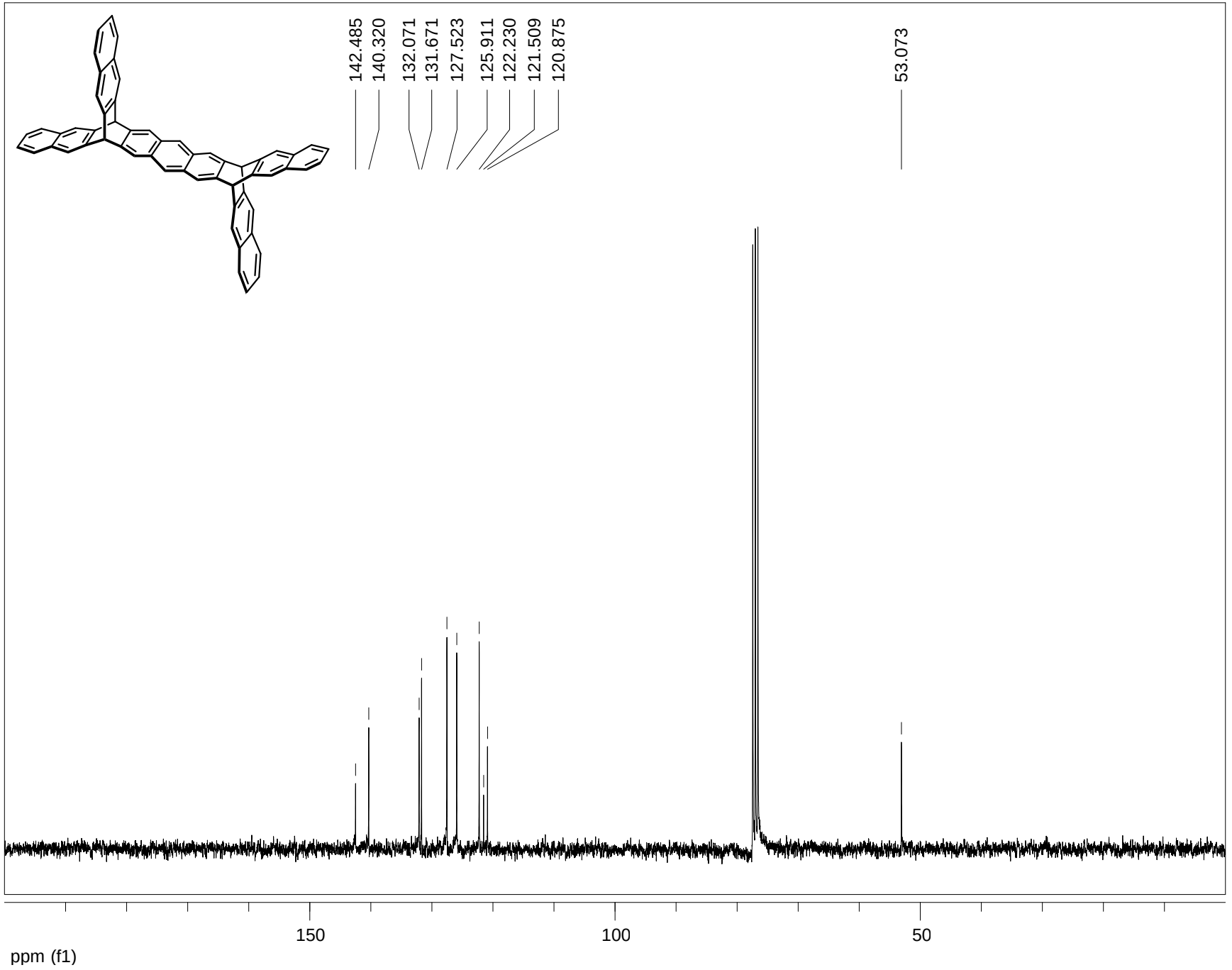

13.13 ^{1}H NMR of tetraethyl (6,8,10,17,19,21-hexahydro-6,21:10,17-bis([2,3]naphthaleno)-8,19-ethenononacene-31,32-diyl)bis(phosphonate) (16)

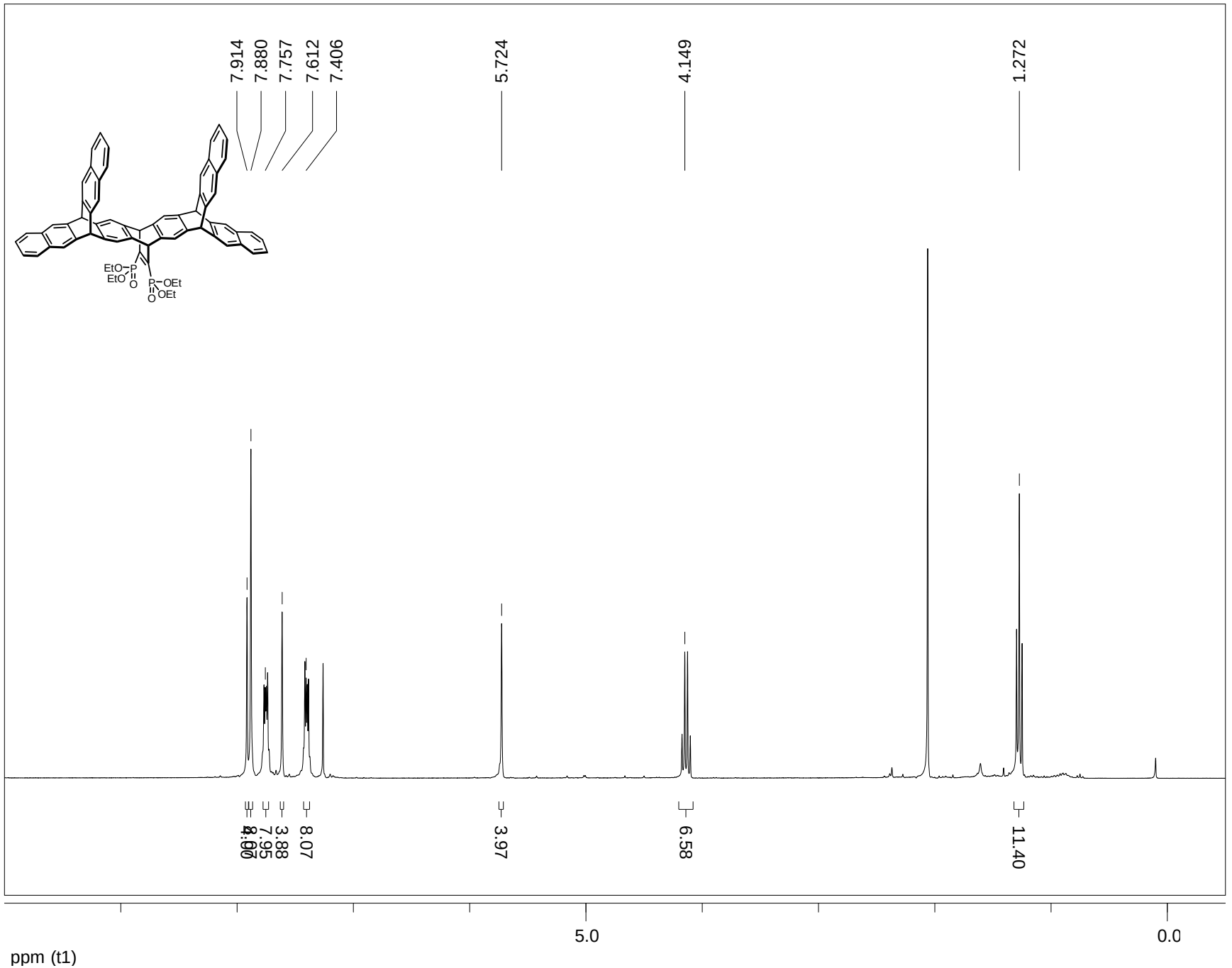

13.14 ^{13}C NMR of tetraethyl (6,8,10,17,19,21-hexahydro-6,21:10,17-bis([2,3]naphthaleno)-8,19-ethenononacene-31,32-diyl)bis(phosphonate) (16)

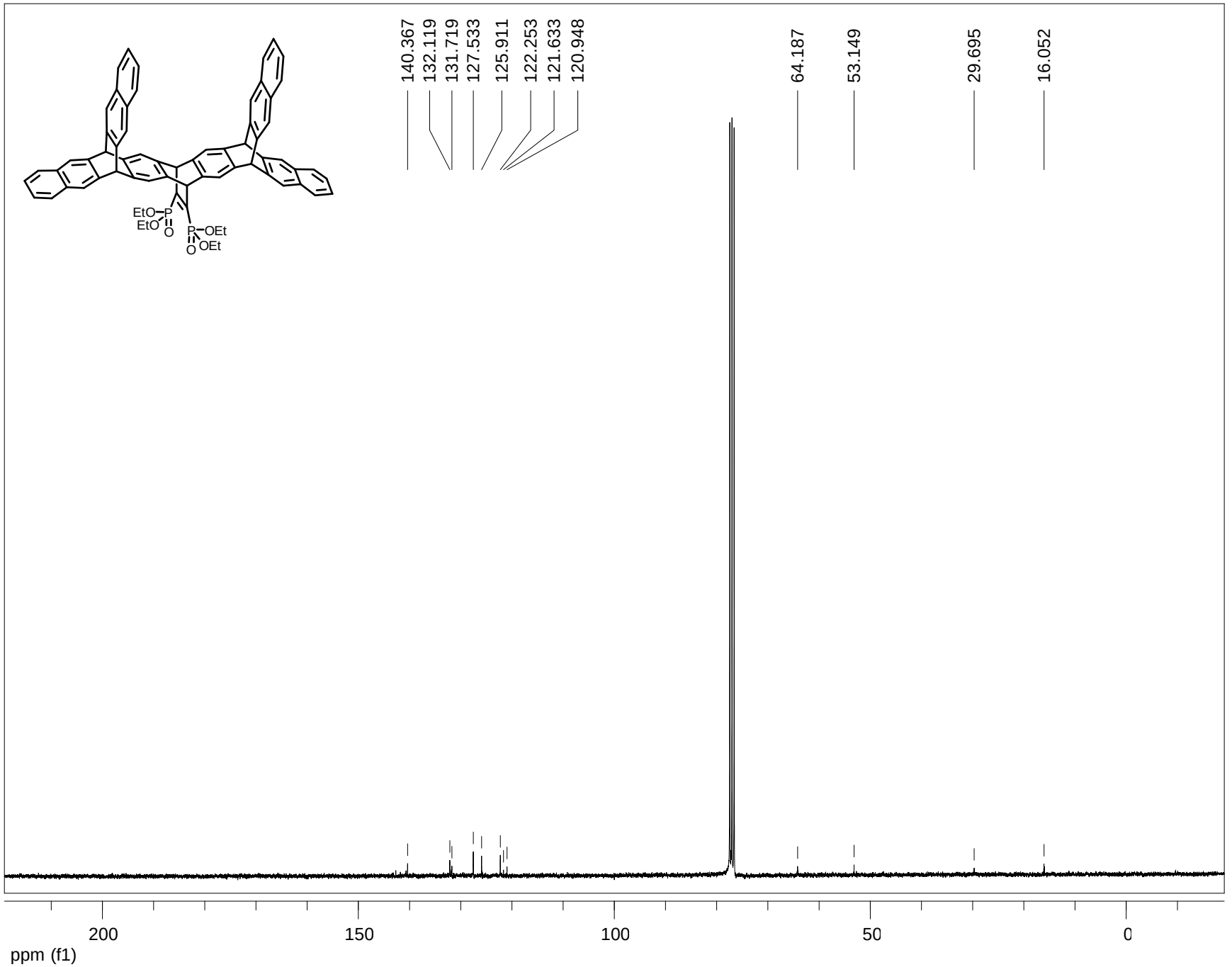

References

(1) Ryzen 5 1600 X https://en.wikichip.org/wiki/amd/ryzen_5/1600x (accessed Jun 14, 2019).

(2) Bergveld, P. The Impact of MOSFET-Based Sensors. *Sensors and Actuators* **1985**, *8*, 109–127.

(3) Kim, F. S.; Guo, X.; Watson, M. D.; Jenekhe, S. A. High-Mobility Ambipolar Transistors and High-gain Inverters from a Donor-Acceptor Copolymer Semiconductor. *Adv. Mater.* **2010**, *22*, 478–482.

(4) Wan, Y.; Samundsett, C.; Bullock, J.; Allen, T.; Hettick, M.; Yan, D.; Zheng, P.; Zhang, X.; Cui, J.; McKeon, J.; Javey, A.; Cuevas, A. Magnesium Fluoride Electron-Selective Contacts for Crystalline Silicon Solar Cells. *ACS Appl. Mater. Interfaces* **2016**, *8*, 14671–14677.

(5) Jaramillo, R.; Ha, S. D.; Silevitch, D. M.; Ramanathan, S. Origins of bad-metal conductivity and the insulator-metal transition in the rare-earth nickelates. *Nat. Phys.* **2014**, *10*, 304–307.

(6) von Hippel, A. R.; Morgan, S. O. Dielectric Materials and Applications. *J. Electrochem. Soc.* **1955**, *102*, 68C.

(7) Li, Q.; Chen, L.; Gadinski, M. R.; Zhang, S.; Zhang, G.; Li, H. U.; Iagodkine, E.; Haque, A.; Chen, L. Q.; Jackson, T. N.; Wang, Q. Flexible high-temperature dielectric materials from polymer nanocomposites. *Nature* **2015**, *523*, 576–579.

(8) Xiang, J.; Lu, W.; Hu, Y.; Wu, Y.; Yan, H.; Lieber, C. M. Ge/Si nanowire heterostructures as high-performance field-effect transistors. *Nature* **2006**, *441*, 489–493.

(9) J. S. Blakemore. Semiconducting and other major properties of gallium arsenide. *J. Appl. Phys.* **1982**, *53*, R123.

(10) Horowitz, G. Oragnic Field-Effect Transistors. *Adv. Mater.* **1998**, *10*, 365–377.

(11) Coropceanu, V.; Cornil, J.; da Silva Filho, D. A.; Olivier, Y.; Silbey, R.; Brédas, J.-L. Charge Transport in Organic Semiconductors. *Chem. Rev.* **2007**, *107*, 926–952.

(12) Forrest, S. R. The path to ubiquitous and low-cost organic electronic appliances on plastic. *Nature* **2004**, *428*, 911–918.

(13) Dong, H.; Zhu, H.; Meng, Q.; Gong, X.; Hu, W. Organic Photoresponse Materials and Devices. *Chem. Soc. Rev.* **2012**, *41*, 1754–1808.

(14) Oehzelt, M.; Koch, N.; Heimel, G. Organic semiconductor density of states controls the energy level alignment at electrode interfaces. *Nat. Commun.* **2014**, *5*, 4174.

(15) Cardona, M.; Pollak, F. H. Energy-Band Structure of Germanium and Silicon: The k·p Method. *Phys. Rev.* **1966**, *142*, 530–543.

(16) Letheby, H. On the production of a blue substance by the electrolysis of sulphate of aniline. *J. Chem. Soc.* **1862**, *15*, 161–163.

(17) Menon, R. Conducting polymers: nobel prize in chemistry, 2000. *Curr. Sci.* **2000**, *79*, 1632–1635.

(18) Kan, B.; Li, M.; Zhang, Q.; Liu, F.; Wan, X.; Wang, Y.; Ni, W.; Long, G.; Yang, X.; Feng, H.; Zuo, Y.; Zhang, M.; Huang, F.; Cao, Y.; Russell, T. P.; Chen, Y. A Series of Simple Oligomer-like Small Molecules Based on Oligothiophenes for Solution-Processed Solar Cells with High Efficiency. *J. Am. Chem. Soc.* **2015**, *137*, 3886–3893.

(19) Wade, L. G.; Simek, J. W. *Organic chemistry*, 9th ed.; Pearson: Glenview, 2017.

(20) Nicolaou, K. C.; Snyder, S. A.; Montagnon, T.; Vassilikogiannakis, G. The Diels–Alder Reaction in Total Synthesis. *Angew. Chem. Int. Ed.* **2002**, *41*, 1668–1698.

(21) Mather, B. D.; Viswanathan, K.; Miller, K. M.; Long, T. E. Michael addition reactions in

macromolecular design for emerging technologies. *Prog. Polym. Sci.* **2006**, *31*, 487–531.

(22) Trost, B. M.; Brindle, C. S. The direct catalytic asymmetric aldol reaction. *Chem. Soc. Rev.* **2010**, *39*, 1600–1632.

(23) Carey, F. A.; Sundberg, R. J. *Advanced Organic Chemistry Part A: Structure and Mechanisms*. Springer: New York, 2007

(24) Glukhovtsev, M. N.; Bach, R. D.; Laiter, S. Isodesmic and homodesmotic stabilization energies of [n]annulenes and their relevance to aromaticity and antiaromaticity: is absolute antiaromaticity possible? *J. Mol. Struct. THEOCHEM* **1997**, *417*, 123–129.

(25) Schleyer, P. von R.; Jiao, H.; Hommes, N. J. R. van E.; Malkin, V. G.; Malkina, O. L. An Evaluation of the Aromaticity of Inorganic Rings: Refined Evidence from Magnetic Properties. *J. Am. Chem. Soc.* **1997**, *119*, 12669–12670.

(26) Cyrański, M. K.; Schleyer, P. V. R.; Krygowski, T. M.; Jiao, H.; Hohlneicher, G. Facts and artifacts about aromatic stability estimation. *Tetrahedron* **2003**, *59*, 1657–1665.

(27) Schleyer, P. V. R.; Manoharan, M.; Jiao, H.; Stahl, F. The Acenes: Is There a Relationship between Aromatic Stabilization and Reactivity? *Org. Lett.* **2001**, *3*, 3643–3646.

(28) Hückel, E. Quantentheoretische Beiträge Zum Benzolproblem - I. Die Elektronenkonfiguration Des Benzols Und Verwandter Verbindungen. *Zeitschrift für Phys.* **1931**, *70*, 204–286.

(29) Hückel, E. Quanstentheoretische Beiträge Zum Benzolproblem - II. Quantentheorie Der Induzierten Polaritäten. *Zeitschrift für Phys.* **1931**, *72*, 310–337.

(30) Hückel, E. Quantentheoretische Beiträge Zum Problem Der Aromatischen Und Ungesättigten Verbindungen. III. *Zeitschrift für Phys.* **1932**, *76*, 628–648.

(31) Pope, M.; Swenberg, C. E. *Electronic Processes in Organic Crystals and Polymers*. Oxford University Press: New York, 1999.

(32) Wannier, G. H. The Structure of Electronic Excitation Levels in Insulating Crystals. *Phys. Rev.* **1937**, *52*, 191–197.

(33) Quattrocchi, C.; Lazzaroni, R.; Bredas, J. L.; Kiebooms, R.; Vanderzande, D.; Gelan, J.; Meervelt, L. V. Optical Absorption Spectra of Aromatic Isothianaphthene Oligomers. Theory and Experiment. *J. Phys. Chem.* **1995**, *99*, 3932–3938.

(34) Tour, J. M.; Wu, R. Synthesis and UV-visible properties of soluble a-thiophene oligomers. Monomer to octamer. *Macromolecules* **1992**, *25*, 1901–1907.

(35) Cheng, Y.-J.; Yang, S.-H.; Hsu, C.-S. Synthesis of Conjugated Polymers for Organic Solar Cell Applications. *Chem. Rev.* **2009**, *109*, 5868–5923.

(36) Dou, L.; Liu, Y.; Hong, Z.; Li, G.; Yang, Y. Low-Bandgap Near-IR Conjugated Polymers/Molecules for Organic Electronics. *Chem. Rev.* **2015**, *115*, 12633–12665.

(37) Li, Y. Molecular Design of Photovoltaic Materials for Polymer Solar Cells: Toward Suitable Electronic Energy Levels and Broad Absorption. *Acc. Chem. Res.* **2012**, *45*, 723–733.

(38) Roncali, J. Synthetic Principles for Bandgap Control in Linear π-Conjugated Systems. *Chem. Rev.* **1997**, *97*, 173–206.

(39) Zhou, H.; Yang, L.; Xiao, S.; Liu, S.; You, W. Donor-Acceptor Polymers Incorporating Alkylated Dithienylbenzothiadiazole for Bulk Heterojunction Solar Cells: Pronounced Effect of Positioning Alkyl Chains. *Macromolecules* **2010**, *43*, 811–820.

(40) Johansson, M. P.; Olsen, J. Torsional Barriers and Equilibrium Angle of Biphenyl: Reconciling Theory

with Experiment. *J. Chem. Theory Comput.* **2008**, *4*, 1460–1471.

(41) Kothai Nayaki, S.; Swaminathan, M. Unusual luminescence characteristics of aminobiphenyls. *Spectrochim. Acta Part A: Mol. Biomol. Spectrosc.* **2002**, *58*, 2931–2940.

(42) Bayrakçeken, F. Triplet-triplet optical energy transfer from benzophenone to naphthalene in the vapor phase. *Spectrochim. Acta Part A: Mol. Biomol. Spectrosc.* **2008**, *71*, 603–608.

(43) Wu, J. S.; Cheng, S. W.; Cheng, Y. J.; Hsu, C. S. Donor-acceptor conjugated polymers based on multifused ladder-type arenes for organic solar cells. *Chem. Soc. Rev.* **2015**, *44*, 1113–1154.

(44) Chen, Y. L.; Chang, C. Y.; Cheng, Y. J.; Hsu, C. S. Synthesis of a New Ladder-Type Benzodi(Cyclopentadithiophene) Arene with Forced Planarization Leading to an Enhanced Efficiency of Organic Photovoltaics. *Chem. Mater.* **2012**, *24*, 3964–3971.

(45) Hermet, P.; Bantignies, J. L.; Rahmani, A.; Sauvajol, J. L.; Johnson, M. R. Density-of-states of crystalline 2,2′-bithiophene: *ab initio* analysis and comparison with inelastic neutron scattering response. *J. Phys. Condens. Matter* **2004**, *16*, 7385–7396.

(46) Zhang, T. G.; Zhao, Y.; Asselberghs, I.; Persoons, A.; Clays, K.; Therien, M. J. Design, Synthesis, Linear, and Nonlinear Optical Properties of Conjugated (Porphinato)zinc(II)-Based Donor-Acceptor Chromophores Featuring Nitrothiophenyl and Nitrooligothiophenyl Electron-Accepting Moieties. *J. Am. Chem. Soc.* **2005**, *127*, 9710–9720.

(47) Roncali, J.; Blanchard, P.; Frère, P. 3,4-Ethylenedioxythiophene (EDOT) as a versatile building block for advanced functional π-conjugated systems. *J. Mater. Chem.* **2005**, *15*, 1589–1610.

(48) Claridge, R. Effect of N-Oxide Incorporation on Thiazole- Containing Conjugated Polymers. MSc. Dissertation, University of Waterloo, Waterloo, ON, 2018.

(49) Lin, J. W. P.; Dudek, L. P. Synthesis and properties of poly(2,5-thienylene). *J. Polym. Sci.* **1980**, *18*, 2869–2873.

(50) Sato, M. A.; Tanaka, S.; Kaeriyama, K. Soluble conducting polythiophenes. *J. Chem. Soc. Chem. Commun.* **1986**, 873–874.

(51) Lei, T.; Dou, J. H.; Pei, J. Influence of Alkyl Chain Branching Positions on the Hole Mobilities of Polymer Thin-Film Transistors. *Adv. Mater.* **2012**, *24*, 6457–6461.

(52) Brédas, J. L. Relationship between band gap and bond length alternation in organic conjugated polymers. *J. Chem. Phys.* **1985**, *82*, 3808–3811.

(53) Wudl, F.; Kobayashi, M.; Heeger, A. J. Poly(Isothianaphthene). *J. Org. Chem.* **1984**, *49*, 3382–3384.

(54) Brédas, J. L.; Heeger, A. J.; Wudl, F. Towards organic polymers with very small intrinsic band gaps. I. Electronic structure of polyisothianaphthene and derivatives. *J. Chem. Phys.* **1986**, *85*, 4673–4678.

(55) Nielsen, C. B.; Holliday, S.; Chen, H. Y.; Cryer, S. J.; McCulloch, I. Non-Fullerene Electron Acceptors for Use in Organic Solar Cells. *Acc. Chem. Res.* **2015**, *48*, 2803–2812.

(56) Kotsuki, H.; Nishizawa, H.; Kitagawa, S.; Ochi, M.; Yamasaki, N.; Matsuoka, K.; Tokoroyama, T. High Pressure Organic Chemistry. III. Diels-Alder Reaction of Thiophene with Maleic Anhydride. *Bull. Chem. Soc. Jpn.* **1979**, *52*, 544–548.

(57) Zhou, Z.; Maruyama, T.; Kanbara, T.; Ikeda, T.; Ichimura, K.; Yamamoto, T.; Tokuda, K. Unique Optical and Electrochemical Properties of π-Conjugated Electrically Conducting Copolymers Consisting of Electron-withdrawing Pyridine Units and Electron-donating Thiophene Units. *J. Chem. Soc. Chem. Commun.* **1991**, 1210–1212.

(58) Bronstein, H.; Chen, Z.; Ashraf, R. S.; Zhang, W.; Du, J.; Durrant, J. R.; Shakya Tuladhar, P.; Song,

K.; Watkins, S. E.; Geerts, Y.; Wienk, M. M.; Janssen, R. A. J.; Anthopoulos, T.; Sirringhaus, H.; Heeney, M.; McCulloch, I. Thieno[3,2-b]thiophene-Diketopyrrolopyrrole-Containing Polymers for High-Performance Organic Field-Effect Transistors and Organic Photovoltaic Devices. *J. Am. Chem. Soc.* **2011**, *133*, 3272–3275.

(59) Ni, Z.; Dong, H.; Wang, H.; Ding, S.; Zou, Y.; Zhao, Q.; Zhen, Y.; Liu, F.; Jiang, L.; Hu, W. Quinoline-Flanked Diketopyrrolopyrrole Copolymers Breaking through Electron Mobility over 6 $cm^2 V^{-1} s^{-1}$ in Flexible Thin Film Devices. *Adv. Mater.* **2018**, *30*, 1704843.

(60) Hou, J.; Chen, H.-Y.; Zhang, S.; Li, G.; Yang, Y. Synthesis, Characterization, and Photovoltaic Properties of a Low Band Gap Polymer Based on Silole-Containing Polythiophenes and 2,1,3-Benzothiadiazole. *J. Am. Chem. Soc.* **2008**, *130*, 16144–16145.

(61) Zhou, H.; Yang, L.; Stuart, A. C.; Price, S. C.; Liu, S.; You, W. Development of Fluorinated Benzothiadiazole as a Structural Unit for a Polymer Solar Cell of 7% Efficiency. *Angew. Chem. Int. Ed.* **2011**, *50*, 2995–2998.

(62) Chen, H.; Hu, Z.; Wang, H.; Liu, L.; Chao, P.; Qu, J.; Chen, W.; Liu, A.; He, F. A Chlorinated π-Conjugated Polymer Donor for Efficient Organic Solar Cells. *Joule* **2018**, *2*, 1623–1634.

(63) Lei, T.; Cao, Y.; Fan, Y.; Liu, C.; Yuan, S.; Pei, J. High-Performance Air-Stable Organic Field-Effect Transistors: Isoindigo-Based Conjugated Polymers. *J. Am. Chem. Soc.* **2011**, *133*, 6099–6101.

(64) Liang, Y.; Feng, D.; Wu, Y.; Tsai, S.-T.; Li, G.; Ray, C.; Yu, Luping. Highly Efficient Solar Cell Polymers Developed via Fine-Tuning of Structural and Electronic Properties. *J. Am. Chem. Soc.* **2009**, *131*, 7792–7799.

(65) Colladet, K.; Fourier, S.; Cleij, T. J.; Lutsen, L.; Gelan, J.; Vanderzande, D.; Nguyen, L. H.;

Neugebauer, H.; Sariciftci, S.; Aguirre, A.; Janssen, G.; Goovaerts, E. Low Band Gap Donor-Acceptor Conjugated Polymers toward Organic Solar Cells Applications. *Macromolecules* **2007**, *40*, 65–72.

(66) Chen, J.; Cao, Y. Development of Novel Conjugated Donor Polymers for High-Efficiency Bulk-Heterojunction Photovoltaic Devices. *Acc. Chem. Res.* **2009**, *42*, 1709–1718.

(67) Price, S. C.; Stuart, A. C.; Yang, L.; Zhou, H.; You, W. Fluorine Substituted Conjugated Polymer of Medium Band Gap Yields 7% Efficiency in Polymer-Fullerene Solar Cells. *J. Am. Chem. Soc.* **2011**, *133*, 4625–4631.

(68) Sumlo Iijima. Helical microtubules of graphitic carbon. *Nature* **1991**, *354*, 56–58.

(69) Rahmat, M.; Hubert, P. Carbon nanotube-polymer interactions in nanocomposites: A review. *Compos. Sci. Technol.* **2011**, *72*, 72–84.

(70) Hirotani, J.; Ohno, Y. Carbon Nanotube Thin Films for High-Performance Flexible Electronics Applications. *Top. Curr. Chem.* **2019**, *377*, 1–14.

(71) Baughman, R. H.; Zakhidov, A. a; de Heer, W. A. Carbon Nanotubes – the Route Toward Applications. *Science* **2002**, *297*, 787–792.

(72) Ribeiro, B.; Botelho, E. C.; Costa, M. L.; Bandeira, C. F. Carbon nanotube buckypaper reinforced polymer composites: a review. *Polímeros* **2017**, *27*, 247–255.

(73) Park, S.; Vosguerichian, M.; Bao, Z. A review of fabrication and applications of carbon nanotube film-based flexible electronics. *Nanoscale* **2013**, *5*, 1727–1752.

(74) Biercuk, M. J.; Llaguno, M. C.; Radosavljevic, M.; Hyun, J. K.; Johnson, A. T.; Fischer, J. E. Carbon nanotube composites for thermal management. *Appl. Phys. Lett.* **2002**, *80*, 2767–2769.

(75) Allaoui, A.; Bai, S.; Cheng, H. M.; Bai, J. B. Mechanical and electrical properties of a MWNT/epoxy

composite. *Compos. Sci. Technol.* **2002**, *62*, 1993–1998.

(76) Li, J.; Ng, H. T.; Cassell, A.; Fan, W.; Chen, H.; Ye, Q.; Koehne, J.; Han, J.; Meyyappan, M. Carbon Nanotube Nanoelectrode Array for Ultrasensitive DNA Detection. *Nano Lett.* **2003**, *3*, 597–602.

(77) Yu, L.; Shearer, C.; Shapter, J. Recent Development of Carbon Nanotube Transparent Conductive Films. *Chem. Rev.* **2016**, *116*, 13413–13453.

(78) Javey, A.; Guo, J.; Wang, Q.; Lundstrom, M.; Dai, H. Ballistic carbon nanotube field-effect transistors. *Nature* **2003**, *424*, 654–657.

(79) Dürkop, T.; Getty, S. A.; Cobas, E.; Fuhrer, M. S. Extraordinary Mobility in Semiconducting Carbon Nanotubes. *Nano Lett.* **2004**, *4*, 35–39.

(80) Byon, H. R.; Choi, H. C. Network Single-Walled Carbon Nanotube-Field Effect Transistors (SWNT-FETs) with Increased Schottky Contact Area for Highly Sensitive Biosensor Applications. *J. Am. Chem. Soc.* **2006**, *128*, 2188–2189.

(81) LeMieux, M. C.; Roberts, M.; Barman, S.; Jin, Y. W.; Kim, J. M.; Bao, Z. Self-Sorted, Aligned Nanotube Networks for Thin-Film Transistors. *Science* **2008**, *321*, 101–104.

(82) Ding, J.; Li, Z.; Lefebvre, J.; Cheng, F.; Dubey, G.; Zou, S.; Finnie, P.; Hrdina, A.; Scoles, L.; Lopinski, G. P.; Kingston, C. T.; Simard, B.; Malenfant, P. R. L. Enrichment of large-diameter semiconducting SWCNTs by polyfluorene extraction for high network density thin film transistors. *Nanoscale* **2014**, *6*, 2328–2339.

(83) Cao, X.; Lau, C.; Liu, Y.; Wu, F.; Gui, H.; Liu, Q.; Ma, Y.; Wan, H.; Amer, M. R.; Zhou, C. Fully Screen-Printed, Large-Area, and Flexible Active-Matrix Electrochromic Displays Using Carbon Nanotube Thin-Film Transistors. *ACS Nano* **2016**, *10*, 9816–9822.

(84) Chopra, S.; McGuire, K.; Gothard, N.; Rao, A. M.; Pham, A. Selective gas detection using a carbon nanotube sensor. *Appl. Phys. Lett.* **2003**, *83*, 2280–2282.

(85) Melzer, K.; Bhatt, V. D.; Schuster, T.; Jaworska, E.; Maksymiuk, K.; Michalska, A.; Lugli, P.; Scarpa, G. Flexible Electrolyte-Gated Ion-Selective Sensors Based on Carbon Nanotube Networks. *IEEE Sens. J.* **2015**, *15*, 3127–3134.

(86) Yang, C.; Denno, M. E.; Pyakurel, P.; Venton, B. J. Recent trends in carbon nanomaterial-based electrochemical sensors for biomolecules: A review. *Anal. Chim. Acta* **2015**, *887*, 17–37.

(87) Besteman, K.; Lee, J.; Wiertz, F. G. M.; Heering, H. A.; Dekker, C. Enzyme-Coated Carbon Nanotubes as Single-Molecule Biosensors. *Nano Lett.* **2003**, *3*, 727–730.

(88) Habisreutinger, S. N.; Leijtens, T.; Eperon, G. E.; Stranks, S. D.; Nicholas, R. J.; Snaith, H. J. Carbon Nanotube/Polymer Composites as a Highly Stable Hole Collection Layer in Perovskite Solar Cells. *Nano Lett.* **2014**, *14,* 5561–5568.

(89) Kymakis, E.; Amaratunga, G. A. J. Single-Wall Carbon Nanotube/Conjugated Polymer Photovoltaic Devices. *Appl. Phys. Lett.* **2002**, *80* (1), 112–114.

(90) Li, H.; Cao, K.; Cui, J.; Liu, S.; Qiao, X.; Shen, Y.; Wang, M. 14.7% efficient mesoscopic perovskite solar cells using single walled carbon nanotubes/carbon composite counter electrodes. *Nanoscale* **2016**, *8*, 6379–6385.

(91) Kataura, H.; Kumazawa, Y.; Maniwa, Y.; Umezu, I.; Suzuki, S.; Ohtsuka, Y.; Achiba, Y. Optical Properties of Single-Wall Carbon Nanotubes. *Synth. Met.* **1999**, *103*, 2555–2558.

(92) Bachilo, S. M.; Strano, M. S.; Kittrell, C.; Hauge, R. H.; Smalley, R. E.; Weisman, R. B. Structure-Assigned Optical Spectra of Single-Walled Carbon Nanotubes. *Science* **2002**, *298*, 2361–2366.

(93) Wallace, P. R. The Band Theory of Graphite. *Phys. Rev.* **1947**, *71*, 622–634.

(94) Park, J.-Y. Band Structure and Electron Transport Physics of One-Dimensional SWNTs. In *Carbon nanotube electronics*; Javey, A.; Kong, J. Springer: New York, 2009. 1–42.

(95) Saito, R.; Fujita, M.; Dresselhaus, G.; Dresselhaus, M. S. Electronic structure of chiral graphene tubules. *Appl. Phys. Lett.* **1992**, *60*, 2204–2206.

(96) Thomsen, C.; Reich, S. Raman Scattering in Carbon Nanotubes. *Top. Appl. Phys.* **2006**, *108*, 115–234.

(97) Cao, Q.; Han, S.; Tulevski, G. S.; Franklin, A. D.; Haensch, W. Evaluation of Field-Effect Mobility and Contact Resistance of Transistors That Use Solution-Processed Single-Walled Carbon Nanotubes. *ACS Nano* **2012**, *6*, 6471–6477.

(98) Zaumseil, J. Single-walled carbon nanotube networks for flexible and printed electronics. *Semicond. Sci. Technol.* **2015**, *30*, 74001.

(99) Hirsch, A. Functionalization of Single-Walled Carbon Nanotubes. *Angew*. *Chem*. *Int*. *Ed*. **2002**, *41*, 1853–1859.

(100) McEuen, P. L.; Fuhrer, M. S.; Park, H. Single-Walled Carbon Nanotube Electronics. *IEEE Trans. Nanotechnol.* **2002**, *1*, 78–85.

(101) Jin, C.; Suenaga, K.; Iijima, S. Vacancy Migrations in Carbon Nanotubes. *Nano Lett.* **2008**, *8*, 1127–1130.

(102) Ishigami, M.; Choi, H. J.; Aloni, S.; Louie, S. G.; Cohen, M. L.; Zettl, A. Identifying Defects in Nanoscale Materials. *Phys. Rev. Lett.* **2004**, *93*, 196803.

(103) Ouyang, M.; Huang, J.; Cheung, C. L.; Lieber, C. M. Atomically Resolved Single-Walled Carbon

Nanotube Intramolecular Junctions. *Science* **2001**, *291*, 97–100.

(104) Choi H.J.; Ihm J.; Louie S.G.; Cohen M.L. Defects, Quasibound States, and Quantum Conductance in Metallic Carbon Nanotubes. *Phys. Rev. Lett.* **2000**, *84*, 2917–2920.

(105) Neophytou, N.; Kienle, D.; Polizzi, E.; Anantram, M. P. Influence of defects on nanotube transistor performance. *Appl. Phys. Lett.* **2006**, *88*, 242106.

(106) Gai, P. L.; Stephan, O.; McGuire, K.; Rao, A. M.; Dresselhaus, M. S.; Dresselhaus, G.; Colliex, C. Structural systematics in boron-doped single wall carbon nanotubes. *J. Mater. Chem.* **2004**, *14*, 669–675.

(107) Chen, Z.; Higgins, D.; Chen, Z. Electrocatalytic activity of nitrogen doped carbon nanotubes with different morphologies for oxygen reduction reaction. *Electrochim. Acta* **2010**, *55*, 4799–4804.

(108) Kang, S. J.; Kocabas, C.; Ozel, T.; Shim, M.; Pimparkar, N.; Alam, M. A.; Rotkin, S. V.; Rogers, J. A. High-performance electronics using dense, perfectly aligned arrays of single-walled carbon nanotubes. *Nat. Nanotechnol.* **2007**, *2*, 230–236.

(109) Ozel, T.; Gaur, A.; Rogers, J. A.; Shim, M. Polymer Electrolyte Gating of Carbon Nanotube Network Transistors. *Nano Lett.* **2005**, *5*, 905–911.

(110) Sun, C. H.; Yin, L. C.; Li, F.; Lu, G. Q.; Cheng, H. M. Van der Waals interactions between two parallel infinitely long single-walled nanotubes. *Chem. Phys. Lett.* **2005**, *403*, 343–346.

(111) Islam, A. E.; Rogers, J. A.; Alam, M. A. Recent Progress in Obtaining Semiconducting Single-Walled Carbon Nanotubes for Transistor Applications. *Adv. Mater.* **2015**, *27*, 7908–7937.

(112) Ajiki, H.; Ando, T. Magnetic Properties of Carbon Nanotubes. *J. Phys. Soc. Japan* **1993**, *62,* 2470–2480.

(113) Mintmire J.; White C. Universal Density of States for Carbon Nanotubes. *Phys. Rev. Lett.* **1998**, *81*, 2506–2509.

(114) Seol, G.; Yoon, Y.; Fodor, J. K.; Guo, J.; Matsudaira, A.; Kienle, D.; Liang, G.; Klimeck, G.; Lundstrom, M.; Saeed, A. I. CNTbands. December 13, 2006.

(115) Miyata, Y.; Kawai, T.; Miyamoto, Y.; Yanagi, K.; Maniwa, Y.; Kataura, H. Chirality-Dependent Combustion of Single-Walled Carbon Nanotubes. *J. Phys. Chem. C* **2007**, *111*, 9671–9677.

(116) Dresselhaus, M. S.; Dresselhaus, G.; Jorio, A.; Souza Filho, A. G.; Saito, R. Raman spectroscopy on isolated single wall carbon nanotubes. *Carbon* **2002**, *40*, 2043–2061.

(117) Doorn, S. K.; Heller, D. A.; Barone, P. W.; Usrey, M. L.; Strano, M. S. Resonant Raman excitation profiles of individually dispersed single walled carbon nanotubes in solution. *Appl. Phys. A-Mater.* **2004**, *78*, 1147–1155.

(118) Dresselhaus, M. S.; Dresselhaus, G.; Saito, R.; Jorio, A. Raman spectroscopy of carbon nanotubes. *Phys. Rep.* **2005**, *409*, 47–99.

(119) Jorio, A.; Saito, R.; Hafner, J. H.; Lieber, C. M.; Hunter, M.; McClure, T.; Dresselhaus, G.; Dresselhaus, M. S. Structural (*n*, *m*) Determination of Isolated Single-Wall Carbon Nanotubes by Resonant Raman Scattering. *Phys. Rev. Lett.* **2001**, *86*, 1118–1121.

(120) Dresselhaus, M. S.; Dresselhaus, G. Intercalation compounds of graphite. *Adv*. *Phys*. **1981**, *30*, 139–326.

(121) Jorio, A.; Souza Filho, A. G.; Dresselhaus, G.; Dresselhaus, M. S.; Swan, A. K.; Ünlü, M. S.; Goldberg, B. B.; Pimenta, M. A.; Hafner, J. H.; Lieber, C. M.; Saito, R. G-band resonant Raman study of 62 isolated single-wall carbon nanotubes. *Phys. Rev. B* **2002**, *65*, 155412.

(122) Tasis, D.; Tagmatarchis, N.; Bianco, A.; Prato, M. Chemistry of Carbon Nanotubes. *Chem. Rev.* **2006**, *106*, 1105–1136.

(123) Karousis, N.; Tagmatarchis, N.; Tasis, D. Current Progress on the Chemical Modification of Carbon Nanotubes. *Chem. Rev.* **2010**, *110*, 5366–5397.

(124) Liu, J.; Rinzler, A. G.; Dai, H.; Hafner, J. H.; Bradley, R. K.; Boul, P. J.; Lu, A.; Iverson, T.; Shelimov, K.; Huffman, C. B.; Rodriguez-Macias, F.; Shon, Y.-S.; Lee, T. R.; Colbert, D. T.; Smalley, R. E. Fullerene Pipes. *Science* **1998**, *280*, 1253–1256.

(125) Xing, Y.; Li, L.; Chusuei, C. C.; Hull, R. V. Sonochemical Oxidation of Multiwalled Carbon Nanotubes. *Langmuir* **2005**, *21*, 4185–4190.

(126) Gromov, A.; Dittmer, S.; Svensson, J.; Nerushev, O. A.; Perez-García, S. A.; Licea-Jiménez, L.; Rychwalski, R.; Campbell, E. E. B. Covalent amino-functionalisation of single-wall carbon nanotubes. *J. Mater. Chem.* **2005**, *15*, 3334–3339.

(127) Chen, J.; Hamon, M. A.; Hu, H.; Chen, Y.; Rao, A. M.; Eklund, P. C.; Haddon, R. C. Solution Properties of Single-Walled Carbon Nanotubes. *Science* **1998**, *282*, 95–98.

(128) Sun, Y.; Huang, W.; Lin, Y.; Fu, K.; Kitaygorodskiy, A.; Riddle, L. A.; Yu, Y. J.; Carroll, D. L. Soluble Dendron-Functionalized Carbon Nanotubes: Preparation, Characterization, and Properties. *Chem. Mater.* **2001**, *13*, 2864–2869.

(129) Hu, H.; Zhao, B.; Hamon, M. A.; Kamaras, K.; Itkis, M. E.; Haddon, R. C. Sidewall Functionalization of Single-Walled Carbon Nanotubes by Addition of Dichlorocarbene. *J. Am. Chem. Soc.* **2003**, *125*, 14893–14900.

(130) Holzinger, M.; Steinmetz, J.; Samaille, D.; Glerup, M.; Paillet, M.; Bernier, P.; Ley, L.; Graupner, R.

[2+1] cycloaddition for cross-linking SWCNTs. *Carbon* **2004**, *42*, 941–947.

(131) Wang, Y.; Iqbal, Z.; Mitra, S. Microwave-induced rapid chemical functionalization of single-walled carbon nanotubes. *Carbon* **2005**, *43*, 1015–1020.

(132) Bahr, J. L.; Dmitry, J. Y.; Kosynkin, D. V.; Bronikowski, M. J.; Smalley, R. E.; Tour, J. M. Functionalization of Carbon Nanotubes by Electrochemical Reduction of Aryl Diazonium Salts: A Bucky Paper Electrode. *J. Am. Chem. Soc.* **2001**, *123*, 6536–6542.

(133) Sun, Y.-P.; Fu, K.; Lin, Y.; Huang, W. Functionalized Carbon Nanotubes: Properties and Applications. *Acc. Chem. Res.* **2002**, *35*, 1096–1104.

(134) Delgado, J. L.; de la Cruz, P.; Urbina, A.; López Navarrete, J. T.; Casado, J.; Langa, F. The first synthesis of a conjugated hybrid of C_{60}-fullerene and a single-wall carbon nanotube. *Carbon* **2007**, *45*, 2250–2252.

(135) Wildgoose, G. G.; Banks, C. E.; Compton, R. G. Metal Nanoparticles and Related Materials Supported on Carbon Nanotubes: Methods and Applications. *Small* **2006**, *2*, 182–193.

(136) An, L.; Fu, Q.; Lu, C.; Liu, J. A Simple Chemical Route To Selectively Eliminate Metallic Carbon Nanotubes in Nanotube Network Devices. *J. Am. Chem. Soc.* **2004**, *126*, 10520–10521.

(137) Strano, M. S.; Dyke, C. A.; Usrey, M. L.; Barone, P. W.; Allen, M. J.; Shan, H.; Kittrell, C.; Hauge, R. H.; Tour, J. M.; Smalley, R. E. Electronic Structure Control of Single-Walled Carbon Nanotube Functionalization. *Science* **2003**, *301*, 1519–1522.

(138) Star, A.; Stoddart, J. F.; Steuerman, D.; Diehl, M.; Boukai, A.; Wong, E. W.; Yang, X.; Chung, S.; Choi, H.; Heath, J. R. Preparation and Properties of Polymer-Wrapped Single-Walled Carbon Nanotubes. *Angew. Chemie, Int. Ed.* **2001**, *40*, 1721–1725.

(139) Backes, C.; Hauke, F.; Hirsch, A. Tuning the adsorption of perylene-based surfactants on the surface of single-walled carbon nanotubes. *Phys. Status Solidi B* **2013**, *250*, 2592–2598.

(140) Kharisov, B. I.; Kharissova, O. V.; Dimas, A. V. The dispersion, solubilization and stabilization in “solution” of single-walled carbon nanotubes. *RSC Adv.* **2016**, *6*, 68760–68787.

(141) Zu, S. Z.; Sun, X. X.; Zhou, D.; Han, B. H. Supramolecular modification of single-walled carbon nanotubes with a water-soluble triptycene derivative. *Carbon* **2011**, *49*, 5339–5347.

(142) Chen, R. J.; Zhang, Y.; Wang, D.; Dai, H. Noncovalent Sidewall Functionalization of Single-Walled Carbon Nanotubes for Protein Immobilization. *J. Am. Chem. Soc.* **2001**, *123*, 3838–3839.

(143) O’Connell, M. J.; Bachilo, S. M.; Huffman, C. B.; Moore, V. C.; Strano, M. S.; Haroz, E. H.; Rialon, K. L.; Boul, P. J.; Noon, W. H.; Kittrell, C.; Ma, J.; Hauge, R. H.; Weisman, R. B.; Smalley, R. E. Band Gap Fluorescence from Individual Single-Walled Carbon Nanotubes. *Science* **2002**, *297,* 593–596.

(144) Lee, H. W.; Yoon, Y.; Park, S.; Oh, J. H.; Hong, S.; Liyanage, L. S.; Wang, H.; Morishita, S.; Patil, N.; Park, Y. J.; Park, J. J.; Spakowitz, A.; Galli, G.; Gygi, F.; Wong, P. H. S.; Tok, J. B. H.; Kim, J. M.; Bao, Z. Selective dispersion of high purity semiconducting single-walled carbon nanotubes with regioregular poly(3-alkylthiophene)s. *Nat. Commun.* **2011**, *2*, 541–548.

(145) Rice, N. A.; Bodnaryk, W. J.; Mirka, B.; Melville, O. A.; Adronov, A.; Lessard, B. H. Polycarbazole-Sorted Semiconducting Single-Walled Carbon Nanotubes for Incorporation into Organic Thin Film Transistors. *Adv. Electron. Mater.* **2019**, *5*, 1800539.

(146) Chortos, A.; Pochorovski, I.; Lin, P.; Pitner, G.; Yan, X.; Gao, T. Z.; To, J. W. F.; Lei, T.; Will, J. W.; Wong, H.-S. P.; Bao, Z. Universal Selective Dispersion of Semiconducting Carbon Nanotubes from Commercial Sources Using a Supramolecular Polymer. *ACS Nano* **2017**, *11*, 5660–5669.

(147) Lei, T.; Chen, X.; Pitner, G.; Wong, H. S. P.; Bao, Z. Removable and Recyclable Conjugated Polymers for Highly Selective and High-Yield Dispersion and Release of Low-Cost Carbon Nanotubes. *J. Am. Chem. Soc.* **2016**, *138*, 802–805.

(148) Modugno, G.; Syrgiannis, Z.; Bonasera, A.; Carraro, M.; Giancane, G.; Valli, L.; Bonchio, M.; Prato, M. The supramolecular design of low-dimensional carbon nano-hybrids encoding a polyoxometalate-bis-pyrene tweezer. *Chem. Commun.* **2014**, *50*, 4881–4883.

(149) Ehli, C.; Guldi, D. M.; Ángeles Herranz, M.; Martín, N.; Campidelli, S.; Prato, M. Pyrene-tetrathiafulvalene supramolecular assembly with different types of carbon nanotubes. *J. Mater. Chem.* **2008**, *18*, 1498–1503.

(150) Zhan, S.; Ahlquist, M. S. G. Dynamics and Reactions of Molecular Ru Catalysts at Carbon Nanotube-Water Interfaces. *J. Am. Chem. Soc.* **2018**, *140*, 7498–7503.

(151) Zhou, J.; Li, H.; Lu, J.; Luo, G.; Lai, L.; Qin, R.; Wang, L.; Nagase, S.; Gao, Z.; Mei, W.; Li, G.; Yu, D.; Sanvito, S. Selection of Single-Walled Carbon Nanotubes According to Both Their Diameter and Chirality via Nanotweezers. *Nano Res*. **2010**, *3*, 296–306.

(152) Hammershøj, P.; Bomans, P. H. H.; Lakshminarayanan, R.; Fock, J.; Jensen, S. H.; Jespersen, T. S.; Brock-Nannestad, T.; Hassenkam, T.; Nygård, J.; Sommerdijk, N. A. J. M.; Kilså, K.; Bjørnholm, T.; Christensen, J. B. A Triptycene-Based Approach to Solubilising Carbon Nanotubes and C_{60}. *Chem. Eur. J.* **2012**, *18*, 8716–8723.

(153) Tromp, R. M.; Afzali, A.; Freitag, M.; Mitzi, D. B.; Chen, Z. Novel Strategy for Diameter-Selective Separation and Functionalization of Single-Wall Carbon Nanotubes. *Nano Lett.* **2008**, *8*, 469–472.

(154) Guo, Z.; Sadler, P. J.; Tsang, S. C. Immobilization and Visualization of DNA and Proteins on Carbon

Nanotubes. *Adv. Mater.* **1998**, *10*, 701–703.

(155) Bradley, K.; Briman, M.; Star, A.; Grüner, G. Charge Transfer from Adsorbed Proteins. *Nano Lett.* **2004**, *4*, 253–256.

(156) Azamian, B. R.; Davis, J. J.; Coleman, K. S.; Bagshaw, C. B.; Green, M. L. H. Bioelectrochemical Single-Walled Carbon Nanotubes. *J. Am. Chem. Soc.* **2002**, *124*, 12664–12665.

(157) Chen, R. J.; Choi, H. C.; Bangsaruntip, S.; Yenilmez, E.; Tang, X.; Wang, Q.; Chang, Y.-L.; Dai, H. An Investigation of the Mechanisms of Electronic Sensing of Protein Adsorption on Carbon Nanotube Devices. *J. Am. Chem. Soc.* **2004**, *126*, 1563–1568.

(158) Najeeb, C. K.; Chang, J.; Lee, J. H.; Lee, M.; Kim, J. H. Preparation of semiconductor-enriched single-walled carbon nanotube dispersion using a neutral pH water soluble chitosan derivative. *J. Colloid Interface Sci.* **2011**, *354*, 461–466.

(159) Zheng, M.; Jagota, A.; Strano, M. S.; Santos, A. P.; Barone, P.; Chou, S. G.; Diner, B. A.; Dresselhaus, M. S.; Mclean, R. S.; Onoa, G. B.; Samsonidze, G. G.; Semke, E. D.; Usrey, M.; Walls, D. J. Structure-Based Carbon Nanotube Sorting by Sequence-Dependent DNA Assembly. *Science* **2003**, *302*, 1545–1548.

(160) Tu, X.; Manohar, S.; Jagota, A.; Zheng, M. DNA sequence motifs for structure-specific recognition and separation of carbon nanotubes. *Nature* **2009**, *460*, 250–253.

(161) Che, Y.; Wang, C.; Liu, J.; Liu, B.; Lin, X.; Parker, J.; Beasley, C.; Wong, H.-S. P.; Zhou, C. Selective Synthesis and Device Applications of Semiconducting Single-Walled Carbon Nanotubes Using Isopropyl Alcohol as Feedstock. *ACS Nano* **2012**, *6*, 7454–7462.

(162) Xu, W.; Zhao, J.; Qian, L.; Han, X.; Wu, L.; Wu, W.; Song, M.; Zhou, L.; Su, W.; Wang, C.; Nie, S.;

Cui, Z. Sorting of large-diameter semiconducting carbon nanotube and printed flexible driving circuit for organic light emitting diode (OLED). *Nanoscale* **2014**, *6*, 1589–1595.

(163) Chien, Y. M.; Lefevre, F.; Shih, I.; Izquierdo, R. A solution processed top emission OLED with transparent carbon nanotube electrodes. *Nanotechnology* **2010**, *21*, 134020.

(164) Lipomi, D. J.; Vosgueritchian, M.; Tee, B. C. K.; Hellstrom, S. L.; Lee, J. A.; Fox, C. H.; Bao, Z. Skin-like pressure and strain sensors based on transparent elastic films of carbon nanotubes. *Nat. Nanotechnol.* **2011**, *6*, 788–792.

(165) Yu, Z.; Niu, X.; Liu, Z.; Pei, Q. Intrinsically Stretchable Polymer Light-Emitting Devices Using Carbon Nanotube-Polymer Composite Electrodes. *Adv. Mater.* **2011**, *23*, 3989–3994.

(166) Sarker, B. K.; Khondaker, S. I. Lower activation energy in organic field effect transistors with carbon nanotube contacts. *Solid. State. Electron.* **2014**, *99*, 55–58.

(167) Southard, A.; Sangwan, V.; Cheng, J.; Williams, E. D.; Fuhrer, M. S. Solution-processed single walled carbon nanotube electrodes for organic thin-film transistors. *Org. Electron.* **2009**, *10*, 1556–1561.

(168) Yang, J. S.; Swager, T. M. Fluorescent Porous Polymer Films as TNT Chemosensors: Electronic and Structural Effects. *J. Am. Chem. Soc.* **1998**, *120*, 11864–11873.

(169) Wang, Y.; Du, J.; Li, Y.; Shan, D.; Zhou, X.; Xue, Z.; Lu, X. A amperometric biosensor for hydrogen peroxide by adsorption of horseradish peroxidase onto single-walled carbon nanotubes. *Colloid*. *Surface*. *B* **2012**, *90*, 62–67.

(170) Qian, T.; Yu, C.; Zhou, X.; Ma, P.; Wu, S.; Shen, J. Ultrasensitive dopamine sensor based on novel molecularly imprinted polypyrrole coated carbon nanotubes. *Biosens. Bioelectron.* **2014**, *58*, 237–241.

(171) Li, W.-S.; Hou, P.-X.; Liu, C.; Sun, D.-M.; Yuan, J.; Zhao, S.-Y.; Yin, L.-C.; Cong, H.; Cheng, H.-M. High-Quality, Highly Concentrated Semiconducting Single-Wall Carbon Nanotubes for Use in Field Effect Transistors and Biosensors. *ACS Nano* **2013**, *7*, 6831–6839.

(172) Kim, J. P.; Lee, B. Y.; Hong, S.; Sim, S. J. Ultrasensitive carbon nanotube-based biosensors using antibody-binding fragments. *Anal. Biochem.* **2008**, *381*, 193–198.

(173) Esser, B.; Schnorr, J. M.; Swager, T. M. Selective Detection of Ethylene Gas Using Carbon Nanotube-based Devices: Utility in Determination of Fruit Ripeness. *Angew. Chem. Int. Ed.* **2012**, *51*, 5752–5756.

(174) Tune, D. D.; Flavel, B. S.; Krupke, R.; Shapter, J. G. Carbon Nanotube-Silicon Solar Cells. *Adv. Energy Mater.* **2012**, *2*, 1043–1055.

(175) Ramuz, M. P.; Vosgueritchian, M.; Wei, P.; Wang, C.; Gao, Y.; Wu, Y.; Chen, Y.; Bao, Z. Evaluation of Solution-Processable Carbon-Based Electrodes for All-Carbon Solar Cells. *ACS Nano* **2012**, *6*, 10384–10395.

(176) Kymakis, E.; Koudoumas, E.; Franghiadakis, I.; Amaratunga, G. A. J. Post-fabrication annealing effects in polymer-nanotube photovoltaic cells. *J. Phys. D: Appl. Phys.* **2006**, *39*, 1058–1062.

(177) Bindl, D. J.; Wu, M. Y.; Prehn, F. C.; Arnold, M. S. Efficiently Harvesting Excitons from Electronic Type-Controlled Semiconducting Carbon Nanotube Films. *Nano Lett.* **2011**, *11*, 455–460.

(178) Jain, R. M.; Howden, R.; Tvrdy, K.; Shimizu, S.; Hilmer, A. J.; McNicholas, T. P.; Gleason, K. K.; Strano, M. S. Polymer-Free Near-Infrared Photovoltaics with Single Chirality (6,5) Semiconducting Carbon Nanotube Active Layers. *Adv. Mater.* **2012**, *24*, 4436–4439.

(179) Fu, X.; Xu, L.; Li, J.; Sun, X.; Peng, H. Flexible solar cells based on carbon nanomaterials. *Carbon*

2018, *139*, 1063–1073.

(180) Shah, K. A.; Tali, B. A. Synthesis of carbon nanotubes by catalytic chemical vapour deposition: A review on carbon sources, catalysts and substrates. *Mater. Sci. Semicond. Process.* **2016**, *41*, 67–82.

(181) Tessonnier, J. P.; Su, D. S. Recent Progress on the Growth Mechanism of Carbon Nanotubes: A Review. *ChemSusChem* **2011**, *4*, 824–847.

(182) Bachilo, S. M.; Balzano, L.; Herrera, J. E.; Pompeo, F.; Resasco, D. E.; Weisman, R. B. Narrow (*n*,*m*)-Distribution of Single-Walled Carbon Nanotubes Grown Using a Solid Supported Catalyst. *J. Am. Chem. Soc.* **2003**, *125*, 11186–11187.

(183) Qu, L.; Du, F.; Dai, L. Preferential Syntheses of Semiconducting Vertically Aligned Single-Walled Carbon Nanotubes for Direct Use in FETs. *Nano Lett.* **2008**, *8*, 2682–2687.

(184) Nasibulin, A. G.; Moisala, A.; Jiang, H.; Kauppinen, E. I. Carbon nanotube synthesis from alcohols by a novel aerosol method. *J. Nanoparticle Res.* **2006**, *8*, 465–475.

(185) Murakami, Y.; Miyauchi, Y.; Chiashi, S.; Maruyama, S. Direct synthesis of high-quality single-walled carbon nanotubes on silicon and quartz substrates. *Chem. Phys. Lett.* **2003**, *377*, 49–54.

(186) Chai, S. P.; Zein, S. H. S.; Mohamed, A. R. Preparation of carbon nanotubes over cobalt-containing catalysts via catalytic decomposition of methane. *Chem. Phys. Lett.* **2006**, *426*, 345–350.

(187) Ding, L.; Tselev, A.; Wang, J.; Yuan, D.; Chu, H.; Mcnicholas, T. P.; Li, Y.; Liu, J. Selective Growth of Well-Aligned Semiconducting Single-Walled Carbon Nanotubes. *Nano Lett.* **2009**, *9*, 800–805.

(188) He, M.; Liu, B.; Chernov, A. I.; Obraztsova, E. D.; Kauppi, I.; Jiang, H.; Anoshkin, I.; Cavalca, F.; Hansen, T. W.; Wagner, J. B.; Nasibulin, A. G.; Kauppinen, E. I.; Linnekoski, J.; Niemelä, M.;

Lehtonen, J. Growth Mechanism of Single-Walled Carbon Nanotubes on Iron-Copper Catalyst and Chirality Studies by Electron Diffraction. *Chem. Mater.* **2012**, *24*, 1796–1801.

(189) Liu, B.; Wu, F.; Gui, H.; Zheng, M.; Zhou, C. Chirality-Controlled Synthesis and Applications of Single-Wall Carbon Nanotubes. *ACS Nano* **2017**, *11*, 31–53.

(190) Murayama, H.; Tomonoh, S.; Alford, J. M.; Karpuk, M. E. Fullerene Production in Tons and More: From Science to Industry. *Fuller*. *Nanotub*. *Car*. *N*. **2004**, *12*, 1–9.

(191) Loutfy, R. O.; Lowe, T. P.; Moravsky, A. P.; Katagiri, S. Commercial Production of Fullerenes and Carbon Nanotubes. *Perspect. Fuller. Nanotechnol.* **2002**, 35–46.

(192) Raymor – Nanotubes for Electronics http://raymor.com/our-products/superpuretubes/ (accessed Jun 17, 2019).

(193) Journet, C.; Maser, W. K.; Bernier, P.; Loiseau, A.; de la Chapelle, M. L.; Lefrant, S.; Deniard, P.; Lee, R.; Fischer, J. E. Large-scale production of single-walled carbon nanotubes by the electric-arc technique. *Nature* **1997**, *388*, 756–758.

(194) Su, Y.; Zhang, Y. Carbon nanomaterials synthesized by arc discharge hot plasma. *Carbon* **2015**, *83*, 90–99.

(195) Das, R.; Shahnavaz, Z.; Ali, M. E.; Islam, M. M.; Abd Hamid, S. B. Can We Optimize Arc Discharge and Laser Ablation for Well-Controlled Carbon Nanotube Synthesis? *Nanoscale Res. Lett.* **2016**, *11*, 510.

(196) Fang, L.; Sheng, L.; An, K.; Yu, L.; Ren, W.; Ando, Y.; Zhao, X. Effect of adding W to Fe catalyst on the synthesis of SWCNTs by arc discharge. *Phys. E* **2013**, *50*, 116–121.

(197) Guo T.; Nikolaev P.; Thess A.; Colbert D. T.; Smalley R.E. Catalytic growth of single-walled

manotubes by laser vaporization. *Chem. Phys. Lett.* **1995**, *243*, 49–54.

(198) Maser, W. K.; Benito, A. M.; Martínez, M. T. Production of carbon nanotubes: the light approach. *Carbon* **2002**, *40*, 1685–1695.

(199) Thess, A.; Lee, R.; Nikolaev, P.; Dai, H.; Petit, P.; Robert, J.; Xu, C.; Lee, Y. H.; Kim, S. G.; Rinzler, A. G.; Colbert, D. T.; Scuseria, G. E.; Tománek, D.; Fischer, J. E.; Smalley, R. E.; Crystalline Ropes of Metallic Carbon Nanotubes. *Science* **1996**, *273*, 483–487.

(200) Naumov, A. V; Kuznetsov, O. A.; Harutyunyan, A. R.; Green, A. A.; Hersam, M. C.; Resasco, D. E.; Nikolaev, P. N.; Weisman, R. B. Quantifying the Semiconducting Fraction in Single-Walled Carbon Nanotube Samples Through Comparative Atomic Force and Photoluminescence Microscopies. *Nano Lett.* **2009**, *9*, 3203–3208.

(201) Bandow, S.; Asaka, S.; Saito, Y.; Rao, A. M.; Grigorian, L.; Richter, E.; Eklund, P. C. Effect of Growth Temperature on the Diameter Distribution and Chirality of Single-Wall Carbon Nanotubes. *Phys. Rev. Lett.* **1998**, *80*, 3779–3782.

(202) Kim, W. J.; Nair, N.; Lee, C. Y.; Strano, M. S. Covalent Functionalization of Single-Walled Carbon Nanotubes Alters Their Densities Allowing Electronic and Other Types of Separation. *J. Phys. Chem. C* **2008**, *112*, 7326–7331.

(203) Hassanien, A.; Tokumoto, M.; Umek, P.; Vrbanič, D.; Mozetič, M.; Mihailović, D.; Venturini, P.; Pejovnik, S. Selective etching of metallic single-wall carbon nanotubes with hydrogen plasma. *Nanotechnology* **2005**, *16*, 278–281.

(204) Zhang, G.; Qi, P.; Wang, X.; Lu, Y.; Li, X.; Tu, R.; Bangsaruntip, S.; Mann, D.; Zhang, L.; Dai, H. Selective Etching of Metallic Carbon Nanotubes by Gas-Phase Reaction. *Science* **2006**, *314*, 974–

977.

(205) Abe, M.; Ogino, K. Dielectric Constants and Electrical Conductivities of Sodium Dodecyl Sulfate in Aqueous Solutions. *J. Colloid Interface Sci.* **1981**, *80*, 58–66.

(206) Krupke, R.; Hennrich, F.; Löhneysen, H. v.; Kappes, M. M. Separation of Metallic from Semiconducting Single-Walled Carbon Nanotubes. *Science* **2003**, *301*, 344–347.

(207) Collins, P. G.; Arnold, M. S.; Avouris, P. Engineering Carbon Nanotubes and Nanotube Circuits Using Electrical Breakdown. *Science* **2001**, *292*, 706–709.

(208) Lin, A.; Patil, N.; Ryu, K.; Badmaev, A.; Arco, L. G. De; Zhou, C.; Mitra, S.; Wong, H.-S. P. Threshold Voltage and On–Off Ratio Tuning for Multiple-Tube Carbon Nanotube FETs. *IEEE Trans. Nanotechnol.* **2009**, *8*, 4–9.

(209) Shulaker, M. M.; Pitner, G.; Hills, G.; Giachino, M.; Wong, H.-S. P.; Mitra, S. High-Performance Carbon Nanotube Field-Effect Transistors. In *2014 IEEE International Electron Devices Meeting*; IEEE, 2014; pp 33.6.1-33.6.4.

(210) Jin, S. H.; Dunham, S. N.; Song, J.; Xie, X.; Kim, J. H.; Lu, C.; Islam, A.; Du, F.; Kim, J.; Felts, J.; Li, Y.; Xiong, F.; Wahab, M. A.; Menon, M.; Cho, E.; Grosse, K. L.; Lee, D. J.; Chung, H. U.; Pop, E.; Alam, M. A.; King, W. P.; Huang, Y.; Rogers, J. A. Using nanoscale thermocapillary flows to create arrays of purely semiconducting single-walled carbon nanotubes. *Nat. Nanotechnol.* **2013**, *8*, 347–355.

(211) Du, F.; Felts, J. R.; Xie, X.; Song, J.; Li, Y.; Rosenberger, M. R.; Islam, A. E.; Jin, S. H.; Dunham, S. N.; Zhang, C.; Wilson, W. L.; Huang, Y.; King, W. P.; Rogers, J. A. Laser-Induced Nanoscale Thermocapillary Flow for Purification of Aligned Arrays of Single-Walled Carbon Nanotubes. *ACS*

Nano **2014**, *8*, 12641–12649.

(212) Zheng, M.; Jagota, A.; Semke, E. D.; Diner, B. A.; McLean, R. S.; Lustig, S. R.; Richardson, R. E.; Tassi, N. G. DNA-assisted dispersion and separation of carbon nanotubes. *Nat. Mater.* **2003**, *2*, 338–342.

(213) Liu, H.; Nishide, D.; Tanaka, T.; Kataura, H. Large-scale single-chirality separation of single-wall carbon nanotubes by simple gel chromatography. *Nat. Commun.* **2011**, *2*.

(214) Han, J.; Ji, Q.; Qiu, S.; Li, H.; Zhang, S.; Jin, H.; Li, Q. Versatile Approach to Obtain High-Purity Semiconducting Single-Walled Carbon Nanotubes Dispersion with Conjugated Polymers. *Chem. Commun.* **2015**, *51*, 4712–4714.

(215) Zheng, M.; Semke, E. D. Enrichment of Single Chirality Carbon Nanotube. *J. Am. Chem. Soc.* **2007**, *129*, 6084–6085.

(216) Arnold, M. S.; Green, A. A.; Hulvat, J. F.; Stupp, S. I.; Hersam, M. C. Sorting carbon nanotubes by electronic structure using density differentiation. *Nat. Nanotechnol.* **2006**, *1*, 60–65.

(217) Selmani, S.; Schipper, D. J. π-Concave Hosts for Curved Carbon Nanomaterials. *Chem. Eur. J.* **2019**, *25*, 6673–6692.

(218) Kroto, H. W.; Heath, J. R.; O'Brien, S. C.; Curl, R. F.; Smalley, R. E. C_{60}: Buckminsterfullerene. *Nature* **1985**, *318*, 162–163.

(219) Zhang, Q. M.; Yi, J. Y.; Bernholc, J. Structure and Dynamics of Solid C_{60}. *Phys. Rev. Lett.* **1991**, *66*, 2633–2636.

(220) Kroto H.W .W.; Heath J.R.R.; O'Brien S.C.C.; Curl R.F.F.; Smalley R.E. E. C60: Buckminsterfullerene. *Nature*. 1985, pp 162–163.

(221) Johnson, R. D.; Bethune, D. S.; Yannoni, C. S. Fullerene Structure and Dynamics: A Magnetic Resonance Potpourri. *Acc. Chem. Res.* **1992**, *25*, 169–175.

(222) Haddon, R. C. Electronic Structure, Conductivity and Superconductivity of Alkali Metal Doped C_{60}. *Acc. Chem. Res.* **1992**, *25*, 127–133.

(223) Haddon, R. C.; Brus, L. E.; Raghavachari, K. Electronic Structure and Bonding in Icosahedral C_{60}. *Chem. Phys. Lett.* **1986**, *125*, 459–464.

(224) P.-M. Allemand A. Koch; Wudl, F.; Y. Rubin; F. Diederich; M. M. Alvarez; S. J. Anz; Whetten, R. L. Two Different Fullerenes Have the Same Cyclic Voltammetry. *J. Am. Chem. Soc.* **1991**, *113*, 1050–1051.

(225) Lof, R. W.; van Veenendaal, M. A.; Koopmans, B.; Jonkman, H. T.; Sawatzky, G. A. Band Gap, Excitons, and Coulomb Interaction in Solid C_{60}. *Phys. Rev. Lett.* **1992**, *68*, 3924–3927.

(226) Howard, J. B.; McKinnon, J. T.; Makarovsky, Y.; Lafleur, A. L.; Johnson, M. E. Fullerenes C_{60} and C_{70} in Flames. *Nature* **1991**, *352*, 139–141.

(227) Gunnarsson, O. Superconductivity in fullerides. *Rev. Mod. Phys.* **1997**, *69*, 575–606.

(228) Fleming, R. M.; Ramirez, A. P.; Rosseinsky, M. J.; Murphy, D. W.; Haddon, R. C.; Zahurak, S. M.; Makhija, A. V. Relation of structure and superconducting transition temperatures in A_3C_{60}. *Nature* **1991**, *352*, 787–788.

(229) Duclos, S. J.; Haddon, R. C.; Glarum, S.; Hebard, A. F.; Lyons, K. B. Raman Studies of Alkali-Metal Doped A_xC_{60} Films (A = Na, K, Rb, and Cs; x = 0, 3, and 6). *Science* **1991**, *254*, 1625–1627.

(230) Maniwa, Y.; Saito, T.; Kume, K.; Kikuchi, K.; Ikemoto, I.; Suzuki, S.; Achiba, Y.; Hirosawa, I.; Kosaka, M.; Tanigaki, K. NMR studies of superconducting Na_2AC_{60} (A = Cs, Rb, and K) fullerides. *Phys. Rev.*

B **1995**, *52*, R7054.

(231) Armaroli, N.; Diederich, F.; Dietrich-Buchecker, C. O.; Flamigni, L.; Marconi, G.; Nierengarten, J.; Sauvage, J. A Copper(I)-Complexed Rotaxane with Two Fullerene Stoppers: Synthesis, Electrochemistry, and Photoinduced Processes. *Chem. Eur. J.* **1998**, *4*, 406–416.

(232) Xu, Y.; Kaur, R.; Wang, B.; Minameyer, M. B.; Gsänger, S.; Meyer, B.; Drewello, T.; Guldi, D. M.; von Delius, M. Concave–Convex π–π Template Approach Enables the Synthesis of [10]Cycloparaphenylene-Fullerene [2]Rotaxanes. *J. Am. Chem. Soc.* **2018**, *140*, 13413–13420.

(233) Xie, Q.; Pérez-Cordero, E.; Echegoyen, L. Electrochemical Detection of C_{60}^{6-} and C_{70}^{6-}: Enhanced Stability of Fullerides in Solution. *J. Am. Chem. Soc.* **1992**, *114*, 3978–3980.

(234) Cataldo, F.; Iglesias-Groth, S.; Hafez, Y. On the Molar Extinction Coefficients of the Electronic Absorption Spectra of C_{60} and C_{70} Fullerenes Radical Cation. *Eur. Chem. Bull.* **2013**, *2*, 1013–1018.

(235) Pfuetzner, S.; Meiss, J.; Petrich, A.; Riede, M.; Leo, K. Improved bulk heterojunction organic solar cells employing C_{70} fullerenes. *Appl. Phys. Lett.* **2009**, *94*, 223307.

(236) Diederich, F.; Whetten, R. L. Beyond C_{60}: The Higher Fullerenes. *Acc. Chem. Res.* **1992**, *25*, 119–126.

(237) Yang, Y.; Arias, F.; Echegoyen, L.; Chibante, L. P. F.; Flanagan, S.; Robertson, A.; Wilson, L. J. Reversible Fullerene Electrochemistry: Correlation with the HOMO-LUMO Energy Difference for C_{60}, C_{70}, C_{76}, C_{78}, and C_{84}. *J. Am. Chem. Soc.* **1995**, *117*, 7801–7804.

(238) Boudon, C.; Gisselbrecht, J-. P.; Gross, M.; Herrmann, A.; Rüttimann, M.; Crassous, J.; Cardullo, F.; Echegoyen, L.; Diederich, F. Redox Characteristics of Covalent Derivatives of the Higher Fullerenes C_{70}, C_{76}, and C_{78}. *J. Am. Chem. Soc.* **1998**, *120*, 7860–7868.

(239) Diederich, F.; Whetten, R. L.; Thilgen, C.; Ettl, R.; Chao, I.; Alvarez, M. M. Fullerene Isomerism: Isolation of C_{2v}-C_{78} and D_3-C_{78}. *Science* **1991**, *254*, 1768–1770.

(240) Cerón, M. R.; Maffeis, V.; Stevenson, S.; Echegoyen, L. Endohedral fullerenes : Synthesis, isolation, *mono*- and *bis*-functionalization. *Inorganica Chim. Acta* **2017**, *468*, 16–27.

(241) Guha, S.; Nakamoto, K. Electronic structures and spectral properties of endohedral fullerenes. *Coord. Chem. Rev.* **2005**, *249*, 1111–1132.

(242) Popov, A.; Yang, S.; Dunsch, L. Endohedral Fullerenes. *Chem. Rev.* **2013**, *113*, 5989–6113.

(243) Stevenson, S.; Rice, G.; Glass, T.; Harich, K.; Cromer, F.; Jordan, M. R.; Craft, J.; Hadju, E.; Bible, R.; Olmstead, M. M.; Maitra, K.; Fisher, A. J.; Balch, A. L.; Dorn, H. C. Small-bandgap endohedral metallofullerenes in high yield and purity. *Nature* **1999**, *401*, 55–57.

(244) Murata, M.; Murata, Y.; Komatsu, K. Surgery of fullerenes. *Chem. Commun.* **2008**, *366*, 6083–6094.

(245) Murphy, T. A.; Pawlik, T.; Weidinger, A.; Höhne, M.; Alcala, R.; Spaeth, J.-M. Observation of Atomlike Nitrogen in Nitrogen-Implanted Solid C_{60}. *Phys. Rev. Lett.* **1996**, *77*, 1075–1078.

(246) Boltalina, O. V.; Sidorov, L. N.; Ya. Borshchevsky, A.; Sukhanova, E. V.; Skokan, E. V. Electron Affinities of Higher Fullerenes. *Rapid Commun. Mass Spectrom.* **1993**, *7*, 1009–1011.

(247) Campanera, J. M.; Bo, C.; Olmstead, M. M.; Balch, A. L.; Poblet, J. M. Bonding within the Endohedral Fullerenes $Sc_3N@C_{78}$ and $Sc_3N@C_{80}$ as Determined by Density Functional Calculations and Reexamination of the Crystal Structure of $\{Sc_3N@C_{78}\}\cdot Co(OEP)\}\cdot 1.5(C_6H_6)\cdot 0.3(CHCl_3)$. *J. Phys. Chem. A* **2002**, *106*, 12356–12364.

(248) Kobayashi, K.; Nagase, S.; Akasaka, T. A theoretical study of C_{80} and $La_2@C_{80}$. *Chem. Phys. Lett.* **1995**, *245*, 230–236.

(249) Kikuchi, K.; Nakao, Y.; Suzuki, S.; Achiba, Y.; Suzuki, T.; Maruyama, Y. Characterization of the Isolated Y@C_{82}. *J. Am. Chem. Soc.* **1994**, *116*, 9367–9368.

(250) Zhang, L.; Chen, N.; Fan, L.; Wang, C.; Yang, S. Electrochemistry of $Sc_3N@C_{78}$ and $Sc_3N@C_{80}$ (I_h): On achieving reversible redox waves of the trimetal nitride endohedral fullerenes. *J. Electroanal. Chem.* **2007**, *608*, 15–21.

(251) Krätschmer, W.; Lamb, L. D.; Fostiropoulos, K.; Huffman, D. R. Solid C_{60}: a new form of carbon. *Nature* **1990**, *347*, 354–358.

(252) Howard, J. B.; Lafleur, A. L.; Makarovsky, Y.; Mitra, S.; Pope, C. J.; Yadav, T. K. Fullerene Synthesis in Combustion. *Carbon* **1992**, *30*, 1183–1201.

(253) Howard, J. B.; Lafleur, A. L.; Makarovsky, Y.; Mitra, S.; Pope, C. J.; Yadav, T. K. Fullerenes Synthesis in Combustion. *Carbon* **1992**, *30*, 1183–1201.

(254) Howard, J. B.; McKinnon, J. T.; Johnson, M. E.; Makarovsky, Y.; Lafleur, A. L. Production of C_{60} and C_{70} Fullerenes in Benzene–Oxygen Flames. *J. Phys. Chem.* **1992**, *96*, 6657–6662.

(255) Osterodt, J.; Zett, A.; Vögtle, F. Fullerenes by Pyrolysis of Hydrocarbons and Synthesis of Isomeric Methanofullerenes. *Tetrahedron* **1996**, *52*, 4949–4962.

(256) Takehara, H.; Fujiwara, M.; Arikawa, M.; Diener, M. D.; Alford, J. M. Experimental study of industrial scale fullerene production by combustion synthesis. *Carbon* **2005**, *43*, 311–319.

(257) Anctil, A.; Babbitt, C. W.; Raffaelle, R. P.; Landi, B. J. Material and Energy Intensity of Fullerene Production. *Environ. Sci. Technol.* **2011**, *45*, 2353–2359.

(258) Sugai, T.; Omote, H.; Bandow, S.; Tanaka, N.; Shinohara, H. Production of fullerenes and single-wall carbon nanotubes by high-temperature pulsed arc discharge. *J. Chem. Phys.* **2000**, *112*, 6000–6005.

(259) Yan, Y.; Miao, J.; Yang, Z.; Xiao, F. X.; Yang, H. Bin; Liu, B.; Yang, Y. Carbon nanotube catalysts: recent advances in synthesis, characterization and applications. *Chem. Soc. Rev.* **2015**, *44*, 3295–3346.

(260) Krestinin, A. V.; Moravsky, A. P. Mechanism of fullerene synthesis in the arc reactor. *Chem. Phys. Lett.* **1998**, *286*, 479–484.

(261) Moravsky, A. P.; Ryabenko, A. G.; Fursikov, P. V.; Ryabenko, A. A. An Invariant of Carbon Arc Synthesis of Fullerenes. *Fuller. Sci. Technol.* **1998**, *6*, 453–467.

(262) Kimura, T.; Sugai, T.; Shinohara, H.; Goto, T.; Tohji, K.; Matsuoka, I. Preferential arc-discharge production of higher fullerenes. *Chem*. *Phys*. *Lett*. **1995**, *246*, 571–576.

(263) Alekseev, N. I.; Filippov, B. M.; Basargin, I. V.; Sedov, A. I. Investigation of Semicommercial Arc Plants for Fullerene-Production. *J. Eng. Phys. Thermophys.* **2011**, *84*, 1087–1098.

(264) Diederich, F.; Ettl, R.; Rubin, Y.; Whetten, R. L.; Beck, R.; Alvarez, M.; Anz, S.; Sensharma, D.; Wudl, F.; Khemani, K. C.; Koch, A. The Higher Fullerenes: Isolation and Characterization of C_{76}, C_{84}, C_{90}, C_{94}, and $C_{70}O$, an Oxide of D_{5h}-C_{70}. *Science* **1991**, *252*, 548–551.

(265) Kimata, K.; Hosoya, K.; Araki, T.; Tanaka, N. [2-(1-Pyrenyl)ethyl]silyl Silica Packing Material for Liquid Chromatographic Separation of Fullerenes. *J. Org. Chem.* **1993**, *58*, 282–283.

(266) Nacalai USA, Inc. | Product | COSMOSIL Buckyprep http://www.nacalaiusa.com/products/view/56/cosmosil-buckyprep (accessed Jun 18, 2019).

(267) Han, J.; Zhuo, Y.; Chai, Y. Q.; Xiang, Y.; Yuan, R. New Type of Redox Nanoprobe: C_{60}-Based Nanomaterial and Its Application in Electrochemical Immunoassay for Doping Detection. *Anal. Chem.* **2015**, *87*, 1669–1675.

(268) Biju, V. Chemical modifications and bioconjugate reactions of nanomaterials for sensing, imaging, drug delivery and therapy. *Chem. Soc. Rev.* **2014**, *43*, 744–764.

(269) Mateo-Alonso, A.; Guldi, D. M.; Paolucci, F.; Prato, M. Fullerenes: Multitask Components in Molecular Machinery. *Angew. Chem. Int. Ed.* **2007**, *46*, 8120–8126.

(270) Wöbkenberg, P. H.; Bradley, D. D. C.; Kronholm, D.; Hummelen, J. C.; de Leeuw, D. M.; Cölle, M.; Anthopoulos, T. D. High mobility n-channel organic field-effect transistors based on soluble C_{60} and C_{70} fullerene derivatives. *Synth. Met.* **2008**, *158*, 468–472.

(271) Thompson, B. C.; Fréchet, J. M. J. Polymer-Fullerene Composite Solar Cells. *Angew. Chem. Int. Ed.* **2008**, *47*, 58–77.

(272) He, Y.; Li, Y. Fullerene derivative acceptors for high performance polymer solar cells. *Phys. Chem. Chem. Phys.* **2011**, *13*, 1970–1983.

(273) Dennler, G.; Scharber, M. C.; Brabec, C. J. Polymer-Fullerene Bulk-Heterojunction Solar Cells. *Adv. Mater.* **2009**, *21*, 1323–1338.

(274) Brabec, C. J.; Sariciftci, N. S.; Hummelen, J. C. Plastic Solar Cells. *Adv. Funct. Mater.* **2001**, *11*, 15–26.

(275) Deng, L. L.; Xie, S. Y.; Gao, F. Fullerene-Based Materials for Photovoltaic Applications: Toward Efficient, Hysteresis-Free, and Stable Perovskite Solar Cells. *Adv. Electron. Mater.* **2018**, *4*, 1–18.

(276) Yan, J.; Saunders, B. R. Third-generation solar cells: a review and comparison of polymer:fullerene, hybrid polymer and perovskite solar cells. *RSC Adv.* **2014**, *4*, 43286–43314.

(277) Echegoyen, L.; Echegoyen, L. E. Electrochemistry of Fullerenes and Their Derivatives. *Acc. Chem. Res.* **1998**, *31*, 593–601.

(278) Günes, S.; Neugebauer, H.; Sariciftci, N. S. Conjugated Polymer-Based Organic Solar Cells. *Chem. Rev*. **2007**, *107*, 1324–1338.

(279) Rispens, M. T.; Meetsma, A.; Rittberger, R.; Brabec, C. J.; Sariciftci, N. S.; Hummelen, J. C. Influence of the solvent on the crystal structure of PCBM and the efficiency of MDMO-PPV:PCBM 'plastic' solar cells. *Chem. Commun.* **2003**, *17*, 2116–2118.

(280) Morvillo, P. Higher fullerenes as electron acceptors for polymer solar cells: A quantum chemical study. *Sol. Energy Mater. Sol. Cells* **2009**, *93*, 1827–1832.

(281) Georgakilas, V.; Tzitzios, V.; Gournis, D.; Petridis, D. Attachment of Magnetic Nanoparticles on Carbon Nanotubes and Their Soluble Derivatives. *Chem. Mater.* **2005**, *17*, 1613–1617.

(282) Zhu, J.; Yudasaka, M.; Zhang, M.; Kasuya, D.; Iijima, S. A Surface Modification Approach to the Patterned Assembly of Single-Walled Carbon Nanomaterials. *Nano Lett.* **2003**, *3*, 1239–1243.

(283) Ehli, C.; Oelsner, C.; Guldi, D. M.; Mateo-Alonso, A.; Prato, M.; Schmidt, C.; Backes, C.; Hauke, F.; Hirsch, A. Manipulating single-wall carbon nanotubes by chemical doping and charge transfer with perylene dyes. *Nat. Chem.* **2009**, *1*, 243–249.

(284) de Juan, A.; López-Moreno, A.; Calbo, J.; Ortí, E.; Pérez, E. M. Determination of association constants towards carbon nanotubes. *Chem. Sci.* **2015**, *6*, 7008–7014.

(285) Hart, H.; Bashir-Hashemi, A.; Luo, J.; Meador, M. A. Iptycenes. *Tetrahedron* **1986**, *42*, 1641–1654.

(286) Chong, J. H.; MacLachlan, M. J. Iptycenes in supramolecular and materials chemistry. *Chem. Soc. Rev.* **2009**, *38*, 3301–3315.

(287) Zu, S. Z.; Sun, X. X.; Liu, Y.; Han, B. H. Supramolecular Surface Modification and Solubilization of Single-Walled Carbon Nanotubes with Cyclodextrin Complexation. *Chem. Asian J.* **2009**, *4*, 1562–

1572.

(288) Marquis, R.; Kulikiewicz, K.; Lebedkin, S.; Kappes, M. M.; Mioskowski, C; Meunier, S.; Wagner, A. Axially Chiral Facial Amphiphiles with a Dihydronaphthopentaphene Structure as Molecular Tweezers for SWNTs. *Chem. Eur. J.* **2009**, *15*, 11187–11196.

(289) Herranz, M. Á.; Ehli, C.; Campidelli, S.; Gutiérrez, M.; Hug, G. L.; Ohkubo, K.; Fukuzumi, S.; Prato, M.; Martín, N.; Guldi, D. M. Spectroscopic Characterization of Photolytically Generated Radical Ion Pairs in Single-Wall Carbon Nanotubes Bearing Surface-Immobilized Tetrathiafulvalenes. *J. Am. Chem. Soc.* **2008**, *130*, 66–73.

(290) Romero-Nieto, C.; García, R.; Herranz, M. Á.; Ehli, C.; Ruppert, M.; Hirsch, A.; Guldi, D. M.; Martín, N. Tetrathiafulvalene-Based Nanotweezers–Noncovalent Binding of Carbon Nanotubes in Aqueous Media with Charge Transfer Implications. *J. Am. Chem. Soc.* **2012**, *134*, 9183–9192.

(291) Peng, X.; Wang, F.; Bauri, A. K.; Rahman, A. F. M. M.; Komatsu, N. Optical Resolution of Single-Walled Carbon Nanotubes through Molecular Recognition with Chiral Diporphyrin Nanotweezers. *Chem. Lett.* **2010**, *39*, 1022–1027.

(292) Ajayan, P. M.; Stephan, O.; Colliex, C.; Trauth, D. Aligned Carbon Nanotube Arrays Formed by Cutting a Polymer Resin-Nanotube Composite. *Science* **1994**, *265*, 1212–1214.

(293) Ren, Z.; Huang, Z.; Xu, J.; Wang, J.; Bush, P.; Siegal, M.; Provencio, P. Synthesis of Large Arrays of Well-Aligned Carbon Nanotubes on Glass. *Science* **1998**, *282*, 1105–1107.

(294) Tulevski, G. S.; Hannon, J.; Afzali, A.; Chen, Z.; Avouris, P.; Kagan, C. R. Chemically Assisted Directed Assembly of Carbon Nanotubes for the Fabrication of Large-Scale Device Arrays. *J. Am. Chem. Soc.* **2007**, *129*, 11964–11968.

(295) Park, H.; Afzali, A.; Han, S.-J.; Tulevski, G. S.; Franklin, A. D.; Tersoff, J.; Hannon, J. B.; Haensch, W. High-density integration of carbon nanotubes via chemical self-assembly. *Nat. Nanotechnol.* **2012**, *7*, 787–791.

(296) Barman, S. N.; Lemieux, M. C.; Baek, J.; Rivera, R.; Bao, Z. Effects of Dispersion Conditions of Single-Walled Carbon Nanotubes on the Electrical Characteristics of Thin Film Network Transistors. *ACS Appl. Mater. Interfaces* **2010**, *2*, 2672–2678.

(297) Yuzvinsky, T. D.; Fennimore, A. M.; Kis, A.; Zettl, A. Controlled placement of highly aligned carbon nanotubes for the manufacture of arrays of nanoscale torsional actuators. *Nanotechnology* **2006**, *17*, 434–438.

(298) Joo, Y.; Brady, G. J.; Arnold, M. S.; Gopalan, P. Dose-Controlled, Floating Evaporative Self-assembly and Alignment of Semiconducting Carbon Nanotubes from Organic Solvents. *Langmuir* **2014**, *30*, 3460–3466.

(299) Cao, Q.; Han, S. J.; Tulevski, G. S.; Zhu, Y.; Lu, D. D.; Haensch, W. Arrays of single-walled carbon nanotubes with full surface coverage for high-performance electronics. *Nat. Nanotechnol.* **2013**, *8*, 180–186.

(300) Tolbert, S. H.; Firouzi, A.; Stucky, G. D.; Chmelka, B. F. Magnetic Field Alignment of Ordered Silicate-Surfactant Composites and Mesoporous Silica. *Science* **1997**, *278*, 264–268.

(301) Helfrich, W. Conduction-Induced Alignment of Nematic Liquid Crystals: Basic Model and Stability Considerations. *J. Chem. Phys.* **1969**, *51*, 4092–4105.

(302) Gibbons, W. M.; Shannon, P. J.; Sun, S.-T.; Swetlin, B. J. Surface-mediated alignment of nematic liquid crystals with polarized laser light. *Nature* **1991**, *351*, 49–50.

(303) Ishihara, S.; Wakemoto, H.; Nakazima, K.; Matsuo, Y. The effect of rubbed polymer films on the liquid crystal alignment. *Liq. Cryst.* **1989**, *4*, 669–675.

(304) Hoogboom, J.; Rasing, T.; Rowan, A. E.; Nolte, R. J. M. LCD alignment layers. Controlling nematic domain properties. *J. Mater. Chem.* **2006**, *16*, 1305–1314.

(305) Demus, D.; Goodby, J.; Gray, G.; Spiess, H.; Vill, V. *Handbook of Liquid Crystals, Volume 1: Fundamentals of Liquid Crystals*; Wiley: New York, 2008.

(306) Meseck, G. R.; Terpstra, A. S.; Maclachlan, M. J. liquid crystal templating of nanomaterials with nature's toolbox. *Curr. Opin. Colloid Interface Sci.* **2017**, *29*, 9–20.

(307) Long, T. M.; Swager, T. M. Minimization of Free Volume : Alignment of Triptycenes in Liquid Crystals and Stretched Polymers. *Adv. Mater.* **2001**, *13*, 601–604.

(308) Pujari, S. P.; Scheres, L.; Marcelis, A. T. M.; Zuilhof, H. Covalent Surface Modification of Oxide Surfaces. *Angew. Chem. Int. Ed.* **2014**, *53*, 6322–6356.

(309) Vega, A.; Thissen, P.; Chabal, Y. J. Environment-Controlled Tethering by Aggregation and Growth of Phosphonic Acid Monolayers on Silicon Oxide. *Langmuir* **2012**, *28*, 8046–8051.

(310) Cattani-Scholz, A.; Pedone, D.; Dubey, M.; Neppl, S.; Nickel, B.; Feulner, P.; Schwartz, J.; Absteiter, G.; Tornow, M. Organophosphonate-Based PNA-Functionalization of Silicon Nanowires for Label-Free DNA Detection. *ACS Nano* **2008**, *2*, 1653–1660.

(311) Chen, X.; Luais, E.; Darwish, N.; Ciampi, S.; Thordarson, P.; Gooding, J. J. Studies on the Effect of Solvents on Self-Assembled Monolayers Formed from Organophosphonic Acids on Indium Tin Oxide. *Langmuir* **2012**, *28*, 9487–9495.

(312) Queffélec, C.; Petit, M.; Janvier, P.; Knight, D. A.; Bujoli, B. Surface Modification Using Phosphonic

Acids and Esters. *Chem. Rev.* **2012**, *112*, 3777–3807.

(313) Ma, H.; Acton, O.; Hutchins, D. O.; Cernetic, N.; Jen, A. K.-Y. Multifunctional phosphonic acid self-assembled monolayers on metal oxides as dielectrics, interface modification layers and semiconductors for low-voltage high-performance organic field-effect transistors. *Phys. Chem. Chem. Phys.* **2012**, *14*, 14110–14126.

(314) Paniagua, S. A.; Hotchkiss, P. J.; Jones, S. C.; Marder, S. R.; Mudalige, A.; Marrikar, F. S.; Pemberton, J. E.; Armstrong, N. R. Phosphonic Acid Modification of Indium-Tin Oxide Electrodes: Combined XPS/UPS/Contact Angle Studies. *J. Phys. Chem. C* **2008**, *112*, 7809–7817.

(315) Gliboff, M.; Sang, L.; Knesting, K. M.; Schalnat, M. C.; Mudalige, A.; Ratcliff, E. L.; Li, H.; Sigdel, A. K.; Giordano, A. J.; Berry, J. J.; Nordlund, D.; Seidler, G. T.; Brédas, J. L.; Marder, S. R.; Pemberton, J. E.; Ginger, D. S. Orientation of Phenylphosphonic Acid Self-Assembled Monolayers on a Transparent Conductive Oxide: A Combined NEXAFS, PM-IRRAS, and DFT Study. *Langmuir* **2013**, *29*, 2166–2174.

(316) Dierking, I. *Textures of Liquid Crystals*; Wiley: New York, 2003.

(317) Miller, M. W.; Williams, E. S. Large-scale assembly of carbon nanotubes. *Nature* **2003**, *425*, 36–37.

(318) Snowdon, M. R.; Selmani, S.; Schipper, D. J. Sonication-Enhanced Alignment Relay Technique for the Orientation of Single-Walled Carbon Nanotubes. *ACS Appl*. *Nano Mater*. **2019**, *2*, 6637–6645.

(319) Yang, J.; Bremer, P. J.; Lamont, I. L.; McQuillan, A. J. Infrared Spectroscopic Studies of Siderophore-Related Hydroxamic Acid Ligands Adsorbed on Titanium Dioxide. *Langmuir* **2006**, *22*, 10109–10117.

(320) Maier, S. A.; Brongersma, M. L.; Kik, P. G.; Meltzer, S.; Requicha, A. A. G.; Atwater, H. A. Plasmonics – A Route to Nanoscale Optical Devices. *Adv. Mater.* **2001**, *13* (19), 1501.

(321) Liu, G.-Y.; Xu, S.; Qian, Y. Nanofabrication of Self-Assembled Monolayers Using Scanning Probe Lithography. *Acc. Chem. Res.* **2000**, *33*, 457–466.

(322) Liu, J.; Casavant, M. J.; Cox, M.; Walters, D. A.; Boul, P.; Lu, W.; Rimberg, A. J.; Smith, K. A.; Colbert, D. T.; Smalley, R. E. Controlled deposition of individual single-walled carbon nanotubes on chemically functionalized templates. *Chem. Phys. Lett.* **1999**, *303*, 125–129.

(323) Kim, S. O.; Solak, H. H.; Stoykovich, M. P.; Ferrier, N. J.; de Pablo, J. J.; Nealey, P. F. Epitaxial self-assembly of block copolymers on lithographically defined nanopatterned substrates. *Nature* **2003**, *424*, 411–414.

(324) Boyd, P. D. W.; Reed, C. A. Fullerene−Porphyrin Constructs. *Acc. Chem. Res.* **2005**, *38*, 235–242.

(325) Tashiro, K.; Aida, T.; Zheng, J. Y.; Kinbara, K.; Saigo, K.; Sakamoto, S.; Yamaguchi, K. A Cyclic Dimer of Metalloporphyrin Forms a Highly Stable Inclusion Complex with C_{60}. *J*. *Am*. *Chem*. *Soc*. **1999**, *121*, 9477–9478.

(326) Zheng, J. Y.; Tashiro, K.; Hirabayashi, Y.; Kinbara, K.; Saigo, K.; Aida, T.; Sakamoto, S.; Yamaguchi, K. Cyclic Dimers of Metalloporphyrins as Tunable Hosts for Fullerenes: A Remarkable Effect of Rhodium(III). *Angew. Chem. Int. Ed.* **2001**, *40*, 1858–1861.

(327) Yanagisawa, M.; Tashiro, K.; Yamasaki, M.; Aida, T. Hosting Fullerenes by Dynamic Bond Formation with an Iridium Porphyrin Cyclic Dimer: A “Chemical Friction” for Rotary Guest Motions. *J. Am. Chem. Soc.* **2007**, *129*, 11912–11913.

(328) Shoji, Y.; Tashiro, K.; Aida, T. One-Pot Enantioselective Extraction of Chiral Fullerene C_{76} Using a Cyclic Host Carrying an Asymmetrically Distorted, Highly π-Basic Porphyrin Module. *J. Am. Chem. Soc.* **2010**, *132*, 5928–5929.

(329) Dawe, L. N.; AlHujran, T. A.; Tran, H. A.; Mercer, J. I.; Jackson, E. A.; Scott, L. T.; Georghiou, P. E. Corannulene and its penta-*tert*-butyl derivative co-crystallize 1:1 with pristine C_{60}-fullerene. *Chem. Commun.* **2012**, *48*, 5563–5565.

(330) Filatov, A. S.; Ferguson, M. V; Spisak, S. N.; Li, B.; Campana, C. F.; Petrukhina, M. A. Bowl-Shaped Polyarenes as Concave-Convex Shape Complementary Hosts for C_{60}- and C_{70}-Fullerenes. *Cryst. Growth Des.* **2014**, *14*, 756–762.

(331) Mizyed, S.; Georghiou, P. E.; Bancu, M.; Cuadra, B.; Rai, A. K.; Cheng, P.; Scott, L. T. Embracing C_{60} with Multiarmed Geodesic Partners. *J. Am. Chem. Soc.* **2001**, *123*, 12770–12774.

(332) Ito, S.; Tokimaru, Y.; Nozaki, K. Benzene-Fused Azacorannulene Bearing an Internal Nitrogen Atom. *Angew. Chem. Int. Ed.* **2015**, *54*, 7256–7260.

(333) Yokoi, H.; Hiraoka, Y.; Hiroto, S.; Sakamaki, D.; Seki, S.; Shinokubo, H. Nitrogen-embedded buckybowl and its assembly with C_{60}. *Nat. Commun.* **2015**, *6*, 1–9.

(334) Sygula, A.; Fronczek, F. R.; Sygula, R.; Rabideau, P. W.; Olmstead, M. M. A Double Concave Hydrocarbon Buckycatcher. *J. Am. Chem. Soc.* **2007**, *129*, 3842–3843.

(335) Yanney, M.; Fronczek, F. R.; Sygula, A. A 2:1 Receptor/C_{60} Complex as a Nanosized Universal Joint. *Angew. Chem. Int. Ed.* **2015**, *54*, 11153–11156.

(336) Abeyratne Kuragama, P. L.; Fronczek, F. R.; Sygula, A. Bis-corannulene Receptors for Fullerenes Based on Klärner's Tethers: Reaching the Affinity Limits. *Org. Lett.* **2015**, *17*, 5292–5295.

(337) Kumarasinghe, K. G. U. R.; Fronczek, F. R.; Valle, H. U.; Sygula, A. Bis-corannulenoanthracene: An Angularly Fused Pentacene as a Precursor for Barrelene-Tethered Receptors for Fullerenes. *Org. Lett.* **2016**, *18*, 3054–3057.

(338) Pérez, E. M.; Sánchez, L.; Fernández, G.; Martín, N. exTTF as a Building Block for Fullerene Receptors. Unexpected Solvent-Dependent Positive Homotropic Cooperativity. *J. Am. Chem. Soc.* **2006**, *128*, 7172–7173.

(339) Pérez, E. M.; Capodilupo, A. L.; Fernández, G.; Sánchez, L.; Viruela, P. M.; Viruela, R.; Ortí, E.; Bietti, M.; Martín, N. Weighting non-covalent forces in the molecular recognition of C_{60}. Relevance of concave–convex complementarity. *Chem. Commun.* **2008**, 38, 4567–4569.

(340) Atwood, J. L.; Koutsantonis, G. A.; Raston, C. L. Purification of C_{60} and C_{70} by selective complexation with calixarenes. *Nature* **1994**, *368*, 229–231.

(341) Skiebe, A.; Hirsch, A.; Klos, H.; Gotschy, B. [DBU]C_{60}. Spin Pairing in a fullerene salt. *Chem. Phys. Lett.* **1994**, *220*, 138–140.

(342) Nagata, K.; Dejima, E.; Kikuchi, Y.; Hashiguchi, M. Efficient and Scalable Method for [60]Fullerene Separation from a Fullerene Mixture: Selective Complexation of Fullerenes with DBU in the Presence of Water. *Org. Process Res. Dev.* **2005**, *9*, 660–662.

(343) Lukeš, I.; Borbaruah, M.; Quin, L. D. Direct Reaction of Phosphorus Acids with Hydroxy of a Silanol and on the Silica Gel Surface. *J Am Chem Soc* **1994**, *116*, 1737–1741.

(344) Selmani, S.; Yue Shen, M.; Schipper, D. J. Iptycene-Functionalized Silica Gel for the Purification of Fullerenes Using Flash Chromatography. *RSC Adv.* **2017**, *7*, 19026–19029.

(345) Rowsell, J. L. C.; Yaghi, O. M. Metal-organic frameworks: a new class of porous materials. *Microporous Mesoporous Mater.* **2004**, *73*, 3–14.

(346) Férey, G.; Mellot-Draznieks, C.; Serre, C.; Millange, F.; Dutour, J.; Surblé, S.; Margiolaki, I. A Chromium Terephthalate-Based Solid with Unusually Large Pore Volumes and Surface Area.

Science **2005**, *309*, 2040–2042.

(347) Sheberla, D.; Bachman, J. C.; Elias, J. S.; Sun, C. J.; Shao-Horn, Y.; Dincă, M. Conductive MOF electrodes for stable supercapacitors with high areal capacitance. *Nat. Mater.* **2017**, *16*, 220–224.

(348) Seo, J. S.; Whang, D.; Lee, H.; Jun, S. I.; Oh, J.; Jeon, Y. J.; Kim, K. A homochiral metal-organic porous material for enantioselective separation and catalysis. *Nature* **2000**, *404*, 982–986.

(349) Hu, A.; Ngo, H. L.; Lin, W. Chiral Porous Hybrid Solids for Practical Heterogeneous Asymmetric Hydrogenation of Aromatic Ketones. *J. Am. Chem. Soc.* **2003**, *125*, 11490–11491.

(350) Dhakshinamoorthy, A.; Garcia, H. Metal-organic frameworks as solid catalysts for the synthesis of nitrogen-containing heterocycles. *Chem. Soc. Rev.* **2014**, *43*, 5750–5765.

(351) Chen, B.; Liang, C.; Yang, J.; Contreras, D. S.; Clancy, Y. L.; Lobkovsky, E. B.; Yaghi, O. M.; Dai, S. A Microporous Metal-Organic Framework for Gas-Chromatographic Separation of Alkanes. *Angew. Chem. Int. Ed.* **2006**, *45*, 1390–1393.

(352) Pan, L.; Parker, B.; Huang, X.; Olson, D. H.; Lee, J.; Li, J. Zn(tbip) (H_2tbip= 5-*tert*-Butyl Isophthalic Acid): A Highly Stable Guest-Free Microporous Metal Organic Framework with Unique Gas Separation Capability. *J. Am. Chem. Soc.* **2006**, *128*, 4180–4181.

(353) Ma, S.; Sun, D.; Wang, X. Sen; Zhou, H. C. A Mesh-Adjustable Molecular Sieve for General Use in Gas Separation. *Angew. Chem. Int. Ed.* **2007**, *46*, 2458–2462.

(354) Xia, B. Y.; Yan, Y.; Li, N.; Wu, H. B.; Lou, X. W. D.; Wang, X. A metal-organic framework-derived bifunctional oxygen electrocatalyst. *Nat. Energy* **2016**, *1*, 1–8.

(355) Chen, B.; Ma, S.; Hurtado, E. J.; Lobkovsky, E. B.; Liang, C.; Zhu, H.; Dai, S. Selective Gas Sorption within a Dynamic Metal-Organic Framework. *Inorg. Chem.* **2007**, *46*, 8705–8709.

(356) Rosi, N. L.; Eckert, J.; Eddaoudi, M.; Vodak, D. T.; Kim, J.; O'Keeffe, M. Hydrogen storage in microporous metal-organic frameworks. *Science* **2003**, *300*, 1127–1129.

(357) Matsuda, R.; Kitaura, R.; Kitagawa, S.; Kubota, Y.; Belosludov, R. V.; Kobayashi, T. C.; Sakamoto, H.; Chiba, T.; Takata, M.; Kawazoe, Y.; Mita, Y. Highly controlled acetylene accommodation in a metal-organic microporous material. *Nature* **2005**, *436*, 238–241.

(358) Choi, K. M.; Kim, D.; Rungtaweevoranit, B.; Trickett, C. A.; Barmanbek, J. T. D.; Alshammari, A. S.; Yang, P.; Yaghi, O. M. Plasmon-Enhanced Photocatalytic CO_2 Conversion within Metal-Organic Frameworks under Visible Light. *J. Am. Chem. Soc.* **2017**, *139*, 356–362.

(359) Du, M.; Jiang, X.; Zhao, X. Molecular Tectonics of Mixed-Ligand Metal−Organic Frameworks: Positional Isomeric Effect, Metal-Directed Assembly, and Structural Diversification. *Inorg*. *Chem*. **2007**, *46*, 3984–3995.

(360) de Lill, D. T.; Gunning, N. S.; Cahill, C. L. Toward Templated Metal − Organic Frameworks : Synthesis, Structures, Thermal Properties, and Luminescence of Three Novel Lanthanide−Adipate Frameworks. *Inorg. Chem.* **2005**, *44*, 258–266.

(361) Zhang, S.; Wang, Z.; Zhang, H.; Cao, Y.; Sun, Y.; Chen, Y.; Huang, C.; Yu, X. Self-assembly of two fluorescent supramolecular frameworks constructed from unsymmetrical benzene tricarboxylate and bipyridine. *Inorganica Chim. Acta* **2007**, *360*, 2704–2710.

(362) Ahrenholtz, S. R.; Epley, C. C.; Morris, A. J. Solvothermal Preparation of an Electrocatalytic Metalloporphyrin MOF Thin Film and its Redox Hopping Charge-Transfer Mechanism. *J*. *Am*. *Chem*. *Soc*. **2014**, *136*, 2464–2472.

(363) D'Alessandro, D. M. Exploiting redox activity in metal–organic frameworks: concepts, trends and

perspectives. *Chem. Commun.* **2016**, *52*, 8957–8971.

(364) Takaishi, S.; Hosoda, M.; Kajiwara, T.; Miyasaka, H.; Yamashita, M.; Nakanishi, Y.; Kitagawa, Y.; Yamaguchi, K.; Kobayashi, A.; Kitagawa, H. Electroconductive Porous Coordination Polymer $Cu[Cu(pdt)_2]$ Composed of Donor and Acceptor Building Units. *Inorg. Chem.* **2009**, *48*, 9048–9050.

(365) Miyasaka, H. Control of Charge Transfer in Donor/Acceptor Metal–Organic Frameworks. *Acc. Chem. Res.* **2013**, *46*, 248–257.

(366) Chen, Z.; Higgins, D.; Yu, A.; Zhang, L.; Zhang, J. A review on non-precious metal electrocatalysts for PEM fuel cells. *Energy Environ. Sci.* **2011**, *4*, 3167–3192.

(367) Wang, Y.; Chen, K. S.; Mishler, J.; Cho, S. C.; Adroher, X. C. A review of polymer electrolyte membrane fuel cells: Technology, applications, and needs on fundamental research. *Appl. Energy* **2011**, *88*, 981–1007.

(368) Murray, L. J.; Dincă, M.; Long, J. R. Hydrogen storage in metal–organic frameworks. *Chem. Soc. Rev.* **2009**, *38*, 1294–1314.

(369) Safizadeh, F.; Ghali, E.; Houlachi, G. Electrocatalysis developments for hydrogen evolution reaction in alkaline solutions - A Review. *Int. J. Hydrogen Energy* **2015**, *40*, 256–274.

(370) Strmcnik, D.; Uchimura, M.; Wang, C.; Subbaraman, R.; Danilovic, N.; van der Vliet, D.; Paulikas, A. P.; Stamenkovic, V. R.; Markovic, N. M. Improving the hydrogen oxidation reaction rate by promotion of hydroxyl adsorption. *Nat. Chem.* **2013**, *5*, 300–306.

(371) Debe, M. K. Electrocatalyst approaches and challenges for automotive fuel cells. *Nature* **2012**, *486*, 43–51.

(372) Wang, J.; Huang, Z.; Liu, W.; Chang, C.; Tang, H.; Li, Z.; Chen, W.; Jia, C.; Yao, T.; Wei, S.; Wu, Y.;

Li, Y. Design of N-Coordinated Dual-Metal Sites: A Stable and Active Pt-Free Catalyst for Acidic Oxygen Reduction Reaction. *J. Am. Chem. Soc.* **2017**, *139*, 17281–17284.

(373) Li, L.; He, J.; Wang, Y.; Lv, X.; Gu, X.; Dai, P.; Liu, D.; Zhao, X. Metal–organic frameworks: a promising platform for constructing non-noble electrocatalysts for the oxygen-reduction reaction. *J. Mater. Chem. A* **2019**, *7*, 1964–1988.

(374) Weekes, D. M.; Salvatore, D. A.; Reyes, A.; Huang, A.; Berlinguette, C. P. Electrolytic CO_2 Reduction in a Flow Cell. *Acc. Chem. Res.* **2018**, *51*, 910–918.

(375) Porosoff, M. D.; Yan, B.; Chen, J. G. Catalytic reduction of CO_2 by H_2 for synthesis of CO, methanol and hydrocarbons: challenges and opportunities. *Energy Environ. Sci.* **2016**, *9*, 62–73.

(376) Wu, J.; Sharifi, T.; Gao, Y.; Zhang, T.; Ajayan, P. M. Emerging Carbon-Based Heterogeneous Catalysts for Electrochemical Reduction of Carbon Dioxide into Value-Added Chemicals. *Adv. Mater.* **2019**, *31*, 1–24.

(377) Zhang, H.; Li, J.; Tan, Q.; Lu, L.; Wang, Z.; Wu, G. Metal–Organic Frameworks and Their Derived Materials as Electrocatalysts and Photocatalysts for CO_2 Reduction: Progress, Challenges, and Perspectives. *Chem. Eur. J.* **2018**, *24*, 18137–18157.

(378) Hori, Y.; Wakebe, H.; Tsukamoto, T.; Koga, O. Electrocatalytic Process of CO Selectivity in Electrochemical Reduction of CO_2 At Metal Electrodes in Aqueous Media. *Electrochim. Acta* **1994**, *39*, 1833–1839.

(379) Kornienko, N.; Zhao, Y.; Kley, C. S.; Zhu, C.; Kim, D.; Lin, S.; Chang, C. J.; Yaghi, O. M.; Yang, P. Metal–Organic Frameworks for Electrocatalytic Reduction of Carbon Dioxide. *J. Am. Chem. Soc.* **2015**, *137*, 14129–14135.

(380) Hod, I.; Sampson, M. D.; Deria, P.; Kubiak, C. P.; Farha, O. K.; Hupp, J. T. Fe-Porphyrin-Based Metal–Organic Framework Films as High-Surface Concentration, Heterogeneous Catalysts for Electrochemical Reduction of CO_2. *ACS Catal.* **2015**, *5*, 6302–6309.

(381) Hinogami, R.; Yotsuhashi, S.; Deguchi, M.; Zenitani, Y.; Hashiba, H.; Yamada, Y. Electrochemical Reduction of Carbon Dioxide Using a Copper Rubeanate Metal Organic Framework. *ECS Electrochem. Lett.* **2012**, *1*, 17–19.

(382) Kumar, S.; Kumar, S.; Kulandainathan, A. Highly selective electrochemical reduction of carbon dioxide using Cu based metal organic framework as an electrocatalyst. *Electrochem. Commun.* **2012**, *25*, 70–73.

(383) Giesbrecht, P. K.; Herbert, D. E. Electrochemical Reduction of Carbon Dioxide to Methanol in the Presence of Benzannulated Dihydropyridine Additives. *ACS Energy Lett.* **2017**, *2*, 549–555.

(384) Cole, E. B.; Lakkaraju, P. S.; Rampulla, D. M.; Morris, A. J.; Abelev, E.; Bocarsly, A. B. Using a One-Electron Shuttle for the Multielectron Reduction of CO_2 to Methanol: Kinetic, Mechanistic, and Structural Insights. *J. Am*. *Chem*. *Soc*. **2010**, *132*, 11539–11551.

(385) Dridi, H.; Comminges, C.; Morais, C.; Meledje, J. C.; Kokoh, K. B.; Costentin, C.; Savéant, J. M. Catalysis and Inhibition in the Electrochemical Reduction of CO_2 on Platinum in the Presence of Protonated Pyridine. New Insights into Mechanisms and Products. *J. Am. Chem. Soc.* **2017**, *139*, 13922–13928.

(386) Seshadri, G.; Lin, C.; Bocarsly, A. B. A new homogeneous electrocatalyst for the reduction of carbon dioxide to methanol at low overpotential. *J. Electroanal. Chem.* **1994**, *372*, 145–150.

(387) Marjolin, A.; Keith, J. A. Thermodynamic Descriptors for Molecules That Catalyze Efficient CO_2

Electroreductions. *ACS Catal.* **2015**, *5*, 1123–1130.

(388) Ruhlmann, L.; Costa-Coquelard, C.; Hao, J.; Jiang, S.; He, C.; Sun, L.; Lampre, I. Association of ruthenium complexes $[Ru(bpy)_3]^{2+}$ or $[Ru(bpy)_2(Mebpy\text{-}py)]^{2+}$ with Dawson polyanions α-$[P_2W_{18}O_{62}]^{6-}$ or α_2-$[Fe^{III}(H_2O)P_2W_{17}O_{61}]^{7-}$. *Can. J. Chem.* **2008**, *86*, 1034–1043.

(389) Helton, M. E.; Chen, P.; Paul, P. P.; Tyeklár, Z.; Sommer, R. D.; Zakharov, L. N.; Rheingold, A. L.; Solomon, E. I.; Karlin, K. D. Reaction of Elemental Sulfur with a Copper(I) Complex Forming a *trans*-*μ*-1,2 End-on Disulfide Complex: New Directions in Copper–Sulfur Chemistry. *J. Am. Chem. Soc.* **2003**, *125*, 1160–1161.

(390) Rasmussen, T.; Berks, B. C.; Sanders-Loehr, J.; Dooley, D. M.; Zumft, W. G.; Thomson, A. J. The Catalytic Center in Nitrous Oxide Reductase, Cu_z, Is a Copper-Sulfide Cluster. *Biochemistry* **2000**, *39*, 12753–12756.

(391) Acheson, R. M.; Ansell, P. J. The Synthesis of Diethyl *p*-Tolylsulphonylethynylphosphonate and Related Acetylenes, and their Reactions with Nucleophiles, Pyridinium-1-dicyanomethylides, and Dienes. *J. Chem. Soc. Perk*. *T. 1* **1987**, *6*, 1275–1281.

(392) Wheeler, S. E.; McNeil, A. J.; Müller, P.; Swager, T. M.; Houk, K. N. Probing Substituent Effects in Aryl–Aryl Interactions Using Stereoselective Diels–Alder Cycloadditions. *J. Am. Chem. Soc.* **2010**, *132*, 3304–3311.